



IntechOpen

Electric Vehicles
Modelling and Simulations

Edited by Seref Soylu



ELECTRIC VEHICLES – MODELLING AND SIMULATIONS

Edited by **Seref Soylu**

Electric Vehicles - Modelling and Simulations

<http://dx.doi.org/10.5772/958>

Edited by Seref Soylu

Contributors

Driss Yousfi, Abdelhadi Elbacha, Abdellah Ait Ouahman, Gheorghe Livint, Vasile Horga, Marcel Ratoi, Mihai Albu, Jaber Karim, Fakhfakh Ahmed, Rafik Neji, Richard Anthony Guinee, Jia-Sheng Hu, Dejun Yin, Feng-Rung Hu, Christophe Versèle, Olivier Deblecker, Jacques Lobry, Lu Xiong, Zhuoping Yu, Monzer Al Sakka, Joeri Van Mierlo, Hamid Gualous, Mohamad Abdul-Hak, Nizar Al-Holou, Utayba Mohammad, Daniel Fodorean, Qianfan Zhang, Xiaofei Liu, Shumei Cui, Shuai Dong, Yifan Yu, Ben Hadj Naourez, Chaeib Mohamed, Kammoun Jalila Kaouthar, Mohamed Amine Fakhfakh, Ricardo de Castro, Rui Esteves Esteves Araújo, Diamantino Freitas, Hartani Kada, Yahia Miloud, Erik Schaltz, John Economou, Kevin Knowles

© The Editor(s) and the Author(s) 2011

The moral rights of the and the author(s) have been asserted.

All rights to the book as a whole are reserved by INTECH. The book as a whole (compilation) cannot be reproduced, distributed or used for commercial or non-commercial purposes without INTECH's written permission.

Enquiries concerning the use of the book should be directed to INTECH rights and permissions department (permissions@intechopen.com).

Violations are liable to prosecution under the governing Copyright Law.



Individual chapters of this publication are distributed under the terms of the Creative Commons Attribution 3.0 Unported License which permits commercial use, distribution and reproduction of the individual chapters, provided the original author(s) and source publication are appropriately acknowledged. If so indicated, certain images may not be included under the Creative Commons license. In such cases users will need to obtain permission from the license holder to reproduce the material. More details and guidelines concerning content reuse and adaptation can be found at <http://www.intechopen.com/copyright-policy.html>.

Notice

Statements and opinions expressed in the chapters are those of the individual contributors and not necessarily those of the editors or publisher. No responsibility is accepted for the accuracy of information contained in the published chapters. The publisher assumes no responsibility for any damage or injury to persons or property arising out of the use of any materials, instructions, methods or ideas contained in the book.

First published in Croatia, 2011 by INTECH d.o.o.

eBook (PDF) Published by IN TECH d.o.o.

Place and year of publication of eBook (PDF): Rijeka, 2019.

IntechOpen is the global imprint of IN TECH d.o.o.

Printed in Croatia

Legal deposit, Croatia: National and University Library in Zagreb

Additional hard and PDF copies can be obtained from orders@intechopen.com

Electric Vehicles - Modelling and Simulations

Edited by Seref Soylu

p. cm.

ISBN 978-953-307-477-1

eBook (PDF) ISBN 978-953-51-6046-5

We are IntechOpen, the world's leading publisher of Open Access books Built by scientists, for scientists

4,000+

Open access books available

116,000+

International authors and editors

120M+

Downloads

151

Countries delivered to

Our authors are among the
Top 1%

most cited scientists

12.2%

Contributors from top 500 universities



WEB OF SCIENCE™

Selection of our books indexed in the Book Citation Index
in Web of Science™ Core Collection (BKCI)

Interested in publishing with us?
Contact book.department@intechopen.com

Numbers displayed above are based on latest data collected.
For more information visit www.intechopen.com



Meet the editor

Dr. Seref Soylu received his Ph.D degree in Mechanical Engineering from Iowa State University in 2001. His Ph.D. research work mostly focused on internal combustion engines and thermodynamic engine modeling that were supported by John Deere Product Engineering Center. Through end of his Ph.D. study, he also worked for Caterpillar Inc. as an analytical engineer in their technical center in Peoria, IL for the development of the advanced diesel engines. After receiving his Ph.D. degree in 2001, Dr. Soylu joined to Sakarya University to perform research and teach thermal science courses. His research interests centered on the development of environmentally friendly road transport vehicles including hybrid electrical vehicles. Dr. Soylu also worked as a visiting scientist in the Joint Research Center of European Commission for a year from November 2004 to November 2005 to provide technical and scientific support to the policymakers of the Commission for their legislative works. His work in the Joint Research Center focused on fuels for internal combustion engines, exhaust emission measurement techniques for zero emission vehicles, portable emission measurement systems, and small engines. Dr. Soylu has also worked as independent expert for European Commission in the field of Energy and Transport to evaluate and review Framework Programme (6 & 7th) projects on behalf of the Commission. Dr. Soylu is currently an Associate Professor of Sakarya University. He is teaching undergraduate and graduate level thermal science courses and leading a research project entitled "Measurement and Modelling of Hybrid City Bus Real-World Emissions" funded by Turkish Ministry of Industry and Trade and TEM-SA R&D.

Contents

- Preface XI**
- Chapter 1 **Electrical Vehicle Design and Modeling 1**
Erik Schaltz
- Chapter 2 **Modeling and Simulation of High Performance Electrical Vehicle Powertrains in VHDL-AMS 25**
K. Jaber, A. Fakhfakh and R. Neji
- Chapter 3 **Control of Hybrid Electrical Vehicles 41**
Gheorghe Livinț, Vasile Horga,
Marcel Rățoi and Mihai Albu
- Chapter 4 **Vehicle Dynamic Control of 4 In-Wheel-Motor Drived Electric Vehicle 67**
Lu Xiong and Zhuoping Yu
- Chapter 5 **A Robust Traction Control for Electric Vehicles Without Chassis Velocity 107**
Jia-Sheng Hu, Dejun Yin and Feng-Rung Hu
- Chapter 6 **Vehicle Stability Enhancement Control for Electric Vehicle Using Behaviour Model Control 127**
Kada Hartani and Yahia Miloud
- Chapter 7 **FPGA Based Powertrain Control for Electric Vehicles 159**
Ricardo de Castro, Rui Esteves Araújo and
Diamantino Freitas
- Chapter 8 **Global Design and Optimization of a Permanent Magnet Synchronous Machine Used for Light Electric Vehicle 177**
Daniel Fodorean
- Chapter 9 **Efficient Sensorless PMSM Drive for Electric Vehicle Traction Systems 199**
Driss Yousfi, Abdelhadi Elbacha and Abdellah Ait Ouahman

- Chapter 10 **Hybrid Switched Reluctance Motor and Drives Applied on a Hybrid Electric Car 215**
Qianfan Zhang, Xiaofei Liu, Shumei Cui, Shuai Dong and Yifan Yu
- Chapter 11 **Mathematical Modelling and Simulation of a PWM Inverter Controlled Brushless Motor Drive System from Physical Principles for Electric Vehicle Propulsion Applications 233**
Richard A. Guinee
- Chapter 12 **Multiobjective Optimal Design of an Inverter Fed Axial Flux Permanent Magnet In-Wheel Motor for Electric Vehicles 287**
Christophe Versèle, Olivier Deblecker and Jacques Lobry
- Chapter 13 **DC/DC Converters for Electric Vehicles 309**
Monzer Al Sakka, Joeri Van Mierlo and Hamid Gualous
- Chapter 14 **A Comparative Thermal Study of Two Permanent Magnets Motors Structures with Interior and Exterior Rotor 333**
Naourez Ben Hadj, Jalila Kaouthar Kammoun, Mohamed Amine Fakhfakh, Mohamed Chaieb and Rafik Neji
- Chapter 15 **Minimization of the Copper Losses in Electrical Vehicle Using Doubly Fed Induction Motor Vector Controlled 347**
Saïd Drid
- Chapter 16 **Predictive Intelligent Battery Management System to Enhance the Performance of Electric Vehicle 365**
Mohamad Abdul-Hak, Nizar Al-Holou and Utayba Mohammad
- Chapter 17 **Design and Analysis of Multi-Node CAN Bus for Diesel Hybrid Electric Vehicle 385**
XiaoJian Mao, Jun hua Song, Junxi Wang, Hang bo Tang and Zhuo bin
- Chapter 18 **Sugeno Inference Perturbation Analysis for Electric Aerial Vehicles 397**
John T. Economou and Kevin Knowles
- Chapter 19 **Extended Simulation of an Embedded Brushless Motor Drive (BLMD) System for Adjustable Speed Control Inclusive of a Novel Impedance Angle Compensation Technique for Improved Torque Control in Electric Vehicle Propulsion Systems 417**
Richard A. Guinee

Preface

Electric vehicles are becoming promising alternatives to be remedy for urban air pollution, green house gases and depletion of the finite fossil fuel resources (the challenging triad) as they use centrally generated electricity as a power source. It is well known that power generation at centralized plants are much more efficient and their emissions can be controlled much easier than those emitted from internal combustion engines that scattered all over the world. Additionally, an electric vehicle can convert the vehicle's kinetic energy to electrical energy and store it during the braking and coasting.

All the benefits of electrical vehicles are starting to justify, a century later, attention of industry, academia and policy makers again as promising alternatives for urban transport. Nowadays, industry and academia are striving to overcome the challenging barriers that block widespread use of electric vehicles. Lifetime, energy density, power density, weight and cost of battery packs are major barriers to overcome. However, modeling and optimization of other components of electric vehicles are also as important as they have strong impacts on the efficiency, drivability and safety of the vehicles. In this sense there is growing demand for knowledge to model and optimize the electrical vehicles.

In this book, modeling and simulation of electric vehicles and their components have been emphasized chapter by chapter with valuable contribution of many researchers who work on both technical and regulatory sides of the field. Mathematical models for electrical vehicles and their components were introduced and merged together to make this book a guide for industry, academia and policy makers.

To be effective chapters of the book were designed in a logical order. It started with the examination of dynamic models and simulation results for electrical vehicles and traction systems. Then, models for alternative electric motors and drive systems were presented. After that, models for power electronic components and various control systems were examined. Finally, to establish the required knowledge as a whole, an intelligent energy management system was introduced.

As the editor of this book, I would like to express my gratitude to the chapter authors for submitting such valuable works that were already published or presented in prestigious journals and conferences. I hope you will get maximum benefit from this book to take the urban transport system to a sustainable level.

Seref Soylu, PhD

Sakarya University, Department of Environmental Engineering, Sakarya,
Turkey

Electrical Vehicle Design and Modeling

Erik Schaltz
Aalborg University
Denmark

1. Introduction

Electric vehicles are by many seen as the cars of the future as they are high efficient, produces no local pollution, are silent, and can be used for power regulation by the grid operator. However, electric vehicles still have critical issues which need to be solved. The three main challenges are limited driving range, long charging time, and high cost. The three main challenges are all related to the battery package of the car. The battery package should both contain enough energy in order to have a certain driving range and it should also have a sufficient power capability for the accelerations and decelerations. In order to be able to estimate the energy consumption of an electric vehicles it is very important to have a proper model of the vehicle (Gao et al., 2007; Mapelli et al., 2010; Schaltz, 2010). The model of an electric vehicle is very complex as it contains many different components, e.g., transmission, electric machine, power electronics, and battery. Each component needs to be modeled properly in order prevent wrong conclusions. The design or rating of each component is a difficult task as the parameters of one component affect the power level of another one. There is therefore a risk that one component is rated inappropriate which might make the vehicle unnecessary expensive or inefficient. In this chapter a method for designing the power system of an electric vehicle is presented. The method insures that the requirements due to driving distance and acceleration is fulfilled.

The focus in this chapter will be on the modeling and design of the power system of a battery electric vehicle. Less attention will therefore be put on the selection of each component (electric machines, power electronics, batteries, etc.) of the power system as this is a very big task in it self. This chapter will therefore concentrate on the methodology of the modeling and design process. However, the method presented here is also suitable for other architectures and choice of components.

The chapter is organized as follows: After the introduction Section 2 describes the modeling of the electric vehicle, Section 3 presents the proposed design method, Section 4 provides a case study in order to demonstrate the proposed method, and Section 5 gives the conclusion remarks.

2. Vehicle modeling

2.1 Architecture

Many different architectures of an electric vehicle exist (Chan et al., 2010) as there are many possibilities, e.g., 1 to 4 electric machines, DC or AC machines, gearbox/no gearbox, high or

low battery voltage, one or three phase charging, etc. However, in this chapter the architecture in Fig. 1 is chosen.

The purpose of the different components in Fig. 1 will here shortly be explained: The traction power of the wheels is delivered by the three phase electric machine. The torque of the left and right wheels are provided by a differential with also has a gear ratio in order to fit the high speed of the electric machine shaft to the lower speed of the wheels. The torque and speed of the machine are controlled by the inverter which inverts the battery DC voltage to a three phase AC voltage suitable for the electric machine. When analyzing the energy consumption of an electric vehicle it is important also to include the losses due to the components which not are a part of the power chain from the grid to the wheels. These losses are denoted as auxiliary loss and includes the lighting system, comfort system, safety systems, etc. During the regenerative braking it is important that the maximum voltage of the battery is not exceeded. For this reason a braking resistor is introduced. The rectifier rectifies the three phase voltages and currents of the grid to DC levels and the boost converter makes it possible to transfer power from the low voltage side of the rectifier to the high voltage side of the battery.

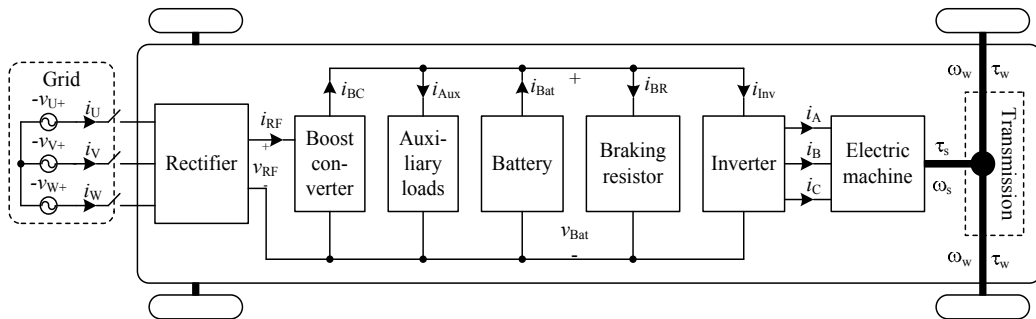


Fig. 1. Architecture of the battery electric vehicle. In the figure the main components of the vehicles which have an influence on the energy consumption of the vehicle is shown.

2.2 Force Model

The forces which the electric machine of the vehicle must overcome are the forces due to gravity, wind, rolling resistance, and inertial effect. These forces can also be seen in Fig. 2 where the forces acting on the vehicle are shown.

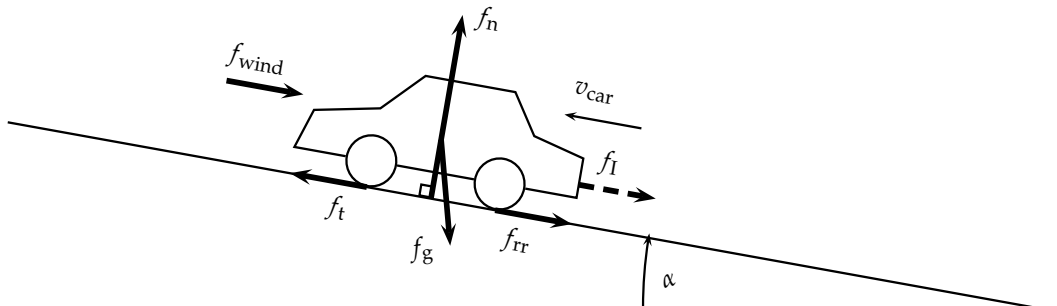


Fig. 2. Free body diagram of the forces (thick arrows) acting on the car.

The traction force of a vehicle can be described by the following two equations (Ehsani et al., 2005):

$$f_t = \underbrace{M_{\text{car}} \dot{v}_{\text{car}}}_{f_I} + \underbrace{M_{\text{car}} \cdot g \cdot \sin(\alpha)}_{f_g} + \text{sign}(v_{\text{car}}) \underbrace{M_{\text{car}} \cdot g \cdot \cos(\alpha)}_{f_n} \cdot c_{\text{rr}} + \underbrace{\text{sign}(v_{\text{car}} + v_{\text{wind}}) \frac{1}{2} \rho_{\text{air}} C_{\text{drag}} A_{\text{front}} (v_{\text{car}} + v_{\text{wind}})^2}_{f_{\text{wind}}} \quad (1)$$

$$c_{\text{rr}} = 0.01 \left(1 + \frac{3.6}{100} v_{\text{car}} \right), \quad (2)$$

where f_t	[N]	Traction force of the vehicle
f_I	[N]	Inertial force of the vehicle
f_{rr}	[N]	Rolling resistance force of the wheels
f_g	[N]	Gravitational force of the vehicle
f_n	[N]	Normal force of the vehicle
f_{wind}	[N]	Force due to wind resistance
α	[rad]	Angle of the driving surface
M_{car}	[kg]	Mass of the vehicle
v_{car}	[m/s]	Velocity of the vehicle
\dot{v}_{car}	[m/s ²]	Acceleration of the vehicle
$g = 9.81$	[m/s ²]	Free fall acceleration
$\rho_{\text{air}} = 1.2041$	[kg/m ³]	Air density of dry air at 20 °C
c_{rr}	[-]	Tire rolling resistance coefficient
C_{drag}	[-]	Aerodynamic drag coefficient
A_{front}	[m ²]	Front area
v_{wind}	[m/s]	Headwind speed

2.3 Auxiliary loads

The main purpose of the battery is to provide power for the wheels. However, a modern car have also other loads which the battery should supply. These loads are either due to safety, e.g., light, wipers, horn, etc. and/or comfort, e.g., radio, heating, air conditioning, etc. These loads are not constant, e.g., the power consumption of the climate system strongly depend on the surrounding temperature. Even though some average values are suggested which can be seen in Table 1. From the table it may be understood that the total average power consumption is $p_{\text{Aux}} = 857 \text{ W}$.

Radio	52 W
Heating Ventilation Air Condition (HVAC)	489 W
Lights	316 W
Total p_{Aux}	857 W

Table 1. Average power level of the auxiliary loads of the vehicle. The values are inspired from (Ehsani et al., 2005; Emadi, 2005; Lukic & Emadi, 2002).

2.4 Transmission

From Fig. 1 it can be understood that the torque, angular velocity, and power of the transmission system are given by the following equations:

$$\tau_t = f_t r_w \quad (3)$$

$$\tau_w = \frac{\tau_t}{2} \quad (4)$$

$$\omega_w = \frac{v_{car}}{r_w} \quad (5)$$

$$p_t = f_t v_{car}, \quad (6)$$

where τ_t [Nm] Traction torque
 τ_w [Nm] Torque of each driving wheel
 r_w [m] Wheel radius
 ω_w [rad/s] Angular velocity of the wheels
 p_t [W] Traction power

It is assumed that the power from the shaft of the electric machine to the two driving wheels has a constant efficiency of $\eta_{TS} = 0.95$ (Ehsani et al., 2005). The shaft torque, angular velocity, and power of the electric machine are therefore

$$\tau_s = \begin{cases} \eta_{TS} \frac{\tau_t}{G}, & p_t < 0 \\ \frac{\tau_t}{\eta_{TS} G}, & p_t \geq 0 \end{cases} \quad (7)$$

$$\omega_s = G \omega_w \quad (8)$$

$$p_s = \tau_s \omega_s, \quad (9)$$

where τ_s [Nm] Shaft torque of electric machine
 ω_s [rad/s] Shaft angular velocity of electric machine
 p_s [W] Shaft power of electric machine
 G [-] Gear ratio of differential

2.5 Electric machine

For propulsion usually the induction machine (IM), permanent magnet synchronous machine (PMSM), and switched reluctance machine (SRM) are considered. The "best" choice is like many other components a trade off between, cost, mass, volume, efficiency, reliability, maintenance, etc. However, due to its high power density and high efficiency the PMSM is selected. The electric machine is divided into an electric part and mechanic part. The electric part of the PMSM is modeled in the DQ-frame, i.e.,

$$v_d = R_s i_d + L_d \frac{di_d}{dt} - \omega_e L_q i_q \quad (10)$$

$$v_q = R_s i_q + L_q \frac{di_q}{dt} + \omega_e L_d i_d + \omega_e \lambda_{pm} \quad (11)$$

$$p_{EM} = \frac{3}{2} (v_d i_d + v_q i_q), \quad (12)$$

where v_d	[V]	D-axis voltage
v_q	[V]	Q-axis voltage
i_d	[A]	D-axis current
i_q	[A]	Q-axis current
R_s	[Ω]	Stator phase resistance
L_d	[H]	D-axis inductance
L_q	[H]	Q-axis inductance
λ_{pm}	[Wb]	Permanent magnet flux linkage
ω_e	[rad/s]	Angular frequency of the stator
λ_{pm}	[Wb]	Permanent magnet flux linkage
p_{EM}	[W]	Electric input power

The mechanical part of the PMSM can be modeled as follows:

$$\tau_e = J_s \frac{d\omega_s}{dt} + B_v \omega_s + \tau_c + \tau_s \quad (13)$$

$$p_s = \tau_s \omega_s, \quad (14)$$

where J_s	[kgm ²]	Shaft moment of inertia
τ_e	[Nm]	Electromechanical torque
τ_c	[Nm]	Coulomb torque
B_v	[Nms/rad]	Viscous friction coefficient

The coupling between the electric and mechanic part is given by

$$\tau_e = \frac{3P}{2} (\lambda_{pm} i_q + (L_d - L_q) i_d i_q) \quad (15)$$

$$\omega_e = \frac{P}{2} \omega_s, \quad (16)$$

where P [-] Number of poles

2.6 Inverter

A circuit diagram of the inverter can be seen in Fig. 3. The inverter transmits power between the electric machine (with phase voltages v_A , v_B , and v_C) and the battery by turning on and off the switches Q_{A+} , Q_{A-} , Q_{B+} , Q_{B-} , Q_{C+} , and Q_{C-} . The switches has an on-resistance $R_{Q,Inv}$. The diodes in parallel of each switch are creating a path for the motor currents during the deadtime, i.e., the time where both switches in one branch are non-conducting in order to avoid a shoot-through.

The average power losses of one switch $p_{Q,Inv}$ and diode $p_{D,Inv}$ in Fig. 3 during one fundamental period are (Casanellas, 1994):

$$p_{Q,Inv} = \left(\frac{1}{8} + \frac{m_i}{3\pi} \right) R_{Q,Inv} \hat{I}_P^2 + \left(\frac{1}{2\pi} + \frac{m_i}{8} \cos(\phi_{EM}) \right) V_{Q,th,Inv} \hat{I}_P \quad (17)$$

$$p_{D,Inv} = \left(\frac{1}{8} - \frac{m_i}{3\pi} \right) R_{D,Inv} \hat{I}_P^2 + \left(\frac{1}{2\pi} - \frac{m_i}{8} \cos(\phi_{EM}) \right) V_{D,th,Inv} \hat{I}_P \quad (18)$$

$$m_i = \frac{2\hat{V}_P}{V_{Bat}}, \quad (19)$$

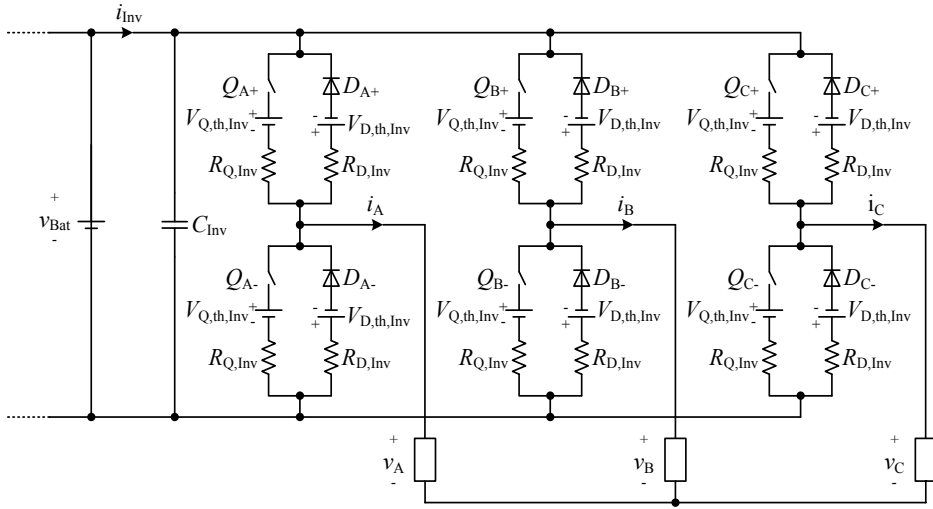


Fig. 3. Circuit diagram of inverter.

where $p_{Q,Inv}$	[W]	Power loss of one switch
$p_{D,Inv}$	[W]	Power loss of one diode
ϕ_{EM}	[rad]	Power factor angle
\hat{I}_p	[A]	Peak phase current
\hat{V}_p	[V]	Peak phase voltage
m_i	[-]	Modulation index
V_{Bat}	[V]	Battery voltage
$R_{Q,Inv}$	[Ω]	Inverter switch resistance
$R_{D,Inv}$	[Ω]	Inverter diode resistance
$V_{Q,th,Inv}$	[V]	Inverter switch threshold voltage
$V_{D,th,Inv}$	[V]	Inverter diode threshold voltage

If it is assumed that the threshold voltage drop of the switches and diodes are equal, i.e., $V_{th,Inv} = V_{Q,th,Inv} = V_{D,th,Inv}$, and that the resistances of the switches and diodes also are equal, i.e., $R_{Inv} = R_{Q,Inv} = R_{D,Inv}$, the total power loss of the inverter is given by

$$P_{Inv,loss} = 6 (P_{Q,Inv} + P_{D,Inv}) = \frac{3}{2} R_{Inv} \hat{I}_p^2 + \frac{6}{\pi} V_{th,Inv} \hat{I}_p. \quad (20)$$

The output power of the inverter is the motor input power p_{EM} . The inverter input power and efficiency are therefore

$$p_{Inv} = v_{Bat} i_{Inv} = p_{EM} + p_{Inv,loss} \quad (21)$$

$$\eta_{Inv} = \begin{cases} \frac{p_{EM}}{p_{Inv}}, & p_{EM} \geq 0 \\ \frac{p_{Inv}}{p_{EM}}, & p_{EM} < 0, \end{cases} \quad (22)$$

where i_{Inv}	[A]	Inverter input current
p_{Inv}	[W]	Inverter input power
η_{Inv}	[-]	Inverter efficiency

2.7 Battery

The battery pack is the heart of an electric vehicle. Many different battery types exist, e.g., lead-acid, nickel-metal hydride, lithium ion, etc. However, today the lithium ion is the preferred choice due to its relatively high specific energy and power. In this chapter the battery model will be based on a Saft VL 37570 lithium ion cell. It's specifications can be seen in Table 2.

Maximum voltage	$V_{\text{Bat,max,cell}}$	4.2 V
Nominal voltage	$V_{\text{Bat,nom,cell}}$	3.7 V
Minimum voltage	$V_{\text{Bat,min,cell}}$	2.5 V
1 h capacity	$Q_{1,\text{cell}}$	7 Ah
Nominal 1 h discharge current	$I_{\text{Bat,1,cell}}$	7 A
Maximum pulse discharge current	$I_{\text{Bat,max,cell}}$	28 A

Table 2. Data sheet specifications of Saft VL 37570 LiIon battery (Saft, 2010).

2.7.1 Electric model

The battery will only be modeled in steady-state, i.e., the dynamic behavior is not considered. The electric equivalent circuit diagram can be seen in Fig.4. The battery model consist of an internal voltage source and two inner resistances used for charging and discharging. The two diodes are ideal and have only symbolics meaning, i.e., to be able to shift between the charging and discharging resistances. Discharging currents are treated as positive currents, i.e., charging currents are then negative.

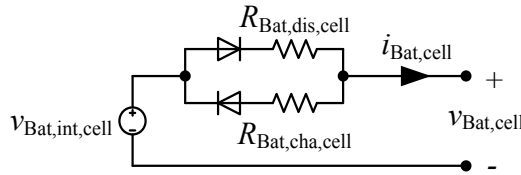


Fig. 4. Electric equivalent circuit diagram of a battery cell.

From Fig. 4 the cell voltage is therefore given by

$$v_{\text{Bat,cell}} = \begin{cases} v_{\text{Bat,int,cell}} - R_{\text{Bat,cell,dis}} i_{\text{Bat,cell}} & , i_{\text{Bat,cell}} \geq 0 \\ v_{\text{Bat,int,cell}} - R_{\text{Bat,cell,cha}} i_{\text{Bat,cell}} & , i_{\text{Bat,cell}} < 0, \end{cases} \quad (23)$$

where $v_{\text{Bat,cell}}$ [V] Battery cell voltage
 $v_{\text{Bat,int,cell}}$ [V] Internal battery cell voltage
 $i_{\text{Bat,cell}}$ [A] Battery cell current
 $R_{\text{Bat,cell,dis}}$ [Ω] Inner battery cell resistance during discharge mode
 $R_{\text{Bat,cell,cha}}$ [Ω] Inner battery cell resistance during charge mode

The inner voltage source and the two resistances in Fig. 4 depend on the depth-of-discharge of the battery. The battery cell have been modeled by the curves given in the data sheet of the battery. It turns out that the voltage source and the resistances can be described as 10th order polynomials, i.e.,

$$R_{\text{Bat,cell,dis}} = a_{10} D_o D_{\text{Bat}}^{10} + a_9 D_o D_{\text{Bat}}^9 + a_8 D_o D_{\text{Bat}}^8 + a_7 D_o D_{\text{Bat}}^7 + a_6 D_o D_{\text{Bat}}^6 + a_5 D_o D_{\text{Bat}}^5 + a_4 D_o D_{\text{Bat}}^4 + a_3 D_o D_{\text{Bat}}^3 + a_2 D_o D_{\text{Bat}}^2 + a_1 D_o D_{\text{Bat}} + a_0 \quad (24)$$

$$v_{\text{Bat,int,cell}} = b_{10}DoD_{\text{Bat}}^{10} + b_9DoD_{\text{Bat}}^9 + b_8DoD_{\text{Bat}}^8 + b_7DoD_{\text{Bat}}^7 + b_6DoD_{\text{Bat}}^6 + b_5DoD_{\text{Bat}}^5 + b_4DoD_{\text{Bat}}^4 + b_3DoD_{\text{Bat}}^3 + b_2DoD_{\text{Bat}}^2 + b_1DoD_{\text{Bat}} + b_0 \quad (25)$$

$$R_{\text{Bat,cell,cha}} = c_{10}DoD_{\text{Bat}}^{10} + c_9DoD_{\text{Bat}}^9 + c_8DoD_{\text{Bat}}^8 + c_7DoD_{\text{Bat}}^7 + c_6DoD_{\text{Bat}}^6 + c_5DoD_{\text{Bat}}^5 + c_4DoD_{\text{Bat}}^4 + c_3DoD_{\text{Bat}}^3 + c_2DoD_{\text{Bat}}^2 + c_1DoD_{\text{Bat}} + c_0 \quad (26)$$

where $a_{10} = -634.0$, $a_9 = 2942.1$, $a_8 = -5790.6$, $a_7 = 6297.4$, $a_6 = -4132.1$, $a_5 = 1677.7$
 $a_4 = -416.4$, $a_3 = 60.5$, $a_2 = -4.8$, $a_1 = 0.2$, $a_0 = 0.0$
 $b_{10} = -8848$, $b_9 = 40727$, $b_8 = -79586$, $b_7 = 86018$, $b_6 = -56135$, $b_5 = -5565$
 $b_4 = 784$, $b_3 = -25$, $b_2 = 55$, $b_1 = 0$, $b_0 = 4$
 $c_{10} = 2056$, $c_9 = -9176$, $c_8 = 17147$, $c_7 = -17330$, $c_6 = 10168$, $c_5 = -3415$
 $c_4 = 578$, $c_3 = 25$, $c_2 = 3$, $c_1 = 0$, $c_0 = 0$

2.7.2 Capacity model

The inner voltage source, charging resistance, and discharge resistance all depend on the depth-of-discharge. The state-of-charge and depth-of-discharge depend on the integral of the current drawn or delivered to the battery, i.e.,

$$DoD_{\text{Bat}} = DoD_{\text{Bat,ini}} + \int \frac{i_{\text{Bat,eq,cell}}}{Q_{\text{Bat,1,cell}}} dt \quad (27)$$

$$SoC_{\text{Bat}} = 1 - DoD_{\text{Bat}} \quad (28)$$

where DoD_{Bat} [-] Depth-of-discharge
 $DoD_{\text{Bat,ini}}$ [-] Initial depth-of-discharge
 SoC_{Bat} [-] Battery state-of-charge
 $i_{\text{Bat,eq,cell}}$ [A] Equivalent battery cell current

The equivalent battery cell current depend on the sign and amplitude of the current (Schaltz, 2010). Therefore

$$i_{\text{Bat,eq,cell}} = \begin{cases} I_{\text{Bat,1,cell}} \left(\frac{i_{\text{Bat,cell}}}{I_{\text{Bat,1,cell}}} \right)^k, & i_{\text{Bat,cell}} \geq 0 \\ \eta_{\text{Bat,cha}} i_{\text{Bat,cell}}, & i_{\text{Bat,cell}} < 0 \end{cases} \quad (29)$$

$$k = \begin{cases} 1, & i_{\text{Bat,cell}} \leq I_{\text{Bat,1,cell}} \\ 1.125, & i_{\text{Bat,cell}} > I_{\text{Bat,1,cell}} \end{cases} \quad (30)$$

where k [-] Peukert number
 $\eta_{\text{Bat,cha}} = 0.95$ [-] Charging efficiency

It is seen that the peukert number has two different values depending on the amplitude of the discharge current. For currents higher than the nominal 1 hour discharge current $I_{\text{Bat,1,cell}}$ the capacity is therefore reduced significant.

2.7.3 Simulation results

In order to verify the methods used to calculate the state-of-charge, internal voltage source, and charging resistance calculations are compared to the data sheet values. The results can be seen in Fig. 5 where the battery cell voltage is shown for different C-values (1 C is the nominal discharge current of $I_{\text{Bat,1,cell}} = 7 \text{ A}$, which means that C/2 is equal to 3.5 A). It is seen that the calculated voltages almost are identical to the data sheet values. It is also noticed that the voltage is strongly depending on the current level and the delivered Ah, and that the voltage drops significant when the battery is almost completely discharged.

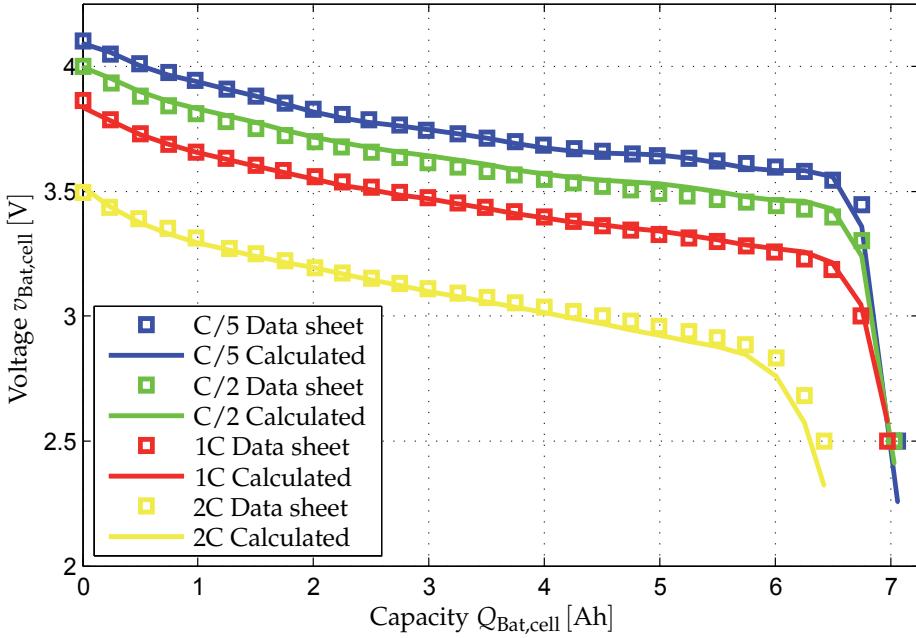


Fig. 5. Data sheet values (Saft, 2010) and calculations of the battery voltage during constant discharge currents.

2.8 Boost converter

The circuit diagram of the boost converter can be seen in Fig. 6. The losses of the boost

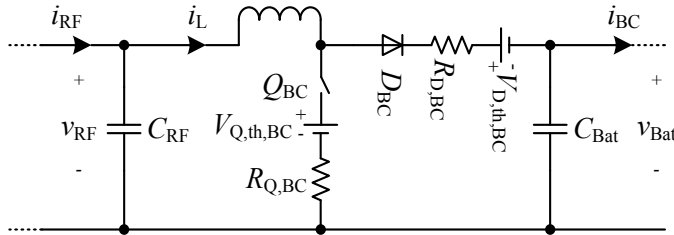


Fig. 6. Electric circuit diagram of the boost converter.

converter are due to the switch resistance $R_{Q,BC}$ and threshold voltage $V_{Q,th,BC}$ and the diodes resistance $R_{D,BC}$ and threshold voltage $V_{D,th,BC}$. In order to simplify it is assumed that the resistances and threshold voltages of the switch Q_{BC} and diode D_{BC} are equal, i.e., $R_{BC} = R_{Q,BC} = R_{D,RF}$ and $V_{th,BC} = V_{Q,th,BC} = V_{D,th,BC}$. The power equations of the boost converter are therefore given by

$$P_{RF} = V_{RF}i_{RF} = P_{BC} + P_{Loss,BC} \quad (31)$$

$$P_{BC} = V_{Bat}i_{BC} \quad (32)$$

$$P_{Loss,BC} = R_{BC}i_{RF}^2 + V_{th,BC}i_{RF} \quad (33)$$

where P_{RF}	[W]	Input power of boost converter
P_{BC}	[W]	Output power of boost converter
$P_{Loss,BC}$	[W]	Power loss of boost converter
V_{RF}	[V]	Input voltage of boost converter
$V_{th,BC}$	[V]	Threshold voltage of switch and diode
R_{BC}	[Ω]	Resistance of switch and diode
i_{RF}	[A]	Input current of boost converter
i_{BC}	[A]	Output current of boost converter

2.9 Rectifier

In order to utilize the three phase voltages of the grid v_U , v_V , and v_W they are rectified by a rectifier as seen in Fig. 7. In the rectifier the loss is due to the resistance $R_{D,RF}$ and threshold voltage $V_{D,th,RF}$.

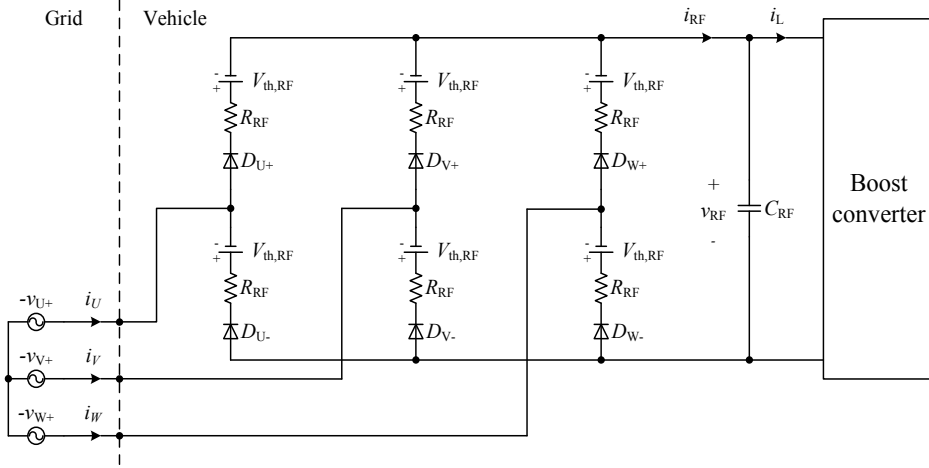


Fig. 7. Electric circuit diagram of the rectifier.

The average rectified current, voltage, and power are given by (Mohan et al., 2003)

$$i_{RF} = I_{Grid} \sqrt{\frac{3}{2}} \quad (34)$$

$$V_{RF} = \frac{3\sqrt{2}}{\pi} V_{LL} - 2R_{RF}i_{RF} - 2V_{th,RF} \quad (35)$$

$$P_{RF} = V_{RF}i_{RF} = P_{Grid} - P_{RF,loss} \quad (36)$$

$$P_{Grid} = \frac{3\sqrt{2}}{\pi} V_{LL} I_{RF} \quad (37)$$

$$P_{RF,loss} = 2R_{RF}i_{RF}^2 + 2V_{th,RF}i_{RF} \quad (38)$$

where I_{Grid}	[A]	Grid RMS-current
P_{Grid}	[W]	Power of three phase grid
$P_{loss,RF}$	[W]	Total loss of the rectifier
R_{RF}	[Ω]	Resistance of switch and diode
$V_{th,RF}$	[V]	Threshold voltage of switch and diode

2.10 Simulation model

The models of each component of the power system in the electric vehicle have now been explained. When combining all the sub models a model of the battery electric vehicle is obtained. In Fig. 8 the implementation in a Matlab/Simulink environment can be seen. The overall vehicle model includes the model of the forces acting on the vehicle (wind, gravity, rolling resistance, etc.), and the individual components of the power train, i.e., transmission, electric machine, inverter, battery, boost converter, rectifier. The wind speed v_{wind} and road angle α have been set to zero for simplicity. The input to the simulation model is a driving cycle (will be explained in Section 4) and the output of the model is all the currents, voltages, powers, torques, etc, inside the vehicle.

3. Design method

3.1 Parameter determination

The parameter determination of the components in the vehicle is an iterative process. The parameters are calculated by using the models given in Section 2 and the outputs of the Matlab/Simulink model shown in Fig. 8.

3.1.1 Battery

The maximum rectified voltage can be calculated from Equation 35 in no-load mode, i.e.,

$$V_{RF,max} = \frac{3\sqrt{2}}{\pi} V_{LL} = \frac{3\sqrt{2}}{\pi} 400 \text{ V} = 540 \text{ V}. \quad (39)$$

In order to insure boost operation during charging the rectified voltage of the rectifier should always be greater than this value. The required number of series connected cells is therefore

$$N_{Bat,s} = \frac{V_{RF,max}}{V_{Bat,cell,min}} = \frac{540 \text{ V}}{2.5 \text{ V}} \approx 216 \text{ cells}. \quad (40)$$

The number of series connected cells $N_{Bat,s}$ is due to the voltage requirement of the battery pack. However, in order to insure that the battery pack contains sufficient power and energy it is probably not enough with only one string of series connected cells. The battery pack will therefore consist of $N_{Bat,s}$ series connected cells and $N_{Bat,p}$ parallel strings. The number of parallel strings $N_{Bat,p}$ are calculated in an iterative process. The flow chart of the sizing procedure of the battery electric vehicle can be seen in Fig. 9. In the "Initialization"-process the base parameters are defined, e.g., wheel radius and nominal bus voltage, initial power ratings of each component of the vehicle are given, and the base driving cycle is loaded into the workspace of Matlab. In the "Is the minimum number of parallel strings obtained?"-decision block it is verified if the minimum number of parallel strings that fulfills both the energy and power requirements of the battery have been reached. If not a "Simulation routine"-process is executed. This process are executed several times during the sizing procedure and its flow chart is therefore shown separately in Fig. 9. This process consist of three sub-processes. The first sub-process is "Design components". In this process the parameters of each component of the battery electric vehicle are determined, e.g., motor and power electronic parameters. The next sub-process is the "Vehicle simulation"-process. In this process the Simulink-model of the vehicle is executed due to the parameters specified in the previous sub-process. In the third and last sub-process, i.e., the "Calculate the power and energy of each component"-process, the energy and power of each component of the vehicle are calculated.

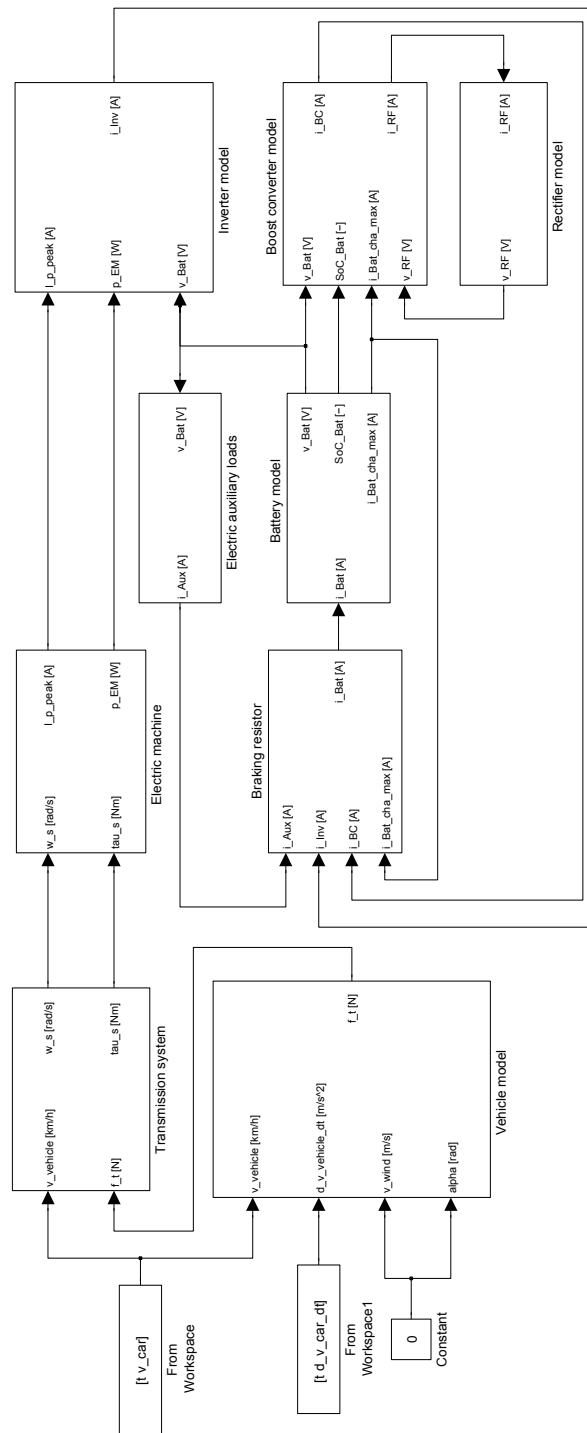


Fig. 8. Matlab/Simulink implementation of the battery electric vehicle.

The three sub-processes in the “Simulation routine”-process are executed three times in order to make sure that parameters converges to the same values for the same input. After the “Simulation routine”-process is finish the “Calculate number of parallel strings”-process is applied. In this process the number of parallel strings $N_{Bat,p}$ is either increased or decreased. When the minimum possible number of parallel strings that fulfills both the energy and power requirements of the battery has been found the “Simulation routine”-process is executed in order to calculate the grid energy due to the final number of parallel strings.

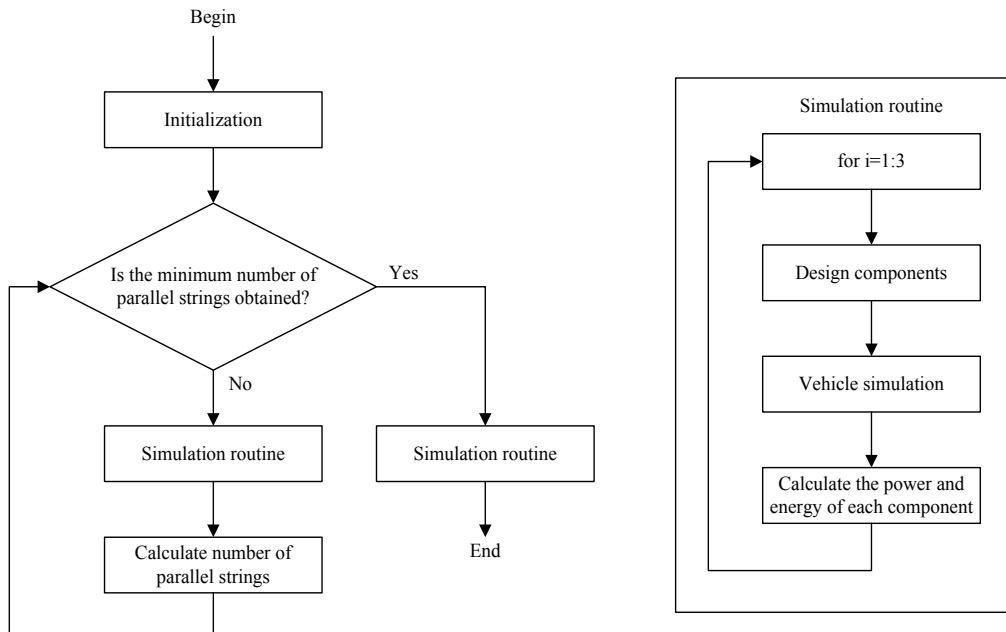


Fig. 9. Sizing procedure of the battery electric vehicle.

In principle all the energy of a battery could be used for the traction. However, in order to prolong the lifetime of the battery it is usually recommended not to charge it to more than 90% of its rated capacity and not to discharge it below $SoC_{Bat,min} = 20\%$, i.e., only 70% of the available energy is therefore utilized. In Fig. 10 it can be seen how the “Calculate number of parallel strings”-process finds the minimum number of parallel strings $N_{Bat,p}$ that fulfills both the energy and power requirements. This process is a part of the sizing procedure shown in Fig. 9. In Fig. 10(a) the minimum state-of-charge $\min(SoC_{Bat})$ is shown and in Fig. 10(b) the maximum battery cell discharge current $\max(i_{Bat,cell})$ is shown. From the figure it is understood that the first iteration is for $N_{Bat,p} = 10$. However, both the minimum state-of-charge and maximum discharge current are satisfying their limits, i.e., $SoC_{Bat,min} = 0.2$ and $I_{Bat,max,cell} = 28$ A, respectively. Therefore the number of parallel strings is reduced to $N_{Bat,p} = 3$ for iteration number two. However, now the state-of-charge limit is exceeded and therefore the number of parallel strings is increased to $N_{Bat,p} = 8$ for iteration three. This process continuous until iteration number six where the number of parallel strings settles to $N_{Bat,p} = 6$, as this is the minimum number of parallel strings which ensures that both the state-of-charge and maximum current requirements are fulfilled.

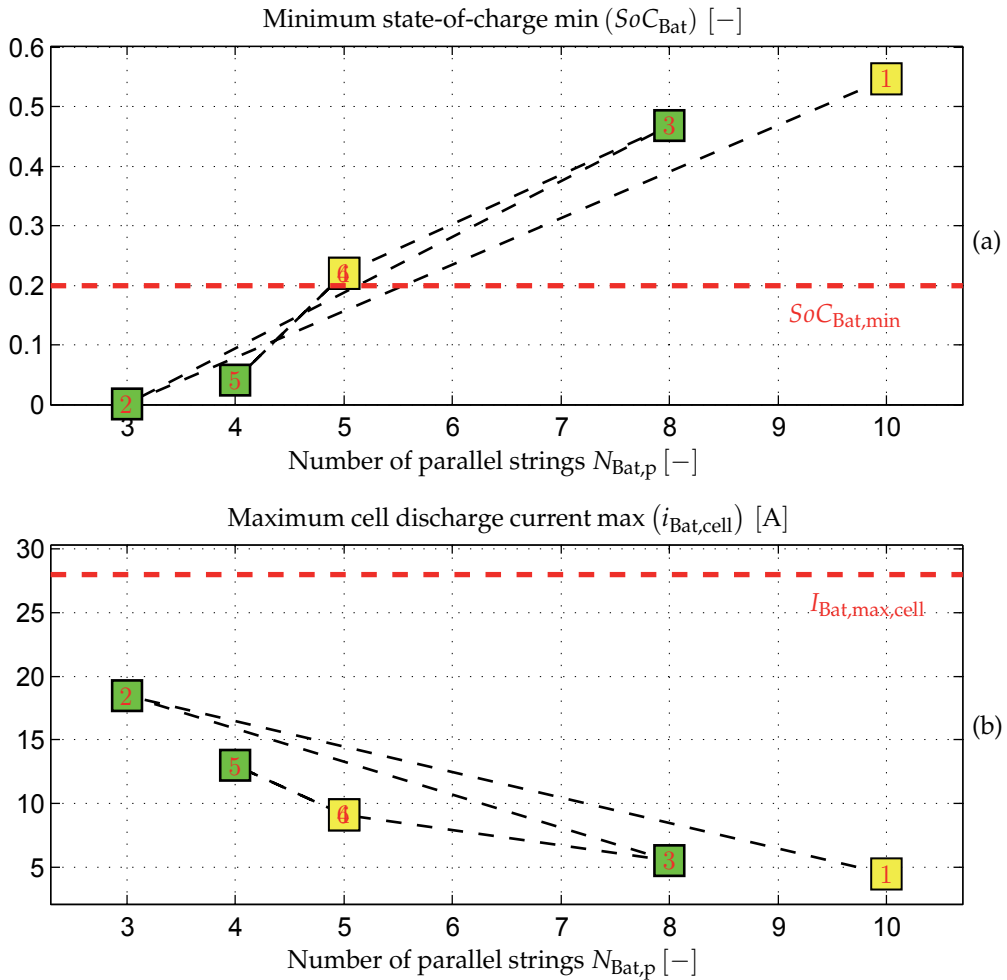


Fig. 10. Number of parallel strings $N_{\text{Bat},p}$ due to the “Calculate number of parallel strings”-process in Fig. 9. The numbers in the green and yellow boxes indicate the iteration number of the design procedure. The yellow boxes are the first and last iteration number. (a) Minimum state-of-charge $SoC_{\text{Bat},\text{min}}$. The red dashed horizontal lines indicates the minimum allowed state-of-charge. (b) Maximum cell discharge current $\max(i_{\text{Bat},\text{cell}})$. The dashed red horizontal line indicates the maximum allowed discharge current.

3.1.2 Electric machine

In order to design the machine design constraints from UQM Technologies (UQM, 2010) are applied. The machine from UQM Technologies is a brushless permanent magnet synchronous machine with the specifications in Table 3.

The phase angle between the voltage and current is not specified, but is assumed to be $\phi_{\text{EM,nom}} = 0.55$ rad, which corresponds to a power factor of $\cos(\phi_{\text{EM,nom}}) = 0.85$. The shaft angular velocity at (maximum power, maximum torque), (maximum power, continuous

Continuous shaft power		45 kW
Peak shaft power	$P_{s,max,UQM}$	75 kW
Maximum speed	$n_{s,max}$	8000 rpm
Shaft speed at peak torque and power	$n_{s,corner}$	3000 rpm
Number of poles (Jensen et al., 2009)	P	18
Continuous shaft torque	$\tau_{s,cont,UQM}$	150 Nm
Peak shaft torque	$\tau_{s,max,UQM}$	240 Nm
Efficiency at maximum shaft power and continuous torque	$\eta_{EM,a}$	94 %
Efficiency at maximum shaft power and maximum speed	$\eta_{EM,b}$	90 %

Table 3. Specifications of UQM PowerPhase 75 (UQM, 2010) from UQM Technologies.

torque), and maximum speed are therefore

$$\omega_{s,corner} = \frac{n_{s,corner}}{60 \text{ s/min}} 2\pi = 314.2 \text{ rad/s} \quad (41)$$

$$\omega_{s,nom} = \frac{P_{s,max,UQM}}{\tau_{s,cont,UQM}} = 500 \text{ rad/s} \quad (42)$$

$$\omega_{s,max} = \frac{n_{s,max}}{60 \text{ s/min}} 2\pi = 837.8 \text{ rad/s.} \quad (43)$$

The relationship between the maximum and continuous shaft torque can be defined as

$$a_{EM} = \frac{\tau_{s,cont,UQM}}{\tau_{s,max,UQM}} = 1.6. \quad (44)$$

It is only possible to have the maximum shaft torque of a PMSM as long as the product of the shaft torque and angular velocity is below the maximum shaft power due to the voltage induced by the permanent magnet. For a PMSM with a given shaft peak torque $\tau_{s,max}$ the speed-torque contour can be written as

$$P_{s,max} = \tau_{s,max} \omega_{s,corner} \quad (45)$$

$$\tau_{s,limit} = \begin{cases} \tau_{s,max} , & \omega_s \leq \omega_{s,corner} \\ \frac{P_{s,max}}{\omega_s} , & \omega_s > \omega_{s,corner}. \end{cases} \quad (46)$$

The peak shaft torque $\tau_{s,max}$ is selected in such a way that the (τ_s, ω_s) -output from the Matlab/Simulink simulation is below the shaft torque contour $\tau_{s,limit}$ calculated by Equation 46.

By trial-and-error-method it turns out that if the coulomb torque and viscous friction are responsible for 2% and 6%, respectively, of the power loss at maximum speed and power, the maximum efficiency is located around the nominal point of operation. Therefore

$$\tau_c = \frac{0.02 P_{s,max}}{\omega_s \eta_{EM,b}} \quad (47)$$

$$B_v = \frac{0.06 P_{s,max}}{\omega_s^2 \eta_{EM,b}}. \quad (48)$$

The nominal electro mechanical torque is:

$$\tau_{s,cont} = \frac{\tau_{s,max}}{a_{EM}} \quad (49)$$

$$\tau_{e,cont} = \tau_c + B_v \omega_{s,nom} + \tau_{s,cont}. \quad (50)$$

The machine will be designed at nominal speed $\omega_{s,nom}$, maximum power $P_{s,max}$, and minimum bus voltage $V_{Bus,min}$. The speed is approximately proportional to the terminal voltage. At the minimum bus voltage the machine should be able run at maximum speed with a modulation index $m_i = 1$. Because the machine is designed at nominal speed, but at the minimum battery voltage, the modulation index is

$$m_{i,nom} = \frac{\omega_{s,nom}}{\omega_{s,max}} = 0.3581. \quad (51)$$

The voltages of the machine are therefore:

$$\hat{V}_{p,nom} = m_{i,nom} \frac{V_{Bat,min}}{2} \quad (52)$$

$$V_{d,nom} = -\hat{V}_{p,nom} \sin(\phi_{EM,nom}) \quad (53)$$

$$V_{q,nom} = \hat{V}_{p,nom} \cos(\phi_{EM,nom}). \quad (54)$$

Several control properties of the PMSM can be applied. Due to its simple implementation the $I_d = 0$ property is selected even though the reluctance then cannot be utilized. Therefore, when using $I_d = 0$ control the machine parameters can be calculated as follows:

$$P_{EM,max} = \frac{P_{s,max}}{\eta_{EM,a}} \quad (55)$$

$$I_{q,cont} = \frac{2}{3} \frac{P_{EM,max}}{V_{q,nom}} \quad (56)$$

$$\lambda_{pm} = \frac{2}{3} \frac{2}{P} \frac{\tau_{e,cont}}{I_{q,cont}} \quad (57)$$

$$\omega_{e,nom} = \omega_{s,nom} \frac{P}{2} = 4500 \text{ rad/s} \quad (58)$$

$$L_q = -\frac{V_{d,nom}}{\omega_{e,nom} I_{q,cont}} \quad (59)$$

$$R_s = \frac{V_{q,nom} - \omega_{e,nom} \lambda_{pm}}{I_{q,cont}}. \quad (60)$$

The efficiency of the machine for different torque-speed characteristics can be seen in Fig. 11. It is seen that the efficiency is highest at continuous torque $\tau_{s,cont}$ and nominal speed $n_{s,nom}$. A common mistake in electric vehicle modeling is to assume a fixed efficiency of the components and it can be understood from Fig. 11 that wrong conclusions therefore can be made if the electric machines not is operating in a sufficient point of operation. The corner speed $n_{s,corner}$, nominal speed $n_{s,nom}$, maximum speed $n_{s,max}$, continuous torque $\tau_{s,cont}$, peak torque $\tau_{s,max}$, and the torque contour $\tau_{s,limit}$ are also shown in the figure.

3.1.3 Transmission

The maximum speed of the electric machine is $n_{s,max} = 8000$ rpm. The required gear ratio of the differential is therefore

$$G = \frac{n_{s,max}}{V_{car,max}} \frac{2\pi}{60} \frac{r_w}{1.1}. \quad (61)$$

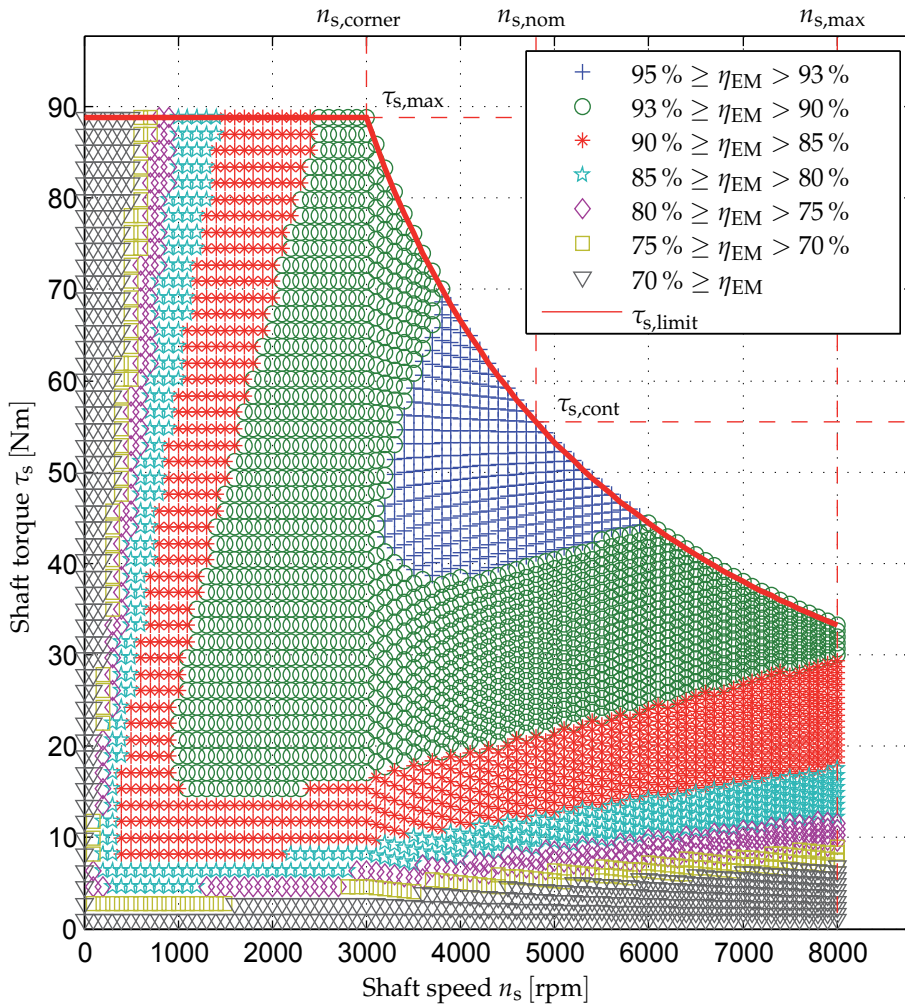


Fig. 11. Efficiency map of the electric machine.

From Equation 61 it is seen that the differential is designed with a 10 % buffer of the maximum speed of the car.

3.1.4 Rectifier

It is expected that most of the charging of the vehicle will take place at private homes, where the maximum RMS-current is $I_{\text{Grid,max}} = 16 \text{ A}$. The maximum grid power and rectifier current are therefore

$$P_{\text{Grid,max}} = \frac{3\sqrt{3}}{\pi} V_{\text{LL}} I_{\text{Grid,max}} = 10.6 \text{ kW} \quad (62)$$

$$I_{\text{RF,max}} = \sqrt{\frac{3}{2}} I_{\text{Grid,max}} = 19.6 \text{ A}. \quad (63)$$

It is assumed that the rectifier has an efficiency of $\eta_{RF,nom} = 0.98$ at maximum grid power. The switch-on resistance can therefore be calculated from Equation 36:

$$P_{RF,max} = \eta_{RF,nom} P_{Grid,max} = P_{Grid,max} - \left(2R_{RF} I_{RF,max}^2 + 2V_{th,RF} I_{RF,max} \right) \quad (64)$$

⇕

$$R_{RF} = \frac{P_{Grid,max} (1 - \eta_{RF,nom}) - 2V_{th,RF} I_{RF,max}}{2I_{RF,max}^2} = 199 \text{ m}\Omega. \quad (65)$$

3.1.5 Boost converter

It is assumed that the boost converter has efficiency $\eta_{BC,nom} = 0.98$ at maximum power. The maximum power of the boost converter is therefore

$$P_{BC,max} = P_{RF,max} \eta_{BC,nom}. \quad (66)$$

The threshold voltage is $V_{th,BC} = 1.5 \text{ V}$. From Equation 31 the resistance of the boost converter is therefore

$$P_{RF,max} = \eta_{BC,nom} P_{RF,max} + R_{BC} I_{RF,max}^2 + V_{th,BC} I_{RF,max} \quad (67)$$

⇕

$$R_{BC} = \frac{P_{RF,max} (1 - \eta_{BC,nom}) - V_{th,BC} I_{RF,max}}{I_{RF,max}^2} = 475 \text{ }\Omega. \quad (68)$$

It might be noticed that the values of the resistances of the rectifier and boost converter are higher than one would expect. However, this is because it is assumed that all the loss is due to the threshold voltage and resistance of the switches and diodes.

3.1.6 Inverter

The inverter is also designed at the maximum power of the electric machine and at minimum battery voltage. However, the inverter is designed at the peak shaft torque instead of at the maximum speed. The inverter is assumed to have an efficiency of $\eta_{Inv,nom} = 0.98$ at this point of operation. The loss $P_{Inv,loss,max}$ and resistance R_{Inv} of the inverter are therefore

$$P_{Inv,loss,max} = \frac{1 - \eta_{Inv,nom}}{\eta_{Inv,nom}} P_{EM,max} \quad (69)$$

$$\tau_{e,max} = \tau_c + B_v \omega_{s,corner} + \tau_{s,max} \quad (70)$$

$$I_{q,max} = \frac{2}{3} \frac{2}{P} \frac{\tau_{e,max}}{\lambda_{pm}} \quad (71)$$

$$R_{Inv} = \frac{P_{Inv,loss,max} - \frac{6}{\pi} V_{th,Inv} I_{q,max}}{\frac{3}{2} I_{q,max}^2}. \quad (72)$$

The threshold voltage is assumed to be $V_{th,Inv} = 1 \text{ V}$.

3.2 Battery charging control

During the charging of the battery, i.e., both due to the regenerative braking and the grid, it is very important that the maximum battery charging current and voltage not are exceeded. The maximum allowed cell charging current can be calculated from the inner and outer voltage of the battery cell, i.e.,

$$i_{\text{Bat,cell,cha,max}} = \begin{cases} \frac{V_{\text{Bat,max,cell}} - v_{\text{Bat,int,cell}}}{R_{\text{Bat,cell,cha}}}, & \frac{V_{\text{Bat,max,cell}} - v_{\text{Bat,int,cell}}}{R_{\text{Bat,cell,cha}}} \leq I_{\text{Bat,1,cell}} \\ I_{\text{Bat,1,cell}} & , \frac{V_{\text{Bat,max,cell}} - v_{\text{Bat,int,cell}}}{R_{\text{Bat,cell,cha}}} > I_{\text{Bat,1,cell}}. \end{cases} \quad (73)$$

In Equation 73 it is insured that neither the maximum allowed voltage or current are exceeded. The battery pack consist of $N_{\text{Bat,s}}$ series connected cells and $N_{\text{Bat,p}}$ parallel connected strings. The total voltage and current of the battery pack can therefore be calculated as

$$v_{\text{Bat}} = N_{\text{Bat,s}} v_{\text{Bat,cell}} \quad (74)$$

$$i_{\text{Bat}} = N_{\text{Bat,p}} i_{\text{Bat,cell}} \quad (75)$$

$$i_{\text{Bat,cha,max}} = N_{\text{Bat,p}} i_{\text{Bat,cell,cha,max}}. \quad (76)$$

During the charging of the battery the battery cell voltage $v_{\text{Bat,cell}}$ should not exceed $V_{\text{Bat,max,cell}} = 4.2 \text{ V}$ and the maximum cell charging current should not be higher than $I_{\text{Bat,1,cell}} = 7 \text{ A}$ (Saft, 2010). In order to charge the battery as fast as possible either the maximum voltage or maximum current should be applied to the battery. The requested battery charging current, i.e., the output current of the boost converter i_{BC} , is therefore

$$i_{\text{BC}}^* = i_{\text{Bat,cha,max}}, \quad (77)$$

which means that the requested output power of the boost converter is

$$p_{\text{BC}}^* = v_{\text{Bat}} i_{\text{BC}}^*. \quad (78)$$

The requested charging current insures that neither the maximum allowed voltage or current are exceeded. However, for a big battery pack the required charging power might be so high that a special charging station is necessary.

The requested input current of the boost converter, i.e., the rectifier current i_{RF} , can be calculated by Equation 31 and 78:

$$i_{\text{RF}}^* = \frac{-(V_{\text{th,BC}} - v_{\text{RF}}) - \sqrt{(V_{\text{th,BC}} - v_{\text{RF}})^2 - 4R_{\text{BC}}p_{\text{BC}}^*}}{2R_{\text{BC}}}. \quad (79)$$

The grid RMS-current can therefore from Equation 34 be calculated as

$$I_{\text{Grid}} = \begin{cases} \sqrt{\frac{2}{3}} i_{\text{RF}}^* & , \sqrt{\frac{2}{3}} i_{\text{RF}}^* < I_{\text{Grid,max}} \\ I_{\text{Grid,max}} & , \sqrt{\frac{2}{3}} i_{\text{RF}}^* \geq I_{\text{Grid,max}}. \end{cases} \quad (80)$$

Glider mass	M_{glider}	670 kg
Wheel radius	r_w	0.2785 m
Front area	A_{front}	1.68 m ²
Aerodynamic drag coefficient	C_{drag}	0.3

Table 4. Parameters of the vehicle used for the case study.

Thereby it is ensured that the maximum RMS grid current is not exceeded. The actual values can therefore be obtained by calculating backwards, i.e.,

$$i_{\text{RF}} = \sqrt{\frac{3}{2}} I_{\text{Grid}} \quad (81)$$

$$p_{\text{RF}} = v_{\text{RF}} i_{\text{RF}} \quad (82)$$

$$p_{\text{BC}} = p_{\text{RF}} - R_{\text{BC}} i_{\text{RF}}^2 - V_{\text{th,BC}} i_{\text{RF}} \quad (83)$$

$$i_{\text{BC}} = \frac{p_{\text{BC}}}{v_{\text{Bat}}} \quad (84)$$

4. Case study

4.1 Driving cycle

When different cars are compared in terms of energy consumption a standard driving cycle is used. An often used driving cycle is the New European Driving Cycle (NEDC) as this driving cycle contains both city driving with several start-and-stops and motorway driving, i.e., it is a good representation of a realistic driving environment. The NEDC has a maximum speed of 120 km/h, an average speed of 33.2 km/h, a duration of 1184 s, and a length of 10.9 km. The NEDC profile can be seen in Fig. 12. The input to the simulation will be the NEDC repeated 14 times as this should provide a driving distance of 153 km which is assumed to be an acceptable driving distance.

4.2 Vehicle parameters

The energy consumption of a given vehicle depend on the physical dimensions and total mass of the vehicle. For this case study the parameters in Table 4 are used. The glider mass is the mass of the vehicle without motor, battery, power electronics, etc. It might be understood from the parameters in Table 4 that it is a rather small vehicle, i.e., similar to a Citroën C1.

4.3 Results

In Fig. 13 the battery state-of-charge, current, voltage, and the power of the grid and battery can be seen. It is understood from Fig. 13(a) that the battery is designed due to its energy requirement rather than the power requirement as the state-of-charge reaches the minimum allowed value of $SoC_{\text{Bat,min}} = 0.2$. In Fig. 13(b) and (c) the battery current and voltage are shown, respectively. It is seen that when the current becomes higher the voltage becomes lower as the power should be the same. In Fig. 13(d) the battery and grid power are shown. It is seen that the charging of the battery is limited by the maximum allowed grid power $P_{\text{Grid,max}}$. After approximately two hours the battery reaches the maximum voltage, and it is therefore seen that the battery then is charged under constant-voltage approach, which means that the battery current and power and grid power slowly are decreased until the battery reaches its initial state-of-charge value.

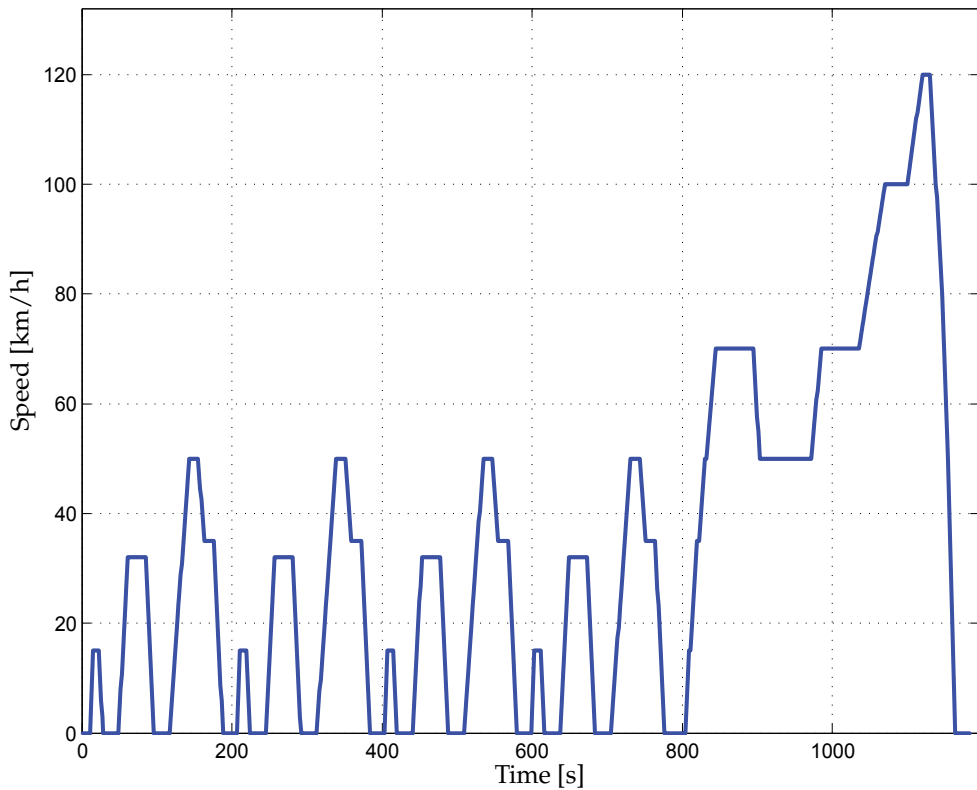


Fig. 12. New European Driving Cycle (NEDC). This driving cycle will be repeated 14 times and thereby serving as the input profile of the Matlab/Simulink simulation model.

Due to the minimum battery pack voltage requirement $N_{\text{Bat},s} = 216$ series connected battery cells are required. The chosen vehicle is designed to be able to handle 14 repetitions of the NEDC. From Fig. 10 it is understood that $N_{\text{Bat},p} = 5$ parallel strings are demanded in order to fulfill this requirement. This means that the battery pack has a capacity of

$$E_{\text{Bat}} = \frac{V_{\text{Bat,nom,cell}} N_{\text{Bat},s} Q_{\text{Bat},1,\text{cell}} N_{\text{Bat},p}}{1000 \text{ Wh/kWh}} = 28.0 \text{ kWh}. \quad (85)$$

The energy distribution of the vehicle can be seen in Fig. 14. During the 14 NEDC repetitions $E_t = 11.2 \text{ kWh}$ is delivered to the surface between the driving wheels and the road, but $E_{\text{Grid}} = 22.7 \text{ kWh}$ charging energy is taken from the grid. This means that only 49% of the charging energy from the grid is used for the traction and that the grid energy consumption is 148.3 Wh/km . The rest of the energy is lost in the path between the wheels and the grid. The auxiliary loads are responsible for the biggest energy loss at 17%. However, it is believed that this can be reduced significant by using diodes for the light instead of bulbs, and to use heat pumps for the heating instead of pure resistive heating.

The battery is responsible for the second largest energy waist as 14% of the grid energy is lost in the battery. The battery was only designed to be able to handle the energy and power requirements. However, in order to reduce the loss of the battery it might be beneficial to oversize the battery as the battery peak currents then will become closer to its nominal current

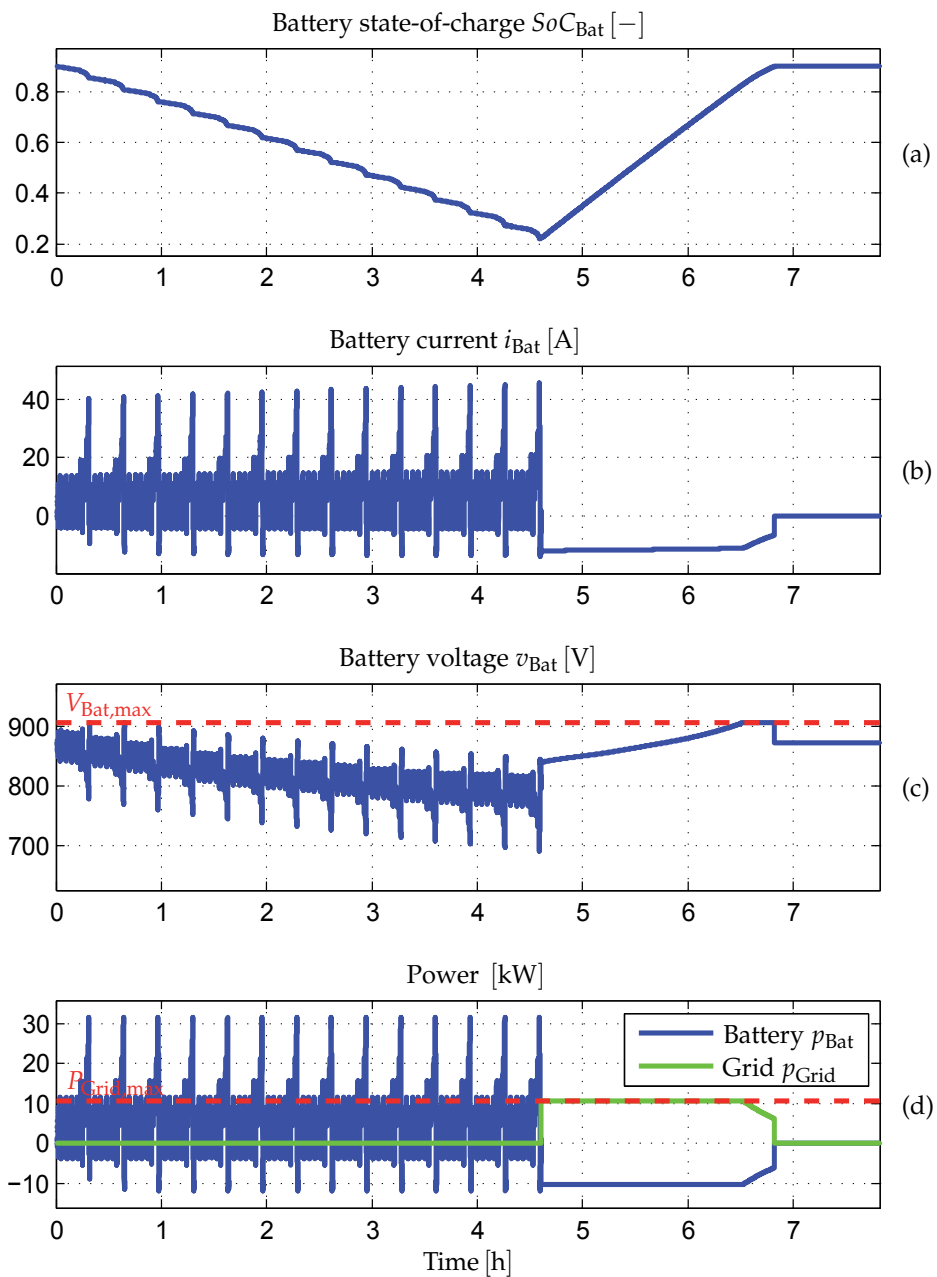


Fig. 13. Simulation results of the vehicle with 14 repeated NEDC cycles as input. (a) Battery state-of-charge. (b) Battery current. (c) Battery voltage. (d) Power of the battery and grid.

which will reduce the negative influence of the peukert phenomena. However, a heavier battery will also increase the traction power, so the gained reduction in battery loss should be higher than the increased traction power. A bigger battery will of course also make the vehicle more expensive, but these issues are left for future work.

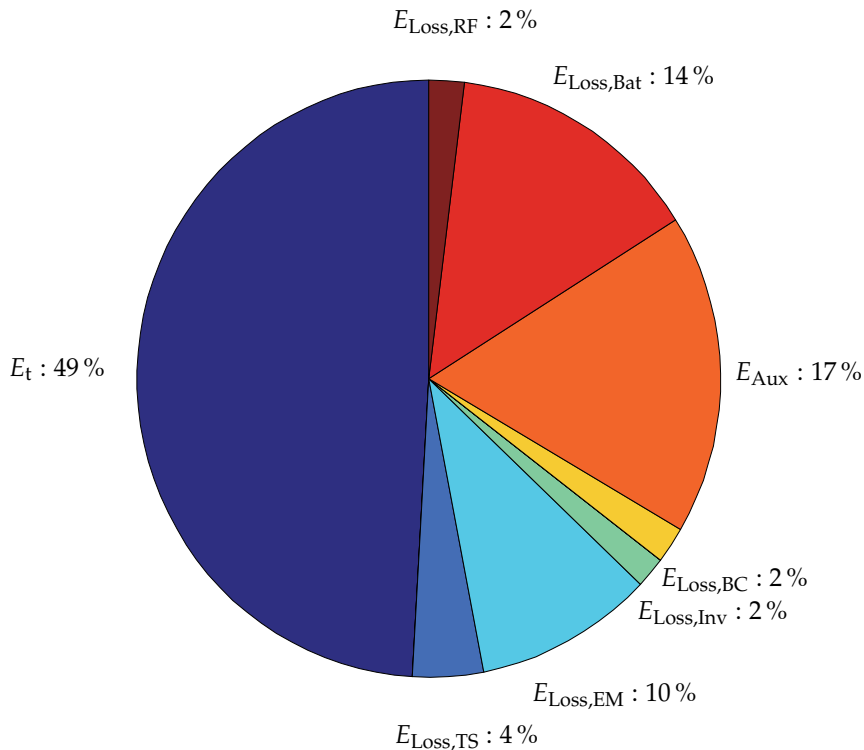


Fig. 14. Energy distribution in the vehicle relative to the grid energy.

5. Conclusion

In this chapter a battery electric vehicle have been modeled and designed. The battery of the electric vehicle is designed in such a way that both the power and energy requirements are fulfilled for a given driving cycle. The design procedure is an iterative process as the power flow inside the vehicle depends on the parameters of each component of the power system between the grid and driving wheels. The loss of each component in the vehicle depend on the internal states of the vehicle, i.e., the voltages, currents, speed, torques, and state-of-charge. These states have been included in the modeling in order to obtain a realistic energy calculation of the vehicle. A case study with a small vehicle undergoing 14 driving cycles of type NEDC resulted in a grid energy consumption of 148.3 Wh/km with an efficiency of 49% from the grid to the driving wheels. However, a relatively big part of the energy loss is due to the auxiliary loads, e.g., light, safety systems, comfort systems, etc., and the battery. For this work the only design constraint of the battery was the voltage limit, and the energy and power requirements. For future work it is recommended also to include the cost and overall efficiency as design parameters. It is also suggested to investigate how the loss due to the auxiliary loads can be reduced.

6. References

- Casanellas, F. (1994). Losses in pwm inverters using igbts, *IEE Proceedings - Electric Power Applications* 141(5): 235 – 239.
- Chan, C. C., Bouscayrol, A. & Chen, K. (2010). Electric, hybrid, and fuel-cell vehicles: Architectures and modeling, *IEEE Transactions on Vehicular Technology* 59(2): 589 – 598.
- Ehsani, M., Gao, Y., Gay, S. E. & Emadi, A. (2005). *Modern Electric, Hybrid Electric, and Fuel Cell Vehicles - Fundamentals, Theory, and Design*, first edn, CRC Press LLC.
- Emadi, A. (2005). *Handbook of Automotive Power Electronics and Motor Drives*, first edn, Taylor & Francis.
- Gao, D. W., Mi, C. & Emadi, A. (2007). Modeling and simulation of electric and hybrid vehicles, *Proceedings of the IEEE* 95(4): 729 – 745.
- Jensen, K. K., Mortensen, K. A., Jessen, K., Frandsen, T., Runólfsson, G. & Thorsdóttir, T. (2009). Design of spmsm drive system for renauld kangoo, *Aalborg University* .
- Lukic, S. & Emadi, A. (2002). Performance analysis of automotive power systems: effects of power electronic intensive loads and electrically-assisted propulsion systems, *Proc. of IEEE Vehicular Technology Conference (VTC)* 3: 1835 – 1839.
- Mapelli, F. L., Tarsitano, D. & Mauri, M. (2010). Plug-in hybrid electric vehicle: Modeling, prototype realization, and inverter losses reduction analysis, *IEEE Transactions on Industrial Electronics* 57(2): 598 – 607.
- Mohan, N., Underland, T. M. & Robbins, W. P. (2003). *Power electronics*, third edn, John Wiley.
- Saft (2010). Saftbatteries. URL: <http://www.saftbatteries.com>
- Schaltz, E. (2010). *Design of a Fuel Cell Hybrid Electric Vehicle Drive System*, Department of Energy Technology, Aalborg University.
- UQM (2010). Uqm technologies. URL: <http://www.uqm.com>

Modeling and Simulation of High Performance Electrical Vehicle Powertrains in VHDL-AMS

K. Jaber, A. Fakhfakh and R. Neji
*National School of Engineers, Sfax
Tunisia*

1. Introduction

Nowadays the air pollution and economical issues are the major driving forces in developing electric vehicles (EVs). In recent years EVs and hybrid electric vehicles (HEVs) are the only alternatives for a clean, efficient and environmentally friendly urban transportation system (Jalalifar *et al.*, 2007). The electric vehicle (EV) appears poised to make a successful entrance to the personal vehicle mass market as a viable alternative to the traditional internal combustion engine vehicles (ICE): Recent advances in battery technology indicate decreasing production costs and increasing energy densities to levels soon acceptable by broad consumer segments. Moreover, excluding the generation of the electricity, EVs emit no greenhouse gases and could contribute to meeting the strict CO₂ emission limits necessary to dampen the effect of global warming. Several countries around the world have therefore initiated measures like consumer tax credits, research grants or recharging station subsidies to support the introduction of the EV. Finally, the success alternative vehicles like the Toyota Prius Hybrid proves a shift in consumer interest towards cleaner cars with lower operating costs (Feller *et al.*, 2009).

Nonetheless, the EV will first need to overcome significant barriers that might delay or even prevent a successful mass market adoption. Permanent Magnet Synchronous Motor (PMSM) is a good candidate for EVs.

In this work, a high level modelling and an optimization is reported for the determination of time response (Tr) and power (P) of Electric Vehicle. The electric constant of back-electromotive-force, stator d- and q- axes inductances, switching period, battery voltage, stator resistance and torque gear ratio were selected as factors being able to influence Tr and P. The optimization process was carried out with Doehlert experimental design (Jaber *et al.*, 2010).

The optimization is based on simulations of the chain of the electric vehicle; every block is simulated with a different abstraction level using the hardware description language VHDL-AMS. The chain of electric traction is shown in Figure 1. It consists of 4 components: Control strategy, Inverter, PMSM model and Dynamic model. A right combination of these four elements determines the performance of electric vehicles.

VHDL (Very High Speed Integrated Circuit Hardware Description Language) is a commonly used modelling language for specifying digital designs and event-driven systems. The popularity of VHDL prompted the development of Analog and Mixed-Signal

(AMS) extensions to the language and these extensions were standardized as IEEE VHDL-AMS in 1999. Some of the main features of this ASCII-based language include Model Portability, Analog and Mixed-Signal modeling, Conserved System and Signal Flow Modeling, Multi-domain modeling, Modeling at different levels of abstraction, and Analysis in time, frequency and quiescent domains. Since VHDL-AMS is an open IEEE standard, VHDL-AMS descriptions are simulator-independent and models are freely portable across tools. This not only prevents model designers from being locked in to a single tool or tool vendor but also allows a design to be verified on multiple platforms to ensure model fidelity.

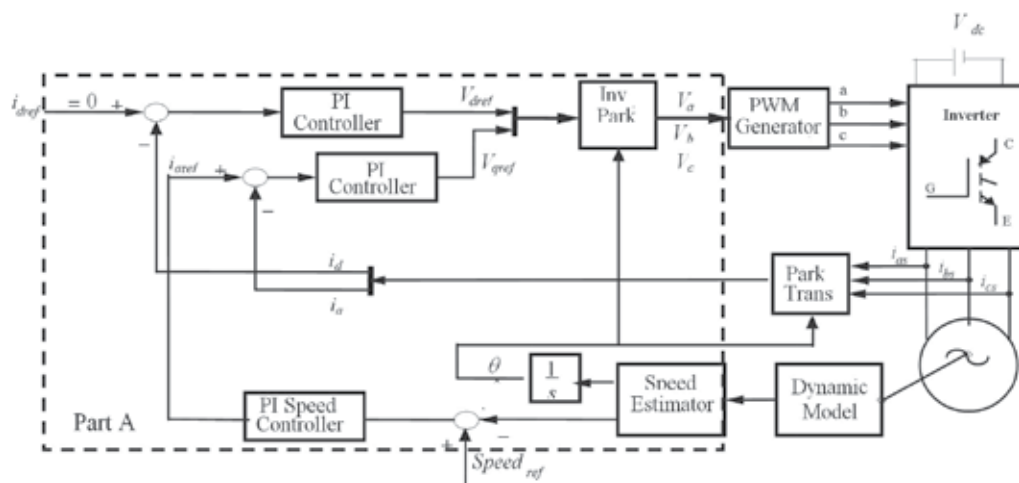


Fig. 1. Model of traction chain

VHDL-AMS is a strict superset of VHDL and inherently includes language support for describing event-driven systems such as finite state machines. The standard not only provides language constructs for digital and analog designs but also specifies the interactions between the analogue and digital solvers for mixed-signal designs. The analog (continuous time) extensions allow the description of conserved energy systems (based on laws of conservation) as well as signal-flow models (based on block diagram modeling).

VHDL-AMS distinguishes between the interface (ENTITY) of a model and its behavior (ARCHITECTURE). VHDL-AMS allows the association of multiple architectures with the same entity and this feature is typically used to describe a model at different levels of abstraction.

With VHDL-AMS, it is possible to specify model behaviour for transient, frequency and quiescent domain simulations. Depending on the user's choice of an analysis type, the appropriate behavior is simulated.

The language is very flexible in that it allows different modeling approaches to be used, both individually and collectively. It is possible to describe model behavior with differential algebraic equations, value assignments and subprograms at a very abstract and mathematical level (McDermott *et al.*, 2006).

The VHDL-AMS language is an undiscovered asset for FPGA designers—a powerful tool to define and verify requirements in a non-digital context.

As an electric vehicle is a multidisciplinary system, the new standard VHDL-AMS is suitable for the modelling and the simulation of such system in the same software environment and with different abstraction levels (Jaber *et al.*, 2009).

2. Dynamic model

The first step in vehicle performance modelling is to write an electric force model. This is the force transmitted to the ground through the drive wheels, and propelling the vehicle forward. This force must overcome the road load and accelerate the vehicle (Sadeghi *et al.*, 2009).

For any mission profile, an electric road vehicle is subjected to forces that the onboard propulsion system has to overcome in order to propel or retard the vehicle. These forces are composed of several components as illustrated in Figure 2. The effort to overcome these forces by transmitting power via the vehicle drive wheels and tyres to the ground is known as the total tractive effort or total tractive force.

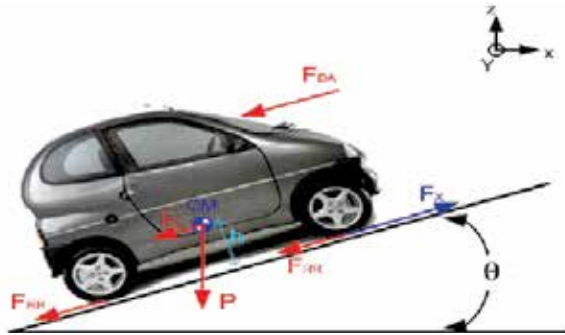


Fig. 2. Forces on a vehicle

The rolling resistance is primarily due to the friction of the vehicle tires on the road and can be written as (Jalalifar *et al.*, 2007):

$$F_{RR} = f \times M_V \times g \quad (1)$$

The aerodynamic drag is due to the friction of the body of vehicle moving through the air. The formula for this component is as in the following:

$$F_{DA} = \frac{1}{2} \cdot \rho \cdot S \cdot C_x \cdot V^2 \quad (2)$$

An other resistance force is applied when the vehicle is climbing of a grade. As a force in the opposite direction of the vehicle movement is applied:

$$F_L = M_v \cdot g \cdot \sin\alpha \quad (3)$$

The power that the EV must develop at stabilized speed is expressed by the following equation:

$$P_a = V \cdot (F_{RR} + F_{DA} + F_L) \quad (4)$$

The power available in the wheels of the vehicle is expressed by:

$$P_m = T_{em} \cdot r_m \cdot \frac{V}{R_{wheels}} \quad (5)$$

According to the fundamental principle of dynamics the acceleration of the vehicle is given by:

$$\gamma = \frac{P_m - P_a}{M_v V} \quad (6)$$

$$\gamma = \frac{T_{em} \cdot r_m - R_{wheels} \cdot (F_{RR} + F_{DA} + F_L)}{M_v \cdot R_{wheels}} \quad (7)$$

$$T_l = R_{wheels} \cdot (F_{RR} + F_{DA} + F_L) \quad (8)$$

$$W_m = \frac{r_m}{R_{wheels}} \cdot \frac{d\gamma}{dt} \quad (9)$$

A VHDL-AMS model for the dynamic model is specified in an “architecture” description as show in Listing 1.

```

ARCHITECTURE behav OF dynamic_model IS
  QUANTITY Speedm_s : REAL := 0.0;
  QUANTITY F_RR : REAL := 0.0;
  QUANTITY F_DA : REAL := 0.0;
  QUANTITY F_L : REAL := 0.0;

  BEGIN
    F_RR = = f*Mv*g;
    F_DA = = 0.5*da*Sf*Cx* Speedm_s * Speedm_s;
    F_L = = Mv*g*sin(alpha)
    Tl = = Rwheels*( F_RR + F_DA + F_L);
    Speedm_s 'dot = = (1.0/(Mv*Rwheels))*(rm*Tem-Tl);
    Speedkm_h = = 3.6 * Speedm_s;
    Wm = = (rm/Rwheels)*Speedm_s;
  END ARCHITECTURE behav;

```

Listing 1. VHDL-AMS dynamic model

3. PMSM model

A permanent magnet synchronous motor (PMSM) has significant advantages, attracting the interest of researchers and industry for use in many applications.

Usage of permanent magnet synchronous motors (PMSMs) as traction motors is common in electric or hybrid road vehicles (Dolecek *et al.*, 2008). The dynamic model of the PMSM can be described in the d-q rotor frame as follows:

$$V_d = R i_d + L_d \frac{di_d}{dt} - \omega_e L_q i_q \quad (10)$$

$$V_q = R i_q + L_q \frac{di_q}{dt} + \omega_e L_d i_d + K \omega_m \quad (11)$$

Where $K = p \phi_m$ is the electric constant of back-electromotive-force (EMF), it is calculated according to the geometrical magnitudes of the motor so that it can function with a high speed. The equations giving the stator current can be written in the following form:

$$I_d = \frac{1}{L_d s + R} (V_d + \omega_e L_q I_q) \quad (12)$$

$$I_q = \frac{1}{L_q s + R} (V_q - \omega_e L_d I_d - K \omega_m) \quad (13)$$

The electromagnetic torque developed by the motor is given by the following equation:

$$T_{em} = \frac{3}{2} K I_q + \frac{1}{2} p (L_d - L_q) I_d I_q \quad (14)$$

The equation giving the angle by the motor can be written in the following form:

$$\frac{d\theta}{dt} = p \omega_m \quad (15)$$

Figure 3 shows the description of the model of the PMSM in Simplerer 7.0 software.

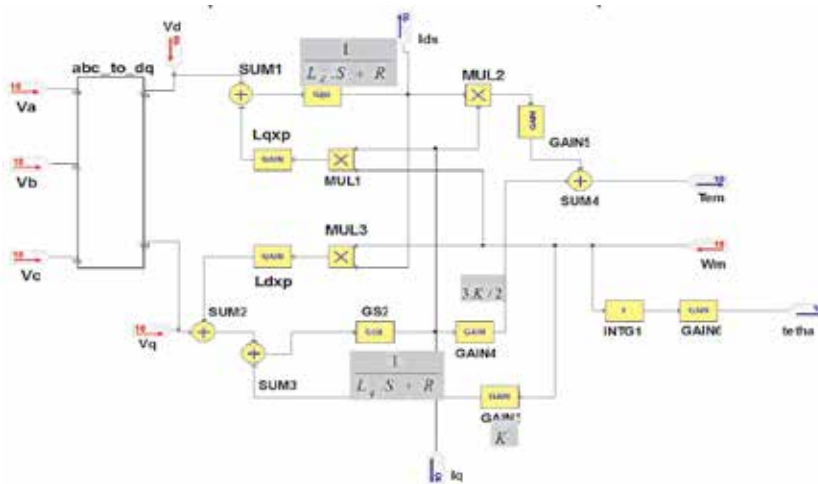


Fig. 3. SIMPLORER model of the PMSM in the d-q rotor frame

4. Control strategy

In recent years, vector-controlled ac motors, such as induction motor, permanent-magnet synchronous motor (PMSM), and synchronous reluctance motor, have become standard in industrial drives and their performance improvement is an important issue. Particularly, improvement of control performance and drive efficiency is essentially required for drives used in electric vehicles (Ben Salah *et al.*, 2008):

$$T_{em} = \frac{3}{2} K_t I_s \sin(\theta_s - p\theta(t)) \quad (16)$$

To achieve an optimal control, which means a maximum torque, it is necessary to satisfy the following condition:

$$\theta_s - p\theta(t) = \pm \frac{\pi}{2} \quad (17)$$

from where

$$I_s = I_q \quad \text{and} \quad I_d = 0 \quad (18)$$

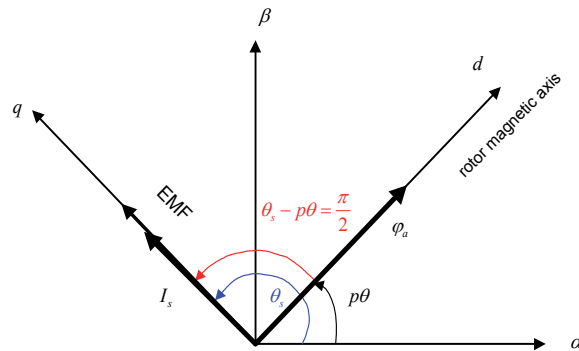


Fig. 4. Stator current and EMF in the d-q rotor frame

The first part (A) in figure 1 illustrates the control strategy. It presents a first **PI** speed control used for speed regulation. The output of the speed control is I_{qref} ; its application to a second **PI** current regulator makes the adjustment of phase and squaring currents. The outputs of current regulators are V_{dref} and V_{qref} ; they are applied to a Park transformation block. Where, V_{dref} and V_{qref} are the forcing function to decide the currents in d-q axis model which may be obtained from 3-phase voltages (V_a , V_b and V_c) through the park transformation technique as:

$$V_a = V_{dref} \cdot \cos(\theta) - V_{qref} \cdot \sin(\theta) \quad (19)$$

$$V_b = V_{dref} \cdot \cos\left(\theta - \frac{2\pi}{3}\right) - V_{qref} \cdot \sin\left(\theta - \frac{2\pi}{3}\right) \quad (20)$$

$$V_c = V_{dref} \cdot \cos\left(\theta - \frac{4\pi}{3}\right) - V_{qref} \cdot \sin\left(\theta - \frac{4\pi}{3}\right) \quad (21)$$

The generation of the control signals of the inverter is made by comparison of the simple tensions obtained following the regulation with a triangular signal. Its period is known as switching period.

The different blocks constituting the traction chain were described in a VHDL-AMS structural model by including all expressions detailed above.

5. Inverter model

The structure of a typical three-phase VSI is shown in figure 6. As shown below, V_a , V_b and V_c are the output voltages of the inverter. S_1 through S_6 are the six power transistors IGBT that shape the output, which are controlled by a , a' , b , b' , c and c' . When an upper transistor is switched on (i.e., when a , b or c are 1), the corresponding lower transistor is switched off (i.e., the corresponding a' , b' or c' is 0). The on and off states of the upper transistors, S_1 , S_3 and S_5 , or equivalently, the state of a , b and c , are sufficient to evaluate the output voltage.

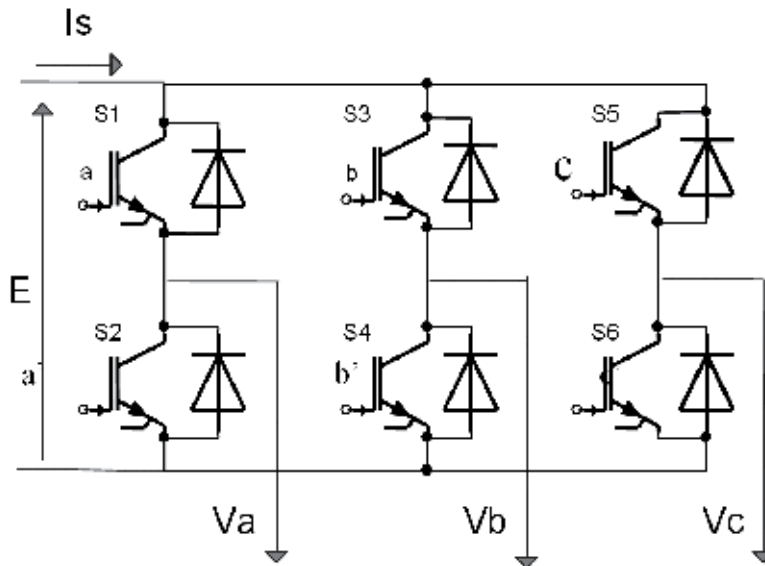


Fig. 5. Inverter connected to a balanced load

The relationship between the switching variable vector $[a, b, c]^t$ and the line-to-line output voltage vector $[V_{ab} V_{bc} V_{ca}]^t$ and the phase (line-to-neutral) output voltage vector $[V_a V_b V_c]^t$ are given by the following relationships, where a , b , c are the orders of S_1 , S_3 , S_5 respectively.

$$\begin{bmatrix} V_{ab} \\ V_{bc} \\ V_{ca} \end{bmatrix} = E \cdot \begin{bmatrix} 1 & -1 & 0 \\ 0 & 1 & -1 \\ -1 & 0 & 1 \end{bmatrix} \cdot \begin{bmatrix} a \\ b \\ c \end{bmatrix} \quad \begin{bmatrix} V_a \\ V_b \\ V_c \end{bmatrix} = \frac{1}{3} \cdot E \cdot \begin{bmatrix} 2 & -1 & -1 \\ -1 & 2 & -1 \\ -1 & -1 & 2 \end{bmatrix} \cdot \begin{bmatrix} a \\ b \\ c \end{bmatrix}$$

The different blocks constituting the traction chain were introduced both in MATLAB and SIMPLORER 7.0 softwares. They were described in structural models by including all expressions detailed above. The different simulation parameters are summarized in table 1:

Parameters	Designation	Values
Vmax	Max Speed	80 km/h
Cx	Drag coefficient of the vehicle	0.55
S	Frontal surface of the vehicle	1.8 m ²
f	Coefficient of rolling friction	0.025
Mv	Total mass of the vehicle	800 kg
p	Pair of pole number	4

Table 1. Simulation parameters

6. Simulation results

6.1 MATLAB environment

Figure 6 details the vector control ($I_d=0$ strategy) of the vehicle, implemented under Matlab/simulink software.

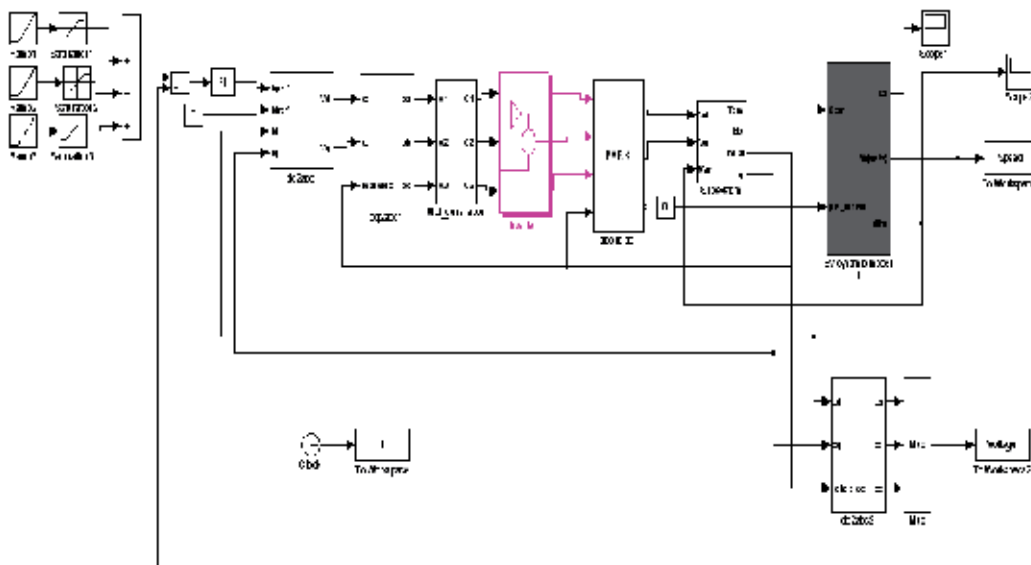


Fig. 6. SIMULINK models for a vector control and his interaction in a chain of traction for vehicle

Figure 7 shows the simulation result. The reference speed of the EV is reached after 8.5s. Simulations with MATLAB are useful to verify that our system works well without any dysfunction. But in this case, the traction chain of the EV is described with ideal functional models. Going down in the hierarchical design level, more suitable software should be applied. For this reason, our system was described in VHDL-AMS and simulated with Simplorer 7.0 software.

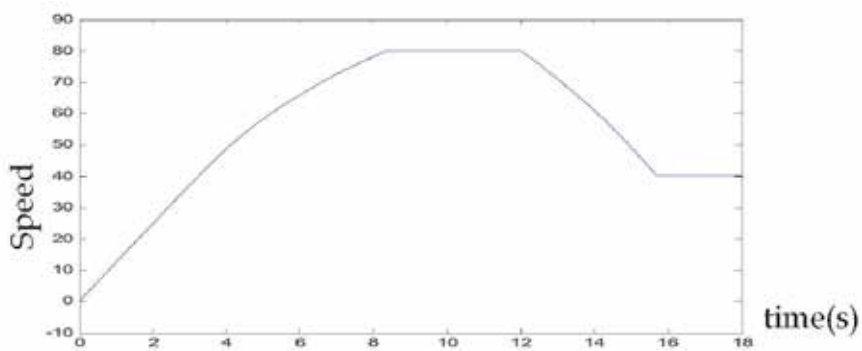


Fig. 7. Vehicle speed response in MATLAB/SIMULINK

6.2 VHDL-AMS virtual prototype

VHDL-AMS descriptions were developed for each block of the electric vehicle including structural models. The obtained blocks were connected in Simplorer 7.0 Software environment to obtain a high level description our system as detailed on figure 8. The exposed blocks include analogue/digital electronic behavioural descriptions. It represents a so complex multi-domain system (Fakhfakh *et al.*, 2006).

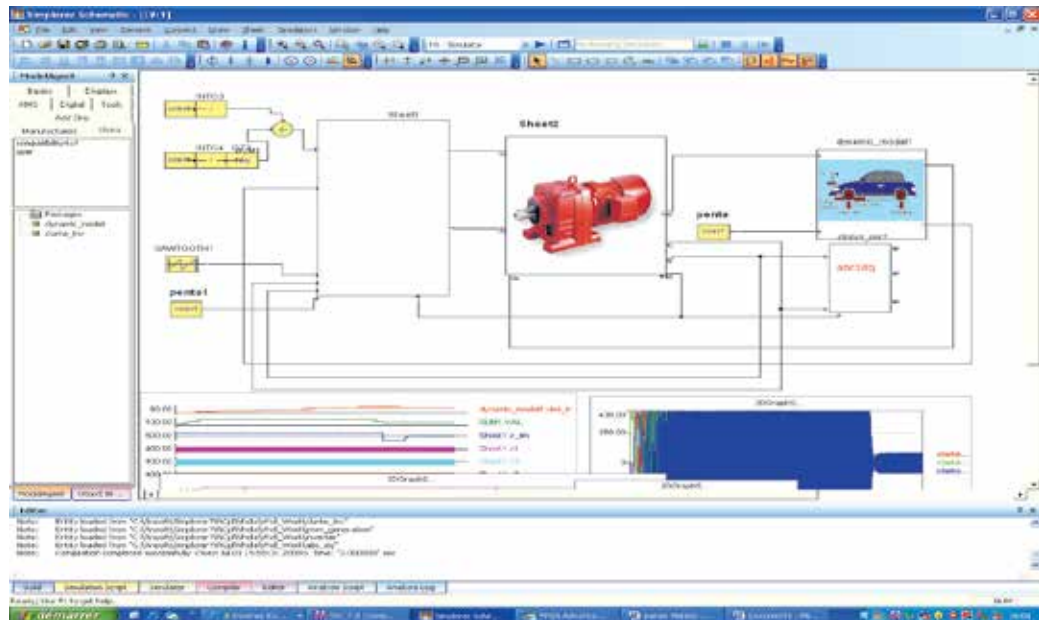


Fig. 8. Electric Vehicle description in Simplorer environment

6.3 Comparison

The dynamic response of the vehicle speed is depicted in figure 9, obtained with both Simplorer and Matlab software. In table 2, we compare the simulation runtime and the obtained response time of the Electric Vehicle. We can distinguish clearly the difference between the two simulation results.

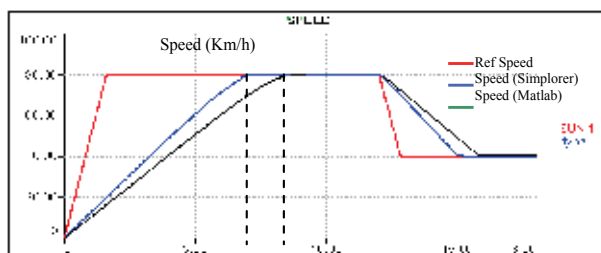


Fig. 9. Dynamic response of the vehicle speed in Simplorer and Matlab

Software	Simulation runtime	Time response of max speed
<i>Matlab</i>	24s	8.5 s
<i>Simplorer</i>	66s	6.5 s

Table 2. Simulation runtime simulation

To conclude, Matlab executes simulations more rapidly (24s); we obtained a dynamic response equal to 8.5s. Simplorer simulation runtime is three times longer due to the fact that the modelling abstraction level is lower compared to the functional description with Matlab; the dynamic response is about 6.5s. The power of the Electric Vehicle is about 42 kW.

To resume, we can clearly conclude that simulating a mathematical model with MATLAB software is useful to verify the ideal response of our EV. But with Simplorer environment we can attend the lower abstraction models. In this case, it is possible to simulate the effect of physical parameters such as temperature, battery voltage, etc.

7. Optimization with experimental designs

To optimize our control strategy, we have adopted an experimental design approach by applying the Doehlert design. Six factors have been considered as shown on table 3: K_e , L_d , T_s , E , R and r_m . According to the number of factors, in order to limit the number of runs and to take into account the major effects, a screening study is necessary. Consequently, a first step of screening was conducted using a fractional factorial design. The last with six factors is a design involving a minimum of 45 experiments (see appendix).

For each factor, we define three levels: low, center and high levels as detailed on table 3.

Naturel Variable	Parameters	Coded variable	Low Level	Center Level	High Level
K_e	electric constant of back-electromotive-force (EMF)	X1	0.05	0.1	0.2
$L_d = L_q$	Stator d- and q- axes inductances (mH).	X2	0.216	0.416	0.616
T_s	Switching period (μ s)	X3	100	300	500
E	Battery voltage (V)	X4	200	300	400
R	Stator resistance (Ω)	X5	0.02	0.05	0.08
r_m	Torque gear ratio	X6	1	3	5

Table 3. Description of experimental variables in the screening design

Our goal is to optimize both the response time and the power of the studied system. The analysis of results and the building of experimental designs were carried out with the NEMRODW mathematical statistical software (El Ati-Hellal *et al.*, 2009).

Because of the none-linearity of the studied system, the experimental response Y_i can be represented by a quadratic equation of the response surface (Elek *et al.*, 2004):

$$Y_{1,2} = b_0 + \sum_{i=1}^6 b_i x_i + \sum_{\substack{i=1 \\ j=2 \\ i \neq j}}^6 b_{ij} x_i x_j \quad (19)$$

Y_1 : response representing the response time;

Y_2 : response representing the power;

To find an optimum, we should minimize (Y_1) and maximize (Y_2). So we define the following experimental response Y :

$$Y = \frac{\alpha}{Y_1} + \beta.Y_2 \quad \text{with } \alpha=350 \text{ and } \beta=0.6 \quad (20)$$

α and β are ponderation factors. In our case, we give the same weight to the response time and the power.

Coefficients b_i of the response surface (19) were calculated with Nemrodw software without taking into account experiment 45 due to high residual.

To decide about the efficiency of the obtained regression equation, we compute R^2 as:

$$R^2 = (\text{Sum of squares attributed to the regression}) / \text{Total Sum of squares}$$

We found $R^2 = 0.976$; it is well within acceptable limits of $R^2 \geq 0.8$ which revealed that the experimental data well fitted the second-order polynomial equation as detailed on table 4.

	Y
Standard error of response	8.4837
R^2	0.976
R^2A	0.939
R^2 pred	0.777
PRESS	11512.167
Degrees of freedom	17

Table 4. Statistical data and coefficients of y response model: $y = f(x_1, x_2, x_3, x_4, x_5, x_6)$

To estimate the quality of the model and validate it, analysis of the variance and the residual values (difference between the calculated and the experimental result) were examined. According to the residual (Figure 10), the choice of the model was appropriate: a systematic behavior was not observed in the plot, for example, an increase in residual suggesting the necessity to transform the response.

After the validation of the proposed second-order polynomial model, we can draw 2D and 3D plots representing the evolution of Y versus 2 factors.

Using contour plot graphs makes the evaluation of the influences of the selected factors easier. Figure 11 illustrates the experimental response obtained by the simultaneous variation of X_2 ($Ld \& Lq$) and X_6 (rm). We concluded that in order to increase the response Y , an increase of X_6 and decrease of X_2 is necessary (Danion *et al.*, 2004) & (El Hajjaji *et al.*, 2005).

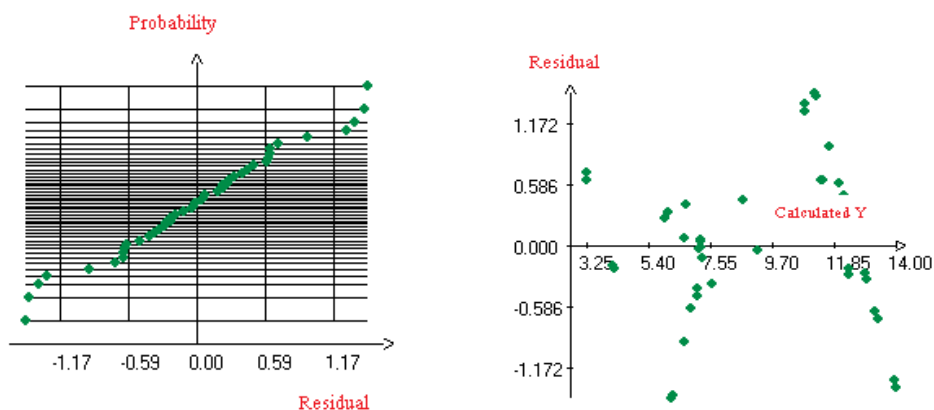


Fig. 10. Overview of residual: Normal probability and residual plot

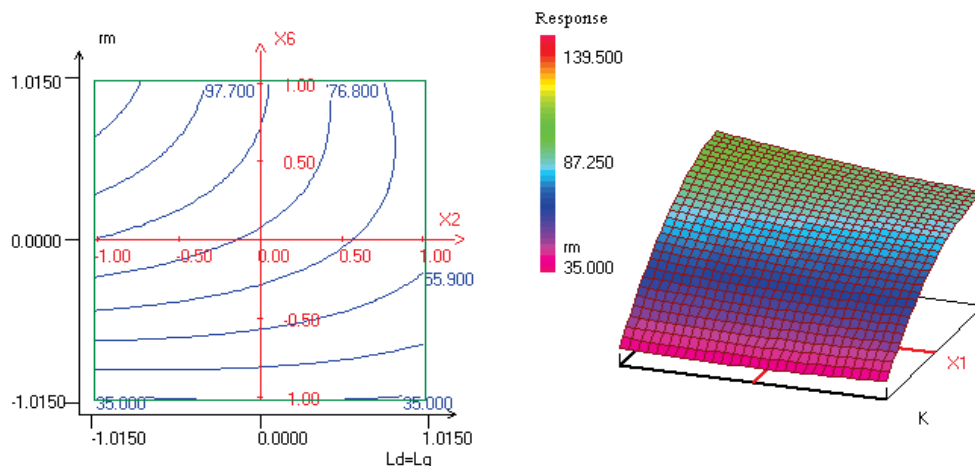


Fig. 11. Contour plot and response surface (Y) of the Torque gear ratio (r_m) and Stator d-q axes inductances (L_d & L_q).

An optimal result of control strategy on the electrical vehicle is obtained with NEMRODW software to obtain an optimal dynamic response. It is detailed on table 5.

Response	Before optimization	After optimization
Tr (Y1)	6.5s	4.65s
P (Y2)	42 Kw	58 Kw

Table 5. Optimization result

The optimal values of variables corresponding to the optimal dynamic response (Tr) and power (P) are resumed on table 6.

Variable	Factor	Optimal value in NEMRODW	Real values before optimization	Real values after optimization
X1	K	1.0094	0.1	0.2
X2	Ld=Lq	0.3976	0.416 mH	0.216 mH
X3	Ts	1.0086	300 μ s	500 μ s
X4	E	1.0052	300 V	400 V
X5	R	1.0061	0.05 Ω	0.08 Ω
X6	rm	0.9934	3	5

Table 6. Optimal values of variables

The speed response shows the good dynamic suggested of our vehicle. The reference speed is attained in 4.65 second. The direct current is equal to zero in the permanent mode, the quadratic current present the image of the electromagnetic torque. The power is increased to reach 58 kW.

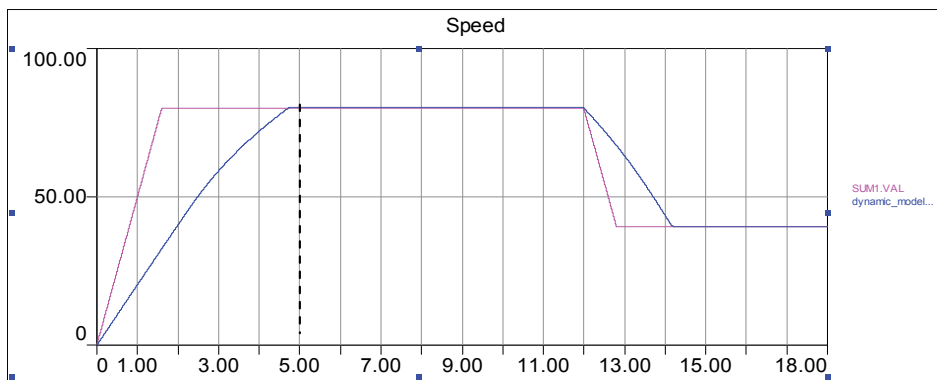


Fig. 10. Dynamic response of the vehicle speed after optimization

10. Conclusion

In this paper, we developed a VHDL-AMS description of a vehicle traction chain and we adopt the vector control $I_d=0$ strategy to drive the designed PMSM. The simulation of the dynamic response of the vehicle shows the effectiveness of this mode of control and the PMSM in the field of the electric traction. The obtained result with Simplorer differs from that obtained with Matlab because we used more accurate models. We think that VHDL-AMS is more suitable to predict the electric vehicle behavior since it is a multidisciplinary HDL. We have shown that response surface analysis coupled with a carefully constructed experimental design is a useful tool to carry out an Optimal Simulation of the Control Strategy of an Electrical Vehicle.

11. Nomenclature

- V_d, V_q Stator d- and q- axes voltages (V).
 i_d, i_q Stator d- and q- axes currents (A).

R	Stator resistance (Ω).
L_d, L_q	Stator d- and q- axes inductances (H).
p	Number of poles pairs.
Φ_m	Flux created by rotor magnets (Wb).
ω_m	Angular speed of the motor (rad/s).
f	Coefficient of rolling friction.
M_v	Total mass of the vehicle (kg).
g	Acceleration of terrestrial gravity (m/s^2).
l	Density of the air (kg/m^3).
S	Frontal surface of the vehicle (m^2).
C_x	Drag coefficient of the vehicle.
V	Speed of vehicle (m/s).
α	Angle that make the road with the horizontal (in $^\circ$).
r_m	Torque gear ratio.
R_{wheels}	Wheels radius (m).
T_{em}	Electromagnetic torque of the motor (N.m)
γ	Acceleration of the vehicle (s^{-2}).
T_l	Load torque (N.m).
E	Battery voltage
T_s	Switching period
V_{max}	Maximum speed

12. Appendix – Doehlert matrix (six factors)

N°Ex p	Factors						Responses $Y=\alpha/Y_1+\beta Y_2$		
	Ke	Ld=Lq [mH]	Ts [μ s]	E [V]	R [ohm]	rm	Y1(Tr) [s]	Y2(P) [Kw]	Response (Y)
1	-1	-1	-1	-1	-1	-1	12.62	13.08	35.582
2	1	-1	-1	-1	-1	1	12.10	52.80	60.600
3	-1	1	-1	-1	-1	1	12.08	20.00	40.973
4	1	1	-1	-1	-1	-1	12.64	12.78	35.358
5	-1	-1	1	-1	-1	1	4.80	58.00	107.710
6	1	-1	1	-1	-1	-1	12.67	12.72	35.256
7	-1	1	1	-1	-1	-1	12.63	12.85	35.422
8	1	1	1	-1	-1	1	12.09	24.70	43.770
9	-1	-1	-1	1	-1	1	3.89	100.00	149.974
10	1	-1	-1	1	-1	-1	12.63	12.50	35.212
11	-1	1	-1	1	-1	-1	12.64	13.00	35.490
12	1	1	-1	1	-1	1	6.60	39.86	76.946
13	-1	-1	1	1	-1	-1	12.64	12.80	35.370

14	1	-1	1	1	-1	1	4.00	98.00	146.300
15	-1	1	1	1	-1	1	6.40	40.00	78.687
16	1	1	1	1	-1	-1	12.64	12.68	35.298
17	-1	-1	-1	-1	1	1	4.71	60.00	110.310
18	1	-1	-1	-1	1	-1	12.66	12.24	35.000
19	-1	1	-1	-1	1	-1	12.66	12.28	35.014
20	1	1	-1	-1	1	1	12.15	20.00	40.806
21	-1	-1	1	-1	1	-1	12.65	12.27	35.030
22	1	-1	1	-1	1	1	12.16	50.00	58.783
23	-1	1	1	-1	1	1	12.02	21.00	41.720
24	1	1	1	-1	1	-1	12.65	12.27	35.030
25	-1	-1	-1	1	1	-1	12.66	12.90	35.386
26	1	-1	-1	1	1	1	4.00	96.80	145.580
27	-1	1	-1	1	1	1	6.24	40.00	80.090
28	1	1	-1	1	1	-1	12.64	12.34	39.094
29	-1	-1	1	1	1	1	3.96	101.00	148.983
30	1	-1	1	1	1	-1	12.65	12.36	35.084
31	-1	1	1	1	1	-1	12.64	12.47	35.172
32	1	1	1	1	1	1	6.28	40.40	79.972
33	-1	0	0	0	0	0	7.11	46.18	76.934
34	1	0	0	0	0	0	7.26	44.77	75.071
35	0	-1	0	0	0	0	6.71	60.40	88.401
36	0	1	0	0	0	0	9.12	31.00	57.000
37	0	0	-1	0	0	0	7.24	45.15	75.432
38	0	0	1	0	0	0	7.18	45.30	76.000
39	0	0	0	-1	0	0	9.14	30.55	56.623
40	0	0	0	1	0	0	6.72	58.37	87.105
41	0	0	0	0	-1	0	7.24	45.50	75.642
42	0	0	0	0	1	0	7.13	46.39	77.000
43	0	0	0	0	0	-1	12.65	12.55	35.198
44	0	0	0	0	0	1	5.73	46.70	89.102
45	0	0	0	0	0	0	7.16	46.00	76.480

13. References

- Jalalifar, M.; Payam, A. F.; Nezhad, S. & Moghbeli, H. (2007). Dynamic Modeling and Simulation of an Induction Motor with Adaptive Backstepping Design of an Input-Output Feedback Linearization Controller in Series Hybrid Electric Vehicle, *Serbian Journal of Electrical Engineering*, Vol.4, No.2, (November 2007), pp. 119-132.
- Feller, A. & Stephan, M. (2009). Modeling Germany' s Transition to the EV until 2040 in System Dynamics, *Thesis*, Vallendar, July 27, 2009.
- Jaber, K.; Fakhfakh, A. & Neji, R. (2010). High Level Optimization of Electric Vehicle Power-Train with Doehlert Experimental Design, *11 th International Workshop on Symbolic and Numerical Methods, Modeling and Applications to Circuit Design, Sm2ACD 2010*, pp. 908-911, ISBN 978-1-4244-5090-9, Tunis-Gammarth, Tunisia, 2010.

- Jaber, K.; Ben Saleh, B.; Fakhfakh, A. & Neji, R. (2009). Modeling and Simulation of electrical vehicle in VHDL-AMS, *16 th IEEE International Conference on, Electronics, Circuits, and Systems, ICECS 2009*, pp. 908-911, ISBN 978-1-4244-5090-9, Yasmine Hammamet, Tunisia, 2009.
- McDermott, T. E.; Juchem, R. & Devarajan, D. (2006). Distribution Feeder and Induction Motor Modeling with VHDL-AMS. 2006 IEEE/PES T&D Conference and Exposition Proceedings, 21-26 May 2006, Dallas.
- Fakhfakh, A., Feki, S., Hervé, Y., Walha, A. & Masmoudi, N., Virtual prototyping in power electronics using VHDL-AMS application to the direct torque control optimisation, *J. Appl. Sci.* 6, 2006, pp. 572-579.
- Sadeghi, S. & Mirsalim, M. (2010). Dynamic Modeling and Simulation of a Switched Reluctance Motor in a Series Hybrid Electric Vehicle, *International peer-reviewed scientific journal of Applied sciences*, Vol.7, No.1, (2010), pp. 51-71, ISBN 1785-8860.
- Dolecek, R.; Novak, J. & Cerny, O. (2009). Traction Permanent Magnet Synchronous Motor Torque Control with Flux Weakening. *Radioengineering*, VOL. 18, NO. 4, DECEMBER 2009.
- Ben Salah, B.; Moalla, A.; Tounsi, S.; Neji, R. & Sellami, F. (2008). Analytic Design of a Permanent Magnet Synchronous Motor Dedicated to EV Traction with a Wide Range of Speed Operation, *International Review of Electrical Engineering (I.R.E.E.)*, Vol.3, No.1, (2008), pp. 110-12.
- El Ati-Hellal, M.; Hellal, F.; Dachraoui, M. & Hedhili, A. (2009). Optimization of Sn determination in macroalgae by microwaves digestion and transversely heated furnace atomic absorption spectrometry analysis. *Canadian Journal of Analytical Sciences and Spectroscopy*, Vol.53, No.6, 2009.
- Elek, J.; Mangelings, D.; Joó, F. & V. Heyden, Y. (2004). Chemometric modelling of the catalytic Hydrogenation of bicarbonate to formate in aqueous Media, *Reaction Kinetics and Catalysis Letters*. Vol.83, No.2, (2004), pp. 321-328.
- Danion, A.; Bordes, C.; Disdier, J.; Gauvrit, J.Y.; Guillard, C.; Lantéri, P. & Renault, N. J. (2004). Optimization of a single TiO₂-coated optical fiber reactor using experimental design, *Elsevier, Journal of Photochemistry and Photobiology A: Chemistry*, Vol.168, No.3, (2004), pp. 161-167.
- El Hajjaji, S.; El Alaoui, M.; Simon, P.; Guenbour, A.; Ben Bachir, A.; Puech-Costes, E.; Maurette, M.-T. & Aries, L. (2005). Preparation and characterization of electrolytic alumina deposit on austenitic stainless steel. *Science and Technology of Advanced Materials*, Vol.6, No.5, (2005), pp. 519-524, ISSN 1468-6996.

Control of Hybrid Electrical Vehicles

Gheorghe Livinț, Vasile Horga, Marcel Rățoi and Mihai Albu
*Gheorghe Asachi Technical University of Iași
Romania*

1. Introduction

Developing cars is a major factor that has determined the increasing of the civilization degree and the continuous stimulation of the society progress. Currently, in Europe, one in five active people and in the US, one in four, directly work in the automotive industry (research, design, manufacture, maintenance) or in related domains (fuel, trade, traffic safety, roads, environmental protection). On our planet the number of the cars increases continuously and he nearly doubled in the last 10 years. With increasing number of cars entered in circulation every year, is held and increasing fuel consumption, increased environmental pollution due to emissions from internal combustion engines (ICE), used to their propulsion. Reducing oil consumption takes into account the limited availability of petroleum reserves and reducing emissions that affect the health of population in large urban agglomerations. The car needs a propulsion source to develop a maximum torque at zero speed. This can not be achieved with the classic ICE. For ICE power conversion efficiency is weak at low speeds and it has the highest values close to the rated speed. Pollution reduction can be achieved by using electric vehicles (EV), whose number is still significant. The idea of an electrical powered vehicle (EV) has been around for almost 200 years. The first electric vehicle was built by Thomas Davenport in 1834 [Westbrook, 2005]] But over time, the batteries used for energy storage could provide the amount of electricity needed to fully electric propulsion vehicles. Electric vehicles are powered by electric batteries which are charged at stations from sources supplied by electrical network with electricity produced in power plants. Currently, a lot of researches are focused on the possibility of using fuel cells for producing energy from hydrogen. EV with fuel cell can be a competitive alternative to the standard ICE that is used in today's cars. If performance is assessed overall thrust of the effort wheel and crude oil consumed for the two solutions: classic car with ICE and car with electric motor powered by electric batteries, the difference between their yields is not spectacular. In terms of exhaust emissions is the net advantage for electric vehicles. Pollutant emissions due to energy that is produced in power plants (plant property, located) are much easier to control than those produced by internal combustion engines of vehicles that are individual and scattered. Power plants are usually located outside urban areas, their emissions affects fewer people living in these cities. By using electric motors and controllers efficient, electric vehicles provide the means to achieve a clean and efficient urban transport system and a friendly environment. Electric vehicles are zero emission vehicles, called ZEV type vehicles (Zero-Emissions Vehicles).

Any vehicle that has more than one power source can be considered hybrid electric vehicle (HEV). But this name is used most often for a vehicle using for propulsion a combination of an electric drive motor and an ICE, which energy source is fossil fuel. The first patent for involving HEV technology was filed in 1905 by the American H. Piper. The change of focus to hybrid technology was done by almost all vehicle manufacturers. Many prototypes and a few mass produced vehicles are now available. For example, there were 23 hybrid electric presented at the North American International Auto Show (NAIAS) in 2000 [Wyczalek, 2000].

There are several configurations of electric and hybrid vehicles [Bayindir, 2011, Ehsani, 2005]: 1. electric vehicles equipped with electric batteries and/or supercapacitors called BEV (Battery Electric Vehicles), 2. hybrid electric vehicles which combine conventional propulsion based on ICE engine with petroleum fuel and electric propulsion with motor powered by batteries or supercapacitors called HEV (Hybrid Electric Vehicles), 3. electric vehicles equipped with fuel cells, called FCEV (Fuel Cell Electric Vehicles).

Concept of hybrid electric vehicle with ICE-electric motor aims to overcome the disadvantages of the pure electric vehicles, whose engines are powered by electric batteries: the limited duration of use (low autonomy) and time recharging for batteries.

2. Hybrid electric vehicles

A hybrid electric vehicle is distinguished from a standard ICE driven by four different parts: a) a device to store a large amount of electrical energy, b) an electrical machine to convert electrical power into mechanical torque on the wheels, c) a modified ICE adapted to hybrid electric use, d) a transmission system between the two different propulsion techniques. Figure 1 shows the possible subsystems of a hybrid vehicle configuration [Chan, 2002], [Ehsani, 2005]

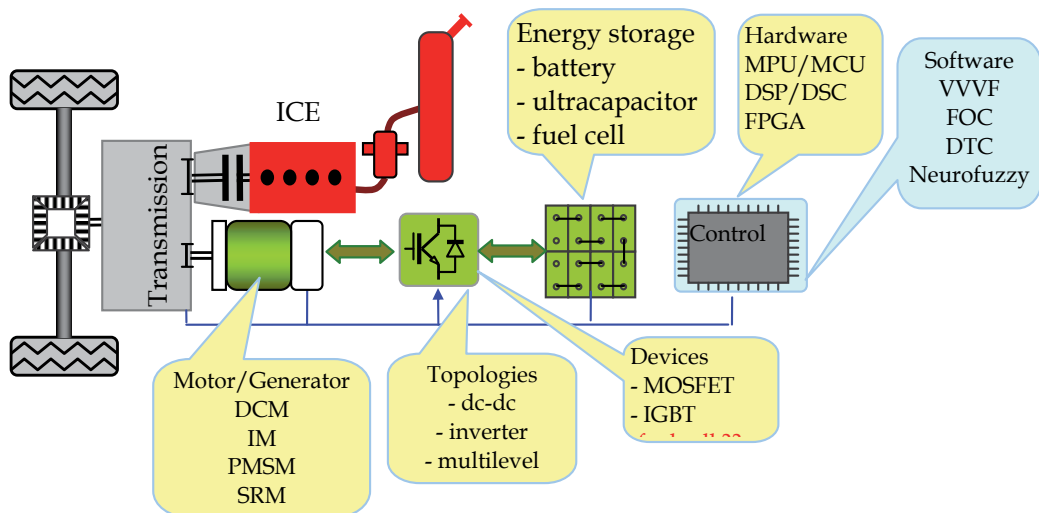


Fig. 1. Main components of a hybrid electric vehicle

The devices used to store electrical energy could be batteries, hydrogen powered fuel cell or supercapacitors. Electric motors used on hybrid vehicles are [Husain 2003], [Fuhs, 2009]: DC motors, induction motors (IM), permanent magnet synchronous motors (PMSM) or switching reluctance motors (SRM). The HEV can use the electrical machine to behave as a generator and thereby produce electrical energy, which can be stored and used later. The ICE may be the same type as those on conventional vehicles, but it must be designed and optimized for hybrid vehicles. The transmission system between the ICE and the electrical machine is typically of series or parallel architecture. For power electronics are used MOSFET or IGBT transistors, and the command can be done with microprocessor, microcontroller or DSP using various techniques (VVVF - variable voltage and variable frequency, FOC -field oriented control, AC - adaptive control, NC - neural control or FC- fuzzy control).

Electric vehicles with two energy sources are also called hybrid vehicles. On hybrid-electric vehicles, in addition to the main battery, special batteries or capacitors, as a secondary energy source are used. These secondary energy sources are designed to provide power for short periods of peak operating conditions - for example, during the ascent of a slope or during acceleration. This is necessary because some batteries with the highest energy density have low power density. Since power density is required at least 150 [W/kg] for a good acceleration and slope climbing performance, a secondary source with high power density is essential. This power density is easily obtained from a lead-based battery and this is an auxiliary battery that is suitable for use with an aluminum-air battery in a hybrid-electric vehicle.

A combination of hybrid electric vehicle that is under development and of great interest, thanks to improvements in fuel cell, is the electric vehicle powered with fuel cell and an auxiliary battery. This battery can provide a high current necessary to start and can also serve as a load limiting device which allows the fuel cell to operate at low power first and then warm for a high power operation. This arrangement enhances the efficiency of the entire system and also allows the vehicle to use the recuperative braking.

Another class of hybrid electric vehicles, called hybrid electromechanical vehicles, use in addition to the main electric drive powered by batteries and a mechanical energy storage device such as a flywheel, or a hydraulic accumulator [Westbrook, 2005]. Hybrid electric vehicles represents a bridge between the present vehicle powered by ICEs and vehicles of the future characterized by a near-zero emissions, ULEV (Ultra-Low-Emission-Vehicle) or, in some cases even without pollution (ZEV-Zero-Emission Vehicle), as it is expected to be electrically propelled vehicles powered by fuel cells supplied with hydrogen.

It is very important to be reminded that without taking the technology steps and to improve the hybrid propulsion systems it is not possible to achieve higher level of the propulsion technology which uses fuel cells.

Currently a number of construction companies sell hybrid electric vehicles in series production: Toyota, Honda, Ford, General Motors. Many other companies have made prototypes of hybrid electric vehicles, the shift in mass production is only a matter of time that depends on the improvement of operating parameters and manufacturing cost reductions. Regarding the line of a hybrid electric vehicle powertrain, it is complex in terms of construction, operation and electronic control system than the most evolved similar vehicle equipped with conventional internal combustion engine.

Viewed from the standpoint of integration components, hybrid electric vehicle represents, compared with the vehicle solution powered ICE, an increase of complexity approximately 25%, while in terms of system control input hardware and software is at least double. These new elements make the price a such vehicle to be higher than that of a vehicle powered

only by internal combustion engine. Thus, as shown in [Ehsani, 2005] the first vehicle (car) series hybrid electric Toyota designed by the company line is the most sophisticated and most advanced integrated powertrain control strategy of the firm ever made known to promote ideas of great ingenuity and technical complexity.

2.1 Architectures of hybrid electric drive trains

The architecture of a hybrid vehicle is defined as the connection between the components of the energy flow routes and control ports. Hybrid electric vehicles were classified into two basic types: series and parallel. But presently HEVs are classified into four kinds: series hybrid, parallel hybrid, series-parallel hybrid and complex. The primary power source (steady power source) is made up of fuel tank and ICE and battery-electric motor is taken as secondary source (dynamic power source).

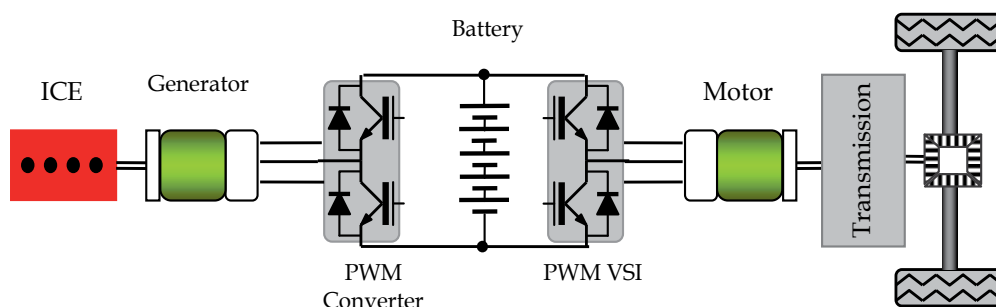


Fig. 2. Series HEV

A series hybrid drive train uses two power sources which feeds a single powerplant (electric motor) that propels the vehicle. In Figure 2 is shown a series hybrid electric drive train where: fuel tank is an unidirectional energy source and the ICE coupled to an electric generator is a unidirectional energy converter. The electric generator is connected to an electric power bus through an electronic converter (rectifier). Electrochemical battery pack is the bidirectional energy source and is connected to the power bus by means of a power electronics converter (DC/DC converter). Also the electric power bus is connected to the controller of the electric traction motor. The traction motor can be controlled either as a motor (when propels the vehicle) or as generator (to vehicle braking). A battery charger can charge batteries with the energy provided by an electrical network.

The possible operating modes of series hybrid electric drive trains are [Ehsani, 2005]: 1. Pure electric: ICE is stopped and the vehicle is propelled only by batteries energy, 2. Pure engine mode: the vehicle is powered with energy provided by electric generator driven by engine. The batteries no provide and do not take energy from the drive train. 3. Hybrid mode: The traction power is drawn from both the engine-generator and the batteries. 4. Engine traction and battery charging mode: The ICE-generator provides the energy needed for the batteries charging and the propulsion vehicle. 5. Regenerative braking mode: the engine is turned off and the traction motor is operated as generator and the energy provided is used to charge the batteries. 6. Batteries charging mode: The engine - generator charges the batteries and the traction motor is not supplied. 7. Hybrid batteries

charging mode: Both the engine-generator and the traction motor operate as generator to charge the batteries.

For series hybrid drive trains the following advantages can be mentioned: 1. Because the ICE is mechanical decoupled from the driven wheels and thus the ICE can operate solely within its maximum efficiency region, at a high-speed where and the emissions are reduced. 2. Electric motors have near-ideal torque-speed characteristics and multigear transmissions are not necessary. 3. The electrical transmission provides the mechanical decoupling and allows the using of a simple control strategy. The series hybrid electric drive trains have some disadvantages: 1. The mechanical energy of the ICE is first converted to electrical energy in the generator and the output energy of generator is converted into mechanical energy in the traction motor. The losses in the generator and the traction motor may be significant and these reduce the system efficiency. 2. The generator adds additional weight and cost. 3. The traction motor must be designed to meet maximum requirements, because only it is used for the vehicle propulsion.

Series hybrid electric vehicles applications include TEMSA – Avenue hybrid bus, Mercedes-Citaro bus and MAN-Lion’s City Hybrid bus. Series hybrid configuration is mostly used in heavy vehicles, military vehicles and buses [Bayindir, 2011].

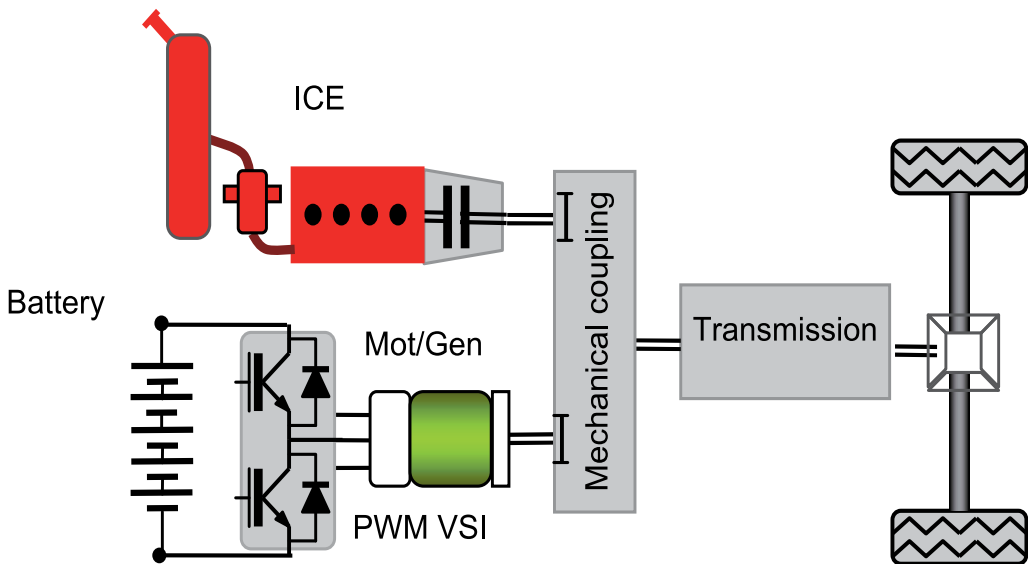


Fig. 3. Parallel HEV

In the parallel configuration the power of the ICE and the electric motor are added into mechanical coupling, as shown in Figure 3 and operate the drive train by the mechanical transmission. There are different combination of the engine and electric motor power:

1. Torque-coupling parallel hybrid electric drive trains, 2. Speed-coupling parallel hybrid electric drive trains, 3. Torque-coupling and speed-coupling parallel hybrid electric drive trains. The torque coupling adds the torques of the engine T_{in1} , and the electric motor, T_{in2} , together or splits the engine torque into two parts: vehicle propelling and battery is charging. In this case the output torque, T_{out} , and speed, ω_{out} , can be described by

$$T_{out} = k_1 T_{in1} + k_2 T_{in2} \quad , \quad \omega_{out} = \frac{\omega_1}{k_1} = \frac{\omega_2}{k_2} \quad (1)$$

where k_1 and k_2 are the constants determined by the parameters of torque coupling. The speed coupling adds the speeds of the engine, ω_{in1} , and the electric motor, ω_{in2} , together by coupling their speeds. The output speed ω_{out} and torque, T_{out} , can be described by:

$$\omega_{out} = k_1 \omega_{in1} + k_2 \omega_{in2} \quad , \quad T_{out} = \frac{T_{in1}}{k_1} + \frac{T_{in2}}{k_2} \quad (2)$$

where k_1 and k_2 are the constants determined by the parameters of speed coupling. In parallel hybrid electric vehicle various control strategies can be used. In the most common strategies, ICE is used in on mode and operates at almost constant power output at its area of maximum efficiency. If the power requested from drive train is higher than the output power of ICE, the electric motor is turned on, ICE and electric motor supply power to the drive train. If the power requested from drive train is less than the output power of the ICE, the remaining power is used for charging the batteries. In this configuration, regenerative braking power on a down slope driving is used to charge the batteries. Examples of the parallel hybrid electric vehicles are [Fuhs, 2009]: Insight model introduced by Honda, Ford Escape Hybrid SUV and Lexus Hybrid SUV.

3. Energy storage for HEV

For hybrid electric vehicles three electromechanical devices are important: batteries supercapacitors and fuel cells (FC). The batteries provide storage of energy that is essential for regenerative braking. Also the batteries are a source of energy that is necessary for electric-only propulsion. Supercapacitors, which have the similar capability, are high-power and low-stored-energy devices. Supercapacitors are used to improve high power peak for short duration. Batteries are heavy and repeated deep discharge adversely affects life. Batteries have much better performance as a provider of peak power for hybrid electric vehicle and/or fuel cell vehicle.

The fuel cell (FC) system has a fuel tank and stores energy in the form of hydrogen. An FC can be used for electric-only propulsion and it cannot be used for regenerative braking.

The batteries can be classified in primary batteries, which cannot be recharged, and secondary batteries, which have reversible reactions and can be charged and discharged. The basic unit of a battery is the voltaic cell. Voltaic cells have the following components parts: the electrodes: anode and cathode, and the electrolyte. Batteries are composed of collections of cells. Each cell has a voltage which depends of the electrochemical potential of the chemicals. Lead acid has a cell potential of 2 V, and Nickel metal hydride (NiMH) has cell potential of 1.2 V. The cells are connected in series for increasing the voltage. Batteries are described by four quantitative features: current, voltage, energy and power. Capacity (C) is the charge that can be taken from the battery under certain conditions, so is the amount of electricity that a battery can provide in continuous discharging. A constant current battery capacity is a function of current values to which they discharge. Battery capacity is expressed in the [Ah] and is given by $C = \int I_d dt$ where I_d is the discharge current and t is the

time of discharge. If the discharge is made at constant current, $C = I_d t$. Cell capacity, C , is determined partially by the mass of available reactants.

3.1 Batteries characteristics

The main batteries characteristics are: specific energy, specific power, self discharge, life, state of charge (SOC).

Specific energy is the ratio between the energy provided of battery and its weight and is expressed in [Wh/kg]. It should be noted that the specific energy storage of gasoline is about 11000 [Wh/kg] versus 90 [Wh/kg] representing a peak through the current batteries. It is noted that lead-based batteries have the lowest energy density as lithium batteries have the highest energy densities. **Specific power**, expressed in [W/kg] or [W/l] represents the ratio between the battery power and its weight or between battery power and its volume. Self discharge consists in the battery power loss due to internal reactions during storage/non-use them, when the external circuit is open (missing load). Self discharge rate depends on battery type, temperature and battery age. Life (number of cycles) is expressed in number of cycles, i.e. the number of complete charge and discharge (until the final voltage permissible or until capacity drops below 80% of initial capacity) that the battery can handle. State of charge - SOC is the ratio of the electric charge Q than can be delivered by the battery at current I , to the nominal battery capacity Q_0

$$SOC = \frac{Q(t)}{Q_0} = \frac{Q_0 - It}{Q_0} \quad (3)$$

Knowing the energy remaining from the initial energy, we get an indication of the time as the battery will continue to work before its charging. SOC decreases as the battery supplies a load and increase SOC when the battery is charging. Note that the SOC does not refer to the maximum capacity that the battery was last charged, but to the initial battery capacity. The degree of discharge (Depth of Discharge - DOD) on each cycle represents the percentage of energy discharged / removed from the battery to each discharge.

3.2 Batteries models used in hybrid electric vehicles

The simplest electrical battery-model is presented in Figure 4.a. It consists of an ideal voltage source V_{OC} , a constant equivalent internal resistance R_i and the terminal voltage represented by V_O [Livint et. al. 2007]. However, the internal resistance is different under discharge and charge conditions. This model does not capture the internal dynamics of the battery, in particular the effect of the diffusion of the electrolytic chemicals between the battery plates. The circuit can be modified as shown in Figure 4.b. for the account the different resistance values under charge and discharge conditions, R_c and R_d . The diodes shown in Figure 4.b have no physical significance in the battery and are included only for modeling purposes.

In order to model the diffusion of the electrolytic through the battery and its resultant effect of causing transient currents in the battery, a capacitor C is added to the model. A dynamical model of the lead-acid battery, presented in Figure 4.c, shows a simplified equivalent circuit proposed in [Livint et al., 2006].

The cell terminal voltage is represented by V_O , and R_i is a lumped resistance due to cell interconnections. A double layer capacitance C_s (surface-capacitor) is shown in parallel with the charge transfer polarization represented by R_t . This double layer capacitor is the results of charge separation at the electrolyte/electrode interface.

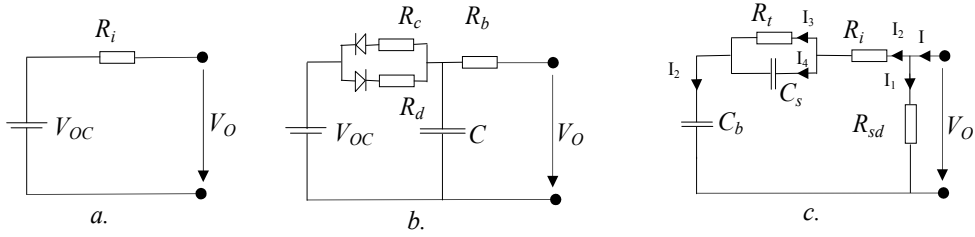


Fig. 4. a. Simple battery model; b. Battery model with the different charging and discharging resistance values and polarization capacitance; c. Simplified equivalent circuit of a lead acid battery

The bulk capacitor C_b models the cell's open circuit voltage, and R_{sd} is included to represent the self-discharge of the cell.

Voltages and currents describing the characteristics of the model shown in Fig.4.c are given by equations

$$\begin{aligned}
 V_O &= R_i I_2 + V_{C_s} + V_{C_b} = R_{sd} I_1 \\
 V_{C_s} &= \frac{1}{C_s} \int I_4 dt = R_i I_3 \\
 V_{C_b} &= \frac{1}{C_b} \int I_2 dt \\
 I &= I_1 + I_2; I_2 = I_3 + I_4
 \end{aligned} \tag{4}$$

where V_{C_b} and V_{C_s} denote the voltages across the bulk- and surface-capacitors, respectively

Taking as state variables the voltages V_O , V_{C_s} , V_{C_b} and assuming that $\frac{dI_2}{dt} \approx 0$ (the rate of change of terminal current per sampling interval, when implemented digitally, is negligible) the complete state variable description (the state model of battery) is obtained:

$$\begin{aligned}
 \begin{bmatrix} \dot{V}_O \\ \dot{V}_{C_s} \\ \dot{V}_{C_b} \end{bmatrix} &= \begin{bmatrix} -\frac{1}{R_{sd}} \left(\frac{1}{C_s} + \frac{1}{C_b} \right) & -\frac{1}{R_i C_s} & 0 \\ -\frac{1}{R_{sd} C_s} & -\frac{1}{R_i C_s} & 0 \\ -\frac{1}{R_{sd} C_b} & 0 & 0 \end{bmatrix} \begin{bmatrix} V_O \\ V_{C_s} \\ V_{C_b} \end{bmatrix} = \begin{bmatrix} \frac{1}{C_s} + \frac{1}{C_b} \\ \frac{1}{C_s} \\ \frac{1}{C_b} \end{bmatrix} I \\
 y = V_O &= [1 \ 0 \ 0] [V_O \ V_{C_s} \ V_{C_b}]^T
 \end{aligned} \tag{5}$$

The control strategies for hybrid and electric vehicles are based on SOC knowledge. The batteries behavior can be modeled with different electrical circuit structures and different linear or nonlinear mathematical models. The different estimation methods can be used for the batteries parameters determination. The method based on continue time model and LIF algorithm assures a good accuracy for parameters estimation. The estimated parameters can be used for the battery SOC determination.

4. Electric motors used for hybrid electric vehicles propulsion

4.1 Motor characteristics versus electric traction selection

The electric motors can operate in two modes: a) as motor which convert electrical energy taken from a source (electric generator, battery, fuel cell) into mechanical energy used to propel the vehicle, b) as generator which convert the mechanical energy taken from a motor (ICE, the wheels during vehicle braking, etc..) in electrical energy used for charging the battery. The motors are the only propulsion system for electric vehicles. Hybrid electric vehicles have two propulsion systems: ICE and electric motor, which can be used in different configurations: serial, parallel, mixed. Compared with ICE electric motors has some important advantages: they produce large amounts couples at low speeds, the instantaneous power values exceed 2-3 times the rated ICE, torque values are easily reproducible, adjustment speed limits are higher. With these characteristics ensure good dynamic performance: large accelerations and small time both at startup and braking.

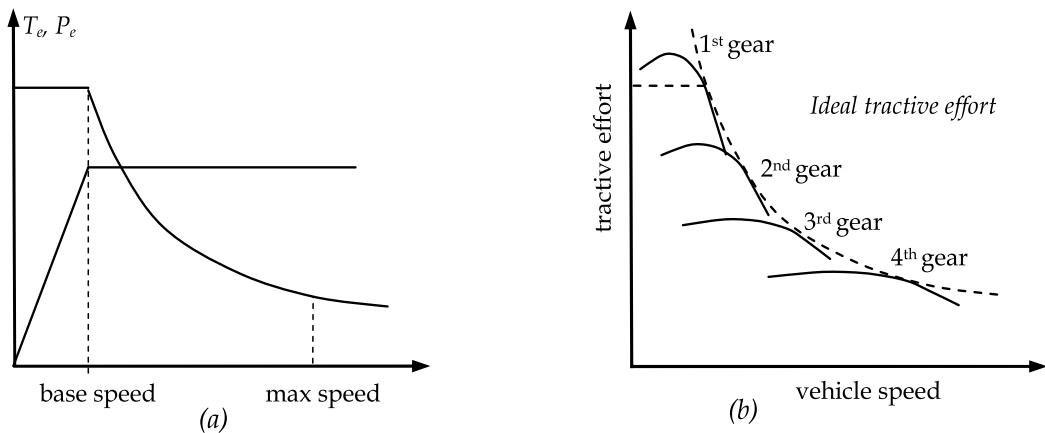


Fig. 5. a. Characteristics of traction motors ; b. Tractive effort characteristics of an ICE vehicle

Figure 5.a illustrates the standard characteristics of an electric motor used in EVs or HEVs. Indeed, in the constant-torque region, the electric motor exerts a constant torque (rated torque) over the entire speed range until the rated speed is reached. Beyond the rated speed of the motor, the torque will decrease proportionally with speed, resulting in a constant power (rated power) output. The constant-power region eventually degrades at high speeds, in which the torque decreases proportionally with the square of the speed. This characteristic corresponds to the profile of the tractive effort versus the speed on the driven wheels [Figure 5. b.]. This profile is derived from the characteristics of the power source and the transmission. Basically, for a power source with a given power rating, the profile of the tractive effort versus the speed should be a constant.

The power of the electric motor on a parallel type hybrid vehicle decisively influences the dynamic performance and fuel consumption. The ratio of the maximum power the electric motor, P_{EM} , and ICE power P_{ICE} is characterized by hybridization factor which is defined by the relation HF

$$HF = \frac{P_{EM}}{P_{EM} + P_{ICE}} = \frac{P_{EM}}{P_{HEV}} \quad (6)$$

where P_{HEV} is the maximum total traction power for vehicle propulsion. It is demonstrated that it reduces fuel consumption and increase the dynamic performance of a hybridization factor optimal point more than one critic ($HF=0.3 \div 0.5$) above the optimal point increase in ICE power hybrid electric vehicle does not improve performance.

The major requirements of HEVs electric propulsion, as mentioned in literature, are summarized as follows [Chan 2005], [Husain 2003], [Ehsani 2005]:

1. a high instant power and a high power density;
2. a high torque at low speeds for starting and climbing, as well as a high power at high speed for cruising;
3. a very wide speed range, including constant-torque and constant-power regions;
4. a fast torque response;
5. a high efficiency over the wide speed and torque ranges;
6. a high efficiency for regenerative braking;
7. a high reliability and robustness for various vehicle operating conditions; and
8. a reasonable cost.

Moreover, in the event of a faulty operation, the electric propulsion should be fault tolerant . Finally, from an industrial point of view, an additional selection criterion is the market acceptance degree of each motor type, which is closely associated with the comparative availability and cost of its associated power converter technology [Emadi 2005].

4.2 Induction motors used in hybrid electric vehicles

4.2.1 Steady state operation of induction motor

Induction motor is the most widely used ac motor in the industry. An induction motor like any other rotating machine consists of a stator (the fixed part) and a rotor (the moving part) separated by air gap. The stator contains electrical windings housed in axial slots. Each phase on the stator has distributed winding, consisting of several coils distributed in a number of slots. The distributed winding results in magnetomotive forces (MMF) due to the current in the winding with a stepped waveform similar to a sine wave. In three-phase machine the three windings have spatial displacement of 120 degrees between them. When balanced three phase currents are applied to these windings, the resultant MMF in the air gap has constant magnitude and rotates at an angular speed of $\omega_s = 2\pi f_s$ electrical radians per second. Here f_s is the frequency of the supply current. The actual speed of rotation of magnetic field depends on the number of poles in the motor. This speed is known as synchronous speed Ω_s of the motor and is given by

$$\Omega_s = \frac{\omega_s}{p} = \frac{2\pi f_s}{p} = \frac{2\pi n_s}{60}; \quad n_s = \frac{60 f_s}{p} \quad (7)$$

where p is number of pole pairs, n_s [rpm], is the synchronous speed of rotating field.

If the rotor of an induction motor has a winding similar to the stator it is known as wound rotor machine. These windings are connected to slip rings mounted on the rotor. There are stationary brushes touching the slip rings through which external electrical connected. The wound rotor machines are used with external resistances connected to their rotor circuit at

the time of starting to get higher starting torque. After the motor is started the slip rings are short circuited. Another type of rotor construction is known as squirrel cage type rotor. In this construction the rotor slots have bars of copper or aluminium shorted together at each end of rotor by end rings. In normal running there is no difference between a cage type or wound rotor machine as far as their electrical characteristics are concerned.

When the stator is energized from a three phase supply a rotating magnetic field is produced in the air gap. The magnetic flux from this field induces voltages in both the stator and rotor windings. The electromagnetic torque resulting from the interaction of the currents in the rotor circuit (since it is shorted) and the air gap flux, results in rotation of rotor. Since electromotive force in the rotor can be induced only when there is a relative motion between air gap field and rotor, the rotor rotates in the same direction as the magnetic field, but it will not run at synchronous speed. An induction motor therefore always runs at a speed less than synchronous speed. The difference between rotor speed and synchronous speed is known as slip. The slip s is given by

$$s = \frac{\Omega_s - \Omega}{\Omega_s} = \frac{\Omega_{sl}}{\Omega_s} = 1 - \frac{\Omega}{\Omega_e}; \text{ or } s = \frac{n_s - n}{n_s} = \frac{n_{sl}}{n_s} = 1 - \frac{n}{n_s} \quad (8)$$

where: n [rpm] is the speed of the rotor.

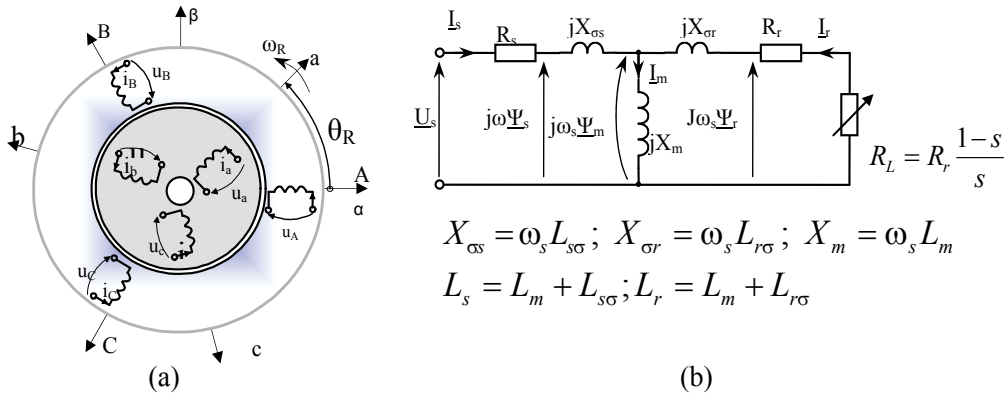


Fig. 6. Cross section of an induction motor (a); Equivalent circuit of an IM (b)

The steady state characteristics of induction machines can be derived from its equivalent circuit. In order to develop a per phase equivalent circuit of a three-phase machine, a wound rotor motor as shown in Figure 6.a. is considered here. In case of a squirrel cage motor, the rotor circuit can be replaced by an equivalent three-phase winding. When three-phase balanced voltages are applied to the stator, the currents flow in them. The equivalent circuit, therefore is identical to that of a transformer, and is shown in Figure 6. b. Here R_s is the stator winding resistance, L_s is self inductance of stator, L_r is self inductance of rotor winding referred to stator, R_r is rotor resistance referred to stator, L_m is magnetizing inductance and s is the slip. The parameters of the equivalent circuit are the stator and rotor leakage reactances $X_{\sigma s}$ and $X_{\sigma r}$, magnetizing reactance X_m , and the equivalent resistance

$$R_L = \frac{1-s}{s} R_r \text{ which depends on the slip } s.$$

The ohmic losses on this "virtual" resistance, R_L , represent the output mechanical power, P_{mec} , transferred to the load. Thus the electromagnetic torque, T_e , is given as

$$T_e = \frac{P_{mec}}{\Omega} = \frac{3p}{(1-s)\omega_s} \frac{(1-s)R_r}{s} I_r^2 = \frac{3p}{\omega_s} \frac{R_r}{s} I_r^2 \quad (9)$$

If statoric leakage reactance is neglected it results

$$T_e = 3p \left(\frac{U_s}{\omega_s} \right)^2 \frac{R_r s}{R_r^2 + (\omega_s L_{r\sigma})^2} \quad (10)$$

For applications where high degree of accuracy in speed control is not required simple methods based on steady state equivalent circuit have been employed. Since the speed of an induction motor, n , in revolutions per minute is given by

$$n = \frac{60 f_s}{p} (1-s) \quad (11)$$

Thus the speed of the motor can be changed by controlling the frequency, or number of poles or the slip. Since, number of poles of a motor is fixed at the time of construction, special motors are required with provision of pole changing windings.

4.2.2 The dynamic model of the induction motor

The dynamic model of ac machine can be developed [Ehsani, 2005], [Husain, 2003], using the concept of "space vectors". Space vectors of three-phase variables, such as the voltage, current, or flux, are very convenient for the analysis and control of ac motors and power converter. A three-phase system defined by $y_A(t)$, $y_B(t)$, and $y_C(t)$ can be represented uniquely by a rotating vector $\underline{y}(t)$ in the complex plane.

$$\underline{y}(t) = \frac{2}{3} (y_A(t) + a \cdot y_B(t) + a^2 \cdot y_C(t)) = y_D(t) + j \cdot y_Q(t) \quad (12)$$

where $a = e^{j(2\pi/3)}$

Under simplifying assumptions (symmetrical windings with sinusoidal distribution, negligible cross-section of the conductors, ideal magnetic circuit) the induction squirrel cage machine may be described in an arbitrary synchronous reference frame, at ω_g speed, by the following complex space vector equations [Livint et al 2006]:

$$\left\{ \begin{array}{l} \underline{u}_{sg} = R_s \cdot \dot{\underline{i}}_{sg} + \frac{d\underline{\psi}_{sg}}{dt} + j\omega_g \underline{\psi}_{sg}; \quad 0 = R_r \cdot \dot{\underline{i}}_{rg} + \frac{d\underline{\psi}_{rg}}{dt} + j(\omega_g - \omega_r) \underline{\psi}_{rg} \\ \underline{\psi}_{sg} = L_s \dot{\underline{i}}_{sg} + L_m \dot{\underline{i}}_{rg}; \quad \underline{\psi}_{rg} = L_m \dot{\underline{i}}_{sg} + L_r \dot{\underline{i}}_{rg} \\ t_e = -\frac{3}{2} p L_m \dot{\underline{i}}_{sg} \times \dot{\underline{i}}_{rg}; \quad J \frac{d\Omega}{dt} = t_e - D\Omega - t_l \end{array} \right. \quad (13)$$

where: $\underline{x}_{sg} = \underline{x}_s e^{-j\theta_s}$; $\underline{x}_{rg} = \underline{x}_r e^{-j(\theta_s - \theta_r)}$; $\omega_g = \frac{d\theta_g}{dt}$ - speed of the arbitrary reference frame,

$\omega_r = p\Omega = \frac{d\theta_r}{dt}$ - speed of the rotor reference frame.

In order to achieve the motor model in stator reference frame on impose $\omega_g=0$, in equations (13).

4.3 Power converters

Power converters play a vital role in Hybrid Electric Vehicle (HEV) systems. Typical HEV drive train consists of a battery, power converter, and a traction motor to drive the vehicle. The power converter could be just a traditional inverter or a dc-dc converter plus an inverter. The latter configuration provides more flexibility and improves the system performance. The dc-dc converter in this system interfaces the battery and the inverter dc bus, and usually is a variable voltage converter so that the inverter can always operate at its optimum operating point. In most commercially available systems, traditional boost converters are used. A power converter architecture is presented in Figure 7.

Voltage source inverters (VSI) are used in hybrid vehicles to control the electric motors and generators. The switches are usually IGBTs for high-voltage high power hybrid configurations, or MOSFETs for low-voltage designs. The output of VSI is controlled by means of a pulse-width-modulated (PWM) signal to produce sinusoidal waveform. Certain harmonics exist in such a switching scheme. High switching frequency is used to move the harmonics away from the fundamental frequency.

A three-phase machine being feed from a VSI receives the symmetrical rectangular three-phase voltages shown in Figure 8.a. Inserting these phase voltage in the space vector definition of stator voltage $\underline{u}_s(t) = \frac{2}{3}(u_{sA}(t) + \underline{a}u_{sB}(t) + \underline{a}^2u_{sC}(t))$, yields the typical set of six active switching state vectors $U_1 \dots U_6$ and two zero vectors U_0 and U_7 as shown in Figure 8.b.

$$\underline{u}_s = \begin{cases} \frac{2}{3}U_{dc}e^{j \cdot k \cdot 2\pi/3} & k = 1, \dots, 6 \\ 0 & k = 0, 7 \end{cases} \quad (14)$$

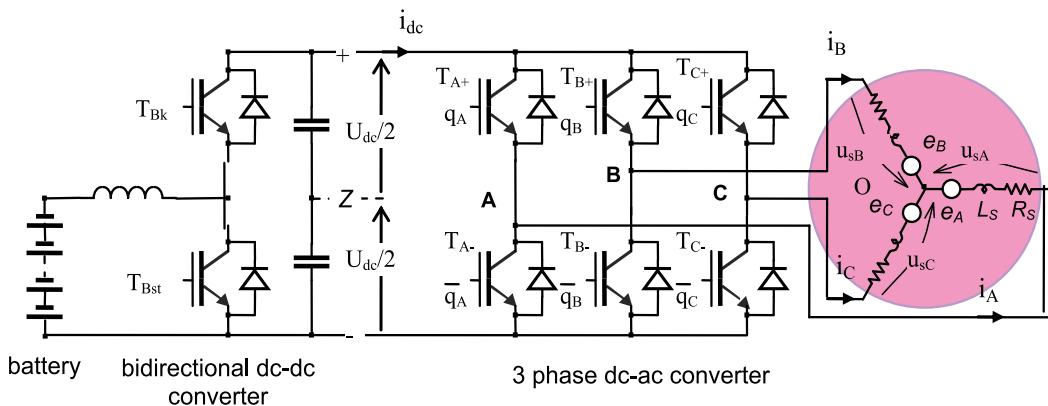


Fig. 7. Power converter architecture

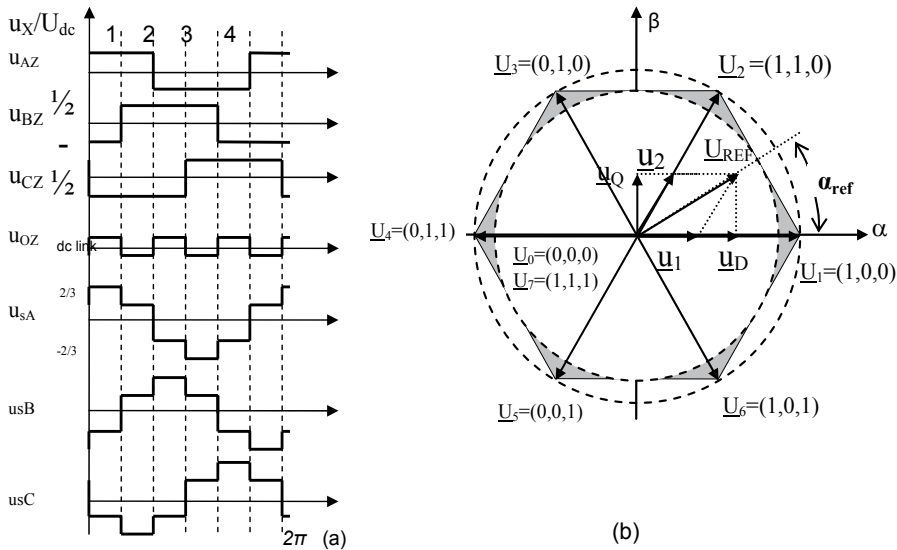


Fig. 8. a. Switched three-phase waveforms ; b. Switching state vectors

5. Control strategies

A number of control strategies can be used in a drive train for vehicles with different mission requirements. The control objectives of the hybrid electric vehicles are [Ehsani, 2005]: 1) to meet the power demand of the driver, 2) to operate each component of the vehicle with optimal efficiency, 3) to recover braking energy as much as possible, 4) to maintain the state-of-charge (SOC) of the battery in a preset window.

The induction motor drive on EV and HEV is supplied by a DC source (battery, fuel cell,) which has a constant terminal voltage, and a DC/AC inverter that provide a variable frequency and variable voltage . The DC/AC inverter is constituted by power electronic switches and power diodes.

As control strategies PWM control is used for DC motor, FOC (field-oriented control) and DTC (direct torque control) are used for induction motors. The control algorithms used are the classical control PID, but and the modern high-performance control techniques: adaptive control, fuzzy control, neuro network control [Seref 2010], [Ehsani 2005], [Livint et al 2008a, 2008c].

5.1 Structures for speed scalar control of induction motor

5.1.1 Voltage and frequency (Volts/Hz) control

Equation (11) indicates that the speed of an induction motor can be controlled by varying the supply frequency f_s . PWM inverters are available that can easily provide variable frequency supply with good quality output wave shape. The open loop volts/Hz control is therefore quite popular method of speed control for induction motor drives where high accuracy in control is not required. The frequency control also requires proportional control in applied voltage, because then the stator flux $\Psi_s = U_s / \omega_s$ (neglecting the resistance drop) remains constant. Otherwise, if frequency alone is controlled, then the flux will change.

When frequency is increased, the flux will decrease, and the torque developed by the motor will decrease as shown in Figure 9.a. When frequency is decreased, the flux will increase and may lead to the saturation of magnetic circuit. Since in PWM inverters the voltage and frequency can be controlled independently, these drives are fed from a PWM inverter.

The control scheme is simple as shown in Figure 9.b with motor being supplied by three-phase supply dc-link and PWM inverter.

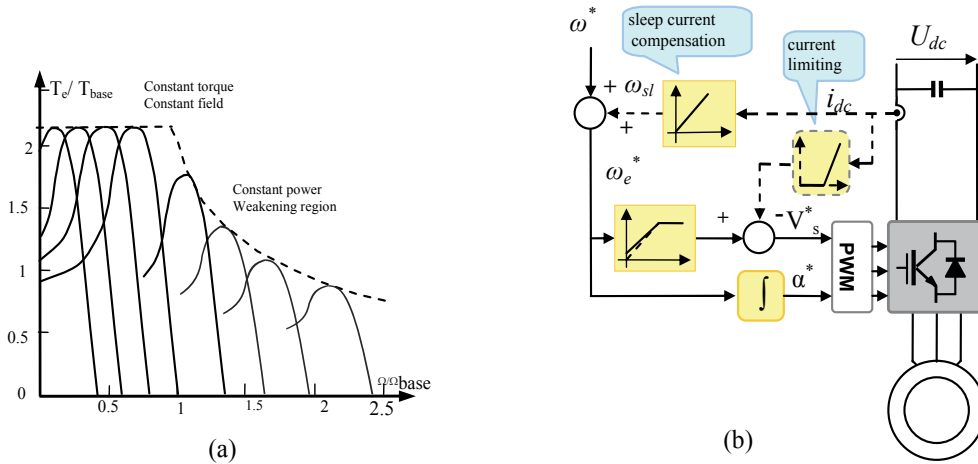


Fig. 9. a. Torque-speed characteristics under V/f control; b. VSI induction motor drive V/f controlled

The drive does not require any feedback and is used in low performance applications where precise speed control is not required. Depending on the desired speed the frequency command is applied to the inverter, and phase voltage command is directly generated from the frequency command by a gain factor, and input dc voltage of inverter is controlled.

The speed of the motor is not precisely controlled by this method as the frequency control only controls the synchronous speed [Emadi, 2005], [Livint et al. 2006] There will be a small variation in speed of the motor under load conditions. This variation is not much when the speed is high. When working at low speeds, the frequency is low, and if the voltage is also reduced then the performance of the motor are deteriorated due to large value of stator resistance drop. For low speed operation the relationship between voltage and frequency is given by

$$U_s = U_0 + kf_s \quad (15)$$

where U_0 is the voltage drop in the stator resistance.

5.2 Structures for speed vector control of induction motor

In order to obtain high performance, and fast dynamic response in induction motors, it is important to develop appropriate control schemes. In separately excited dc machine, fast transient response is obtained by maintaining the flux constant, and controlling the torque by controlling the armature current.

The vector control or *field oriented control* (FOC) of ac machines makes it possible to control ac motor in a manner similar to the control of a separately excited dc motor. In ac machines also, the torque is produced by the interaction of current and flux. But in induction motor the power is fed to the stator only, the current responsible for producing flux, and the current responsible for producing torque are not easily separable. The basic principle of vector control is to separate the components of stator current responsible for production of flux, and the torque. The vector control in ac machines is obtained by controlling the magnitude, frequency, and phase of stator current, by inverter control. Since, the control of the motor is obtained by controlling both magnitude and phase angle of the current, this method of control is given the name vector control.

In order to achieve independent control of flux and torque in induction machines, the stator (or rotor) flux linkages phasor is maintained constant in its magnitude and its phase is stationary with respect to current phasor .

The vector control structure can be classified in: 1. direct control structure, when the oriented flux position is determined with the flux sensors and 2. indirect control structure, then the oriented flux position is estimated using the measured rotor speed.

For indirect vector control, the induction machine will be represented in the synchronously rotating reference frame. For indirect vector control the control equations can be derived with the help of d-q model of the motor in synchronous reference frame as given in 13.

The block diagram of the rotor flux oriented control a VSI induction machine drive is presented in Figure 10.

Generally, a closed loop vector control scheme results in a complex control structure as it consists of the following components: 1. PID controller for motor flux and torque, 2. Current and/or voltage decoupling network, 3. Complex coordinate transformation, 4. Two axis to three axis transformation, 5. Voltage or current modulator , 6. Flux and torque estimator, 7. PID speed controller

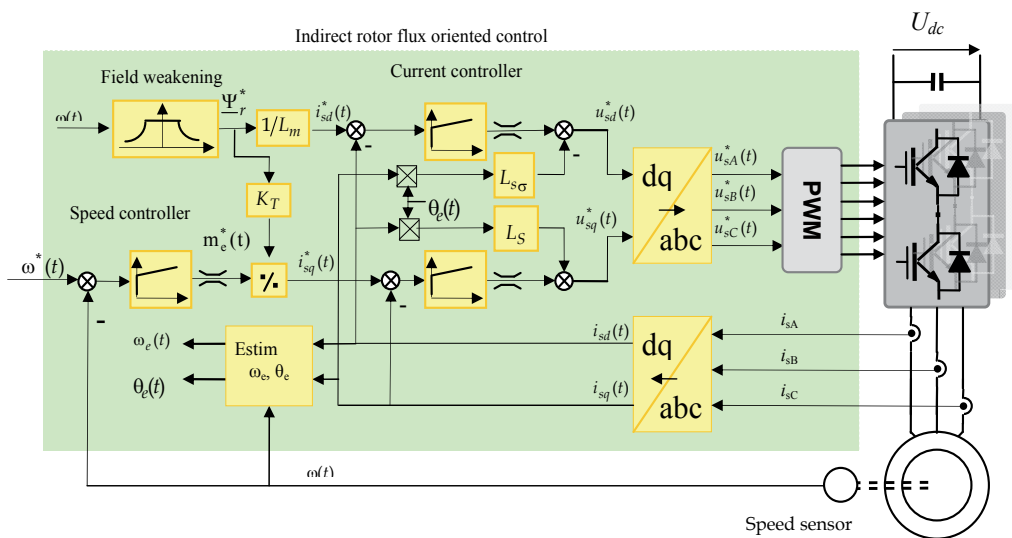


Fig. 10. Block diagram of the rotor flux oriented control of a VSI induction machine drive

6. Experimental model of hybrid electric vehicle

The structure of the experimental model of the hybrid vehicle is presented in Figure 11. The model includes the two power propulsion (ICE, and the electric motor/generator M/G) with allow the energetically optimization by implementing the real time control algorithms. The model has no wheels and the longitudinal characteristics emulation is realized with a corresponding load system. The ICE is a diesel F8Q of 1.9l capacity and 64[HP]. The electronic unit control (ECU) is a Lucas DCN R04080012J-80759M. The coupling with the motor/generator system is assured by a clutch, a gearbox and a belt transmission.

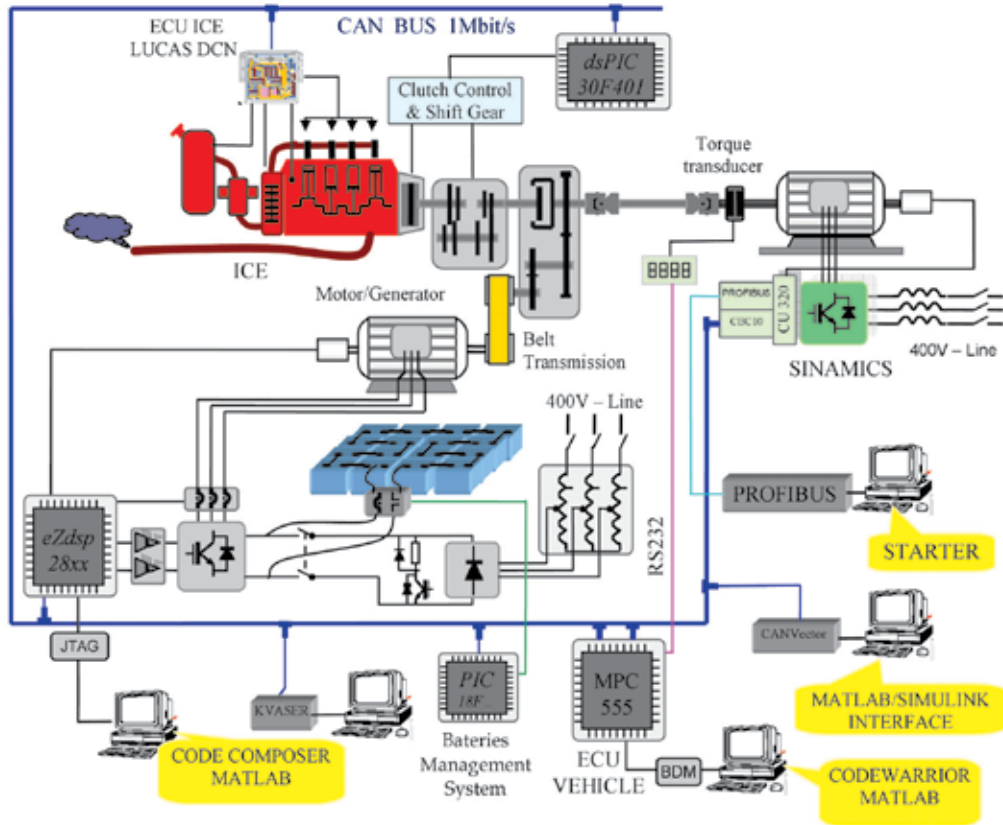


Fig. 11. The structure of the experimental model of the hybrid electric vehicle

The electric machine is a squirrel cage asynchronous machine (15kW, 380V, 30.5A, 50Hz, 2940 rpm) supplied by a PWM inverter implemented with IGBT modules (SKM200GB122D). The motor is supplied by 26 batteries (12V/45Ah). The hardware structure of the motor/generator system is presented in Figure 12. The hardware resources assured by the control system eZdsp 2808 permit the implementation of the local dynamic control algorithms and for a CAN communication network, necessary for the distributed control used on the hybrid electric vehicle, [Livint et all 2008, 2010]

With the peripheral elements (8 ePWM channels, 2x8 AD channels with a resolution of 12 bits, incremental transducer interface eQEP) and the specific peripheral for the

communication assure the necessary resources for the power converters command and for the signal acquisition in system. For the command and state signal conditioning it was designed and realized an interface module.

6.1 The emulation of the longitudinal dynamics characteristics of the vehicle

The longitudinal dynamics characteristics of the vehicle are emulated with an electric machine with torque control, Figure 13. As a mechanical load emulator, the electric machine operates both in motor and generator regimes. An asynchronous machine with vector control technique assures a good dynamic for torque. This asynchronous machine with parameters (15KW, 28.5A, 400V, 1460rpm) is supplied by a SINAMICS S120 converter from Siemens which contains a rectifier PWM, a voltage dc link and a PWM inverter [Siemens 2007]. This converter assures a sinusoidal current at the network interface and the possibility to recover into the network the electric energy given by the electric machine when it operates in generator regime.

The main objective is to emulate the static, dynamics and operating characteristics of the drive line. The power demand for the vehicle driving at a constant speed and on a flat road [Ehsani, 2005], can be expressed as

$$P_e = \frac{v}{1000\eta_{t,e}} (m_v g f_r + \frac{1}{2} \rho_a C_D A_f v^2 + m_v g i) \text{ [kW]} \quad (16)$$

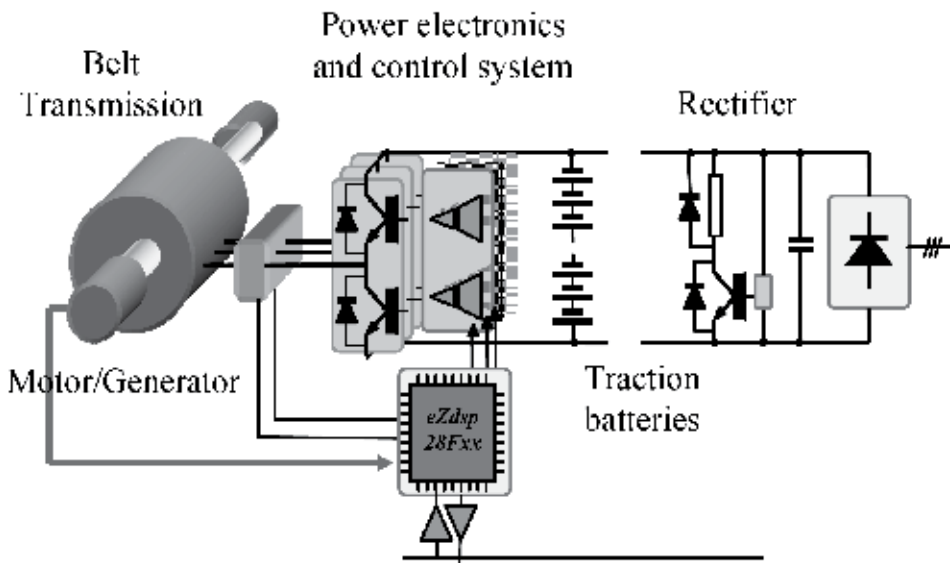


Fig. 12. Electric motor/generator system

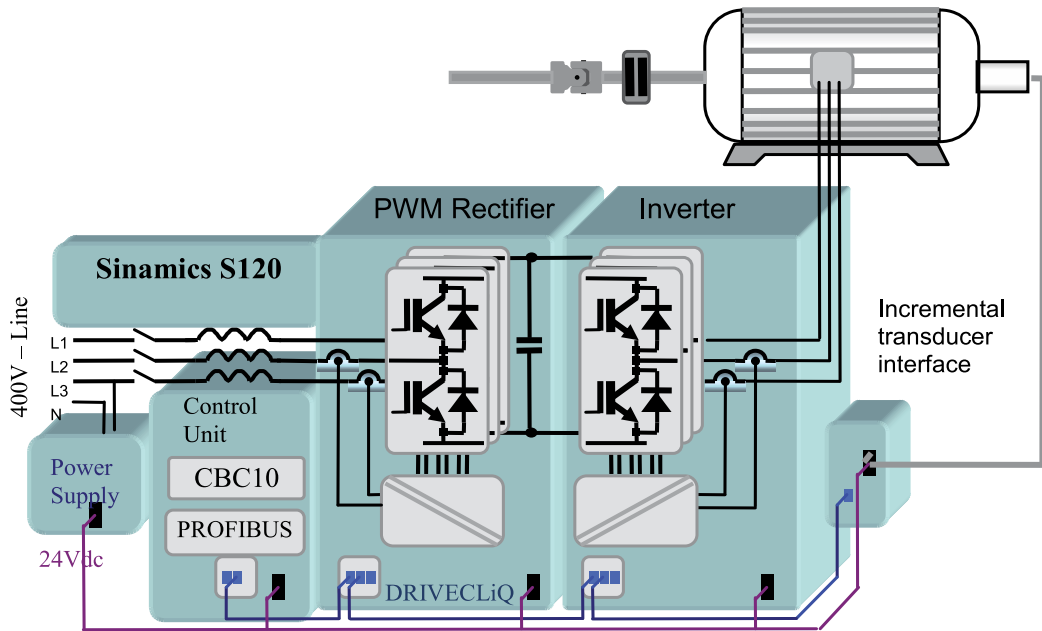


Fig. 13. Emulation system of the longitudinal dynamics characteristics of the vehicle

6.2 The distributed system of the real-time control of the hybrid electric vehicle model

The coordinated control of the sub-systems of the parallel hybrid vehicle can be realized with a hierarchical structure, [Livint et. al, 2006, 2008]. Its main element is the Electronic Control Unit vehicle of the vehicle (ECU vehicle) which supervises and coordinates the whole systems.

It has to monitor permanently the driver demands, the motion conditions and the state of the sub-systems in order to estimate the optimum topology of the whole system and to assure minimum fuel consumption at high running performances. The main system must to assure the maneuverability demanded by the driver in any running conditions. These supervising and coordinating tasks are realized by a control structure that includes both state automata elements and dynamic control elements corresponding to each state. The dynamic control of each sub-system is realized by every local control system. The dynamic control is integrated at the level of the coordinating system only when it is necessary a smooth transition between states or for a dynamic change into a state with more than a sub-system (starting engine with the electric machine).

The optimization of the performances objectives is realized logically by the state automata. The optimum operating state is determined by the coordinating and supervising system based on the analysis of the centralized data.

The state machine design is achieved in three stages:

- the identification of the all possible operating modes of the vehicle,
- the evaluation of the all possible transitions between the operating modes,
- the arbitration of the priorities between the concurrent transitions.

For the first stage it is realized a list with the possible operating modes for each sub-system. For example, for the engine the possible operating modes are running engine and stop engine.

After the identification of the all possible operating modes of each sub-system, it is generated a set of all the possible combinations of the operating modes for the vehicle.

Due to the complexity of the real time control for a parallel hybrid electric vehicle it is necessary to integrate all the elements in a high speed CAN communication network (1Mbps) to assure the distributed control of all resources [CANopen, 2004], [Chacko, 2005]. The experimental model uses a CANopen network with four slave nodes and one master node. The master node is implemented on phyCORE-mpc555 system and assures the network management and supervises the nodes control connected by NMT services, the nodes operating states, the emergency messages analysis and the modifications appeared into the communication network. The first CANopen slave node, at an inferior level, is dedicated for the motor/generator system and includes the speed control loop for the vehicle electrical propulsion. The second slave node is used to take over the torque data given on the RS-232 serial line by the DTR torque transducer and to convert the data for the proper utilization on the CANopen network.

The third slave node of the CANopen network is used for the emulation system for the longitudinal dynamics characteristics of the vehicle, implemented with the asynchronous motor and the SINAMICS S120 converter.

The fourth slave node of the CANopen network is the system of automatic gear shift, which involves control of clutch and gear. Control is achieved with a numerical dsPIC-30F4011.

The CAN protocol utilizes versatile message identifiers that can be mapped to specific control information categories. With predefined priority of the communication message, non-destructive bit-wise arbitration with error detection signaling, the CAN protocol supports distributed real-time control in vehicles applications with a very high level of security .

The content of a message is named by an *identifier*. The *identifier* describes the meaning of the data, but not indicates the destination of the message. All nodes in the network are able to decide by *message filtering* whether the data is to be accepted. If two or more nodes attempt to transmit at the same time, a non-destructive arbitration technique guarantees the messages transmission in order of priority and that no messages are lost.

It is guaranteed that a message is simultaneously accepted by all nodes of a CAN network. When a receiver detects an error in the last bit that cares about it will send an error frame and the transmitter will retransmit the message.

The CAN network provides standardized communication objects for real-time data (PDO – Process Data Objects), configuration data (SDO – Service Data objects), and special functions (Emergency message), network management data (NMT message, Error control).

Service Data Object (SDO) supports the mandatory OD (Object Dictionary) entries, slave support for the next slave services: `Reset_Node`, `Enter_Preoperational_State`, `Start_Remote_Node`, `Stop_Remote_Node`, `Reset_Communication`, COB (Communication Data Object).

For the software design it was in attention the modularity and a scalar structure of the final product that can be easy configured for the automation necessities of the communication node. For this the CANopen stack was structured in two modules [Livint et al, 2008, 2009]:

- Module I, dependent on the hardware resources of the numerical system,
- Module II, specific for the application, independent on the hardware resources. To pass the product on other numerical systems it is enough to rewrite the first module.

The functional structure of the slave CANOpen software is presented in Figure 14. Module I is specific for the numerical system (phyCORE-mpc555, eZdsp-F2808, dsPIC-30F4011) and module II is common all three systems. To implement the CANOpen protocol it was used both the graphical programming and the classic (textual) programming.

6.3 Module I implementation on the eZdsp-F2808 or dsPIC-30F4011 numerical systems

The Simulink model visible structure of the slave CANOpen communication node is presented in Figure 15.

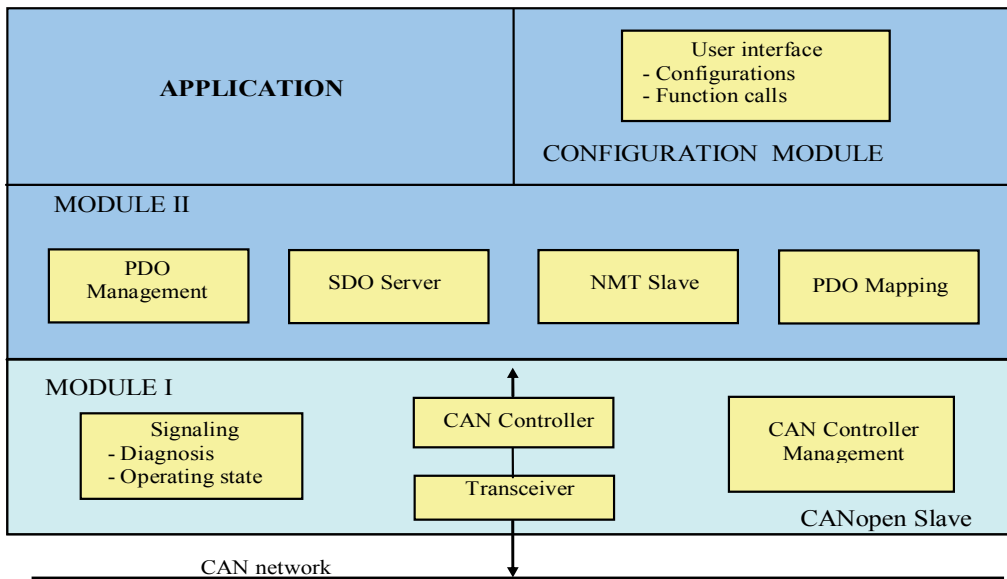


Fig. 14. The functional structure of a CANOpen slave

The CANOpen Message Receive (dsPIC30F4011 or eZdsp 2808) sub-system realizes the messages reception into the CANOpen stack buffer. The messages are transmitted by the CANOpen Message Send (dsPIC30F4011 or eZdsp 2808) sub-system.

They are part of the Module I from the Figure 16. In the same module there is also the CANOpen Err & Run LED's sub-system which commands the two LEDs of the numerical system. The stack initialization and its periodical interrogation are realized by the Init CANOpen, and SW_TimerISR sub-systems.

The data transfer between the graphical and textual modules is made with global variables which are defined by the state flow chart. It is to mention that was necessary to interfere with the C-code generating files (Target Language Compiler – TLC) to obtain the necessary functionality.

An important aspect of the CANOpen implementation is the generation of relative references of time to administrate the data transfer messages (timestamp) and the administrative data (node guarding, heartbeat). For this it was used a software which call both the CANOpen stack and the timer with 1 ms period.

Module I implementation on phyCORE-mpc555 numerical system

The Simulink model for the CANopen node of the second numerical system is similar with the model from Figure 17 but eZdsp 2808 is changed with phyCORE-mpc 555. Thus, for a user which knows a model it is easy to operate with the other. The communication speed is established with the MPC555 Resource Configuration module.

Module II implementation of slave CANopen communication node

The graphical programming is operative and suggestive. It also has limits especially for the complex algorithms processing. In this case the programmer makes a compromise: hardware resources are realized with the graphical libraries and the complex algorithms processing are implemented with textual code lines. The Matlab/Simulink embraces such a combined programming.

Thus, the second module was implemented by a textual programming. The function call is realized with a 1KHz frequency by the SW_TimerISR sub-system. SDO services are assured by the object dictionary SDOResponseTable and by the functions Search_OD (WORD index, BYTE subindex), Send_SDO_Abort (DWORD ErrorCode) and Handle_SDO_Request (BYTE*pData). The functions Prepare_TPDOs (void) and TransmitPDO (BYTE PDONr) realize the administration of the data transmission messages between the numerical systems

The node initialization is realized by the function CANOpen_Init (BYTE Node_ID, WORD Heartbeat) and the communication network administration (NMT slave) are incorporate into the function CANOpen_ProcessStack(void).

The connections (mapping) between the data on the CAN communication bus can be static realized by the initialization function CANOpen_InitRPDO (BYTE PDO_NR, WORD CAN_ID, BYTE len, BYTE *dat), CANOpen_InitTPDO (BYTE PDO_NR, WORD CAN_ID, WORD event_time, WORD inhibit_time, BYTE len, BYTE *pDat).

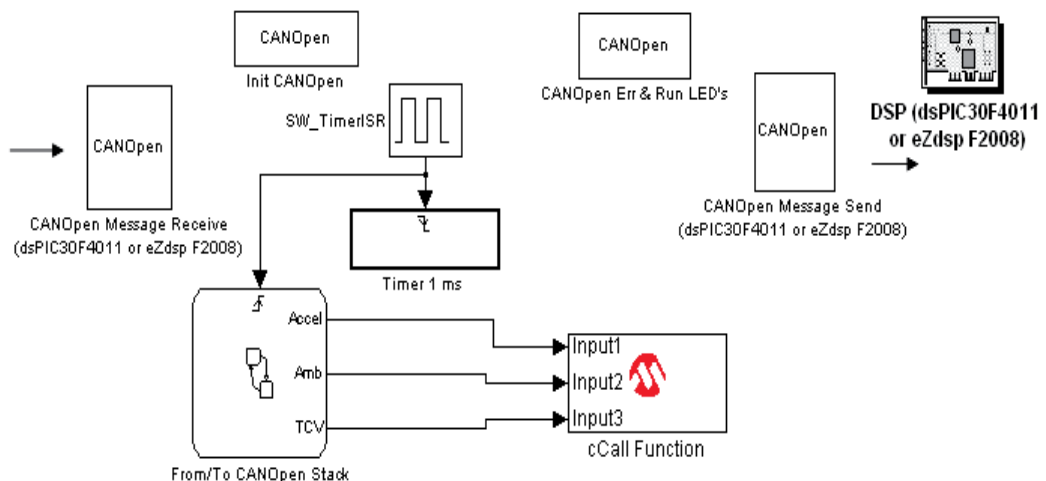


Fig. 15. The Simulink model assigned to the slave CANopen communication node

6.4 Experimental results

In Figure 16 is presented the hybrid electric vehicle model realized into the Energy Conversion and Motion Control laboratory of the Electrical Engineering Faculty from Iasi. Finally several diagrams are presented highlighting the behaviour of the electric traction motor and the mechanical load emulator. It was considered a standard operating cycle UDDS (Urban Dynamometer Driving Schedule).

A velocity diagram UDDS cycle operation is shown in Figure 17-a. It is the speed reference for electric traction motor and the measured speed is presented in Figure 17-b.

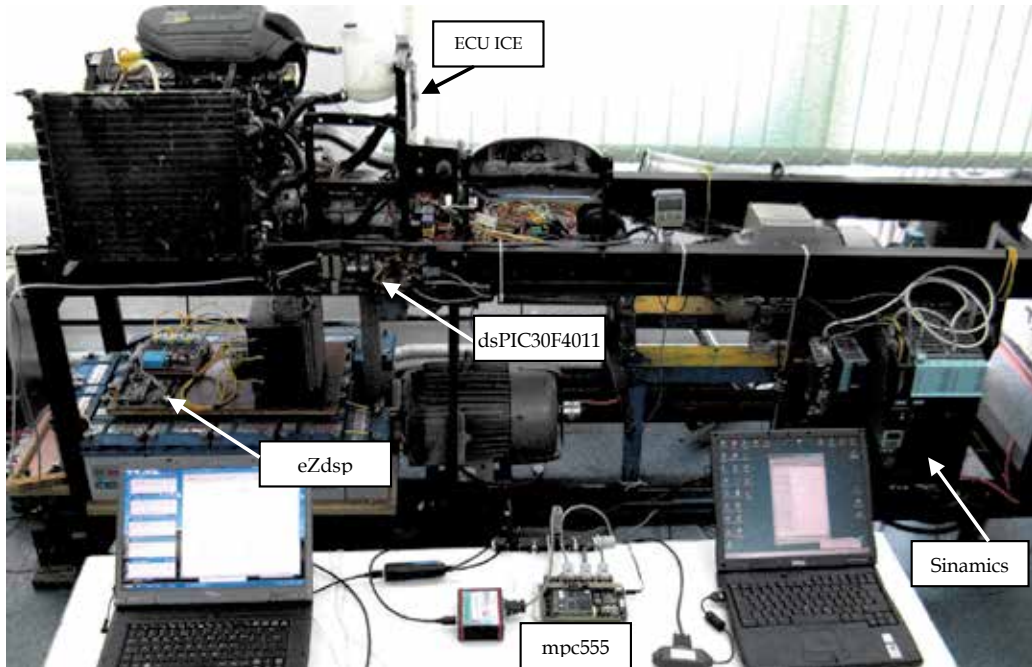


Fig. 16. Hybrid electric vehicle experimental model

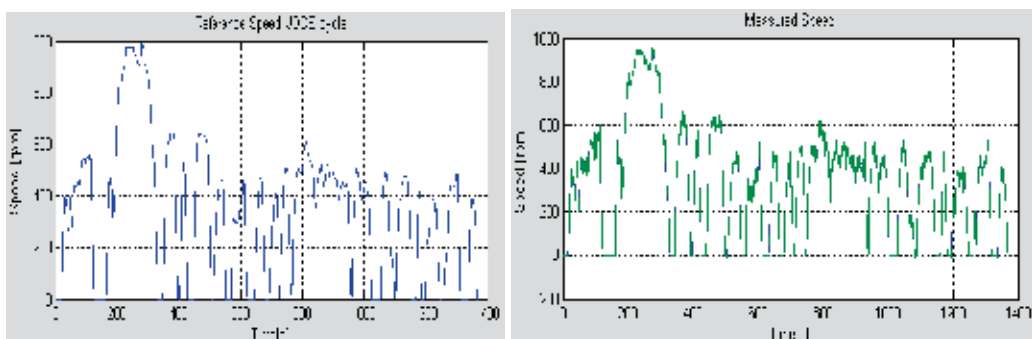


Fig. 17. a) Reference speed for UDSS cycle b) Measured speed for electrical motor

The active current from electrical traction motor is shown in Figure 18-a. Also the mechanical load emulator is an electrical motor with torque control and the torque reference shown in Figure 18-b. In Figure 19 is presented the estimated torque from mechanical load emulator.

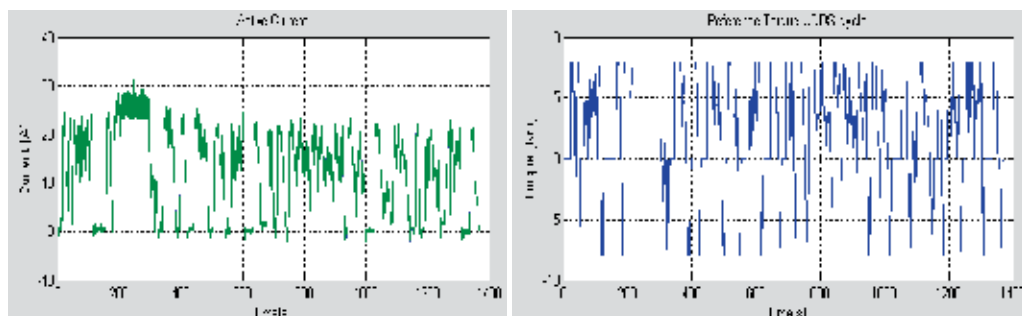


Fig. 18. a) The active current from electric traction motor b) The reference torque for Sinamics system

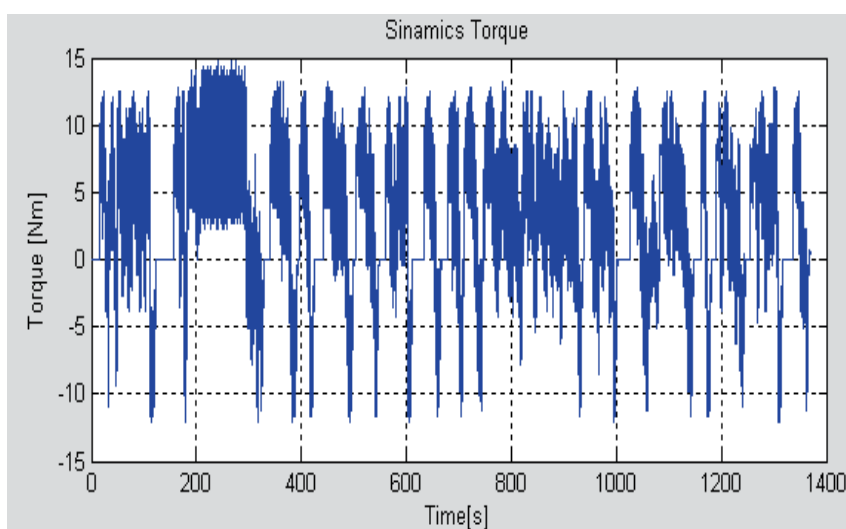


Fig. 19. The estimated torque from mechanical load emulator

7. Conclusions

The hybrid electric vehicles are very complex dynamic systems and have an important number of interconnected electrical systems to achieve the required operating performances. Because of the complexity of the real time control for a hybrid electric vehicle it is necessary to integrate all the elements in a high speed CAN communication network to assure the distributed control of all the resources. For the hybrid electric vehicle experimental model is used a CANopen network with one master node and four slave nodes. The distributed system control with the CANopen protocol on a CAN bus permits the control of the electrical drives systems in safe conditions and with improved dynamic performances.

8. References

- Bayindir , K. C., Gozukucuk, M.A., Teke, A. , (2011). A comprehensive overview of hybrid electric vehicle: Powertrain configurations, powertrain control techniques and electronic control units, *Energy Conversion and Management*, Elsevier, nr. 52, 1305-1313.
- CANopen, *User Manual, Software Manual*, (2004), PHYTE Technology Holding Company
- Chacko, V.R., Lahaparampil, V.Z., Chandrasekar, V., (2005). CAN based distributed real time controller implementation for hybrid electric vehicle, *IEEE*, 247- 251, ISBN 0-7803-9280-9-05
- Chan, C.C, (2002), The state of the art of electric and hybrid vehicles, *Proc. IEEE*, vol. 90, no. 2, pp. 247-275
- Comigan , S., (2002). *Introduction to the Controller Area Network (CAN)*, Texas Instruments Application Report, SLOA101-August 2002, pp. 1-16
- Duan, J., Xiao, J., Zhang, M., (2007). Framework of CANopen protocol for a hybrid electric vehicle, *Proceedings of the IEEE Intelligent Vehicles Symposium*, Istanbul, Turkey, June 13-15, 2007.
- Ehsani M., Gao Y., Gay E.S. Emadi A, (2005). *Modern Electric, Hybrid Electric, and Fuel Cell Vehicles* CRC PRESS, Boca Raton London, New York, ISBN 0-8493-3154-4
- Emadi Ali, (2005). *Hanbook of Automotive power electronics and MotorDrives*, CRC PRESS, Taylor&Francis Group, LLC, 2005, ISBN 0-8247-2361-9
- Fuhs A.E., (2009). *Hybrid Vehicles*, CRC PRESS 2009, Taylor Francis Group, LLC, ISBN 978-1-4200-7534-2
- Guzzella L., Sciarretta A., (2007). *Vehicle Propulsion Systems*, Second Edition, Springer-Verlag Berlin Heidelberg, ISBN 978-3-540-74691-1
- Husain I., (2003), *Electric and Hybrid Vehicles Design Fundamentals*, CRC PRESS, ISBN 0-8493-1466-6
- Livint, Gh., Gaiginschi, R., Horga, V., Drosescu R., Chiriac, G., Albu, M., Ratoi, M., Damian, I, Petrescu M., (2006). *Vehicule electrice hibride*, Casa de Editura Venus, Iasi, Romania
- Livinț, Gh., Rățoi, M., Horga, V., Albu, M, (2007). Estimation of Battery Parameters Based on Continuous-Time Model, *Proceedings International Symposium on Signals, Circuits&Systems-ISSCS* , July 12-13, 2007, Iasi, Romania, pp. 613-617, IE.EE. Catalog Number: 07EX1678C, ISBN: 1-4244-0969-1
- Livinț Gh., Horga, V., Albu, M., Rățoi, M, (2007). Evaluation of Control Algorithms for Hybrid Electric Vehicles, *WSEAS TRANSACTIONS on SYSTEMS*, Issue 1, Vol. 6, January 2007, pp. 133-140, ISSN 1109-2777, <http://www.wseas.org>
- Livint, Gh., Horga, V., Ratoi, M., (2008), Distributed control system for a hybrid electric vehicle implemented with CANopen protocol, -Part I, *Bulletin of the Polytechnic Institute of Iasi*, Tom LIV (LVIII), FASC. 4, ISSN 1223-8139, pp. 1019-1026
- Livint, Gh., Horga, V., Ratoi, M., Albu, M., Petrescu, M., Chiriac, G., (2008). Distributed control system for a hybrid electric vehicle implemented with CANopen protocol- Part II, *Bulletin of the Polytechnic Institute of Iasi*, Tom LIV (LVIII), FASC. 4, ISSN 1223-8139, pp. 1027-1032
- Livint, Gh., Horga, V., Ratoi, M., Damian, I., Albu, M., Chiriac, G., (2008). Advanced real rime control algorithms for hybrid electric vehicles optimization, *CEEX Program, Simposion "Contributii Stiintifice "*, UCP AMTRANS, Bucuresti, Romania, noiembrie 2008, pp. 209-214

- Livint, Gh., Horga, V., Ratoi, M., Albu, M., Chiriac, G., (2009), Implementing the CANopen protocol for distributed control for a hybrid electric vehicle, *Proceedings The 8th International Symposium on Advanced Electromechanical Motion Systems*, Lille , July 1-3, CD., ISBN: 978-2-915913-25-5/EAN: 978-2-91 5913-26-5 IEEEExplore, <http://ieeexplore.ieee.org/xpl/RecentCon.jsp?punumber=5234983>
- Livint, Gh., Horga, V., Sticea, D., Rațoi, M., Albu, M., (2009) Electrical drives control of a hybrid electric vehicle experimental model, *Proceedings of the 7th International Conference of Electromechanical and Power Systems*, Editura PIM, 2009, vol. II, pp. 21-27, ISBN vol II, 978-606-520-623-6, October 8-9, 2009, Iași, Romania,
- Livint Gh., Horga V., Sticea D., Rațoi M., Albu M., (2010). Hybrid electric vehicle experimental model with CAN network real time control, in *Advances in Electrical and Computer Engineering*, nr. 2., 2010, pp. 102-108, ISSN 1582-7445, Stefan cel Mare University of Suceava, Romania
- Petrescu, M., Livint, Gh., Lucache, D. (2008), Vehicles dynamic control using fuzzy logic, *Proceedings of 9th WSEAS International Conference on Automation and Information*, pag. 488-493, 2008
- Seref Soylu, (2010) *Urban Transport and Hybrid Vehicles*, Published by Sciyo, Janeza Trdine 9, 51000 Rijeka, Croatia, ISBN 978-953-307-100-8
- Siemens, Sinamics, *S120 Control Unit and additional system components*, (2007), Equipment Manual 03, Edition
- Sticea D., Livint Gh., Albu M., Chiriac G., (2009). Experimental stand for the dynamical cycle study of the batteries used on hybrid electrical vehicle, *Proceedings of the 7th International Conference of Electromechanical and Power Systems*, Editura PIM, 2009, vol. II, pp. 172-175, ISBN vol II, 978-606-520-623-6, October 8-9, 2009, Iași, Romania,
- Yamada, E., and Zhao, Z., (2000). Applications of electrical machine for vehicle driving system, *Proceedings of the Power Electronics and Motion Control Conference (PIEMC)*, vol 3., pp. 1359-1364, Aug. 15-18, 2000.
- Westbrook H. M., (2005). *The Electric Car, Development and future of battery, hybrid and fuel-cell cars*, The Institution of Electrical Engineers, London, 2005, ISBN 0 85296 013 1
- Wyczalek, F.A., (2000) Hybrid electric vehicles year 2000, *Proceedings of the Energy Conversion Engineering Conference and Exhibit (IECEC) 35th Intersociety*, vol.1, pp. 349-355, July 24-28, 2000

Vehicle Dynamic Control of 4 In-Wheel-Motor Driven Electric Vehicle

Lu Xiong and Zhuoping Yu
Tongji University
China

1. Introduction

Thanks to the development of electric motors and batteries, the performance of EV is greatly improved in the past few years. The most distinct advantage of an EV is the quick and precise torque response of the electric motors. A further merit of a 4 in-wheel-motor driven electric vehicle (4WD EV) is that, the driving/braking torque of each wheel is independently adjustable due to small but powerful motors, which can be housed in vehicle wheel assemblies. Besides, important information including wheel angular velocity and torque can be achieved much easier by measuring the electric current passing through the motor. Based on these remarkable advantages, a couple of advanced motion controllers are developed, in order to improve the handling and stability of a 4WD EV.

2. Traction control

The fast and accurate torque generation of each driving wheel enables a great enhancement in traction control during acceleration.

In this section, an anti-slip controller for a 4WD EV using VSC (Variable Structure Control) method is presented. The control algorithm is independent on the identification of the road adhesion coefficient and has excellent robustness to the estimation error of the vehicle velocity. Regarding the high-frequency-chattering on the sliding surface, a new control method which combines the advantage of the VSC and MFC (Model Following Control) in order to decrease the fluctuation to the e-motor torque and slip ratio of the tire is proposed. The result of the simulation indicates that the proposed control method is effective for the ASR control and improves the performance of e-motor's output torque and the slip ratio of the tire.

2.1 VSC ASR controller

2.1.1 One-wheel-model

An accurate simulation model is important to verify the effect of the designed controller. Fig.2.1-1 shows a two degrees of freedom vehicle model. It only contains the vehicle's longitudinal motion and ignores air resistance and rotating resistance. Formula 2.1-1 shows the mathematical model:

$$M\dot{v}_x = F_d$$

$$I_w \dot{\omega} = T_m - F_x R \quad (2.1-1)$$

Here, M is the 1/4 vehicle mass, kg; v_x represents the longitudinal velocity, m/s; F_x is the driving force of the road, N; I_w is the wheel rotational inertia, kg m²; R is the wheel radius, m; ω is the angular velocity, rad/s and T_m is the motor torque, N m.

The Magic Formula tire model is applied as the tire model, so the driving force F_d can be expressed as follows:

$$F_d = \mu_{Max} \cdot F_z \cdot \sin\left(C \cdot \arctan\left\{B(1-E)\lambda + E \cdot \arctan(B\lambda)\right\}\right) \quad (2.1-2)$$

The meanings of the parameters can be found in the literature [1].

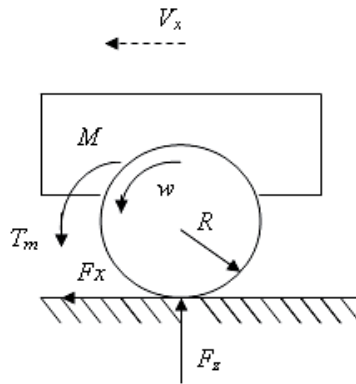


Fig. 2.1-1. One-wheel-Model

2.1.2 Design of VSC ASR controller

VSC with sliding mode has good robustness to the input signals so that this strategy has advantage to the ASR control system which needs the vehicle velocity observation and signal identification. But there is always high-frequency-chattering on the sliding surface. In the following text a VSC controller, which doesn't depend on the identification of the optimal slip ratio, is designed and its performance will be analyzed through simulation.

In order to make the VSC possess excellent robustness to the additional uncertainties and interferences, the control law adopted here is equivalent control with switching control. Hence, the output torque of the e-motors can be expressed as [2]:

$$T_m = T_{m,eq} - \Delta T \operatorname{sgn}(s) \quad (2.1-3)$$

In this equation, $T_{m,eq}$ is the equivalent torque of the e-motor, ΔT is the hitting control drive torque, $\operatorname{sgn}(s)$ is the switching function of the system.

The sliding motion includes two processes: approaching motion and sliding motion. The approaching motion can make the system at any time in any position approach to the sliding face in limited time. The sliding motion occurs only when the system reaches sliding surface:

$$s = \lambda - \lambda_{reference} = 0.$$

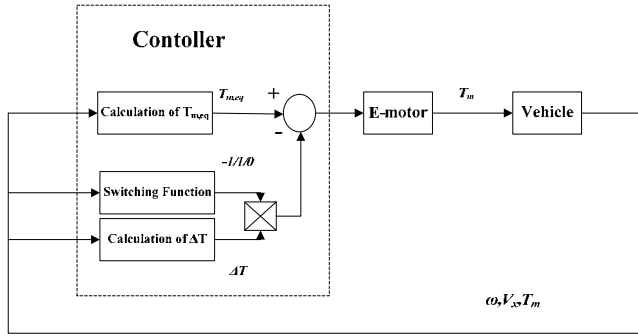


Fig. 2.1-2. Diagram of VSC ASR Strategy

To reach the ideal sliding mode, the requirement $s=0$ should be fulfilled. Assuming the reference slip is constant, so $\dot{\lambda}_{reference} = 0$. So, on the sliding face there is:

$$\dot{\lambda} = \dot{\lambda}_{reference} = 0 \quad (2.1-4)$$

According to the one-wheel model:

$$I_{\omega} \dot{\omega} = T_m - F_x R$$

During driving process, the slip ratio of the wheel can be expressed as:

$$\lambda = \frac{\omega R - v}{\omega R}$$

Combining Formula (2.1-1) and (2.1-4), we can get:

$$\frac{d\lambda}{dt} = -\frac{1}{\omega R} \left[v - (1-\lambda)R \frac{T_m - F_x R}{I_{\omega}} \right] = 0$$

Then, we can obtain the e-motor's equivalent torque:

$$T_{m,eq} = \frac{I_{\omega}}{R(1-\lambda)} \dot{v} + F_x R$$

As the tire's longitudinal velocity is difficult to be measured accurately, \hat{v} is the estimated value. Then the above formula can be rewritten as:

$$\hat{T}_{m,eq} = \frac{I_{\omega}}{R(1-\lambda)} \dot{\hat{v}} + F_x R \quad (2.1-5)$$

In the actual driving progress, there are many kinds of road surfaces and their respective optimal slip ratios. The identification for them is difficult. Through Fig. 2.1-3, we can see that, although the slip ratios for different roads are different, the basic shapes for μ - λ curves are

similar. It means, before the optimal slip ratio, the bigger the slip ratio, the larger the longitudinal adhesion coefficient is. While after the optimal slip ratio, the bigger the slip ratio, the smaller the longitudinal adhesion coefficient is^[3].

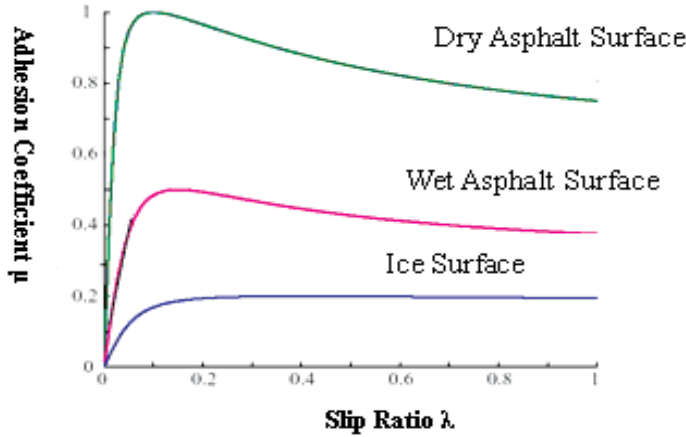


Fig. 2.1-3. Slip ratio-Longitudinal adhesion coefficient on different road surface

From Fig. 2.1-3, we can get:

When $\frac{d\mu}{d\lambda} > 0$, $\lambda < \lambda_{reference}$, λ needs increasing so as to get larger adhesion coefficient and the driving torque should be increased.

When $\frac{d\mu}{d\lambda} = 0$, $\lambda = \lambda_{reference}$, λ needs keeping so as to get larger adhesion coefficient and the driving torque should be maintained.

When $\frac{d\mu}{d\lambda} < 0$, $\lambda > \lambda_{reference}$, λ needs decreasing so as to get larger adhesion coefficient and the driving torque should be reduced.

According to the one-wheel model, we can acquire: $\mu = \frac{T_m - I_\omega \dot{\omega}}{F_Z R}$

Then we can get:

$$\frac{d\mu}{d\lambda} = \frac{d\mu / dt}{d\lambda / dt} = \frac{\frac{T_m - I_\omega \ddot{\omega}}{F_Z R}}{\frac{v \dot{\omega} R - v \dot{\omega} R}{(\omega R)^2}} = \frac{\omega^2}{F_Z} \cdot \frac{T_m - I_\omega \ddot{\omega}}{v \dot{\omega} - v \dot{\omega}}$$

Now, we can get the judgment condition:

When $\frac{T_m - I_\omega \ddot{\omega}}{v \dot{\omega} - v \dot{\omega}} > 0$, the e-motor's output torque needs increasing;

When $\frac{\dot{T}_m - I_\omega \ddot{\omega}}{v\omega - v\omega} = 0$, the e-motor's output torque needs keeping;

When $\frac{\dot{T}_m - I_\omega \ddot{\omega}}{v\omega - v\omega} < 0$, the e-motor's output torque needs decreasing.

From above we can find that what the switching function needs is not the slip ratio and the reference slip ratio any more, but the angular speed, e-motor's torque and driving torque, which need not identification. Although there is still longitudinal velocity estimation value in the controller, the controller itself has solved this problem which can be seen in Formula 8. So this VSC strategy is considered as feasible.

When the system is not on the sliding surface, it needs approaching the sliding surface from any state. This motion is called approaching motion. And during this motion the slip ratio will be approaching 0.

Under the generalized sliding condition, the switching function should meet:

$$\dot{s}s \leq -\eta|s| \quad (2.1-6)$$

Here the parameter $\eta > 0$. η represents the velocity, in which the system approaches the sliding surface. The larger the η is, the faster the approaching velocity is. Whereas, the chattering on the sliding surface will be bigger.

When Formula (2.1-1) is put into Formula (2.1-6), we can get:

$$-\frac{s}{\omega R} \left[v - (1 - \lambda)R \frac{\hat{T}_m - \Delta T \operatorname{sgn}(s) - F_x R}{I_\omega} \right] \leq -\eta|s| \quad (2.1-7)$$

Here the hitting control driving torque is assumed as

$$\Delta T = \frac{\omega I_\omega}{(1 - \lambda)} (F + \eta) \quad (2.1-8)$$

Putting Formula 2.1-7 into Formula 2.1-6, we can get:

$$\left| \frac{1}{\omega R} (\dot{v}_x - \dot{\hat{v}}_x) \right| |s| \leq F|s|$$

That is:

$$F \geq \frac{1}{\omega R} \left| \dot{v}_x - \dot{\hat{v}}_x \right| \quad (2.1-9)$$

So the e-motor's output torque can be shown as

$$T_m = \hat{T}_{m,eq} - \Delta T \operatorname{sgn}(s) \quad (2.1-10)$$

The simulation results for vehicle that starts on the road surface with a low adhesion coefficient ($\mu=0.2$) is shown in Fig.2.1-4.

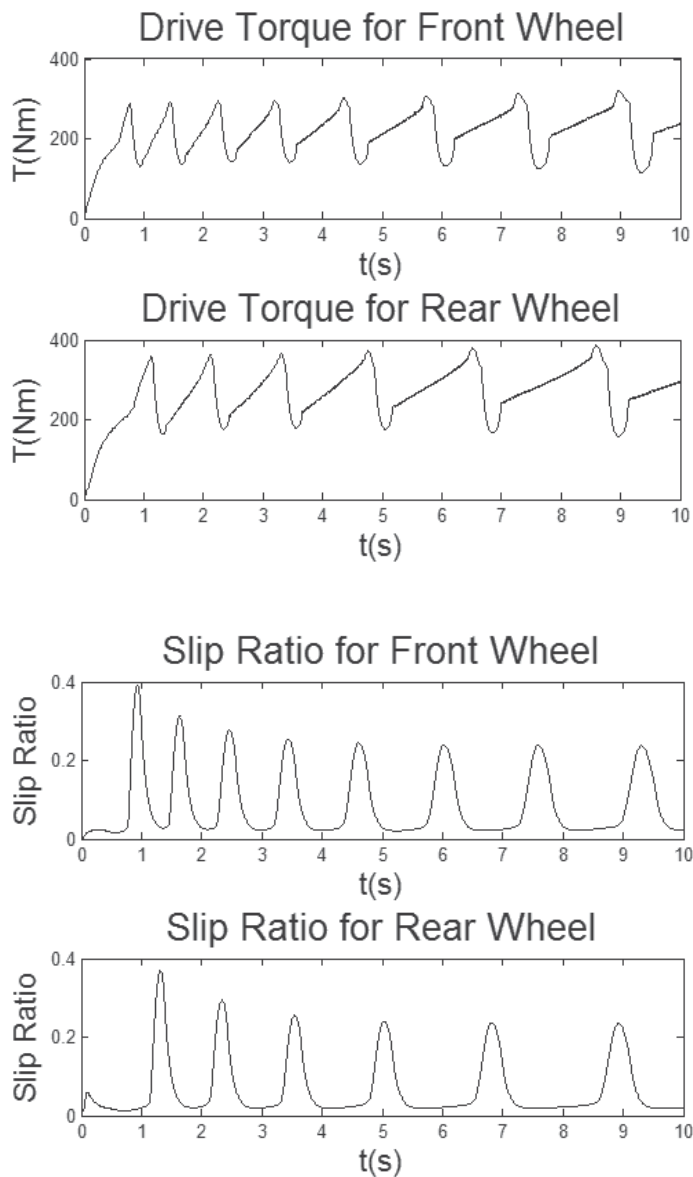


Fig. 2.1-4. Start on a low adhesion surface ($\mu=0.2$)

From the simulation results we can get that the vehicle can keep away from skipping and the acceleration performance is good when it starts. But the slip ratio occurs fluctuation when it's among 0 to 0.3 and the e-motor's output torque also fluctuates near 300Nm. In reality, big fluctuation is harmful to the e-motor and sometimes the e-motor can't fully realize what the controller requires. Therefore, there are some defects in this method.

2.2 ASR combined controller
2.2.1 MFC controller

According to the research results from Tokyo University [4, 5], when the tire is completely adhered, the vehicle’s equivalent mass is equal to the sum of the sprung mass and non-sprung mass. When the tire slips, the angular speed changes significantly. During acceleration, the angular speed is obviously smaller than the ideal value which is outputted by the standard model. In light of this principal, the tire’s angular speed should be compared to the angular speed from the standard model at any time. And then the difference is used as the basis for a correction value through a simple proportional control to adjust the e-motor’s output torque. So that the tire can avoid slipping.

MFC strategy only requires the e-motor’s output driving torque and the tire’s angular speed signal to put ASR into practice. Consequently the estimation of the longitudinal velocity and the optimal slip ratio identification can be ignored. Therefore, this strategy is practical. The system diagram is shown in Fig.2.2-1.

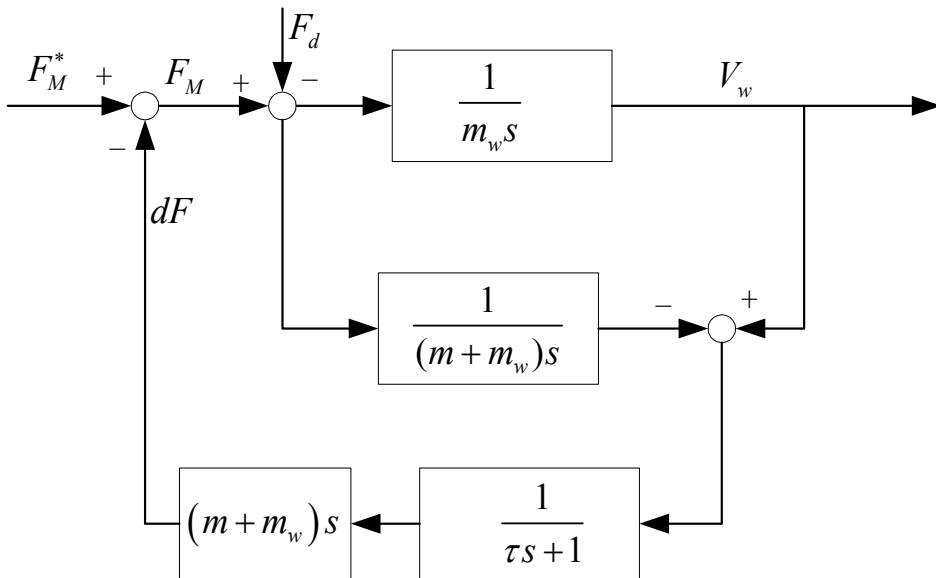


Fig. 2.2-1. MFC control block diagram

The standard model of MFC is got under the condition that the slip ratio is set to 0. It means that the road’s adhesion force isn’t fully utilized and the driving performance will be bad. So this control strategy is not perfect. Secondly, MFC hasn’t good robustness to the input signals. Especially when the angular speed is disturbed, deviation of the controller will happen.

2.2.2 Combined controller

Based on the characters of VSC and MFC, in this section an area near the sliding surface will be set, within which the MFC strategy is applied. And out of this area, the VSC strategy is used. Thus, the high-frequency-chattering near the sliding surface can be avoided. The system diagram is shown in Fig.2.2-2 and Fig.2.2-3.

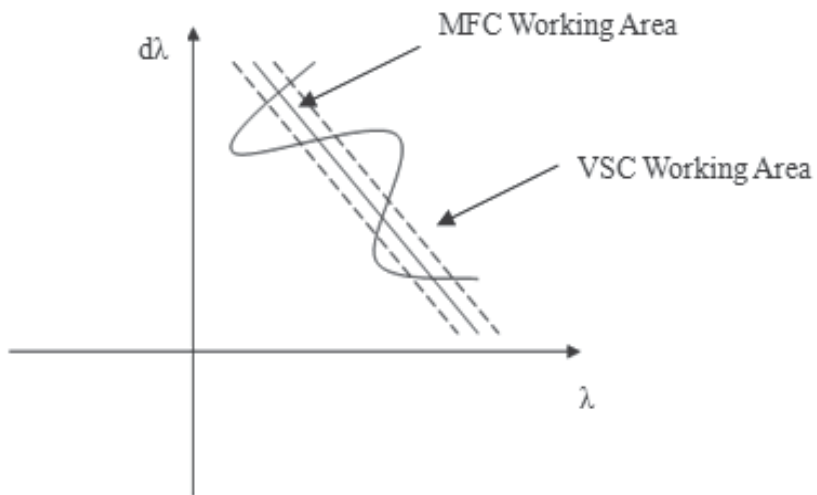


Fig. 2.2-2. Schematic diagram of switch region of combined control

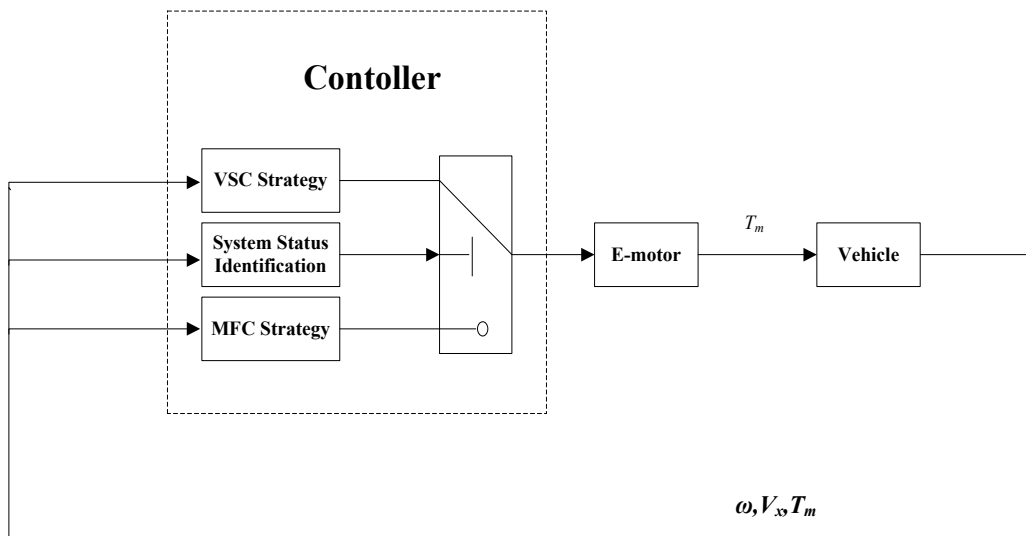


Fig. 2.2-3. Combined control block diagram

The simulation results for the vehicle that starts on the road surface with a low adhesion coefficient ($\mu=0.2$) is shown in Fig.2.2-4.

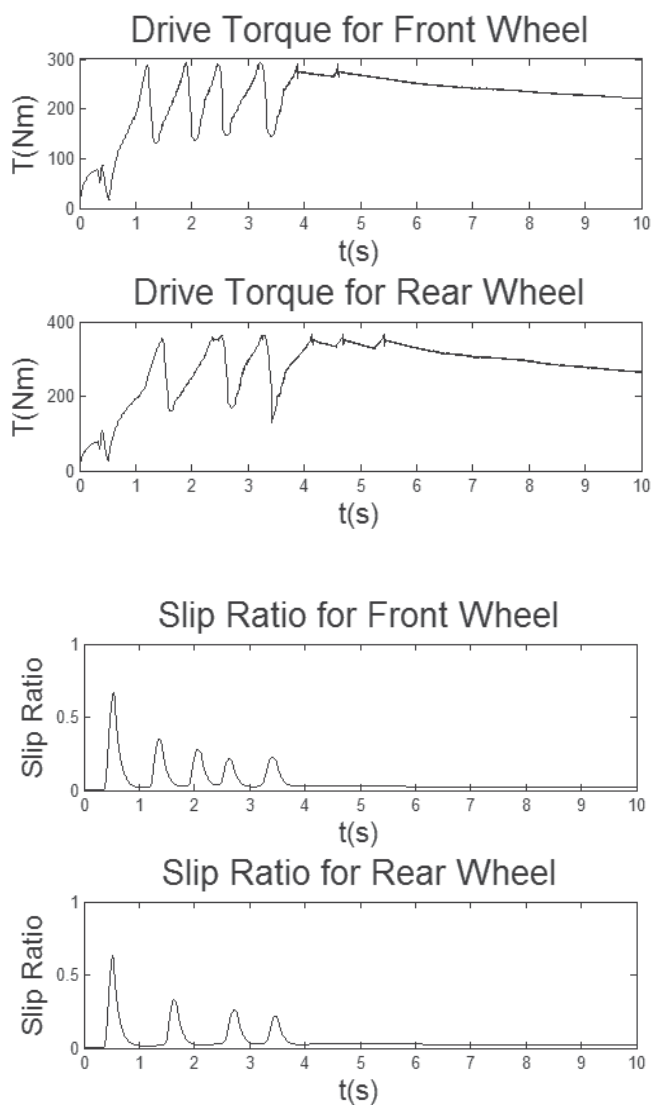


Fig. 2.2-4. Start on a low adhesion surface($\mu=0.2$)

From Fig.2.2-4, we can see that, on a low adhesion coefficient road surface, the vehicle doesn't slip. The slip ratio is in the ideal scope. Comparing with the above mentioned VSC strategy, the fluctuation of the slip ratio for combined control is improved. The fluctuation time continues 2.5s before stable convergence range occurs and the peak of the fluctuation of the slip ratio is 0.5. With the work of the combined control strategy the fluctuation scope is narrowed and the same to the e-motor's output torque. The drive performance for the combined control strategy is also excellent. On the low adhesion surface, the longitudinal velocity can reach 17m/s after 10s from starting.

Table 1 shows the driving performance for different control methods on road surface with low adhesion coefficient ($\mu=0.2$).

	Drive distance(m)	Time(s)	Average acceleration(m/s ²)	Utilization of adhesion coefficient
Without Control	36	7.5	1.33	68%
MFC	29	5.8	1.72	88%
Combined control	26	5.7	1.75	89%

Table 1. Accelerate to 10m / s on road surface with low adhesion coefficient from starting

Fig. 2.2-5 displays the simulation results on the jump μ road (from $\mu=0.2$ to $\mu=0.7$). The tire doesn't slip on this kind of surface. It demonstrates that the combined control strategy is effective to such surface, too.

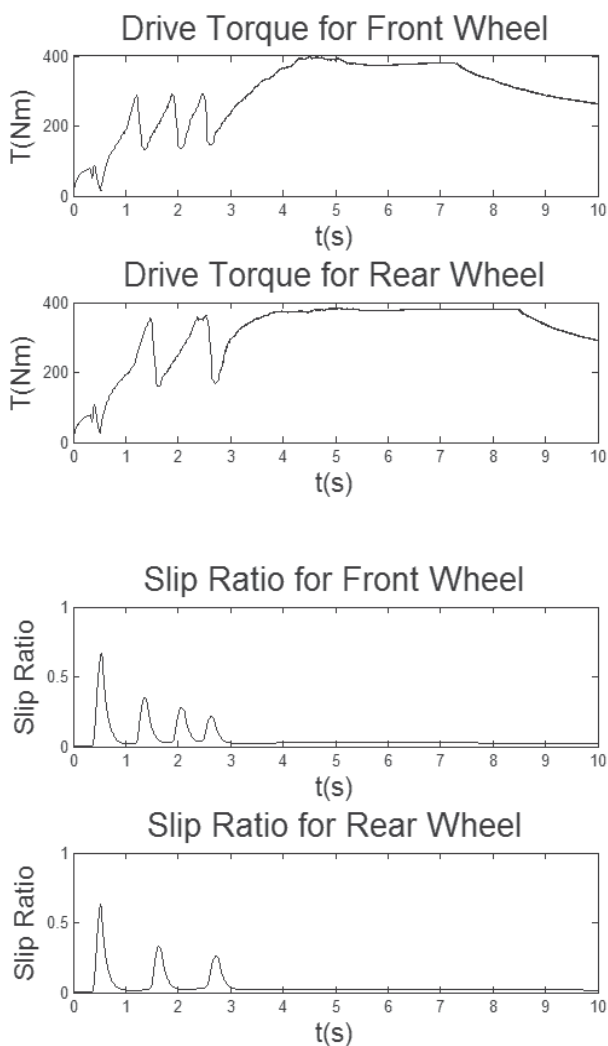


Fig. 2.2-5. Start on the jump μ road (from $\mu=0.2$ to $\mu=0.7$)

Fig.2.2-6 shows the simulation results with MFC strategy which is on the low adhesion coefficient road surface. In this simulation test, the wheel speed is disturbed that is manually offset by white noise(0.1kw) in order to verify the effectiveness to the disturb of the velocity signal.

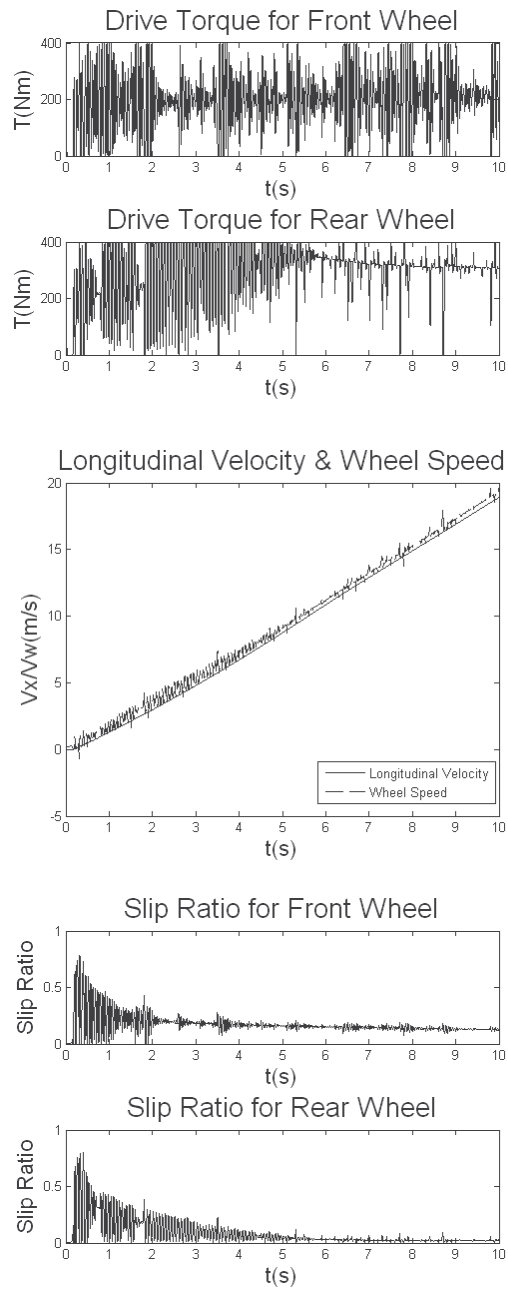


Fig. 2.2-6. Effectiveness to the disturb of the wheel speed signal for MFC control

From Fig.2.2-6, we can get that MFC has not good performance to the disturb of the wheel speed because the output drive torque is out of control. As we all known, the wheel speed is the only control parameter to this kind of strategy so that MFC control isn't regarded as an excellent control method to realize ASR function.

Fig.2.2-7 shows the simulation results on the low adhesion coefficient road surface which the longitudinal velocity is disturbed with combined control method. In this paper the longitudinal velocity is manually offset by a positive 2m/s and white noise. According to the results, the character of the combined control strategy is confirmed.

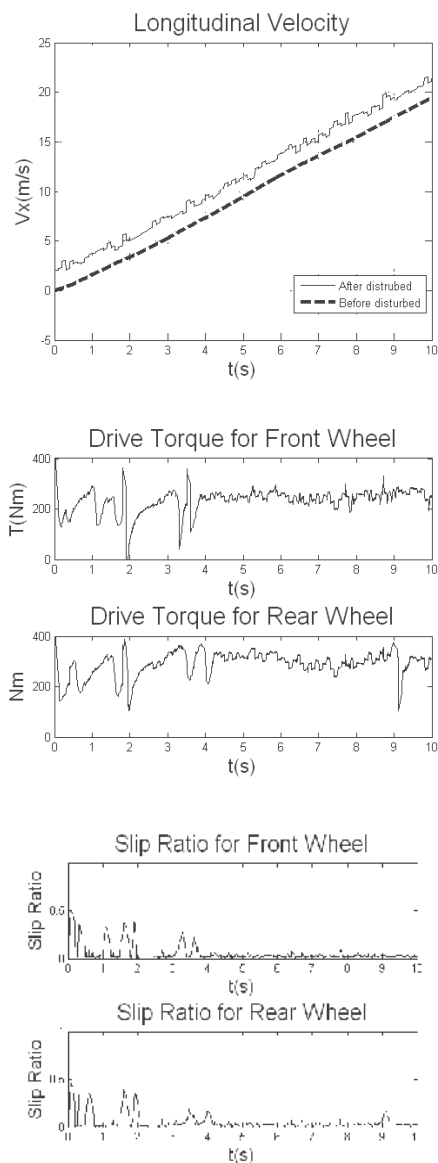


Fig. 2.2-7. Effectiveness to the disturb of the longitudinal velocity signal

According to results from Fig.2.2-6 and Fig.2.2-7, we can get that the combined control method has better robustness to the input signal's disturb. This point is very important to the usage of the control method.

3. Anti-lock brake control

For electric vehicles, the motor inside each wheel is able to provide braking torque during deceleration by working as a generator. Moreover, the torque response of an electric motor is much faster than that of a hydraulic system. Thanks to the synergy of electric and hydraulic brake system, the performance of the ABS (Anti-lock Brake System) on board is considerably improved.

In this section, a new anti-skidding method based on the model following control method is proposed. With the new feedback function and control parameter, the braking performance, especially the phase-delay of the electric motor's torque is, according to the result of the simulation, improved. Combined with the advantage of the origin MFC, the improved MFC can be widely applied in anti-skidding brake control.

Furthermore, a braking torque dynamic distributor based on the adjustable hybrid braking system is designed, so that the output torque can track the input torque accurately. Meanwhile a sliding mode controller is constructed, which doesn't perform with the slip ratio value as the main control parameter. Accordingly, the total torque is regulated in order to prevent the skidding of the wheel, so that the braking safety can be guaranteed.

3.1 Model following controller

3.1.1 One wheel model

When braking, slip ratio λ is generally given by,

$$\lambda = \frac{V_w - V}{V}$$

Where V is the vehicle longitudinal velocity and V_w is the wheel velocity. $V_w = R\omega$, where R , ω are the wheel radius and angular velocity respectively.

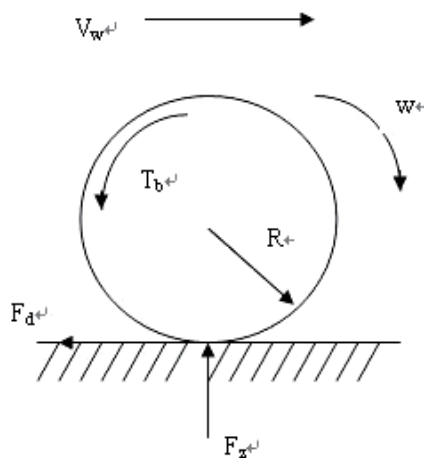


Fig. 3.1-1. One wheel model dynamic analysis

In the light of Fig. 3.1-1, the motion equations of one wheel model can be represented as

$$I_w \frac{dw}{dt} = \frac{I_w}{R} \frac{dV_w}{dt} = F_d \cdot R - T_b \quad (3.1-1)$$

$$M_w \frac{dV}{dt} = -F_d \quad (3.1-2)$$

In these equations, air resistance and rotating resistance are ignored. M_w is the weight of one wheel; I_w is the wheel rotational inertia; T_b is the braking torque, i.e. The sum of the hydraulic braking torque and the braking torque offered by the electric motor, and F_d is the braking force between the wheel and the road surface.

3.1.2 Design of MFC controller

The slip ratio is an important measurement for wheel's braking performance. For practical vehicle, it is difficult to survey this velocity. Therefore the slip ratio is hard to obtain. Compared with usual anti-skidding method, the method MFC(model following control) does not depend on the information-slip ratio. Consequently it is beneficial for the practical use.

According to the result by Tokyo University:

For the situation-skidding, the transmit function is $P(s)_{skid} = \frac{V_w}{F_{brake}} = -\frac{1}{M_w} \frac{1}{s}$

For the situation-adhesion, the transmit function is $P(s)_{adh} = \frac{V_w}{F_{brake}} = -\frac{1}{M/4 + M_w} \frac{1}{s}$

The equation above is used as the nominal model in designing the controller "Model Following Controller". M represents the mass of the vehicle. Applying the controller, the dynamics of the going to be locked wheel becomes close to that of the adhesive wheel, through which the dynamics of the vehicle will be in the emergency situation.

3.1.3 Improved MFC controller

The above listed method, especially the feedback function is based on the one-wheel-model, but in fact there is always load-transfer for each wheel so that it cannot appropriately reflect the vehicle's state. According to the origin feedback function for one-wheel-model ($M/4+M_w$), which is introduced in the above-mentioned text, the information of the vertical load of each wheel can be used to substitute for ($M/4+M_w$). Here it is called equivalent mass and then the controller will automatically follow the state of the vehicle, especially for acceleration and deceleration situation.

The specific way to achieve this idea is to use each wheel's vertical load F_z to represent its equivalent weight. So the feedback function should be F_z/g instead of ($M/4+M_w$). When necessary, there should be a wave filter to obtain a better effect.

Another aspect, which needs no modify is its control parameter. For the method above, the control parameter is the wheel velocity V_w . In order to have a better improvement of the braking performance, the wheel angular acceleration $\frac{dw}{dt}$ as the control parameter is taken advantage of.

Therefore the feedback function accordingly should be $\frac{R}{I_t + M/4 * R^2}$.

With the idea of the equivalent mass, the feedback function should be $\frac{R}{I_t + F_z / g * R^2}$.

The reason why we take use of this control parameter is the electric motor itself also shows a delay (5~10ms) in an actual situation while the phase of the wheel angular acceleration $\frac{dw}{dt}$ precedes that of the wheel velocity V_w . Consequently this control method can compensate the phases-delay of the electric motor.

3.1.4 Simulation and results

3.1.4.1 Simulation results with the wheel velocity as the control parameter

In the simulation, the peak road coefficient in the longitudinal direction is set to 0.2, which represents the low adhesive road. The top output torque of the electric motor is 136Nm and the delay time due to the physical characteristic of the electric motor 5 ms.

Fig. 3.1-2 shows the simulation result using the wheel velocity V_w as the control parameter. The braking distance is apparently decreased. The slip ratio is restrained under 20%. The unexpected increased amplitude of the slip ratio is mainly due to the delay of the electric motor's output, which can be proved in Fig. 3.1-2 (b). This can cause contradiction in the braking process. Fig. 3.1-2 (c) shows longitudinal vehicle velocity and wheel velocity under this control parameter.

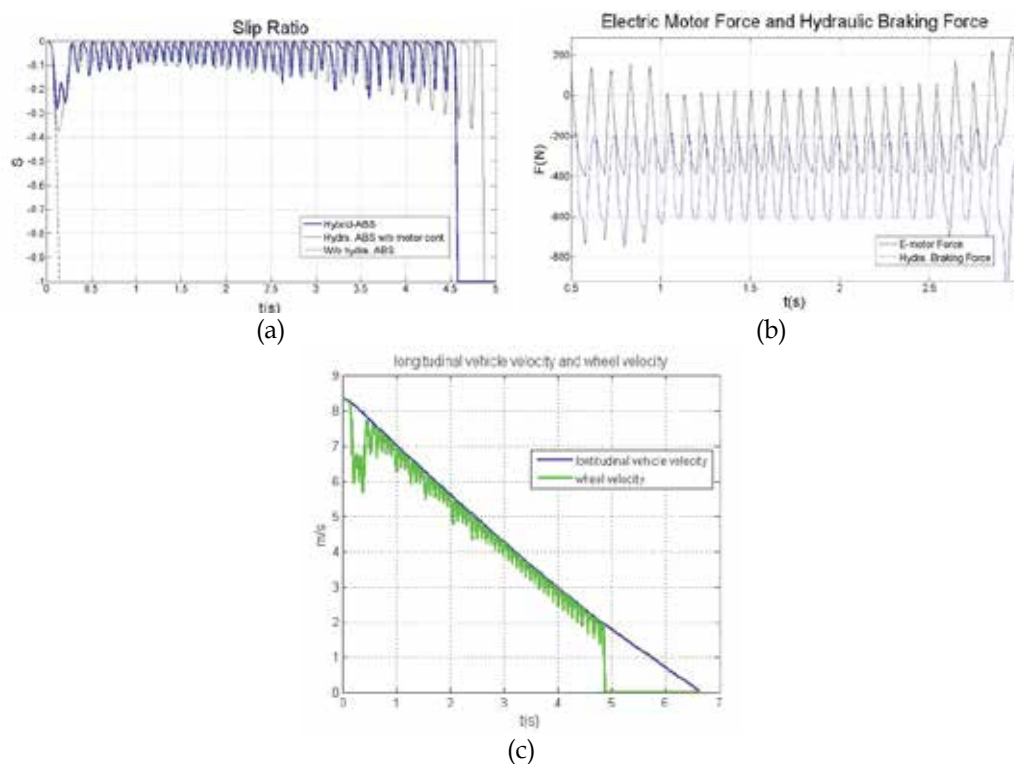


Fig. 3.1-2. Simulation Result of the Hybrid-ABS with the wheel velocity as the control parameter

3.1.4.2 The simulation results with the angular acceleration as the control parameter

Fig. 3.1-3 shows the simulation result using the wheel angular acceleration $\frac{dw}{dt}$ as the control parameter and increase the top output torque of the electric motor. Compared with the previous simulation result, it is clear that the braking distance is further shortened (compared with the system without electric motor control). The slip ratio is also restrained under 20% and is controlled better than the previous control algorithm. From Fig. 3.1-3 (b) we can see the phase-delay of the electric motor is greatly improved so that the two kinds of the torques can be simply coordinated regulated.

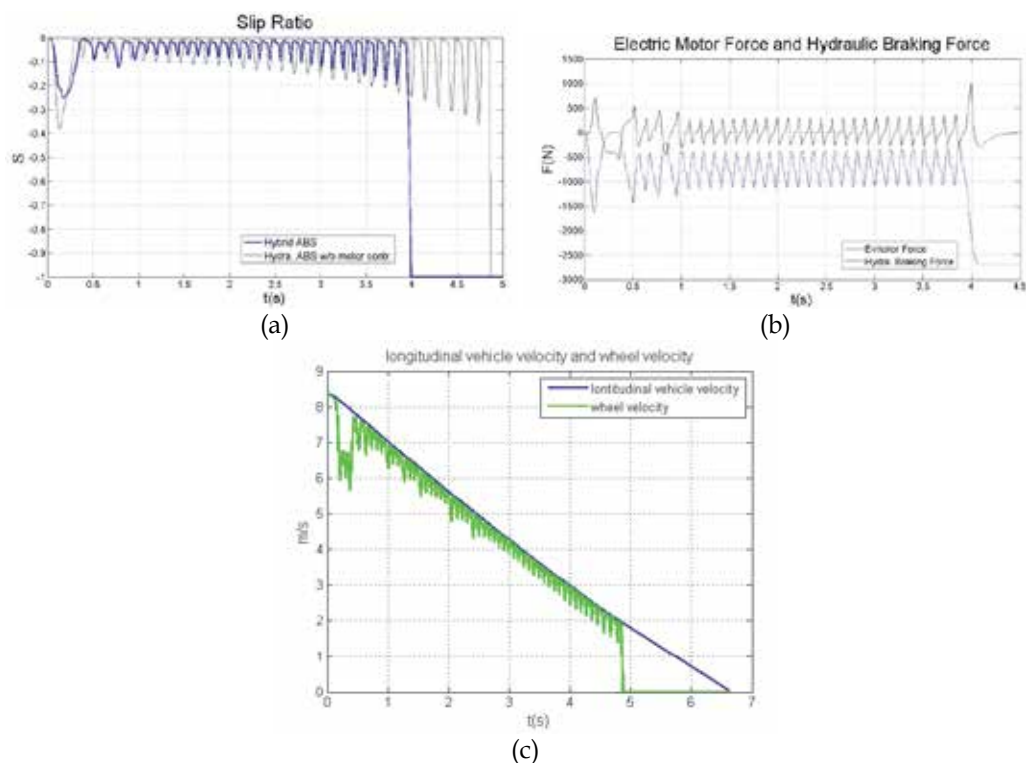


Fig. 3.1-3. Simulation results of the Hybrid-ABS with the angular acceleration as the control parameter

Table 2 shows the result of the braking distance and the braking time under three above-mentioned methods.

	Hydraulic ABS without motor control	Hybrid ABS with MFC	Hybrid ABS with improved MFC
Braking distance(m)	27.9	26.8	26.5
Braking time(s)	5.12	4.87	4.83

Table 2. Results of the braking distance and the braking time under three different methods

3.1.5 Conclusion

According to the simulation results, the braking performance of the improved MFC is better than the performance of the origin MFC, proposed by Tokyo University. In future can we modify the MFC theory through the choice of the best slip ratio, because we know the value of the best slip ratio is not 0 but about 2.0. When we can rectify MFC theory in this aspect, the effect of the braking process will be better.

3.2 Design of the braking torque dynamic distributor

The distributor's basic design idea is to make the hydraulic system to take over the low frequency band of the target braking torque, and the motor to take over the high frequency band. Then the function of the rapid adjustment can be reached.

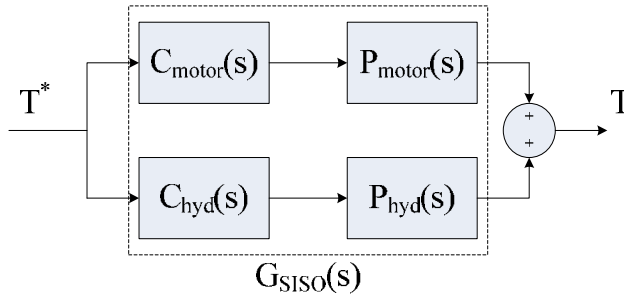


Fig. 3.2-1. The block diagram of the braking torque dynamic distributor

According to Fig. 3.2-1, $C_1(s)$ and $C_2(s)$ in Fig. 3.2-1 are the model of motor and hydraulic system. They can be written expressed as (1) and (2):

$$C_1(s) = \frac{1}{\tau_M s + 1} \quad (3.2-1)$$

$$C_2(s) = \frac{1}{\tau_H s + 1} \quad (3.2-2)$$

Here, τ_M and τ_H are time constants for motor and hydraulic system relatively.

In order to reach the goal to track the braking torque, $G_{SISO}(s) = 1$, that is,

$$C_1(s) \cdot G_1(s) + C_2(s) \cdot G_2(s) = 1 \quad (3.2-3)$$

We can put formula (3.2-1) and formula (3.2-2) into formula (3.2-3),

$$C_{motor}(s) \cdot \frac{1}{\tau_M s + 1} + C_{hyd}(s) \cdot \frac{1}{\tau_H s + 1} = \frac{1}{\tau s + 1} \quad (3.2-4)$$

$$\begin{aligned} C_{motor}(s) &= \left[\frac{1}{\tau s + 1} - C_{hyd}(s) \cdot \frac{1}{\tau_H s + 1} \right] \cdot (\tau_M s + 1) \\ &= \frac{\tau_M s + 1}{\tau s + 1} - C_{hyd}(s) \cdot \frac{\tau_M s + 1}{\tau_H s + 1} \end{aligned} \quad (3.2-5)$$

Here, τ is the sampling step

$C_{\text{hyd}}(s)$ is chosen as the second-order Butterworth filter, and then according to (3.2-5) we can get $C_{\text{motor}}(s)$. And the saturation torque of the motor is limited by the speed itself.

3.3 Design of the sliding mode controller

3.3.1 Design of switching function

The control target is to drive the slip ratio to the desired slip ratio. Here a switching function is defined as:

$$s = \lambda - \lambda_{\text{reference}} \quad (3.3-1)$$

The switching function is the basis to change the structure of the model. And the commonest way to change the structure is to use sign function- $\text{sgn}(s)$. The control law here combines equivalent control with switching control so that the controller can have excellent robustness in face with the uncertainty and interference of the environment.

So the control law can be expressed as:

$$u = u_{\text{eq}} + u_{\text{vss}} \quad (3.3-2)$$

Therefore the braking torque can be represented as:

$$T_b = T_{b,\text{eq}} - \Delta T \text{sgn}(s) \quad (3.3-3)$$

In practical engineering applications, the chattering may appear when sign function is used. Therefore the Saturation function 'sat ()' is used to substitute for sign function.

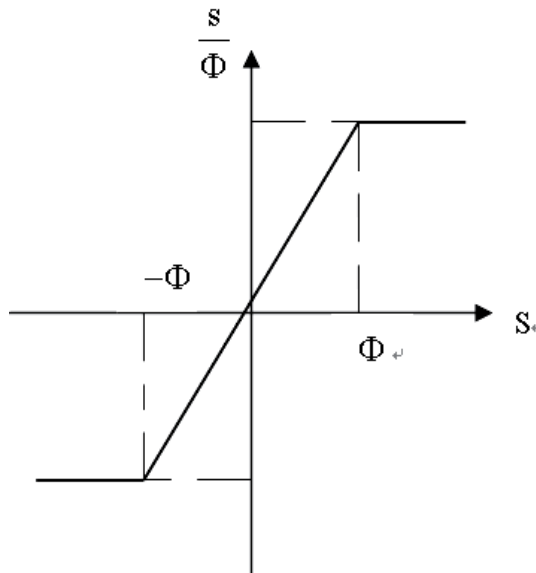


Fig. 3.3-1. Saturation function

So the braking torque can be expressed as:

$$T_b = T_{b,eq} - \Delta T_{sat} \left(\frac{s}{\Phi} \right) \tag{3.3-4}$$

3.3.2 The improved sliding mode controller

One desired slip ratio can't achieve the best braking effect because of the inaccurate measurement of the vehicle speed and the change of the road surface. Then, a new method based on sliding mode control will be proposed according to the characteristic of the $\mu - \lambda$ curve. It can seek the optimal slip ratio automatically. The typical $\mu - \lambda$ curve is shown in Fig.3.3-2.

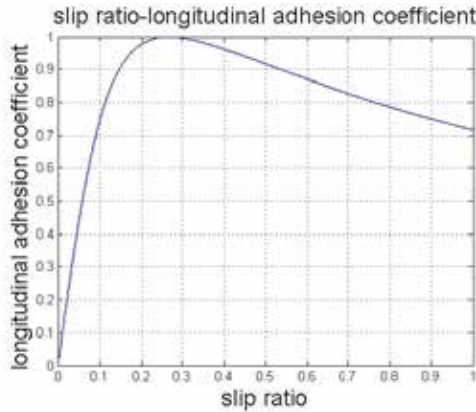


Fig. 3.3-2. $\mu - \lambda$ curve

From Fig. 3.3-2, we can see:

When $\frac{d\mu}{d\lambda} > 0, \lambda < \lambda_{reference}$, λ needs increasing in order to obtain larger μ . At this point we can increase the braking torque on the wheel;

When $\frac{d\mu}{d\lambda} = 0, \lambda = \lambda_{reference}$, λ needs maintaining in order to obtain larger μ . At this point we can maintain the braking torque on the wheel;

When $\frac{d\mu}{d\lambda} < 0, \lambda > \lambda_{reference}$, λ needs decreasing in order to obtain larger μ . At this point we can decrease the braking torque on the wheel.

According to the one wheel model and the definition of slip ratio, we can receive:

$$\begin{aligned} \frac{d\mu}{d\lambda} &= \frac{d\mu / dt}{d\lambda / dt} = - \frac{\dot{T}_b + I_w \ddot{\omega}}{F_Z R} * \frac{V_x}{R \dot{\omega}} \\ &= - \frac{\dot{T}_b + I_w \ddot{\omega}}{\dot{\omega}} * \frac{V_x}{F_Z R} \end{aligned} \tag{3.3-5}$$

That is:

$$\text{When } -\frac{\dot{T}_b + I_w \ddot{w}}{\dot{w}} > 0, \lambda < \lambda_{reference}, s = \lambda - \lambda_{reference} < 0$$

$$\text{When } -\frac{\dot{T}_b + I_w \ddot{w}}{\dot{w}} = 0, \lambda = \lambda_{reference}, s = \lambda - \lambda_{reference} = 0$$

$$\text{When } -\frac{\dot{T}_b + I_w \ddot{w}}{\dot{w}} < 0, \lambda > \lambda_{reference}, s = \lambda - \lambda_{reference} > 0$$

The interval of the optimal slip ratio is commonly from 0.1 to 0.2. Therefore, when the slip ratio calculated by $\lambda = \frac{\omega R - V_x}{V_x}$ is larger than 0.3, we can judge that the current slip ratio is surely larger than the optimal slip ratio. The output of the sign function is 1.

So the algorithm based on $\mu - \lambda$ curve can be improved as:

When the slip ratio calculated by $\lambda = \frac{\omega R - V_x}{V_x}$ is bigger than 0.3, then we know that the actual slip ratio must be bigger than the optimal slip ratio, then the output of the sign function is 1;

When the slip ratio calculated by $\lambda = \frac{\omega R - V_x}{V_x}$ is smaller than 0.3,

i. If $|\dot{w}| > \phi_w$,

$$\left\{ \begin{array}{l} \frac{J_w \ddot{w} + \dot{T}_b}{\dot{w} + \phi_w} > 0 \quad \text{sgn}(s) = 1 \\ \frac{J_w \ddot{w} + \dot{T}_b}{\dot{w} + \phi_w} < 0 \quad \text{sgn}(s) = -1 \end{array} \right.$$

ii. If $|\dot{w}| \leq \phi_w$

Sign function maintains the output of the last step, that is: $\text{sgn}(s)_t = \text{sgn}(s)_{t-1}$.

3.3.3 Simulation and results

Fig. 3.3-3 shows the effect of the braking torque dynamic distributor. Since the existence of the saturation torque of the motor, it can't track the input torque when the input torque too large. When the demand torque is not too large, the braking torque dynamic distributor illustrates excellent capability.

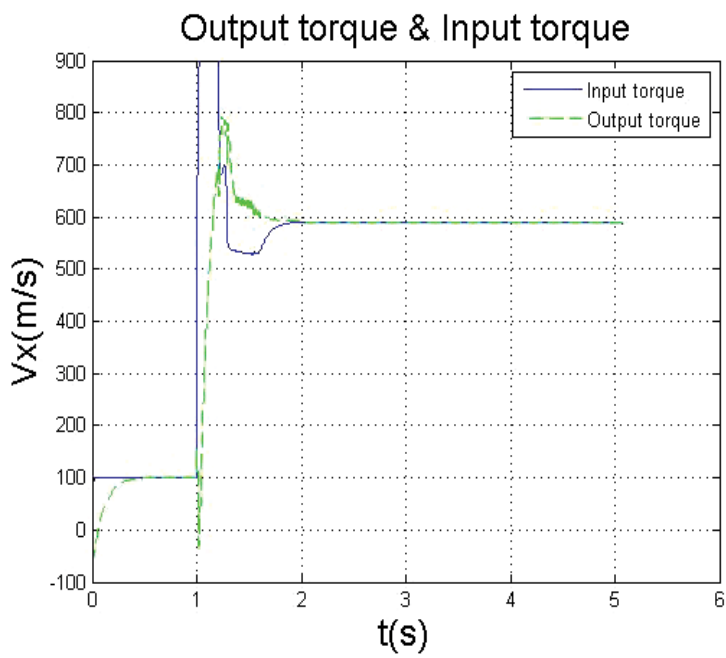


Fig. 3.3-3. The character of the braking torque dynamic distributor

Fig.3.3-4 - Fig.3.3-6 is the simulation results, which get from the improved sliding mode controller, and the initial velocity of the vehicle is 80km/h, the saturation torque of the motor is 180Nm :

i. When adhesion coefficient $\mu = 0.9$:

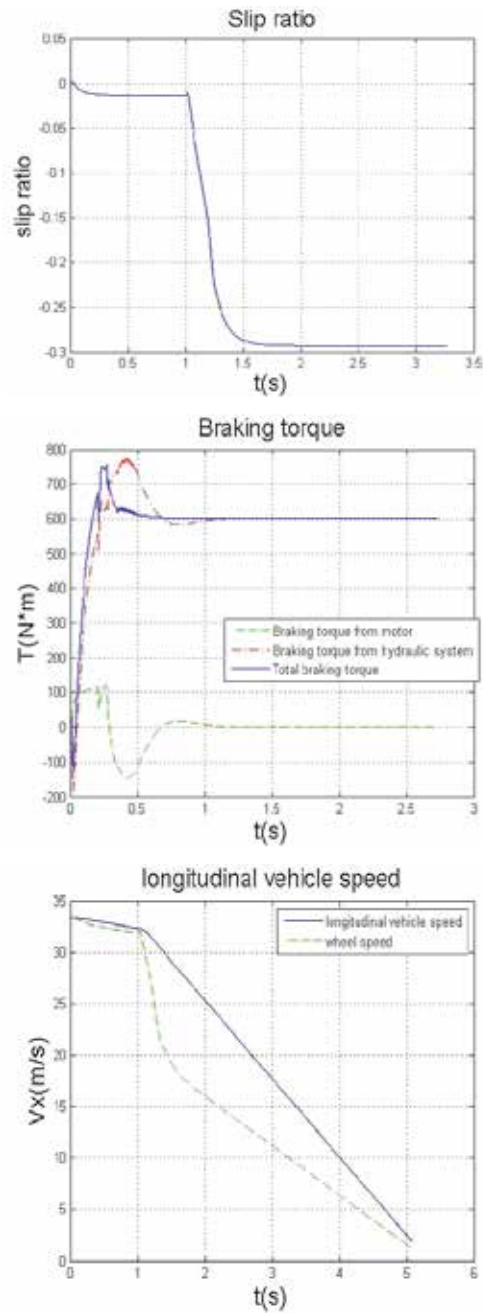


Fig. 3.3-4. Simulation results on the road with $\mu = 0.9$

ii. When adhesion coefficient $\mu = 0.2$:

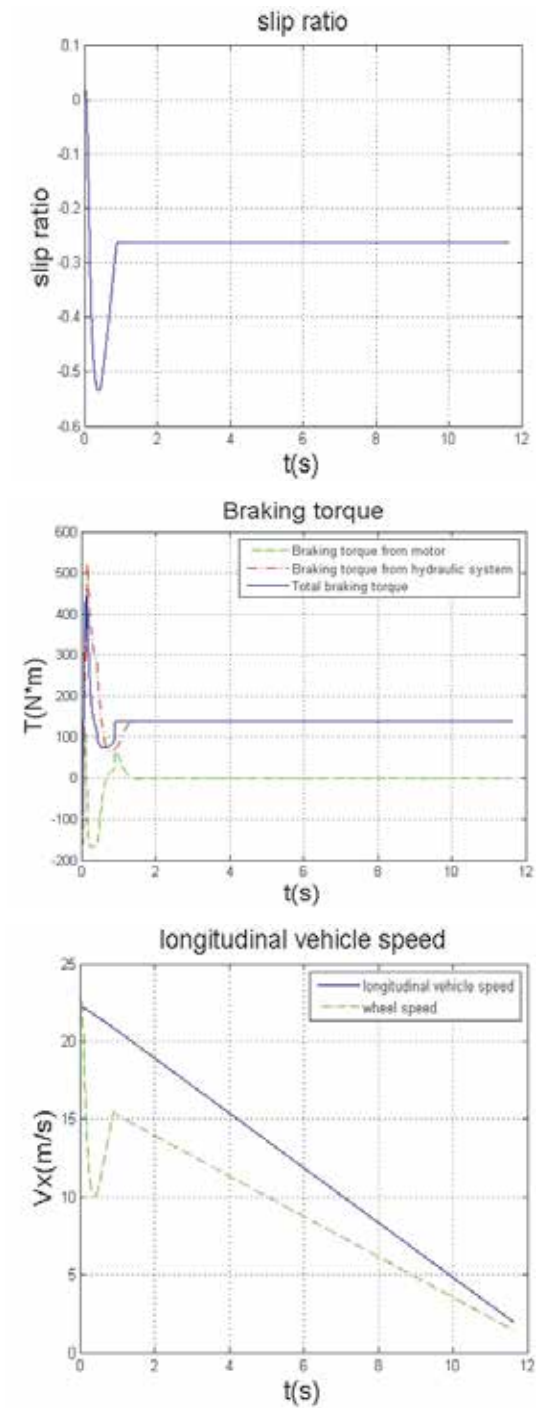


Fig. 3.3-5. Simulation results on the road with $\mu = 0.2$

iii. When adhesion coefficient changes in 1st second from 0.2 to 0.9:

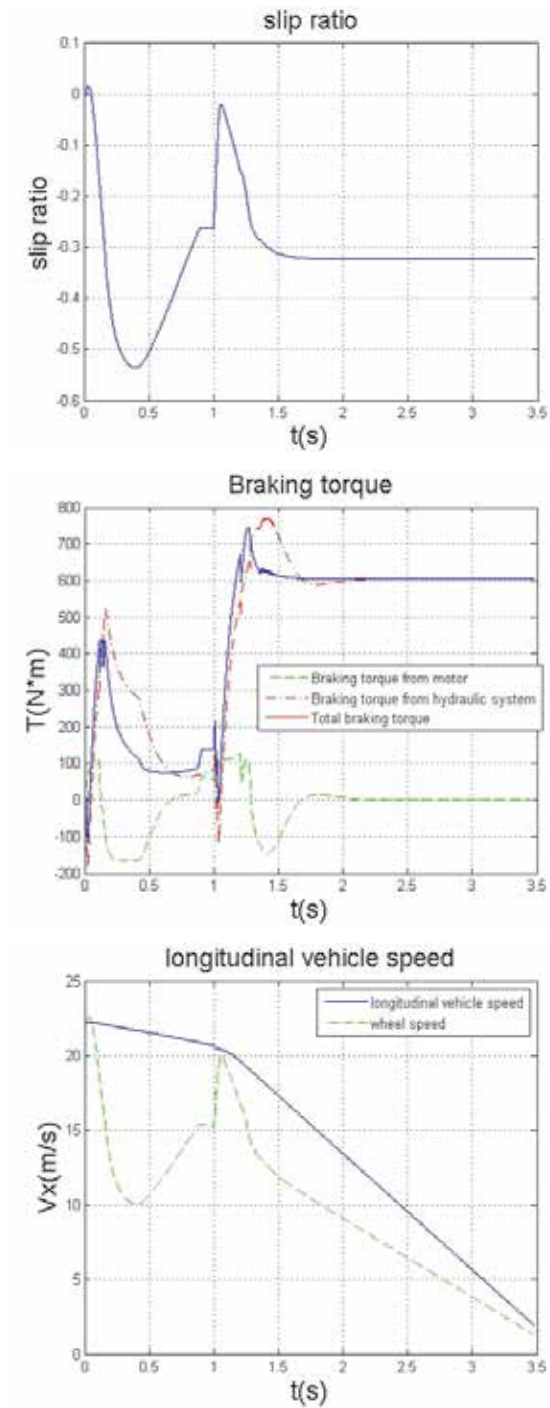


Fig. 3.3-6. The road adhesion coefficient changes from $\mu = 0.2$ to $\mu = 0.9$ at the 1st second

From Fig.3.3-4 -Fig.3.3-6, we know that, although this method doesn't regard slip rate as the main control information, this sliding mode can track the optimal slip ratio automatically. That means, both the longitudinal adhesion force and the lateral adhesion force can be made use of fully. Even on the road, whose adhesion coefficient increases suddenly, the controller can also find the optimal slip ratio.

During the braking process, the torque offered by the motor and hydraulic system doesn't oscillate distinctly. It indicates, the hybrid-braking system can achieve target braking torque actually.

Table 3 shows the braking distance and braking time on the different road. From the datum we know the braking safety can be guaranteed with this anti-skidding controller.

Number	Adhesion coefficient	Braking distance(m)	Braking time(s)
a)	0.9	33.99	2.71
b)	0.2	136.6	11.62
c)	0.2-0.9	50.23	3.47

Table 3. Braking distance and braking time on the different road

3.3.4 Conclusion

The braking torque dynamic distributor, which combines the merits of the two actuators motor and hydraulic system, can track the demanded torque promptly and effectively. The sliding mode controller has two sorts. One is to track the desired slip ratio, which is set manually and the effect of the controller good. However, the measurement of the vehicle velocity and the identification of the road limit the promotion of the usage. The other kind of controller can seek the optimal slip ratio automatically. Through the result of the simulation, the effectiveness of this controller is proved. It can have a wider range of application.

4. Vehicle stability control

Many researchers in the last decade have reported that direct yaw moment control is one of the most effective methods of active chassis control, which could considerably enhance the vehicle stability and controllability. The direct yaw moment control of a traditional ICE (Internal Combustion Engine) vehicle is based on the individual control of wheel braking force known as the differential braking. However, for EVs, the generation of desired yaw moment for stabilizing the vehicle under critical driving conditions can be achieved by rapid and precise traction/braking force control of each in-wheel-motor.

In this section, a hierarchical vehicle stability control strategy is introduced.

The high level of the control strategy is the vehicle motion control level. A dynamic control system of a 4 in-wheel-motored electric vehicle which improves the controlling stability under critical situation is presented. By providing the method of estimating the cornering stiffness and combining the controller with optimal control allocation algorithm, which takes account of the couple characteristic of the longitudinal/lateral force for tire under critical situation, the vehicle stability control system is designed. The double lane change simulation was carried out to verify the validity of the control method. Simulation result shows the proposed control method could stabilize the vehicle posture well under critical condition. Compared with the LQR with fixed cornering stiffness, the feedback from

identifying cornering stiffness to correct the parameters of the controller helps a lot in improving the robustness of the stability control.

The low level of the control strategy is the control allocation level, in which the longitudinal force's distribution is the focal point. Through the analysis of the tire characteristics under the combined longitudinal and lateral forces, an effectiveness matrix for the control allocation considering the longitudinal force's impact on the lateral force was proposed. Based on Quadratic Programming method the longitudinal forces on each wheel are optimal distributed. The simulation results indicate that the proposed method can enhance the vehicle handling stability, meanwhile the control efficiency is improved as well.

4.1 Vehicle dynamic control structure

Studies have shown that hierarchical control of the dynamics control method has a clear, modular control structure, as well as better control robustness, which is easy for real vehicle applications of the control algorithms. This hierarchical control architecture is widely adopted by general chassis's integrated control. VDC (vehicle dynamic control) introduces the hierarchical control structure, as shown in Fig. 4.1-1, the upper level is the vehicle motion control and the bottom level is the control allocation for each actuator.

The motion controller which belongs to the first level in the stability algorithm, collects the signals from the steering wheel's angle and the accelerator pedal, and calculates the generalized forces required by the stability control, including the longitudinal forces F_{xT} and yaw moment M_{zT} . The longitudinal forces can be directly calculated according to the accelerator pedal signals. The yaw moment can be got by following the reference model.

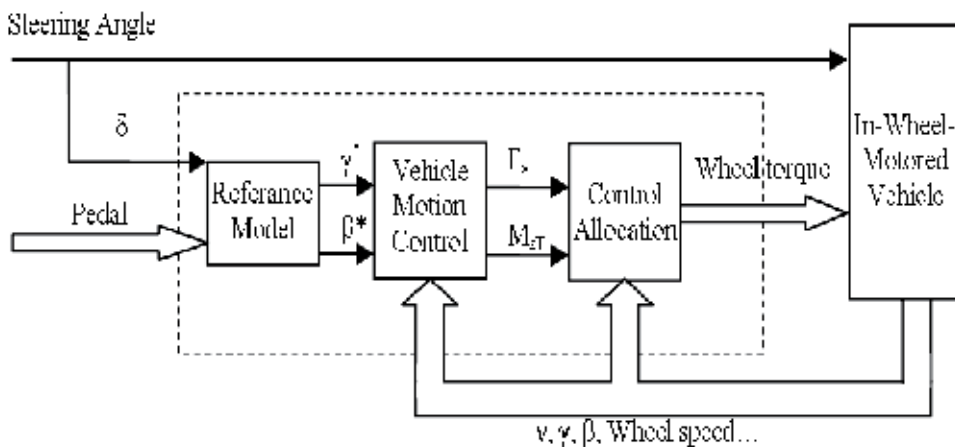


Fig. 4.1-1. Vehicle dynamic control structure

The control allocation is the second level of the vehicle controller. It is responsible to convert the "generalized forces" to the sub-forces on each actuator according to certain distribution rules and under some external constraint conditions (such as the maximum output of the motor and the road adhesion coefficient, etc.). And then to realize the optimum distribution of the each motor's torque. For a 4WD electric vehicle driven by 4 in-wheel-motors, the sub-force on each actuator is just the tire longitudinal force formed by the motor's output torque.

4.2 Vehicle motion controller

The yaw moment control is based on the MFC (model follow control) method. As reference model, the DYC model could keep slip angle zero for stability. The gain scheduling control algorithm can revise the parameters real-timely through the cornering stiffness identification to improve the adaptability of the algorithm to the environment and the change of the model parameters. The variable structure control (VSC) is applied to design control algorithm, for considering the strong robust characteristic during uncertainty. With proposed non-linear vehicle model, a precise gain value for switch function will be calculated, in order to reduce chattering effect.

4.2.1 Vehicle model

4.2.1.1 Linear vehicle model

The simplified linear two freedom model make the side slip angle and the yaw rate as its state variables. As the control input, the yaw moment M_{zT} is gained from the longitudinal force allocation by the motors according to the required moment, the function is:

$$m \cdot V \left(\frac{d\beta}{dt} + \gamma \right) = F_{yf} + F_{yr} \quad (4.2-1)$$

$$J_z \frac{d\gamma}{dt} = M_y + M_{zT} \quad (4.2-2)$$

The description of the state space is:

$$\dot{X} = AX + E\delta + Bu \quad (4.2-3)$$

Here : $x = [\beta \ \gamma]^T$, $u = M_{zT}$

$$A = \begin{bmatrix} -\frac{2(C_f + C_r)}{mV} & -1 - \frac{2(C_f l_f - C_r l_r)}{mV^2} \\ -\frac{2(C_f l_f - C_r l_r)}{J_z} & -\frac{2(C_f l_f^2 + C_r l_r^2)}{J_z V} \end{bmatrix}$$

$$E = \begin{bmatrix} \frac{2C_f}{mV} \\ \frac{2C_f l_f}{J_z} \end{bmatrix}, B = \begin{bmatrix} 0 \\ \frac{1}{J_z} \end{bmatrix} \quad (4.2-4)$$

$M_y = F_{yf} l_f - F_{yr} l_r$ represents the yaw motion caused by the lateral force acting on each wheel, F_{yf} , F_{yr} are the total front/rear wheel lateral forces. Other parameters are shown in Fig.4.2-1.

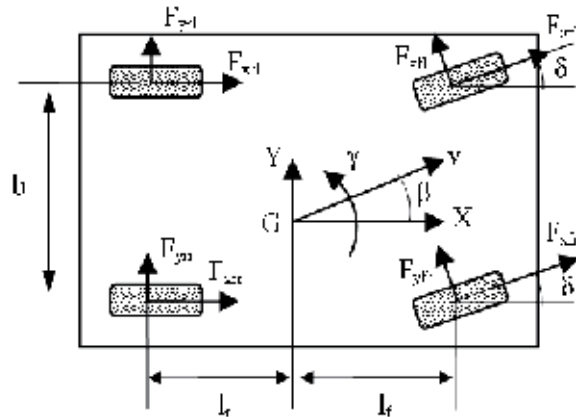


Fig. 4.2-1. Planar vehicle motion model

4.2.1.2 Non-linear vehicle model

In this paper the arc-tangent function is used to fit the lateral force formula, then a simple non-linear vehicle model can be obtained, the arc-tangent function contains two fitting parameters c_1, c_2 , the fitting effect is show below:

The state space of One-track non-linear vehicle model can be express as: $\mathbf{x} = [x_1 \ x_2]^T = [\beta \ \psi]^T, h(x) = \beta = x_1, \beta$ is the centroid-side angle of the vehicle, ψ is the course angle of the vehicle, u means additional yaw moment input M_{zT} , the complete function is:

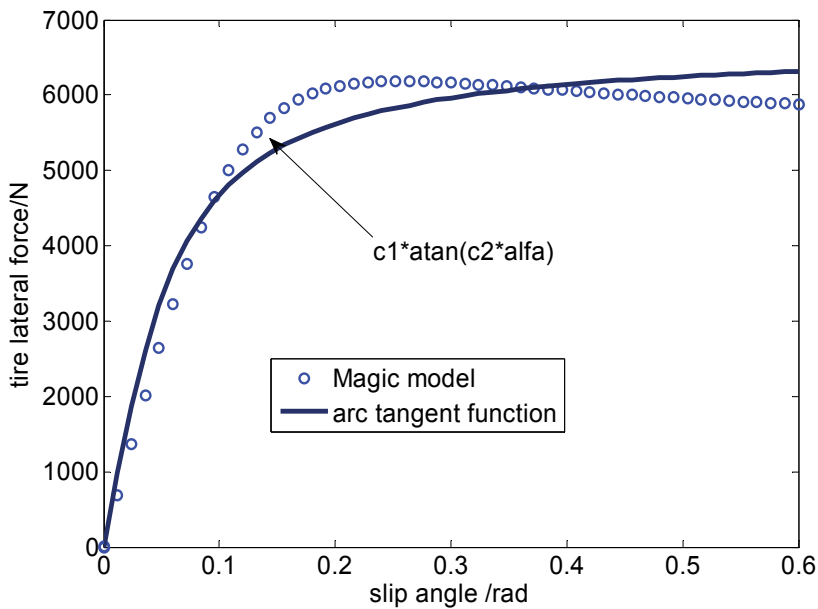


Fig. 4.2-2. Arc-tangent function vs. magic model

$$\begin{bmatrix} \dot{x}_1 \\ \dot{x}_2 \end{bmatrix} = \begin{cases} \frac{1}{mV} \{c_{f1} a \tan[c_{f2}(\delta_f - x_1 - \frac{l_f}{V}x_2)] \cos \delta_f \\ \quad + c_{r1} a \tan[c_{r2}(-x_1 + \frac{l_r}{V}x_2)]\} - x_2 \\ \frac{1}{J_z} \{l_f c_{f1} a \tan[c_{f2}(\delta_f - x_1 - \frac{l_f}{V}x_2)] \cos \delta_f \\ \quad - l_r c_{r1} a \tan[c_{r2}(-x_1 + \frac{l_r}{V}x_2)] + u \end{cases} \quad (4.2-5)$$

Here, m represents the mass of the vehicle, J_z represents the yaw rotational inertia of the vehicle, c_{f1} and c_{f2} are the fitting parameters for the front wheel, c_{r1} and c_{r2} are the fitting parameters for the rear wheel, l_f is the distance from the gravity point to the front axle and l_r is the distance from the gravity point to the rear axle, V is the gravity point velocity of the vehicle, δ_f is the steering angle for the front wheel.

Based on non-linear model mention above, we can design yaw-rate follow controller. In our case, the dynamic function of yaw rate is second-order system:

$$\begin{aligned} \ddot{\psi} &= f(X,t) + \Delta f(X,t) + g(u) + d(t) \\ &= \frac{1}{J_z} (F_{yf}(\alpha_f, F_{fz}, \mu) \cdot l_f - F_{yr}(\alpha_r, F_{rz}, \mu) \cdot l_r) \\ &\quad + \Delta f(X,t) + \frac{1}{J_z} u + d(t) \end{aligned} \quad (4.2-6)$$

Here, α_f is the side slip angle for the front wheel, α_r is the side slip angle for the rear wheel, F_{yf} and F_{yr} are the side slip force for the front and rear wheel, F_{fz} and F_{rz} are the vertical load for the front and rear wheel, μ is the road adhesion coefficient.

$f(X,t)$ indicates non-linear system function; $g(u)$ indicates non-linear continued function; $\Delta f(X,t)$ and $d(t)$ stand for uncertainty and external disturbance of controlled object, which are supposed to be zeros.

4.2.2 Reference model

The desired yaw-rate output is calculated from the reference model (DYC):

$$\dot{\gamma}_d = -\frac{1}{\tau_d} \cdot \gamma_d + \frac{k_d}{\tau_d} \delta \quad (4.2-7)$$

$$\text{Here: } k_d = \frac{2C_f V}{mV^2 + 2(C_f l_f - C_r l_r)} ; \tau_d = \frac{J_z \cdot V}{2(C_f l_f^2 + C_r l_r^2)}$$

4.2.3 Controller design

4.2.3.1 Gain scheduling controller

Based on the linear vehicle model, the controller adapts the LQR stability control algorithm. It is composed of feed-forward and feedback. Supposing the relationship between the feed-forward yaw moment and the front-wheel steering angle as:

$$M_{ff}(s) = G_{ff}\delta(s) \quad (4.2-8)$$

Here: G_{ff} is the feed-forward yaw moment coefficient. It can be calculated through the transfer function from vehicle side slip angle to front-wheel steering angle under stable condition, i.e. $\beta(s)/\delta(s)$ when $\beta(0) = 0$. Then.

$$G_{ff} = \frac{4C_f C_r l_f l_r - 2C_f l_f m V^2}{m V^2 + 2(C_f l_f - C_r l_r)} \quad (4.2-9)$$

Feedback control is used to decrease the control system's error caused by the unknown perturbation and the imprecise of the model, and to improve the reliability of the control system.

Define the state error $E = X - X_d$, from function (4.2-3), (4.2-7):

$$\dot{E} = AE + BM_{fb} + (A - A_d)X_d + (E - E_d)\delta \quad (4.2-10)$$

Considering the last two as perturbation, and according to LQR, assure the target function below to be least:

$$J = \int_0^{\infty} (EQE^T + uRu^T)dt \quad (4.2-11)$$

By solving the Riccati function, feedback coefficient G_{fb} is gained. And the feedback moment is:

$$M_{fb} = -G_{fb}E = -g_{fb1}(\beta - \beta_d) - g_{fb2}(\dot{\psi} - \dot{\psi}_d) \quad (4.2-12)$$

Total yaw moment required is:

$$M_{zT} = M_{ff} + M_{fb} \quad (4.2-13)$$

From the analysis above, we know the total yaw moment is decided by the feed-forward coefficient G_{ff} and feed-back coefficient G_{fb} together. And the coefficients can be adjusted on time according to the front and rear cornering stiffness identified and the vehicle speed measured. The control algorithm refers to the linear optimization calculation and on-line resolution of the Riccati function, which can affect the real time performance. On the real car the coefficients corresponding to different cornering stiffness and the vehicle speed are calculated off-line previously. Then a look-up table will be made from that and will be downloaded to the ECU for control. To easily show the movement of the feed-forward and feed-back coefficients, the following figure will illustrate the change of the front and rear cornering stiffness together through supposing the front cornering stiffness is changing, while the rear one is a fixed proportion to it.

Cornering stiffness is an important parameter for the controller. It will change along with the road condition or under the critical condition of the vehicle, which will further affect the control precise of the vehicle stability. The cornering stiffness that DYC control relies on is linear to the cornering stiffness under the current condition. So the cornering stiffness in this paper is estimated based on the two freedom linear model.

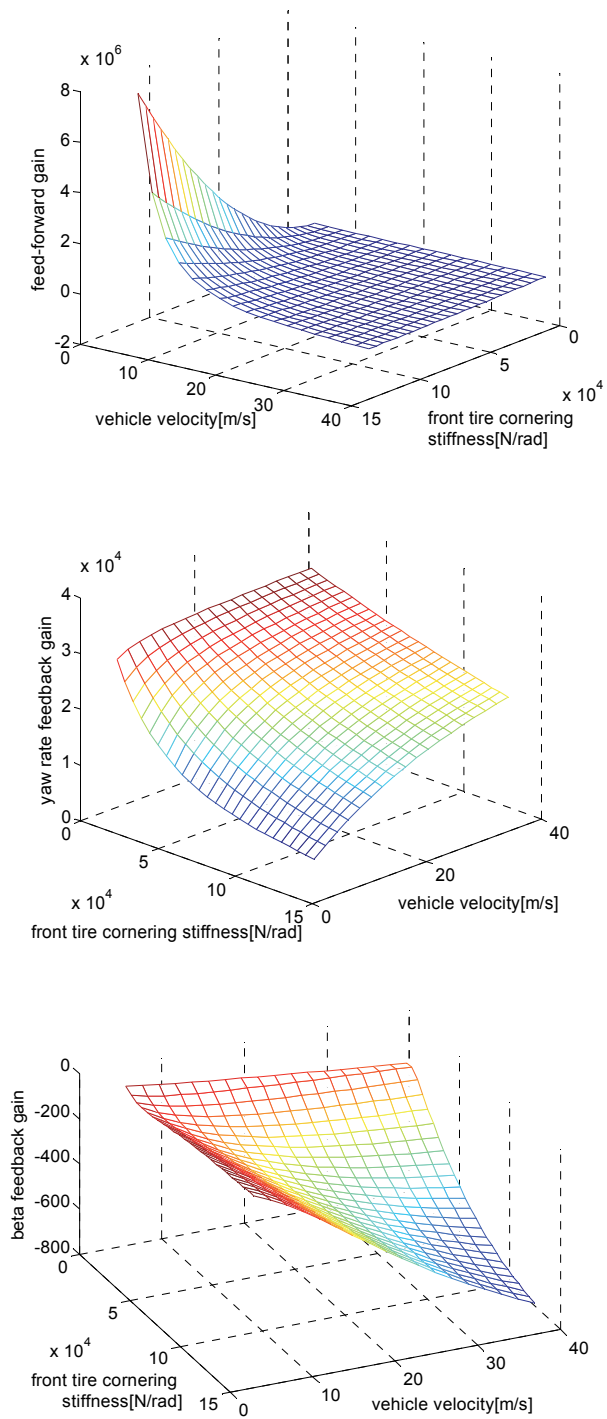


Fig. 4.2-3. Feed-forward/Feed-back Map

From function (4.2-2), M_y is:

$$M_y = 2C_f(\beta + \frac{l_f}{V} - \delta)l_f - 2C_r(\beta - \frac{l_r}{V})l_r \quad (4.2-14)$$

Here C_f, C_r are front and rear nominal cornering stiffness. M_y above needs to be estimated by the yaw moment observation(YMO) below:

$$\hat{M}_y = F(s)(J_z \dot{\gamma} - M_{zT}) \quad (4.2-15)$$

Here: $F(s) = \omega_c / (s + \omega_c)$ is a filter function to gain $\dot{\gamma}$. ω_c is truncation frequency.

From function (4.2-14): to estimate the front and rear cornering stiffness separately, the estimator must provide the information of β . Therefore a united estimation of C_f, C_r, β needs to be established. To simplify the design, some change has been made to the function above. According to the magic tire model, the wheel cornering stiffness is pro rata to the load under a certain load range ($C_f l_f \approx C_r l_r$). And as β is a small value, then:

$$C_f l_f \beta - C_r l_r \beta \ll M_y \quad ; \quad (4.2-16)$$

Thus function (4.2-14) can be :

$$M_y = -2C_f l_f (\frac{l_f + l_r}{V} \gamma - \delta) \quad (4.2-17)$$

$$\hat{M}_y(t) = \theta^T \cdot \varepsilon(t), \theta^T = C_f, \quad (4.2-18)$$

$$\varepsilon(t) = F(s) \cdot \left(-2l_f (\frac{l_f + l_r}{V} \gamma - \delta) \right) \quad (4.2-19)$$

Based on the above model, the front and rear cornering stiffness C_f, C_r will be gained by RLS estimation, as follows:

$$\begin{aligned} \hat{\theta}(k) &= \hat{\theta}(k-1) - \frac{\Gamma(k-1)\varepsilon(k)}{\sigma + \varepsilon^T(k)\Gamma(k-1)\varepsilon(k)} \\ &\quad \cdot \{ \varepsilon^T(k)\hat{\theta}(k-1) - y(k) \} \\ \Gamma(k) &= \frac{1}{\sigma} \left\{ \begin{array}{l} \Gamma(k-1) - \\ \frac{\Gamma(k-1)\varepsilon(k)\varepsilon^T(k)\Gamma(k-1)}{\sigma + \varepsilon^T(k)\Gamma(k-1)\varepsilon(k)} \end{array} \right\} \quad (4.2-20) \end{aligned}$$

σ is forget factor and can be properly selected according to the road condition.

With the estimation result the controller parameters can be corrected on time. And a more precise general force can be gained to improve the allocation control of the vehicle.

4.3 Control allocation algorithm

Through the control of the upper level, the yaw moment M_{zT} is gained, which will be allocated to each actuator to realize the control target (on 4WD EV is the motor torque).

4.3.1 Effectiveness matrix

Making approximation: $\sin \delta \approx 0$ and $\cos \delta \approx 1$, the total vehicle longitudinal force and the yaw moment caused by the longitudinal force are as follows:

$$\begin{aligned} F_{xT} &= F_{xfl} + F_{xfr} + F_{xrl} + F_{xrr} \\ M_{zxT} &= \frac{b}{2}(-F_{xfl} + F_{xfr} - F_{xrl} + F_{xrr}) \end{aligned} \quad (4.3-1)$$

Expressed as:

$$\begin{aligned} F_{xT} &= B_x \mathbf{F}_x \\ M_{zT} &= B_{zx} \mathbf{F}_x \end{aligned} \quad (4.3-2)$$

Where: $\mathbf{F}_x = [F_{xfl} \ F_{xfr} \ F_{xrl} \ F_{xrr}]^T$; $B_x = [1 \ 1 \ 1 \ 1]$, $B_{zx} = [-\frac{b}{2} \ \frac{b}{2} \ -\frac{b}{2} \ \frac{b}{2}]$, B_x and B_{zx} are named as the effectiveness matrix.

In most researches, the vehicle yaw moment was directly obtained by (4.3-1). As the coupling characteristics of tires, the change of the tire longitudinal forces leads to the change of its' lateral force, especially in the critical conditions. So it's necessary to consider the additional yaw moment caused by the change of the lateral force.

Under certain tire sideslip angle α , the relationship between the four wheels' lateral and longitudinal forces can be expressed as:

$$\mathbf{F}_y = f_{yx}^\alpha(\mathbf{F}_x) \quad (4.3-3)$$

Where: $\mathbf{F}_y = [F_{yfl} \ F_{yfr} \ F_{yrl} \ F_{yrr}]^T$
 f_{yx}^α is a non-linear function, which brings complexity in the computation of the effectiveness matrix and the optimization of the control distribution. While if direct linear approximation was made to it, it would be too simplistic.

Discretization of the total yaw moment demand from the vehicle motion controller comes to:

$$M_{zT}(t+1) = M_{zT}(t) + \Delta M_{zT} \quad (4.3-4)$$

Supposing that δ is a small value, then $\sin \delta \approx 0$ and $\cos \delta \approx 1$. The increment of the total yaw moment can be expressed as:

$$\Delta M_{zT} = B_{zx} \Delta \mathbf{F}_x + B_{zy} \Delta \mathbf{F}_y \quad (4.3-5)$$

Here: $B_{zx} = \begin{bmatrix} -\frac{b}{2} & \frac{b}{2} & -\frac{b}{2} & \frac{b}{2} \end{bmatrix}$, $B_{zy} = \begin{bmatrix} l_f & l_f & -l_r & -l_r \end{bmatrix}$

$$\Delta \mathbf{F}_x = [\Delta F_{xfl} \quad \Delta F_{xfr} \quad \Delta F_{xrl} \quad \Delta F_{xrr}]^T$$

$$\Delta \mathbf{F}_y = [\Delta F_{yfl} \quad \Delta F_{yfr} \quad \Delta F_{yrl} \quad \Delta F_{yrr}]^T$$

Under a certain tire cornering angle α , the coupling relation of the tire longitudinal/lateral forces can be expressed as:

$$\mathbf{F}_y = f_{yx}^\alpha(\mathbf{F}_x) \quad (4.3-6)$$

Here: $\mathbf{F}_x = [F_{xfl} \quad F_{xfr} \quad F_{xrl} \quad F_{xrr}]^T$, $\mathbf{F}_y = [F_{yfl} \quad F_{yfr} \quad F_{yrl} \quad F_{yrr}]^T$.

then: $\Delta \mathbf{F}_y = \nabla f_{yx}^\alpha(\Delta \mathbf{F}_x)$

Magic formula can describe the tire characteristics under the combined working condition, but too complex. According to tire friction ellipse, the tire characteristics can be

approximated expressed as: $\left(\frac{F_y}{F_{y0}^\alpha}\right)^2 + \left(\frac{F_x}{F_{x\max}^\alpha}\right)^2 = 1$, where F_{y0}^α is lateral tire force under tire

sideslip angle α when longitudinal force equal zero, and $F_{x\max}^\alpha$ is maximum longitudinal tire force under tire sideslip angle α .

$$\left(\nabla f_{yx}^\alpha\right)_{ij} = \begin{cases} -\frac{F_{y0i}^i \cdot F_{xi}}{F_{yi} \cdot F_{x\max i}^2} & i = j \\ 0 & i \neq j \end{cases} \quad (4.3-7)$$

To substitute function (4.3-5) with (4.3-7), then:

$$\Delta M_z = (B_{zx} + B_{zy} \nabla f_{yx}^\alpha) \Delta F_x \quad (4.3-8)$$

Then:

Set virtual control vector $v = [\Delta F_{xT} \quad \Delta M_{zT}]^T$,

where the total longitudinal forces F_{xT} are created by the driver's pedal command. And the actual control vector $u = [\Delta F_{xfl} \quad \Delta F_{xfr} \quad \Delta F_{xrl} \quad \Delta F_{xrr}]^T$. Then the control allocation should meet the following equation:

$$v = B \cdot u \quad (4.3-9)$$

Where: the effectiveness matrix $B = \begin{bmatrix} B_x \\ B_{zx} + B_{zy} \nabla f_{yx}^\alpha \end{bmatrix}$

4.3.2 Optimal allocation algorithm

One objective of the control allocation can be expressed as to minimize the allocation error:

$$\begin{aligned} & \min \|W_v(Bu - v)\| \\ & \text{s.t. } u^- \leq u \leq u^+ \end{aligned} \quad (4.3-10)$$

W_v is the weight matrix, reflecting the priority of each generalized force. The constraints include the limited capacity of the actuator, ie. the maximum torque range of in-wheel-motors, and the road adhesion ability.

At the same time, we also hope to minimize the energy consumption of the actuator. Considering the characteristics of the tire adhesion, different wheels with different vertical load F_z , then the longitudinal forces and the lateral forces provided by each wheel are not the same. So the weight matrix W_u is introduced. It is a diagonal matrix, and the diagonal elements are:

$$w_{ii} = \frac{1}{\sqrt{(\mu_{ii}F_{zii})^2 - (F_{xii}^2 + F_{yii}^2)}} \quad (4.3-11)$$

Where μ is the road adhesion coefficient of each wheel. F_x , F_y and F_z are the longitudinal force, the lateral force and the vertical load of each wheel of the time.

Then another objective can be expressed as:

$$\begin{aligned} & \min \|W_u(u - u_d)\| \\ & \text{s.t. } u^- \leq u \leq u^+ \end{aligned} \quad (4.3-12)$$

W_u considerate the characteristic of each tire adhesion, because different wheel is with different vertical load F_z .

The above (4.3-10) and (4.3-12) can be combined as followed Quadratic Programming (QP) problem:

$$u = \arg \min_{u^- \leq u \leq u^+} (\|W_u(u - u_d)\|_2^2 + \lambda \|W_v(Bu - v)\|_2^2) \quad (4.3-13)$$

Thus the computation time can be reduced largely. The parameter λ is usually set to very large in order to minimize the allocation error. The optimization problem can be solved through active set methods.

4.4 Simulation results and analysis

Using vehicle dynamics analysis software veDYNA, combined with the proposed vehicle stability control algorithm above, the high velocity double lane change operation is simulated to verify the validity of the control algorithm.

The vehicle is to carry out double lane change operation with the velocity of about 100km/h, which should be as constant as possible during the operation. Fig.4.4-2 shows the contrast between the vehicle trajectories with and without stability control. The vehicle could keep a steady posture and avoid obviously lateral slippage. Meanwhile compared to the LQR control without identification of the cornering stiffness, the algorithm designed in this paper can decrease the impact of the change of the model's parameters on the control effect. In addition a little under steering during lane change presents the steering characteristic of DYC reference model to restrain over large side slip angle.

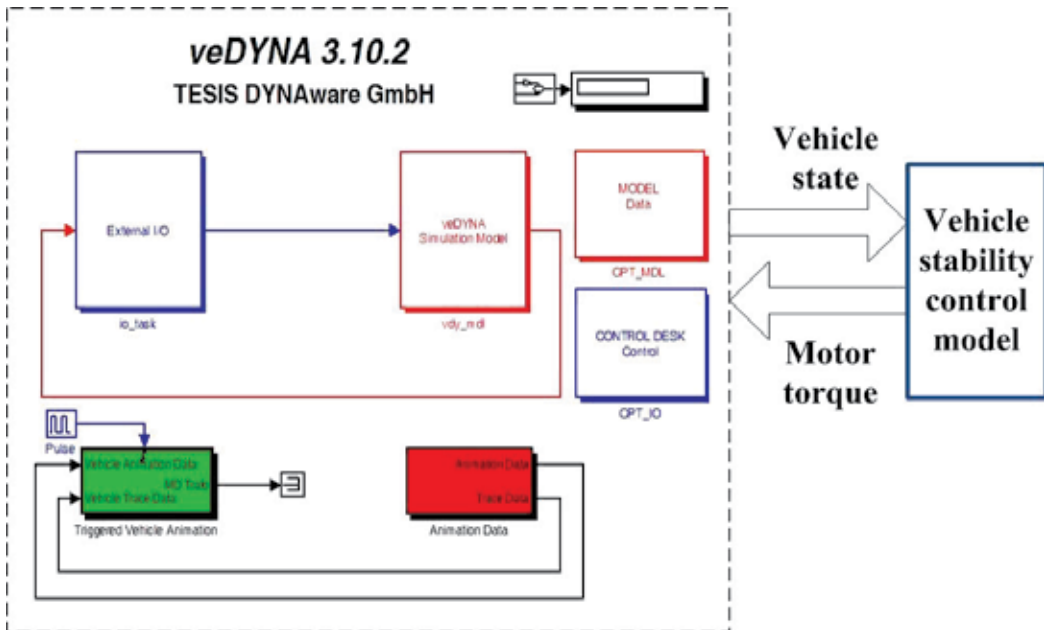


Fig. 4.4-1. veDYNA Simulation Model

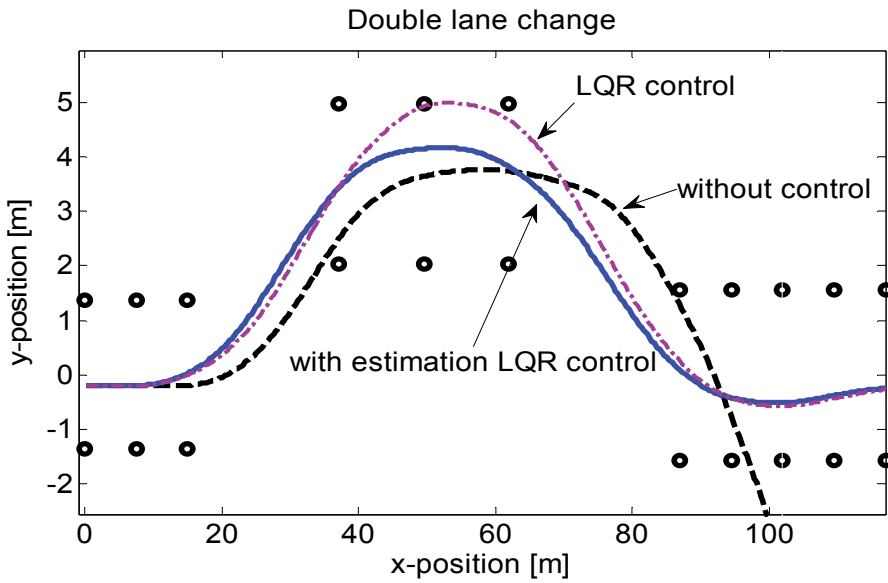


Fig. 4.4-2. Vehicle Trajectory

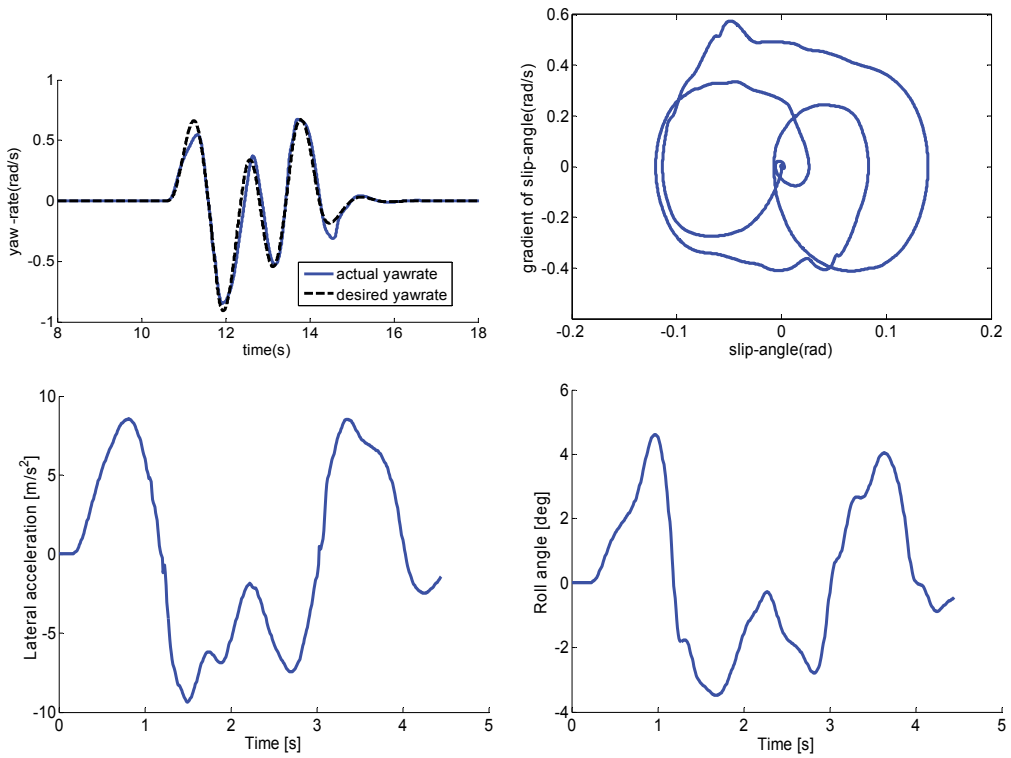


Fig. 4.4-3. Vehicle States

Fig. 4.4-3 presents the behaviors of several state values of the vehicle during such operation. Among them the yaw rate response can match the desired value well. Supposing on level and smooth road, when the peak value of the lateral acceleration is close to 1.0g, the vehicle has been working under critical condition. The $\beta - \dot{\beta}$ phase trajectory indicates that the vehicle can keep steady even when the slip angle reaches 8 degree.

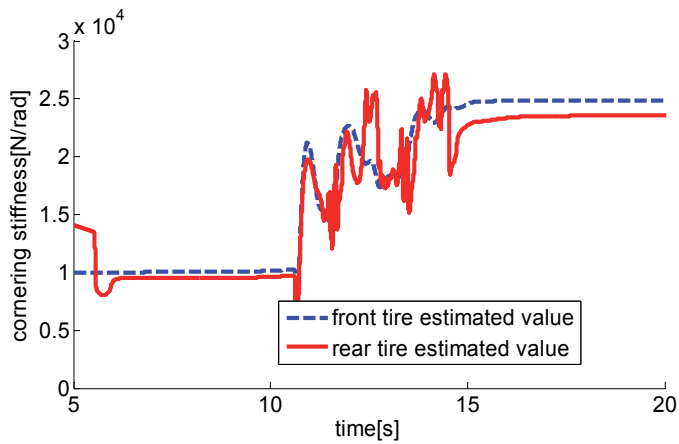


Fig. 4.4-4. Estimated Cornering Stiffness of Tire

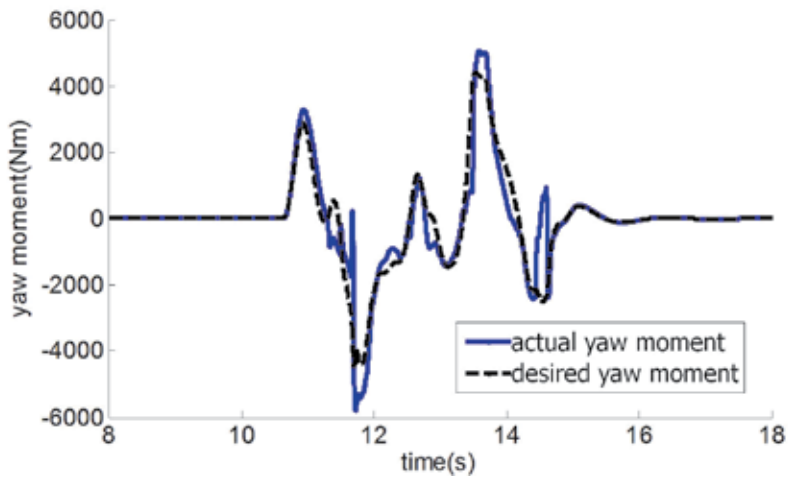


Fig. 4.4-5. Actual vs Desired Yaw Moment

Fig. 4.4-4 shows the estimated values of the cornering stiffness in the double lane change simulation, the vehicle lateral motion characteristic adjusts acutely during lane change. If the LQR controller were designed according to the fixed value of the cornering stiffness, the control effect would get worse along with the fluctuation of the cornering stiffness. Fig. 4.4-5 illustrates how the actual yaw moment follows the requirement of the control during the whole control process. It's clear that the optimize allocation algorithm can finely meet the requirement of the stability control even under the critical condition.

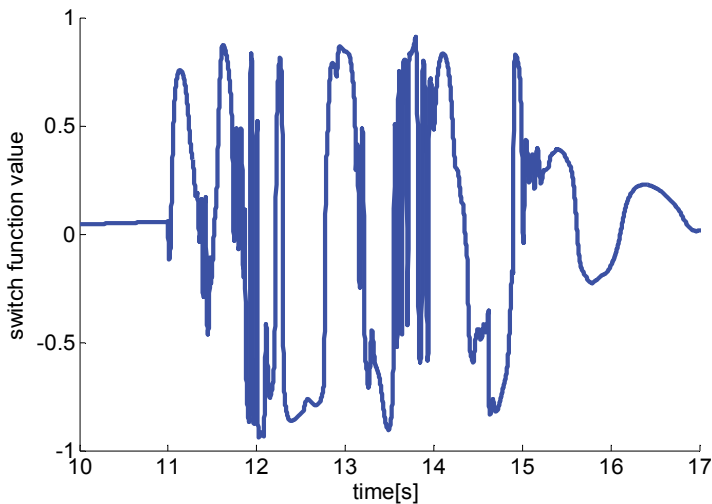


Fig. 4.4-6. Switch function value

Figure shows the adjustment of switch function value during operation; there is obvious chattering when simulation time is near 12s and 14s, but that causes no severe fluctuate to general yaw moment. Figure illustrates the actual yaw moment can realize the general control requirement basically, which guarantees the achievement of motion follow control.

4.5 Conclusion

In this section, a motion follow controller is designed based on the linear optimal control theory with the real time identification of the cornering stiffness and VSC theory with non-linear vehicle model. Considering the longitudinal/lateral forces' couple characteristic of tire under critical condition, the optimal control allocation algorithm realized the vehicle stability control successfully. Using veDYNA software, the double lane change simulation is carried out to verify the validity of the control method above.

The results of the simulation show: the proposed control method could stabilize the vehicle posture well under critical condition (i.e. the peak lateral acceleration is close to 1.0g and the slip angle reaches 8 degree). The reference model plays an important role on restraining the vehicle from losing stability. Compared with the LQR with fixed cornering stiffness, the feedback from identifying cornering stiffness to correct the parameters of the controller helps a lot in improving the robustness of the stability control. Actual control allocation could match the general requirement well by taking into account of tire force characteristic.

5. References

- [1] D. Foito, A. Roque, J. Esteves, J. Maia, Electric Vehicle with two Independent Wheel Drives-Improving the Performance with A Traction Control System, Proceedings on the "17th International Electric Vehicle Symposium & Exposition - EVS 17", Montreal, Canada, October 2000.
- [2] Buckholtz K R. Reference Input Wheel Slip Tracking Using Sliding Mode Control [R]. SAE 2002 World Congress, 2002.
- [3] Zhaoliang Zhang, Lu Xiong and Zhuoping Yu. The Anti-skidding Control for Combined- braking System based on theadjustable Hydraulic System. 2010 IEEE International Conference on VehicularElectronics and Safety, Qingdao, 2010.
- [4] Yoichi HORI , Future Vehicle driven by Electricity and Control -Research on Four Wheel Motored "UOT Electric March II", IEEE, Vol 51, 2004 P954 - 962.
- [5] Shin-ichiro Sakai , Takahiro Okano, Tai Chien Hwa , 4 Wheel Motored Vehicle "UOT Electric March II" -Experimental EV for Novel Motion Control Studies-, Proc. of INTERMAC2001 Joint Technical Conference, Tokyo, Japan, 2001.
- [6] Yoichi Hori, Yasushi Tyoda, and Yoshimasa Tsuruoka. Traction Control of Electric Vehicle: Basic Experimental Results Using the Test EV "UOT Electric March". IEEE Transactions on Industry Applications, vol.34, pp.1131-1137, September/October 1998.
- [7] Buckholtz K R. Reference Input Wheel Slip Tracking Using Sliding Mode Control [R]. SAE 2002 World Congress, 2002.
- [8] Y.Chamaillard, G.L. Gissinger, J.M.Perronne and M.Renner. An original braking controller with torque sensor. Proceedings of the Third IEEE Conference on Control Applications, 1994.
- [9] A.El Hadri, J. C. Cadiou, K. N.M'Sirdi and Y. Delanne. Wheel-slip regulation based on sliding mode approach. SAE 2001 World Congress, 2001.UC Berkeley, November 1993.
- [10] Kachroo P. Nonlinear Control Strategies and Vehicle Traction Control [D]. Ph.D .dissertation

- [11] Shino,M.,Wang,Y.,Nagai,M., Motion Control of Electric Vehicle Considering Vehicle Stability. Proc.of AVEC2000,2000, pp.705-711
- [12] Motoki Shino, Masao Nagai, "Yaw moment control of electric vehicle for improving handling and stability", JSAE Review 2001, pp.473-480
- [13] Peng He and Yoichi Hori, "Optimum Traction Force Distribution for Stability Improvement of 4WD EV in Critical Driving Condition", 9thIEEE International Advanced Motion Control, Workshop, Istanbul, 2006
- [14] Zhuoping Yu, Wei Jiang and Lijun Zhang, "Torque distribution control for four wheel in-wheel-motor electric vehicle", Tongji Daxue Xuebao/Journal of Tongji University, Vol. 36, No. 8, 2008, pp.1115-1119
- [15] Sakai,S.,Hori,Y., Advanced Vehicle Motion Control of Electric Vehicle Based on The Fast Motor Torque Response. Proc.of AVEC2000, 2000 ,pp .729-736
- [16] Chumsamutr,R., Fujioka,T., Improvement of Electric Vehicle's Cornering Performance by Direct Yaw Moment Control. Proc. of AVEC2000, 2000, pp.729-736
- [17] H .Fujimoto, N .Takahashi, A. Tsumasaka and T. Noguchi. motion control of electric vehicle based on cornering stiffness estimation with yaw-moment observer. IEEE Int. Workshop Advanced Motion Control, 2006,pp. 206-211
- [18] Peng He and Yoichi Hori, "Optimum Traction Force Distribution for Stability Improvement of 4WD EV in Critical Driving Condition", 9th IEEE International Advanced Motion Control, Workshop, Istanbul, 2006
- [19] Zhuoping Yu, Wei Jiang and Lijun Zhang, "Torque distribution control for four wheel in-wheel-motor electric vehicle", Tongji Daxue Xuebao/Journal of Tongji University, Vol. 36, No. 8, 2008, pp.1115-1119
- [20] H.B.Pacejka, "Tyre and Vehicle Dynamics", Butterworth Heinemann, 2002
- [21] Brad Schofield and Tore Haeggglund, "Optimal Control Allocation in Vehicle Dynamics Control for Rollover Mitigation", 2008 American Control Conferance, Washington, 2008
- [22] O. haerkegard, "Backstepping and control allocation with applications to flight control", Ph.D. dissertation, Linkping University, 2003

A Robust Traction Control for Electric Vehicles Without Chassis Velocity

Jia-Sheng Hu¹, Dejun Yin² and Feng-Rung Hu³

¹*National University of Tainan,*

²*Keio University,*

³*National Taichung University,*

^{1,3}*Taiwan*

²*Japan*

1. Introduction

As the rapid development of technology, the control technology and daily livings are interrelated. However, unanticipated breakdowns can happen in any control system due to the internal malfunctions or external distractions. Since the prices in most of the home electronic appliances are reasonable and affordable, malfunctions can simply be solved by purchasing new ones, however, for complex control systems with high social costs, the consequences of these passive solutions result in paying more prices. For example, systems such as aircrafts, ships, satellites, nuclear power plants, space shuttles, high speed rails are all extremely high in manufacturing costs, and if malfunction happens and is not able to eliminate or repair, the price paying afterward is tremendous.

Traction control is an example. For passenger involved in electric automobile systems, traction control is a core for stabilizing the movements of automobiles. In addition to guarantee the safety of automobile system in any driving conditions, one must also has adequate ability of fault-tolerant. Under a slippery, a muddy, and a flat tire conditions, wheel inertia changes, and results in deteriorating of controllability in traction control. Hence, researches have been focusing on adopting robust control theory, which can endow electric vehicles with fault-tolerant performance. Fully electric vehicles powered by batteries can achieve quieter and pollution-free operation, which has offered a solution to next generation vehicles. Unlike internal combustion engine vehicles, electric vehicles use independently equipped motors to drive each wheel. The independently equipped motors provide higher power/weight density, higher reliability for safety and better dynamic performance. These aspects make it easy to estimate the driving or braking forces between tires and road surfaces in real time, which contributes a great deal to the application of new traction control strategies based on road condition estimation (Hori, 2004; He & Hori, 2006; Yang & Lo, 2008).

For advanced vehicles today, many technologies embedded in the micro controller unit (MCU) that enhance the vehicle stability and handling performance in critically dynamic situations. For example, the antilock braking system (ABS) (Schinkel & Hunt, 2002; Patil et al., 2003), electronic differential (ED) (Urakubo et al., 2001; Tsai & Hu, 2007), direct yaw-

posture control (DYC) (Tahami et al., 2004; Mizushima et al., 2006), traction control (Bennett et al., 1999; Poursamad & Montazeri, 2008), and so on, are all solutions implemented to improve both vehicle stability and handling. Traction control is often interested in the performance of anti-slip mechanisms. When a vehicle is driven or brakes on a slippery road, traction control must not only guarantee the effectiveness of the torque output to maintain vehicle stability, but also provide some information about tire-road conditions to other vehicle control systems. Moreover, a well-managed traction control system can cover the functions of ABS, because motors can generate deceleration torque as easily as acceleration one (Mutoh et al., 2007). However, in practice, vehicle systems actually face challenges on restricting the development of traction control. For example, when the real chassis velocity is not available, the friction force which drives the vehicle is immeasurable (Baffet et al., 2009). In general traction control systems that need chassis velocity, the non-driven wheels are utilized to provide an approximate vehicle velocity due to physical and economic reasons. However, this method is not applicable when the vehicle is accelerated by 4WD systems or decelerated by brakes equipped in these wheels. For this reason, the accelerometer measurement is also used to calculate the velocity value, but it cannot avoid offset and error problems. Other sensors, e.g., optical sensors (Saito et al., 2002), sensors of magnetic markers (Fujimoto et al., 2004), etc., can also obtain chassis velocity. However, they are too sensitive and reliant on the driving environment or too expensive to be applied in actual vehicles. Some anti-slip control systems (Schinkel & Hunt, 2002; Patil et al., 2003; Fujii & Fujimoto, 2007) try to realize optimal slip-ratio controls according to the Magic Formula (Pacejka & Bakker, 1992). These systems not only need extra sensors for the acquisition of chassis velocity or acceleration, but are also more difficult to realize than expected. This is because the tuned algorithms and parameters for specific tire-road conditions cannot be adapted quickly enough to compensate the significant variation found in the instantaneous, immeasurable relationship between the slip ratio and the friction coefficient. In order to overcome these problems, the Model Following Control (MFC) approaches (Sakai & Hori, 2001; Saito et al., 2002; Fujimoto et al., 2004), do not need information on chassis velocity or even acceleration sensors are proposed. In these systems, the controllers only make use of torque and wheel rotation as input variables for calculation. Fewer sensors contribute not only to lower costs, but also to increase reliability and independence from driving conditions, which are the most outstanding features of this class of control systems. Nevertheless, these control designs based on compensation have to consider the worst stability case to decide the compensation gain, which impairs the performance of anti-slip control. Furthermore, gain tuning for some specific tire-road conditions also limits the practicability of this method. Recently, the MTTE approach (Yin et al., 2009) that requires neither chassis velocity nor information about tire-road conditions further upgrades the anti-slip performance of electric vehicles. In this system, use is only made of the torque reference and the wheel rotation speed to estimate the maximum transmissible torque to the road surface, then the estimated torque is applied for anti-slip control implementation. This approach also shows its benefits for vehicle mass-perturbed operation. Since a human being is involved in the operation of a vehicle, the total mass potentially varies with different drivers and passengers.

Model uncertainties are considered as systematic faults (Patton et al., 2000; Campos-Delgado et al., 2005), and these faults are unpreventable and non-measurable in automobile control systems. Normally, due to the existence of different levels of faults in general automobile

control system, the anti-slip function of traction control will deteriorate and even malfunction occur (Ikeda et al., 1992). For example, different passengers are with different weights, and this causes the vehicle mass to be unpredictable. In addition, the wheel inertia changes because of abrasion, repairs, tire flattening, and practical adhesion of mud and stones. For traction control, these two factors have significant impacts on anti-slip function in traction control. Additionally, feedback control is established upon the output measurement. Sensor faults deteriorate the measurement signals and decline the stability. Therefore, a fine traction control of electric vehicle should equip the ability of fault-tolerant against these faults. Truly, to develop traction control with fault-tolerant technique is practically competitive. This paper aims to make use of the advantages of electric vehicles to discuss the robustness of MTTE-based traction control systems and is structured as follows. Section 2 describes the MTTE approach for anti-slip control. Section 3 discusses the concepts of disturbance estimation. Details of the robustness analysis to the discussed systems are presented in Section 4. The specifications of the experiments and practical examples for evaluating the presented anti-slip strategy are given in Section 5. Finally, Section 6 offers some concluding remarks.

2. Traction control without chassis velocity

Consider a longitudinal motion of a four-wheeled vehicle, as depicted in Fig. 1, the dynamic differential equations for the longitudinal motion of the vehicle can be described as

$$J_w \dot{\omega} = T - rF_d \quad (1)$$

$$M\dot{V} = F_d - F_{dr} \quad (2)$$

$$V_w = r\omega \quad (3)$$

$$F_d(\lambda) = \mu N \quad (4)$$

Generally, the nonlinear interrelationships between the slip ratio λ and friction coefficient μ formed by tire's dynamics can be modeled by the widely adopted Magic Formula (Pacejka & Bakker, 1992) as shown in Fig. 2.

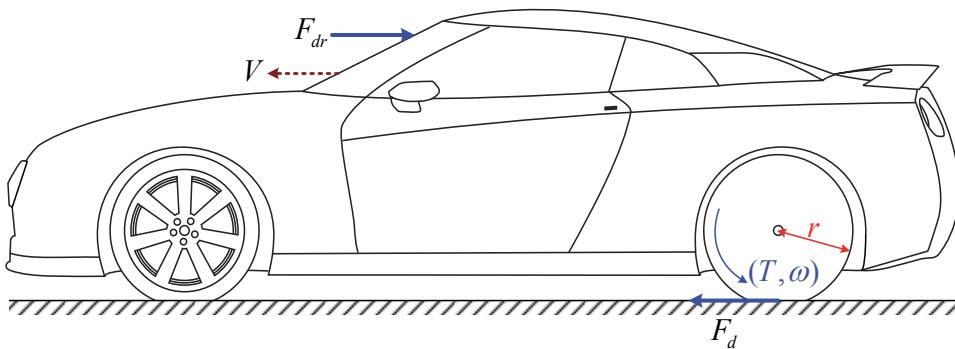


Fig. 1. Dynamic longitudinal model of vehicle.

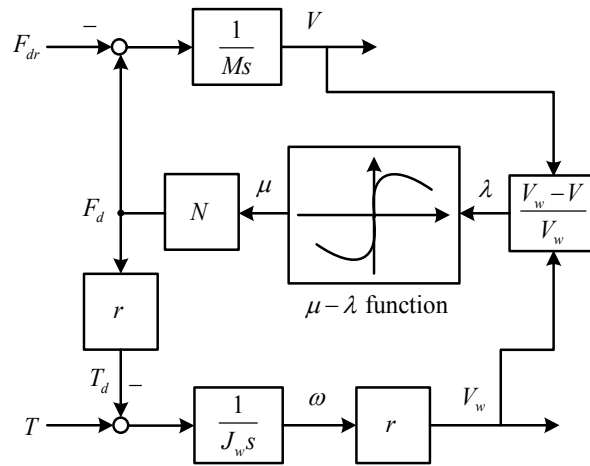


Fig. 2. One wheel of vehicle model with magic formula.

The concept of MTTE approach for vehicle anti-slip control is firstly proposed in (Yin et al., 2009). The MTTE approach can achieve an acceptable anti-slip control performance under common operation requirements. However, the MTTE approach is sensitive to the varying of the wheel inertia. If the wheel inertia varies, the anti-slip performance of the MTTE will deteriorate gradually. This paper is devoted to improve the anti-slip performance of the MTTE approach under such concerned abnormal operations. An advanced MTTE approach with fault-tolerant performance is then proposed. Based on the MTTE approaches, the following considerations are concerned.

1. No matter what kind of tire-road condition the vehicle is driven on, the kinematic relationship between the wheel and the chassis is always fixed and known.
2. During the acceleration phase, considering stability and tire abrasion, well-managed control of the velocity difference between wheel and chassis is more important than the mere pursuit of absolute maximum acceleration.
3. If the wheel and the chassis accelerations are well controlled, the difference between the wheel and the chassis velocities, i.e. the slip is also well controlled.

Here from Eqs. (1) and (3), the driving force, i.e. the friction force between the tire and the road surface, can be calculated as

$$F_d = \frac{T}{r} - \frac{J_w \dot{V}_w}{r^2} \quad (5)$$

In normal road conditions, F_d is less than the maximum friction force from the road and increases as T goes up. However, when slip occurs, F_d cannot increase by T . Thus when slip is occurring, the difference between the velocities of the wheel and the chassis become larger and larger, i.e. the acceleration of the wheel is larger than that of the chassis. Moreover, considering the $\mu - \lambda$ relation described in the Magic Formula, an appropriate difference between chassis velocity and wheel velocity is necessary to support the desired friction force. In this paper, α is defined as

$$\alpha = \frac{\dot{V}_w}{V_w}, \text{ i.e. } \alpha = \frac{(F_d - F_{dr})/M}{(T_{\max} - rF_d)r/J_w} \quad (6)$$

It serves as a relaxation factor for smoothing the control system. In order to satisfy the condition that slip does not occur or become larger, α should be close to 1. With a designated α , when the vehicle encounters a slippery road, T_{\max} must be reduced adaptively according to the decrease of F_d . If the friction force F_d is estimable, the maximum transmissible torque, T_{\max} can be formulated as

$$T_{\max} = \left(\frac{J_w}{\alpha M r^2} + 1 \right) r \hat{F}_d \quad (7)$$

This formula indicates that a given estimated friction force \hat{F}_d allows a certain maximum torque output from the wheel so as not to increase the slip. Hence, the MTTE scheme utilizes T_{\max} to construct and constrain the driving torque T as

$$\begin{aligned} -|T_{\max}| < T^* < |T_{\max}|, T = T^*; \\ T^* \geq |T_{\max}|, T = |T_{\max}|; \\ T^* \leq -|T_{\max}|, T = -|T_{\max}|. \end{aligned} \quad (8)$$

Note that from Eq. (2), it is clear that the driving resistance F_{dr} can be regarded as one of the perturbation sources of the dynamic vehicle mass M . Although the vehicle mass M can also be estimated online (Ikeda et al., 1992; Vahidi et al., 2005; Winstead & Kolmanovsky, 2005), in this paper, it is assumed to be a nominal value.

Figure 3 shows the main control scheme of the MTTE. As shown in Fig. 3, a limiter with a variable saturation value is expected to realize the control of driving torque according to the dynamic situation. The estimated disturbance force \hat{F}_d is driven from the model inversion of the controlled plant and driving torque T . Consequently, a differentiator is needed. Under normal conditions, the torque reference is expected to pass through the controller without any effect. Conversely, when on a slippery road, the controller can constrain the torque output to be close to T_{\max} . Based on Eq. (7), an open-loop friction force estimator is employed based on the linear nominal model of the wheeled motor to produce the maximum transmissible torque. For practical convenience, two low pass filters (LPF) with the time constants of τ_1 and τ_2 respectively, are employed to smoothen the noises of digital signals and the differentiator which follows.

3. Disturbance estimation

The disturbance estimation is often employed in motion control to improve the disturbance rejection ability. Figure 4 shows the structure of open-loop disturbance estimation. As can be seen in this figure, we can obtain

$$\hat{T}_d = \left[(T^* + T_d)(G(s) + \Delta(s)) \right] G(s)^{-1} - T^* \quad (9)$$

If $\Delta(s) \neq 0$, then $\hat{T}_d \neq T_d$. Without the adjustment mechanism, the estimation accuracy decreases based on the deterioration of modeling error. Figure 5 shows the structure of closed-loop disturbance estimation. As seen in this figure, we can obtain

$$\hat{T}_d = C(s) \left[(G(s) + \Delta(s))(T^* + T_d) - G(s)(T^* + \hat{T}_d) \right] \quad (10)$$

If $\Delta(s) = 0$, Eq. (10) becomes a low pass dynamics as $\hat{T}_d = \frac{C(s)G(s)}{1 + C(s)G(s)} T_d$. Moreover, from

Eq. (10), without considering the feed-forward term of T^* , the closed-loop observer system of Eq. (10) can be reconstructed into a compensation problem as illustrated in Fig. 6. It is obvious that, the compensator $C(s)$ in the closed-loop structure offers a mechanism to minimize the modeling error caused by $\Delta(s)$ in a short time. Consequently, the compensator enhances the robust estimation performance against modeling error. Since the modeling error is unpredictable, the disturbance estimation based on closed-loop observer is preferred.

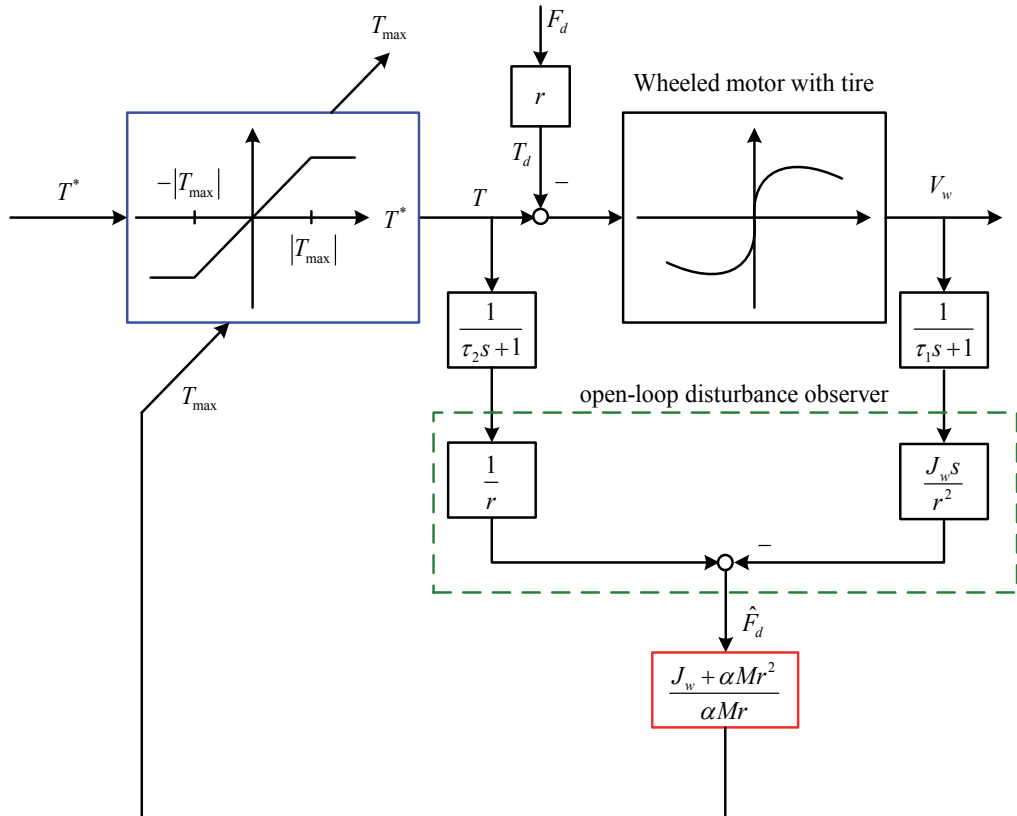


Fig. 3. Conventional MTTE system.

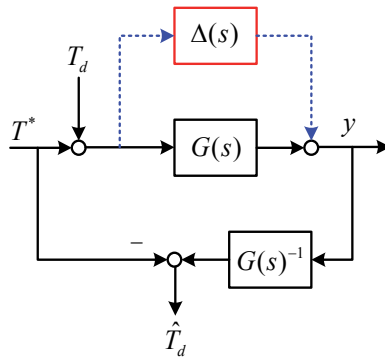


Fig. 4. Disturbance estimation based on open-loop observer.

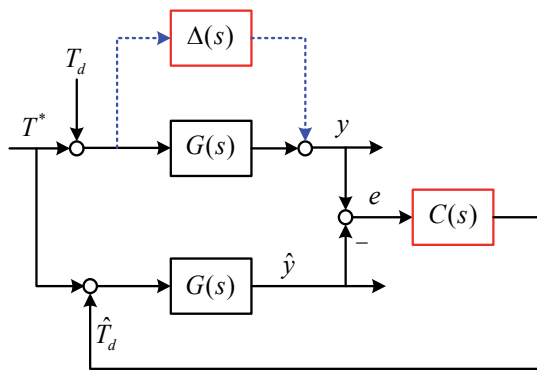


Fig. 5. Disturbance estimation based on closed-loop observer.

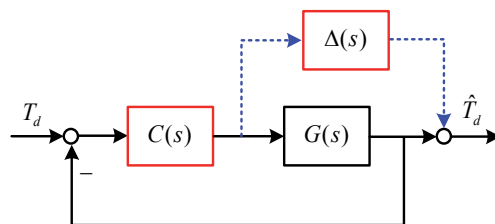


Fig. 6. Equivalent control block diagram of disturbance estimation.

4. Robustness analysis

Firstly, consider the conventional scheme of MTTE. The follow will show that the MTTE scheme is robust to the varying of vehicle mass. Note that the bandwidth of LPF is often designed to be double or higher than the system's bandwidth. Hence in motion control analysis, the LPFs can be ignored. Figure 7 shows a simplified linear model of MTTE scheme where M_n denotes the nominal value of vehicle mass M and $\Delta_d(s)$ stands for the perturbation caused by passenger and driving resistance F_{dr} . Here from Fig. 7, we have

$$\frac{T_{\max}}{F_d} = \frac{J_w}{\alpha M_n r} + r \tag{11}$$

Note that, if

$$\alpha M_n r \gg J_w \tag{12}$$

It is convinced that the condition of Eq. (12) is satisfied in most of the commercial vehicles. Then

$$\frac{T_{\max}}{F_d} \approx r \tag{13}$$

Now consider the mass perturbation of ΔM . From Eq. (11), it yields

$$\frac{T_{\max}}{F_d} = \frac{J_w}{\alpha(M_n + \Delta M)r} + r \tag{14}$$

Obviously, from Eq. (11), the anti-slip performance of MTTE will be enhanced when ΔM is a positive value and reduced when ΔM is a negative value. Additionally, in common vehicles, the MTTE approach is insensitive to the varying of M_n . Since passenger and driving resistance are the primary perturbations of M_n , the MTTE approach reveals its merits for general driving environments. The fact shows that the MTTE control scheme is robust to the varying of the vehicle mass M .

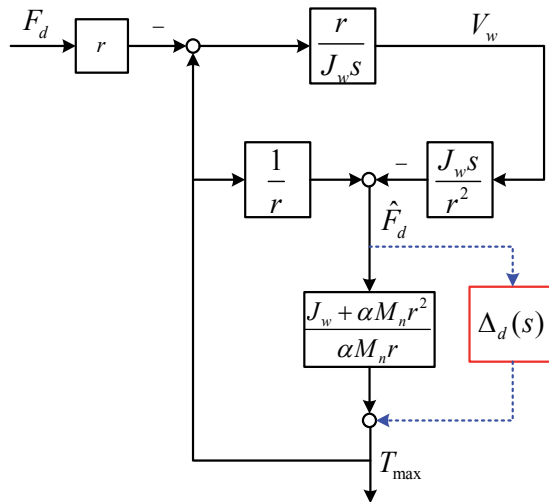


Fig. 7. Simplified MTTE control scheme.

Model uncertainty and sensor fault are the main faults concerned in this study. Since the conventional MTTE approach is based on the open-loop disturbance estimation, the system is hence sensitive to the varying of wheel inertia. If the tires are getting flat, the anti-slip performance of MTTE will deteriorate gradually. Figure 8 illustrates the advanced MTTE scheme which endows the MTTE with fault-tolerant performance. The disturbance torque

T_d comes from the operation friction. When the vehicle is operated on a slippery road, it causes the T_d to become very small, and due to that the tires cannot provide sufficient friction. Skidding often happens in braking and racing of an operated vehicle when the tire's adhesion cannot firmly grip the surface of the road. This phenomenon is often referred as the magic formula (i.e., the $\mu - \lambda$ relation). However, the $\mu - \lambda$ relation is immeasurable in real time. Therefore, in the advanced MTTE, the nonlinear behavior between the tire and road (i.e., the magic formula) is regarded as an uncertain source which deteriorates the steering stability and causes some abnormal malfunction in deriving.

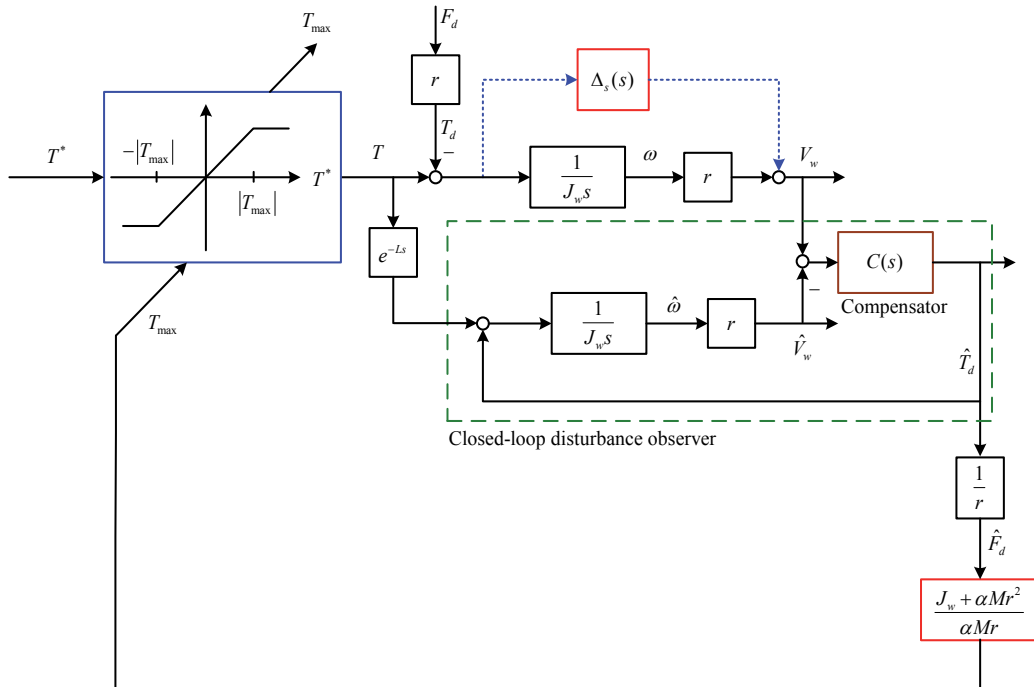


Fig. 8. Advanced MTTE control system.

Faults such as noise will always exist in a regular process; however not all faults will cause the system to fail. To design a robust strategy against different faults, the model uncertainties and system faults have to be integrated (Campos-Delgado et al., 2005). In addition, the sensor fault can be modeled as output model uncertainty (Hu & Tsai, 2008). Hence in this study, the model uncertainty and sensor fault are integrated as $\Delta_s(s)$ in the proposed system, which has significant affects to the vehicle skidding. Here, let $\Delta_s(s)$ denote the slip perturbation caused by model uncertainty and sensor fault on the wheeled motor. The uncertain dynamics of $\Delta_s(s)$ represent different slippery driving situations. When $\Delta_s(s) \approx 0$, it means the driving condition is normal. For a slippery road surface, the $\Delta_s(s) \neq 0$. It is commonly known that an open-loop disturbance observer has the following drawbacks.

1. An open-loop disturbance observer does not have a feedback mechanism to compensate for the modeling errors. Therefore its robustness is often not sufficient.

2. An open-loop disturbance observer utilizes the inversion of a controlled plant to acquire the disturbance estimation information. However, sometimes the inversion is not easy to carry out.

Due to the compensation of the closed-loop feedback, the closed-loop disturbance observer enhances the performance of advanced MTTE against skidding. It also offers better robustness against the parameter varying. Unlike the conventional MTTE approach, the advanced MTTE does not need to utilize the differentiator. Note that the advanced MTTE employs a closed-loop observer to counteract the effects of disturbance. Hence it is sensitive to the phase of the estimated disturbance. Consequently, the preview delay element e^{-Ls} is setup for compensating the digital delay of fully digital power electronics driver. This preview strategy coordinates the phase of the estimated disturbance torque.

The advanced MTTE is fault-tolerant against the model uncertainties and slightly sensor faults. Its verification is discussed in the following. Figure 9 shows a simplified linear model of the advanced MTTE scheme where J_{wn} denotes the nominal value of wheel inertia J_w and $\Delta_s(s)$ stands for the slippery perturbation caused by model uncertainties and sensor faults.

Formulate the proposed system into the standard control configuration as Fig. 10, the system's robustness reveals by determining $\|T_{zw}(s)\|_\infty \leq \gamma$ such that $\|\Delta_s(s)\|_\infty < \frac{1}{\gamma}$. For convenience, the compensator employed in the closed-loop observer stage is set as

$$C(s) = K_p + K_i \frac{1}{s} \quad (15)$$

Note that the dynamics of delay element can be approximated as

$$e^{-Ls} \approx \frac{1}{1 + Ls} \quad (16)$$

The delay time in practical system is less than 30ms. Hence it has higher bandwidth of dynamics than the vehicle system. Consequently, it can be omitted in the formulation. Then from Fig. 9, we have

$$T_{zw}(s) = \frac{T_{\max}}{F_d} = - \frac{K_p(J_{wn} + \alpha Mr^2)s + K_i(J_{wn} + \alpha Mr^2)}{J_{wn}\alpha Ms^2 + K_p\alpha Mrs + K_i\alpha Mr} \quad (17)$$

As stated in Section 2, α should be close to 1. Therefore, if

$$\alpha Mr^2 \gg J_{wn} \quad (18)$$

then Eq. (17) can be simplified as

$$\frac{T_{\max}}{F_d} = - \frac{K_p r^2 s + K_i r^2}{J_{wn} s^2 + K_p r s + K_i r} \quad (19)$$

It is convinced that the condition of Eq. (18) is satisfied in most commercial vehicles. Accordingly, when the anti-slip system confronts the Type I (Step type) or Type II (Ramp type) disturbances (Franklin et al., 1995), equation Eq. (19) can be further simplified as

$$\frac{T_{\max}}{E_d} \approx -r \tag{20}$$

This means the system of $\|T_{zw}\|_{\infty} \approx r$ is stable if and only if $\|\Delta_s(s)\|_{\infty} < \frac{1}{r}$.

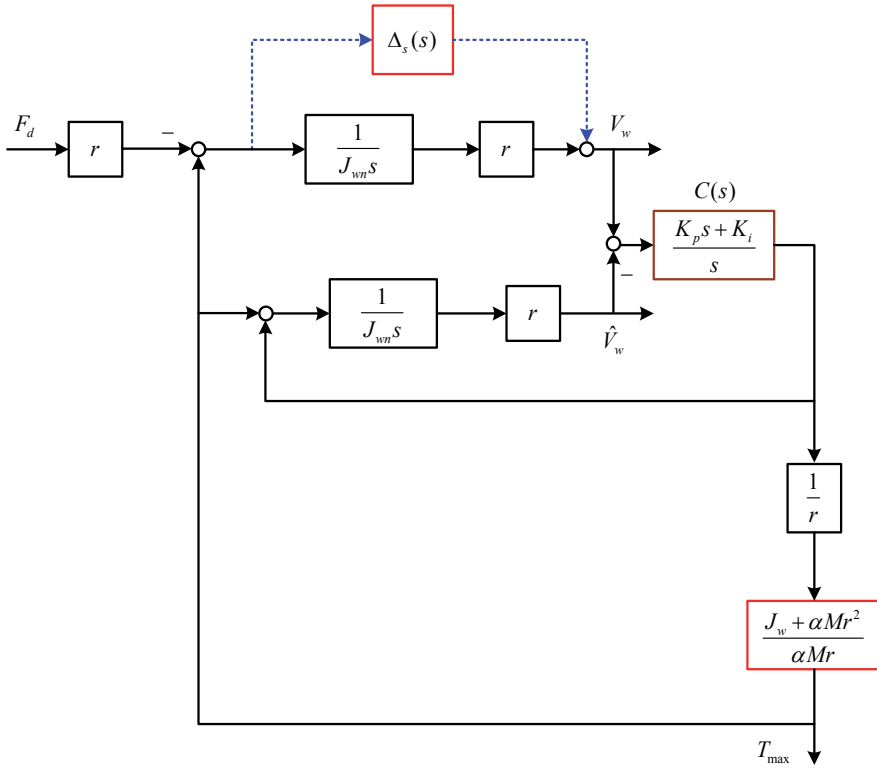


Fig. 9. A simplified scheme of proposed control.

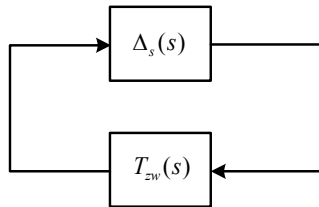


Fig. 10. Standard control configuration.

Now consider the affection of model uncertainty ΔJ_w to wheel inertia J_w . It yields $J_w = \Delta J_w + J_{wn}$. Since the mass of vehicle is larger than the wheels, in most of the commercial vehicle, $\alpha Mr^2 \gg \Delta J_w + J_{wn}$ is always held. Especially, the mass of passengers can also increase M to convince the condition of Eq. (18). Since the varying of J_w caused by ΔJ_w cannot affect the anti-slip control system so much. This means that the proposed control

approach for vehicle traction control is insensitive to the varying of J_w . Recall that the advanced MTTE scheme is MTTE-based. Consequently, by the discussions above, the proposed traction control approach reveals its fault-tolerant merits for dealing with certain dynamic modeling inaccuracies.

5. Examples and discussions

In order to implement and evaluate the proposed control system, a commercial electric vehicle, COMS3, which is assembled by TOYOTA Auto Body Co. Ltd., shown in Fig. 11 was modified to carry out the experiments' requirements. As illustrated in Fig. 12, a control computer is embedded to take the place of the previous Electronic Control Unit (ECU) to operate the motion control. The corresponding calculated torque reference of the left and the right rear wheel are independently sent to the inverter by two analog signal lines. Table 1 lists the main specifications.

Total Weight	360kg
Maximum Power/per wheel	2000W
Maximum Torque/per wheel	100Nm
Wheel Inertia/per wheel	0.5kgm ²
Wheel Radius	0.22m
Sampling Time	0.01s
Controller	Pentium M1.8G, 1GB RAM using Linux
A/D and D/A	12 bits
Shaft Encoder	36 pulses/round

Table 1. Specification of COMS3.



Fig. 11. Experimental electric vehicle and setting of slippery road for experiment.

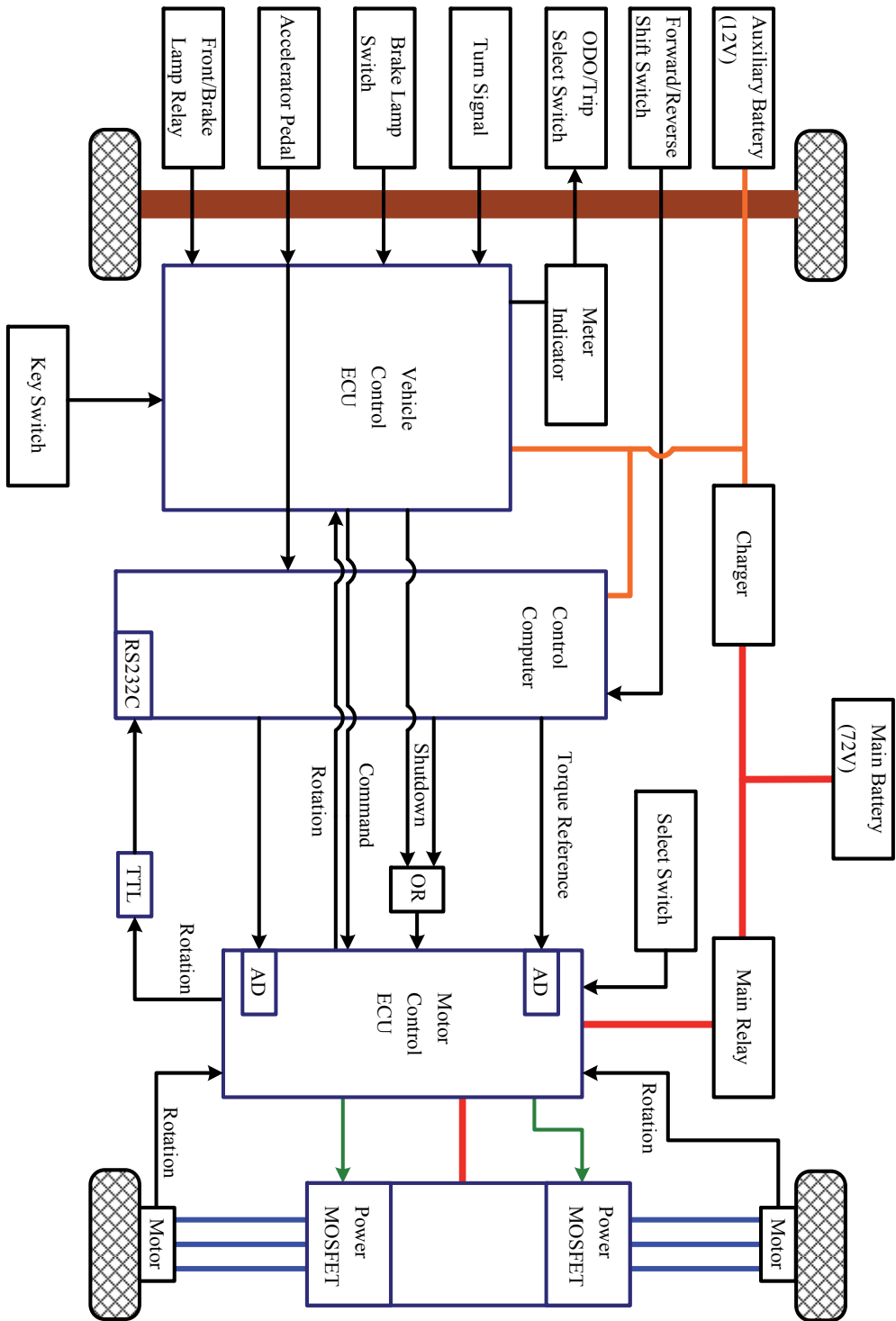


Fig. 12. Schematic of electrical system of COMS3.

In the experiments, the relation factor of MTTE scheme is set as $\alpha = 0.9$. The time constants of LPFs in the comparison experiment are set as $\tau_1 = \tau_2 = 0.05$. It is known that the passenger's weight varies. Hence, this paper adopts the PI compensator as the kernel of disturbance estimation. The PI gains are set as $K_p = 70$, and $K_i = 60$. As shown in Fig. 11, the slippery road was set by an acrylic sheet with a length of 1.2m and lubricated with water. The initial velocity of the vehicle was set higher than 1m/s to avoid the immeasurable zone of the shaft sensors installed in the wheels. The driving torque delay in the advanced MTTE approach is exploited to adjust the phase of the estimated disturbance. Under a proper anti-slip control, the wheel velocity should be as closed to the chassis velocity as possible. As can be seen in Fig. 13, the advanced MTTE cannot achieve any anti-slip performance (i.e. the vehicle is skidded) if the reference signal is no delayed. Figure 13 also shows the measured results, and obviously, the digital delay of motor driver has significant affections to the advanced MTTE. According to the practical tests of Fig. 13, with proper command delay of 20ms, the advanced MTTE can achieve a feasible performance. Hence, in the following, all experiments to the advanced MTTE utilize this delay parameter.

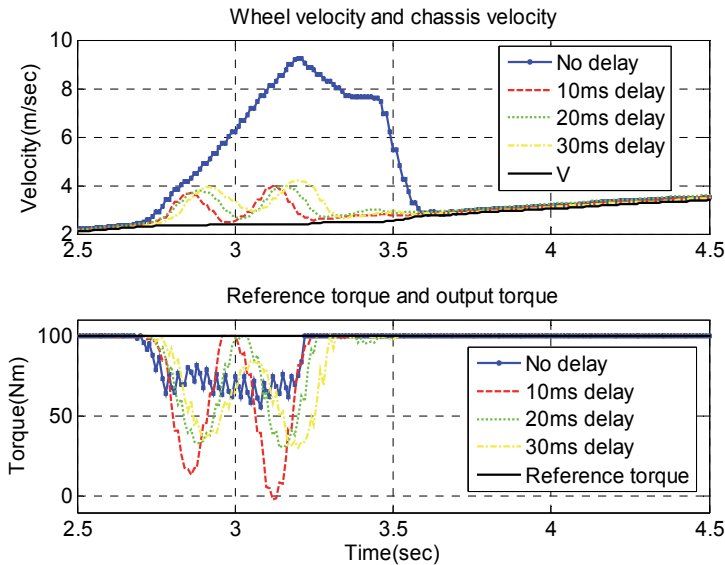


Fig. 13. Experimental results to different delay time L to advanced MTTE.

The MTTE-based schemes can prevent vehicle skid. These approaches compensate the reference torque into a limited value when encountering a slippery road. Based on the experimental result of Fig. 14, the reference torque of MTTE-based approaches is constrained without divergence. Figure 14 is evaluated under the nominal wheel inertia. As can be seen in this figure, both the conventional MTTE and advanced MTTE are with good anti-slip performance. Nevertheless, as indicated in the practical results in Fig. 15, the anti-slip performance of MTTE impairs with the varying of wheel inertia. In addition, Fig. 16 shows the same testing on the advanced MTTE. Apparently, the advanced MTTE overcomes this problem. The advanced MTTE has fault-tolerant anti-slip performance against the

wheel inertia varying in real time. Figures 17 and 18 show the performance tests of MTTE and advanced MTTE against different vehicle mass. It is no doubt that the MTTE-based control schemes are robust in spite of different passengers setting in the vehicle. From experimental evidences, it is evident that the advanced MTTE traction control approach has consistent performance to the varying of wheel inertia J_w and vehicle mass M . As shown in these figures, the proposed anti-slip system offers an effective performance in maintaining the driving stability under more common situations, and therefore the steering safety of the electric vehicles can be further enhanced.

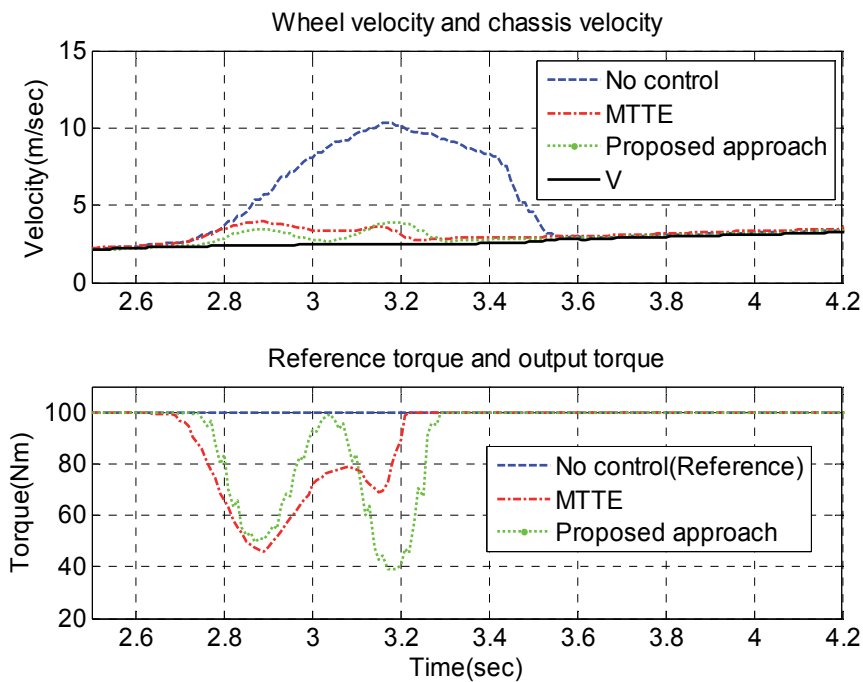


Fig. 14. Practical comparisons between MTTE and advanced MTTE to nominal J_w .

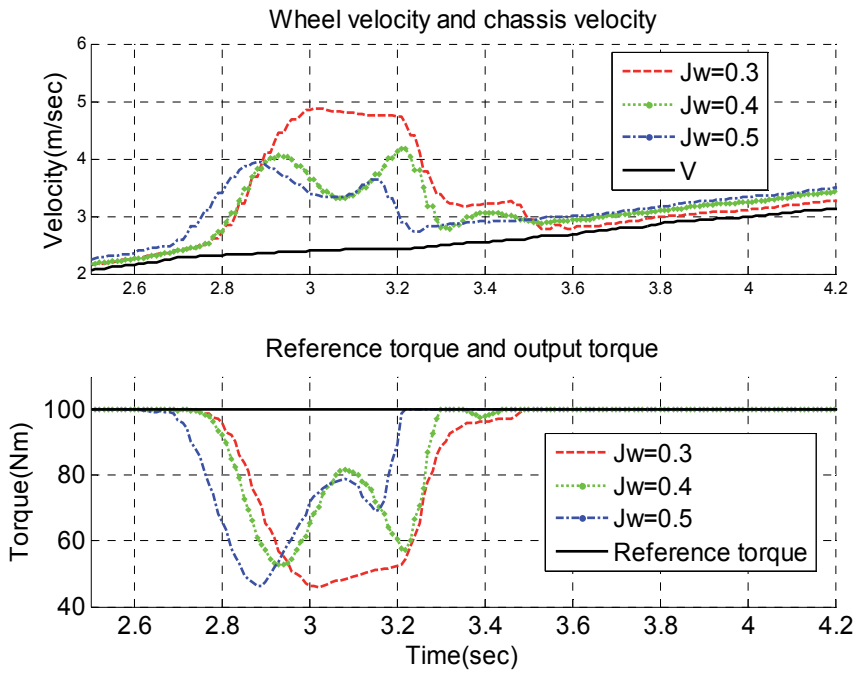


Fig. 15. Experimental results of MTTE to different J_w .

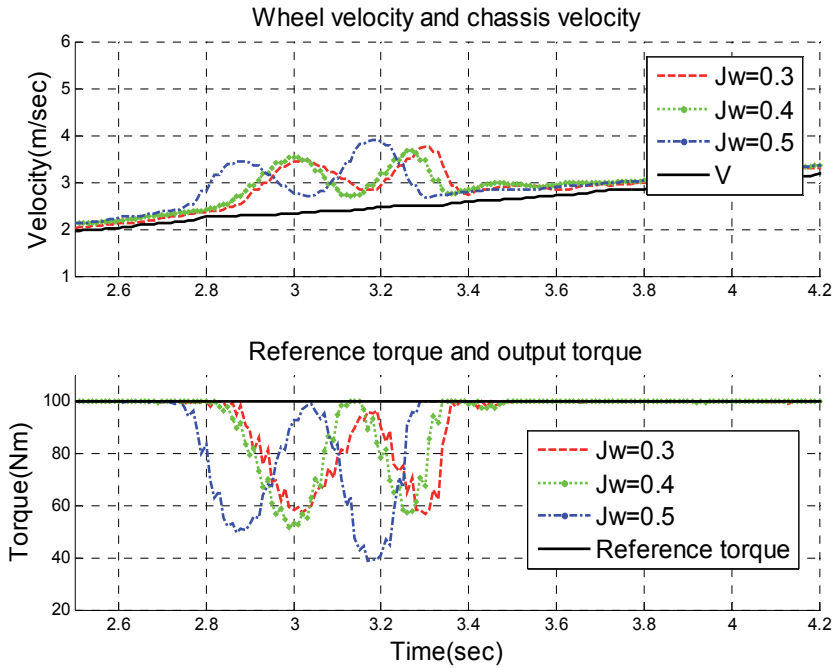


Fig. 16. Experimental results of advanced MTTE to different J_w .

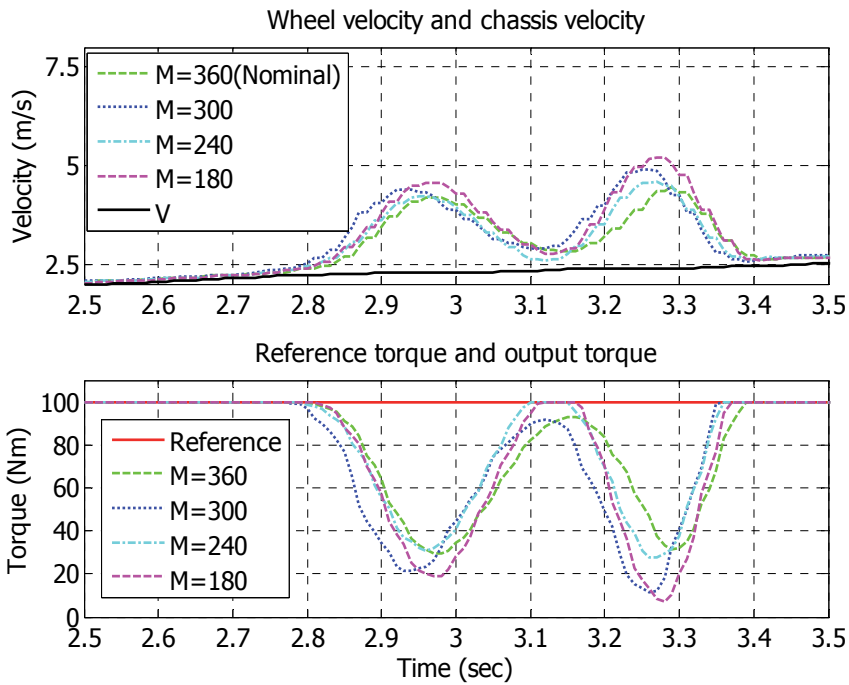


Fig. 17. Experimental results of MTTE to different M.

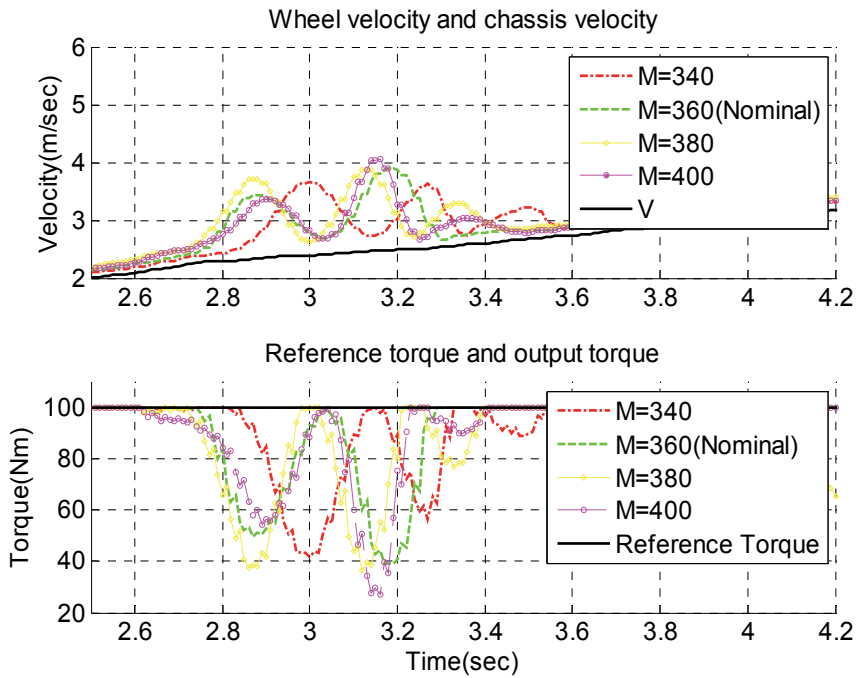


Fig. 18. Experimental results of advanced MTTE to different M.

6. Conclusions

This paper has presented a robustness analysis to the traction control of MTTE based approach in electric vehicles. The schemes of conventional MTTE and advanced MTTE were introduced. The conventional MTTE was confirmed by analysis and experiment of its robustness to the perturbation of vehicle mass. This advanced MTTE endowed the conventional MTTE approach with a fault-tolerant ability for preventing driving skid of electric vehicles in many common steering situations. It provided a good basis for anti-slip control as well as other more advanced motion control systems in vehicles. The phase lag problem of disturbance estimation to closed-loop observer and digital implementation has been overcome by the driving torque delay in the advanced MTTE. The experimental results have substantiated that the advanced MTTE has benefits such as preventing potential failures in a slippery driving situation. In addition, the MTTE approaches have made cost effective traction control for electric vehicles possible.

7. Nomenclature

F_d	Friction Force (Driving Force)
F_{dr}	Driving Resistance
J_w	Wheel Inertia
M	Vehicle Mass
N	Vehicle Weight
r	Wheel Radius
T	Driving Torque
V	Chassis Velocity (Vehicle Velocity)
V_w	Wheel Velocity (Circumferential Velocity)
λ	Slip Ratio
μ	Friction Coefficient
ω	Wheel Rotation

8. References

- Hori, Y. (2001). Future Vehicle Driven by Electricity and Control-research on four-wheel-motored "UOT electric march II. *IEEE Transactions on Industrial Electronics*, Vol.51, pp. 954-962.
- He, P & Hori, Y. (2006). Optimum Traction Force Distribution for Stability Improvement of 4WD EV in Critical Driving Condition. *Proceedings of IEEE International Workshop on Advanced Motion Control*, pp. 596-601, Istanbul, Turkey.
- Yang, Y.-P. & Lo, C.-P. (2008). Current Distribution Control of Dual Directly Driven Wheel Motors for Electric Vehicles. *Control Engineering Practice*, Vol.16, pp. 1285-1292.
- Schinkel, M. & Hunt, K. (2002). Anti-lock Braking Control Using a Sliding Mode Like Approach, *Proceedings of the American Control Conference*, pp. 2386-2391, Anchorage, USA.

- Patil, C. B.; Longoria, R. G. & Limroth, J. (2003). Control Prototyping for an Anti-lock Braking Control System on a Scaled Vehicle, *Proceedings of the IEEE Conference on Decision and Control*, pp. 4962-4967, Hawaii, USA.
- Urakubo, T.; Tsuchiya, K. & Tsujita, K. (2001). Motion Control of a Two-wheeled Mobile Robot. *Advanced Robotics*, Vol.15, pp. 711-728.
- Tsai, M.-C. & Hu, J.-S. (2007). Pilot Control of an Auto-balancing Two-wheeled Cart. *Advanced Robotics*, Vol.21, pp. 817-827.
- Tahami, F.; Farhangi, S. & Kazemi, R. (2004). A Fuzzy Logic Direct Yaw-moment Control System for All-wheel-drive Electric Vehicles. *Vehicle System Dynamics*, Vol.41, pp. 203-221.
- Mizushima, T.; Raksincharoensak, P. & Nagai, M. (2006). Direct Yaw-moment Control Adapted to Driver Behavior Recognition, *Proceedings of SICE-ICASE International Joint Conference*, pp. 534-539, Busan, Korea.
- Bennett, S. M.; Patton, R. J. & Daley, S. (1999). Sensor Fault-tolerant Control of a Rail Traction Drive. *Control Engineering Practice*, Vol.7, pp. 217-225.
- Poursamad, A. & Montazeri, M. (2008). Design of Genetic-fuzzy Control Strategy for Parallel Hybrid Electric Vehicles. *Control Engineering Practice*, Vol.16, pp. 861-873.
- Mutoh, N.; Hayano, Y.; Yahagi, H. & Takita, K. (2007). Electric Braking Control Methods for Electric Vehicles with Independently Driven Front and Rear Wheels. *IEEE Transactions on Industrial Electronics*, Vol.54, pp. 1168-1176.
- Baffet, G.; Charara, A. & Lechner, D. (2009) Estimation of Vehicle Sideslip, Tire Force and Wheel Cornering Stiffness. *Control Engineering Practice*, Vol. 17, pp. 1255-1264.
- Saito, T.; Fujimoto, H. & Noguchi, T. (2002). Yaw-moment stabilization control of small electric vehicle, *Proceedings of the IEEE Technical Meeting on Industrial Instrumentation and Control*, IIC-02, Tokyo, Japan.
- Fujimoto, H.; Saito, T. & Noguchi, T. (2004). Motion stabilization control of electric vehicle under snowy conditions based on yaw-moment observer, *Proceedings of IEEE International Workshop on Advanced Motion Control*, pp. 35-40, Kawasaki, Japan.
- Fujii K. & Fujimoto, H. (2007). Traction Control Based on Slip Ratio Estimation without Detecting Vehicle Speed for Electric Vehicle, *Proceedings of 4th Power Conversion Conference*, pp. 688-693, Nagoya, Japan.
- Pacejka, H. B. & Bakker, E. (1992). The Magic Formula Tyre Model. *Vehicle System Dynamics*, Vol.21, pp. 1-18.
- Sakai, S. & Hori, Y. (2001). Advantage of Electric Motor for Anti Skid Control of Electric Vehicle. *European Power Electronics Journal*, Vol.11, pp. 26-32.
- Yin, D.; Hu, J.-S. & Hori, Y. (2009). Robustness Analysis of Traction Control Based on Maximum Transmission Torque Estimation in Electric Vehicles. *Proceedings of the IEEE Technical Meeting on Industrial Instrumentation and Control*, IIC-09-027, Tokyo, Japan.
- Patton, R. J.; Frank, P. M. & Clark., R. N. (2000). *Issues of Fault Diagnosis for Dynamic Systems*, Springer, New York, USA.
- Campos-Delgado, D. U.; Martinez-Martinez, S. & Zhou, K. (2005). Integrated Fault-tolerant Scheme for a DC Speed Drive. *IEEE Transactions on Mechatronics*, Vol.10, pp. 419-427.

- Ikeda, M.; Ono, T. & Aoki, N. (1992). Dynamic mass measurement of moving vehicles. *Transactions of the Society of Instrument and Control Engineers*, Vol.28, pp. 50-58.
- Vahidi, A.; Stefanopoulou, A. & Peng, H. (2005). Recursive Least Squares with Forgetting for Online Estimation of Vehicle Mass and Road Grade: Theory and Experiments. *Vehicle System Dynamics*, Vol.43, pp. 31-55.
- Winstead, V. & Kolmanovsky, I. V. (2005). Estimation of Road Grade and Vehicle Mass via Model Predictive Control, *Proceedings of IEEE Conference on Control Applications*, pp. 1588-1593, Toronto, Canada.
- Hu, J.-S. & Tsai, M.-C. (2008). *Control and Fault Diagnosis of an Auto-balancing Two-wheeled Cart: Remote Pilot and Sensor/actuator Fault Diagnosis for Coaxial Two-wheeled Electric Vehicle*, VDM Verlag, Saarbrücken, Germany.
- Franklin, G. F.; Powell, J. D. & Emami-Naeini, A. (1995). *Feedback Control of Dynamic Systems*, Addison Wesley, New York, USA.

Vehicle Stability Enhancement Control for Electric Vehicle Using Behaviour Model Control

Kada Hartani and Yahia Miloud
*Electrical Engineering Department,
University of Saida
Algeria*

1. Introduction

In this chapter, two permanent magnet synchronous motors which are supplied by two voltage inverters are used. The system of traction studied Fig.1, belongs to the category of the multi-machines multi-converters systems (MMS). The number of systems using several electrical machines and/or static converters is increasing in electromechanical applications. These systems are called multi-machines multi-converters systems (Bouscayrol, 2003). In such systems, common physical devices are shared between the different energetic conversion components. This induces couplings (electrical, mechanical or magnetic) which are quite difficult to solve (Bouscayrol, 2000).

The complexity of such systems requires a synthetic representation in which classical modeling tools cannot always be obtained. Then, a specific formalism for electromechanical system is presented based on a causal representation of the energetic exchanges between the different conversion structures which is called energetic macroscopic representation (EMR). It has developed to propose a synthetic description of electromechanical conversion systems. A maximum control structure (MCS) can be deduced by from EMR using inversion rules. The studied MMS is an electric vehicle. This system has a mechanical coupling, Fig.1. The main problem of the mechanical coupling is induced by the non-linear wheel-road adhesion characteristic. A specific control structure well adapted to the non-linear system (the Behaviour Model Control) is used to overcome this problem. The BMC has been applied to a non-linear process; therefore, the wheel-road contact law of a traction system can be solved by a linear model.

The control of the traction effort transmitted by each wheel is at the base of the command strategies aiming to improve the stability of a vehicle. Each wheel is controlled independently by using an electric motorization. However, the traditional thermal motorization always requires the use of a mechanical differential to ensure the distribution of power on each wheel. The mechanical differential usually imposes a balanced transmitted torques. For an electric traction system, this balance can be obtained by using a multi-motor structure which is shown in Fig.1. An identical torque on each motor is imposed using a fuzzy direct torque control (FDTC) (Miloudi, 2004; Tang, 2004; Sun, 2004, Miloudi, 2007). The difficulty of controlling such a system is its highly nonlinear character of the traction forces expressions. The loss of adherence of one of the two wheels which is likely to destabilize the vehicle needs to be solved in this chapter.

2. Presentation of the traction system proposed

The proposed traction system is an electric vehicle with two drives, Fig.1. Two machines thus replace the standard case with a single machine and a differential mechanical. The power structure in this paper is composed of two permanent magnet synchronous motors which are supplied by two three-phase inverters and driving the two rear wheels of a vehicle through gearboxes, Fig. 2. The traction system gives different torque to in-wheel-motor, in order to improve vehicle stability. However, the control method used in this chapter for the motors is the fuzzy direct torque control with will give the vehicle a dynamic behaviour similar to that imposed by a mechanical differential (Arnet, 1997; Hartani, 2005; Hartani, 2007). The objective of the structure is to reproduce at least the behaviour of a mechanical differential by adding to it a safety anti skid function.

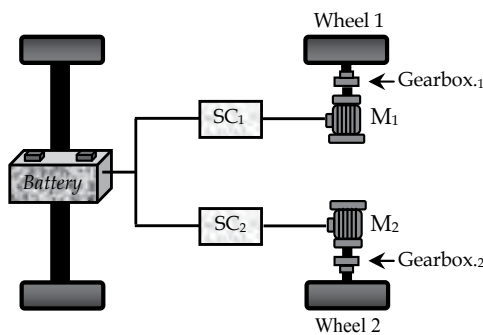


Fig. 1. Configuration of the traction system proposed

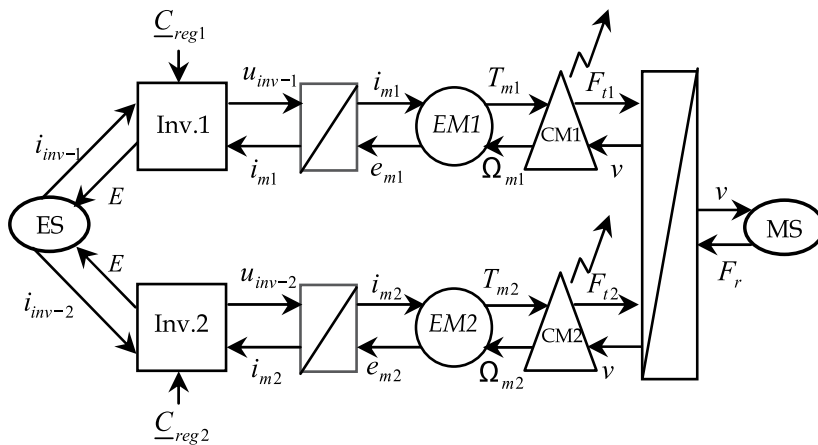


Fig. 2. EMR of the studied traction chain

2.1 Energetic macroscopic representation of the traction system

The energetic macroscopic representation is a synthetic graphical tool on the principle of the action and the reaction between elements connected (Merciera, 2004). The energetic macroscopic representation of the traction system proposed, Fig. 3, revealed the existence of

only one coupling called overhead mechanical type which is on the mechanical part of the traction chain.

The energetic macroscopic representation of the mechanical part of the electric vehicle (EV) does not take into account the stated phenomenon. However, a fine modeling of the contact wheel-road is necessary and will be detailed in the following sections.

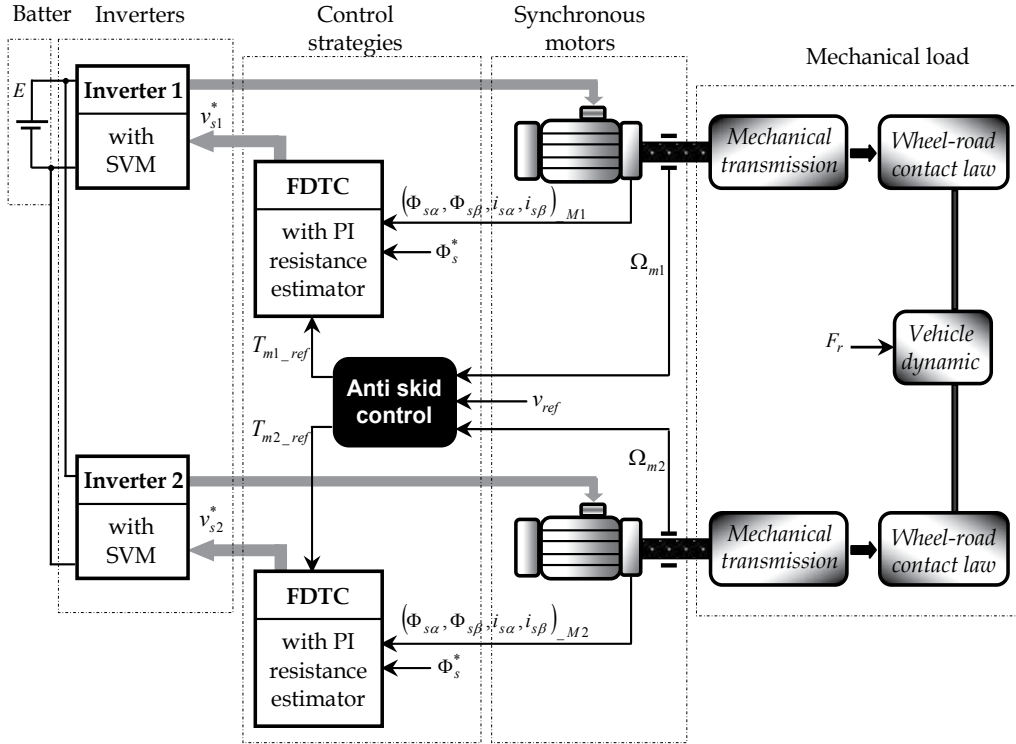


Fig. 3. Components of the traction system proposed

2.2 Traction motor model

The PMSM model can be described in the stator reference frame as follows (Pragasen, 1989):

$$\begin{cases} \frac{di_{s\alpha}}{dt} = -\frac{R_s}{L_s}i_{s\alpha} + \frac{\Phi_f}{L_s}\omega_m \sin\theta + \frac{1}{L_s}v_{s\alpha} \\ \frac{di_{s\beta}}{dt} = -\frac{R_s}{L_s}i_{s\beta} - \frac{\Phi_f}{L_s}\omega_m \cos\theta + \frac{1}{L_s}v_{s\beta} \\ \frac{d\omega_m}{dt} = -\frac{f}{J}\omega_m + \frac{p}{J}(T_{em} - T_{rm}) \end{cases} \quad (1)$$

and the electromagnetic torque equation

$$T_{em} = \frac{3}{2}p\Phi_f(-i_{s\alpha} \sin\theta + i_{s\beta} \cos\theta) \quad (2)$$

2.3 Inverter model

In this electric traction system, we use a voltage inverter to obtain three balanced phases of alternating current with variable frequency. The voltages generated by the inverter are given as follows:

$$\begin{bmatrix} v_a \\ v_b \\ v_c \end{bmatrix} = \frac{E}{3} \begin{bmatrix} 2 & -1 & -1 \\ -1 & 2 & -1 \\ -1 & -1 & 2 \end{bmatrix} \begin{bmatrix} S_a \\ S_b \\ S_c \end{bmatrix} \quad (3)$$

2.4 Mechanical transmission modeling of an EV

2.4.1 Modeling of the contact wheel-road

The traction force between the wheel and the road, Fig. 4(a), is given by

$$F_t = \mu N \quad (4)$$

where N is the normal force on the wheel and μ the adhesion coefficient. This coefficient depends on several factors, particularly on the slip λ and the contact wheel-road characteristics (Gustafsson, 1997; Gustafsson, 1998), Fig. 4(b). For an accelerating vehicle, it is defined by (Hori, 1998):

$$\lambda = \frac{v_\Omega - v}{v_\Omega} \quad (5)$$

The wheel speed can be expressed as:

$$v_\Omega = r\Omega \quad (6)$$

where Ω is the wheel rotating speed, r is the wheel radius and v is the vehicle speed. When $\lambda = 0$ means perfect adhesion and $\lambda = 1$ complete skid.

Principal non-linearity affecting the vehicle stability is the adhesion function which is given by Eq. (7) and represented on Fig. 4(b).

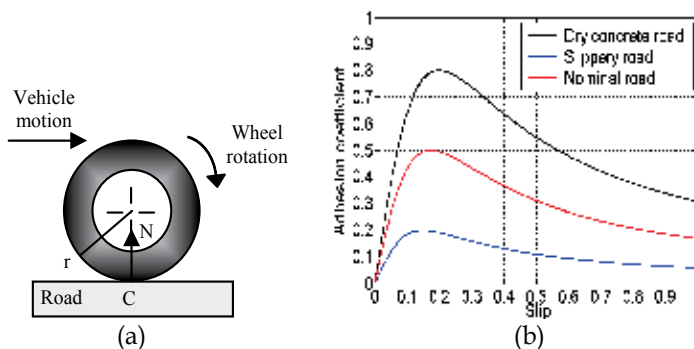


Fig. 4. (a) One wheel model, (b) contact wheel-road characteristics.

We now represent in the form of a COG (Guillaud, 2000) and an EMR, the mechanical conversion induced by the contact wheel-road, Fig. 5.

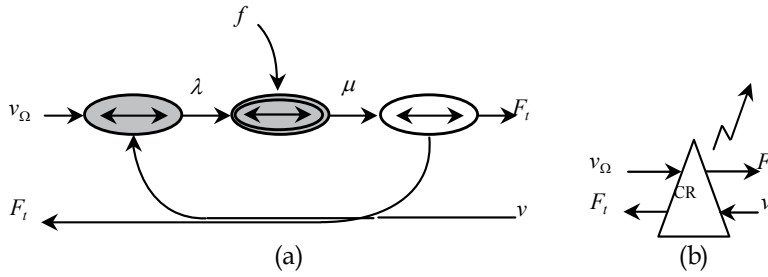


Fig. 5. Modeling of the contact wheel-road: (a) COG and (b) EMR.

2.4.2 Modeling of the transmission gearbox-wheel

Modeling of the transmission gearbox-wheel is carried out in a classical way which is given by:

$$\begin{cases} v_{\Omega} = r\Omega \\ T_r = rF_t \end{cases} \quad (7)$$

$$\begin{cases} \Omega = k_{red}\Omega_m \\ T_{rm} = k_{red}T_m \end{cases} \quad (8)$$

where r is the wheel radius, k_{red} the gearbox ratio, T_r the transferred resistive torque on the wheel shafts and T_{rm} the transferred resistive torque on the motor axle shafts, Fig. 6.

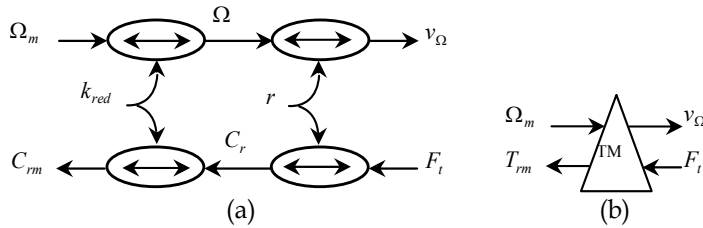


Fig. 6. Modeling of the mechanical drive: (a) COG and (b) EMR.

2.4.3 Modeling of the environment

The external environment is represented by a mechanical source (MS) on Fig. 3, leading to the resistance force of the vehicle motion F_r (Ehsani, 1997), where:

$$F_r = F_{aero} + F_{roll} + F_{slope} \quad (9)$$

F_{roll} is the rolling resistance, F_{aero} is the aerodynamic drag force and F_{slope} is the slope resistance.

The rolling resistance is obtained by Eq. (10), where μ_r is the rolling resistance coefficient, M is the vehicle mass and g is the gravitational acceleration constant.

$$F_{roll} = \mu_r Mg \quad (10)$$

The resistance of the air acting upon the vehicle is the aerodynamic drag, which is given by Eq. (11), where ρ is the air density, C_D is the aerodynamic drag coefficient, A_f is the vehicle frontal area and v is the vehicle speed (Wong, 1993).

$$F_{acero} = \frac{1}{2} \rho C_D A_f v^2 \tag{11}$$

The slope resistance and down grade is given by Eq. (12)

$$F_{slope} = Mg p_{\%} \tag{12}$$

2.5 EMR of the mechanical coupling

The modeling of the phenomenon related to the contact wheel-road enables us to separate the energy accumulators of the process from the contact wheel-road. However, the energy accumulators which are given by the inertia moments of the elements in rotation can be represented by the total inertia moments of each shaft motor J_{Ω} and the vehicle mass M , where:

$$J_{\Omega} \frac{d\Omega_m}{dt} = T_m - T_{rm} - f\Omega_m \tag{13}$$

and

$$M \frac{dv}{dt} = F_{t1} + F_{t2} - F_r \tag{14}$$

F_{t1} , F_{t2} are the traction forces developed by the left and right wheels and F_r is the resistance force of the motion of the vehicle.

The final modeling of the mechanical transmission is represented by the EMR, Fig. 7.

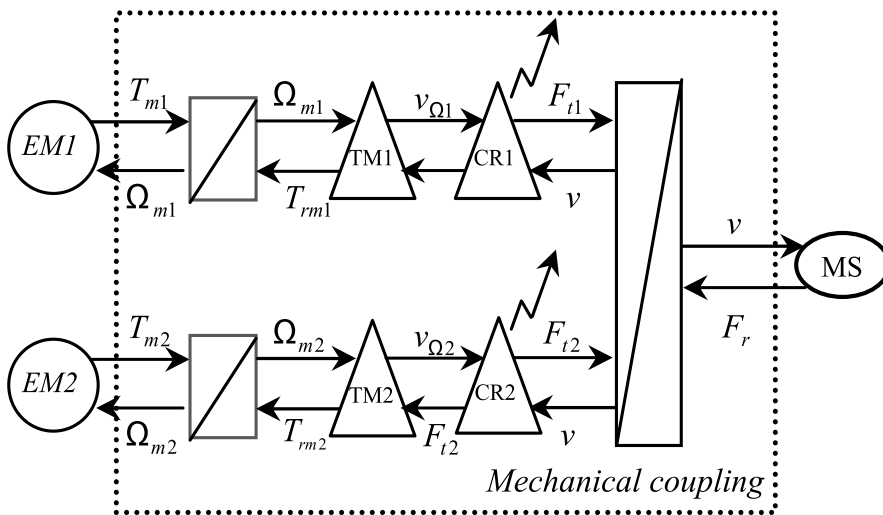


Fig. 7. Detailed EMR of the mechanical coupling

3. Control strategy

3.1 Fuzzy direct torque control

A fuzzy logic method was used in this chapter to improve the steady-state performance of a conventional DTC system. Fig. 8 depicts schematically a direct torque fuzzy control, in which the fuzzy controllers replace the flux linkage and torque hysteresis controllers and the switching table normally used in conventional DTC system (Takahachi, 1986; French, 1996; Vyncke, 2006; Vasudevan, 2004).

The proposed fuzzy DTC scheme uses the stator flux amplitude and the electromagnetic torque errors through two fuzzy logic controllers (i.e., FLC1 and FLC2) to generate a voltage space vector V_s^* (reference voltage); it does so by acting on both the amplitude and the angle of its components, which uses a space vector modulation to generate the inverter switching states. In Fig. 8 The errors of the stator flux amplitude and the torque were selected as the inputs, the reference voltage amplitude as the output of the fuzzy logic controller (FLC1), and the increment angle as the output of the fuzzy logic controller (FLC2) that were added to the angle of the stator flux vector. The results were delivered to the space vector modulation, which calculated the switching states S_a , S_b , and S_c .

The Mamdani and Sugeno methods were used for the fuzzy reasoning algorithms in the FLC1 and FLC2, respectively. Figs. 9 and 10 show the membership functions for the fuzzy logic controllers FLC1 and FLC2, respectively. Fig. 11 shows the fuzzy logic controller structure.

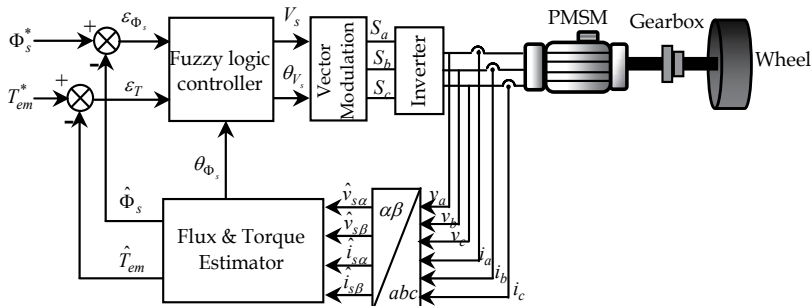


Fig. 8. System diagram of a PMSM-fuzzy DTC drive system with stator PI resistance estimator

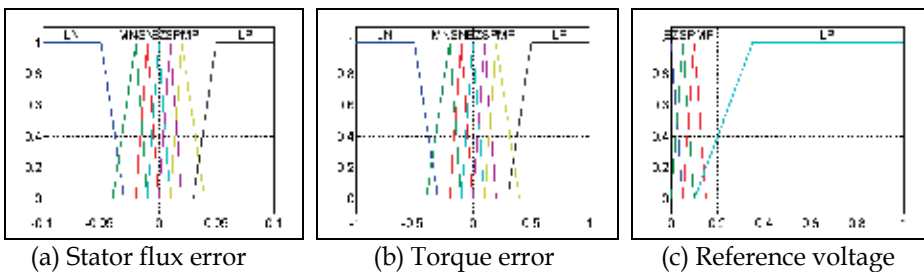


Fig. 9. Membership functions for the FLC1

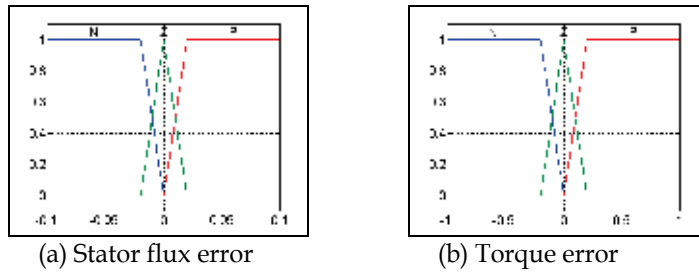


Fig. 10. Membership functions for the FLC2

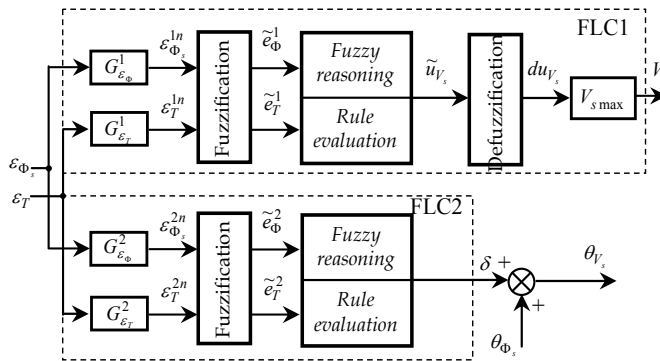


Fig. 11. Fuzzy logic controller structure

\tilde{e}_T \tilde{e}_Φ	NG	NM	NP	EZ	PP	PM	PG
NG	PG	PM	PP	PP	PP	PM	PG
NM	PG	PM	PP	PP	PP	PM	PG
NP	PG	PM	PP	EZ	PP	PM	PG
EZ	PG	PM	PP	EZ	PP	PM	PG
PP	PG	PM	PP	EZ	PP	PM	PG
PM	PG	PM	PP	PP	PP	PM	PG
PG	PG	PM	PP	PP	PP	PM	PG

Table 1. FLC 1 rules

$\varepsilon_{\Phi_s}^n$	P			Z			N		
ε_T^n	P	Z	N	P	Z	N	P	Z	N
δ	$\frac{\pi}{4}$	0	$-\frac{\pi}{4}$	$\frac{\pi}{2}$	$\frac{\pi}{2}$	$-\frac{\pi}{2}$	$\frac{3\pi}{2}$	π	$-\frac{3\pi}{4}$

Table 2. Reference voltage increment angle

3.2 PI resistance estimator for PMSM-fuzzy DTC drive

The system diagram can be shown in Fig. 11. It is seen that the input to the PI resistance estimator is torque and flux reference, together with the stator current. Rotor position is not needed for the PI estimator (Mir, 1998; Hartani, 2010).

When the stator resistance changes, the compensation process will be applied. Therefore, the change of stator resistance will change the amplitude of the current vector. So, the error between the amplitude of current vector and that of the reference current vector will be used to compensate the change in stator resistance until the error becomes zero.

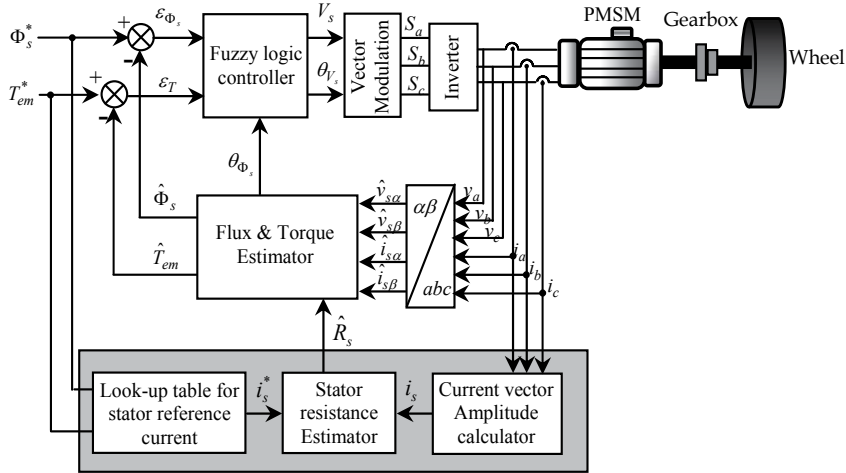


Fig. 12. System diagram of a PMSM-fuzzy DTC drive system with stator PI resistance estimator

Based on the relationship between change of resistance and change of current, a PI resistance estimator can be constructed by Eq. (15), as shown in Fig. 13. Here, i_s^* is the current vector corresponding to the flux and torque, and i_s is the measured stator current vector.

$$\Delta R_s = \left(kp + \frac{ki}{s} \right) \Delta i_s \tag{15}$$

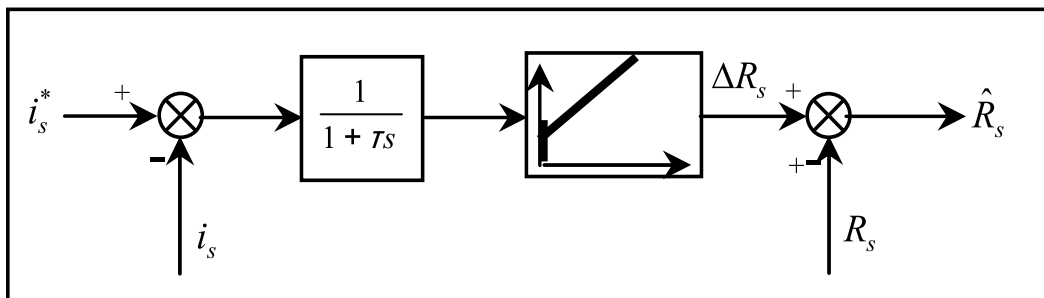


Fig. 13. PI resistance estimator for FDTC-PMSM drive system

3.2.1 Amplitude of stator reference current

The PMS machine's torque and flux vector are given by (16) and (17) in the vector reference frame. The amplitude of flux vector can be calculated using (19).

$$T_{em} = \frac{3}{2}p \left[\Phi_f i_q - (L_q - L_d) i_d i_q \right] \quad (16)$$

$$\begin{cases} \Phi_d = L_d i_d + \Phi_f \\ \Phi_q = L_q i_q \end{cases} \quad (17)$$

$$|\Phi_s| = \sqrt{\Phi_d^2 + \Phi_q^2} \quad (18)$$

The reference torque and flux are given, respectively, by:

$$\begin{cases} T_{em}^* = \frac{3}{2}p \left[\Phi_f i_q^* - (L_q - L_d) i_d^* i_q^* \right] \\ |\Phi_s^*| = \sqrt{(L_d i_d^* + \Phi_f)^2 + (L_q i_q^*)^2} \end{cases} \quad (19)$$

The stator current amplitude is obtained using the relation given by:

$$|i_s^*| = \sqrt{i_d^{*2} + i_q^{*2}} \quad (20)$$

A Matlab/Simulink model was built in order to verify the performance of the PI resistance estimator. The system performances with and without the resistance estimator were then compared. Fig. 14 shows the result of flux, torque, and amplitude of current of the system with PI stator resistance estimator.

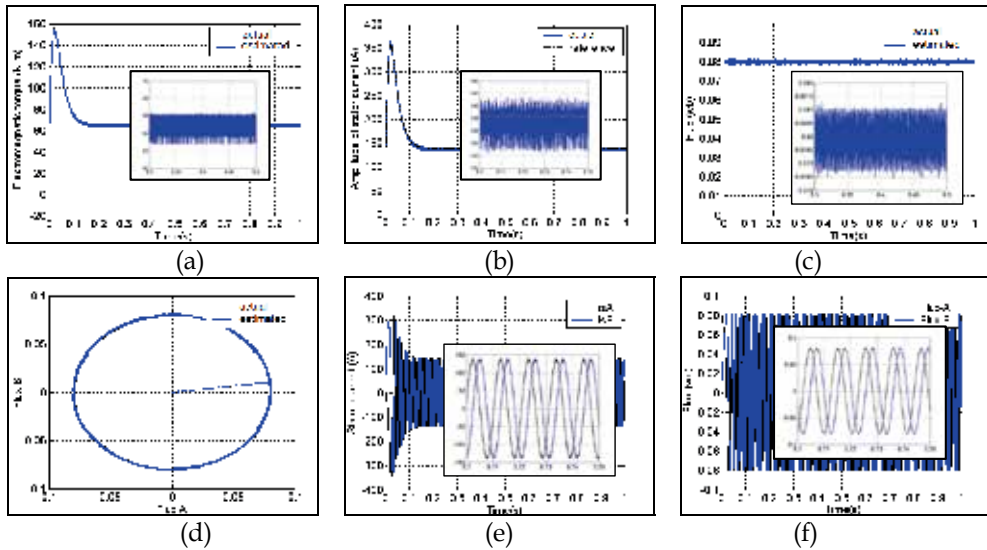


Fig. 14. Performances of the FDTC-PMSM drive system with a ramp-up in stator resistance with compensation

3.3 Maximum control structure

The maximum control structure (MCS) is obtained systematically by applying the principles of inversion to the model EMR of the process (Bouscayrol, 2002). We define by this method the control structure relating to the mechanical model of the vehicle. In our application, the variable to be controlled is the vehicle speed by acting on the motor torques of both wheels. The maximum control structure is shown in Fig. 15, by taking into account only one wheel for simplification.

This structure shows the problems involved in the inversions of the mechanical coupling by the accumulation element and of non-linearity relating to the contact wheel-road.

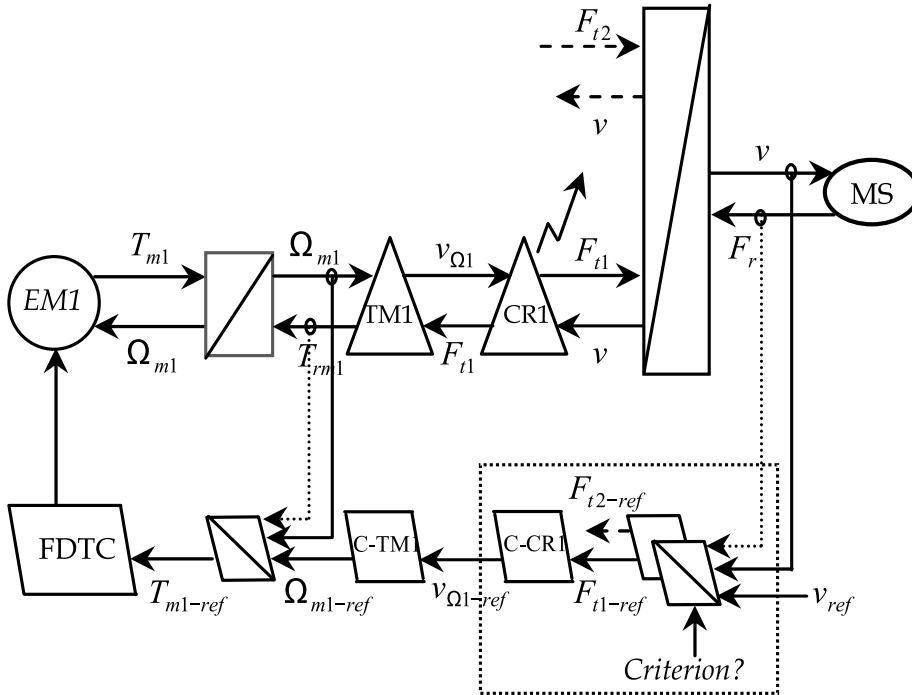


Fig. 15. EMR of the maximum control of the vehicle

3.3.1 Inversion of the coupling by accumulation elements

The inversion of the relation (15) shows that this control is done by controlling a traction effort $(F_{t1} + F_{t2})$ where each wheel contributes to the advance of the vehicle. However, the inversion of the COG requires the use of a controller where the ergonomic analyzes showed that the driver wishes to keep the control of traction effort by acting on an accelerator pedal in order to control the vehicle speed. In this work, we admit that the action of the driver provides the reference of the total traction effort $(F_{t1} + F_{t2})_{ref}$, Fig. 16. The difficulty of this reference is how to distribute the forces between both wheels $(F_{t1-ref}$ and $F_{t2-ref})$. The solution of this difficulty can be solved by adding a condition to the inversion of the rigid relation. This condition $(F_{t1-ref} = F_{t2-ref})$ is relating to the stability of the vehicle to imbalance the forces transmitted to each wheel which is closer to the equivalent torques imposed by the classical mechanical differential.

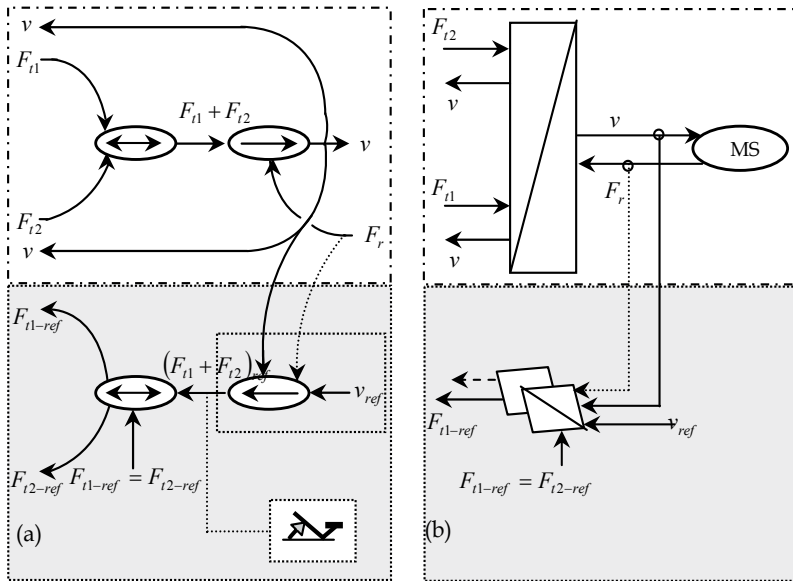


Fig. 16. Modulation of the traction effort: (a) COG and (b) EMR.

3.3.2 Inversion of the converter CR

We should now define the speed of each wheel in order to ensure the balance of the traction forces. However, the problems which we will face are the nonlinearity and the badly known of the relation to reverse which depends of the road conditions. In the following work, we propose two methods to solve these problems.

3.4 Anti skid strategy by slip control

The proposed solution will be obtained from the maximum control structure, Fig. 15. In this case, the solution to be used to reverse the converter CR is based on the principle of inversion of a badly known rigid relation. We can now apply with this type of relation, the principles of inversion of a causal relation which will minimize the difference between the output and its reference by using a classical controller. The principle of this strategy is based on Fig. 17.

3.4.1 Inversion of relation CR1

Figure 18, shows the COG inversion of relation CR1. We need now the measurements or estimations of the variables speed and traction effort of each wheel.

The linear velocity estimation permits a true decoupling in the control of both wheels (Pierquin, 2001) and the definition of the reference speed which is given by the following equation:

$$v_{\Omega 1-ref} = \frac{v}{1 - \lambda_{1-ref}} \tag{22}$$

In the control structure, the maximum slip is limited to 10% which constitutes the real function anti skidding.

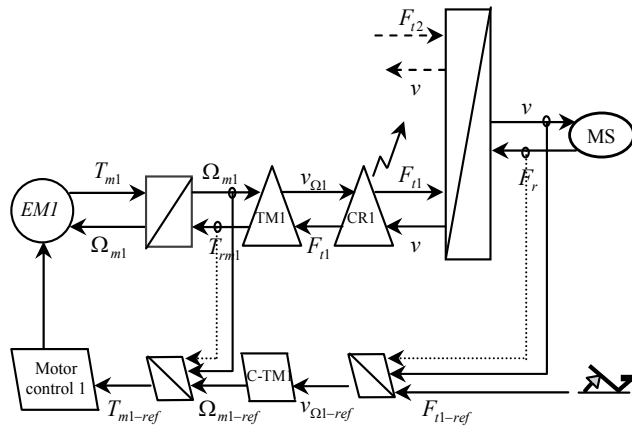


Fig. 17. Control structure deduced from the inversion

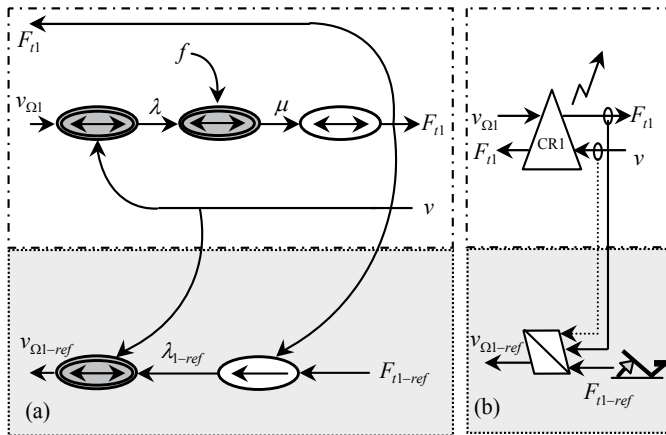


Fig. 18. Inversion of the converter CR: (a) COG; (b) EMR

3.5 Anti skid strategy by BMC

3.5.1 The BMC structure

The behaviour model control (BMC) can be an alternative to other robust control strategies. It is based on a supplementary input of the process to make it follow the model (Hautier, 1997 ; Vulturescu, 2000; Pierquin, 2000).

The process block corresponds to the real plant, Fig. 19. It can be characterised by its input vector u and its output vector y .

The control block has to define an appropriated control variable u , in order to obtain the desired reference vector y_{ref} .

The model block is a process simulation. This block can be a simplified model of the process. The difference between the process output y and the model output y_{mod} is taken into account by the adaptation block. The output of this block acts directly on the process by a supplementary input, Fig. 19. The adaptation mechanism can be a simple gain or a classical controller (Vulturescu, 2004).

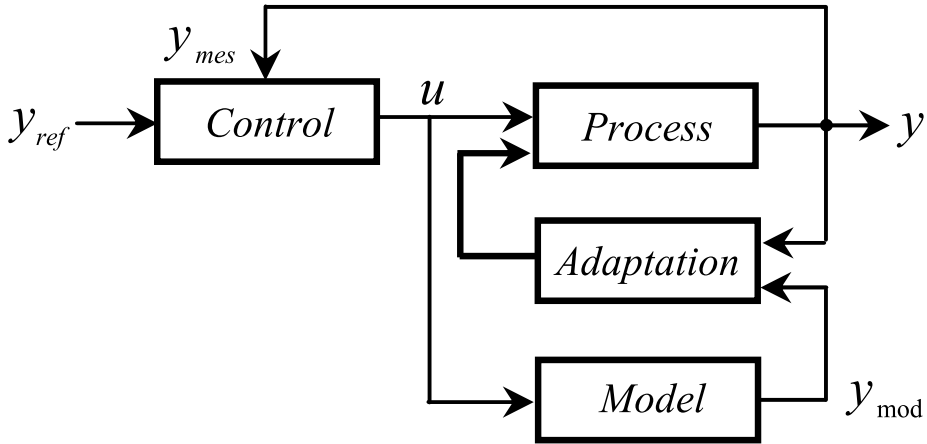


Fig. 19. Example of a BMC structure

3.5.2 Application of the BMC control to the traction system

The first step to be made is to establish a behaviour model. In this case, we choose a mechanical model without slip, which will be equivalent to the contact wheel-road in the areas known as pseudo-slip. This model can be considered as an ideal model. However, the inertia moments of the elements in rotation and the vehicle mass can be represented by the total inertia moments J_{t_mod} of each shaft motor which is given by:

$$J_{t_mod} = \tilde{J}_{\Omega} + \tilde{M} \left(\tilde{k}_{red} \tilde{r} \right)^2 \quad (23)$$

The dynamic equation of the model is given by:

$$J_{t_mod} \frac{d\Omega_{mod}}{dt} = T_{m_mod} - T_{rm_mod} \quad (24)$$

By taking into account the wheel slip, the total inertia moments will become:

$$J_t = J_{\Omega} + M(1-\lambda)(k_{red}r)^2 \quad (25)$$

We now apply the BMC structure for one wheel to solve the skid phenomenon described before. In Fig. 20, we have as an input the reference torque and as an output the speed of the motor which drives the wheel. However, the main goal of this structure of control is to force the speed Ω_m of the process to track the speed Ω_{m_mod} of the model by using a behaviour controller.

It was shown that the state variables of each accumulator are not affected with the same manner by the skid phenomenon. The speed wheel is more sensitive to this phenomenon than that of vehicle in a homogeneous ratio to the kinetic energies, Fig. 5(a). Hence, the motor speed is taken as the output variable of the model used in the BMC control. The proposed control structure is given by Fig. 20.

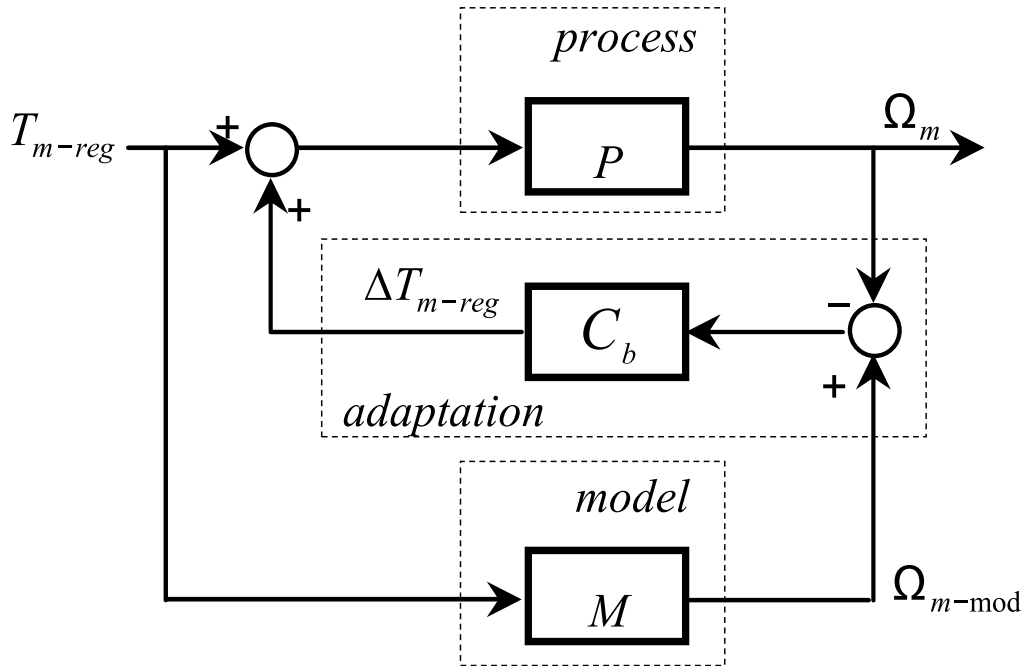


Fig. 20. BMC control applied to one wheel

The influence of the disturbance on the wheel speeds in both controls is shown in Fig. 21. An error is used to compare the transient performances of the MCS and the BMC. This figure shows clearly that the perturbation effect is negligible in the case of BMC control and demonstrates again the robustness of this new control.

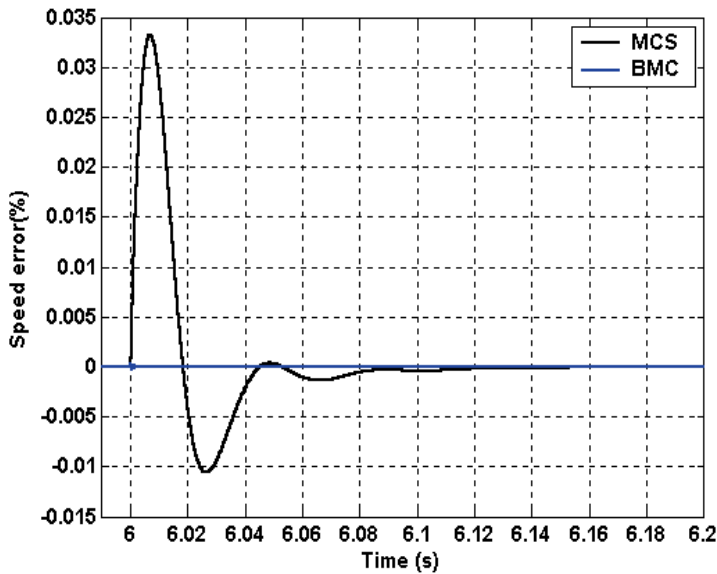


Fig. 21. Effect of a loss of adherence of MCS and BMC controls

4. Simulation results

We have simulated by using different blocks of Matlab/Simulink the proposed traction system. This system is controlled by the behaviour model control (BMC) based on the DTC strategy applied to each motor, Fig. 20, for the various conditions of environment (skid phenomenon), Fig. 22.

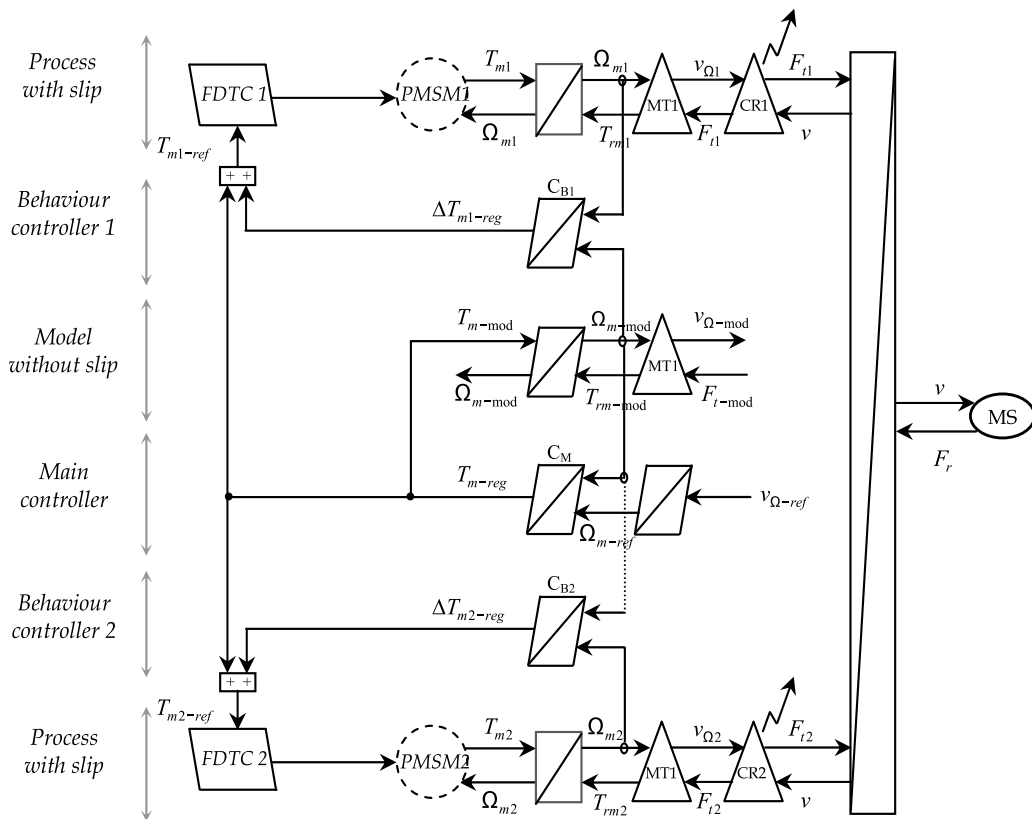


Fig. 22. BMC structure applied to the traction system

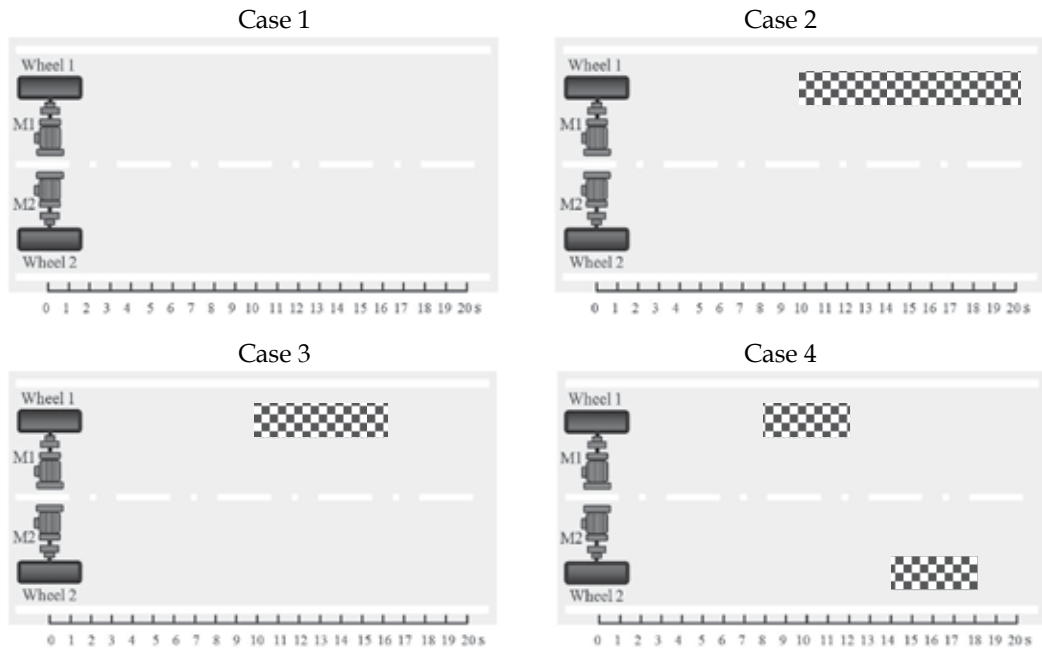


Fig. 23. Simulation cases.  Dry road  Slippery road

4.1 Case 1

Initially, we suppose that the two wheels are not skidding and are not disturbed. Then, a 80 km/h step speed is applied to our system. We notice that the speeds of both wheels and vehicle are almost identical. These speeds are illustrated in the Fig. 24(a) and (b). Fig. 24(c) shows that the two motor speeds have the same behaviour to its model. The difference between these speeds is represented in the Fig. 24(d). From Fig. 24(e) we notice that the slips λ_1 and λ_2 of both wheels respectively, are maintained in the adhesive region and the traction forces which are illustrated by the Fig. 24(f) are identical, due to the same conditions taken of both contact wheel-road. The motor torques are represented in Fig. 24(g) and the imposed torques of the main controller and the behaviour controllers are shown in Fig. 24(h). The resistive force of the vehicle is shown by the Fig. 24(i).

4.2 Case 2

We simulate now the system by using the BMC control and then applying a skidding phenomenon at $t = 10\text{s}$ to wheel 1 which is driven by motor 1 when the vehicle is moving at a speed of 80 km/h . The skidding occurs when moving from a dry road ($\mu_1(\lambda)$) to a slippery road ($\mu_2(\lambda)$) which leads to a loss of adherence.

The BMC control has a great effect on the adaptation blocks and by using the behaviour controllers to maintain permanently the speed of the vehicle and those of the wheels close to their profiles, Fig. 25(a). However, both driving wheel speeds give similar responses as shown in Fig. 25(b).

Figure 25(c) shows that the two motor speeds have the same behaviour with the model during the loss of adherence. The difference between these speeds which is negligible is represented in the Fig. 25(d).

The loss of adherence imposed on wheel 1 results to a reduction in the load torque applied to this wheel, consequently its speed increases during the transient time which induces a small variation of the slip on wheel 2, Fig. 25(e). The effect of this variation, leads to a temporary increase in the traction force, Fig. 18(i). However, the BMC control establishes a self-regulation by reducing the electromagnetic torque T_{m1} of motor 1 and at the same time increases the electromagnetic torque T_{m2} to compensate the load torque of motor 2, Fig. 25(j) and Fig. 25(k). Figures 25(n) and 25(o) show the phase currents of motor 1 and motor 2 respectively.

4.3 Case 3

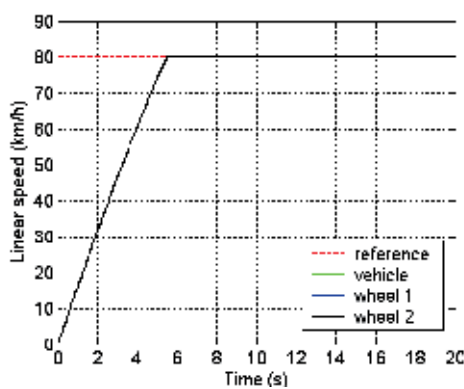
In this case, the simulation is carried out by applying a skid phenomenon between $t = 10\text{s}$ and $t = 16\text{s}$ only to wheel 1.

As shown in Fig. 26(i). and during the loss of adherence, the traction forces applied to both driving wheels have different values. At $t = 16\text{s}$, when moving from a slippery road ($\mu_2(\lambda)$) to a dry road ($\mu_1(\lambda)$), the BMC control establishes a self-regulation by increasing the electromagnetic torque T_{m1} of motor 1 and at the same time decreases the electromagnetic torque T_{m2} of motor 2, Fig. 26(j) and (k) which results to a negligible drop of speeds, Fig. 26(d), (e) and (f).

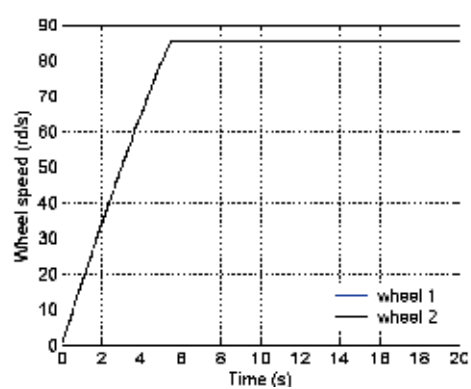
4.4 Case 4

The simulation is carried out by applying a skid phenomenon to both wheels successively at different times. Figure 27(c) shows that the two motor speeds have the same behaviour to the model. The difference between these speeds is represented in the Fig. 27(g).

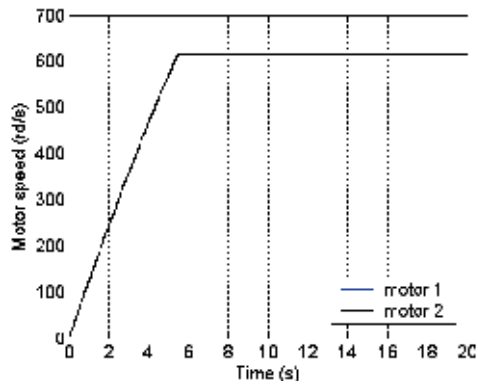
When the adherence of the wheel decreases, the slip increases which results to a reduction in the load torque applied to this wheel. However, the BMC control reduces significantly the speed errors which permits the re-adhesion of the skidding wheel. Therefore, it is confirmed that the anti-skid control could maintain the slip ratio around its optimal value, Fig. 27(h).



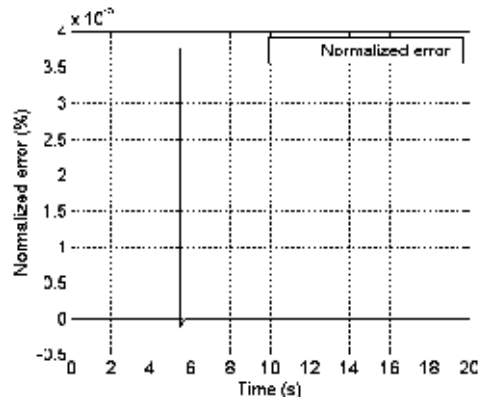
(a)



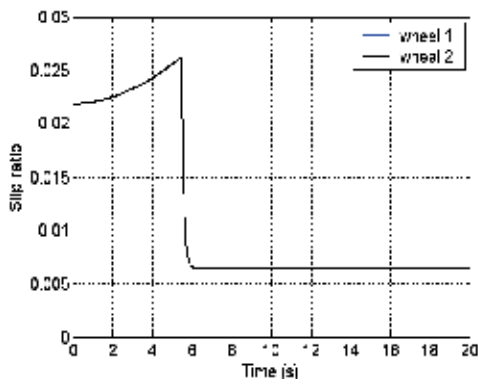
(b)



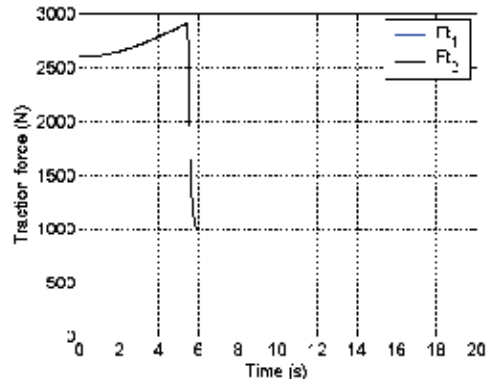
(c)



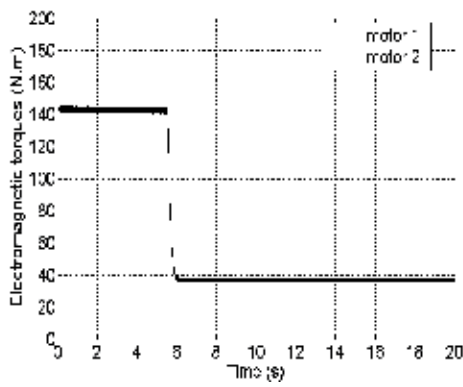
(d)



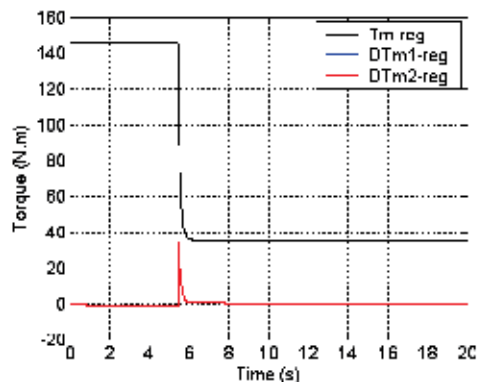
(e)



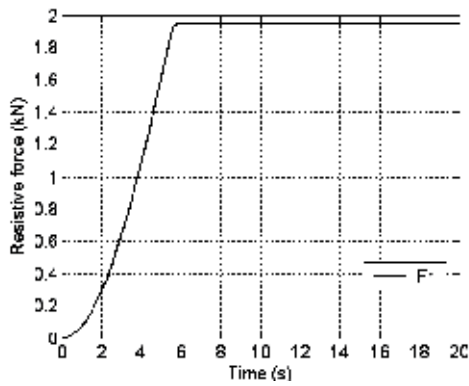
(f)



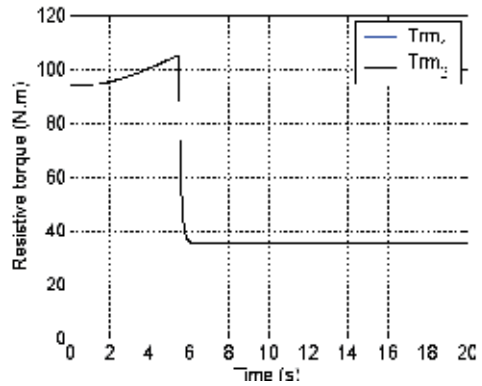
(g)



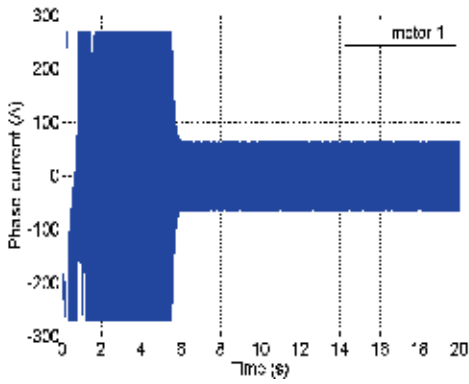
(h)



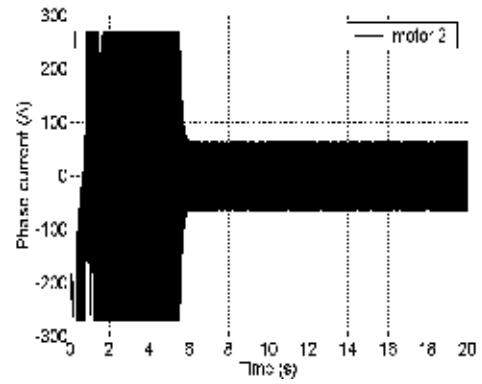
(i)



(j)

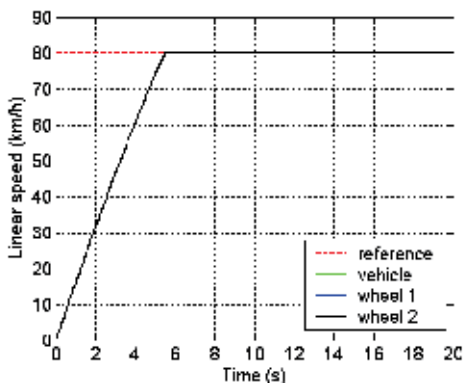


(k)

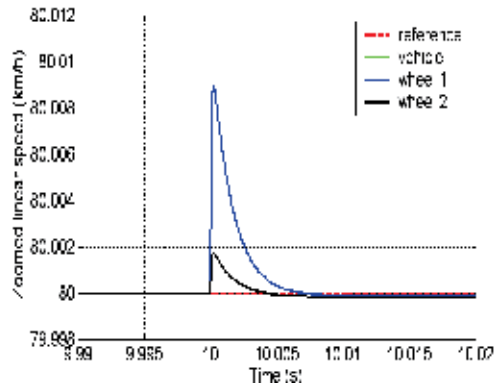


(l)

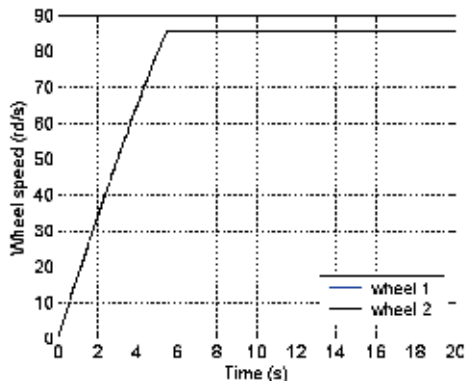
Fig. 24. Simulation results for case 1



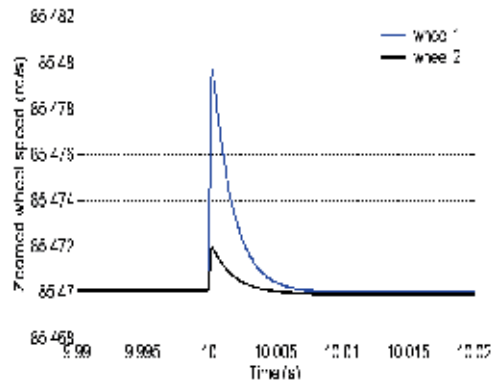
(a)



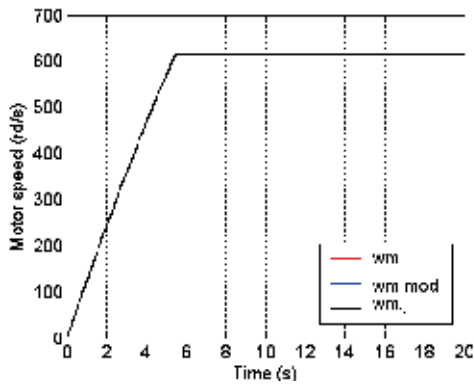
(b)



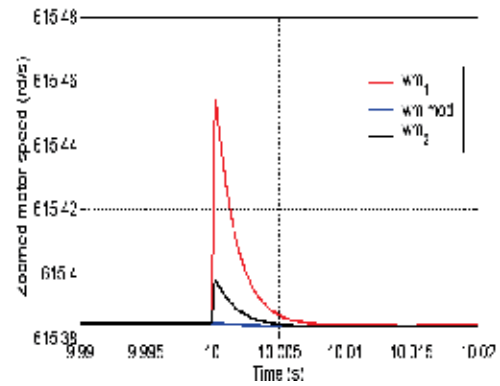
(c)



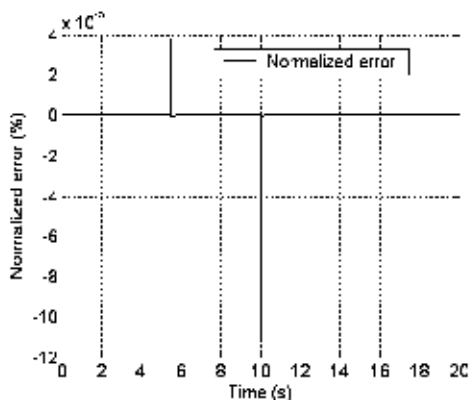
(d)



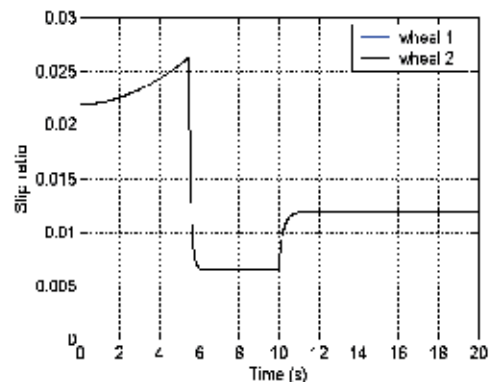
(e)



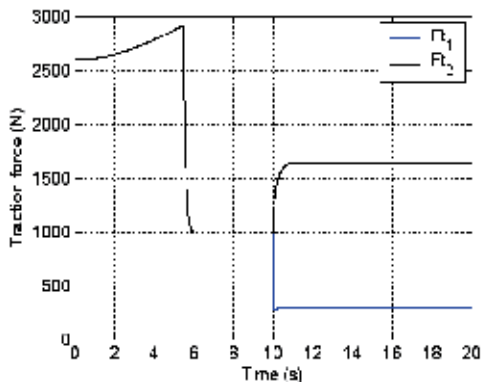
(f)



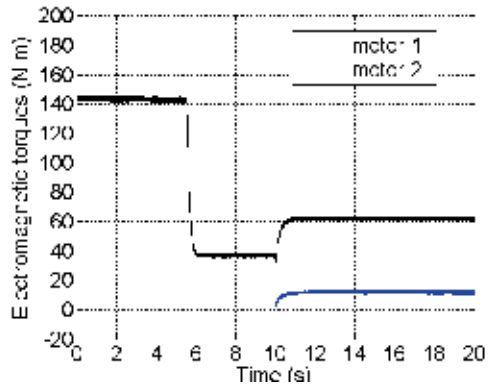
(g)



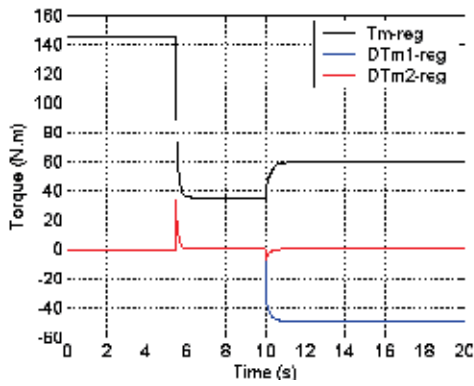
(h)



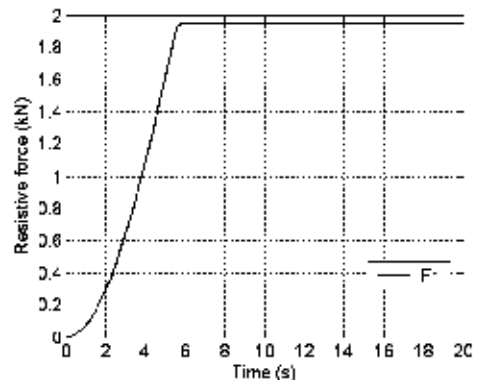
(i)



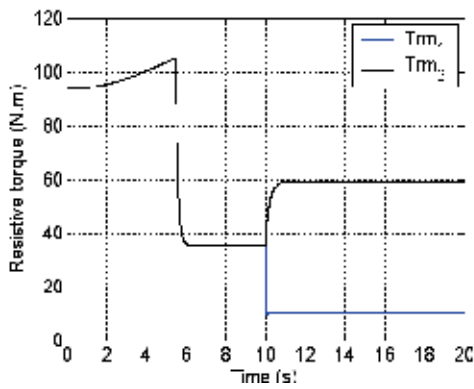
(j)



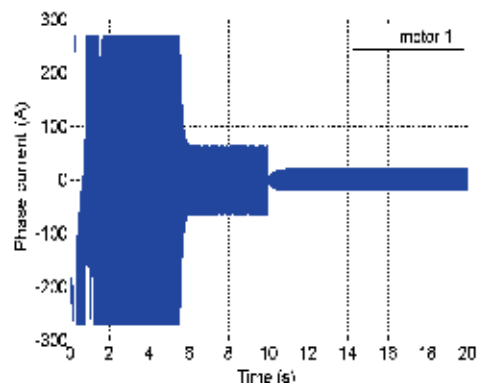
(k)



(l)



(m)



(n)

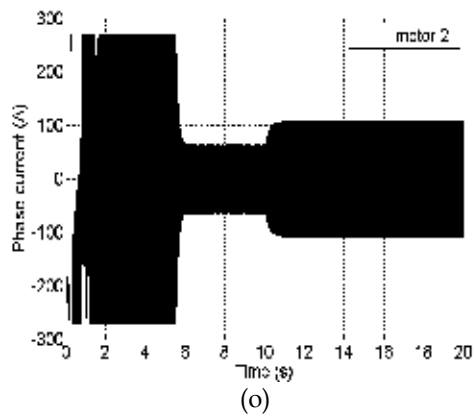
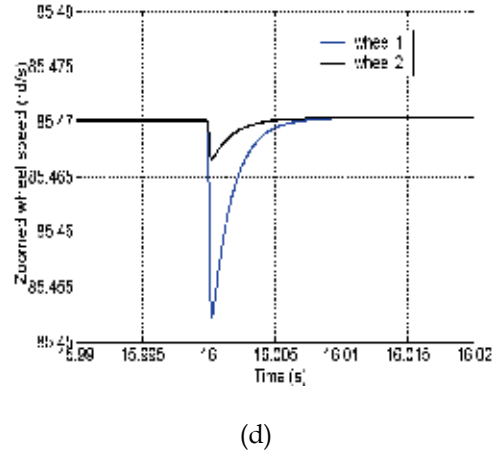
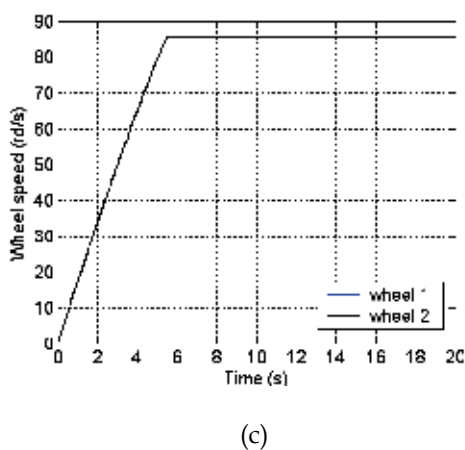
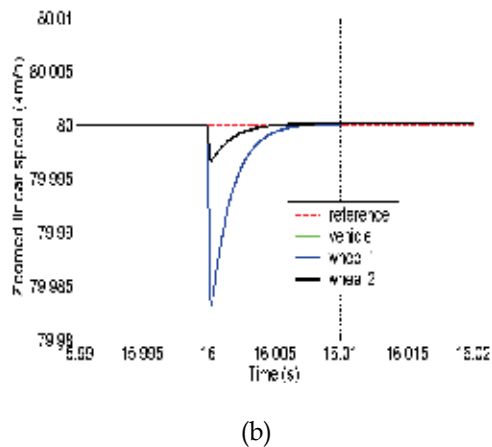
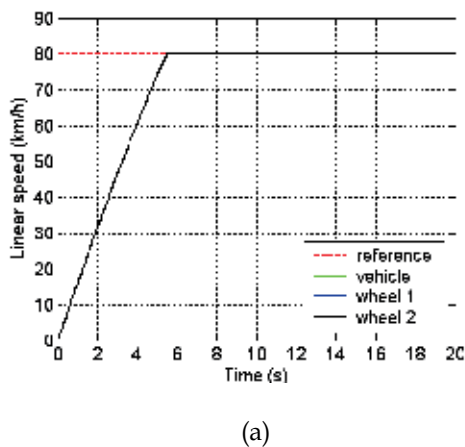
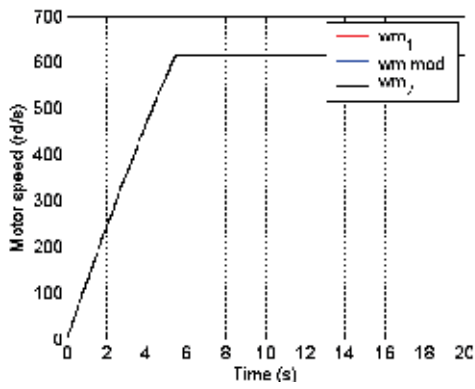
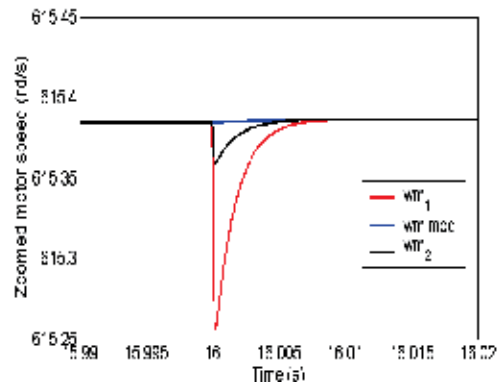


Fig. 25. Simulation results for case 2

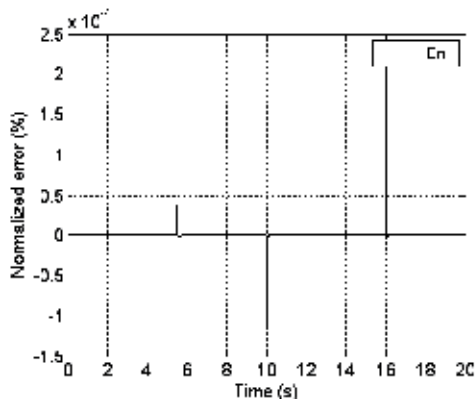




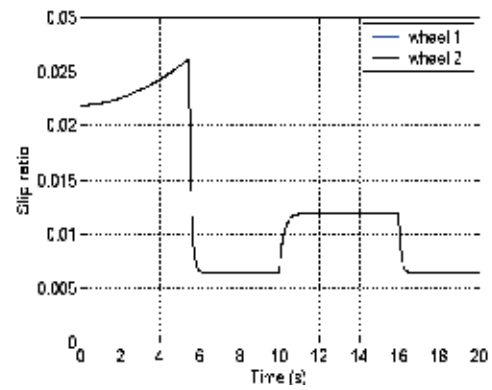
(e)



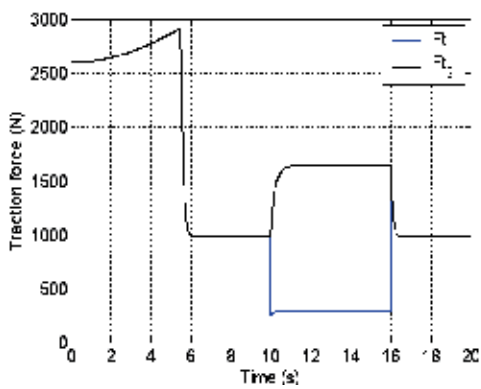
(f)



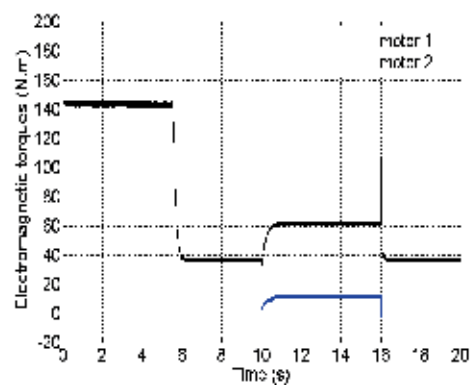
(g)



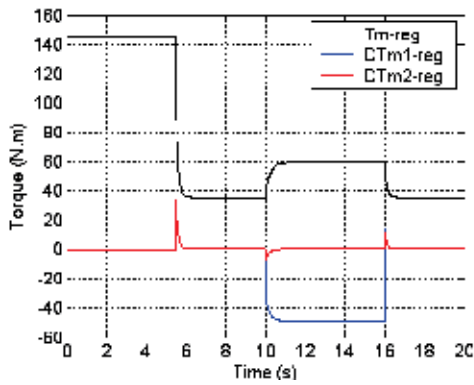
(h)



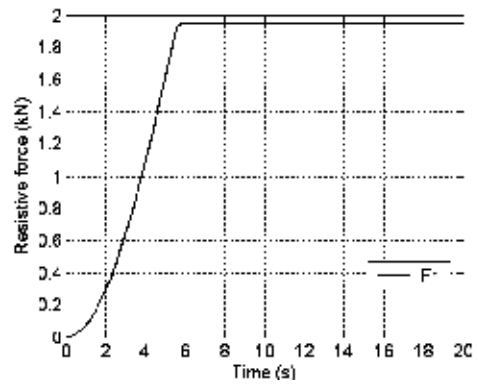
(i)



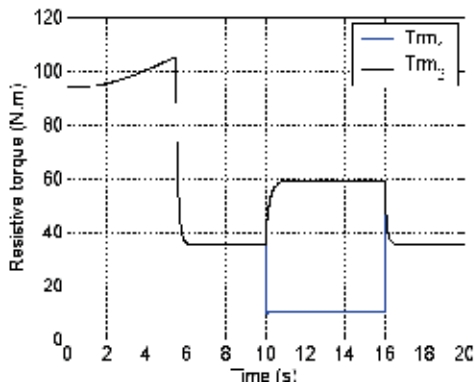
(j)



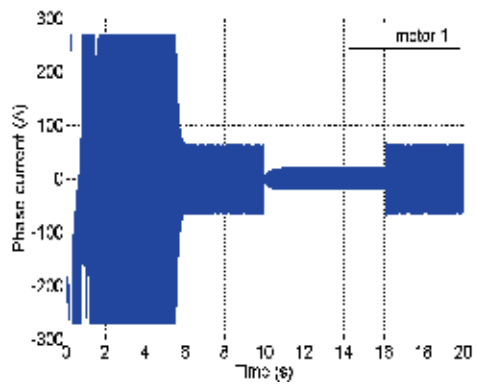
(k)



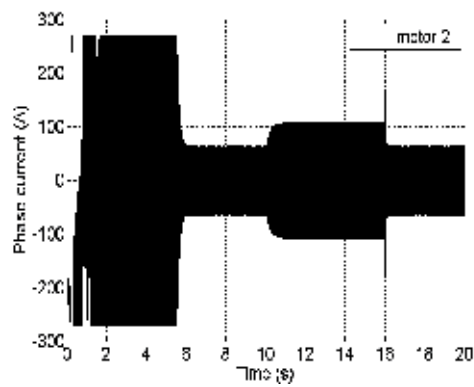
(l)



(m)

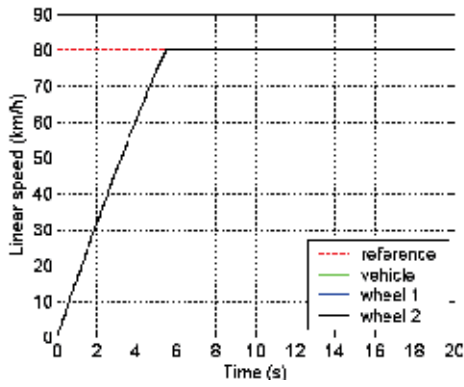


(n)

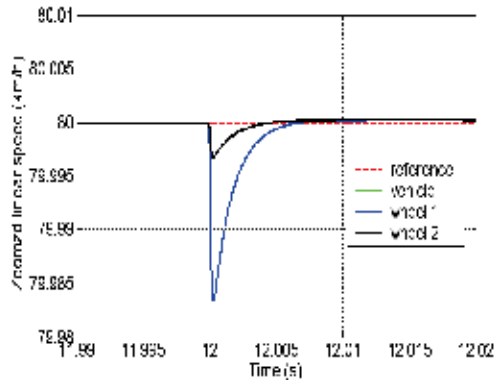


(o)

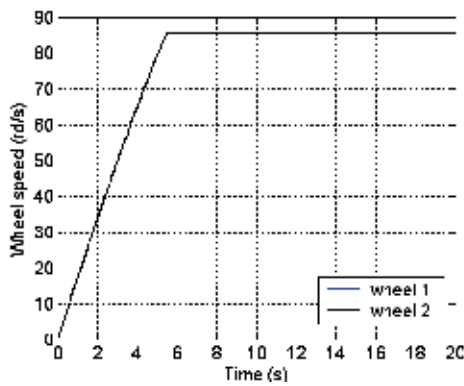
Fig. 26. Simulation results for case 3



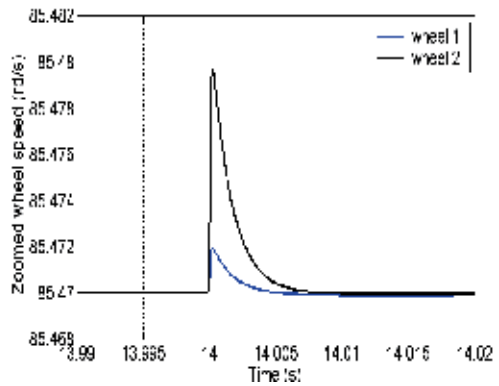
(a)



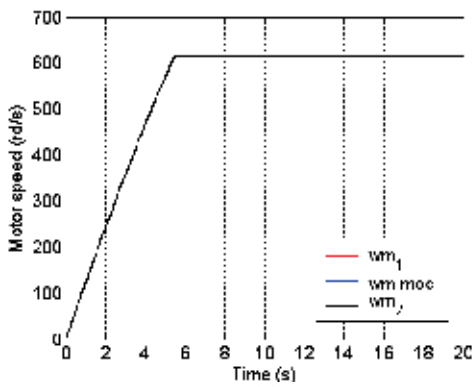
(b)



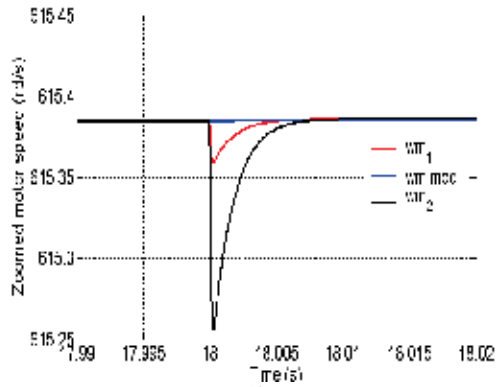
(c)



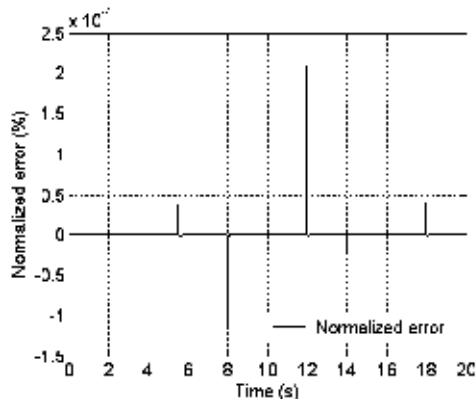
(d)



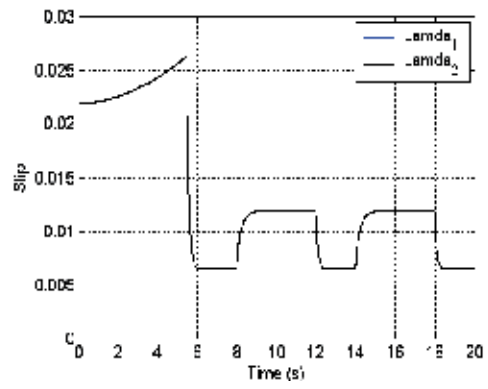
(e)



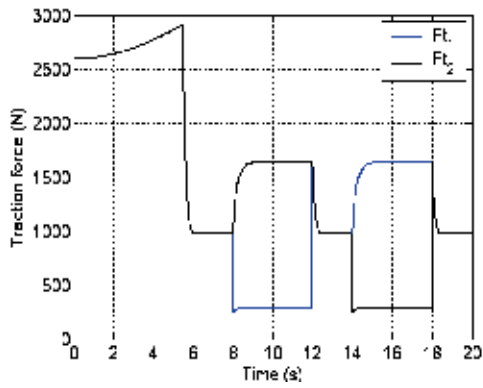
(f)



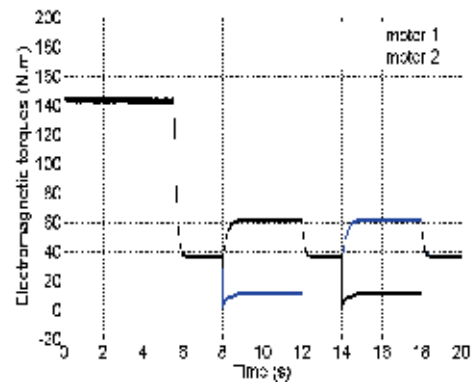
(g)



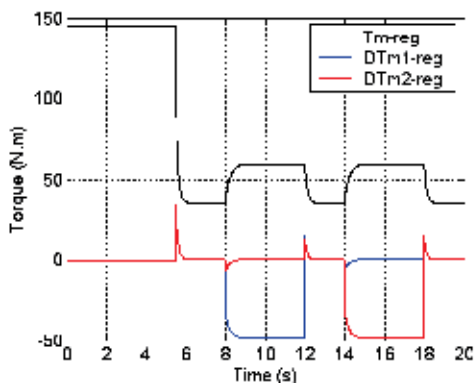
(h)



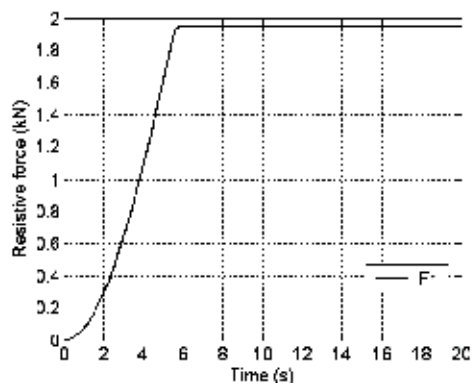
(i)



(j)



(k)



(l)

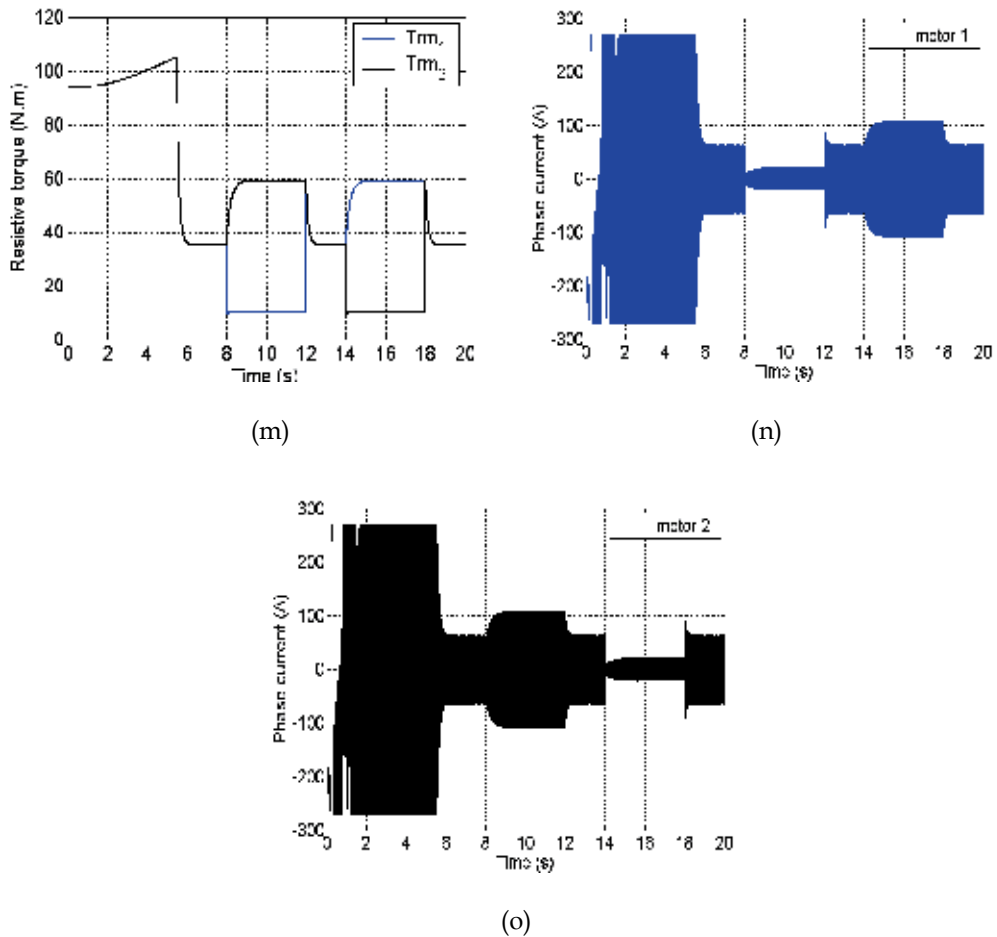


Fig. 27. Simulation results for case 4

5. Conclusion

In this chapter, a new anti-skid control for electric vehicle is proposed and discussed. This work contributes to the improvement of the electric vehicle stability using behaviour model control. According to the results obtained by simulations for all the cases, the proposed traction system shows a very stable behaviour of the electric vehicle during the various conditions of adherence.

6. Abbreviations

COG	: Causal Ordering Graph
DTFC	: Direct Torque Fuzzy Control
EC	: Electrical Coupling
EM	: Electrical machine

EMR : Energetic Macroscopic Representation
 ES : Electrical Source
 EV : Electric Vehicle
 MC : Mechanical Coupling
 MCS : Maximum Control Structure
 MMS : Multi-machine Multi-converter Systems
 MS : Mechanical Source
 PMSM : Permanent Magnet synchronous Machine
 SC : Static converter

7. Appendix

Parameter	Symbol	Unit	Value
Vehicle total mass	M	Kg	1200
Wheel radius	r	m	0,26
Aerodynamic drag coefficient	C_D	N/(ms) ²	0,25
Vehicle frontal area	S	m ²	1,9
Gearbox ratio	k_{red}	-	1/7,2
Efficiency of the gearbox	η	-	0,98

Table 3. The Specifications of the Vehicle Used in Simulation

Parameter	Symbol	Unit	Value
Resistance	R	Ω	0,03
d -axis inductance	L_d	H	$2 \cdot 10^{-4}$
q -axis inductance	L_q	H	$2 \cdot 10^{-4}$
Permanent magnet flux	Φ_f	Wb	0,08
Pole pairs	p	-	4

Table 4. The specifications of motors

8. References

- Bouscayrol, A.; Davat, B.; de Fornel, B.; François, B.; Hautier, J.P.; Meibody-Tabar, F.; Monmasson, E.; Pietrzak-David, M.; Razik, H.; Semail, E.; Benkhoris, F. (2003), Control structures for multi-machine multi-converter systems with upstream coupling. *Elsevier, Mathematics and computers in simulation* Vol. 63, pp. 261-270, 2003.
- Bouscayrol, A.; Davat, B.; de Fornel, B.; François, B.; Hautier, J.P.; Meibody-Tabar, F.; Pietrzak-David, M. (2000), Multi-machine multi-converter systems for drives: analysis of couplings by a global modelling. in: *Proceedings of the IEEE-IAS Annual Meeting, Rome, October 2000*.
- Arnet, B.; Jufer, M. (1997), Torque control on Electric vehicles with separate wheel drives. *Proceeding of EPE'97, Trondhein, Vol. 4, pp. 39-40, 1997*.
- Hartani, K.; Bourahla, M.; Mazari, B. (2005), New driving wheels control of electric vehicle, *Journal of Electrical Engineering, Vol. 5, pp. 36-43*.
- Hartani, K.; Bourahla, M.; Miloud, Y. (2007), Electric vehicle with two independent wheel drive – Performance improvement by an electronic differential using sliding-mode control, *Electromotion, Vol. 14, No. 2, pp. 99-113*.
- Merciera, J.C.; Verhille, J.N.; Bouscyrol, A. (2004), Energetic Macroscopic Representation of a subway traction system for a simulation model, *IEEE-ISIE'04, Ajaccio (France), Vol. 2, pp. 1519-1524, May 2004*.
- Pragasen, P.; Krishnan, R. (1989), Modeling, Simulation, and Analysis of Permanent Magnets Motor Drives, Part I: The Permanent Magnets Synchronous Motor Drive, *IEEE Transactions on Industry Applications, 25 (2), 265-273*.
- Miloudi, A.; Eid, A.; Al-radadi, A.; Draou, D. (2007), A variable gain PI controller used for speed control of a direct torque neuro fuzzy controlled induction machine drive, *Turk. J. Elec. Engin. Vol. 15 No. 1, pp. 37-49*.
- Miloudi, A.; Eid, A.; Al-radadi, A.; Draou A.; Miloud, Y. (2004), Simulation and modelling of a variable gain PI controller for speed control of a direct torque neuro fuzzy controlled induction machine drive, in proc. *PESC'04, Aechan, Germany, June. 20-25, pp. 3493-3498*.
- Tang, L.; Zhang, L.; Rahman, M. F.; Yumen, Hu. (2004), A novel direct torque controlled interior permanent magnet synchronous machine drive with low ripple in flux and torque and fixed frequency, *IEEE Trans. on Power Electronics, Vol. 19, No. 2, pp. 346-354*.
- Sun, D.; Yikang, He.; Zhu, J. G. (2004), Fuzzy logic direct torque control for permanent magnet synchronous motors, *Proc. Of the 5th world congress on intelligent control and automation, Hanzzhou, P.R. China, June 15-19, 2004*.
- Gustafsson, F. (1998), Monotiring tire-road friction using the wheel slip," *IEEE Control Systems Magazines. Vol.18, No.4, pp. 42-49, 1998*.
- Gustafsson, F. (1997), Slip based tire-road friction estimation, *Automatica. Vol.33, No.6, pp. 1087-1099, 1997*.
- Hori, Y.; Toyoda, Y.; Tsuruoka, Y. (1998), Traction control of electric vehicle based on the estimation of road surface condition. Basic experimental results using the test EV

- "UOT electric march, *IEEE. Trans. on Industry Applications*. Vol. 34, No.5, pp. 1131-1138, 1998.
- Guillaud, X.; Degobert, P.; Hautier, J.P. (2000), Modeling, control and causality: the causal ordering graph," *16th IMACS world congress*, CD-ROM, Lausanne, Switzerland; August 2000.
- Ehsani, M.; Rahman, K. M.; Toliyat, H.A. (1997), Propulsion system design and Hybrid vehicles," *IEEE Transactions on Industrial Electronics*, Vol. 44, No.1, pp.19-27, 1997.
- Wong, J. Y. (1993), The theory of ground vehicle, *Wiley-Interscience Publication* 1993, ISBN 0-471-58496-4.
- Bouscayrol, A.; Delarue, Ph. (2002), Simplifications of the Maximum Control Structure of a wind energy conversion system with an induction generator, *Int. J. Renew Energy Eng.*, Vol.4, no.2, pp. 479-485, 2002.
- Pierquin, J.; Vulturescu, B.; Bouscayrol, A.; Hautier, J. P. (2001), Behaviour model control structures for an electric vehicle, *EPE'2001*, CD-ROM, Graz (Austria), August, 2001.
- Hautier, J.P.; Garon, J.P. (1997), Systèmes automatiques, *Tome 2, Commande de processus*, Edition Ellipses, Paris, 1997.
- Vulturescu, B.; Bouscayrol. A.; Hautier, J.P.; Guillaud, X.; Ionescu, F. (2000), Behaviour model control of a DC machine, *ICEM2000, Conference Espoo* (Finland). August 2000.
- Pierquin, J.; Escane, P.; Bouscayrol, A.; Pietrzak-David, M.; Hautier, J.P.; de Fornel, B. (2000), Behaviour model control of a high speed railway traction system, *EPE-PEMC 2000 Conference*, Kocise (Slovak Republic), Vol. 6, pp. 197-202, September 2000.
- Vulturescu, B.; Bouscayrol, A.; Ionescu, F.; Hautier, J.P. (2004), Behaviour model control for cascaded processes: Application to an electrical drive, *Elsevier, Computers and Electrical Engineering*, vol.30, pp. 509-526, 2004.
- Sado, H.; Sakai, S., Hori, Y. (1999), Road condition estimation for traction control in electric vehicle, *In Proc. IEEE Int. Symp. Industrial Electronic*, Solvenia, pp. 973-978, 1999.
- Okano, T.; Tai, C.; Inoue, T.; Uchida, T.; Sakai, S., Hori, Y. (2002), Vehicle stability improvement Based on MFC independently installed on 4 wheels-Basic experiments using "UOT Electric March II", *In proc. PCC-Osaka*, Vol. 2, pp. 582-587, 2002.
- Sakai, S.; Hori, Y. (2001), Advantage of electric motor for antiskid control of electric vehicle, *EPE Journal*, Vol. 1.11, No.4, pp. 26-32, 2001.
- Takahachi, I.; Noguchi, T. (1986), A new quick-response and high-efficiency control strategy of an induction motor, *IEEE Trans. Ind. Applicat.*, Vol. 22, No. 5, pp. 820-827, 1986.
- French, C.; Acarnley, P. (1996), Direct torque control of permanent magnet drives, *IEEE Trans. Ind. Appl.* Vol. 32, No. 5, pp. 1080-1088, Sep./Oct. 1996.
- Vyncke, T.J.; Melkebeek, J. A.; Boel, R. K. (2006), Direct torque control of permanent magnet synchronous motors - an overview, *in conf.Proc. 3rd IEEE Benelux Young Research Symposium in Electrical Power Engineering*, No. 28, Ghent, Belgium, Apr. 27-28, p.5, 2006.
- Vasudevan, M.; Arumugam, R. (2004), New direct torque control scheme of induction motor for electric vehicles, *5th Asian Control Conference*, Vol. 2, 20-23, pp. 1377 - 1383, 2004.

- Mir, S.; Elbuluk, M. E.; Zinger, D. S. (1998), PI and Fuzzy Estimators for Tuning the stator resistance in direct torque control of induction machines, *IEEE Transactions Power Electronics*, Vol. 13, No. 2, pp. 279 – 287, March, 1998.
- Hartani, K.; Miloud, Y.; Miloudi, A. (2010), Improved Direct Torque Control of Permanent Magnet Synchronous Electrical Vehicle Motor with Proportional-Integral Resistance Estimator, *Journal of Electrical Engineering & Technology*, Vol. 5, N°3, pp. 451-461, September 2010, ISSN 1975-0102.

FPGA Based Powertrain Control for Electric Vehicles

Ricardo de Castro, Rui Esteves Araújo and Diamantino Freitas
Faculdade de Engenharia da Universidade do Porto
Portugal

1. Introduction

Current legislation in European countries, as well as in other parts of the world, is putting stricter limits on pollutant emissions from road vehicles. This issue, in conjunction with the increase awareness of consumer for the environmental problems, will require the development of new clean propulsion systems in disruption with the current mobility solutions based on internal combustion engine. Electric, hybrid and fuel-cells vehicles (Chan, 2007) are now recognized as an indispensable mean to meet the challenges associated with sustainable mobility of people and goods. In this paradigm shift, the electric motor (EM) will assume a key role in the propulsion of future vehicles and, unlike vehicles based on internal combustion engines, the high energy and power densities will facilitate the development of new powertrains configurations. In particular, multi-motor configurations, where several EMs are allocated to each driven wheel of the vehicle, represent an attractive configuration for electric vehicles (EVs), due to the independent wheel torque control and the elimination of some mechanical systems, like the differential. These features, allied with the fast dynamics of EMs, are being explored to increase the vehicle maneuverability and safety (Geng et al., 2009) and improve the performance of the EV traction system (Hori, 2004).

To cope with this rise in functional and computational complexity that current (and future) EVs require, in this work we explore the new Field-programmable Gate Array (FPGA) platform to address the powertrain control, i.e. involving the electric motor and the power converters control, of multi-motor EVs.

In the past two decades, motor control applications have been dominated by software based solutions implemented in DSPs (Digital Signal Processors), due to the low cost and ease of programming (Cecati, 1999). However, these DSP solutions are facing increasing difficulties to respond to the ever-increasing computational, functional and timing specifications that modern industrial and vehicular applications require (Monmasson & Cirstea, 2007). For instance, when single-core DSP based solutions needs to incorporate complex and time-critical functions, e.g. multi-motor control, the sequential processing of this approach decrease the controller bandwidth (see Fig. 1), which may compromise the application timing specification. Multi-core DSPs are a possible alternative to address this concern, but they also add costs and interconnection complexity. Consequently, in the last years, FPGAs received an increased interest by the academy and industry as an option to offload time-critical tasks from the DSPs (Lopez et al., 2008; Rahul et al., 2007; Ying-Yu & Hau-Jean, 1997), or even replace the DSPs control platform by a System on Chip (SOC) based on FPGAs (Idkhajine et al., 2009).

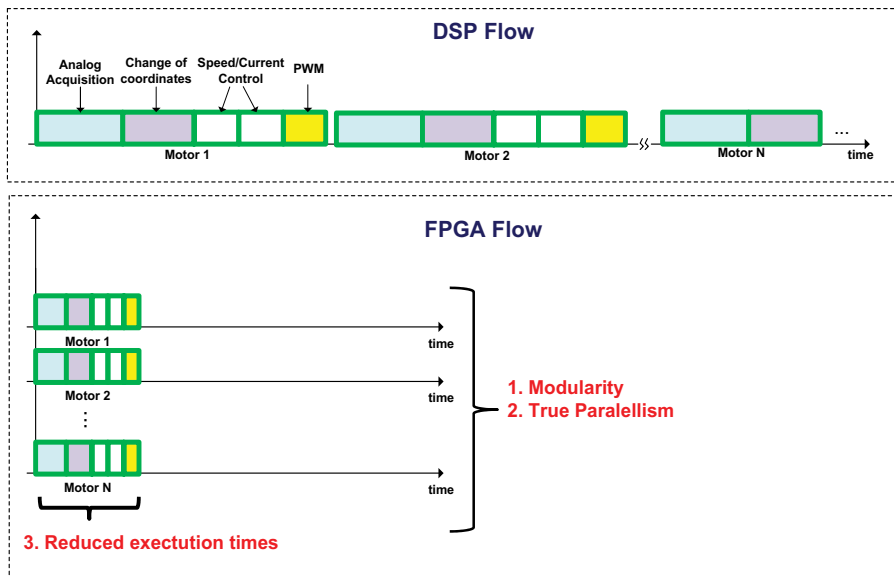


Fig. 1. Some advantages of FPGA use when controlling multiple electric motors.

The main motivation behind the FPGA introduction lies in the following properties: *i*) high processing speed; *ii*) modularity and parallel capabilities (see Fig. 1) and *iii*) hardware reconfigurability. The first feature, high processing speed, enables a reduction in execution times of the motor control algorithm, which can be explored to increase the bandwidth of torque control (Takahashi & Goetz, 2004) and decrease the discretization effects of some control and estimation techniques (Delli Colli et al., 2010; Naouar et al., 2007). Similarly, the FPGA parallelism and modularity features open up new possibilities to incorporate multi-motor control in a single chip, a useful property in multi-axis robotic manipulator arm (Jung Uk et al., 2009) and in process control applications (Tazi et al., 1999), and develop fault tolerant control systems with physical redundancy (Seo et al., 2010). Furthermore, even software based solution implemented in DSPs relies on some special hardware peripherals to boost time critical tasks, e.g. the pulse with modulators (PWM). Although these fixed hardware peripherals can be parameterized to address a wide variety of application, there are some cases where this architecture is unsuitable. The special modulation hardware blocks that multi-level converters demand is a paradigmatic example of the limitations present in the fixed DSP architecture. In this case, the FPGA hardware reconfigurability property is pivotal to effectively solve the multi-level modulation problem by allowing the development of custom PWM blocks in FPGA logic (Lopez et al., 2008). As additional benefits, the FPGAs offers the possibility to migrate, if large production volumes are needed, to ASICs - application specific integrated circuits (Fasang, 2009) - and avoid components obsolescence by emulating in FPGAs the behaviour of discontinued products, such as processors and others digital circuits (Guzman-Miranda et al., 2011).

On the other hand, FPGAs also present some potential difficulties and pitfalls that must be carefully considered before adopting this technology. Firstly, the FPGA unit cost have been the main obstacle to achieve a wider penetration of this technology, but,

owing to the continuous cost reduction in the fabrication processes, this issue is being attenuated (Rodriguez-Andina et al., 2007). In second place, the designing times and the learning curve associated with the FPGA tools can also pose some concerns. The most common approach to design these types of systems is to code directly in hardware description languages, like Verilog or VHDL. This approach has potential to produce very efficient and optimized code, but the developing time, although inferior to ASICs (Winters et al., 2006), is still very high when compared with DSPs. To overcome these difficulties, graphical based design tools, such as Simulink HDL Coder (MathWorks, 2010) or the System Generator (Xilinx, 2005), were included on the top of the FPGA tool-chain, allowing faster developing times and a jump start for designers without previous knowledge on hardware design. Another factor that helps to reduce the developing effort is the integration of processors (hard or soft) within the FPGA. As a result, the designer has an additional degree of freedom to partitioning the system project into two components, namely the software and hardware components. The former runs inside the processor and is responsible for non-time critical tasks, giving easier and faster develop environments (Barat et al., 2002), while the later is implemented in FPGA logic and handles the faster algorithms.

Finally, another traditional limitation in the majority of the FPGAs is the absence of analog peripherals, like analog to digital converters, forcing the inclusion of additional external components on the control board, which may poses undesirable limitations on embedded system with high-level of integration requirements. A notable exception to this trend is the Actel Fusion family (Actel, 2010) that supports mixed-signal processing, and is being used to develop complete SOC solutions for motor drives applications (Idkhajine et al., 2009).

To sum up, the FPGAs cost reductions made in the last years, coupled with the new graphical oriented design tools and the increasingly computational demands in industrial and vehicular electronics, are making these reconfigurable system a competitive alternative to ASICs and DSPs. For that reason, in this work, we explore the FPGAs properties to design and implement an advanced motion control library for EVs, addressing the most relevant control needs in modern powertrains, i.e. (multi) motor control, energy loss minimization and vehicle safety functionalities.

The remaining of the article is structured as follows. Section 2 presents an overview of the library developed to control the powertrain of multi-motor EV's. Next, in Section 3, this powertrain library is used to build a FPGA control system for the uCar EV prototype, including experimental validation. And finally, Section 4 discusses the conclusions and future work.

2. Overview of the powertrain IP core library

Inspired by the vector control signal processing blockset for use with Matlab - Simulink (Araujo & Freitas, 1998), in recent years our team developed a set of Intellectual Properties (IP) cores, targeting the advanced and efficient powertrain control of EV's with multiple motors (Araujo et al., 2009; 2008; de Castro et al., 2010a;b; 2009a;b). This IP core library, whose main components are depicted in Fig. 2, can be divided in 3 main classes. Firstly, a low level class was created containing basic control blocks, like Proportional and Integral controllers, modulators, mathematical transforms, etc., that were efficient and carefully designed to be reused in the control of power electronics applications and other higher level functions. Secondly, a middle layer incorporating motor control and estimation blocks was developed, in order to regulate the electric motor torque and flux, while

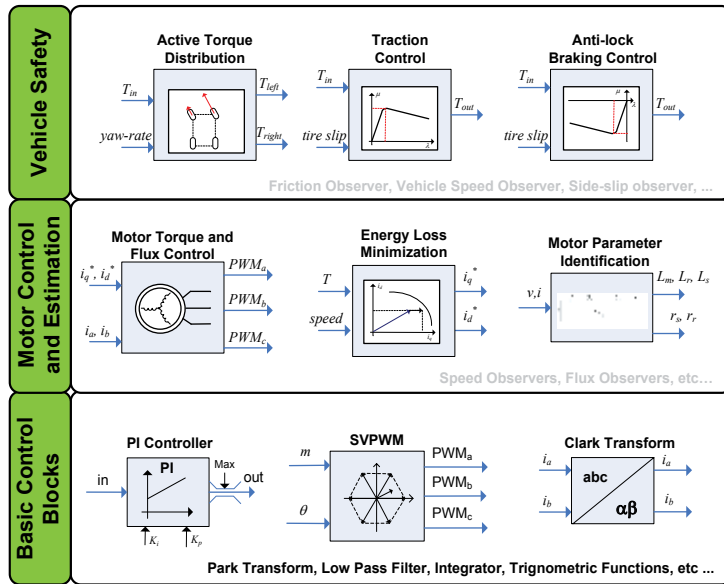


Fig. 2. Powertrain IP Core library for the control of Electric Vehicles.

minimizing the energy losses in the process. On top of that, a control layer related with the vehicle safety functions is also available, which aid the driver avoiding high tire slips during acceleration (traction control) and braking (ABS) manoeuvres and to perform active torque distribution in multi-motor EVs.

One of the main strengths in this library is that the system designer has a great flexibility to specify the controller architecture that best fits the design goals, ranging from basic powertrain controllers (just the motor control) to more advanced solutions with energy minimization and driving aid systems. The FPGA parallel features also allow the multiple instantiation of the same IP core, without degrading the control response time, which is very beneficial for multi-motor EVs where many blocks may need to be replicated in the same control unit (de Castro et al., 2010b). Moreover, the library is implemented in a generic hardware description language (Verilog), so it can be easily ported between different FPGA vendors, introducing more freedom in the hardware selection for the controller implementation.

It is worth pointing out that the IP core blocks represent "out-of-box" solutions to specific powertrain control problems, without requiring extensive development times, so the designer can focus more in the application problems and tuning and less in the technology development. Although not explicitly represented in Fig. 2, there is also available other auxiliary IP cores related with communications (UART, SPI, CAN, etc.), memory controllers, quadrature decoder, soft processors etc., which are normally supplied from the FPGA manufactures and allow the interface with external peripherals. In the remaining of this section, a brief overview of the main functionalities of the powertrain library will be discussed.

2.1 Vehicle safety

Active safety systems are of paramount importance in modern transportation applications and represent an unavoidable functionality to reduce and prevent road accidents (van Zanten, 2002). Therefore, the powertrain control of EVs must address this concern by offering driving aid mechanisms to mitigate the effects of a loss of the vehicle longitudinal and/or

lateral controllability. Such cases may appear due to aggressive driving patterns or, more importantly, by unavoidable external conditions that limit the vehicle operation range and make driving more difficult. For example, when the road present low grip conditions, such as wet tarmac, snow or ice, it is easy for the driver to apply excessive torque to the wheels and generate high tire slips. As a consequence, this excessive slip may produce tire wear, reduce the longitudinal force transmitted to the vehicle and compromise the tire capability to generate lateral forces, i.e. the steerability. In order to improve the longitudinal EV safety our powertrain control library contains IP cores for performing the traction controller (TC) and anti-lock braking functions. These control blocks are based on the sliding mode control framework and, when excessive tire slips are detected, they reduce the wheel torque magnitude to levels where the tire slip is constrained to a safe range, i.e. to a point where the tire longitudinal force is maximized. The main merit of this approach is the implementation simplicity and robustness to the model's parametric variations, such as the grip levels present on the road. These IP cores were experimental verified in our EV prototypes, demonstrating satisfactory competence in preventing excessive tire slip, particularly under low friction conditions. For further details about these control blocks, the interested reader is referred to (de Castro et al., 2010a).

A second important safety function that the powertrain control must address is the torque allocation/distribution strategy for EV's driven by multiple motors. Unlike traditional vehicles, based on internal combustion engine, the high specific power and energy densities offered by the electric motor opens up new possibilities for the powertrain configuration, in particular the distribution of several motors by the EV wheels. With these new configurations, normally composed by 2 or 4 electric motors, the traditional mechanical differentials are eliminated from the powertrain, as well as its energy losses, and the torque transmitted to each driven wheel can be independently controlled. Accordingly, this new degree of control can be explored to perform torque allocation based on the vehicle yaw-rate and side-slip control, which improve the vehicle handling (He et al., 2005) and the lateral safety (Geng et al., 2009). Although important, this block is still under internal development by our team (de Castro, 2010) and we are planning to incorporate it, as soon as possible, in the powertrain library. Nevertheless, while this block is not completely developed we are employing a simple constant torque allocation (de Castro et al., 2009b), whose features will be discussed in a later section.

2.2 Motor control, identification and energy minimization

To address the control of EVs based on induction motors, the well known indirect field oriented method (Araujo, 1991; Novotny & Lipo, 1996) was incorporated in the library, achieving a decoupled control of torque and flux by regulating the motor currents, which are formulated in the synchronous reference frame and will be briefly discussed in the next section. Besides the decoupled control, the current feedback loops, on which the vector control builds, also increases the system robustness against load overloads, peak current protection and compensation of non-linear effects (e.g. semiconductor voltage drop, dead-times, DC-link voltage variations, etc.), making this approach very attractive for EV applications. Furthermore, this module can also be used, with little modifications, to control other types of motors frequently employed in the EV applications, such as permanent magnet and brushless DC motors (Araujo et al., 2009), and be easily replicated inside the control unit to address EVs with multi-motor configurations (de Castro et al., 2010b).

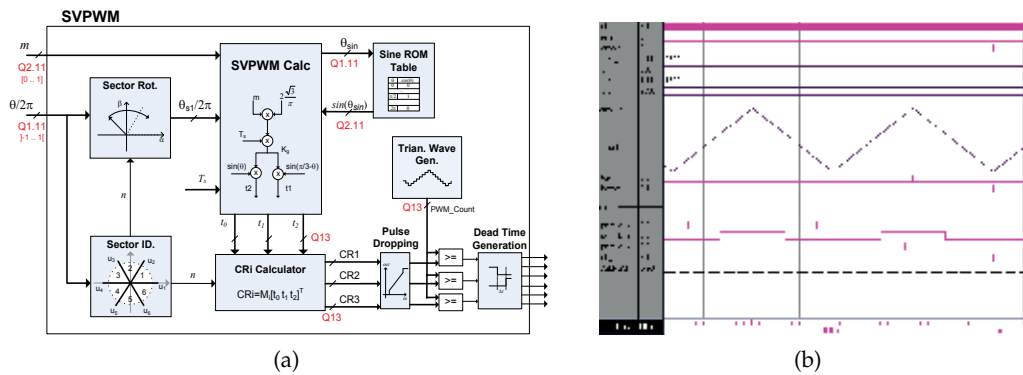


Fig. 3. Space Vector PWM implementation (a) and simulation validation (b).

Another important feature of the powertrain library is the energy loss minimization block of induction motors (IMs). It is a well known fact that IMs, although robust and cheap, are less efficient than other electric motors, like the permanent magnets motors (Zeraouia et al., 2006). To partially attenuate this drawback, our IP core library incorporates a loss minimization algorithm (Araujo et al., 2008) which, based on the IM losses model, finds the flux current setpoint that minimizes the energy losses for each operating point (torque, speed) of the motor. Experimental studies conducted in our prototypes showed that, in urban driving cycles, energy savings between 10% and 20% can be achieved, which contribute to increase the vehicle efficiency and range per charge metric (Araujo et al., 2008). Since the motor control and the energy minimization are model based, the effectiveness of these algorithms relies on good estimates of the motor parameters. To address this limitation, our team developed an additional IP core for performing the identification of the IM model parameters, whose output data is employed to tune the motor controller and the loss minimization algorithm (Cerqueira et al., 2007).

2.3 Basic control blocks

The majority of the control blocks that comprise the low layer depicted in Fig. 2 are intrinsic connected with the operations needed in the motor control algorithms, such as the pulse-width modulators, mathematical transformations and the linear PI controllers. To start with, the analysis and controller design of electric motors, in particular induction and synchronous, is greatly simplified if the equations of the motor model are represented in a rotating coordinate systems. These change of coordinates are normally known as the Park and Clark transformations and lays the mathematical foundations on which the vector control of induction and synchronous motors builds (Novotny & Lipo, 1996). Therefore, these transformations were added to the powertrain library, and, due to the high amount of multiplication operation involved, special attention was taken in the efficient use of the multiplier operator, employing time-sharing methodologies (de Castro et al., 2009a). Along with these change of coordinates, the pulse-width modulators (PWM) represent another fundamental cornerstone to regulate the energy flow in modern power electronics (Kazmierkowski et al., 2002). Since three phase electric motors are the most common type in EVs applications, three-phase voltage source converters are a natural choice to feed the motor. To control these converters we implemented the Space Vector PWM (SVPWM) method which, compared with the carrier-based modulation

techniques, allows a 15% increase in the linear zone of operation and a low current distortion (Kazmierkowski et al., 2002). The SVPWM implementation, depicted in Fig. 3, was designed using polar coordinates, represented in the stationary reference frame (α, β), having as inputs the normalized magnitude (m) and angle (θ) of the desired voltage vector to be applied to the motor. Based on this information, and employing simple trigonometric relations (de Castro et al., 2009b), the SVPWM calculates the duty cycles to be applied to each arm in the inverter. Before generating the final PWM signals, dead-times are inserted in the switching signals, as a mean to prevent upper and lower arm short-circuits, and pulses less than a minimum width (2 times the inverter dead-times) are dropped to ensure the proper operation of the inverter when high modulation indexes are requested.

The modulators and the mathematical transformations described above are usually employed in conjunction with Linear PI controllers, i.e. the motor voltage vector is defined by current PI controllers that operate in a synchronous reference frame. This class of linear controllers are widely used, not only in the motor controller, but also in many control application due to the implementation simplicity and robustness to constant disturbances. For that reason, a discrete version of the PI controller was coded in Verilog and reused in several high-level control blocks. Other functions, like low pass filters to attenuate the noise effects in the feedback loops, the calculation of trigonometric functions and inverse numbers were also included in the library.

And finally, it is worth point out that, even though these low level modules have been implemented in the context of powertrain control, they can also be reused in other industrial and power electronics applications, e.g. with three phase rectifiers and grid interface, a feature to be explored in future works.

3. The uCar case study

After describing the main components of the powertrain library, we will discuss in this section how these modules can be assembled in order to build a complete controller for an bi-motor EV prototype, named uCar. In order to reduce the FPGA resource usage, as well as the costs, we will focus our attention on designing a minimal EV control system, comprising only essential functions to operate the vehicle. As a consequence, the high-value functions associated with the energy minimization and vehicle safety will not be considered in the current controller design.

The architecture of this minimal control system, depicted in Fig. 4, is built around a single FPGA XC3S1000 unit, and has as main features the ability to control two inductions motors, thanks to the double instantiation of the motor control IP core, and a soft processor, the PicoBlaze (Xilinx, 2010), used to manage the global operation of the EV controller. To complement the operation of the motor control IP core and the soft processor, the FPGA unit has a set of peripheral interfaces (UART, SPI, ADC interface, quadrature decoder, etc.), enabling the FPGA to interact with the external entities, like sensors, driving commands and host systems (computer).

The processing flow in the EV controller evolves as follows. In first place, the soft processor acquires the analog commands requested by the driver, such as throttle, brake and also digital signals, like the key and vehicle direction, using for this purpose the I/O and ADC peripherals, which are accessed by the soft processor via a dedicated data bus. Based on this information a state machine (task 2), responsible for defining the EV operating mode (run, stop, fault, etc.), is updated; if the EV is in run mode, then the soft processor executes the

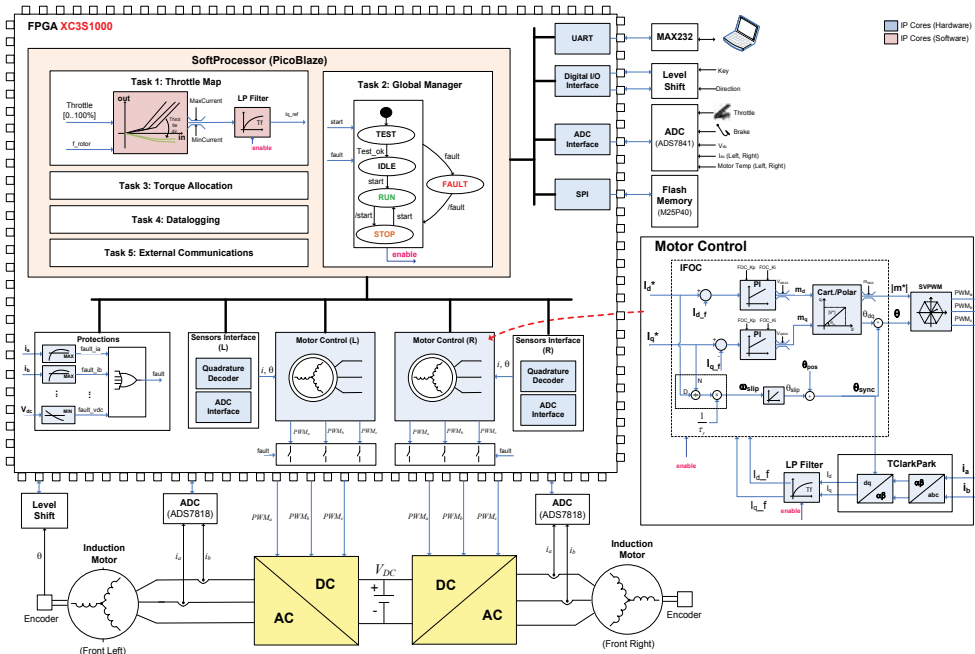


Fig. 4. Diagram of the uCar EV controller.

throttlemap module, where the throttle signal is mapped on a current reference (task 2), and the torque allocation task (3) to define the current (or torque) level that must be imposed to each electric motor in the uCar. After completing task 3, the soft processor sends the current references to the motor control IP cores that command the power converters to achieve the motor torque and flux regulation.

An interesting feature that is worth mention is the hardware/software partitioning on which the EV controller relies. On one hand, the algorithms that needs a fast response times or parallel execution, such as the motor control and the protection module, are directly coded in FPGA logic with boosts the system performance. On the other hand, for implementing slow algorithms and designing control sequences based on state machines, like the EV global state machine or the communication protocols, the soft processor offers a better solution, easier to program and with faster developing times (Xilinx, 2010).

3.1 Soft processor tasks

The soft processor, i.e. a processor implemented in FPGA logic, employed in the current system was the 8-bit PicoBlaze processor, which was selected due to the low resource usage and the free access to the soft processor VHDL source-level code. This processor is used to perform 5 non time-critical tasks (throttlemap, global manager, torque allocation, datalogging and external communications), which are described in this section.

3.1.1 Task 1: ThrottleMap

The ThrottleMap task implements a static function that translates the throttle signal (t_i), defined by the driver, in a current reference (in our case i_q , which is proportional to the motor torque) to be applied to the motor controller. This mapping is normally composed

by a initial dead-zone, to avoid the pedal offset, a liner gain, followed by a saturation to limit the maximum torque, and is described by the following relation:

$$t_1 = \begin{cases} 0, & \text{if } t_i - \underline{t} < 0 \\ t_i - \underline{t}, & \text{if } 0 \leq t_i - \underline{t} \leq 100 \\ 100, & \text{if } t_i - \underline{t} > 100 \end{cases} \quad (1)$$

where $t_i, t_1 \in [0\%, 100\%]$ are the normalized input and output throttle signals and \underline{t} represents the throttle deadzone. A second feature that needs to be addressed by the throttlemap is the "engine braking" emulation: in vehicles based on internal combustion engine, when the driver release the throttle pedal the vehicle experience a deceleration, caused by "engine braking". In EVs this behaviour must be emulated by the control unit, which, in our controller, is performed by the ThrottleMap module and described by:

$$t_2 = \begin{cases} -t_{brk}, & \text{if } t_i - \bar{t} < -t_{brk} \\ t_i - \bar{t}, & \text{if } -t_{brk} \leq t_i - \bar{t} \leq 0 \\ 0, & \text{if } t_i - \bar{t} > 0 \end{cases} \quad (2)$$

where $-t_{brk}$ is the minimum value for the equivalent "engine braking" torque and \bar{t} the throttle point where the braking begins. Putting (1) and (2) together, and considering a scale factor k_{t2i} that translates the throttle signal to current, the final motor current reference (i_q^*) is defined as:

$$i_q^* = (t_1 + t_2 i_{move}(v)) k_{t2i} \quad (3)$$

where $i_{move}(v) \in \{0, 1\}$ is a flag that is activated when the vehicle is moving above a given speed threshold. This flag intents to disable the "engine braking" when the vehicle is close to a complete stop.

Based on several experimental roadtests conducted in our EV prototypes, it was verified that the throttlemap module is a fundamental tool to improve the driving experience, and, in particular, the "engine braking" contributes to a more pleasant and predictable driving.

3.1.2 Task 2: Global state machine

To keep track of the EV operating mode, the soft processor also runs a simple state machine (task 2), whose simplified behaviour is shown in Fig. 4. When the controller is first initiated, the state machine goes to the TEST state, where a series of validation tests (check current and voltage sensors, throttle signal, etc) are performed; if these checks do not shown any anomaly, then the state machine jumps to the IDLE state, where it waits for the start signal generated by the driver. After performing this initialization phase, the EV switches between the RUN and STOP mode, depending on the start signal defined by the driver, and if an EV protection becomes active, the FAULT mode is enabled. Since the switching between the state machine depends on external digital signals, which are subject to be bouncing and other fast transient disturbances, a preprocessing was also included in the task 2 in order to filter these signals.

3.1.3 Task 3: Constant torque allocation

While the active torque allocation method discussed in Section 2.1 is not implemented, a uniform torque distribution strategy has been used, with both motor controllers receiving the same torque reference ($i_{q,left}^* = i_{q,right}^* = i_q^*$), defined by the throttle position and throttlemap.

This strategy emulates the basic features of a single axis mechanical open differential, widely used in conventional vehicles. Typically, the open differential has 2 objectives: *i*) transfer the motor power to the driven wheels, applying the same torque to both wheels; *ii*) allow the driven wheels to rotate at different speeds (critical feature during the vehicle cornering). In the case of multi-motor EV, the first feature can be easily emulated by applying the same current/torque reference to both motor controllers, and assuming that both motors have similar characteristics. The second problem addressed by the mechanical differential, related with different wheel speeds, is not an issue in a multi-motor EV configuration. Note that in a multi-motor configuration each motor is free to rotate at any speed, and can be seen as an independent system: all motors receive equal value of acceleration/braking torque, but the load torque experience by each motor is different, especially during cornering manoeuvres, which naturally leads to different wheel speeds. These observations are corroborated by the experimental results obtained in the multi-motor uCar prototype (de Castro et al., 2009b) and allow us to employ a simple and low cost torque allocation to operate the EV.

3.1.4 Task 4 and 5: Datalogging and external communications

The soft processor also run a datalogger task (4) that stores, in an external 4 Mbit flash memory (M25P40) accessed by an SPI interface, the evolution of several EV variables, helpful for debug purposes and characterization of the vehicle behaviour. Finally, a communication task (5) is responsible for implementing a simple communication protocol (Oliveira et al., 2006), on top of a RS232 link, to enable the interaction between the FPGA controller and a host system, e.g. a computer.

3.2 Motor Controller (MC)

In order to address the motor controller needs, which are the most time-critical and computational intensive in the EV controller, we employed some of the IP cores from the powertrain library described in Section 2. As a result, the SVPWM, PIs and the mathematical transformations were assembled together to build the indirect field oriented control of induction motors, represented in the right part of Fig. 4, offloading much of the processing demands from the soft processor to the FPGA logic. Due to the parallel features of the FPGA, the second motor in the uCar prototype can be straightforwardly handled by instantiating a second motor control (MC) module, which does not degrade the bandwidth and response time of modules already in place. In addition, each MC has a dedicated module to acquire the feedback information from the motor position, though an incremental encoder, and motor currents, as well as a protection module to detect and process faults produced by overcurrents, over and under-battery voltage and thermal overloads.

3.3 Latency and resource analysis

Figure 5 shows the latency cycles introduced by the most time-critical IP core in the EV controller: the MC sub-modules. Before beginning the mathematical calculations, the MC must acquire the motor currents. Due to the absence of an internal ADC in the FPGA, the currents measurements is done through ADCs (TI ADS7818) external to the FPGA and its value transmitted by a high-speed serial protocol. This acquisition process takes 250 latency cycles and represents the largest delay in the MC (73% of the total time). The MC computational blocks (Clark and Park transformation, PIs and SVPWM), introduces a latency of just 90 cycles. In total, the MC control cycles is performed in less than 340 cycles (6.8 μ s),

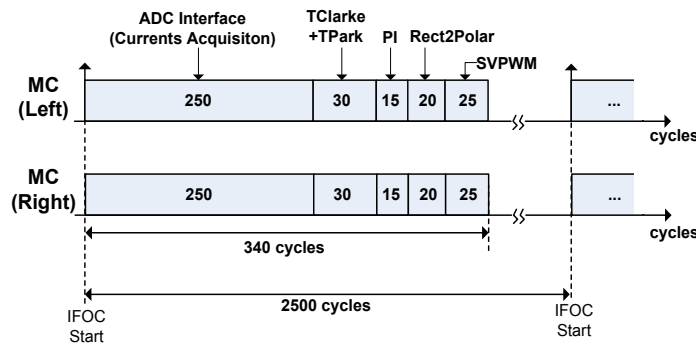


Fig. 5. Latency introduced by the MC sub-modules (the main clock in the FPGA has a frequency of 50MHz, thus 2500cycles \Leftrightarrow 50us)

Type	Module	Slices	Mul.	BRAM.	FMax(MHz)
Motor Control	SVPWM	316	1	1	86
	TClarke+TPark	212	2	1	78
	2xPI's + Cart2Polar	1012	6	1	92
	Field Weakening	59	2	1	125
Sensor Interface	ADC Interface (ADS7818)	47			190
	Quadrature Decoder	37			134
Protections	Protections	75			183
Soft Processor	PicoBlaze + SPI + UART + ...	501		3	85

Table 1. Resource utilization of the main IP cores (Note: the design tool was the ISE WebPack 8.2.03i, FPGA family: Spartan 3, Speed Grade: -5).

Module	Num. Instances	Slices	Mul.
Motor Control(MC)	2	3198	22
Sensor Interface	2	168	
Protections	1	75	
Soft Processor	1	501	
Others	1	789	
Total		4731 (61%)	22 (92%)

Table 2. Resource utilization of the XC3S1000 FPGA used to control the uCar prototype (Note: the design tool was the ISE WebPack 8.2.03i, FPGA family: Spartan 3, Speed Grade: -5).

representing 14% of the 2500 cycles associated with the MC minimum execution rate (20kHz). This minimum rate is the result of the energy dissipation limits in the power semiconductors, which, in hard-switching, high current traction applications, is normally constrained to a maximum of 20kHz switching frequency. Albeit the MC modules have been specifically developed for electric traction applications, with the 20 kHz update rate limit, the low value of latency permits a higher execution rate, up to 147 kHz. This feature enables the MC modules to be reused in other industrial applications, where a high-bandwidth control of torque and

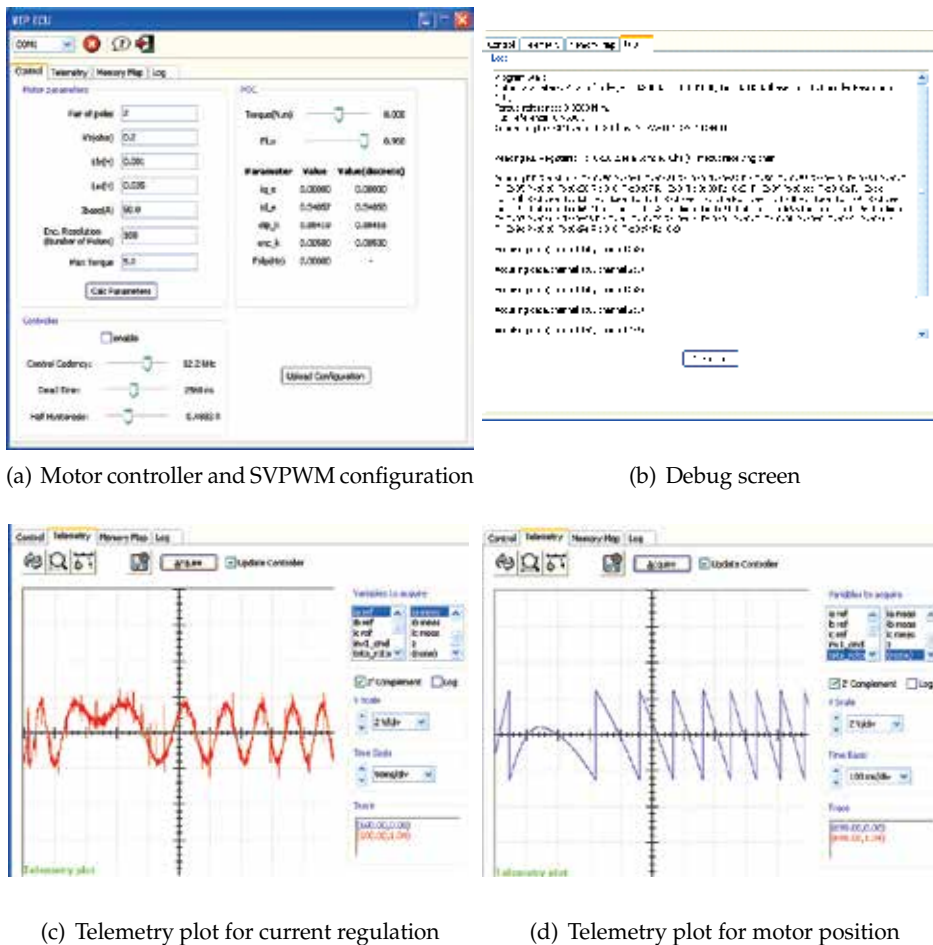


Fig. 6. User interfaces of the software developed to configure and debug the EV controller.

speed is necessary. Figure 5 also shows the parallel processing capabilities of FPGA, which allows multiple instantiations of the MC to run simultaneously, independently and without compromising the bandwidth of other modules.

A summary of the resource utilization in the IP cores implementation, such as slices, dedicated multipliers and Block Ram (BRAM), is presented in Tables 1 and 2. The two Motor Controllers instantiated in control unit are the most demanding on the FPGA resources, requiring 44% of the slices and 92% of the dedicated multipliers available on the chip. Although there are a considerable number of slices available (39%), the low number of free multipliers prevents the inclusion of additional MC, presenting a restriction for future improvements in this FPGA; in other words, such improvements would need an FPGA with more computational resources, thus more costly. In addition to the MC, there are also others modules to perform auxiliary functions (sensor interface, protections, soft processor), described in the previous section, and which consume 17% of the FPGA area.

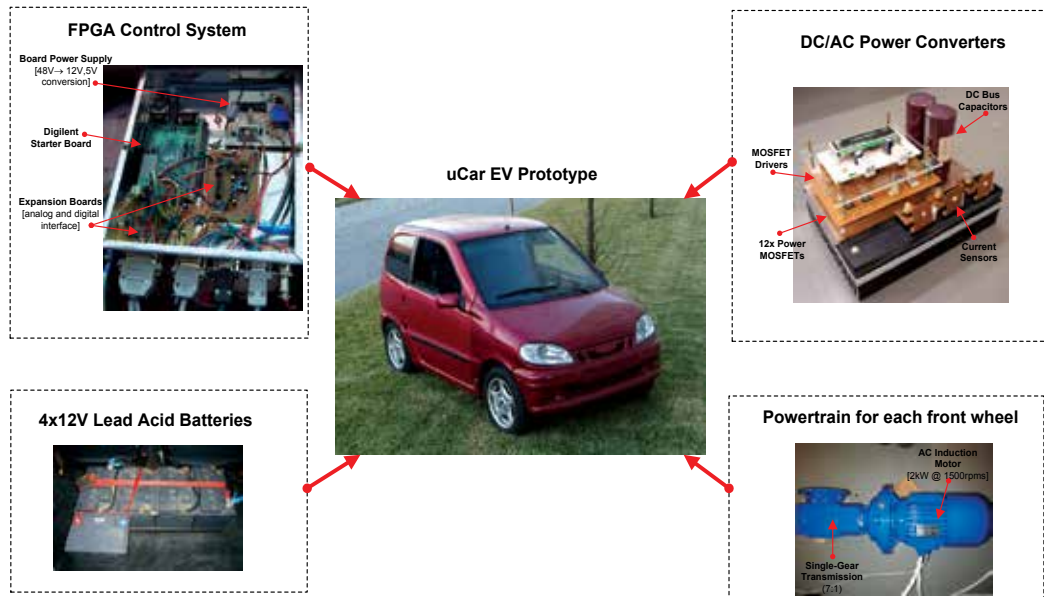


Fig. 7. uCar electric vehicle prototype.

3.4 Configuration software

During the EV development, it is necessary to exchange configuration and debugging data with the FPGA control unit. To this aim, we built a graphical application based on the cross-platform wxWidgets library, whose main user interfaces are depicted in Fig. 6. This application, running on a convention computer, establishes a communication channel with the tasks 4 and 5, briefly described in Section 3.1.4. Based on this interface, the EV designer has the possibility to change the EV control parameters associated with the motor controller (current and flux limits, pair of poles, etc.), peripherals (encoder pulses), modulation (switching frequency, dead-times, etc.), among other modules. For debugging the controller we also have a datalogger interface (Fig. 6(c)), which enables the real-time acquisition of the EV controller variables, like the motor currents, voltages and mechanical position, providing an effective mechanism to inspect the performance of the control loops during fast transients and aid the controller tuning process.

3.5 Experimental results

In order to evaluate the control system discussed in the previous sections, an EV prototype, named uCar, was built to accommodate the electric powertrain (see Fig. 7). The vehicle is based on a two-seater quadricycle, manufactured by the MicroCar company, and is very popular among elderly people of southern Europe, mainly due to non-compulsory driving license. The original propulsion structure, based on the internal combustion engine, was replaced by a new electric powertrain composed by two electric motors (26 Vrms, 2.2 kW @ 1410 rpm), each one coupled to the front wheels by single gear (7 : 1) transmissions. Due to low cost, lead acid batteries (4x12V@110Ah) were selected as the main energy storage of the EV, providing a range of 40 km per charge, a sufficient autonomy for urban driving. After the conversion, the uCar prototype weights 590 kg and reaches a top speed of 45 km/h.

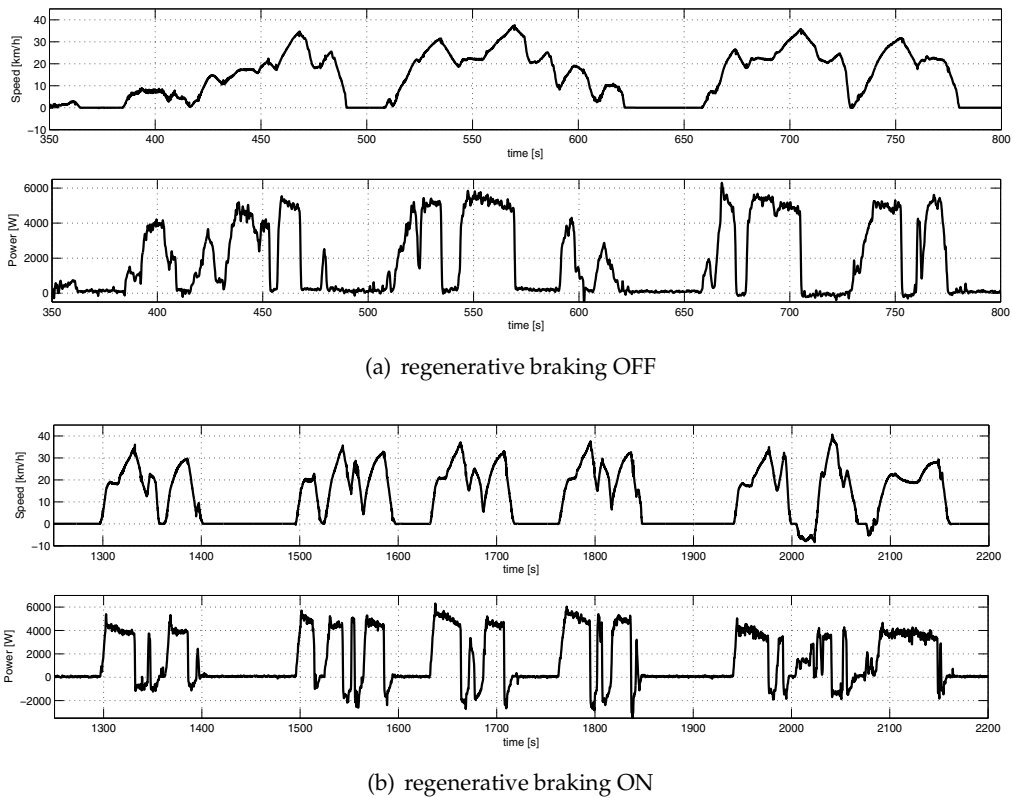


Fig. 8. Experimental results of a typical driving cycle performed by the uCar inside the university campus, with and without regenerative braking active.

All the powertrain control functions of the EV are concentrated on the Digilent Spartan 3 Start Board, containing, besides the XC3S1000 FPGA, several useful peripherals such as flash memory (2 Mbit) for storing data, serial interface for communications and 4 expansion ports for I/O with the FPGA. To extend the functionalities of these main peripherals, two additional boards were constructed and connected to the main board, containing analog to digital converters (TIADS7818 and TIADS7848) to allow the acquisition of analog variables, and voltage level shifters (3.3 \leftrightarrow 5.0V) to perform the interface with the external digital I/O. This EV controller interacts with two DC/AC power converters, featuring 120Arms@30Vrms and 20kHz switching frequency, in order to regulate the current and voltage delivered to the electric motors, as discussed in the previous sections.

To validate the experimental performance of the uCar, several roadtests were conducted inside the FEUP university campus, characterized by low speed driving cycles, similar to urban conditions (see Fig. 8). From these roadtests, we selected two representative cycles for assess the influence of the regenerative braking in the energy consumption of the uCar. In the first situation, with the regenerative braking disabled, the vehicle travels approximately 2.36 km and shows consumption metrics close to 100 Wh/km (see Table 3). On the other hand, when the reg. braking is active the EV consumption decreases 13.2%, to 86.8 Wh/km, representing an important contribute to increase the EV range per charge.

Mode	Distance	Energy Delivered	Energy Regenerated	Consump.	Max. Power	Min. Power
Reg. OFF	2.37km	236.7 W.h	0W.h	99.9 Wh/km	6.3 kW	0 kW
Reg. ON	4.26km	417.6 W.h	48.3W.h	86.8 Wh/km	6.3 kW	-3.5 kW

Table 3. Performance metrics of the uCar over the driving cycles described in Fig. 8.

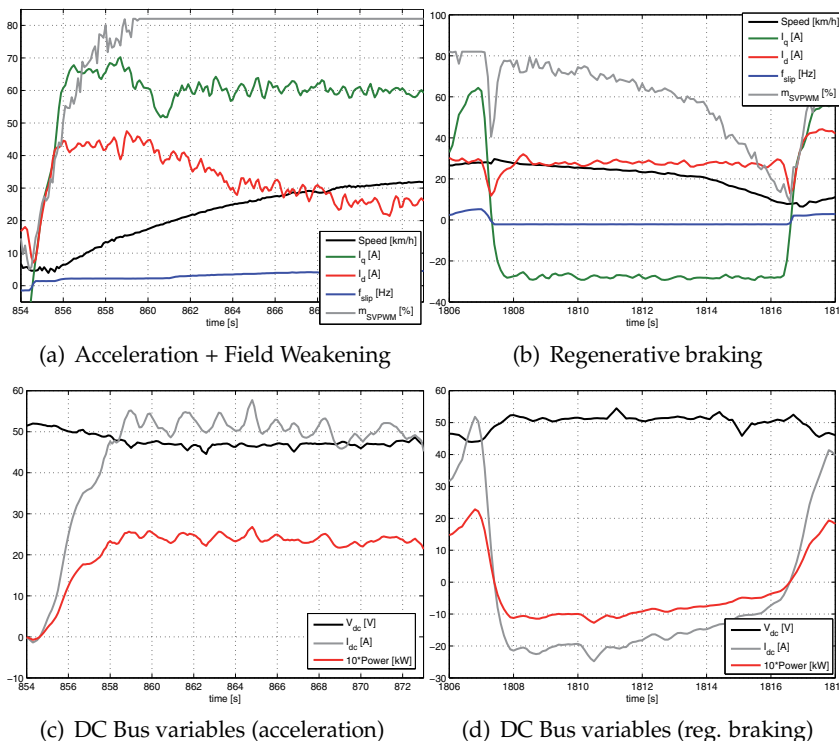


Fig. 9. Detailed view of the uCar (left motor) results during accelerating, field weakening and regenerative braking.

To further validate the EV control unit performance, Fig. 9 show the detailed results of the left motor controller for three different operating modes: acceleration, field weakening and regenerative braking. The data depicted in these figures was acquired with the controller internal datalogger, which enable us to keep track of the most relevant EV variables, such as: mechanical (motor speed), energy source (voltage, current and power) and the motor controller (torque (i_q) and flux (i_d) currents, modulation index (m) and the slip frequency (f_{slip})) variables. During the acceleration mode (Fig.9(a), 9(c)), performed with the throttle at 100%, the i_q and i_d currents are set at the maximum value in order to extract the maximum motor torque and vehicle acceleration (2.2km/h/s). When the EV reaches 18km/h the motor voltage saturates at 83% and the flux current is reduced to allow the vehicle to operate in the field weakening area, with a power consumption of 2.5kW per motor. In fact, analyzing the evolution of the power supplied by the batteries during the experimental driving cycles (Fig. 8), it is interesting to note that the electric motors spend most of the time operating in this field weakening zone. Fig. 9(b) and 9(d) shows the detailed results of third EV operation

mode: the regenerative braking. In the depicted manoeuvre, the driver is requesting a torque current of -25A to decelerate the vehicle from 30 km/h to 5 km/h in 10s, which enable a conversion of 1kW peak power and emphasizing one of the most promising features in EVs: energy recovering during braking.

4. Conclusion

In this article an FPGA based solution for the advance control of multi-motor EVs was proposed. The design was build around a powertrain IP Core library containing the most relevant functions for the EV operation: motor torque and flux regulation, energy loss minimization and vehicle safety. Due to the parallel, modularity and reconfigurability features of FPGAs, this library can be reused in the development of several control architectures that best suits the EV powertrain configuration (single or multi-motor) and functional requirements. As proof of concept, the powertrain library was employed in the design of minimal control system for a bi-motor EV prototype and implemented in a low cost Xilinx Spartan 3 FPGA. Experimental verification of the control unit was provided, showing reasonable consumption metrics and illustrating the energy benefits from regenerative braking.

In future works, we are planning the inclusion, in the powertrain library, of active torque methods in order to improve the handling and safety of multi-motor EVs. On the technological level, we also intent to validate the library on EV prototypes with 4 in-wheel motors.

5. References

- Actel (2010). Fusion Family of Mixed Signal FPGAs datasheet.
- Araujo, R. E. (1991). *Control System of Three-phase Induction Motor based on the Principle of Field Orientation*, Master thesis, Faculdade de Engenharia da Universidade do Porto.
- Araujo, R. E. & Freitas, D. S. (1998). The Development of Vector Control Signal Processing Blockset for Simulink: Philosophy and Implementation, *Proceedings of the 24th Annual Conference of the IEEE Industrial Electronics Society*.
- Araujo, R. E., Oliveira, H. S., Soares, J. R., Cerqueira, N. M. & de Castro, R. (2009). Diferencial Electronico. Patent PT103817.
- Araujo, R. E., Ribeiro, G., de Castro, R. P. & Oliveira, H. S. (2008). Experimental evaluation of a loss-minimization control of induction motors used in EV, *34th Annual Conference of IEEE Industrial Electronics*, Orlando, FL, pp. 1194–1199.
- Barat, F., Lauwereins, R. & Deconinck, G. (2002). Reconfigurable instruction set processors from a hardware/software perspective, *IEEE Transactions on Software Engineering* 28(9): 847–862.
- Cecati, C. (1999). Microprocessors for power electronics and electrical drives applications, *IEEE Industrial Electronics Society Newsletter* 46(3): 5–9.
- Cerqueira, N. M., Soares, J. R., de Castro, R. P., Oliveira, H. S. & Araujo, R. E. (2007). Experimental evaluation on parameter identification of induction motor using continuous-time approaches, *International Conference on Power Engineering, Energy and Electrical Drives*, Setubal, Portugal.
- Chan, C. C. (2007). The State of the Art of Electric, Hybrid, and Fuel Cell Vehicles, *Proceedings of the IEEE* 95(4): 704–718.

- de Castro, R. (2010). Main Solutions to the Control Allocation Problem, *Technical report*, Universidade do Porto.
- de Castro, R., Araujo, R. E. & Freitas, D. (2010a). A Single Motion Chip for Multi-Motor EV Control, *10th International Symposium on Advanced Vehicle Control (AVEC)*, Loughborough, UK.
- de Castro, R., Araujo, R. E. & Freitas, D. (2010b). Reusable IP Cores Library for EV Propulsion Systems., *IEEE International Symposium on Industrial Electronics*, Bari, Italy.
- de Castro, R., Araujo, R. E. & Oliveira, H. (2009a). Control in Multi-Motor Electric Vehicle with a FPGA platform, *IEEE International Symposium on Industrial Embedded Systems*, Lausanne, Switzerland, pp. 219–227.
- de Castro, R., Araujo, R. E. & Oliveira, H. (2009b). Design, Development and Characterisation of a FPGA Platform for Multi-Motor Electric Vehicle Control, *The 5th IEEE Vehicle Power and Propulsion Conference*, Dearborn, USA.
- Delli Colli, V., Di Stefano, R. & Marignetti, F. (2010). A System-on-Chip Sensorless Control for a Permanent-Magnet Synchronous Motor, *IEEE Transactions on Industrial Electronics* 57(11): 3822–3829.
- Fasang, P. P. (2009). Prototyping for Industrial Applications, *IEEE Industrial Electronics Magazine* 3(1): 4–7.
- Geng, C., Mostefai, L., Denai, M. & Hori, Y. (2009). Direct Yaw-Moment Control of an In-Wheel-Motored Electric Vehicle Based on Body Slip Angle Fuzzy Observer, *IEEE Transactions on Industrial Electronics* 56(5): 1411–1419.
- Guzman-Miranda, H., Sterpone, L., Violante, M., Aguirre, M. & Gutierrez-Rizo, M. (2011). Coping With the Obsolescence of Safety - or Mission-Critical Embedded Systems Using FPGAS, *IEEE Transactions on Industrial Electronics* 58(3): 814 – 821.
- He, P., Hori, Y., Kamachi, M., Walters, K. & Yoshida, H. (2005). Future motion control to be realized by in-wheel motored electric vehicle, *31st Annual Conference of IEEE Industrial Electronics Society*.
- Hori, Y. (2004). Future vehicle driven by electricity and control - Research on four-wheel-motored UOT Electric March II, *IEEE Transactions on Industrial Electronics* 51(5): 954–962.
- Idkhajine, L., Monmasson, E., Naouar, M. W., Prata, A. & Bouallaga, K. (2009). Fully Integrated FPGA-Based Controller for Synchronous Motor Drive, *IEEE Transactions on Industrial Electronics* 56(10): 4006–4017.
- Jung Uk, C., Quy Ngoc, L. & Jae Wook, J. (2009). An FPGA-Based Multiple-Axis Motion Control Chip, *IEEE Transactions on Industrial Electronics* 56(3): 856–870.
- Kazmierkowski, M., Krishnan, R. & Blaabjerg, F. (2002). *Control in Power Electronics: Selected Problems*, Academic Press.
- Lopez, O., Alvarez, J., Doval-Gandoy, J., Freijedo, F. D., Nogueiras, A., Lago, A. & Penalver, C. M. (2008). Comparison of the FPGA Implementation of Two Multilevel Space Vector PWM Algorithms, *IEEE Transactions on Industrial Electronics* 55(4): 1537–1547.
- MathWorks (2010). Simulink HDL Coder 2.0 User Guide.
- Monmasson, E. & Cirstea, M. N. (2007). FPGA Design Methodology for Industrial Control Systems-A Review, *IEEE Transactions on Industrial Electronics* 54(4): 1824–1842.
- Naouar, M. W., Monmasson, E., Naassani, A. A., Slama-Belkhdja, I. & Patin, N. (2007). FPGA-Based Current Controllers for AC Machine Drives-A Review, *IEEE Transactions on Industrial Electronics* 54(4): 1907–1925.
- Novotny, D. & Lipo, T. (1996). *Vector control and dynamics of AC drives*, Oxford University Press.

- Oliveira, H. S., Soares, J. R., Cerqueira, N. M. & de Castro, R. (2006). *Veiculo Electrico de Proximidade com Diferencial Electronico*, Licenciatura thesis, Universidade do Porto.
- Rahul, D., Pramod, A. & Vasantha, M. K. (2007). Programmable Logic Devices for Motion Control-A Review, *IEEE Transactions on Industrial Electronics* 54(1): 559–566.
- Rodriguez-Andina, J. J., Moure, M. J. & Valdes, M. D. (2007). Features, Design Tools, and Application Domains of FPGAs, *IEEE Transactions on Industrial Electronics* 54(4): 1810–1823.
- Seo, K., Yoon, J., Kim, J., Chung, T., Yi, K. & Chang, N. (2010). Coordinated implementation and processing of a unified chassis control algorithm with multi-central processing unit, *Proceedings of the Institution of Mechanical Engineers, Part D: Journal of Automobile Engineering* 224(5): 565–586.
- Takahashi, T. & Goetz, J. (2004). Implementation of complete AC servo control in a low cost FPGA and subsequent ASSP conversion, *Nineteenth Annual IEEE Applied Power Electronics Conference and Exposition*.
- Tazi, K., Monmasson, E. & Louis, J. P. (1999). Description of an entirely reconfigurable architecture dedicated to the current vector control of a set of AC machines, *The 25th Annual Conference of the IEEE Industrial Electronics Society*.
- van Zanten, A. T. (2002). Evolution of electronic control systems for improving the vehicle dynamic behavior, *Proceedings of the International Symposium on Advanced Vehicle Control (AVEC)*, Hiroshima, Japan, pp. 7–15.
- Winters, F., Nicholson, R., Young, B., Gabrick, M. & Patton, J. (2006). FPGA Considerations for Automotive Applications, *SAE 2006 World Congress and Exhibition*, Detroit, MI.
- Xilinx (2005). System Generator User Guide.
- Xilinx (2010). PicoBlaze 8-bit Embedded Microcontroller User Guide.
- Ying-Yu, T. & Hau-Jean, H. (1997). FPGA realization of space-vector PWM control IC for three-phase PWM inverters, *Power Electronics, IEEE Transactions on* 12(6): 953–963.
- Zeraouia, M., Benbouzid, M. E. H. & Diallo, D. (2006). Electric Motor Drive Selection Issues for HEV Propulsion Systems: A Comparative Study, *IEEE Transactions on Vehicular Technology* 55(6): 1756–1764.

Global Design and Optimization of a Permanent Magnet Synchronous Machine Used for Light Electric Vehicle

Daniel Fodorean

*Technical University of Cluj-Napoca, Electrical Engineering Department
Romania*

1. Introduction

One of the most common problems of modern society, these days, particularly for industrialized countries, is the pollution (Fuhs, 2009; Ehsani et al., 2005; Vogel, 2009; Ceraolo et al., 2006; Chenh-Hu & Ming-Yang, 2007; Naidu et al., 2005). According to several studies, the largest share of pollution from urban areas comes from vehicle emissions and because of this explosive growth of the number of cars. The pollution effect is more and more obvious, especially in large cities. Consequently, finding a solution to reduce (or eliminate) the pollution is a vital need. If in public transports (trains, buses and trams) were found non-polluted solutions (electrical ones), for the individual transport the present solutions can not yet meet the current need in autonomy. Even though historically the electric vehicle precedes the thermal engine, the power/fuel-consumption ratio and the reduced time to refill the tank has made the car powered by diesel or gasoline the ideal candidate for private transport. Although lately there were some rumors regarding the depletion of fossil resources, according to recent studies, America's oil availability is assured for the next 500 years (Fuhs, 2009; Ehsani et al., 2005). So, the need of breathing clean air remains the main argument for using electric vehicles (EV). However, all over the world, one of the current research topics concerns the use of renewable energy sources and EVs.

With regard to automobiles, there have been made several attempts to establish a maximum acceptable level of pollution. Thus, several car manufacturers have prepared a declaration of Partnership for a New Generation of Vehicles (PNGV), also called *SUPERCAR*. This concept provides, for a certain power, the expected performance of a thermal or hybrid car. Virtually, every car manufacturer proposes its own version of electric or hybrid car, at *SUPERCAR* standard, see Table 1 (Fuhs, 2009).

Of course, at concept level, the investment is not a criterion for the construction of EVs, as in the case of series manufacturing (where profits are severely quantified). For example, nowadays the price of 1 kW of power provided by fuel cell (FC) is around 4,500 €; thus, a FC of 100 kW would cost 450,000 € (those costs are practically prohibitive, for series manufacturing). By consulting Table 1, it can be noticed the interest of all car manufacturers to get a reduced pollution, with highest autonomy. Nowadays, the hybrid vehicles can be seen on streets. Although the cost of a hybrid car is not much higher than for the classical engine (about 15-25% higher), however, the first one requires supplementary maintenance costs which cannot be quantified in this moment.

Concept Cars	Technical Data	Performances
AUDI metroproject quattro	turbocharged four-cylinder engine and an electric machine of 30 kW; lithium-ion battery	maximum range on electric-only of 100 km; 0-100 km/h in 7.8 s; maximum speed 200 km/h
BMW x5 hybrid SUV	for 1000 rpm, there is a V-8 engine providing 1000 Nm; the electric motor gives 660 Nm	fuel economy is improved by an estimated 20%.
CHRYSLER eco voyager FCV	propulsion of 200 kW; hydrogen is feed to a PEM fuel cell (FC)	range of 482 km and a 0-60 km/h in less than 8 s.
CITROËN c-cactus hybrid	diesel engine provides 52 kW and the electric motor gives 22 kW	fuel consumption is 2.0 L/100 km; maximum speed is 150 km/h
FORD hySeries EDGE	Li-ion battery has maximum power of 130 kW, and the FC provides 35 kW	range of 363 km (limited by the amount of hydrogen for the FC)
HONDA FCX	electric vehicle with 80 kW propulsion engine, combining ultracapacitors (UC) and PEM FC	55% for overall efficiency, driving range of 430 km
HYUNDAI I-blue FCV	FC stack produces 100 kW; there is a 100 kW electric machine (front wheels) and 20 kW motor for each rear wheel	estimated range is 600 km
JEEP renegade diesel-electric	1.5 L diesel engine provides 86 kW and is teamed with 4 electric motors (4WD) of 85 kW combined power	the diesel provides range extension up to 645 km beyond the 64 km electric-only range (diesel fuel tank holds 38 L)
KIA FCV	a 100 kW FC supplants a 100 kW front wheel electric motor, while the motor driving the rear wheels is 20 kW	range is stated to be 610 km
MERCEDES BENZ s-class direct hybrid	3.5 L (V-6) gasoline engine with motor/generator combined power of 225 kW and combined torque of 388 Nm	acceleration time from 0-100 km/h in 7.5 s
MITSUBISHI pure EV	Li-ion battery and wheel-in-motors of 20 kW	150 kg Li-ion battery give a range of 150 km (2010 prospective range of 250 km)
OPEL flextreame	a series hybrid configuration (with diesel engine) with Li-ion battery; the electric motor has peak power of 120 kW	fuel consumption of 1.5 L/100 km; electric only mode has range of 55 km
PEUGEOT 307 hybrid	it is diesel/electric hybrid automobile	the estimated fuel economy is 82 mpg; this is a hybrid that matches the PNGV goals
SUBARU G4E	five passengers EV, using Li-ion batteries	driving range is 200 km; the battery can be fully charged at home in 8 h (an 80% charge is possible in 15 min)
TOYOTA 1/X plug-in hybrid	thermal engine 0.5 L, with a huge reduction of mass to 420 kg (use of carbon fiber composites, although expensive)	low mass also means low engine power and fuel consumption
VOLKSWAGEN Blue FC	a 12 kW FC mounted in the front charges 12 Li-ion batteries at the rear; The 40 kW motor is located at the rear	the electric-only range is 108 km; top speed is 125 km/h, and the acceleration time from 0-100 km/h is 13.7 s
VOLVO recharge	series hybrid with lithium polymer batteries; the engine is of 4-cylinder type with 1.6 L; it has 4 electric wheels motors (AWD)	electric-only range is 100 km; for a 150 km trip, the fuel economy is 1.4 L/100 km

Table 1. Several types of hybrid vehicle concepts.

Some predictions on the EV's were considered by (Fuhs, 2009). In the nearest future the thermal automobiles number will decrease, while the hybrid ones are taking their place. By 2037 the fully electric vehicle (called *kit car*) will replace the engine and then, after a fuzzy period all vehicles will be powered based on clean energy sources, when a new philosophy of building and using the cars will be put in place.

So, one of the challenges of individual transport refers to finding clean solutions, with enhanced autonomy (Ceraolo et al., 2006; Chenh-Hu & Ming-Yang, 2007; Naidu et al., 2005).

This is the motivation of this research work. For that, an electric scooter will be studied from the motorization, supplying and control point of view. The global steps of the design process will be presented here. Firstly, the considered load and expected mechanical performances will be introduced. The electromagnetic design of the electrical motor, capable to fulfill the mechanical performances, will be presented too. The obtained analytical performances should be validated; for that, the finite element method will be used. Also, the machine optimization will fulfill the global designing process of the electrical machine.

2. Design of studied electrical machine

The research study presented here concerns the design of a three phase permanent magnet synchronous machine (PMSM) used for the propulsion of an electric scooter. It is widely recognized that the common solution, the dc motor, has usually poor performances against ac motor. However, for low small power electrical machines, this advantage is not always obvious. Also, a special attention should be paid for the efficiency and power factor of ac machines. This will be analyzed here. The validation of the obtained results will be made based on finite element method (FEM) analysis. The goal is to increase the autonomy of the light electric vehicle, based on a PMSM, with a proper control, and after the optimization of the designed machine.

The analytical approach, employed here, can be used for any type of electric vehicle. First of all, for a given maximum load, it will be established the necessary power needed for the propulsion of the vehicle. Secondly, the main steps in the design process of the studied machine will be given. Next, the energetic performances and electro-mechanical characteristics will be presented. The validation of the analytical obtained results is made based on finite element method (FEM). By means of numerical computation, it will be demonstrated that a unity power factor control is possible when using ac machines, by employing a field oriented control strategy. The optimization of the studied machine will be realized based on gradient type algorithm and the obtained results will show the benefits of using a PMSM for the propulsion of the light electric vehicle.

2.1 The needed mechanical performances

The maximum speed and weight of the vehicle are 12 km/h and 158 kg, respectively. The considered vehicle has 4 tires of 11 inches in diameter. The vehicle dimensions are: 1290 mm in length, 580 mm in width and 1150 mm in height. The vehicle will be supplied from a battery of 24 Vcc.

First of all, it is needed to compute the output power of the electric motor which is capable to run the vehicle. Since the mechanical power is the product between the mechanical torque and angular speed, it is possible to establish the speed of the vehicle at the wheel:

$$n_t = v \cdot 60 / (\pi \cdot D_t) \quad (1)$$

where n_t is the velocity measured at the vehicle's wheels (measured in min⁻¹), v is the vehicle speed (in m/s), D_t is the outer diameter of the wheel (the tire height included, in m). The resulted velocity is $n_t=244.4 \text{ min}^{-1}$. From mechanical and controllability considerations, it is desirable to have an electric motor operating at higher speed, so it is considered a gear ratio of 6.1 to 1. Thus the electric motor rated speed is imposed at 1500 min⁻¹.

Next, the rated torque has to be established. Since the motor torque is proportional to the wheel radius and the force acting on it, one should determine the force involved by the

vehicle's weight and rolling conditions. The electric motor has to be capable to produce a mechanical force to balance all other forces which interfere in vehicle's rolling. Thus, the motor force is:

$$F_m = F_{acc} + F_h + F_d + F_w + F_r \quad (2)$$

where F_{acc} is the acceleration force, F_h is the climbing force, F_d is the aerodynamic drag force, F_w is a resistive force due to the wind, and F_r is the rolling force.

Since the vehicle studied here is not for racing, and will be controlled to start smoothly, no acceleration constraints are imposed.

When the vehicle goes hill climbing, based on angle of incline θ , the climbing force is:

$$F_h = M_{tot} \cdot g \cdot \sin(\theta) \quad (3)$$

where M_{tot} is the total mass of the vehicle (in kg), g is the gravitational constant (9.8 m/s^2).

Usually, the degree of incline is given in percentage. For this special electric scooter it is considered a maximum 8% degree of incline. 1% degree of incline represents the ratio of 1 meter of rise, on a distance of 100 meters. Thus, $1\% = \text{atan}(0.01) = 0^\circ 34'$ (zero degrees and 34 minutes). For an incline of 8%, the angle is $4^\circ 34'$ (or 4.57 degrees).

The drag force takes into account the aerodynamics of the vehicle. This force is proportional with the square of the speed, the frontal area of the vehicle (A_{fr} , here 0.668 m^2) and the aerodynamic coefficient, k_d , (empirically determined, for each specific vehicle (Vogel, 2009)):

$$F_d = A_{fr} \cdot v^2 \cdot g \cdot k_d \quad (4)$$

The resistant force due to wind, cannot be precisely computed. It depends on various conditions, like (for common automobiles) the fact that windows are entirely or partially open etc... Also, the wind will never blow at constant speed. However, an expression, determined empirically, which will take into account the speed of wind, v_w , can be written as (Vogel, 2009):

$$F_w = \left((0.98 \cdot (v_w/v)^2 + 0.63 \cdot (v_w/v)) \cdot k_{rw} - 0.4 \cdot (v_w/v) \right) \cdot F_d \quad (5)$$

where k_{rw} is the wind relative coefficient, depending on the vehicle's aerodynamics, (here is 1.6).

The resistant force due to rolling depends on the hardness of the road's surface, being proportional with the weight of the vehicle and the angle of incline:

$$F_r = k_r \cdot M_{tot} \cdot g \cdot \cos(\theta) \quad (6)$$

(here, the road surface coefficient, k_r , is 0.011).

A more precise computation of the rolling resistant force could take into account also the shape and the width of the tires, but these elements are not critical at low speeds, like in this case.

After the computation of the resistant forces, it can be determined the needed torque at the wheel, see Table 2, and finally the rated torque of the electrical machine.

For this specific value of the torque at the wheel, a power of 505.1 W is required. Nevertheless, for small power electrical traction systems, the efficiency is quite poor. Here, the efficiency is estimated at 75%. This means that the output power of the electrical motor, capable to operate in the specified road/mechanical conditions, it has to be at least of 673.5 W. Thus, rounding the power, it is obtained a 700 W electrical machine.

It is now possible to identify the mechanical characteristics of the electrical machines. Two traction motors are considered, with a gear ratio of 6.1 to 1. Thus, the rated mechanical characteristics for one motor are: 350 W, 1500 rpm, 2.2 N·m.

F_h (N)	F_d (N)	F_w (N)	F_r (N)	F_m (N)	torque at the wheel (N·m)
123.5	0.026	0.667	16.98	141.2	19.73

Table 2. Computed resistant forces and the torque at the wheel.

2.2 Electromagnetic design of the PMSM

The permanent magnet synchronous machine (PMSM) has to provide a maximum power density. For that, good quality materials should be used. The permanent magnet (PM) material is of Nd-Fe-B type, with 1.25 T remanent flux density. The steel used for the construction of PMSM is M530-50A. The material characteristics are presented in Fig. 1.

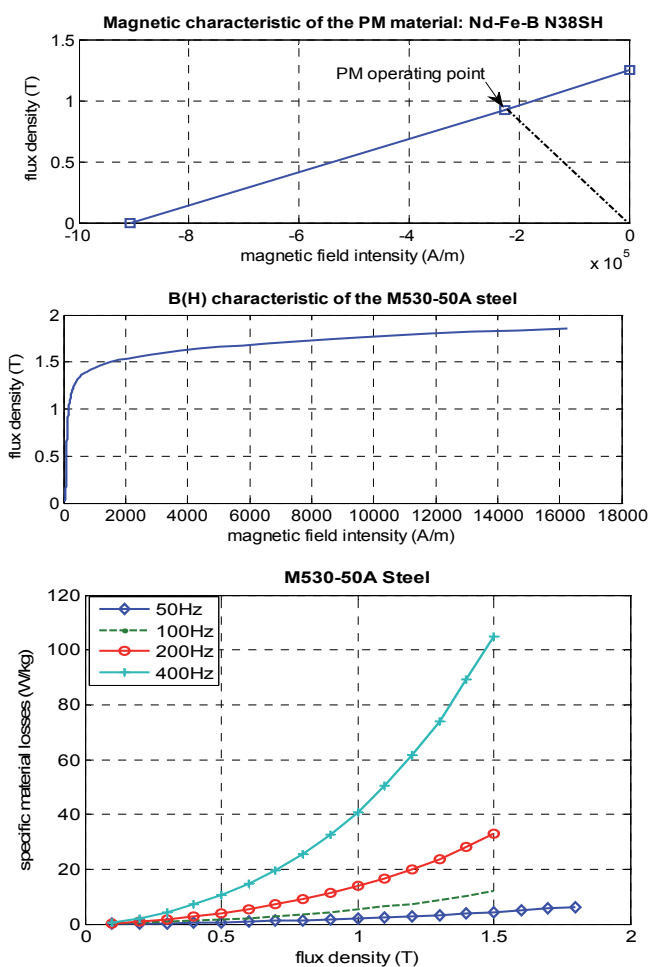


Fig. 1. The PM and steel characteristics used as the active part's materials of the PMSM.

For the PM, the N38SH material was used. This rare earth magnet can be irreversibly demagnetized starting from 120°C. The 1.25 T remanent flux density (at 20°C) is however affected with the temperature increase. In order to compute the real value of the PM's remanent flux density, for a temperature derivative coefficient of 0.1% and for an increase in temperature of 110 K, the rated operating point of the PM is 1.11 T (based on the mathematical expression $X_{20^\circ\text{C}+\Delta T} = X_{20^\circ\text{C}} \cdot (1 - \alpha_x \cdot \Delta T)$).

In order to obtain a smooth torque wave, a fractioned winding type is used. Thus, the PMSM has 8 pair of poles and 18 slots. The geometry of the PMSM, the winding configuration and the obtained phase resultant vectors are shown in Fig. 2.

The design approach is based on the scientific literature presented in (Pyrhonen et al., 2008; Fitzgerald et al., 2003; Huang et al., 1998). The output power (measured in W) of an electric machine, when the leakage reactance is neglected, is proportional with the number of phases of the machine, n_{ph} , the phase current, $i(t)$, and the induced electromotive force (emf), $e(t)$:

$$P_{out} = \eta \cdot \frac{n_{ph}}{T} \cdot \int_0^T e(t) \cdot i(t) dt = \eta \cdot n_{ph} \cdot k_p \cdot E_{max} \cdot I_{max} \quad (7)$$

where T is the period of one cycle of emf, E_{max} , and I_{max} represent the peak values of the emf and phase current, k_p is the power coefficient, and η is the estimated efficiency.

The peak value of the emf is expressed by introducing the electromotive force coefficient, k_E :

$$E_{max} = k_E \cdot N_t \cdot B_{gap} \cdot D_{gap} \cdot L_m \cdot f_s / p \quad (8)$$

where N_t is the number of turns per phase, B_{gap} and D_{gap} are the air-gap flux density and diameter, L_m is the length of the machine, f_s is the supplying frequency and p is the number of pole pairs.

By introducing a geometric coefficient, $k_L = L_m / D_{gap}$, and a current coefficient (related to its wave form) $k_i = I_{max} / I_{rms}$, and defining the phase load ampere-turns,

$$A_{th} = 2 / \pi \cdot N_t \cdot I_{rms} / D_{gap} \quad (9)$$

it is possible to define the air-gap diameter of the machine:

$$D_{gap} = \sqrt[3]{\frac{2 \cdot p \cdot P_{out}}{\pi \cdot n_{ph} \cdot A_{th} \cdot k_e \cdot k_i \cdot k_p \cdot k_L \cdot \eta \cdot B_{gap} \cdot f_s}} \quad (10)$$

Based on the type of the current wave form, it is possible to define the current and power coefficients (Huang et al., 1998). Thus, for sinusoidal current wave form, $k_i = \sqrt{2}$, $k_p = 0.5$, for rectangular current wave $k_i = 1$, $k_p = 1$ and for trapezoidal current wave $k_i = 1.134$, $k_p = 0.777$.

All the other geometric parameters will be computed based on this air-gap diameter. The designer has to choose only the PMs shape and stator slots.

The air-gap flux density is computed based on the next formula:

$$B_{gap} = \frac{h_m \cdot B_{rm}}{\frac{D_{gap}}{2} \cdot \left(\ln \left(\frac{R_{si} - gap}{R_{cr}} \right) + \ln \left(\frac{R_{si}}{R_{si} - gap} \right) \right)} \quad (11)$$

where, h_m and B_{rm} are the PM length on magnetization direction (in m) and the remanent flux-density (in $tesla$), respectively, R_{si} and R_{cr} are inner stator radius and rotor core radius, respectively.

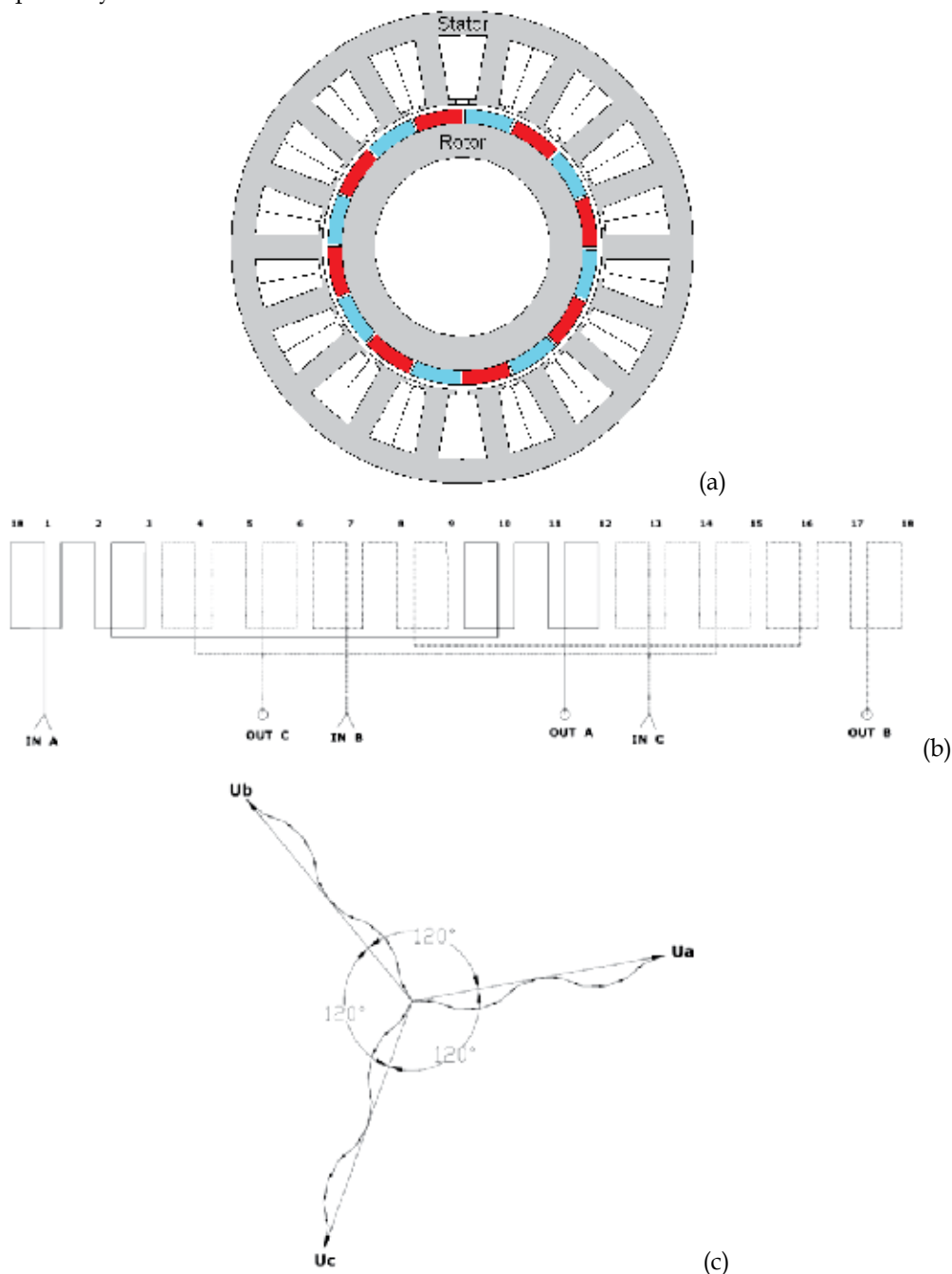


Fig. 2. The PMSM: (a) geometry; (b) fractioned type winding configuration; (c) the resultant voltage vectors.

The saturation factor, k_s , has to be computed in order to take into account the non-linearity of the steel. k_s depends on the equivalent magnetomotive force, F_{mv} , in each active part of the machine and in the air-gap:

$$k_s = (2 \cdot F_{mt} + F_{my} + F_{mr} + 2 \cdot F_{mg}) / (2 \cdot F_{mg}) \quad (12)$$

where 't', 'y', 'r' and 'g' indices refer to the stator teeth and yoke, rotor core and air-gap, respectively. Each magnetomotive force is computed based on the magnetic field intensity (H) and the length (l) of the active part of the machine, on the flux direction:

$$F_{mx} = H_x \cdot l_x \quad (13)$$

Equation (13) is general and used for the computation of the magnetomotive force in each active part of the machine, while 'x' replaces 't', 'y', 'r' and 'g' indices. The parameter l_x can be easily expressed. Further on, the magnetic field intensity is computed. The H_x value can be chosen from the supplier B(H) magnetic characteristic (for each computed value of the flux density).

Next, the electromagnetic parameters of the PMSM should be determined. The phase resistance depends on: copper resistivity, ρ_{co} , length of series turns, l_t , and conductor cross section, S_c :

$$R_{ph} = \rho_{co} \cdot l_t / S_c \quad (14)$$

The d - q axis reactances are computed based on magnetizing (X_m) and leakage (X_σ) reactances:

$$X_{d,q} = X_\sigma + X_{m,d,q} \cdot k_{a,d,q} / k_s \quad (15)$$

where d - q magnetizing reactances depend on the saliency coefficient, $k_{a,d,q}$ (which equals unity for surface mounted PM machines: $X_{m,d} = X_{m,q}$):

$$X_{m,d,q} = 4 \cdot n_{ph} \cdot f_s \cdot \tau_p \cdot L_m \cdot (N_t \cdot k_{ws})^2 \cdot \mu_0 \cdot k_{a,d,q} / (\pi \cdot p \cdot \text{gap}) \quad (16)$$

$$X_\sigma = 4 \cdot \pi \cdot f_s \cdot (N_t)^2 \cdot \mu_0 \cdot \sum \Lambda_\sigma / (p \cdot q) \quad (17)$$

where τ_p is the polar pitch, k_{ws} is the winding factor, q is the number of slots per pole and per phase, and $\sum \Lambda_\sigma$ is the sum of leakage permeances. The saliency ratios (for saliency rotors) are:

$$k_{a,d} = \frac{\pi \cdot \alpha_{mp} + \sin(\pi \cdot \alpha_{mp})}{4 \cdot \sin(\alpha_{mp} \cdot \pi / 2)} \quad (18)$$

$$k_{a,q} = \frac{\pi \cdot \alpha_{mp} - \sin(\pi \cdot \alpha_{mp}) + 2 / 3 \cdot \cos(\alpha_{mp} \cdot \pi / 2)}{4 \cdot \sin(\alpha_{mp} \cdot \pi / 2)}$$

where α_{mp} is a coefficient representing the percentage of magnet covering the rotor pole. For motor operation of PMSM (with magnetic anisotropy), we can use the typical load phasor diagram, in d - q reference frame, Fig. 3. From this phasor diagram one will get the d - q axis reactances equations, function of phase voltage, U_{phv} phase electromotive force, E_{phv} phase resistance, R_{phv} d - q axis currents and internal angle, δ :

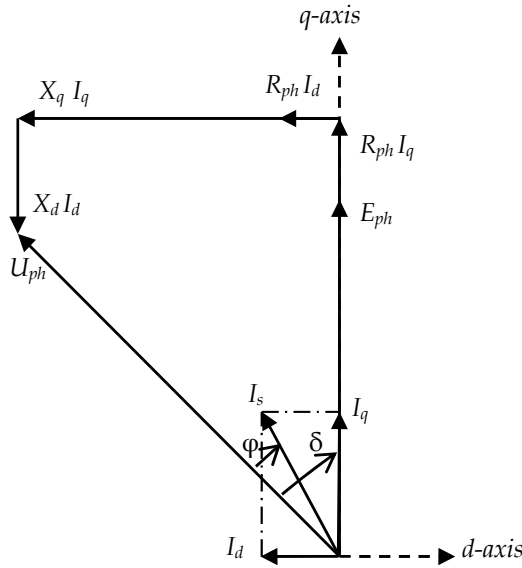


Fig. 3. Phasor diagram for PMSM in motor-load conditions.

$$\begin{aligned} X_d &= (U_{ph} \cdot \cos(\delta) - E - R_{ph} \cdot I_q) / I_d \\ X_q &= (U_{ph} \cdot \sin(\delta) + R_{ph} \cdot I_d) / I_q \end{aligned} \quad (19)$$

Also, it is possible to compute the source current, $I_s = \sqrt{I_d^2 + I_q^2}$, knowing that the direct and quadrature current are obtained by developing (19):

$$\begin{aligned} I_d &= \frac{U_{ph} \cdot (X_q \cdot \cos(\delta) - R_{ph} \cdot \sin(\delta)) - E_{ph} \cdot X_q}{R_{ph}^2 + X_d \cdot X_q} \\ I_q &= \frac{U_{ph} \cdot (X_d \cdot \cos(\delta) + R_{ph} \cdot \sin(\delta)) - E_{ph} \cdot R_{ph}}{R_{ph}^2 + X_d \cdot X_q} \end{aligned} \quad (20)$$

The electromotive force is proportional with the frequency, the number of turns, the air-gap flux per pole and a demagnetization coefficient, k_d (given by the PMs material supplier, usually between 0.8 – 0.9 for rare earth PMs):

$$E_{ph} = \sqrt{2} \cdot \pi \cdot f_s \cdot N_t \cdot k_{ws} \cdot \Psi_{gap} \cdot k_d \quad (21)$$

Next, the common electromechanical characteristics can be also computed, namely: the input power:

$$P_{in} = n_{ph} \cdot U_{ph} \cdot (I_q \cdot \cos(\delta) - I_d \cdot \sin(\delta)) \quad (22)$$

the output power (function of the sum of losses) and axis torque:

$$P_{out} = P_{in} - \sum Losses \quad (23)$$

$$T_m = P_{out} / \omega \quad (24)$$

the energetic performances (power factor and efficiency, respectively):

$$\begin{aligned} \cos \varphi &= P_{in} / (n_{ph} \cdot U_{ph} \cdot I_s) \\ \eta &= P_{in} / P_{out} \end{aligned} \quad (25)$$

The sum of losses contains the copper (the product between the phase resistance and square current), iron, mechanical (neglected here) and supplementary (estimated to 0.5% of output power) losses.

After the designing process, the following results have been obtained, see Table 3. The reader's attention is now oriented towards the energetic performances of the PMSM.

Parameter	PMSM
Output power (W)	350
Rated speed (rpm)	1500
Rated torque (N·m)	2.2
Battery voltage (V)	24
Number of phases (-)	3
Number of pole pairs (-)	8
Number of slots (-)	18
Outer diameter (mm)	98.7
Machine length (mm)	43.5
Airgap length (mm)	1
Airgap flux density (T)	0.83
Phase resistance (Ω)	0.0424
<i>d</i> axis inductance (mH)	0.30515
<i>q</i> axis inductance (mH)	0.30515
Phase emf (V)	9.058
Rated current (A)	16.64
Losses (W)	71.4
Power factor (%)	60.9
Efficiency (%)	83.06
Active part costs (€)	27.15
Active part mass (kg)	2.69
Power/mass (W/kg)	130.1

Table 3. Comparison of obtained results for the designed PMSM.

2.3 Drive modeling for controlling the PMSM

The power factor for the PMSM is quite reduced (as it can be seen in Table 3). In order to increase the power factor, it is possible to use capacitor battery connected to stator winding. This solution is expensive and non-reliable. On the other hand, the current, and finally the power factor are depending on angle δ and φ (see Fig. 3).

It is possible to rewrite the d,q-axis currents by imposing $\beta = (\delta - \varphi)$. Thus, the currents are $I_d = -I_s \cdot \sin(\beta)$ and $I_q = I_s \cdot \cos(\beta)$. If one will choose the q axis as phase origin, in Fig. 2, the electric motor will operate to unity power factor ($\cos \varphi = 1$) if $\beta = \delta$.

The purpose of this subsection is to introduce the control modeling of a PMSM and the controllability of the motor at unity power factor.

First of all, the motor model will be presented. After a short review of the vector control technique, the results of the PMSM control are presented.

From the PMSM equivalent circuit (Fig. 4), one can obtain the machine's mathematical model. The model takes into account the iron loss. The voltage equations, as a matrix, are:

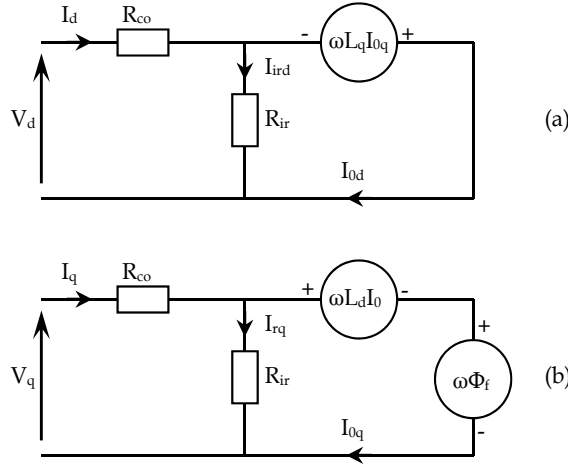


Fig. 4. The d (a) and q (b) axis equivalent circuits.

$$\begin{bmatrix} V_d \\ V_q \end{bmatrix} = R_{ph} \cdot \begin{bmatrix} I_d \\ I_q \end{bmatrix} + \left(1 + \frac{R_{ph}}{R_{ir}}\right) \cdot \begin{bmatrix} 0 & -\omega \cdot L_q \\ \omega \cdot L_d & 0 \end{bmatrix} \cdot \begin{bmatrix} I_{0d} \\ I_{0q} \end{bmatrix} + \begin{bmatrix} 0 \\ \omega \cdot \lambda_f \end{bmatrix} \quad (26)$$

where: $V_{d,q}$, $L_{d,q}$ are the d - q axis voltages and inductances, respectively; λ_f represents the excitation flux produced by the PMs; R_{ir} , is the resistance corresponding to the iron loss.

The phase voltage and total torque equations are:

$$V^2 = (\omega \cdot \lambda_f + \omega \cdot L_d \cdot I_{0d} + R_{ph} \cdot I_q)^2 + (-\omega \cdot L_q \cdot I_{0q} + R_{ph} \cdot I_d)^2 \quad (27)$$

$$T = p \cdot [\lambda_f \cdot I_{0q} + (L_d - L_q) \cdot I_{0d} \cdot I_{0q}] \quad (28)$$

with $I_{0d} = I_d - I_{ird}$ and $I_{0q} = I_q - I_{irq}$; representing the d, q axis equivalent currents.

The copper and iron losses are:

$$P_{ph} = R_{ph} \cdot (I_d^2 + I_q^2) \quad (29)$$

$$P_{ir} = R_{ir} \cdot (I_{ird}^2 + I_{irq}^2) = \frac{(\omega \cdot L_q \cdot I_{0q})^2 + (\omega \cdot \lambda_f + \omega \cdot L_d \cdot I_{0d})^2}{R_{ir}} \quad (30)$$

The motor speed equation is:

$$\Omega_s = \frac{V^2}{p \cdot \sqrt{(\lambda_f - L_d \cdot I_d)^2 + (L_q \cdot I_q)^2}} \quad (31)$$

Vector-controlled drives were introduced about 30 years ago (as was stated in Buja & Kazmierkowski, 2004) and they have achieved a high degree of maturity, being very popular in a wide range of applications in our days. It is an important feature of various types of vector controlled drives that they allow dynamic performance of AC drives to match or sometimes even to surpass that of the DC drive. At the present, the main trend is to use sensorless vector drives, where the speed and position information is obtained by monitoring input voltages or currents.

The vector control (VC) consists in controlling the spatial orientation of the electromagnetic field and has led to the name of field orientation. The FOC usually refers to controllers which maintain a 90° electrical angle between the rotor d-axis and the stator field components. Thus, with a FOC strategy, the field and armature flux are held orthogonal; moreover, the armature flux does not affect the field flux and the motor torque responds immediately to a change in the armature flux (or armature current). Hence, the AC motor behaves like a DC one.

A basic scheme of the FOC technique was used for the PMSM control. Having a speed and direct axis current as references and using PI controllers, one can obtain the needed stator voltage components for the motor supply. The employed simplified FOC scheme for our simulations is given in Fig. 5.

Direct torque control (DTC) technique was introduced about 20 years ago (as was stated in Bae et al., 2003). The principle of DTC is to directly select voltage vectors according to the difference between the reference and the actual value of the torque and the flux linkage. Thus, the torque and flux errors are compared in hysteresis comparators. Depending on the comparators a voltage vector is selected from the well known switching table of the DTC technique.

In general, compared to the conventional FOC scheme, the DTC is inherently a sensorless control method; it has a simple and robust control structure (however, the performances of DTC strongly depends on the quality of the estimation of the actual stator flux and torque).

The implemented simplified DTC scheme is given in Fig. 6. Here, from the current and speed controllers, it is possible to get the flux and torque references. The reference values are compared with the measured ones. From the obtained errors, one can get the voltage vector selection in order to assure the PMSM supply after an $abc \Rightarrow dq$ transformation.

In contrast to induction motors the initial value of the stator flux in PMSM is not zero and depends on the rotor position. In motion-sensorless PMSM drives the initial position of the rotor is unknown and this often causes initial backward rotation and problems of synchronization. Otherwise, the DTC system possesses good dynamic performances, but in steady state regime the torque-current-flux ripples present high levels.

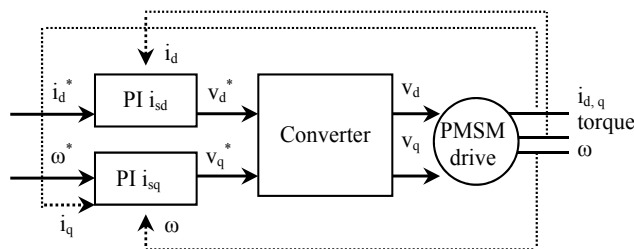


Fig. 5. Simplified basic scheme of the implemented FOC technique.

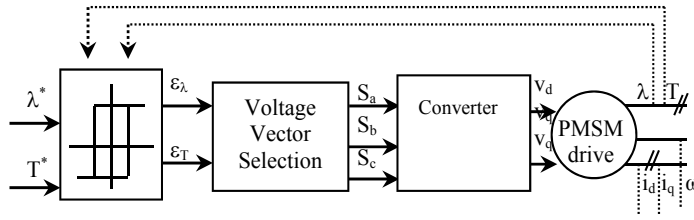


Fig. 6. Simplified basic scheme of the implemented DTC technique.

Both techniques can be used for controlling the PMSM at unity power factor. Here, the FOC was employed.

The internal angle of the PMSM can be expressed function of d,q axis voltages: $\tan \delta = -V_d/V_q$. Then, in stationary regime (derivate terms are suppressed), one will get:

$$\tan \delta = \frac{R_{ph} \cdot I_s \cdot \sin \beta + \omega \cdot L_q \cdot I_s \cdot \cos \beta}{R_{ph} \cdot I_{ph} \cos \beta - \omega \cdot L_d \cdot I_s \cdot \sin \beta + \omega \cdot \Psi_m} \quad (32)$$

Neglecting the phase resistance, the internal angle tangent becomes:

$$\tan \delta = \frac{\omega \cdot L_q \cdot I_s \cdot \cos \beta}{-\omega \cdot L_d \cdot I_s \cdot \sin \beta + \omega \cdot \Psi_m} \quad (33)$$

For unity power factor, β equals δ and the following expression is obtained:

$$\frac{\sin \beta}{\cos \beta} = \frac{\omega \cdot L_q \cdot I_s \cdot \cos \beta}{-\omega \cdot L_d \cdot I_s \cdot \sin \beta + \omega \cdot \Psi_m} \quad (34)$$

One will get, after calculation, a second degree equation which solution is:

$$\sin \beta = \frac{1 \pm \sqrt{1 - 4 \cdot \frac{L_d \cdot L_q \cdot I_s^2}{\Psi_d} \cdot \left(1 - \frac{L_q}{L_d}\right)}}{2 \cdot \frac{L_d \cdot I_s}{\Psi_m} \cdot \left(1 - \frac{L_q}{L_d}\right)} \quad (35)$$

In this way, the d,q currents will be computed for unity power factor.

The simulations results are presented in Fig. 7-Fig. 8. After 0.5 seconds, a reference speed is imposed. The measured speed follows the reference one, and in a very short time it reaches the desired value. This acceleration is accompanied by a current supply, from the electric source. Since the motor is of orthogonal type (a Park transformation was used to transform the 3 phase equation system in a 2 phase one), we will exploit the direct and quadrature axis currents to produce de torque and to evaluate the active and reactive power. To maximize the torque, the I_d should be imposed to zero. Thus, the I_q is the image of the axis torque.

The active and reactive powers are computed based on direct and quadrature currents and voltages, respectively. From those values, one can compute the energetic performances of the designed PMSM, Fig. 8. For a load torque of 2.2 N·m, the absorbed electric power (corresponding to the active power P) is of 379 W, meaning that an efficiency of 92.3% is obtained through this vector control strategy. The reactive power is used for the computation of the power factor.

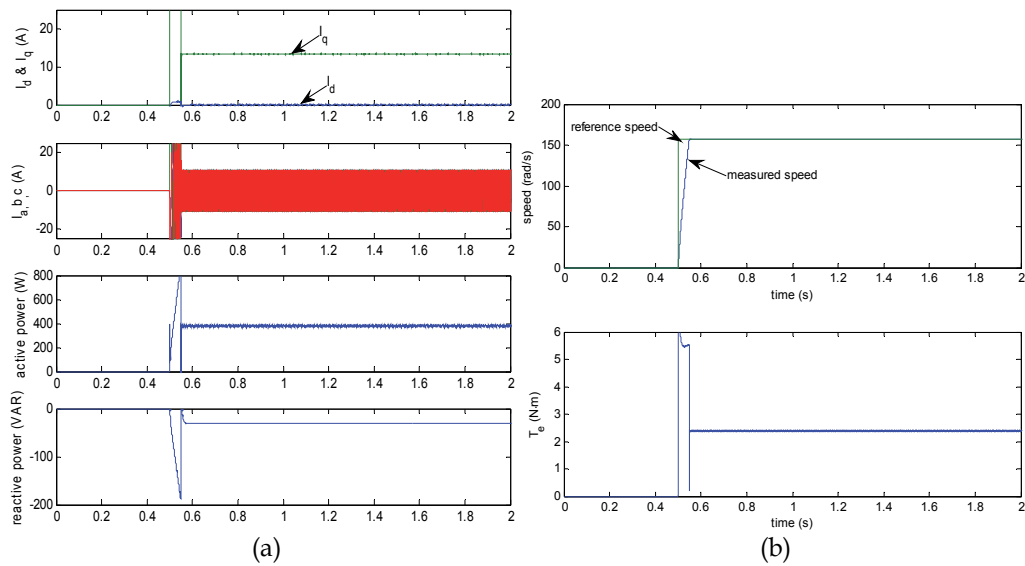


Fig. 7. PMSM simulation results: (a) electrical performances; (b) mechanical performances.

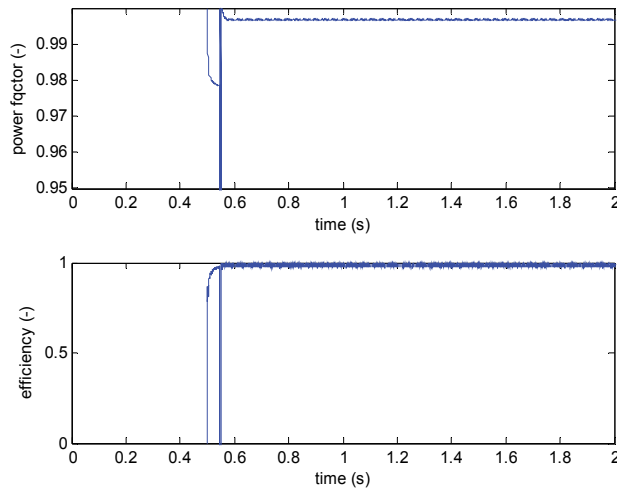


Fig. 8. PMSM simulation results: energetic performances.

Based on the obtained simulation results, it can be said that the analytical approach was validated. The unity power-factor control strategy has been successfully employed since the simulated results show a power factor over 99%!

3. Numerical validation of the designed PMSM

In order to prove the electromagnetic design validity, it has been employed a numerical computation based on finite element method (FEM). This analysis has been carried out by using Flux2D. The FEM analysis of PMSM in motor operation regime is employed at rated speed (1500 min^{-1}), while the stator is fed with three currents delayed in time by 120° .

The saturation level can be observed in Fig. 9. In Fig. 10 have been plotted the air-gap flux density, the 3-phase sinusoidal currents, axis torque and iron loss. It can be observed that the air-gap flux-density value is very close to the one obtained from analytical approach, 0.826 T. On the other hand, the rated torque is obtained based on rated current. Also, thanks to the proper winding-slots-poles configurations, the torque ripples are significantly reduced. In fact, the ratio of torque ripple is of 0.8% (maximum at 2.222 N·m and minimum at 2.204 N·m)! For the computed iron loss (average value) a supplementary explanation is needed.

It has been observed that from analytical approach the iron loss is of 34.42 W. From FEM analysis, the average value of iron loss is 27.573 W, meaning that an improved efficiency is obtained. This difference can be explained regarding Fig. 9, where the flux density is depicted in the machine's active part. Here, the flux density varies significantly in the stator iron, while in the analytical approach a fixed maximum flux density was used. Since the FEM analysis has more credit, it can be said that 2% improved efficiency is obtained!

4. Optimization of the designed PMSM

After the design process and numerical validation, the optimization approach of the studied electrical machine will be presented. Since we want to obtain a specific power for the PMSM, we could say that our optimization objective will be to reduce the volume of the machine (consequently the mass of the active parts of the machine), while the output power is maintained constant (or very close to the desired value). Thus, the objective function is to minimize the mass of the active parts of the PMSM. This mass, called m_{tot} is defined by the mathematical expression:

$$m_{tot} = m_{copper} + m_{rs} + m_{ss} + m_{pm} \quad (36)$$

where m_{copper} refers to the mass of the winding copper, m_{rs} is the mass of the rotor steel, m_{ss} is the mass of the stator steel and m_{pm} is the mass of the permanent magnet.

4.1 The optimization method

The optimization of studied electrical machine is based on gradient algorithm, (Tutelea & Boldea, 2007). The main steps in the optimization algorithm are:

- Step 1. Choose the optimization variables (which will be modified in the process; starting value and boundaries of the optimization variables are imposed).
- Step 2. Impose special limitations of other variables which can be altered during process.
- Step 3. Define the objective function.
- Step 4. Set initial and final value of global increment. The objective values will be initially modified with larger increment, which will be further decreased in order to refine the search space.
- Step 5. Compute geometrical dimensions, the electromagnetic parameters and the characteristics (given in section 2.c), and evaluate the objective function.
- Step 6. Make a movement in the solution space and recompute the objective function and its gradient. Use partial derivative to find the worse and the track points.
- Step 7. Move to the better solution, while the objective function is decreasing.
- Step 8. Reduce the variation step and repeat the previous steps. The algorithm stops when the research movement cannot find better solution, even with smallest variation step. The found value represents a local minimum; a different value can be found by changing the initial starting point.

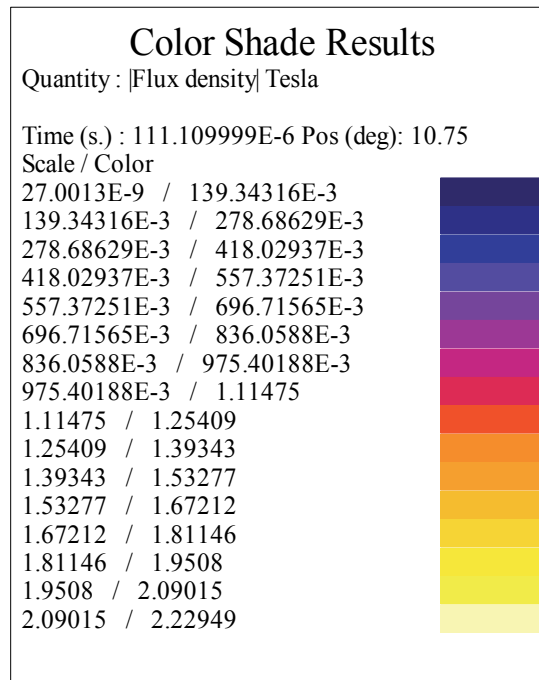
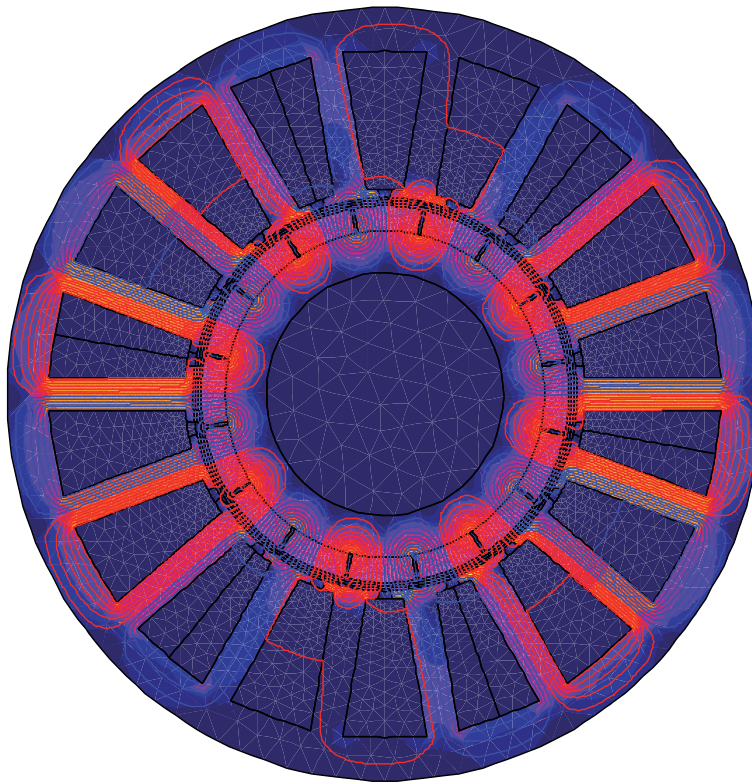


Fig. 9. Flux-density and field lines for studied PMSM.

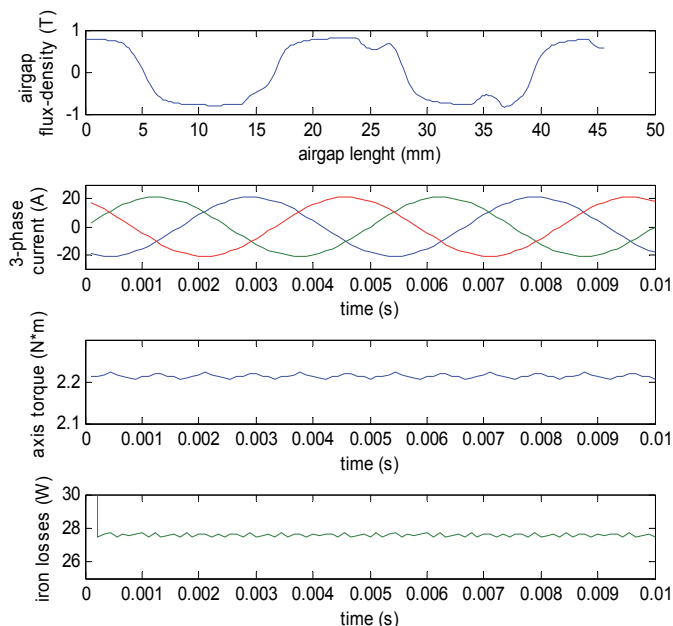


Fig. 10. FEM results of PMSM in motor regime.

The goal of the optimization process is to maximize the *power density* (power/mass ratio) – this is our objective function. The parameters to be varied, in the optimization process, are: the length of the machine, the air-gap length, the PM length (on the magnetization direction), the inner stator diameter, the stator slot’s height, the tooth width, the stator yoke height and isthmus height. The initial values and the boundaries are given in Table 4.

parameter	Initial value	Boundaries
inner stator diameter (mm)	59	[30 ...80]
slot height (mm)	13.4	[8 ...18]
isthmus height (mm)	1.5	[0.7 ...3]
height of the stator yoke	5	[3 ...9]
width of stator tooth (mm)	4	[3 ...8]
air-gap length (mm)	1	[0.5 ...1.5]
height of the PM on magnetization direction (mm)	3	[2 ...6]
length of the machine (mm)	43.5	[20 ...60]

Table 4. Optimization variables: initial values and boundaries.

Supplementary constraints were considered for the mechanical outputs (torque and power) and electrical (supplied current) characteristics, see Table 5.

parameter	Bouderies
Axis torque (N·m)	[2.1 ... 2.3]
Output power (W)	[340 ... 360]
Supplied current (A)	[13 ... 18]

Table 5. Optimization variables: supplementary constraints.

4.2 Obtained results

The optimization procedure was launched. The iterative process has reached its optimum after 672 steps, the simulation time being 5.58 seconds on an Intel Core 2 of 2Ghz processor, 2 Gb RAM.

In Fig. 11 have been plotted the current source, the output power and axis torque, to prove that the supplementary constraints were satisfied. The current reaches its upper limit after 672 steps, thus the optimization process is stopped. It is true, the copper loss will increase a little bit, but will not affect drastically the efficiency.

Next, the evolution of the geometric and energetic parameters is plotted in Fig. 12. Not all the geometric parameters are shown. Here, only the stator tooth width, the PM's height and stator yoke's height are presented as a sample. It can be seen that some parameters are maintained constant, while others are varied. The gradient type optimization algorithms are sometimes limited and they do not exploit every possible solution (meaning that a local optimum was reached, and the algorithm cannot exit from this local optimum). In order to see other possible geometrical solutions, the user needs to change the starting values; thus, new solution could appear.

It is obvious that, if the current source will increase, the copper loss will increase too. This is a normal behavior, since we want to keep the same number of turns per phase, and not to increase the copper volume. On the other hand, since the geometry volume was reduced, the iron loss is decreased too. Thus, there is compensation on the efficiency.

Practically, the efficiency of the machine has, globally, increased with 1.6%. The power factor has kept the starting value. Thus, with a proper control, this parameter can be optimized.

Finally, the objective function evolution, and the power density ratio are plotted in Fig. 13. If the initial mass of the active parts of the machine was 2.6 kg, the optimized PMS has only 1.93 kg, meaning a mass gain of 28%.

The resume of the optimized results of the PMSM are given in Table 6.

parameter	PMSM-RF	Gain (%)
Rated current (A)	18	-7.6
Losses (W)	67.4	+5.6
Power factor (%)	59.8	-1.8
Efficiency (%)	84.4	+1.6
Active part costs (€)	22.79	+16.1
Active part weight (kg)	1.93	+28.3
Power/weight (W/kg)	194.3	+33.1

Table 6. Main optimization results, at rated operating point, of the PMSM.

(In order to validate the obtained optimization results, the author has introduced again the modified parameters into the FEM software to re-compute the performances of the designed machine. The optimization results have been confirmed by the FEM analysis, like the results presented in Section 3.)

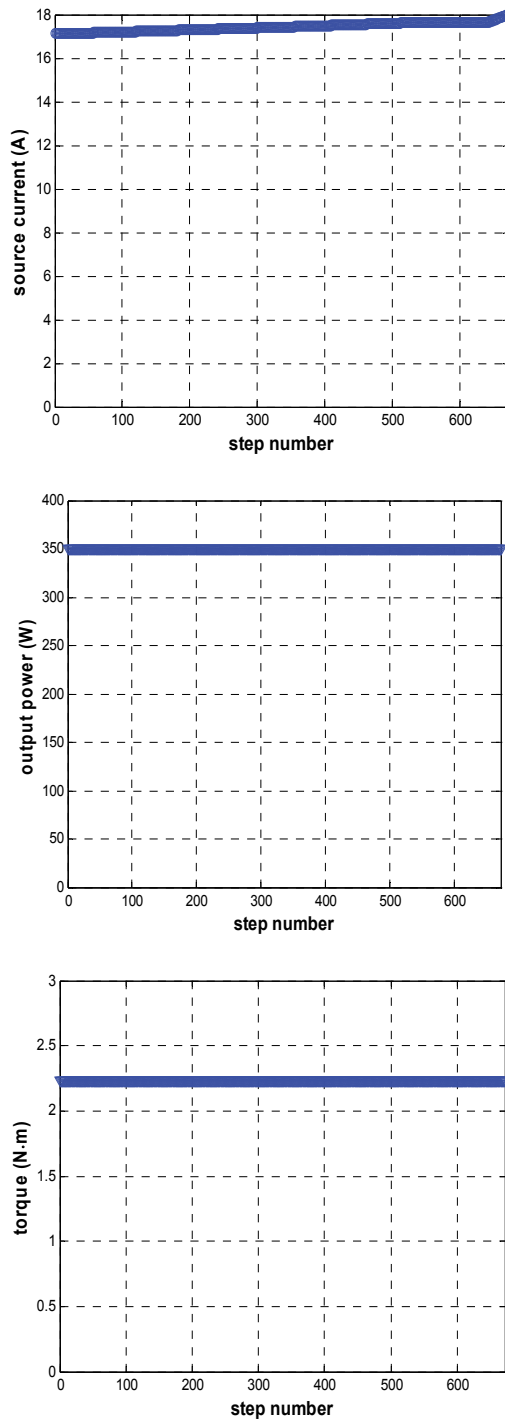


Fig. 11. Optimization results of PMSM: source current and mechanical performances constraints.

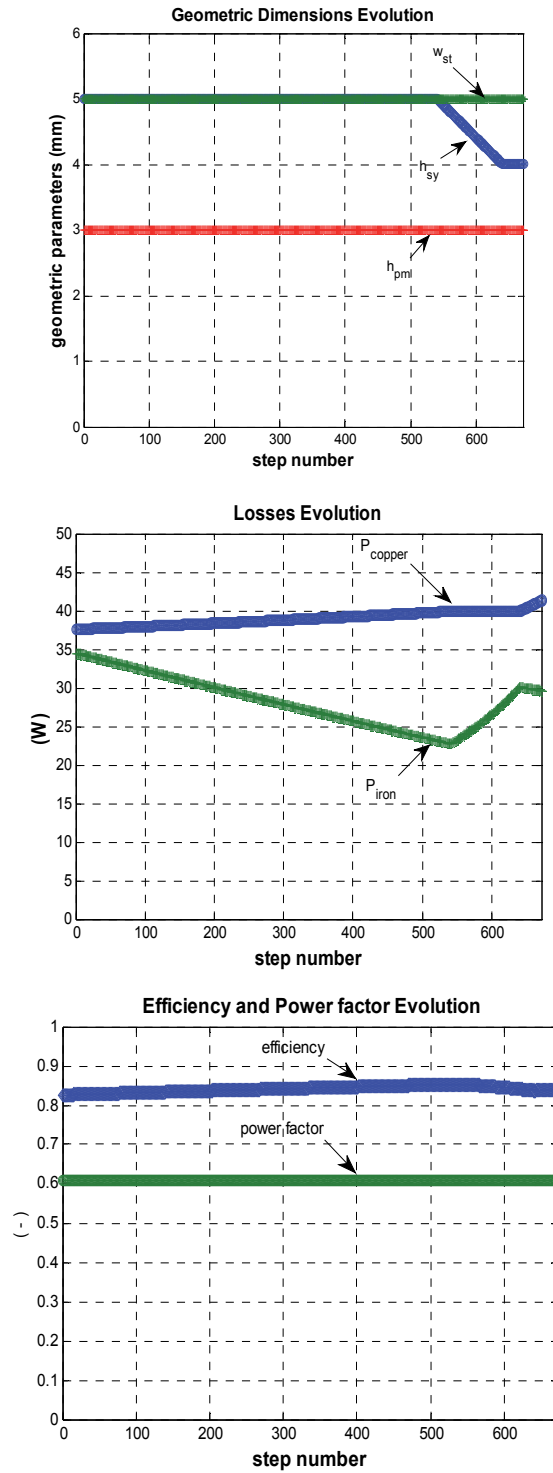


Fig. 12. Optimization results of PMSM: evolution of geometrical and energetic parameters.

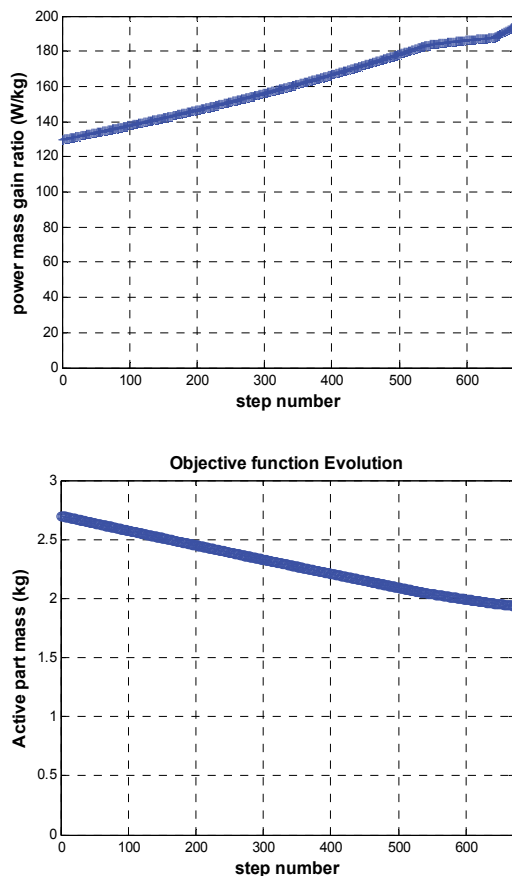


Fig. 13. Optimization results of PMSM: power density and mass improvement.

5. Conclusions

The paper presents the main steps to be followed in the design process of a permanent magnet synchronous machine used for light electric vehicles. Even if the analytical approach is not completely detailed, it contains the major elements which need to be discussed. Detailed equations are presented for the calculation of the desired output characteristics, based on certain mechanical performances. Thus, for a specific load and taking into account the vehicle's weight and the road profile, it is possible to get the needed output power which will be capable to run the vehicle.

Usually, the traction of light electric vehicles is employed with dc motors. The disadvantage of such a motor is related to its poor efficiency and power density. The permanent magnet synchronous machine (PMSM) has the best power/mass ratio, and very high efficiency. Nevertheless, two problems need to be solved for the PMSM: one is related to the poor power factor and the other one to the torque ripples. The first problem is solved with a proper vector control technique, while the second issue is solved with a proper winding configuration. A fractioned type winding configuration was used for the PMSM, and a very smooth torque was obtained: the torque ripples are of 0.8%.

The design of the PMSM is completed with the optimization of the motor, based on gradient type algorithm. The objective function of the problem is the minimization of the machine's active parts mass, while the output power is kept practically constant. After the optimization process, the mass of the PMSM was reduced with 28%, at the same energetic performances (efficiency and power factor). This mass decrease involves also an investment decrease of 16%.

6. Acknowledgments

This research work was supported by *CNCSIS-UEFISCDI*, project type TE-250, contract number 32/28-07-2010.

7. References

- Bae, B.H.; Sul, S.K., Kwon, J.H. & Shin, J.S. (2003). Implementation of sensorless vector control for super high speed PMSM of turbo-compressor. *IEEE Transactions on Industry Applications*, Vol.39, No.3, (May-June 2003), pp.811-818, ISSN: 0093-9994.
- Buja, G.S. & Kazmierkowski, P. (2004). Direct torque control of PWM inverter fed AC motor – A survey. *IEEE Transactions on Industrial Electronics*, Vol.51, No.4, (August 2004), pp.744-757, ISSN: 0278-0046.
- Ceraolo, M., Caleo, A., Campozella, P. & Marcacci, M. (2006). A parallel-hybrid drive-train for propulsion of a small scooter. *IEEE Transactions on Power Electronics*, Vol.21, No.3, (March 2006), pp.768-778, ISSN: 0885-8993.
- Chen-Hu C. & Ming-Yang, C. (2007). Implementation of a highly reliable hybrid electric scooter drive. *IEEE Transactions on Industrial Electronics*, Vol.54, No.5, (March 2007), pp.2462-2473, ISSN: 0278-0046.
- Ehsani, M., Gao, Y., Gay, S.E. & Emadi, A. (2005). *Hybrid Electric, and Fuel Cell Vehicles: Fundamentals, Theory, and Design*. CRC Press.
- Fitzgerald, A.E., et al. (2003). *Electric Machinery – 6th edition*, McGraw-Hill.
- Fuhs, A.E. (2009). *Hybrid vehicle and the future of personal transportation*. CRC Press.
- Huang, A.S., Luo, J., Leonardi, F. & Lipo, T.A. (1998). A general approach to sizing power density equation for comparison of electrical machines. *IEEE Trans. on Industry Applications*, Vol.34, No.1, (January 1998), pp.92-97, ISSN: 0093-9994.
- Naidu, M., Nehl, T.W., Gopalakrishnan, S. & Würth, L. (2005). A semi-integrated, sensorless PM brushless drive for a 42-V automotive HVAC compressor. *IEEE Industry Application Magazine*, July-August 2005, pp.20-28, ISSN: 1077-2618.
- Pyrhonen, J., Jokinen, T. & Hrabovcova, V. (2008). *Design of Rotating Electrical Machines*, John Wiley & Sons.
- Tutelea, L. & Boldea, I. (2007). Optimal design of residential brushless d.c. permanent magnet motors with FEM validation, *International AGEAN Conference on Electrical Machines and Power Electronics*, Antalya, Turkey, 2007, pp.435-439.
- Vogel, C. (2009). *Build Your Own Electric Motorcycle*, McGraw-Hill Companies.

Efficient Sensorless PMSM Drive for Electric Vehicle Traction Systems

Driss Yousfi, Abdelhadi Elbacha and Abdellah Ait Ouahman
*Cadi Ayyad University, ENSA-Marrakech
Morocco*

1. Introduction

With ever increasing oil prices and concerns for the natural environment, there is a fast growing interest in electric vehicles (EVs). However, energy storage is the weak point of the EVs that delays their progress. For this reason, a need arises to build more efficient, light weight, and compact electric propulsion systems, so as to maximize driving range per charge. There are basically two ways to achieve high power density and high efficiency drives. The first technique is to employ high-speed motors, so that motor volume and weight are greatly reduced for the same rated output power. However, mechanical losses are incurred by the clutch, reduction and differential gears, during power transmission from the motor to the wheels. With such driveline transmission, losses amount up to 20% of the total power generated (Jain & Williamson, 2009).

A more attractive solution involves employing high-torque, low-speed motors (around 1000rpm); which can be directly mounted inside the wheel, known as in-wheel motors or hub motors. By applying wheel motors in EVs, power transmission equipment can be eliminated. Therefore, transmission losses are minimized and operating efficiency is improved (Chau et al., 2008).

The basic requirements of wheel motors are large starting torque, overload capability, wide speed range, and high power density in order to reduce motor weight. A low motor weight is essential when the motor is fitted inside the wheel to reduce un-sprung mass, thus maintaining the quality of road holding. Hence, high efficiency/weight ratio is required for a wheel motor.

Considering these requirements, several types of motors have been reported in literature for use as an in-wheel motor: Induction motor, Permanent Magnet Brushless motor and switched reluctance motor (Emadi, 2005; Jain & Williamson, 2009). Amongst these solutions, PM Brushless motors might play a major role in the future development of in-wheel applications, because of its high power density and efficiency, smooth torque, and simple control drive.

The PM Brushless motor has either a trapezoidal-wave or a sine-wave Back-EMF. In the trapezoidal-wave motor, cheap Hall-effect sensors are used to control commutation. The interaction between the fed trapezoidal-wave current and magnetic field, produces more frequency harmonics and a larger torque ripple. In the PM Brushless motor with sinusoidal Back-EMF a continuous rotor position sensor is indispensable. In addition to commutation purposes, this measurement is used to eliminate the problems associated with the

trapezoidal-wave version. Because these types of sensors are expensive and cumbersome, a number of position measurement elimination techniques have been reported to operate such motors with sensorless strategies. When reviewing papers published in this field i.e. sensorless control applied to wheel motors, it is evident that there has not been so many published contrary to other industrial applications.

Some of reported rotor position estimation techniques are based on the vector control principle of AC motors (Chen, et al., 2010; Genduso et al., 2010; Jingbo, et al., 2010). The state estimation algorithms, such as a state observer or an extended Kalman filter, are also adopted to estimate the rotor position and the speed (Batzel & Lee, 2005). Other rotor position estimation techniques reported in (Carpaneto, et al., 2009; Cheng & Tzou, 2003; Johnson, et al., 1999; Sungyoon, et al., 2010; Yousfi, 2009) are based on the flux linkages, which can be obtained from the stator voltages and the currents of the motors. The flux linkage based methods operate accurately over a wide speed range and can be applied to the PM Brushless motors with either trapezoidal or sinusoidal Back-EMFs. However, the performance of the position estimation depends very much on the quality and the accuracy of the estimated flux linkages.

In all of these algorithms, extensive computational power and accurate measurement of the voltages and currents, as well as accurate knowledge of the motor parameters are required. Moreover, the methods proposed so far ultimately fail at low and zero speed in wheel motor tests due to the absence of measurable signals. Indeed, the position error and the torque losses are relatively large in these conditions.

From the mathematical model of the PM Brushless Motor, it can be observed that the Back-EMF or flux linkage varies as a function of the rotor position. Therefore, if these quantities are measured or estimated, the rotor position information can be determined. However, it is difficult to measure the Back-EMFs, specifically at low operating speeds, or the flux linkages directly because of the integration drift and/or shift.

To solve the aforementioned position estimation problems, this chapter presents a direct algebraic calculation method of the flux linkage, instead of the Back-EMF integration. Hence, sensorless vector control of the PM Brushless Motor could be applied in order to raise the efficiency of the drive. During the initial operation, the motor is started up using the Hall-effect signals to develop the required high starting torque.

2. PM Brushless motor commutation

In many EV applications, PM Brushless in-wheel Motor is preferred for its high efficiency. In such configuration, the motor is integrated in the wheel in order to eliminate transmission losses and simplify the mechanical design. A basic EV system with in-wheel motors is shown in Fig.1.

2.1 Brushless motor types

There are two main types of Brushless motors (Gieras et al., 2004; Hanselman, 2006 ; Krishnan, 2010). One is known as the Brushless DC Motor (BLDCM), characterized by constant flux density in the air gap around the pole faces. The motor windings should be supplied with currents in the form of rectangular pulses.

The other motor ideally has sinusoidal flux and sinusoidal distribution of its windings. It is supplied with a sinusoidal current and is known as the Permanent Magnet Synchronous Motor (PMSM).

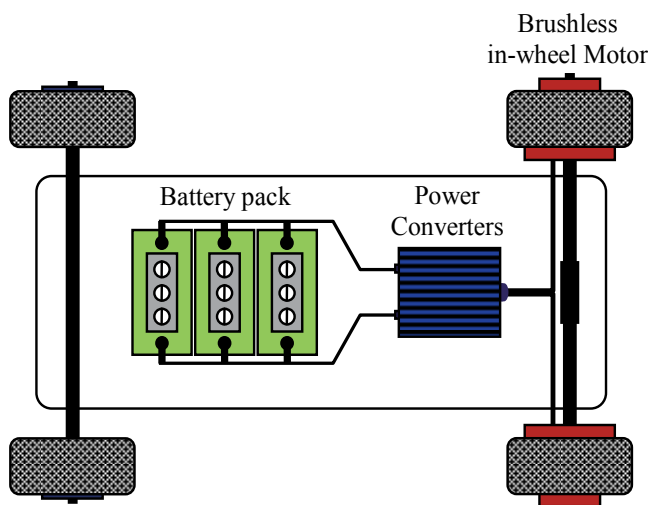


Fig. 1. Schematic of an Electric Vehicle with in-wheel motors.

The commutation process has to ensure that the action of switching the current direction is synchronized with the movement of the flux in the air gap, and so the motor must have a sensor for measuring the position of the flux wave relative to that of the stator windings.

Simple Hall-effect sensors are used with BLDCM in order to manage the commutation sequence and form the appropriate current waveform. On the other hand, a high resolution encoder or resolver is necessary for the PMSM control mode to generate sinusoidal currents.

2.2 Current and torque waveforms

Fig. 2 shows experimental currents and torques for the same motor used in BLDCM (120° commutation) and PMSM control modes under the same operating conditions. By driving the motor with rectangular current commutation, more frequency harmonics are present in the current waveform as shown in Fig. 2-a. That is reflected, at the level of the generated torque, as a relatively intense ripple at 6 times the fundamental frequency and weighing 13% of the rated torque. As a result, the ageing process of the motor is accelerated.

In the PMSM control mode (Fig. 2-b), these problems practically disappear and a larger torque is produced for the same RMS current. Thus, an immediate reduction in power losses occurs. The sinusoidally driven motor gains 7.5% in energy consumption compared to BLDC mode. Although this rate might be worthless in conventional electric drive applications, it is valuable in EV case where batteries are the only source of energy.

The smoothness of the PMSM output torque is only affected by the ripple in the flat top caused by stator slotting and the fringing effects. However, in BLDCM, further irregularities in the rotor output torque arise from stator current waveforms which are never perfectly rectangular in practice.

Most EV dedicated brushless hub motors come with Hall-effect sensors for BLDC control end. Unfortunately, PMSM control mode requires more precise angle measurements. Consequently, position and speed estimators would be an effective solution to carry out the PMSM control and benefit from its advantages, without using cumbersome mechanical sensors.

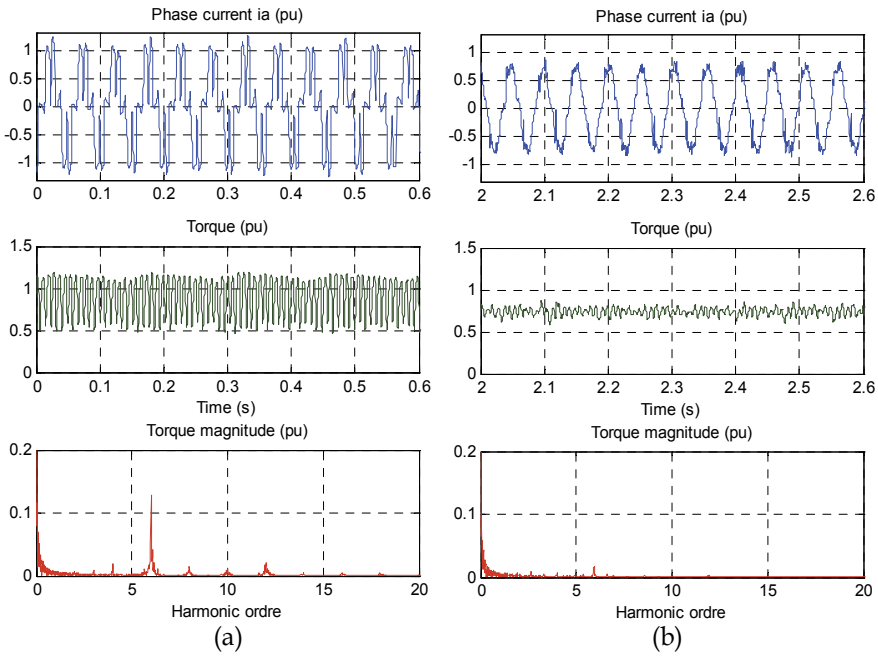


Fig. 2. Phase current, torque and torque spectrum at 50 rpm in (a) BLDCM and (b) PMSM control modes

3. Mathematical model of the motor

In this section, a brief description of the PMSM model is presented since the investigated estimation method needs to manipulate the equations of the machine. The model of the PMSM in the stationary frame (α - β) is:

$$\begin{aligned} v_{\alpha} &= R i_{\alpha} + e_{\alpha} \\ v_{\beta} &= R i_{\beta} + e_{\beta} \end{aligned} \quad (1)$$

$$\begin{aligned} e_{\alpha} &= \frac{d\psi_{\alpha}}{dt} \\ e_{\beta} &= \frac{d\psi_{\beta}}{dt} \end{aligned} \quad (2)$$

where $e_{\alpha\beta}$, $\psi_{\alpha\beta}$, $v_{\alpha\beta}$ and $i_{\alpha\beta}$ are respectively the Back-EMF, flux linkages, terminal voltages and phase currents in $\alpha\beta$ -frame, and R the winding resistance.

The flux linkages are generated in term of position as:

$$\begin{aligned} \psi_{\alpha} &= L_{\alpha} i_{\alpha} + \psi_m \cos \theta \\ \psi_{\beta} &= L_{\beta} i_{\beta} + \psi_m \sin \theta \end{aligned} \quad (3)$$

θ is the actual rotor angle.

ψ_m is the maximum flux linkage of the permanent magnet.

L_α, L_β are the inductances in $\alpha\beta$ -frame.

The used Brushless motor is a non-salient machine with sinusoidal Back-EMF. So the inductances in the model are equal i.e. $L_\alpha=L_\beta=L$.

The above electrical and magnetic equations are the basis for the position and speed extraction from the voltage and current measurement.

4. Position and speed estimation

In the PMSM operating mode, in order to generate smooth torque and thus reduce power losses, vibration and noise, the current waveform should match the shape of the sinusoidal motor Back-EMF. Consequently, high resolution rotor position feedback is of critical importance. On the other hand, speed feedback is required for accurate velocity tracking. Hence, in the absence of an optical encoder, suitable strategies must be developed to determine these parameters. Figure 3 illustrates a common vector control scheme with a position and speed estimator instead of an encoder.

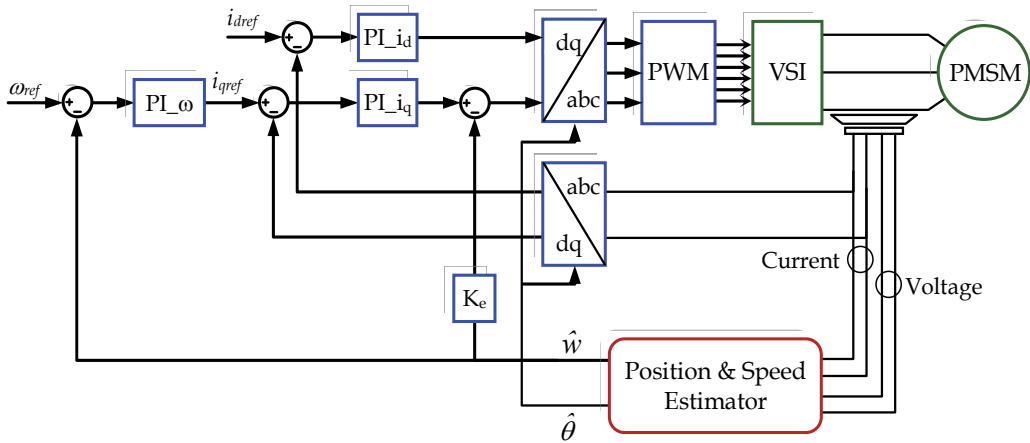


Fig. 3. PMSM sensorless vector control with position and speed estimator.

4.1 Rotor position estimation using hall-effect signals

Simple rotor position estimation can be obtained through direct digital signal processing of the Hall-effect sensor outputs (Johnson, et al., 1999; Morimoto et al., 1996). The electric angular position is generally given by:

$$\theta(t) = \int_{t_k}^t \omega(t) dt + \theta_k \tag{4}$$

$\omega(t)$ is the instantaneous electric angular velocity and θ_k is the initial angle of sector k measured from a fixed reference axis.

t_k is the instant when the magnetic axis enters sector k ($k=1, 2, \dots, 6$).

The zeroth-order position estimation algorithm is obtained by taking into account the zeroth-order term of an approximated Taylor series expansion.

The Hall-effect sensors detect when the rotor magnetic axis enters a 60° sector. Then, the speed can be expressed as the approximation:

$$\omega(t) \approx \hat{\omega}_{0k} = \frac{\pi/3}{\Delta t_{k-1}} \quad (5)$$

Δt_{k-1} is the time interval taken by the rotor magnetic axis to cross the previous sector $k-1$.

The electric angular position can be obtained by numerical integration of (4), applying the constraint that the resulting angular position value has to be within sector k limits. The angular position is, thus, calculated as:

$$\begin{aligned} \hat{\theta}(t) &= \theta_k + \hat{\omega}_{0k} \times (t - t_k) \\ \text{with } \theta_k &\leq \hat{\theta}(t) \leq \theta_k + \pi/3 \end{aligned} \quad (6)$$

The position estimate can be also derived as a second-order algorithm by taking into account higher order terms of the Taylor series expansion.

The block diagram of this estimation technique is shown in Fig. 4.

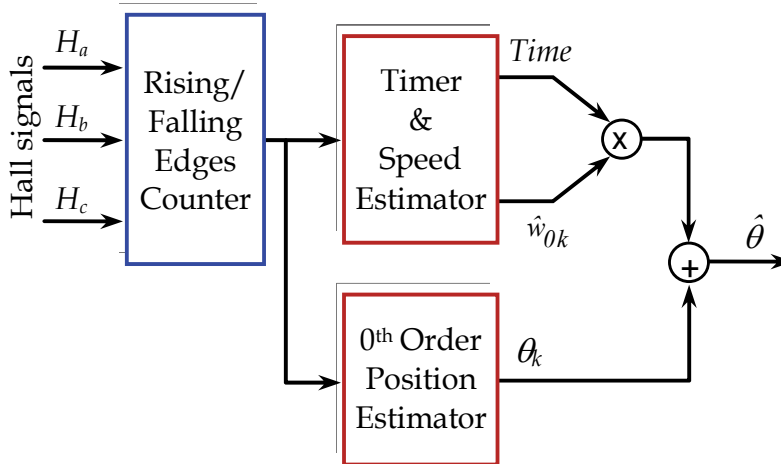


Fig. 4. Block diagram of the Hall-effect sensor based estimator.

The estimation here depends exclusively on the motor speed and the sampling time. So, more attention should be paid to the sampling time in high speed operation particularly. For the test motor, the frequency of the Hall signals goes beyond 1.4 kHz at rated speed; therefore relatively fast sampling time should be used for the estimation ($100 \mu\text{s}$).

The estimation weakness in this method intensifies during velocity transitions, as shown in Fig. 5. When the motor accelerates, the estimated position deviates from the real position between the Hall-effect signals. This is due to the error between the actual speed and the time based estimated speed from Hall sensors. Such a position error affects current regulation and degrades torque production.

Furthermore, the position estimation error is proportional to the rotor speed. Consequently, the estimation capability could entirely deteriorate when the speed becomes relatively high as in Fig. 6.

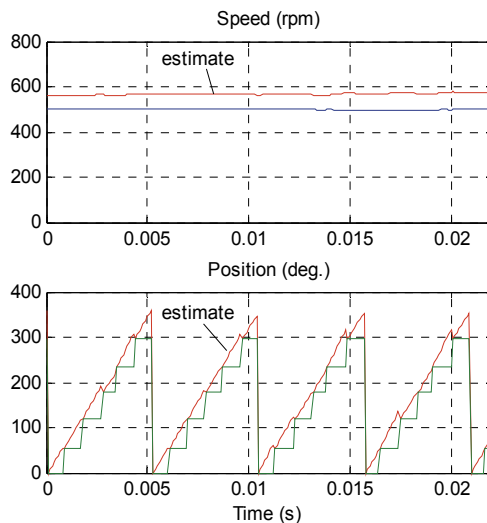


Fig. 5. Speed and 1st order position estimates deviation during motor acceleration around 500 rpm.

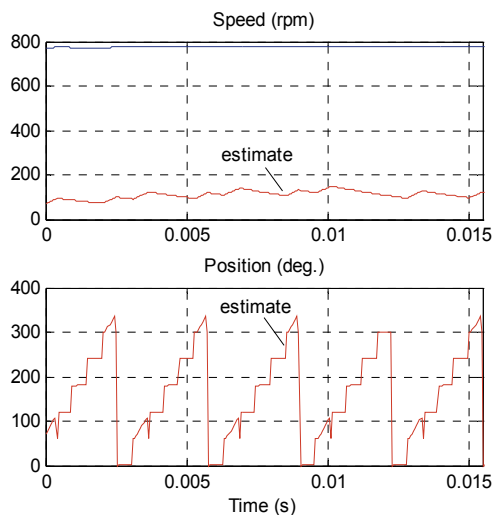


Fig. 6. Deterioration of the estimator at 780 rpm.

4.2 Back-EMF based rotor position estimator

The flux can be used to estimate the rotor angular position. Especially in steady-state, the actual flux linkage vector is synchronized to the rotor and the flux linkage vector position is the true rotor position.

However, because of the measurement imperfection which must be corrected by means of a filter, an error occurs in the phase angle and magnitude of the flux linkage estimation. This uncertainty depends on the speed, and it increases when the motor operates at a frequency lower than the filter cut-off frequency. A correction routine is set up for this reason.

Commonly, direct measurements of the line current and phase voltage allow estimation of the flux linkage through the well-known integration:

$$\begin{aligned}\psi_{\alpha} &= \int e_{\alpha} dt = \int (v_{\alpha} - Ri_{\alpha}) dt \\ \psi_{\beta} &= \int e_{\beta} dt = \int (v_{\beta} - Ri_{\beta}) dt\end{aligned}\quad (7)$$

From the estimation of ψ_{α} and ψ_{β} , the rotor angle estimate may be determined as:

$$\operatorname{tg} \theta = \frac{\sin \theta}{\cos \theta} = \frac{\psi_{\alpha} - L i_{\alpha}}{\psi_{\beta} - L i_{\beta}} \quad (8)$$

Thus

$$\hat{\theta} = \operatorname{arctg} \frac{\psi_{\alpha} - L i_{\alpha}}{\psi_{\beta} - L i_{\beta}} \quad (9)$$

At this stage a four-quadrant arctan function is used.

The integration of Eq. 7 by pure integrator involves drift and saturation problems. Since the integration at $t=0$ s time instant requires initial condition, the rotor must be brought to a known position. However, this prior setting is not possible in EV context.

To avoid the pure integrator and solve the problems, one can benefit from the fact that the flux ψ_{α} and ψ_{β} are respectively cosine and sine function of the position (Yousfi & El Adnani, 2007). They can be derived, immediately, from the Back-EMFs e_{α} and e_{β} by using the following algebraic calculation:

$$\begin{aligned}\psi_{\alpha} &= \frac{e_{\alpha}}{\omega} \\ \psi_{\beta} &= -\frac{e_{\beta}}{\omega}\end{aligned}\quad (10)$$

In this way, there is no need of position or flux linkage initial values.

In practice the Back-EMF measurement, used to evaluate the flux estimate, contains an offset which causes additional position errors. The solution consists of detecting this offset with a very low cut-off frequency LP Filter and subtracting it from the original signal.

4.3 Rotor speed estimation

It is clear from Eq. 10 that the rotor speed is required first for the implementation of the rotor position estimator. Eq. 1 can be used to extract the speed, since the Back-EMF magnitude E_m already contains this quantity:

$$e_{\alpha}^2 + e_{\beta}^2 = L^2 \left(\frac{di_{\alpha}}{dt}^2 + \frac{di_{\beta}}{dt}^2 \right) - 2LE_m \left(\frac{di_{\alpha}}{dt} \sin \theta - \frac{di_{\beta}}{dt} \cos \theta \right) + E_m^2 \quad (11)$$

where

$$E_m = \omega \psi_m \quad (12)$$

Until the rated speed operation, the first term on the right hand of Eq. 11 stays below 5% of the overall magnitude because the motor inductance is very small. However, the second term reaches 45% near this speed and cannot be neglected.

Consequently, when the motor operates relatively far from the rated conditions the following approximation is valid:

$$e_{\alpha}^2 + e_{\beta}^2 \approx \omega^2 \psi_m^2 \quad (13)$$

This leads to a simple manner of estimating the speed magnitude:

$$|\hat{\omega}| \approx \frac{\sqrt{e_{\alpha}^2 + e_{\beta}^2}}{\delta \psi_m} \quad (14)$$

Here, δ is an adjustment coefficient introduced to compensate the neglected term in Eq. 11. The direction of the speed estimate at sampling interval kT_e is then obtained from the Back-EMF angle evolution, as follow:

$$\varphi(k) = \text{arctg} \left(-\frac{e_{\alpha}(k)}{e_{\beta}(k)} \right) \quad (15)$$

$$\hat{\omega}(k) = \text{sgn}(\varphi(k) - \varphi(k-1)) |\hat{\omega}(k)| \quad (16)$$

The strength of this method is its ability to determine speed, even at low speed. The weakness is its dependence on motor parameters.

The above model based speed estimator may not be a good solution when the speed increases and approaches the rated value. A simpler manner of estimating the speed magnitude, at this speed range, is the derivation of the position estimate:

$$\hat{\omega} = \frac{d\hat{\theta}}{dt} \quad (17)$$

Obviously, the resulting speed needs to be Low-Pass filtered.

4.4 Position error correction

The open-loop structure of the position estimator that uses stator voltage and current measurement as well as speed-division, leads to cumulative position estimation error. In addition, the use of LP filters in the estimation line induces a phase shift, and thus, an additional error. The position error affects current regulation and degrades torque production. Based on the above considerations, a position correction procedure using Hall-effect signals, is implemented to compensate all sources of position estimation error.

It is important to note that the position estimation cannot be achieved near zero-speed when the electric measurements are weak and the speed-based division is unstable (Capponi et al., 2004; Yousfi, 2009).

For this reason, the motor is started up as a BLDC motor using Hall-effect signals until the rotor speed reaches convenient level for angle estimation.

Complete structure of the proposed position and speed estimator is presented in Fig. 7.

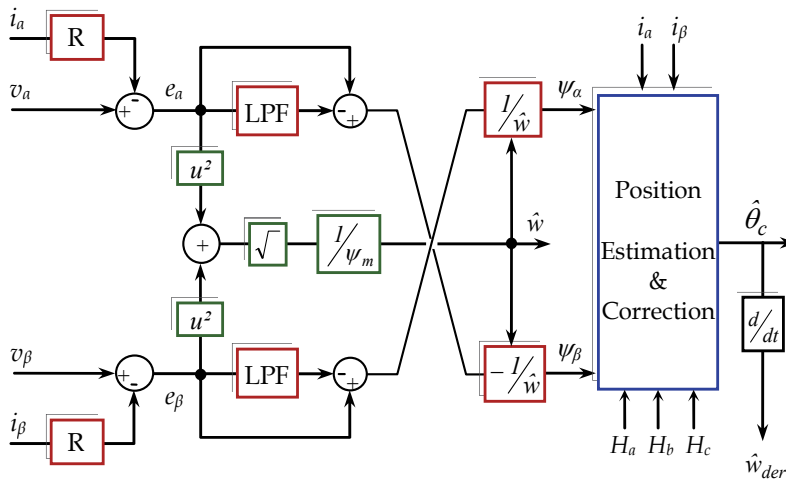


Fig. 7. Block diagram of the Back-EMF/Hall-effect based position and speed estimator.

This estimation method depends mainly on two machine parameters i.e. the winding resistance R and the inductance L . The second advantage of this method is its estimation capability even at low speed range and high load rate. In addition, thanks to the BLDC starting mode using Hall-effect sensors, high torque is possible at any initial moment.

5. Experimental setup and results

An experimental set up was fabricated in the laboratory using a 48V/2kW in-wheel gearless Brushless motor which is fed by a three-phase full bridge inverter built using compact Intelligent Power Module (IPM) (Fig. 8). This system is powered by 48V/75AH battery pack. For estimation and control tasks, an eZdsp2812 board has been used. To keep an eye on the control mode of the motor, the Park frame currents (d-q) are measured.



Fig. 8. Experimental setup for the in-wheel brushless motor drive validation and the IPM based power circuit.

In EV applications, current and voltage measurements are often required in order to carry out advanced motor control strategies, to estimate the position and speed of the machine or to carry out online energy management. In the current application, phase currents are provided by the LEM transducers used for the implementation of the motor vector control. On the other hand, an indirect voltage measurement that uses the PWM duty cycle and the DC bus voltage to estimate the inverter output voltage is used to reduce the drive sensors number. Thus, for each phase the voltages are reconstructed every sample period using the following method:

$$v = DV_{dc} - v_{comp} \tag{18}$$

V_{dc} is the DC Link voltage measured via LEM sensor that already exists for battery energy management purposes, and D is the PWM duty cycle.

The compensation term v_{comp} is associated with the inverter device losses and is determined from non-linear tables relating inverter device voltage drop to phase current.

The block diagram of the developed control scheme is shown in Fig. 9. Inputs to the position estimator are motor stator currents and voltages as well Hall sensor signals. The output is a high resolution estimate of the rotor position and speed estimation.

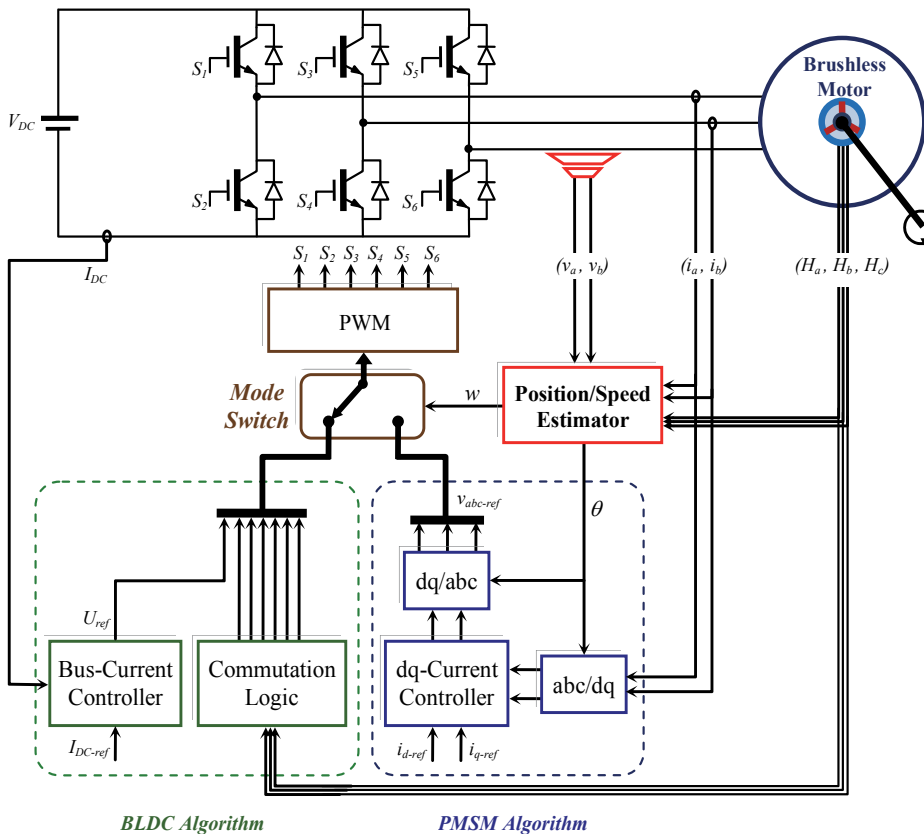


Fig. 9. Overall scheme of the combined BLDCM/Sensorless PMSM control strategy.

The three Hall-effect sensors are positioned in the machine stator in order to provide 60 electrical deg. resolution in rotor position sensing. Thus, the error on the rotor position estimation is reset every time the rotor magnetic axes enter a new 60°. sector univocally identified by means of the three Hall-effect sensors stats as shown in Fig. 10. The position error $\Delta\theta$ is taken to be the angular difference at these special instants because no encoder is used in the drive.

To meet the low-speed/high-torque demand, which is crucial for effective EV traction systems, the three Hall-effect sensors are used to start up the motor in BLDC mode. Until the motor overcomes the vehicle inertia and the speed is high enough that mechanical quantities can be accurately estimated with the Back-EMF/Hall sensors estimation method, the operation algorithm is switched to the PMSM vector control mode.

Fig. 11 shows the curves of a-phase, d-q currents and torque as well as speed and position error at a transition moment from BLDC to PMSM operating mode. The motor runs at 50 rpm under 75% of the rated load in this test. The a-phase current wave-form reflects the six-step excitation mode, using only Hall-effect data, and the sensorless sinusoidal drive. The cancellation of the direct current i_d (black line) reflects the change to vector control with maximum torque strategy. Clearly, the generated torque and current are much smoother in PMSM control zone i.e. after 0.5s. That justifies the effectiveness of the technique in reducing power losses, noises and mechanical vibrations.

The position estimation error is delimited by a $\pm 10^\circ$ band but it is small on average. The speed estimate remains unaffected by the transition. Furthermore, it can be noticed especially during BLDC mode, that position error peaks appear six times per electrical period. They arise from the position refreshing at Hall-effect sensor edges.

The results given in Fig. 12 show successful starting up from standstill to 600rpm. The switching instant from BLDC to PMSM control mode is dictated by the speed when it reaches 50rpm (4 km/h). The speed threshold is chosen to have not only accurate estimation but also proper operation with considerable load. This speed value should be low and it is defined by tests. The transition behavior of the drive is highlighted by current and torque zoom. The technique provides an excellent mode transition and sensorless control with good position estimation ($\Delta\theta \leq 1^\circ$). Thanks to the BLDC mode, the motor can start with a very high torque that exceeds 200% of the rated torque. At the transition instant, the maximal rotor position error is around 15° which may generate 3.4% of torque loss. With this loss value, the sensorless PMSM drive keeps perfectly the ability to develop the large torque required to startup and maintain the motion. The motor current and torque, in the figure, exhibit the high efficiency and performance of the PMSM vector control, except for the first short interval.

The dynamic performances of the in-wheel motor drive are tested in an acceleration/deceleration speed profile from 200 rpm to 600 rpm (Fig. 13). The maximum continuous torque is about 80% of the rated load. The proposed position estimation works very reliably during such relatively severe conditions. The position error average is always very small (1°). The residual ripple is not usually a problem because it will be filtered out by the vehicle inertia.

The position error that arises from Hall sensors alignment defect, remains constant. So, it could be easily eliminated from the position estimate.

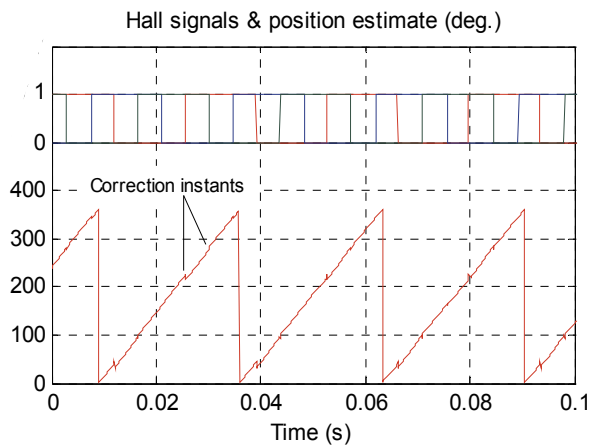


Fig. 10. Hall-effect signals and estimated position.

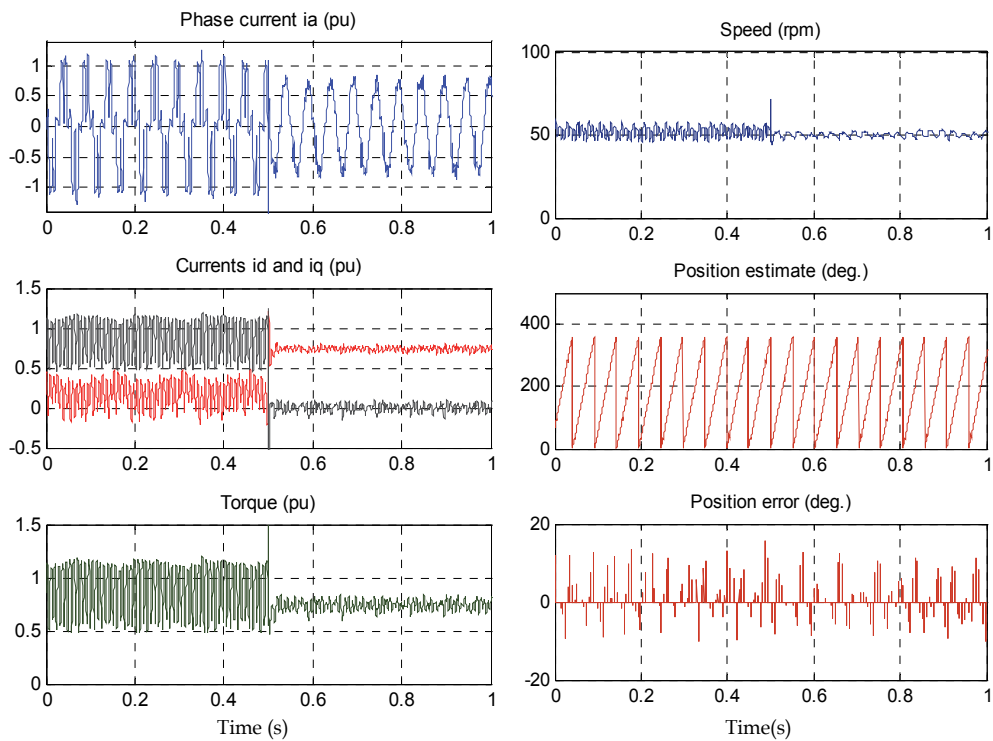


Fig. 11. Commutation from BLDCM mode to PMSM mode at 50 rpm.

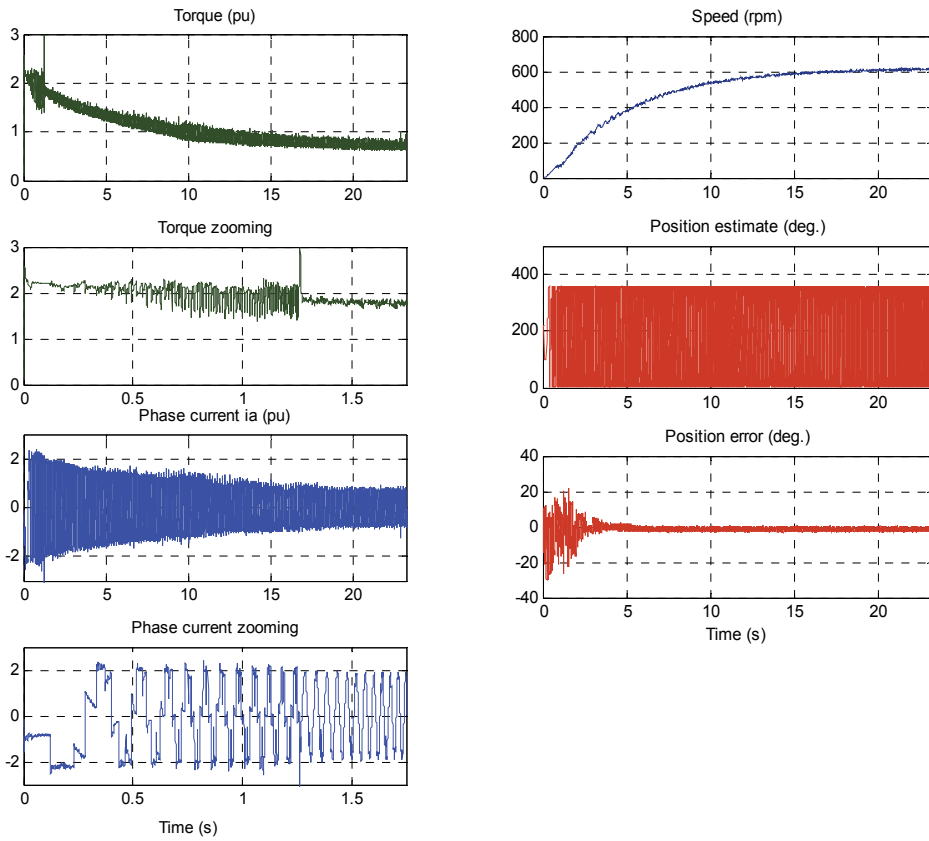


Fig. 12. Starting up with complete BLDCM/Sensorless PMSM control strategy.

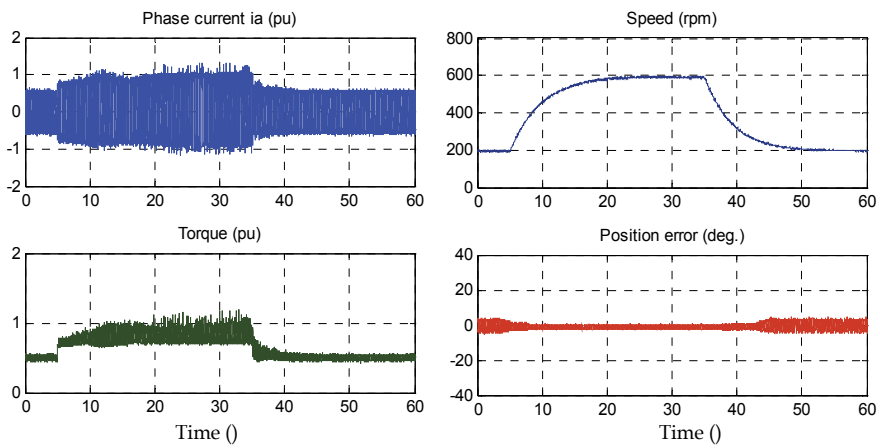


Fig. 13. Dynamic behavior of the drive in Sensorless PMSM control mode

6. Conclusion

The presented position and speed estimation technique is based on Hall-effect sensors and is dedicated to Electric Vehicle applications. The starting problem commonly encountered in such a field, is completely surmounted by using the Hall-effect pulses to start the machine as a BLDC Motor. Next, the Back-EMF based estimator in conjunction with Hall-effect sensors are used to achieve a very accurate estimation of the rotor position and speed for sensorless vector control of the motor in PMSM mode. That means the drive is not in need of special initial position detection or starting up technique.

The experimental results show that the presented sensorless estimation algorithm provides high accuracy rotor position and speed. There are three major advantages associated with the proposed method:

- Minor sensitivity to the motor parameters and electrical measurement imperfections. The refreshment of the position estimation at every Hall signal edge, eliminates any position error whichever origin induces it.
- Extra-load starting up capability, as the Hall-effect sensors provides enough information for proper BLDC operation.
- Low computation time requirement and high reliability; the algorithm can be easily implemented by a microcontroller or DSP.

7. References

- Batzel, T.D. & Lee, K. Y. (2005). Electric Propulsion with the Sensorless Permanent Magnet Synchronous Motor: Model and Approach, *IEEE Transaction on Energy Conversion*, Vol. 20, No. 4, (December 2005), pp. 818–825.
- Capponi, F. G.; De Donato, G.; Del Ferraro, L.; Honorati, O.; Harke, M. C. & Lorenz, R. D. (2006). AC Brushless Drive With Low-Resolution Hall-Effect Sensors for Surface-Mounted PM Machines, *IEEE Transaction on Industry Applications*, Vol. 42, No. 2, (March/April 2006), pp. 526-535.
- Capponi, G. ; De Donato, G. & Del Ferraro, L. (2004). Brushless AC Drive Using an Axial Flux Synchronous Motor with Low Resolution Position Sensors, *Proceeding of the IEEE 35th Annual Power Electronics Specialists Conference*, Vol. 3, pp. 2287-2292, Aachen, Germany, June 20-25, 2004.
- Carpaneto, M.; Maragliano, G.; Marchesoni, M. & Vaccaro, L. (2009). A New Sensorless Permanent Magnet Synchronous Motor Algorithm Based on Algebraic Method, *Proceeding of the 13th European Conference on Power Electronics and Applications*, pp. 1-10, Barcelona, Spain, September 8-10, 2009.
- Chau, K. T.; Chan, C. C. & Liu, C. (2008). Overview of Permanent-Magnet Brushless Drives for Electric and Hybrid Electric Vehicles, *IEEE Transaction on Industrial Electronics*, Vol. 55, No. 6, (June 2008), pp. 2246-2256.
- Chen, J.-L.; Liu, T.-H. & Chen, C.-L. (2010). Design and Implementation of a Novel High-Performance Sensorless Control System for Interior Permanent Magnet Synchronous Motors, *Electric Power Applications (IET)*, Vol. 4, No. 4, (April 2010), pp. 226-240.

- Cheng, K.-Y. & Tzou, Y.-Y. (2003). Design of a Sensorless Commutation IC for BLDC Motors, *IEEE Transaction on Power Electronics*, Vol. 18, No. 6, (November 2003), pp. 1365-1375.
- Emadi, A. (2005). *Handbook of Automotive Power Electronics and Motor Drives*, CRC Press-Taylor & Francis Group, ISBN: 0-8247-2361-9, USA.
- Genduso, F.; Miceli, R.; Rando, C. & Galluzzo, G. R. (2010). Back EMF Sensorless-Control Algorithm for High-Dynamic Performance PMSM, *IEEE Transaction on Industrial Electronics*, Vol. 57, No. 6, (June 2010), pp. 2092-2100.
- Gieras, J. F.; Rong-Jie Wang, R. J. & Kamper, M. J. (2004). *Axial Flux Permanent Magnet Brushless Machines*, Springer Science+Business Media B.V.-Kluwer Academic Publishers, ISBN: 1-4020-2661-7, Netherlands.
- Hanselman, D. C. (Second Edition, 2006). *Brushless Permanent Magnet Motor Design*, Magna Physics Publishing, ISBN: 1881855155, USA.
- Jain, M. & Williamson, S.S. (2009). Suitability Analysis of In-wheel Motor Direct Drives for Electric and Hybrid Electric Vehicles, *Proceeding of IEEE Electrical Power & Energy Conference*, pp 1-5, Montreal QC, Canada, October 22-23, 2009.
- Jingbo, L.; Nondahl, T.; Schmidt, P.; Royak, S. & Harbaugh, M. (2010). Equivalent EMF Based Position Observers for Sensorless Synchronous Machines, *Proceeding of the 25th Annual IEEE Applied Power Electronics Conference and Exposition*, pp. 425-432, Palm Springs, CA, February 21-25, 2010.
- Johnson, J. P.; Ehsani, M. & Guzelgunler, Y. (1999). Review of Sensorless Methods for Brushless DC, *Proceeding of IEEE Industry Application Society Annual Meeting*, Vol. 1, pp. 143-150, Phoenix, AZ, USA, October 3-7, 1999.
- Krishnan, R. (2010). *Permanent Magnet Synchronous and Brushless DC Motor Drives*, CRC Press-Taylor & Francis Group, ISBN: 978-0-8247-5384-9, USA.
- Morimoto, S.; Sanada, M. & Takeda, Y. (1996). Sinusoidal Current Drive System of Permanent Magnet Synchronous Motor with Low Resolution Position Sensor, *Proceeding of IEEE Industry Application Society Annual Meeting*, pp. 9-13, San Diego, CA, USA, October 6-10, 1996.
- Sungyoon, J.; Beomseok, L. & Kwanghee, N. (2010). PMSM Control Based on Edge Field Measurements by Hall Sensors, *Proceeding of the 25th Annual IEEE Applied Power Electronics Conference and Exposition*, pp. 2002-2006, Palm Springs, CA, USA, February 21-25, 2010.
- Yousfi, D. & El Adnani, M. (2007). PMSM Sensorless Control with Simple and Efficient Estimation Method, *Proceeding of the 7th International Conference on Power Electronics and Drive Systems*, Bangkok, Thailand, November 27-30, 2007.
- Yousfi, D. (2009). Encoderless PM Brushless Drive For Electric Vehicle Traction, *Proceeding of the 35th Annual Conference of the IEEE Industrial Electronics Society*, Porto, Portugal, November 3-5, 2009.
- Yousfi, D.; Ait Ouahman, A.; Elbacha A. & Boulghasoul Z. (2010). Combined BLDCM and Encoderless PMSM Control for Electric Hub Motor Drives, *Proceeding of the XIX International Conference on Electrical Machines*, Rome, Italy, September 6-8, 2010.

Hybrid Switched Reluctance Motor and Drives Applied on a Hybrid Electric Car

Qianfan Zhang, Xiaofei Liu, Shumei Cui, Shuai Dong and Yifan Yu
*Harbin Institute of technology
China*

1. Introduction

Electric machine is one of key parts in hybrid electric vehicles which affect dynamical and fuel consumption features and is the kernel to realize all kinds of strategy. Induction motor, PM synchronous motor, brushless DC motor, and switched reluctance motor are all applied in HEV. Traction motors for HEV are different from motors applied in industry. Load changes frequently and widely. Characteristics such as high maximum torque and maximum speed, high ratio of maximum speed to base speed usually larger than 4, high efficiency over whole work area, smaller volume and lighter weight with high power are demanded. Moreover, electric machine is usually installed on the chassis on which the environment is vibrative, dusty and moist. So characteristics of traction motors for HEV should be as follows, high power and torque density, extended speed range, high efficiency over whole working area, shockproof, waterproof, and dustproof.^[1] A novel hybrid switched reluctance motor drives are developed. With simple flux adjusting, large torque and high speed are achieved. With a coil stationary in the motor, rotor position is detected and speed is calculated.

The torque-speed characteristic curve and system efficiency map of the electric machinery applied on HEV are important items in power assembly test. The electric machinery will help to start the engine or the vehicle, assist to drive the vehicle, charge the battery and absorb the braking power or sometimes reverse the vehicle. So the electric machines often work in both motor and generator mode, and sometimes run both forward and reversal. It is to say that the working torque-speed area is distributed in 2 or 4 quadrants. The magnetic particle brake and electric eddy current load as in normal electric machinery test bed cannot work because they cannot drag the tested electric machinery. Some electrical dynamometer can do that kind of test. But with the unit of generating to the grid, the system is expensive. A bench is developed to test the motor drives. It is energy saving and no power flows to the grid.

2. Power train and control strategy of the hybrid electric car

Fig.1 shows the structure of drive assembly of hybrid electric car. There are 3 electric machineries, G/M, starter and M, in the figure. G/M is an integrated started and generator (ISG) which connects with the internal combustion engine (ICE) with belt. The starter is a standby one. The M, which is subject of the paper, is called main motor. It connects with the wheels through the final gear. The batteries are NiH batteries (288V, 10Ah).

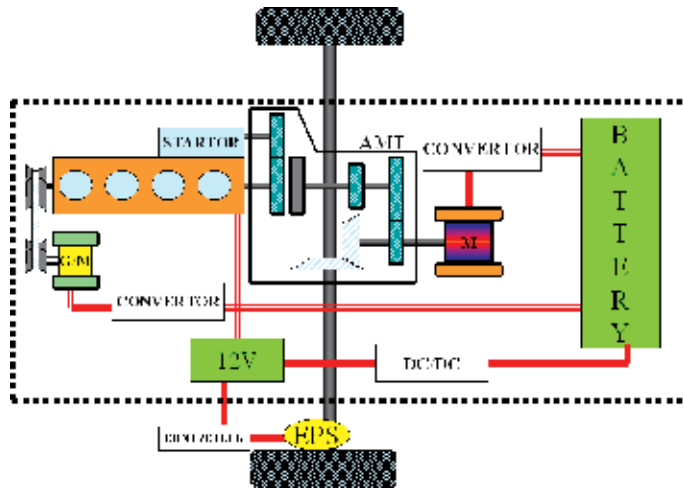


Fig. 1. Power assembly diagram of hybrid electric car

The hybrid electric car has 8 working modes: idle stop, ICE drive, motor drive, serial mode, parallel mode, serial & parallel mode, ICE drive & battery charge and regenerative brake. Fig.2 shows power flowing in 4 modes of them.

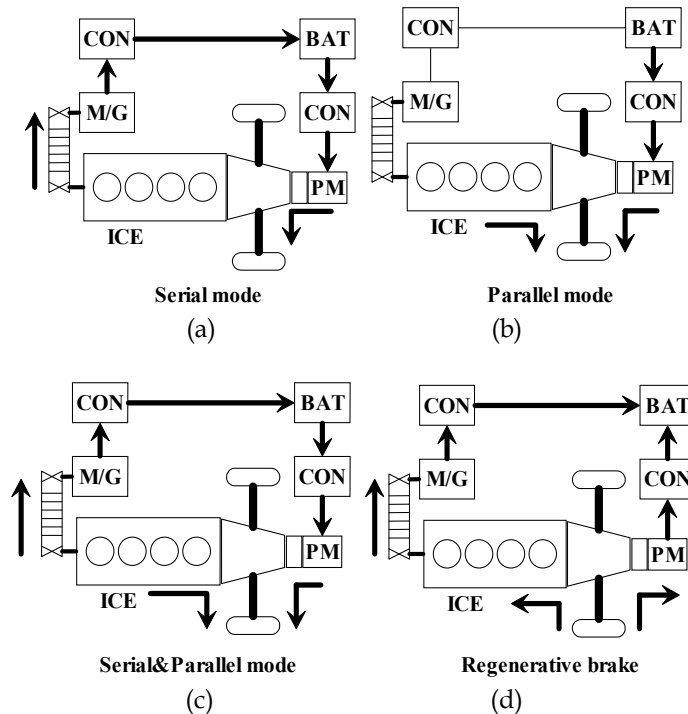


Fig. 2. Working modes and power flow route of hybrid electric car

ICE stops running when it is in idle running state and started in no more than 100ms by M/G to work again. The idle stop mode will eliminate fuel consume and emission in idle

running state. ICE drive mode is the same as the traditional car and will occur in most efficient working area of ICE. The motor drive mode is the same as the battery electric car and will occur in very low speed. In serial mode which is shown in Fig.2 (a), ICE drags M/G to charge the battery, and M drives the wheel. In parallel mode which is shown in Fig.2 (b), both ICE and M drive the wheel. It will occur when high output is needed. Serial & parallel mode is shown in Fig2 (c). When the state of charge (SOC) is low, ICE drags M/G to charge the battery and drives the wheels at the same time. In regenerative brake mode shown in Fig.2 (d), M/G and M work in generator mode to charge the battery. These will distinctly decrease the fuel consume

3. Operating points simulation of the electric machine

In order to design the speed and torque range of electric the machine, especially the base speed, the simulation based on vehicle drive mode and control strategy is developed on Simulink ADVISOR, an electric vehicle simulation software. Under the ECE-EUDC drive cycle, the working points of electric machinery are simulated. According to it, the base speed of the electric machinery is decided. The electric machinery drives system is designed according to the frequently working points. The main electric machinery is the subject of the paper. The design process of the M/G is the same.

According to the hybrid degree of this hybrid car, the power of M is 20kW; the maximum rotation speed is 5000rpm. According to the simulation, the large torque and low base speed electric machinery is fit for the car. The simulation results of two electric machineries with the same power are presented here. One with base speed of 1280rpm is called low base speed electric machinery. The other with base speed of 4000rpm is called high base speed one.

The basic parameters of the vehicle are shown in the Table 1.

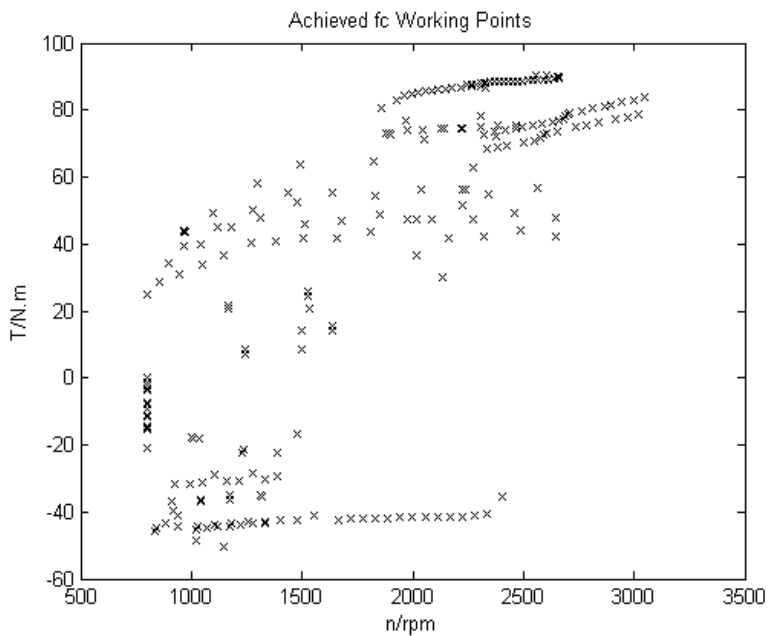
The power of 1.5l ICE is 43kW. The transmission is auto transmission. Power of G/M is 8kW. Table.2 shows the simulation results of ICE drive only, with high base speed electric machinery and with low base speed electric machinery. The simulation condition is the same. With the highest torque, the drive assembly with low base speed electric machinery obtains better dynamic performance. And its fuel consume is lower, because the ICE work in more efficient area. These can be found in simulated ICE working points under 1 ECE-EUDC cycle in Fig.3.

Mass/ kg	Coefficient of rolling resistance	Coefficient of aerodynamic drag C_d	Vehicle frontal area/ m^2	Wheel radius/m	Transmission efficiency
1655	0.00917	0.31	2.15P	0.301	0.92
1 st gear ratio	2 nd gear ratio	3 rd gear ratio	4 th gear ratio	Final gear ratio	
3.6	2.125	1.32	0.857	3.889	

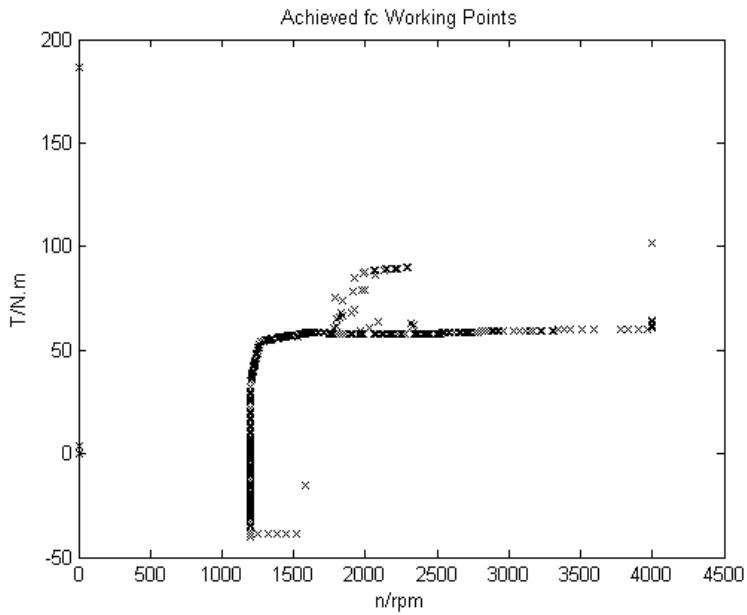
Table 1. Basic parameters of the vehicle

	Fuel consuming per 100km/l	0-96.6km/h acceleration rate/s	64.4-96.6km/h acceleration rate/s	Grade with speed of 88.5km/h
Only ICE drive	6.7	84	53.9	3.5%
With high base speed motor	6.1	33	10.9	5.7%
With low base speed motor	5.2	21.5	9.5	6.3%

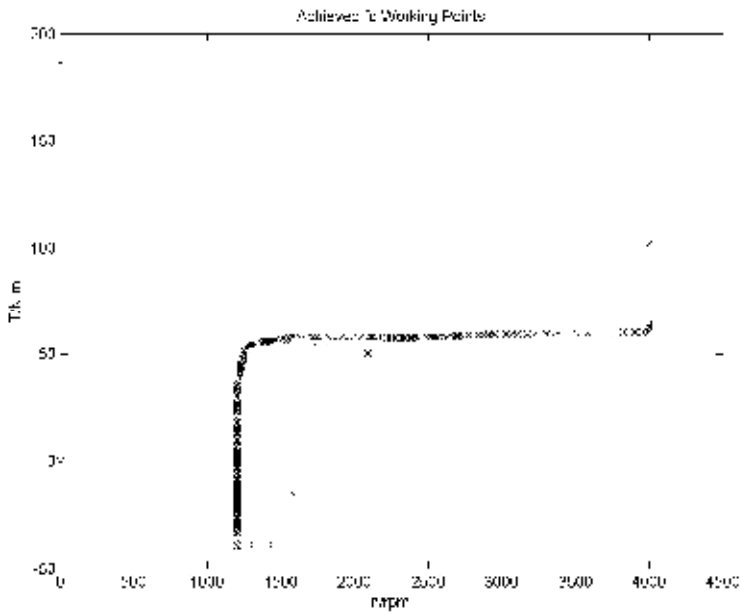
Table 2. Simulation result



(a) ICE working alone without any motors



(b) ICE working with high base speed main motor



(c) ICE working with low base speed main motor

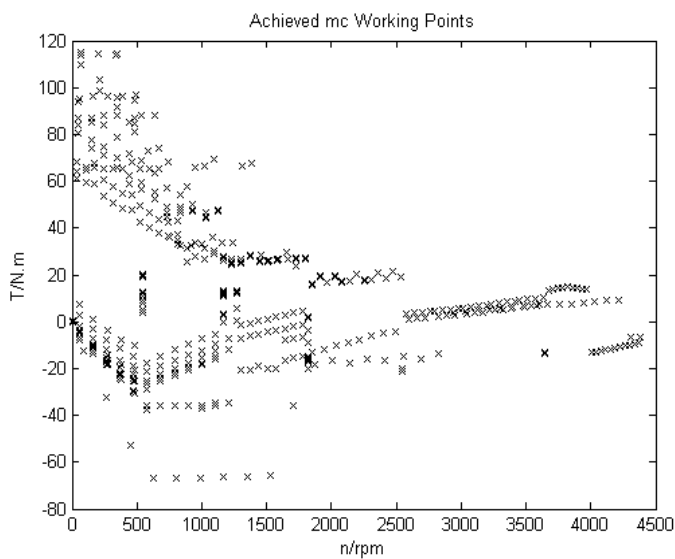
Fig. 3. Working points of ICE

Base on the simulation analysis and considering other factor, the parameter of the main electric machinery is as the data in table 3.

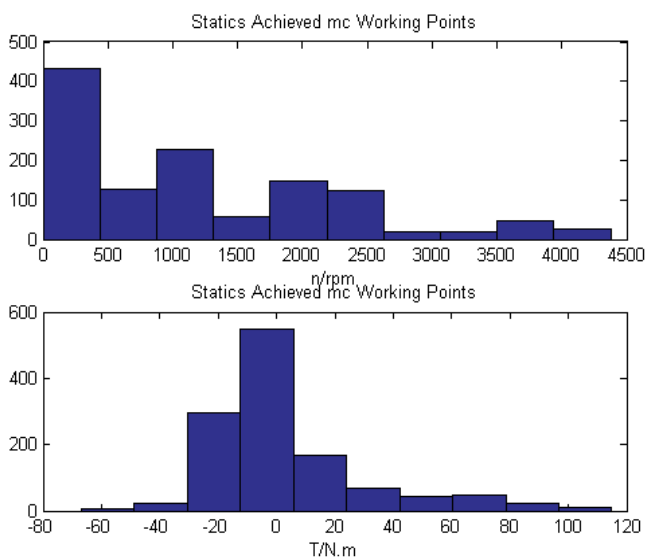
Power/kW	Max torque/ N.m	Rate torque/ N.m	Base speed/rpm
20	150	63	1280

Table 3. Parameters of the main electric machinery

During 1 ECE-EUDC cycle, the main electric machinery working points are shown in Fig.4. The drive system design will emphasize on frequently working points.



(a) Working points



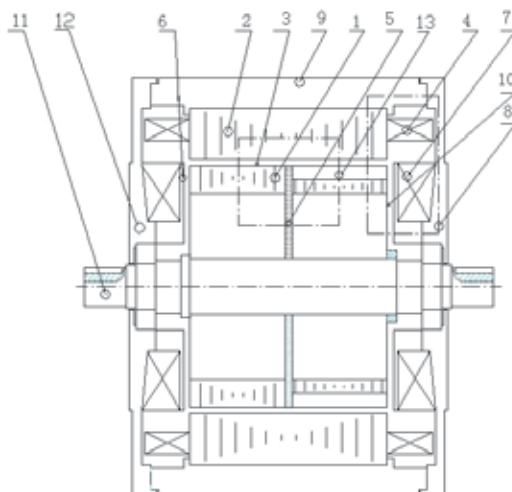
(b) Statistical data

Fig. 4. Working points of low base speed main motor during one ECE-EUDC cycle

4. Architecture and principle of the novel electric machine

According to the analysis above, a hybrid switched reluctance motor with flux adjustment is developed to obtain low base speed torque-speed features of the main motor. Hybrid switched reluctance motor is developed from Hybrid Stepper Motor. In the motor, there are axial excitation coils on both sides of end cover, which is different from HB stepper motor. These coils produce axial flux which is controlled to compensate and adjust PM flux.

A structure figure of a three-phase hybrid switched reluctance motor is shown in Figure 5. The motor consists of: rotor core 1, stator core 2, radial air gap 3, radial three phase excitation coil 4, axial magnetization permanent magnet 5, axial compensatory excitation coil core 6, axial compensatory excitation coil 7, magnetized end cover 8, magnetized housing 9, axial air gap 10, and axes 11. 12 indicates the path of flux produced by axial compensatory excitation coil and 13 indicates the path of PM flux. Except for 6, 7 and 10, the structure is same as HB stepper motor. Axial compensatory excitation coil and core are coaxial in line with PM through axial air gap. Controlling the value and direction of currents flowing in axial coil will compensate and adjust axial flux mainly produced by PM. Consequentially, the main flux is adjustable.



1 - rotor core, 2 - stator core, 3 - radial air gap, 4 - radial three phase excitation coil (armature), 5 - magnetization permanent magnet, 6 - axial compensatory excitation coil core, 7 - axial compensatory excitation coil, 8 - magnetized end cover, 9 - magnetized housing, 10 - axial air gap, 11 - axes, 12 - flux path produced by axial compensatory excitation coil, 13 - flux path produced by permanent magnet

Fig. 5. Structure figure of 3-phase axial excited hybrid reluctant motor

Like the three-phase hybrid HB stepper motor, there are six big poles on stator core 2. Radial coils 4 are wound on the pole. On the pole face, are several teeth. Rotor core 1 consists of two parts, core 1-1 and core 1-2. Permanent magnet 5 is laid between 1-1 and 1-2, it is magnetized in the direction of the axe. On the rotor core 1, are several teeth. Pitch is same as that of the stator teeth. Relative departure of centerline of teeth on 1-1 from that on 1-2 is half pitch. To the two neighborhood stator poles, relative departure of centerline of stator tooth from rotor tooth is different by one-third pitch. It means that, to one stator pole, the centerline of stator tooth aligns with that of the rotor tooth, and then on the neighborhood

stator pole, the centerline of stator tooth departs from that of rotor tooth by one-third pitch. Stator core 2 and rotor core 1 is connected by bearing, and the gap between 1 and 2 is the air gap 3.

The path of flux produced by PM is shown in Figure 5 by 13. Flux flows through rotor core 1-1, radial air gap 3, stator core 2, radial air gap 3 and rotor core 1-2. Path of flux produced by axial coils is shown in Figure 5 by 12. Flux flows through core 6, axial air gap 10, rotor core 1, radial air gap 3, stator core 2, magnetized housing 9 and magnetized end cover 8. Flux produced by three-phase coil 4 flows through stator pole body, radial air gap 3, rotor core 1, radial air gap 3, neighborhood stator pole body and yoke. MMF produced by 5, 7 and 4 constitutes hybrid space flux path. Commutating currents in three-phase coils 4 produces rotating space magnetic field and then motor will rotate. Controlling currents in axial coils and radial coils will adjust main flux in air gap.

5. Rotor position sensing

Consider the axial coil on the side of 1-1 in Fig.5. When current flows in the coil, main flux linking the coil is produced by coil itself and radial excitation coil on the stator poles. Because of the drop of MMF on the sheet gap of rotor core, the effect of flux by PM is weak. This effect is ignored in analysis. The equivalent circuit of flux path on side of 1-1 is shown in Figure 6.

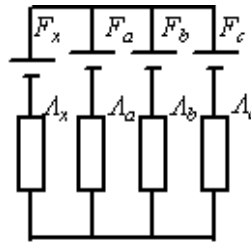


Fig. 6. Equivalent circuit of flux path on side of 1-1

Consider that MMF F_x , F_a , F_b and F_c apply respectively, then flux flows through Λ_x is Φ_0 , Φ_1 , Φ_2 , Φ_3 respectively, and

$$\begin{aligned}
 \Phi_0 &= \frac{F_x}{\frac{1}{\Lambda_x} + \frac{1}{\Lambda_a + \Lambda_b + \Lambda_c}} \\
 \Phi_1 &= \frac{F_a}{\frac{1}{\Lambda_a} + \frac{1}{\Lambda_x + \Lambda_b + \Lambda_c}} \cdot \frac{\Lambda_x}{\Lambda_x + \Lambda_b + \Lambda_c} \\
 \Phi_2 &= \frac{F_b}{\frac{1}{\Lambda_b} + \frac{1}{\Lambda_x + \Lambda_a + \Lambda_c}} \cdot \frac{\Lambda_x}{\Lambda_x + \Lambda_a + \Lambda_c} \\
 \Phi_3 &= \frac{F_c}{\frac{1}{\Lambda_c} + \frac{1}{\Lambda_x + \Lambda_b + \Lambda_a}} \cdot \frac{\Lambda_x}{\Lambda_x + \Lambda_b + \Lambda_a}
 \end{aligned} \tag{1}$$

It is DC current in axial coils, and three-phase AC current in radial coils. Only consider basic-frequency component of AC current, then

$$\begin{aligned} F_x &= NI_x \\ F_a &= NI \sin \omega t \\ F_b &= NI \sin \left(\omega t - \frac{2}{3} \pi \right) \\ F_c &= NI \sin \left(\omega t - \frac{4}{3} \pi \right) \end{aligned} \quad (2)$$

where

I maximum value of basic-frequency component current in radial excitation coil.
Ignore saturate effect, flux Φ linking axial coil is

$$\Phi = \Phi_0 + \Phi_1 + \Phi_2 + \Phi_3 \quad (3)$$

When (3) is substituted by (1) and (2), we obtain

$$\begin{aligned} \Phi &= \left(\Lambda_x - \frac{\Lambda_x^2}{\Lambda_x + 3\Lambda_0} \right) \cdot NI_x + \frac{3\Lambda_3 NI_x \Lambda_x^2}{(\Lambda_x + 3\Lambda_0)^2} \cos(3 \cdot \omega \cdot t) + \\ &\frac{3}{2} \frac{N\Lambda_x \Lambda_2 I}{(\Lambda_x + 3\Lambda_0)} \sin(3 \cdot \omega \cdot t) - \frac{9\Lambda_3 \Lambda_2 \Lambda_x NI}{4(\Lambda_x + 3\Lambda_0)^2} \sin(6 \cdot \omega \cdot t) \end{aligned} \quad (4)$$

From (4), we see that when 3-phase balance AC current flows in radial coils and DC current flows in axial coils, flux linking the axial coil consists of constant component and frequency components of value multiplied by 3.

EMF E in axial coil is

$$E = -N \frac{d}{dt} \Phi \quad (5)$$

Substitutes (5) by (4), we obtain

$$E = \frac{9}{2} \frac{N\Lambda_x \omega}{(\Lambda_x + 3\Lambda_0)^2} \left(\begin{array}{l} 2\Lambda_3 \Lambda_x I_x \sin(3 \cdot \omega \cdot t) - \\ N I \Lambda_2 (\Lambda_x + 3\Lambda_0) \cos(3 \cdot \omega \cdot t) + \\ 3\Lambda_3 \Lambda_2 NI \cos(6 \cdot \omega \cdot t) \end{array} \right) \quad (6)$$

Frequency component of EMF in axial coil is third order and the order multiplied by 3. It means that the axial coil can be the position sensor of rotor by detecting zero value of the signal.

6. Motor drives

6.1 Flux adjustment control method

Vector control is executed to achieve flux weakening control in permanent magnet synchronous motor. The current in the armature is resolved into direct axis current and

quadrature axis current. Controlling the direct axis current to produce anti-direction flux with main flux by magnetic pole, the flux weaken control is achieved. To the axial excited hybrid reluctance motor, flux-weakening control can be achieved by simply controlling the current magnitude in the axial exciting coil. The control is simplified. The following is the resolve of the torque and maximum speed of the motor. They theoretically show how the flux weakening and strengthening control of the motor is achieved.

The phase voltage equation of the 3-phase motor is

$$\begin{bmatrix} u_A \\ u_B \\ u_C \end{bmatrix} = R \begin{bmatrix} i_A \\ i_B \\ i_C \end{bmatrix} + \begin{bmatrix} L & M & M \\ M & L & M \\ M & M & L \end{bmatrix} \cdot \frac{d}{dt} \begin{bmatrix} i_A \\ i_B \\ i_C \end{bmatrix} + \frac{d}{dt} \begin{bmatrix} \psi_{Am} + \psi_{Az} \\ \psi_{Bm} + \psi_{Bz} \\ \psi_{Cm} + \psi_{Cz} \end{bmatrix} \quad (7)$$

Where u_A, u_B, u_C voltage of A, B, C phase,

i_A, i_B, i_C current of A, B, C phase,

R resistance of the coil,

L self-inductance of the coil,

M mutual inductance of the coil,

$\psi_{Am}, \psi_{Bm}, \psi_{Cm}$ magnet flux in A, B, C phase coils induced by permanent magnet,

$\psi_{Az}, \psi_{Bz}, \psi_{Cz}$ magnet flux in A, B, C phase coils induced by axial coil current.

Ignoring effect of the coil resistance, one phase voltage equation is

$$u = (L - M) \frac{di}{dt} + \frac{d}{dt} (\psi_m + \psi_z) \quad (8)$$

The vector equation is

$$\dot{U} = j\omega(L - M)\dot{I} + j\omega(\dot{\Psi}_m + \dot{\Psi}_z) \quad (9)$$

Let the current and voltage vector in the same phase angle, we get

$$U = \omega \sqrt{(L - M)^2 I^2 + (\Psi_m + \Psi_z)^2} \quad (10)$$

In the equation, $U = |\dot{U}|$, $I = |\dot{I}|$, $\Psi_m = |\dot{\Psi}_m|$, $\Psi_z = |\dot{\Psi}_z|$.

From (10),

$$I = \frac{1}{L - M} \sqrt{\frac{U^2}{\omega^2} - (\Psi_m + \Psi_z)^2} \quad (11)$$

When the voltage across the phase coil is the maximum value which power supply can outputs, the maximum speed of the motor is

$$n = \frac{30}{\pi \cdot Z_r} \frac{U}{\Psi_m + \Psi_z} \quad (12)$$

The magnet flux induced by axial exciting coil current is

$$\Psi_z = L_{zs} I_z \quad (13)$$

where L_{zs} mutual inductance between armature and axial exciting coils,
 I_z current flowing in the axial exciting coils.

From (12) and (13), we get

$$n = \frac{30}{\pi \cdot Z_r} \frac{U}{\Psi_m + L_{zs} I_z} \quad (14)$$

From (14), we can find that the maximum speed of the motor will increase if the I_z is negative. It means that when the magnet flux in the phase coil induced by the axial coil current is not in the same direction with that induced by the permanent magnet, the maximum speed of the motor increases. The flux weakening control is achieved. When the 3 phase coil currents are powered simultaneously, the electromagnetic torque is

$$T_{em} = \frac{3}{2} Z_r (\Psi_m + \Psi_z) I + \frac{3}{4} L_2 I^2 \quad (15)$$

From (11) and (15), we get

$$T_{em} = \frac{3}{2} \frac{Z_r (\Psi_m + L_{zs} I_z)}{L - M} \sqrt{\frac{U^2}{\omega^2} - (\Psi_m + L_{zs} I_z)^2} + \frac{3}{4} \frac{Z_r L_2}{(L - M)^2} \left(\frac{U^2}{\omega^2} - (\Psi_m + L_{zs} I_z)^2 \right) \quad (16)$$

where, Z_r number of teeth on rotor;
 Ψ_m flux linkage produced by permanent magnet;
 U voltage on armature;
 Ω rotation speed of the rotor;
 L_2 increment inductance.

The simulation result of torque-rotation speed curves under different axial coil current is shown in Figure 7. In the figure, the bigger the positive axial coil current is, the larger the maximum torque is. The bigger the negative axial coil current is, the higher the working speed with torque is. The electromagnetic torque is not printed in the figure. It is determined by the given maximum current of the armature. We can see that large torque during low speed and acceptable torque during high speed are achieved only by controlling the axial coil current (magnitude and direction).

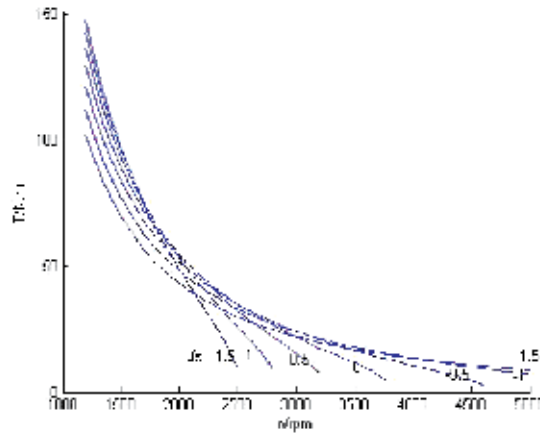


Fig. 7. Torque-rotation speed curve under different axial coil current I_z

In the simulation, the motor parameters are as shown in the table 4.

Λ_m/H	Λ_z/H	Λ_0/H	Λ_1/H	N	I_m/A	I_z/A
3.654×10^{-6}	7.792×10^{-6}	1.4625×10^{-5}	1.2922×10^{-5}	16	200	$43.75 \times I_{z0}$
D/mm	l/mm	Z_r	N_z			
250	130	16	700			

Table 4. Parameters of the type motor

In the table, Λ_m equivalent permeance of the permanent magnet,
 Λ_z equivalent permeance of the axial exciting coils,
 Λ_0 permanent value of main air gap permeance,
 Λ_1 fundamental value of main air gap permeance
 D Diameter of the motor,
 l length of the motor,
 N_z turns of the axial exciting coils,
 I_{z0} axial coil current,

6.2 Principle of hybrid switched reluctance motor drives

As a main motor in hybrid drive train, torque control is needed in the motor drives. Motor executes the positive torque command in motoring mode and negative torque in regenerative braking and generating mode. When the rotor speed is high, the flux weakening control is needed with limited battery voltage across DC bus. We can control the electromagnetic torque according to equation (16) in the hybrid switched reluctance motor drives.

In order to control the electromagnetic torque according to equation (16), two conditions are needed, which is

1. Vector EMF and current in each armature are in the same angle phase;
2. Current in three phases are powered simultaneously at every time.

We control three phase armature current as shown in Fig.8. The signal in the axial coils can be modulated into sinusoidal signal with frequency three times of that of the armature EMF. The zero detect pulse of this signal is applied to control the armature current as shown in Fig.8. Two conditions above are satisfied.

Motor drive is developed. The torque control motor drive block diagram of it is shown in Fig.9. Sensor processing section processes the axial coil signal and works as a rotor position and speed sensor. Only controlling the magnitude and direction of the current in the axial exciting coils, the flux strengthening (giving positive current to the axial exciting coils) and flux weakening (giving negative current to the axial exciting coils) control are realized. When large torque is needed, as starting the vehicle immediately, flux strengthening control is executed. Flux weaken control is executed when charging the battery in high speed. The armature current and EMF keep in the same angle phase.

Simple armature current commutation and axial coil flux adjusting control are developed to achieve large torque and high speed. The control block diagram is shown in figure 9.

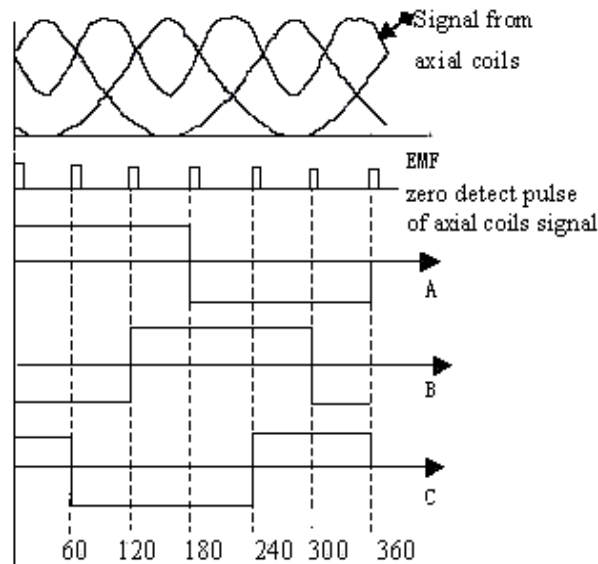


Fig. 8. Diagram of the current control

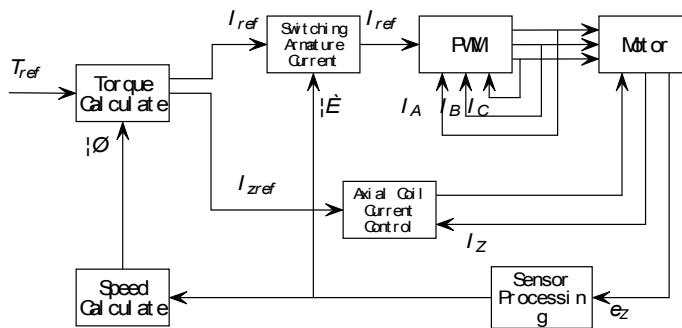


Fig. 9. Block diagram of motor drive control

7. Experiment validation

7.1 Experiment setup

The block diagram is shown in the figure 10 to test motor drives in the lab. An electric machine is controlled to simulate load. AC grid, instead of battery, powers motor drives in the lab. The bus voltage value of tested motor drive is 288V as in so many EV and HEV. So the voltage of load converter is AC220V. The tested converter and load converter are common DC bus. When tested electric machinery works as a motor, the load electric machinery works as a generator which generates electric power to drive the tested machinery through DC bus, whereas, the tested electric machinery generates power to drive the load machinery. Power flows on the DC bus between the tested and load sides. The power consume is the loss of both the tested system and the load system.

The output power, torque and rotation speed of the tested electric machinery are measured by torque speed sensor. The electric power, AC voltages and currents, and DC voltage and current are measured by the digital power meter.

The speed and torque reference to both the tested and load converter are produced by the computer. All of measured data are acquired by the computer, too. The tested curves are outputted by the post procedure very quickly.

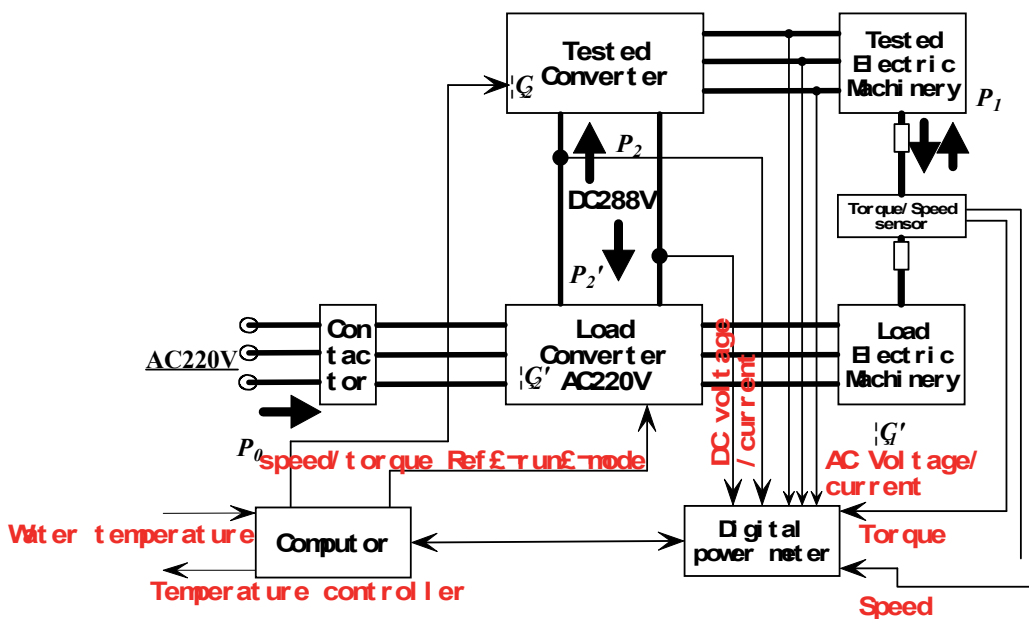
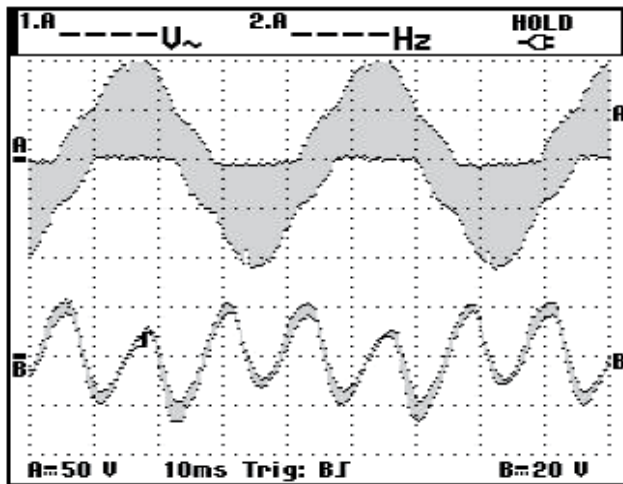


Fig. 10. Block diagram of the test system

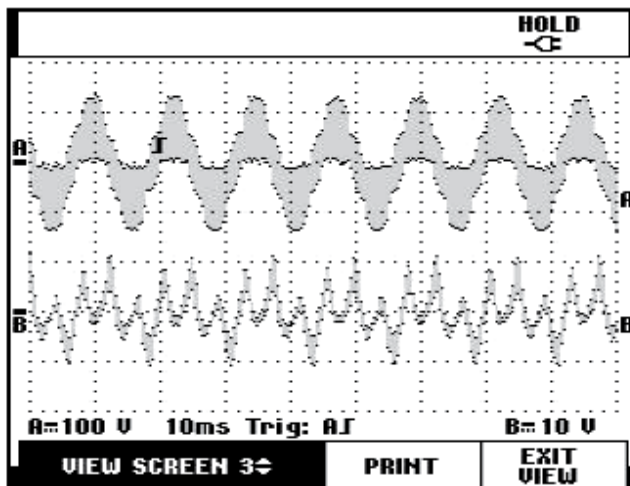
7.2 Results

Fig.11, Fig.12 and Fig.13 are the measured wave form of armature EMF (upper one) and axial coil EMF when rotor speeds are 300 rpm, 1200rpm and 2400rpm. It is seen that there are 6 zero points in the axial coil EMF signal corresponding in 1 cycle of armature EMF signal which can be the commuted signals to drive motor.



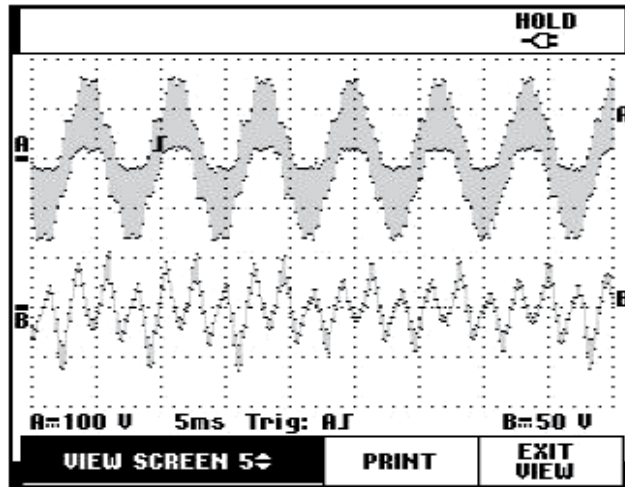
(B: Axial coil EMF, A: Armature EMF)

Fig. 11. Measured wave form of axial coil emf and armature emf when 300rpm



(B: Axial coil EMF, A: Armature EMF)

Fig. 12. Measured wave form of axial coil emf and armature emf when 1200rpm



(B: Axial coil EMF, A: Armature EMF)

Fig. 13. Measured wave form of armature EMF and axial coil EMF when 2400rpm

Fig.14 is torque-speed characteristic and efficiency map of the motor drives. Large torque and high speed are obtained by flux adjusting control.

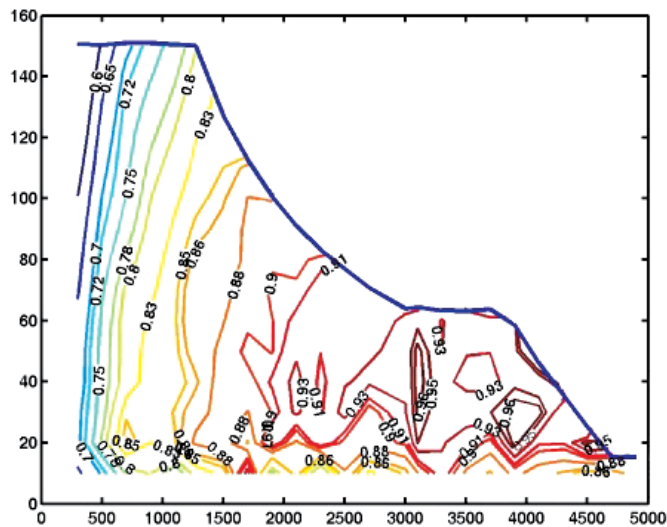


Fig. 14. Efficiency map of the motor drives

8. Conclusion

Demands of motor drive for a Mid-size hybrid electric car are analyzed by simulation. A novel hybrid switched reluctance motor drive is developed which is suitable for applying in electric vehicles. Frequency of EMF in axial coil is three times of that of terminal voltage over one phase of radial coil, and is three times of that of EMF in radial coil. It means that the axial coil can be the position sensor of rotor. Simple flux adjusting control is developed to achieve large torque and high speed. An energy saving test bed is developed. With applying the common DC bus technique, 4-quadrant electric machinery drive characteristic testing is done simply without regenerative power to power grid.

9. Acknowledgment

This research is supported by Natural Scientific Research Innovation in Harbin Institute of Technology (HIT. NSRIF. 2009042) and Scientific Research Foundation for Returned Scholars by Harbin Science and Technology Bureau (RC2009LX007004).

10. References

- [1] Z. Q. Zhu, David Howe. Electrical Machines and Drives for Electric, Hybrid, and Fuel Cell Vehicles. Proceedings of the IEEE, 2007, 95(4):746-765.
- [2] Avoki M. Omekanda. A New Technique for Multidimensional Performance Optimization of Switched Reluctance Motors for Vehicle Propulsion. IEEE Transactions on Industry Applications. 2003, 39(3): 672-676
- [3] Teven E. Schulz, Khwaja M. Rahman. High-Performance Digital PI Current Regulator for EV Switched Reluctance Motor Drives. IEEE Transactions on Industry Applications. 2003,39(4): 1118-~1126
- [4] Wei Cai, Pragasen Pillay, Zhangjun Tang. Low-Vibration Design of Switched Reluctance Motors for Automotive Applications Using Modal Analysis. IEEE Transactions on Industry Applications. 2003, 39(4): 971~977
- [5] Cheng Shukang, Zheng Ping, Cui Shumei et al. Fundamental Research on Hybrid-magnetic-circuit multi-couple Electric Machine, Proceedings of the CSEE, vol.20, no. 4, pp.50-58, 2000.
- [6] Zheng Ping, Cheng Shukang. Mechanism of Hybrid- Magnetic-circuit multi-couple Motor. Journal of Harbin Institute of Technology, 2000, E-3(3), pp.66-69.
- [7] Zheng Ping, Liu Yong, Wang Tiecheng et al. Theoretical and Experimental Research on Hybrid-magnetic-circuit Multi-couple Motor. Seattle, USA: 39th IAS Annual Meeting, 2004.
- [8] Zhang Qianfan, Cheng Shukang, Song Liwei et al. Axial Excited Hybrid Reluctant Motor Applied in Electric Vehicles and Research of its Axial Coil Signal. Magnetics, IEEE Transactions, 2005, 41(1), pp.518-521.
- [9] Pei Yulong, Zhang Qianfan, Cheng Shukang. Axial and Radial Air Gap Hybrid Magnet Circuit Multi-coupling Motor and Resolution of Motor Electromagnetic Torque. Power system technology, 2005, supplement.
- [10] Zhang, Qian-Fan; Pei, Yu-Long; Cheng, Shu-Kang. Position sensor principle and axial exciting coil EMF of axial and radial air gap hybrid magnet circuit multi-coupling

motor. Proceedings of the Chinese Society of Electrical Engineering, v 25, n 22, Nov 16, 2005, p 136-141

- [11] Zhang Qianfan, Chai Feng, Cheng Shukang, C.C. Chan. Hybrid Switched Reluctance Integrated Starter and Generator. Vehicle Power and Propulsion Conference VPP 2006. September 6-8, 2006. Windsor, UK.

Mathematical Modelling and Simulation of a PWM Inverter Controlled Brushless Motor Drive System from Physical Principles for Electric Vehicle Propulsion Applications

Richard A. Guinee
*Cork Institute of Technology,
Ireland*

1. Introduction

High performance electric motor drive systems are central to modern electric vehicle propulsion systems (Emadi et al. , 2003) and are also widely used in industrial automation (Dote, 1990) in such scenarios as numerical control (NC) machine tools and robotics. The benefits accruing from the application of such drives are precision control of torque, speed and position which promote superior electric vehicle dynamical performance (Miller, 2010) with reduced greenhouse carbon gaseous emissions resulting in increased overall automotive efficiencies. These electric motor drive attributes also contribute to enhanced productivity in the industrial sector with high quality manufactured products. These benefits arise from the fusion of modern adaptive control techniques (El Sarkawi, 1991) with advances in motor technology, such as permanent magnet brushless motors, and high speed solid-state switching converters which constitute the three essential ingredients of a high performance embedded drive system. The controllers of these machine drives are adaptively tuned to meet the essential requirements of system robustness and high tracking performance without overstressing the hardware components (Demerdash et al, 1980; Dawson et al, 1998). Conventional d.c. motors were traditionally used in adjustable speed drive (ASD) applications because torque and flux control were easily achieved by the respective adjustment of the armature and field currents in separately excited systems where fast response was a requirement with high performance at very low speeds (Vas, 1998). These dc motors suffer from the drawback of a mechanical commutator assembly fitted with brushes for electrical continuity of the rotor mounted armature coil which increases the shaft inertia and reduces speed of response. Furthermore they require periodic maintenance because of brush wear which limits motor life and the effectiveness of the commutator for high speed applications due to arcing and heating with high current carrying capacity (Murugesan, 1981).

Brushless motor drive (BLMD) systems, which incorporate wide bandwidth speed and torque control loops, are extensively used in modern high performance EV and industrial motive power applications as control kernels instead of conventional dc motors. Typical high performance servodrive applications (Kuo, 1978; Electrocraft Corp, 1980) which require high torque and precision control, include chemical processing, CNC machines, supervised

actuation in aerospace and guided robotic manipulations (Asada et al, 1987). This is due largely to the high torque-to-weight ratio and compactness of permanent magnet (PM) drives and the virtually maintenance free operation of brushless motors in inaccessible locations when compared to conventional DC motors. These PM machines are also used for electricity generation (Spooner et al, 1996) and electric vehicle propulsion (Friedrick et al, 1998) because of their higher power factor and efficiency. Furthermore the reported annual World growth rate of 25% per annum (Mohan, 1998) in the demand for of all types of adjustable speed drives guarantees an increased stable market share for PM motors over conventional dc motors in high performance EV and industrial drive applications. This growth is propelled by the need for energy conservation and by technical advances in Power Electronics and DSP controllers.

The use of low inertia and high energy Samarium Cobalt-rare earth magnetic materials in PM rotor construction (Noodleman, 1975), which produces a fixed magnetic field of high coercivity, results in significant advantages over dc machines by virtue of the elimination of mechanical commutation and brush arcing radio frequency interference (RFI). These benefits include the replacement of the classical rotor armature winding and brush assembly which means less wear and simpler machine construction. Consequently the PM rotor assembly is light and has a relatively small diameter which results in a low rotor inertia. The rotating PM structure is rugged and resistant to both mechanical and thermal shock at high EV speeds. Furthermore high standstill/peak torque is attainable due to the absence of brushes and high air-gap flux density. When this high torque feature is coupled with the low rotor inertia extremely high dynamic performance is produced for EV propulsion due to rapid acceleration and deceleration over short time spans. The reduction in weight and volume for a given horsepower rating results in the greatest possible motor power-to-mass ratio with a wide operating speed range and lower response times thus makes PM motors more suitable for variable speed applications. Greater heat dissipation is afforded by the stationary machine housing, which provides large surface area and improved heat transfer characteristics, as the bulk of the losses occur in the stator windings (Murugesan, 1981). The operating temperature of the rotor is low since the permanent magnets do not generate heat internally and consequently the lifetime of the motor shaft bearings is increased.

There are three basic types of PM motor available depending on the magnetic alignment and mounting on the rotor frame. The permanent magnet synchronous motor (PMSM) behaves like a uniform gap machine with rotor surface-mounted magnets. This magnetic configuration results in equal direct d -axis and quadrature q -axis synchronous inductance components and consequently only a magnetic torque is produced. If the PM magnets are inset into the rotor surface then salient pole machine behaviour results with unequal d and q inductances in which both magnetic and reluctance torque are produced. A PMSM with buried magnets in the rotor frame also produces both magnetic and reluctance torque. There are three types of PM machine with buried magnetic field orientation which include radial, axial and inclined interior rotor magnet placement (Boldea, 1996). Brushless motor drives (Hendershot et al, 1994; Basak, 1996) are categorized into two main groups based on (a) current source inverter fed BLMD systems with a trapezoidal flux distribution (Persson, 1976) and (b) machines fed with sinusoidal stator currents with a sinusoidal air-gap flux distribution (Leu et al, 1989).

BLMD systems also have a number of significant operational features in addition to the above stated advantages, that are key requirements in high performance embedded drive applications, by comparison with conventional dc motor implementations which can be summarized as follows:

- i. DC motor emulation is made possible through electronic commutation of the PM synchronous motor three phase stator winding in accordance with sensed rotor position (Demerdash et al, 1980; Dohmeki, 1985).
- ii. In addition to (i) pulse-width modulation (PWM) (Tal, 1976), which is generally used in brushless motor inverter control as the preferred method of power dispatch as a form of class S amplification (Kraus et al, 1980), provides a wide range of continuous power output. This is much more energy efficient than its linear class A counterpart in servo-amplifier operation.
- iii. BLMD systems have a linear torque-speed characteristic (Murugesan, *ibid*) because of the high PM coercivity which ensures fixed magnetic flux at all loads. If the PMSM is fed by a current controlled voltage source inverter (VSI) then the instantaneous currents in the stator winding are forced to track the reference values determined by the torque command or speed reference.
- iv. Direct torque drive capability with higher coupling stiffness and smooth torque operation at very low shaft speeds, without torque ripple, is feasible without gears resulting in better positional accuracy in EVs.

The decision as to the eventual choice of a particular drive type ultimately depends on the embedded drive system application in terms of operational drive performance specification, accessible space available to house the physical size of the motor, and to meet drive ventilation requirements for dissipated motor heating. The decision will also be influenced by operational efficiency consideration of embedded drive power and torque delivery and the required level of accuracy needed for the application controlled variable be it position, velocity or acceleration.

Consideration of the benefits of using PM motors in high performance electric vehicle (EV) propulsion illustrates the need for an accurate model description (Leu et al, *ibid*) of the complete BLMD system based on internal physical structures for the purpose of simulation and parameter identification of the nonlinear drive electrodynamics. This is necessary for behavioural simulation accuracy and performance related prediction in feasibility studies where new embedded motor drives in EV systems are proposed. Furthermore an accurate discrete time BLMD simulation model is an essential prerequisite in EV optimal controller design where system identification is an implicit feature (Ljung, 1991, 1992). Concurrent with model development is the requirement for an efficient optimization search strategy in parameter space for accurate extraction of the system dynamics. Two important interrelated areas where system modelling with parameter identification plays a key role in controller design and performance for industrial automation include PID auto-tuning and adaptive control. PID auto-tuning (Astrom et al, 1989) of wide bandwidth current loops in torque controlled motor drives make it possible to speed EV commissioning and facilitate control optimization through regular retuning by comparison with the manual application of the empirical Ziegler-Nichols tuning rule using transient step response data. Typical methods employed in auto-tuner PID controllers (Astrom et al, 1988, 1989; Hang et al, 1991) are pattern recognition and relay feedback, which is the simplest. Implementation of the self oscillating relay feedback method in the current loops of a brushless motor drive is difficult and complex because of internal system structure and connectivity with three phase current (3Φ) commutation. Proper selection of the PID term parameters in PID controller setup, from dynamical parameter identification, is necessary to avoid significant overshoot and oscillations in precision control applications (Sarkawi, *ibid*). This is dependent to a great

extent on an accurate physical model of the nonlinear electromechanical system (Krause et al, 1989) including the PWM controlled inverter with substantial transistor turnon delay as this reflects the standard closed loop drive system configuration and complexity during normal online operation. Motor parameter identification, based on input/output (I/O) data records, enable suitable PID settings to be chosen and subsequent overall system performance can be validated from model simulation trial runs with further retuning if necessary. Auto-tuning can also be used for pre-tuning more complex adaptive structures such as self tuning (STR) and model reference adaptive systems (MRAS). The method of identification of EV motor drive shaft load inertia and viscous damping parameters, based on the chosen physical model of BLMD operation, is one of constrained optimization in such circumstances. This is a minimization search procedure manifested in the reduction of an objective function, generally based on the least mean squares error (MSE) criterion (Soderstrom, 1989) as a penalty cost measure, in accordance with the optimal adjustment of the model parameter set. The objective function is expressed as the mean squared difference, for sampled data time records, between actual drive chosen output (o/p) as the target function and its model equivalent. This quadratic error performance index, which provides a measure of the goodness of fit of the model simulation and should ideally have a paraboloidal landscape in parameter hyperspace, may have a multim minima response surface because of the target data used making it difficult to obtain a global minimum in the search process. The existence of a stochastic or 'noisy' cost surface, which results in a proliferation of 'false' local minima about the global minimum, is unavoidable because of model complexity and depends on the accuracy with which inverter PWM switching instants with subsequent delay turnon are resolved during model simulation (Guinee et al, 1999). Furthermore the number of genuine local minima, besides cost function noise, is governed by the choice of data training record used as the target function in the objective function formulation which in the case of step response testing with motor current feedback is similar to a sinc function profile (Guinee et al, 2001). The cost function is, however, reduced to one of its local minima during identification, preferably in the vicinity of its global minimizer, with respect to the BLMD model parameter set to be extracted. The presence of local minima will result in a large spread of parameter estimates about the optimum value with model accuracy and subsequent controller performance very much dependent on the minimization technique adopted and initial search point chosen. Besides adequate system modelling there is thus a need for a good identification search strategy (Guinee et al, 2000). over a noisy multim minima response surface.

Adaptive control of dc servomotors rely on such techniques as Self Tuning pole assignment [Brickwedde, 1985; Weerasooriya et al, 1989; El-Sharkawi et al, 1990], Model Reference [Naitoh et al, 1987; Chalam, 1987] and Variable Structure Control (VSC) (El-Sharkawi et al, 1989) for preselected trajectory tracking performance in guidance systems and robustness in high performance applications. This is in response to changing process operating conditions (El-Sharkawi et al, 1994) typified by changing load inertia in robots, EVs and machine tools. The essential feature of adaptation is the regulator design (Astrom et al, *ibid*), in which the controller parameters are computed directly from the online input/output response of the system using implicit identification of the plant dynamics, based on the principle of general minimum variance control in the two former methods with slide mode control implementation in VSC. Although no apriori knowledge of the physical nature of the systems dynamics is required, identification in this scenario relies on the application of

black box linear system modelling of the motor and load dynamics. This modelling strategy is based on a general family of transfer function structures (Ljung, 1987; Johansson, 1993) with an ARMAX model being the most suitable choice (Dote, *ibid*; Ljung, *ibid*). The parameter estimates of the model predictor are then obtained recursively from pseudolinear regression at regular intervals of multiple sampling periods. This type of modelling approach is particularly suitable for conventional dc machine drives because of their near linear performance with constant field current despite the complex DSP solution of the adaptive controller. However the PM motor drive, in contrast, is essentially nonlinear both in terms of its operation electrodynamically (Krause, 1986, 1989) and in the functionality of the switching converter where considerable dead time is required in the protective operation of the power transistor bridge network. When the state space method is employed in this case, as in for example variable structure tracking control, a considerable degree of idealization is introduced in the linearization of the model equations about the process operating point, which are essentially nonlinear, for controller design. The above modelling schemes therefore suffer from the drawback of not adequately describing nonlinearities encountered in real systems and are thus inaccurate. Furthermore in high performance PM drive applications, characterized by large excursion and rapid variation in the setpoint tracking signal, other nonlinearities such as magnetic saturation, slew rate limitation and dead zone effects are encountered in the dynamic range of operation. Effective modelling of the physical attributes of a real PM drive system (Guinee et al, 1998, 1999) is a therefore necessary prerequisite for controller design accuracy in high performance BLMD applications.

1.1 Objectives

This chapter is concerned with the presentation of a detailed model of a BLMD system including PWM inverter switching operation with dead time (Guinee, 2003). This model can then be used as an accurate benchmark reference to gauge the speed and torque performance characteristics of proposed embedded BLMD systems via simulation in EV applications. The decomposition of BLMD network structure into various subsystem component entities is demonstrated (Guinee et al, 1998). The physical modelling procedure of the individual subsystems into linear functional elements, using Laplacian transfer function synthesis, with non linearities described by difference equations is explained. The solution of the model equations using numerical integration techniques with very small step sizes (0.5% of PWM period T_s) is discussed and the application of the regula-falsi method for accurate resolution of natural sampled PWM edge transitions within a fixed time step is explained. Very accurate simulation traces are produced, based on step response transients, for the BLMD in torque control mode which has wide bandwidth configuration, when compared with similar test data for a typical BLMD system. BLMD model accuracy is further amplified by the high correlation of fit of unfiltered current feedback simulation waveforms with experimental test data, which exhibit the presence of high frequency carrier harmonics associated with PWM inverter switching. Model validation is provided with a goodness of fit measure based on motor current feedback (FC) using frequency and phase coherence. A novel delay compensation technique, with zener clamping of the triangular carrier waveform during PWM generation, is presented for simultaneous three-phase inverter dead time cancellation which is verified through BLMD waveform simulation (Guinee, 2005, 2009).

2. Mathematical modelling of a BLMD system

In this chapter an accurate mathematical model for high performance three phase permanent magnet motor drive systems, including interaction with the servoamplifier power conditioner, based on physical principles is presented (Guinee et al, 1999) for performance related prediction studies in embedded systems, through comparison with actual drive experimental test data for model fidelity and accuracy, and for subsequent dynamical parameter identification strategies where required. The BLMD system (Moog GmbH, 1988, 1989), which is modelled here as an example, can be configured for either torque control operation or as an adjustable speed drive in high performance EV applications (Emadi et al, *ibid*; Crowder, 1995). The motor drive incorporates two feedback loops for precision control with (a) a fast tracking high gain inner current loop, which forces the stator winding current equal to the required torque demand current via pulsewidth modulation and (b) an outer velocity loop for adjustable speed operation of the motor drive shaft in high performance applications.

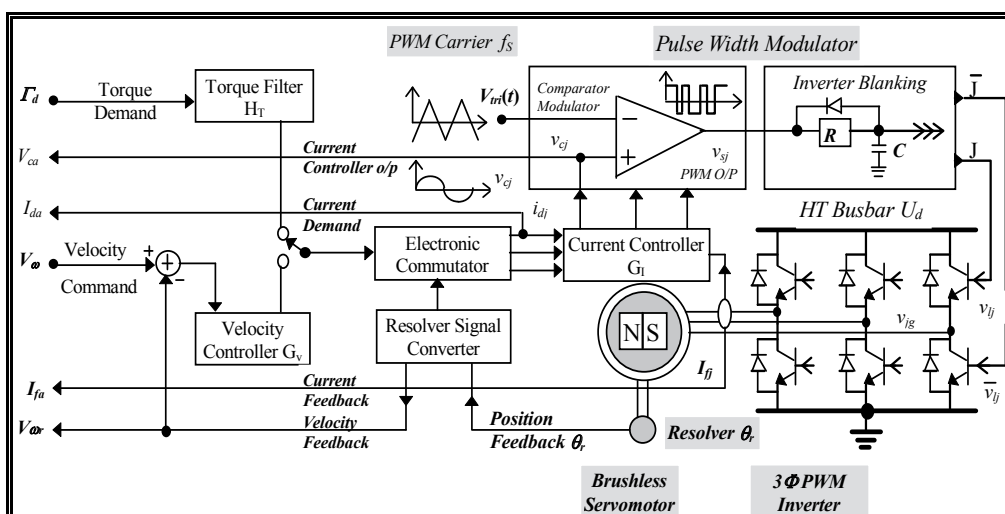


Fig. 1. Network structure of a typical brushless motor drive system (Guinee et al, 1999)

When configured for adjustable speed drive (ASD) operation the outer BLMD velocity loop of low bandwidth encloses the inner wideband current loop and tends to partially obscure its operation as a result of outer loop coupling. It is for this reason that the BLMD is initially modelled with a separate torque loop, uncoupled from the outer velocity feedback loop, for complete visibility of its high frequency PWM current control loop operation. The most difficult aspect of the BLMD modelling exercise for torque control operation that has to be addressed concerns the simulation of the current controlled PWM output voltage, from the three phase inverter to the motor stator windings, with sufficient accuracy to incorporate the effects of inverter dead-time. This issue arises when the modulating control signal to the pulsewidth modulator is non deterministic during the transient phase of motor operation for random step changes in command input that may occur during normal online operation of the embedded drive in industrial applications eventhough the modulation employed is sinusoidal PWM. It could be argued that a simplified model of the PWM process is adequate in this instance in that only the low frequency filtered components of current feedback and speed are

necessary, since these are uncoupled from the actual PWM process except for the dead time, for accurate BLMD simulation with minimal run time. This simplified low frequency model strategy, based on the fundamental component of the PWM process, can only be used when there is negligible inverter delay and is the approach that is adopted in such circumstances for simulation purposes as the 'average' BLMD model. The presence of inverter dead time, however, requires additional BLMD model processing in that the current flow direction must be checked in each phase, during every PWM switching period, in order to determine whether a delay pulse or correction term is to be added or subtracted to the fundamental signal components. Consequently the modulated pulse edge transitions have to be accurately known to include the exact instances of fixed delay triggering of the basedrives controlling power transistor inverter ON/OFF switching. Once a satisfactory BLMD model of sufficient functional accuracy has been generated and 'mapped' to an actual embedded drive system, through parameter identification of the motor dynamics, the addition of the outer velocity control loop can then be completed in a holistic BLMD model for ASD simulation. Correlation accuracy of this complete model with an actual ASD is established through subsequent step response simulation and comparison with experimental shaft velocity test data.

Power Supply Unit (Moog Series - T157)	
Power o/p = 18 kW	
3 Φ rms Voltage i/p $U_s = 220$ V	
DC Voltage o/p $U_d = 310$ V _{DC}	
Motor Controller Unit (Moog Series - T158)	
Current o/p $I_c = 15$ A Continuous, 30 A Peak	
Motor Controller Optimizer [MCO-402B]	Lag Compensator: $K=19.5$, $\tau_a = 225\mu s$, $\tau_b = 1.5ms$
Max. Motor Speed $n_{max} = 10,000$ RPM	Inverter Transistor Blanking $\delta = 20\mu s$
Transistor Switching Frequency $f_s = 5$ kHz	Current Loop Bandwidth = 3 kHz
Brushless 1.5kW PM Servomotor (Moog Series - D314...L20)	
Continuous Stall Torque $M_O = 5.0$ Nm	Peak Torque $M_{max} = 15$ Nm
Continuous Stall Current $I_O = 9.3$ A	Nominal Speed ($U=310$ V) $n_n = 4000$ rpm
Mass without Brake $m = 5.1$ kg	Rotor Inertia $J = 2.8$ kg.cm ²
Mass Factor $M_O/m = 0.98$ Nm.kg ⁻¹	Dynamic Factor $M_O/J = 19,000$ s ⁻²
Volume Factor $M_O/V = 2.8$ Nm.m ⁻³	No. PM Rotor Pole Pairs $p = 6$
Torque Constant $K_T = 0.32$ Nm.A ⁻¹	Calculation Factor 1.5 $K_T = 0.48$ Mm.A ⁻¹
Motor Terminal Resistance $R_{tt} = 1.5$ Ω	Motor Terminal Inductance $L_{tt} = 3.88$ mH
Mech. Time Constant $\tau_m = 1$ ms	Elec. Time Constant $\tau_e = 2.6$ ms

Table I. Moog BLMD System Component Specification

The motor drive system (Moog GmbH, *ibid*), used as the focus of investigation in the mathematical development of the BLMD system based on physical principles, is shown in Figure 1 and is typical of most high performance PM motor drives available. This drive system is required for verification and validation of the BLMD modelling process at critical internal observation nodes through comparison of experimental test results with model simulation runs for accuracy. The servomotor system consists of a Power Supply Unit, Motor Controller Unit and a PM brushless motor with component specification details as summarised in Table I. The BLMD system, that is modelled here, has a considerable inverter dead time (20 μs) by comparison with the nominal PWM switching period (200 μs). Each phase of the motor stator winding has a separate PWM current controller with a 20 μs inverter delay for

protection from current 'shoot through'. This delay, which is dependent on the direction of winding current flow, is manifested as a reduction in the overall modulated pulsewidth voltage supply to the stator winding and developed motor drive torque. If the current flow is directed into the phase winding then there is a reduction of $20\mu\text{s}$ at the leading edge of the modulated pulsewidth and if the current flow is negative an extension of $20\mu\text{s}$ is appended at the trailing edge of the modulated pulse. An accurate model of the BLMD system must account for the presence of such a delay. During simulation of the BLMD model the current flow direction has to be sensed to determine whether a fixed $20\mu\text{s}$ delay pulse is to be subtracted from or added to the modulated pulse duration. Detailed evaluation of the width modulated pulse edge transition times is required for accurate BLMD modelling in such circumstances in torque control mode to ensure numerical accuracy of PWM inverter simulation and subsequent positioning of the inverter trigger delay associated with the large dead time present. This is afforded by the use of small step sizes ($\sim 0.5\%T_s$) by comparison with the overall PWM switching period (T_s) and application of the regula-falsi iterative search method (Press et al, 1990) during BLMD simulation. Model accuracy is guaranteed through numerical waveform simulation, which is shown to give excellent agreement in terms of correlation with BLMD experimental test data at critical observation nodes for model fidelity purposes. Consequently the BLMD model can be used for the specific purpose of accurate simulation of circuit functionality within an actual typical EV motor drive system with special emphasis on the inner torque loop as it embraces the PWM motor current control operation with inverter delay during rapid EV acceleration.

2.1 Overall system description

The 1.5 kW motor drive system, used as the subject of this BLMD modelling procedure, has the component block diagram sketched in Figure 2. This system is an electronic self commutated, PM synchronous machine (Tomasek, 1979), which is sinusoidally controlled (Tomasek, 1986) and is typical of most high performance PM motor drives available. The BLMD consists of a Power Supply Unit (PSU), Motor Controller Unit (MCU) and a Brushless Servomotor with specification details itemized in Table I. The PSU converts the matched three phase (3Φ), $220V_{\text{rms}}$ mains supply (U_s) into a full wave rectified stiff 310 volt dc supply (U_d) with 18kW continuous power output thus permitting multiple motor controller connection. A large smoothing capacitor maintains a constant dc link voltage which provides a low impedance dc source for voltage-fed inverter operation. The PSU can also fitted with an external dynamic braking resistor which bleeds excess energy from the DC busbar U_d during motor regeneration when the ASD is overhauled by the rotor mechanical load. This resistor prevents overcharging of the filter capacitor and thus a rise in the DC link voltage during rapid deceleration. The MCU contains the following functional elements, as depicted in Figure 3, which are essential for proper operation of the brushless servomotor: (a) Power converter, (b) PWM modulator, (c) Current controller, (d) 3Φ commutator, (e) Velocity controller and (e) Circuit protection.

This provides brushless motor commutation and subharmonic PWM power control with a 30 Amp continuous output (o/p) current per phase to facilitate peak motor torque. The controller outputs a synthesized variable frequency and variable amplitude 3Φ sinusoidal current which accurately controls motor speed (n) and torque (Γ). This is facilitated by a configuration of six Darlington transistor-diode switches which form the three-leg inverter amplifier shown in Figure 1.

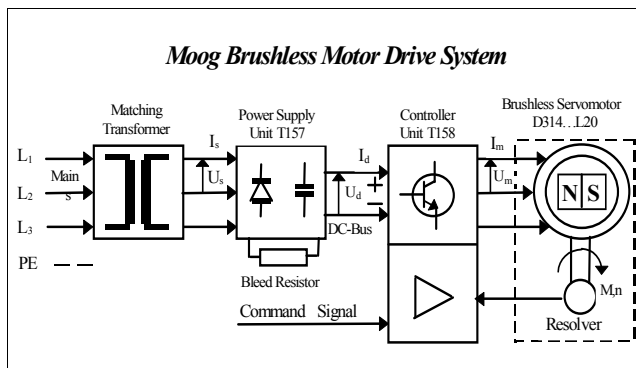


Fig. 2. Typical BLMD system components (Moog, 1989)

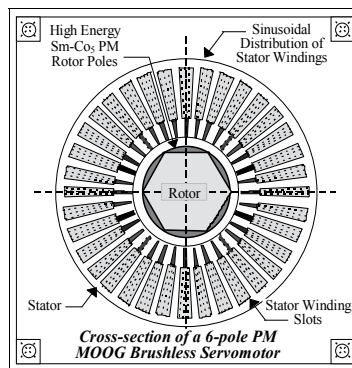


Fig. 4. Motor cross section

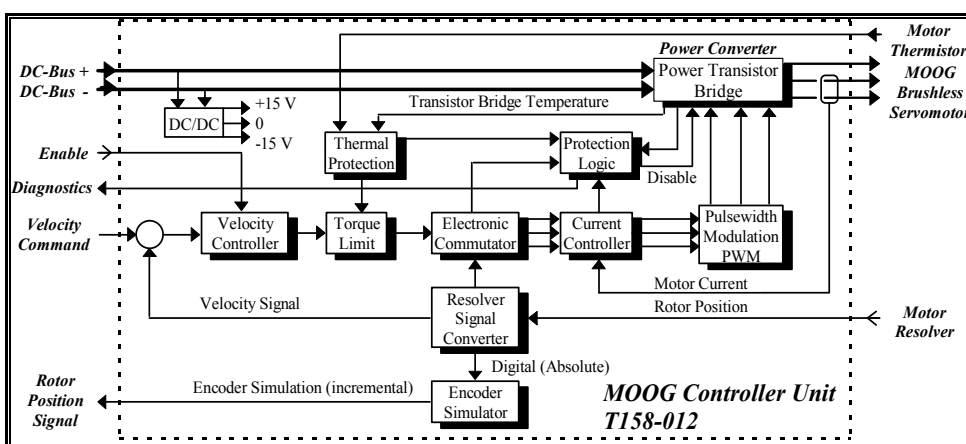


Fig. 3. Block schematic of a typical BLMD controller module

The brushless motor consists of a 12-pole PM rotor, a wound multiple pole stator, a 2-pole transmitter type pancake resolver and a ntc thermistor embedded in the stator end turns with a typical cross-section sketched in Figure 4. Stator current is provided by a 3Φ power cable with a protective earth while a signal cable routes rotor position information from the pancake resolver located at the rear side of the motor structure. The outer motor casing (stator) houses the 3Φ stationary winding in a lamination stack. The Y-connected floating neutral winding is embedded in slots around the air gap periphery with a sinusoidal spatial distribution. This has the effect of producing a time dependent rotating sinusoidal MMF space wave centred on the magnetic axes of the respective phases, which are displaced 120 electrical degrees apart in space. The inner member (rotor) contains the Samarium-Cobalt magnets, which have a high holding force with an energy product of 18 MGO_e (Demerdash et al, 1980), in the form of arc segments assembled as salient poles on an iron rotor structure. The fixed radially directed magnetic field, produced by the rotor magnets, is held perpendicular to the electromagnetic field generated by the stator coils and consequently yields maximum rotor torque for a given stator current. This stator-to-rotor vector field interaction is achieved by electronic commutation, which processes rotor position information from the shaft resolver to provide a balanced three phase sinusoidal stator current. The high peak torque achievable, which is

about eight to ten times the rated torque for Sm-Co₅ PM motors (Tomasek, 1983), and low rotor inertia J result in high dynamic motor performance which is evident from the large dynamic factor given in Table I. A high continuous torque-to-volume ratio is achieved due to the high pole number in the motor stator.

2.1.1 General features of a typical BLMD system

A network structure for this BLMD system, showing the functional subsystems and their interconnection into an overall organizational pattern, is illustrated in Figure 1A. This provides indication of the type and complexity of model required as the first step in the development of a comprehensive and accurate model for embedded system parameter identification and EV performance evaluation. The dynamic system consists of an inner current loop for torque control and an outer velocity loop for motor shaft speed control each of which can be individually selected according to the control operation required. The major functional elements of the system are:

- a. a velocity PI control governor G_V for wide bandwidth speed tracking. This compares the velocity command V_ω with the estimated motor shaft velocity V_{ω_r} from the resolver-to-digital converter (RDC) and from which an optimized velocity error signal e_v is derived.
- b. a torque demand filter H_T with limiter for command input Γ_d slew rate limitation and circuit protection in the event of excessive temperature in the motor winding and MCU baseplate.
- c. a phase generation ROM lookup table which issues sinewaves corresponding to position of the rotor magnetic pole. The phase angles are determined, with angular displacement of 120 degrees apart, from the RDC position θ_r for current vector $I(t)$ commutation
- d. a 3 Φ commutation circuit for generation of variable frequency and variable amplitude phase sequence current command signals. The command amplitudes are determined by mixing the velocity error or torque demand with the phase generator output using an 8-bit multiplying Digital-to-Analog Converter (DAC).
- e. current command low pass filtering H_{DI} for high frequency harmonic rejection.
- f. current controllers G_I which close a wide bandwidth current loop around three phases of the motor winding in response to the filtered commutator current output. Current feedback sensing from the stator windings is accomplished through Hall Effect Devices (HED) which is then filtered (H_{FI}) to remove unwanted noise.
- g. a 3 Φ pulse width modulator giving an output set of amplitude limited ($\pm V_S$) switching pulse trains to drive the inverter power transistor bridge. The pulse aperture times are modulated by the error voltages from the respective phase current controllers when compared with a fixed frequency triangular waveform $v_{tri}(t)$.
- h. RC delay networks which provide a fixed delay δ , related to the turn-off time of power transistors, between inverter switching instants. These "lockout" circuits are necessary during commutation of the inverter power transistors to avoid dc link short circuit with current "shoot-through".
- i. a six step inverter which consists of the PWM controlled three-leg power transistor bridge and the base drive circuitry which include the switch delay networks. As the motor rotates the commutation logic switches over the power transistor bridge legs via the base drive circuits in a proper sequence. During a given commutation interval the power transistor bridge is reduced to one of the three possible (a-b, a-c, b-c) two-leg configurations. The PWM pulse trains are effectively amplified to the dc bus voltage supply U_d before application to the three phase motor stator windings.

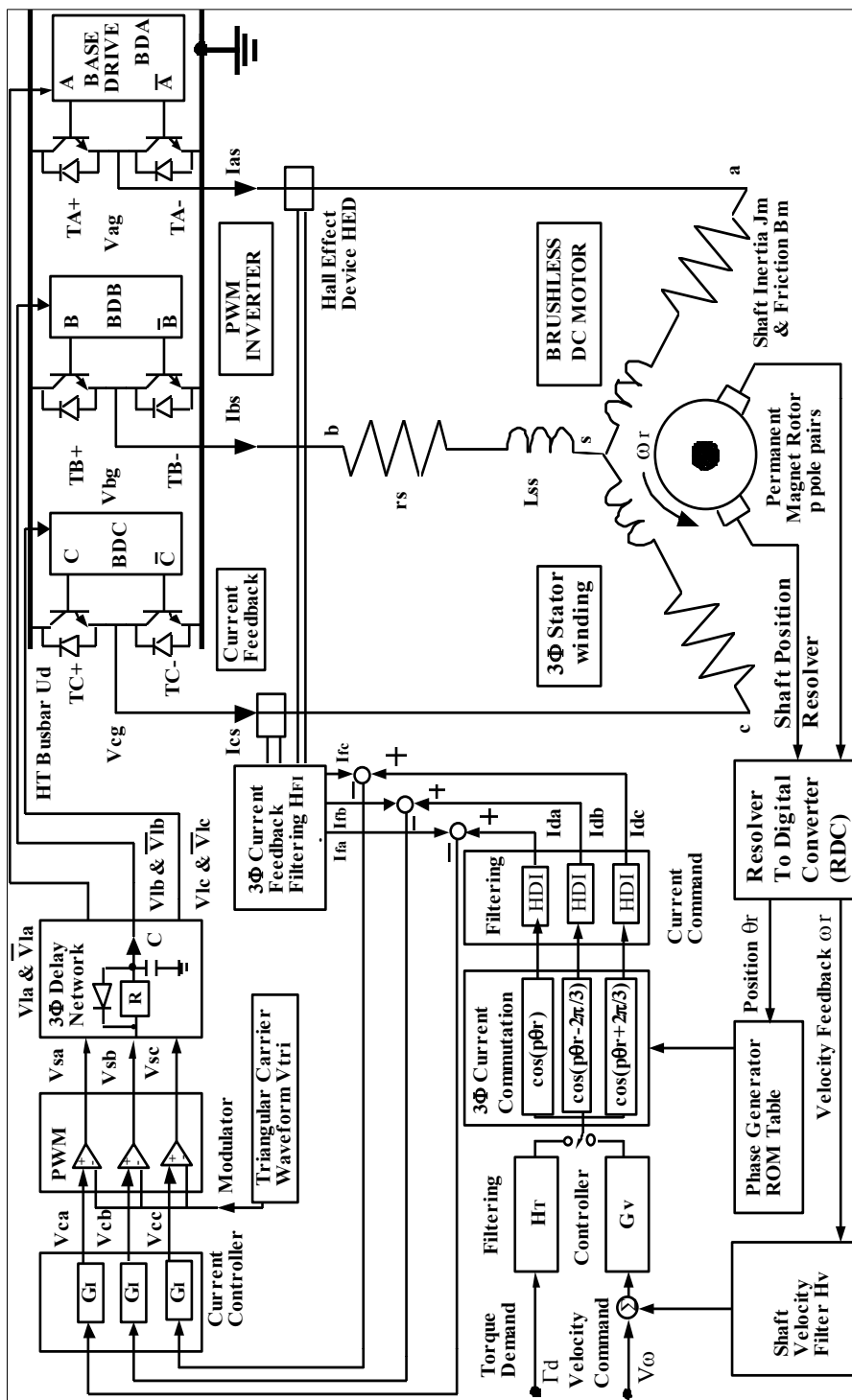


Fig. 1A. Network structure of a typical brushless motor drive system (Guinee, 1998)

- j. an RDC (Figure 1A) which provides a 12 bits/rev natural binary motor shaft position signal, with the 10MSB's used for motor commutation, and an analogue linear voltage signal proportional to motor speed ω_r . The estimated speed signal is subsequently filtered to give a velocity tracking signal $V\omega_r$ which can be used for motor tuning via G_V and performance evaluation.
- k. a shaft velocity filter H_V for speed signal noise reduction before feeding to the velocity controller.
- l. three phase motor with a high coercivity permanent magnet rotor.

2.2 Mathematical behavioural model of BLMD system

The behaviour of the BLMD system can be ascertained from physical principles in terms of its electromechanical operation during energy conversion. The system operation is described in terms of its Kirchhoff's law voltage equations and electromagnetic torque which are derived in subsequent sections. These equations can be used to

- a. develop a complete mathematical model for the BLMD system whereby its performance can be evaluated
- b. understand and analyse the electromechanical energy conversion process in the PM motor and
- c. in system design techniques and optimization for specific requirements.

The result is a set of nonlinear equations describing the dynamic performance of the BLMD system. The 3Φ motor stator windings are \mathbf{Y} connected and are sinusoidally distributed with an angular separation of $2\pi/3$ radians, associated with the mechanical location of the phase coils, as illustrated in Figure 4. The rotor consists of p pairs of permanent magnet pole face slabs, anchored to the solid steel shaft, which provide a sinusoidal magnetic flux distribution vector $\Lambda(\theta_r)$ in the air gap between the rotor and stator. If the PM pole face geometry admits to a nonuniform air gap then the reluctance variation, due to the effects of rotor saliency, as a function of rotor position is generally considered in the evaluation of the stator winding inductances. The effects of rotor saliency as shown in Figure 5, where the a_s , b_s , c_s and d axes denote the positive direction of the magnetic axes of the symmetrical windings and PM poles in stationary (s) and rotating (r) coordinate reference frames, will be included initially as a generalization of the analytical model of the BLMD system.

2.2.1 Stator winding flux linkages and inductances

Angular displacements can be referred to either the rotor or stator frames as shown in Figure 5 with the interrelationship

$$\phi_s = \phi_r + \theta_r \quad (I)$$

where ϕ_s and θ_r are the respective stator and rotor angular displacements referred to the \mathbf{a}_s axis. The air-gap MMF space vector for the 3Φ distributed stator winding, with N_s equivalent coil turns per phase, can be written in terms of the space angle $p\phi_s$ around the air gap periphery as

$$\mathfrak{F}_s(\phi_s, t) = \begin{bmatrix} \mathfrak{F}_{as} \\ \mathfrak{F}_{bs} \\ \mathfrak{F}_{cs} \end{bmatrix} = \left(\frac{N_s}{2p}\right) \begin{bmatrix} i_{as} \cos(p\phi_s) \\ i_{bs} \cos(p\phi_s - \frac{2\pi}{3}) \\ i_{cs} \cos(p\phi_s + \frac{2\pi}{3}) \end{bmatrix} \quad (II)$$

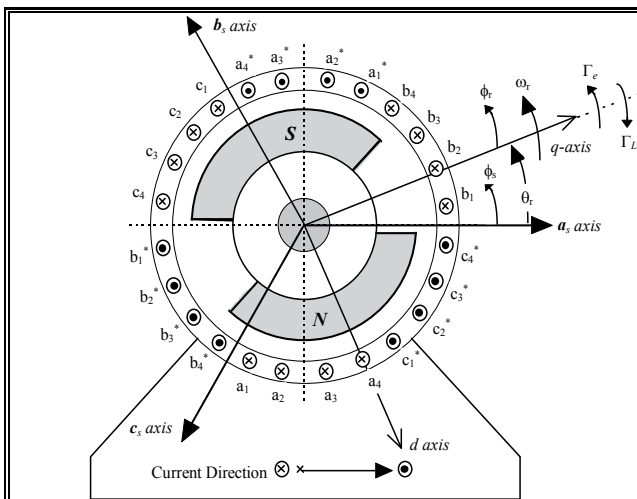


Fig. 5. Salient 2-pole synchronous PM Motor with non-uniform air gap (Guinee, 2003)

The MMF standing wave, which is wrapped around the air gap periphery, is effectively produced by a sinusoidally distributed current sheet located on the inner stator circumference as shown in Figure 6 for phase-a. The standing space wave components are modulated by the time varying balanced 3Φ stator current, with electrical angular frequency ω_e , represented by

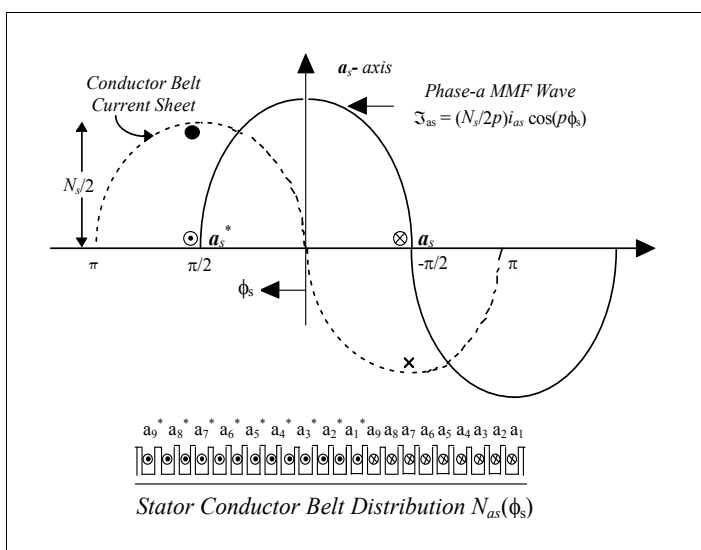


Fig. 6. Phase-a MMF standing space wave

$$\mathbf{I}_s(t) = \begin{bmatrix} i_{as}(t) \\ i_{bs}(t) \\ i_{cs}(t) \end{bmatrix} = \begin{bmatrix} I_m \cos(\omega_e t) \\ I_m \cos(\omega_e t - \frac{2\pi}{3}) \\ I_m \cos(\omega_e t + \frac{2\pi}{3}) \end{bmatrix} \quad (III)$$

These pulsating standing waves, with amplitudes proportional to the instantaneous phase currents and directed along the magnetic axes of the respective phases, produce a travelling MMF_s wave that rotates counterclockwise about the air gap as a set of magnetic poles given by

$$\mathfrak{F}_s(\phi_s, t) = \left(\frac{3}{2}\right) \left(\frac{N_s}{p} I_m\right) \cos(\omega_e t - p\phi_s) \quad (\text{IV})$$

with synchronous speed

$$\frac{d\phi_s}{dt} = \frac{\omega_e}{p} = \omega_r \quad (\text{V})$$

The motor shaft also rotates at synchronous speed with the result that the stator MMF is stationary with respect to the rotor. The length of the air gap $g(\phi_r)$ between the rotor and stator changes with rotor position ϕ_r which for a $2p$ -pole rotor, using Figure 5, is given by $g(\phi_r) = (\alpha_1 - \alpha_2 \cos(2p\phi_r))^{-1}$ with upper and lower bound limits given as $(\alpha_1 + \alpha_2)^{-1} \leq g \leq (\alpha_1 - \alpha_2)^{-1}$. Consequently this affects the reluctance of the flux path with a cyclic variation that occurs $2p$ times during one period of revolution of the rotor. As a result of reluctance variation, the inductances of the stator windings change periodically with PM pole rotation. The net magnetic flux in the motor air gap can be regarded as a combination of that due to the rotating armature MMF and a separate independent PM polar field contribution. The effect of armature reaction MMF on the magnitude and distribution of the air gap flux in a PM motor can be controlled by altering the winding current using an electronic converter which is self-synchronized by a shaft position sensor as in a BLMD system. The corresponding flux density radial vector $B_s(\phi_s, \theta_r)$ contributions in the air gap can be determined from the MMF for each phase acting separately due to its own current flow, using Amperes's magnetic circuit law, as

$$\mathbf{B}_s(\phi_s, \theta_r) = \begin{bmatrix} B_{as} \\ B_{bs} \\ B_{cs} \end{bmatrix} = \frac{\mu_0}{g(p\phi_s - p\theta_r)} \begin{bmatrix} \mathfrak{F}_{as} \\ \mathfrak{F}_{ab} \\ \mathfrak{F}_{cs} \end{bmatrix} \quad (\text{VI})$$

The flux linkage $\Phi_s(\phi_s, \theta_s)$ of a single turn of a stator winding, which spans π radians with angular orientation ϕ_s from the a_s axis, can be determined by integration (Krause, *ibid*) as

$$\Phi_s(\phi_s, \theta_r) = \int_{\phi_s}^{\phi_s + \pi/p} \mathbf{B}_s(\xi, \theta_r) r l d\xi \quad (\text{VII})$$

over the cylindrical surface defined by the air gap mean radius r and axial length l . The flux linkage of an entire stator phase winding, due to its own current flow, can be determined from integration over all turns of a conductor belt with sinusoidal distribution $N_s(\phi_s)$ given by

$$\mathbf{N}_s(\phi_s) = \begin{bmatrix} N_{as} \\ N_{bs} \\ N_{cs} \end{bmatrix} = \left(\frac{N_s}{2p}\right) \begin{bmatrix} \sin(p\phi_s) \\ \sin(p\phi_s - \frac{2\pi}{3}) \\ \sin(p\phi_s + \frac{2\pi}{3}) \end{bmatrix} \quad (\text{VIII})$$

If linear magnetic structures are assumed for non saturated stator conditions the flux linkage for phase-a, with similar calculations for the other two phases, is given by

$$\begin{aligned}\lambda_{asas} &= L_{ls}i_{as} + p \int_0^{\pi/p} N_{as}(\phi_s) \Phi_{as}(\phi_s, \theta_r) d\phi_s \\ &= L_{ls}i_{as} + \left(\frac{N_s}{2p}\right)^2 p\pi\mu_0 rl \left(\alpha_1 - \frac{\alpha_2}{2} \cos(2p\theta_r)\right) i_{as}\end{aligned}\quad (IX)$$

where L_{ls} is the leakage inductance. The second term in (IX), when divided by the current i_{as} , defines the phase-a winding self inductance

$$L_{asas} = L_{ss} - L_G \cos(2p\theta_r) \quad (X)$$

with $L_{ss} = \left(\frac{N_s}{2p}\right)^2 p\pi\mu_0 rl \alpha_1$ and $L_G = \frac{1}{2} \left(\frac{N_s}{2p}\right)^2 p\pi\mu_0 rl \alpha_2$. This consists of the nominal inductance L_{ss} as the default value for round rotor geometry and the variable air gap reluctance contribution which pulsates with amplitude L_G with rotor position. Similar self inductance expressions can be deduced for the other two phases, by allowing for the 120° phase displacement in the air gap reluctance contribution, as

$$\begin{aligned}L_{bsbs} &= L_{ss} - L_G \cos 2(p\theta_r - \frac{2\pi}{3}) \\ L_{cscs} &= L_{ss} - L_G \cos 2(p\theta_r + \frac{2\pi}{3})\end{aligned}\quad (XI)$$

The flux linkage contribution from mutual magnetic coupling between phases is obtained, via (IX), by evaluating the flux linking of a particular phase winding due to current flow in any of the two other phases. The magnetic interaction between phases a and b, for example, is given by

$$\begin{aligned}\lambda_{asbs} &= \int N_{as}(\phi_s) \Phi_{bs}(\phi_s, \theta_r) d\phi_s = -\left(\frac{N_s}{2p}\right)^2 p \frac{\pi}{2} \mu_0 rl \left[\alpha_1 + \alpha_2 \cos(2p\theta_r - \frac{2\pi}{3})\right] i_{bs} \\ &= \left[-\frac{1}{2}L_{ss} - L_G \cos(2p\theta_r - \frac{2\pi}{3})\right] i_{bs}\end{aligned}\quad (XII)$$

with similar expressions for the other cross phase interactions. The corresponding mutual inductance is determined as, upon dividing (XII) by i_{bs} ,

$$L_{asbs} = L_{bsas} = -\frac{1}{2}L_{ss} - L_G \cos(2p\theta_r - \frac{2\pi}{3}) \quad (XIII)$$

This consists of the nominal value ($-L_{ss}/2$) normally associated with a uniform air gap or round rotor and a variable component due to rotor saliency. The mutual inductance components associated with other flux linkage phase interactions are reciprocal and are similarly obtained with

$$\begin{aligned}L_{ascs} &= L_{csas} = -\frac{1}{2}L_{ss} - L_G \cos(2p\theta_r + \frac{2\pi}{3}) \\ L_{bscs} &= L_{csbs} = -\frac{1}{2}L_{ss} - L_G \cos(2p\theta_r)\end{aligned}\quad (XIV)$$

The cumulative flux linkage for each of the three phases, using (IX) and (XII) as examples for phase-a, may be expressed as

$$\Lambda_s(\mathbf{I}, \theta_r) = [\lambda_{as} \quad \lambda_{bs} \quad \lambda_{cs}]^T \quad (\text{XV})$$

with

$$\begin{aligned} \lambda_{as} &= \lambda_{asas} + \lambda_{asbs} + \lambda_{ascs} + \lambda_{asm} = \lambda_{ass} + \lambda_{asm} \\ \lambda_{bs} &= \lambda_{bsas} + \lambda_{bsbs} + \lambda_{bscs} + \lambda_{bsm} = \lambda_{bss} + \lambda_{bsm} \\ \lambda_{cs} &= \lambda_{csas} + \lambda_{csbs} + \lambda_{cscs} + \lambda_{csm} = \lambda_{css} + \lambda_{csm} \end{aligned}$$

where $\{\lambda_{asm}, \lambda_{bsm}, \lambda_{csm}\}$ represent the PM rotor phase-flux linkages which have a 120° relative phase disposition and $\{\lambda_{ass}, \lambda_{bss}, \lambda_{css}\}$ are the 3-phase armature reaction flux linkages. The general form of the flux linkage expression (XV) can be evaluated, via (IX) and (XII), using numerical integration techniques without resorting to the linear magnetic circuit constraint. This approach is relevant only when magnetic saturation is an issue during very high current demand in peak torque applications. In this instance the time varying inductances, associated with salient PM rotor rotation, are nonlinear with values that depend on the saturation status of the armature iron. However the assumption of linear magnetic structures greatly simplifies the modelling process with considerable savings in numerical computation. This assumption is applicable in the absence of magnetic saturation and can be used to provide a very good model approximation with negligible error during brief periods of magnetic saturation associated with over current drive. The total magnetic flux vector $\Lambda_s(I, \theta_r)$ may be rewritten in terms of winding inductance matrix $L_s(\theta_r)$, stator current $I_s(t)$ and rotor field coupling $\Lambda_{sm}(\theta_r)$, for linear magnetic operation, as

$$\begin{bmatrix} \lambda_{as} \\ \lambda_{bs} \\ \lambda_{cs} \end{bmatrix} = \begin{bmatrix} L_{ls} + L_{asas} & L_{asbs} & L_{ascs} \\ L_{bsas} & L_{ls} + L_{bsbs} & L_{bscs} \\ L_{csas} & L_{csbs} & L_{ls} + L_{cscs} \end{bmatrix} \begin{bmatrix} i_{as} \\ i_{bs} \\ i_{cs} \end{bmatrix} + \begin{bmatrix} \lambda_{asm} \\ \lambda_{bsm} \\ \lambda_{csm} \end{bmatrix} \quad (\text{XVI})$$

This can also be expressed in the compact matrix form as

$$\Lambda_s(\mathbf{I}, \theta_r) = \Lambda_{ss}(\mathbf{I}, \theta_r) + \Lambda_{sm}(\theta_r) = \mathbf{L}_s(\theta_r)\mathbf{I}_s(t) + \Lambda_{sm}(\theta_r) \quad (\text{XVII})$$

with total flux $\Lambda_s(\mathbf{I}, \theta_r) = [\lambda_{as} \quad \lambda_{bs} \quad \lambda_{cs}]$, rotor flux

$$\Lambda_{sm}(\theta_r) = [\lambda_{asm} \quad \lambda_{bsm} \quad \lambda_{csm}]^T = [\lambda_m \sin(p\theta_r) \quad \lambda_m \sin(p\theta_r - \frac{2\pi}{3}) \quad \lambda_m \sin(p\theta_r + \frac{2\pi}{3})]^T \text{ and stator}$$

$$\text{flux } \Lambda_{ss}(\mathbf{I}, \theta_r) = [\lambda_{ass} \quad \lambda_{bss} \quad \lambda_{css}]^T = \mathbf{L}_s(\theta_r)\mathbf{I}_s(t)$$

Since the machine windings are Y-connected the algebraic sum of the branch currents is zero with

$$i_{as} + i_{bs} + i_{cs} = 0 \quad (\text{XVIII})$$

and the flux linkage equation (XVI) can be written in terms of the symmetric inductance matrix as

$$\begin{bmatrix} \lambda_{as} \\ \lambda_{bs} \\ \lambda_{cs} \end{bmatrix} = \begin{bmatrix} L_{ls} + L_s - L_G \cos(2p\theta_r) & -L_G \cos(2p\theta_r - \frac{2\pi}{3}) & -L_G \cos(2p\theta_r + \frac{2\pi}{3}) \\ -L_G \cos(2p\theta_r - \frac{2\pi}{3}) & L_{ls} + L_s - L_G \cos(2p\theta_r + \frac{2\pi}{3}) & -L_G \cos(2p\theta_r) \\ -L_G \cos(2p\theta_r + \frac{2\pi}{3}) & -L_G \cos(2p\theta_r) & L_{ls} + L_s - L_G \cos(2p\theta_r - \frac{2\pi}{3}) \end{bmatrix} \begin{bmatrix} i_{as} \\ i_{bs} \\ i_{cs} \end{bmatrix} + \begin{bmatrix} \lambda_{asm} \\ \lambda_{bsm} \\ \lambda_{csm} \end{bmatrix} \quad (\text{XIX})$$

where L_s is the synchronous inductance for a non salient rotor given by $L_s = \frac{3}{2}L_{ss}$. If leakage inductance is neglected and a round rotor structure is assumed the inductance variation L_G in (XIX) disappears with the elimination of the air gap factor α_2 . This results in the synchronous inductance matrix, which is diagonal, with constant entries L_s .

The phase voltage equations governing the BLMD electrical behaviour can be determined from the stator winding flux linkages using Faraday's law as follows

$$\mathbf{V}_s(t) = \mathbf{R}_s \mathbf{I}_s(t) + \frac{d\Lambda_s(I,t)}{dt} = \mathbf{R}_s \mathbf{I}_s(t) + \mathbf{L}_s(\theta_r) \frac{d\mathbf{I}_s(t)}{dt} + \mathbf{I}_s(t) \frac{d\mathbf{L}_s(\theta_r)}{dt} + \frac{d\Lambda_{sm}(\theta_r)}{dt} \quad (\text{XX})$$

which phase index notation change $\{1 \equiv a; 2 \equiv b; 3 \equiv c\}$ where $\mathbf{V}_s(t) = [v_{1s}(t) \ v_{2s}(t) \ v_{3s}(t)]^T$, $\mathbf{I}_s(t) = [i_{1s}(t) \ i_{2s}(t) \ i_{3s}(t)]^T$, $\mathbf{R}_s = \text{diag}[r_s]$ and r_s is the phase winding resistance and $L_s(\theta_r)$ is the time varying inductance matrix in (XIX).

2.2.2 Phase voltage equations in the stator reference frame

The voltage expression (XX) in stationary coordinates is used to determine the phase voltage differential equations based on the assumption of a round rotor structure as follows:

$$v_{js} = r_s i_{js} + \frac{d\lambda_{js}(i_{js}, \theta_r)}{dt} \quad \text{for } j = 1, 2, 3 \quad (\text{XXI})$$

The total mutual air gap magnetic flux for phase- j given by

$$\lambda_{js}(i_{js}, \theta_r) = \lambda_{jss}(i_{js}, \theta_r) + \lambda_{mj}(\theta_r) = L_s i_{js} + \lambda_{mj}(\theta_r) \quad (\text{XXII})$$

where

$$\lambda_{mj}(\theta_r) = \lambda_m \sin(p\theta_r - \frac{2(j-1)\pi}{3}).$$

Expression (XXI) may be rewritten as

$$v_{js} = r_s i_{js} + L_s \frac{di_{js}}{dt} + v_{ej} \quad \text{for } j = 1, 2, 3 \quad (\text{XXIII})$$

where v_{ej} is the internally generated phase- j back emf voltage given by

$$v_{ej} = K_e \omega_r \cos(p\theta_r - \frac{2(j-1)\pi}{3}) \quad (\text{XXIV})$$

with motor voltage back EMF constant K_e given by $K_e = p\lambda_m$ and rotor shaft velocity ω_r as in (V). The alternative compact matrix form for (XXIII) is given by

$$\begin{bmatrix} v_{1s} \\ v_{2s} \\ v_{3s} \end{bmatrix} = \begin{bmatrix} r_s & 0 & 0 \\ 0 & r_s & 0 \\ 0 & 0 & r_s \end{bmatrix} \begin{bmatrix} i_{1s} \\ i_{2s} \\ i_{3s} \end{bmatrix} + \begin{bmatrix} L_{ls} + L_s & 0 & 0 \\ 0 & L_{ls} + L_s & 0 \\ 0 & 0 & L_{ls} + L_s \end{bmatrix} \cdot \frac{d}{dt} \begin{bmatrix} i_{1s} \\ i_{2s} \\ i_{3s} \end{bmatrix} + K_e \begin{bmatrix} \cos(p\theta_r) \\ \cos(p\theta_r - \frac{2\pi}{3}) \\ \cos(p\theta_r + \frac{2\pi}{3}) \end{bmatrix} \quad (\text{XXV})$$

The uniform air gap assumption results in a diagonal inductance matrix, which allows for current variable decoupling in (XXV) and thus a tractable model structure. This approach is somewhat justified, in the absence of magnetic saturation, from previous studies (Persson et al, 1976; Demerdash et al, 1980) where the independence of stator inductance with salient

rotor displacement has been explained. The *raison d'être* of this simplifying assumption is that the permeability of the magnetically hard Samarium-Cobalt (SmCo_5) material is almost equal to that of air. As a consequence of this property the SmCo_5 material has some desirable features from a BLMD modelling perspective in terms of its intrinsic demagnetization characteristic. The PM rotor air gap line (Matsch, 1972) is a design feature which is optimized in terms of the maximum energy product of 160 kJm^{-3} (Crangle, 1991) for a given machine configuration and magnet geometry. In Figure 7 the locus of operation of the air gap line, due to changes in gap width, is a minor hysteresis loop (Match, *ibid*) with axis tangent to the magnetization curve through the retention flux Φ_0 .

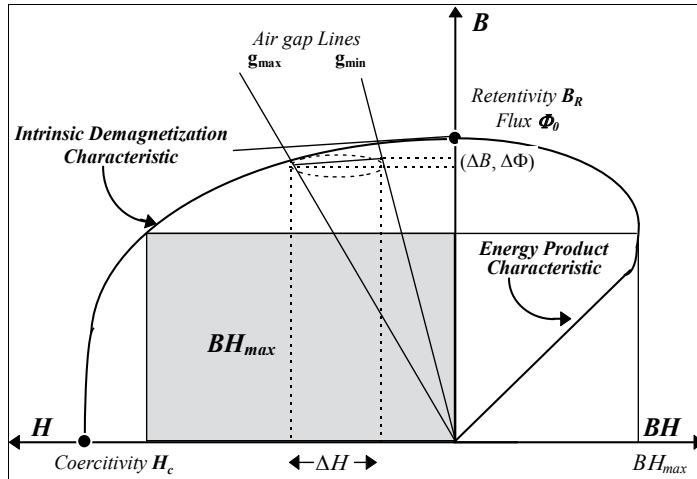


Fig. 7. PM flux variation with air gap width

The corresponding oscillating PM flux variations $\Delta\Phi$, which occur p times per rotor revolution, are practically negligible ($\Delta\Phi \ll \Phi_0$) with little impact on the overall rotor flux linkage contribution to the stator windings.

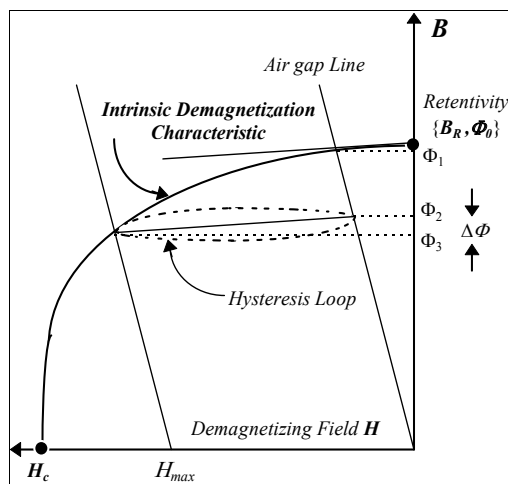


Fig. 8. Demagnetizing MMF effect

In Figure 8 the repeated application of a demagnetizing MMF, generated by the stator windings, results in a negligibly small flux variation ($\Delta\Phi \ll \Phi_0$) associated with the minor hysteresis loop on the demagnetization curve. The applied radial stator H -field, which is designed to lie on the knee of the intrinsic demagnetization characteristic (Pesson et al, 1976) corresponding to the energy product figure BH_{max} , has its maximum value associated with the air gap line at H_{max} . Since the PM relative permeability (μ_r) is almost unity, the applied field generated in the stator windings is not affected by rotor position.

2.2.3 Electromechanical energy conversion and torque production

In a BLMD system the electromechanical energy conversion process involves the exchange of energy between the electrical and mechanical subsystems through the interacting medium of a magnetic coupling field. This energy transfer mechanism is manifested by the action of the coupling field on output mechanical motion of the rotor shaft masses and its stator winding input reaction to the electrical power supply. This reaction, which is necessary for the coupling field to absorb energy from the electrical supply, is the emf $V_s^*(t)$ induced across the coupling field by the magnetic field interaction of the stator winding with the PM rotor. Energy conversion during motor action is maintained by the incremental supply of internal electrical energy dW_e , associated with sustained current flow $I_s(t)$ against the reaction emf, to balance the differential energy dW_f absorbed by the reservoir coupling field and that released by the coupling field dW_m to mechanical form. This results in the replenished energy transfer for sustained motion with stator flux change $d\Lambda_s(I, \theta_r)$, using (V), as

$$dW_e = I_s(t)V_s^*(t)dt = I_s(t)d\Lambda_s(I, \theta_r) = dW_f + dW_m \tag{XXVI}$$

where mechanical and field losses are included in the electrical source $V_s^*(t)$ and are thus ignored for convenience. In a motor system most of the stator winding MMF is used to overcome the reluctance of the air gap separating the fixed armature from the moving rotor in the magnetic circuit. Consequently most of the magnetic field energy is stored in the air gap so that when the field is reduced most of this energy is returned to the electrical source. Furthermore since stacked ferromagnetic laminations are used in the stator winding assembly the magnetic field core losses are minimal whereupon the magnetic coupling fields are assumed conservative. The field energy state function $W_f(\lambda_{1s}, \lambda_{2s}, \lambda_{3s}, \theta_r)$ can be expressed in terms of the flux linkages ($\lambda_{1s}, \lambda_{2s}, \lambda_{3s}$) in (XVI), for multiple stator winding controlled excitations with appropriate index change, and the mechanical angular displacement θ_r of the rotor. This can be expressed in differential form using (XXVI) in terms of the stator winding flux linkages λ_{js} and currents i_{js} as

$$dW_f = \sum_{j=1}^3 \frac{\partial W_f}{\partial \lambda_{js}} d\lambda_{js} + \frac{\partial W_f}{\partial \theta_r} d\theta_r = \sum_{j=1}^3 i_{js} d\lambda_{js} - dW_m \tag{XXVII}$$

The mechanical energy transfer dW_m with incremental change $d\theta_r$ in rotor position θ_r due to developed electromagnetic torque $\Gamma_e(I_s, \theta_r)$ by the coupling field is expressed by

$$dW_m = \Gamma_e(I_s, \theta_r) d\theta_r \tag{XXVIII}$$

By coefficient matching the state variables θ_r and λ_{js} for $j \in \{1, 2, 3\}$ in (XXVII) and (XXVIII) an analytical expression for the electromagnetic (EM) torque Γ_e is obtained with

$$\Gamma_e(\Lambda_s, \theta_r) = - \frac{\partial W_f(\Lambda_s, \theta_r)}{\partial \theta_r} \tag{XXIX}$$

in terms of the coupling field stored energy as a function of the flux linkages Λ_s . The coupling field energy is first determined by integration of the other coefficient partial differential equations

$$i_{js} = \frac{\partial W_f(\Lambda_s, \theta_r)}{\partial \lambda_{js}} \quad \forall j \in \{1,2,3\} \tag{XXX}$$

with respect to the flux linkages of the connected system for restrained rotor conditions as

$$W_f(\Lambda_s, \theta_r) \Big|_{(d\theta_r=0)} = \sum_j \int \frac{\partial W_f(\Lambda_s, \theta_r)}{\partial \lambda_{js}} d\lambda_{js} = \sum_{j=1}^3 \int i_{js} d\lambda_{js}(i_{1s}, i_{2s}, i_{3s}, \theta_r) \tag{XXXI}$$

as shown in Figure 9 before evaluation of the drive torque. Since the flux linkages are functions of the stator winding current, complex and lengthy numerical integration of (XXX) would be required over the nonlinear λ - i magnetization characteristic in Figure 9, which must be known, if saturation effects are to be included. However if magnetic nonlinearity is neglected, with the assumption that the flux linkages and MMFs are directly proportional for the entire magnetic circuit as in air, the resulting analysis and integral expression (XXXI) is greatly simplified. In this case the flux linkages are assumed to be linear with current magnitude, which is often done in the analysis of practical devices, in the winding inductances as in (XXII). However a simpler and more convenient alternative (Krause, 1986) than obtaining the EM torque as a function of Λ_s via $W_i(\Lambda_s, \theta_r)$ in (XXXI), relies on the coenergy state function $W_c(I_s, \theta_r)$ to determine the applied torque Γ_e in terms of the stator currents I_s as the independent PWM controlled state variables in BLMD system operation. This methodology is more effective during BLMD model simulation as the motor winding currents are immediately available for motor torque computation.

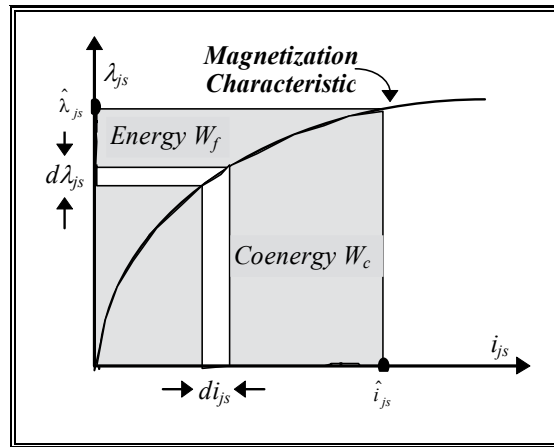


Fig. 9. Stored energy and coenergy

The coenergy $W_c(I_s, \theta_r)$, which has no physical basis or use other than to simplify the torque calculation, is the dual form of the coupling field energy $W_i(\Lambda_s, \theta_r)$ as shown in Figure 9 with

$$W_c(I_s, \theta_r) = \hat{I}_s^T \hat{\Lambda}_s - W_f(\Lambda_s, \theta_r) \tag{XXXII}$$

The following equivalent expressions result for the differential forms of the coenergy in (XXXII) using the substitutions (XVII) and (XVIII) for $W_f(\mathbf{I}_s, \theta_r)$

$$dW_c(\mathbf{I}_s, \theta_r) = \left[\sum_{j=1}^3 (i_{js} d\lambda_{js} + \lambda_{js} di_{js}) \right] - \left[\sum_{j=1}^3 i_{js} d\lambda_{js} - \Gamma_e(\mathbf{I}_s, \theta_r) d\theta_r \right] \quad (XXXIII)$$

$$dW_c(\mathbf{I}_s, \theta_r) = \sum_{j=1}^3 \frac{\partial W_c}{\partial i_{js}} di_{js} + \frac{\partial W_c}{\partial \theta_r} d\theta_r \quad (XXXIV)$$

which when coefficient matched yield the parametric equations

$$\lambda_{js} = \frac{\partial W_c(\mathbf{I}_s, \theta_r)}{\partial i_{js}} \quad \forall j \in \{1, 2, 3\} \quad (XXXV)$$

$$\Gamma_e(\mathbf{I}_s, \theta_r) = \frac{\partial W_c(\mathbf{I}_s, \theta_r)}{\partial \theta_r} \quad (XXXVI)$$

The coupling field coenergy is determined from (XXXV) by integrating the cumulative stator flux linkages in (XV) with respect to the appropriate phase currents for restrained rotor movement as

$$W_c(\mathbf{I}_s, \theta_r) = \int \sum_{j=1}^3 \frac{\partial W_c(\mathbf{I}_s, \theta_r)}{\partial i_{js}} di_{js} = \int \sum_{j=1}^3 \lambda_{js} di_{js} \quad (XXXVII)$$

If magnetic nonlinear saturation effects and field losses are negligible then the flux linkages are linearly related to the currents, which establish the magnetic coupling field, through the inductance circuit elements as in (XIX) for a salient pole rotor with

$$\lambda_{js} = \sum_{k=1}^3 (L_{jk} i_{ks} + \lambda_{jm}) \quad (XXXVIII)$$

The resulting coenergy W_c , from substitution of (XXXVIII) into (XXXVII), is given by

$$W_c(\mathbf{I}_s, \theta_r) \Big|_{d\theta_r=0} = \frac{1}{2} \sum_{j=1}^3 L_{jj} \cdot i_{js}^2 + \sum_{j=1}^3 \sum_{\substack{k=1 \\ k \neq j}}^3 L_{jk} i_{ks} i_{js} + \sum_{j=1}^3 \lambda_{jm} \cdot i_{js} \quad (XXXIX)$$

from which the EM torque is evaluated using (XXXVI) as

$$\Gamma_e(\mathbf{I}_s, \theta_r) = \frac{1}{2} \sum_{j=1}^3 i_{js}^2 \frac{dL_{jj}}{d\theta_r} + \sum_{j=1}^3 \sum_{\substack{k=1 \\ k \neq j}}^3 i_{ks} i_{js} \frac{dL_{jk}}{d\theta_r} + \sum_{j=1}^3 i_{js} \frac{d\lambda_{jm}}{d\theta_r} \quad (XL)$$

This may be expanded in terms of the stator winding inductances for a salient pole machine as

$$\Gamma_e(\mathbf{I}_s, \theta_r) = pL_G \sum_{j=1}^3 \left[\sin\left(2p\theta_r - \frac{2(j-1)\pi}{3}\right) \cdot i_{js}^2 + 2 \sum_{\substack{k=1 \\ k \neq j}}^3 \sin\left(2p\theta_r - \frac{2(k-1)\pi}{3}\right) \cdot i_{ks} i_{js} \right] + K_t \sum_{j=1}^3 \cos\left(p\theta_r - \frac{2(j-1)\pi}{3}\right) i_{js} \quad (XLI)$$

with torque constant $K_t = p\lambda_m$ which is the same as K_e if proper units are used. If a round rotor structure is assumed, then the L_G terms in (XLI) disappear and the resulting developed motor torque, due to the coupling field reaction EMF , in general terms is given by

$$\begin{aligned}\Gamma_e(\mathbf{I}_s, \theta_r) &= \sum_{j=1}^3 i_{js} \frac{d\lambda_{jm}}{d\theta_r} = \sum_{j=1}^3 p\lambda_m \cos\left(p\theta_r - \frac{2(j-1)\pi}{3}\right) \cdot i_{js} \\ &= K_e \sum_{j=1}^3 \cos\left(p\theta_r - \frac{2(j-1)\pi}{3}\right) \cdot i_{js}\end{aligned}\quad (\text{XLII})$$

or in a more compact general form, using (XVII), as

$$\Gamma_e(\mathbf{I}_s, \theta_r) = \mathbf{I}_s^T \frac{d}{d\theta_r} \{\Lambda_{sm}(\theta_r)\} = \frac{1}{L_s} \Lambda_{ss}^T(\mathbf{I}, \theta_r) \frac{d}{d\theta_r} \{\Lambda_{sm}(\theta_r)\} \quad (\text{XLIII})$$

The first two terms in (XL), which vanish in (XLII), represent the reluctance torque that tends to align the salient poles in the minimum reluctance position with rotating air gap flux. Motor torque control in high performance industrial drives is achieved by an electronically commutated 3-phase PWM inverter which forces the armature phase currents i_{js} in (XLII) to follow the sinusoidal reference currents i_{dj} generated from a prescribed torque demand signal i/p T_d using rotor position information θ_r . In the 3 Φ commutated BLMD system in Figure 1A the reference sinusoids, issued from the phase generator, are amplitude modulated (AM) by the i/p torque demand T_d or velocity error signal via a multiplying DAC. This AM effect is reflected in winding current amplitudes I_{jm} which vary with time as $I_{jm}(t)$ in symphony with the current demand signals $\{I_{da}, I_{db}, I_{dc}\}$. These winding currents can be thus written in the following vector form, with amplitude variation included, as

$$\mathbf{I}_s(t) = \begin{bmatrix} i_{1s} \\ i_{2s} \\ i_{3s} \end{bmatrix} = \begin{bmatrix} I_{1m}(t) \cos(\omega_e t) \\ I_{2m}(t) \cos(\omega_e t - \frac{2\pi}{3}) \\ I_{3m}(t) \cos(\omega_e t + \frac{2\pi}{3}) \end{bmatrix} \quad (\text{XLIV})$$

Consequently the developed torque is expressed by (XLII) in its most general form to allow for current amplitude variations which track the i/p torque demand signal excursions during transient step changes. Expression (XLII) is employed during BLMD model simulation to compute the motor torque from the derived stator winding currents for simulation of the rotor shaft drive dynamics. The steady state motor torque is determined from (XLIII), for balanced 3 Φ phase conditions with constant amplitude stator winding currents as in (III), with

$$\Gamma_e(\mathbf{I}_s, \theta_r) = K_e I_m \sum_{j=1}^3 \cos\left(p\theta_r - \frac{2(j-1)\pi}{3}\right)^2 = \frac{3}{2} I_m K_e \quad (\text{XLV})$$

The mechanical power P_m delivered by the magnetic coupling field can be determined from the applied motor torque in (XLII) which holds the rotor drive shaft load at an angular velocity ω_r as

$$P_m = \Gamma_e \omega_r = K_e \omega_r \sum_{j=1}^3 \cos\left(p\theta_r - \frac{2(j-1)\pi}{3}\right) \cdot i_{js} \quad (\text{XLVI})$$

This is identical to electrical power P_e provided to each of the stator phase windings ignoring losses, by the PSU, in sustaining the magnetic coupling field from collapse during mechanical energy transfer. The electric power is accomplished by means of phase current i_{js} injection against coupling field back-emf v_{ej} . The PSU contribution P_e is expressed by means of (XIV) and (XLIV) as $V_e^T I_s$ with

$$P_e = P_m = K_e \omega_r \sum_{j=1}^3 \cos(p\theta_r - \frac{2(j-1)\pi}{3}) \cdot i_{js} \tag{XLVII}$$

which defaults to (XLVI) for zero internal power factor angle ϕ_I in the phasor diagram of Figure 10 and for constant amplitude winding currents.

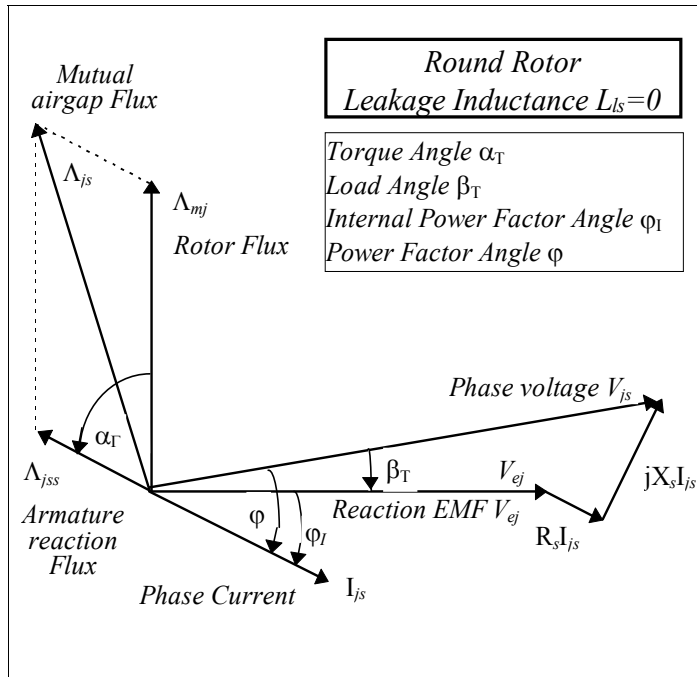


Fig. 10. Phasor diagram for PM motor

The physical manifestation of motor torque production, which is expressed as the product of stator current and the rotor air gap flux given in (XLIII), results from a tendency of the stator and rotor air gap flux fields to align their magnetic axes with minimum energy configuration. Consequently maximum torque is developed by the motor as in (XLIII) when the torque angle α_T , defined as the angle between the armature reaction $\Lambda_{ss}(I, \theta_r)$ and PM flux $\Lambda_{sm}(\theta_r)$ space vectors in (XVII), is maintained at 90 degrees. Optimum torque angle control can be achieved in a BLMD system by means of self synchronization, via a rotor shaft position resolver as shown in Figure 1, in which a current controlled PWM inverter ensures an orthogonal spatial relationship between the stator and rotor flux vectors. This can be visualized with the aid of the phasor diagram in Figure 10 where the torque angle α_T , given by

$$\alpha_T = \pi / 2 - \phi_I \tag{XLVIII}$$

with internal power factor angle φ_1 for steady state conditions, is forced towards 90 degrees by adjustment of the armature reaction field Λ_{js} . This adjustment is accomplished with stator phase current I_{js} angle control, via electronic commutation, which also implies that the internal power factor angle φ_1 between the reaction EMF V_e and armature current I_s in (XLVII) is held at zero.

The PM air gap flux Λ_{mj} generates a phase-j reaction EMF V_{ej} in Figure 10 at steady state rotor angular velocity ω_r . This EMF has a maximum value for a given shaft speed when the phase winding axis is displaced 90 electrical degrees relative to the rotor flux axis in which case the phase winding conductors are opposite the rotor magnetic poles with zero flux linkage. Consequently the emf phasor V_{ej} lags the flux phasor Λ_{mj} by 90 degrees. The developed EM torque Γ_e results in sustained mechanical motion of motor drive shaft against a coupled load torque Γ_l , with angular velocity ω_r , expressed by the torque balance differential equation as

$$\Gamma_e - \Gamma_l = (J_m + J_l) \frac{d\omega_r}{dt} + B_m \omega_r \quad (\text{IL})$$

where J_m and J_l are the respective shaft and load moments of inertia and B_m is the motor shaft friction or damping coefficient. The motor shaft position θ_r is obtained from the rotor angular velocity by numerical integration during BLMD model simulation using

$$\theta_r = \int_0^t \omega_r(\xi) d\xi \quad (\text{L})$$

The equations (XXIII) and (XXIV) governing the electrical behaviour and the dynamical expressions (XXXII), (IL) and (L), together with the Laplace transform, form the basis of a mathematical model shown in Figure 1 of a brushless dc motor for complete simulation of the drive system.

2.2.4 Modelling of BLMD power converter with inverter blanking

Brushless motor speed or torque control is achieved by adjusting the amplitude and frequency of the stator winding phase voltages which are synchronized in phase with instantaneous rotor position. Several different methods of power converter operation in regulating the 3-phase motor winding voltage excitation have been reported in the literature (Murphy et al, 1989). The widely used method of ASD stator winding voltage control which relies on three-phase six-step inverter operation, with a basic 60 degree commutation interval over a 120 degree conduction mode and an adjustable dc link voltage, suffers from low order harmonics with resultant low speed motor torque pulsations (Jahns, 1984). An effective alternative to the six-step mode of operation relies on voltage control within the inverter using pulsewidth modulation. The PWM control strategy results in better overall transient response with the elimination of low frequency harmonic content and motor cogging if a large carrier to reference frequency ratio is employed. A wide variety of PWM techniques are available (Adams et al, 1975) such as synchronized square-wave (Pollack, 1972) and sinusoidal PWM (Grant et al, 1981, 1983) with the latter being the preferred choice in asynchronous form with a very large fixed carrier ratio in commercial applications. Smooth motor shaft rotation down to standstill is obtained via a sinusoidal asynchronous PWM inverter which delivers a high fidelity fundamental o/p voltage waveform to the stator windings. The accompanying distortion frequency components, due to modulated pulse shaping, are concentrated about the high frequency carrier and its harmonics and are easily attenuated by the stator winding inductances.

In a 3Φ current-controlled PWM inverter each current loop is equipped with a current controller and comparator modulator which provides wide bandwidth dynamic control of the stator current for high performance drive torque applications. Each current controller is fed with a sinusoidal current command reference i_{dj} from the 3Φ current commutator, shown in Figure 1, along with the sensed stator winding current feedback i_{fj} via Hall effect measuring devices. The rapidly adjusted error o/p $v_{cj}(t)$ from the current compensator forces the actual motor current i_{js} in each phase, via the high gain PWM controlled voltage-source inverter, to track the command reference in both phase and magnitude with minimal error.

A mathematical model of 3-phase inverter operation can be obtained by describing the control action of the pulsewidth modulator in each phase, fed with a fixed voltage dc supply U_{dr} , on the amplitude and frequency adjustment of the BLMD stator winding voltage in response to the current compensator error output. Modulation proceeds in two steps in accordance with the current controller output as shown in Figure 1. A symmetrical double edge width modulated pulse train is generated for each phase by means of a voltage comparator as the first step. A triangular carrier waveform $V_{tri}(t)$, of fixed frequency f_s and common to all three phases, establishes the switching period T_s and the current control error reference $v_{cj}(t)$ then modulates the switch duty cycle as shown in Figure 11 for phase-a.

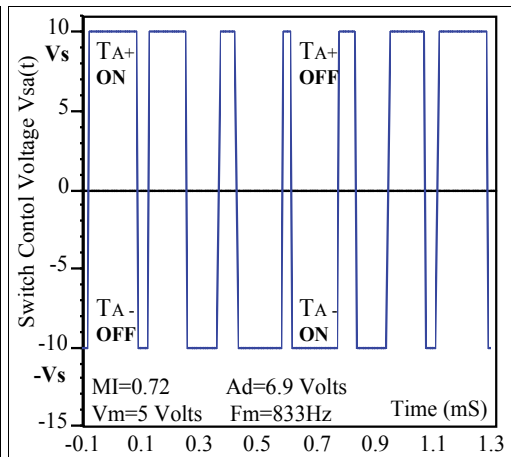
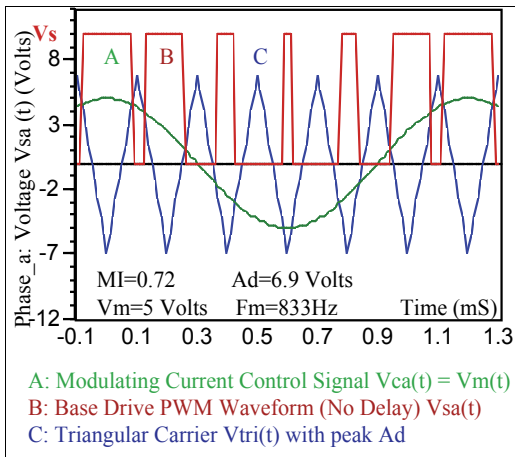


Fig. 11. Comparator modulator waveforms

Fig. 12. Phase-a switch control voltage

The modulated bipolar switch pulse train $v_{sj}(t)$ is then used as the firing signal, at the modulator o/p as shown in Figure 12 for phase-a, to control the “ON” and “OFF” periods of the power transistors, via the base drive circuitry (BDA), in each half-bridge of the 3Φ inverter as the subsequent step. Similar switching sequences, with a phase angle separation of 120 degrees, are obtained for control of the other two phases of the inverter bridge resulting in a 3Φ PWM voltage supply to the motor stator windings. In practical inverters the finite turn-off time of the power transistor bridge necessitates the use of a finite blanking switch time in the PWM process to avoid short circuiting the dc busbar to ground (Murai, 1985; Evans et al, 1987; Dodson et al, 1990). This fixed ‘interlock delay’ δ , which is typically 20 μ S, is conservatively chosen for slow switching Darlington transistors in medium power motor drives in the low kilowatt range.

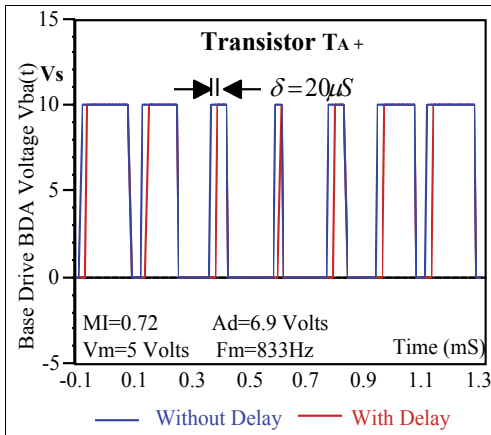


Fig. 13. Base drive voltage for TA+

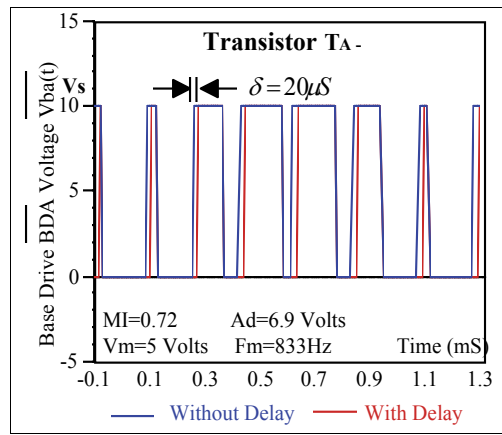


Fig. 14. Base drive voltage for TA-

This dwell time, between successive power transistor switching instants, is effected through an integrate and dump RC 'lockout' network connected to a voltage threshold in the base drive circuitry. A switching delay of this magnitude, for inverter frequencies in the audio range (5kHz), has to be included in the motor drive modelling process for accurate simulation studies. The effect of the switching delay can be modelled as follows by considering phase-a only with a similar procedure for the other two phases (Guinee et al, 1998, 1999).

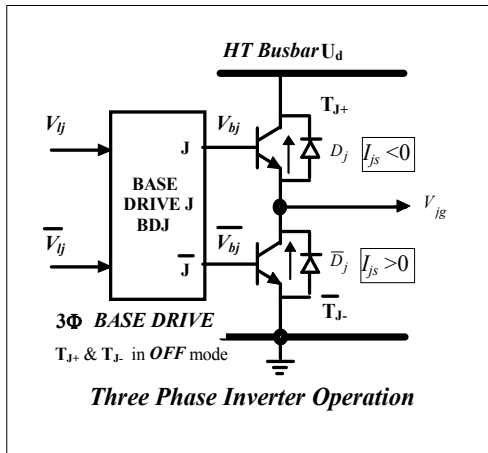


Fig. 15. Phase-j inverter operation

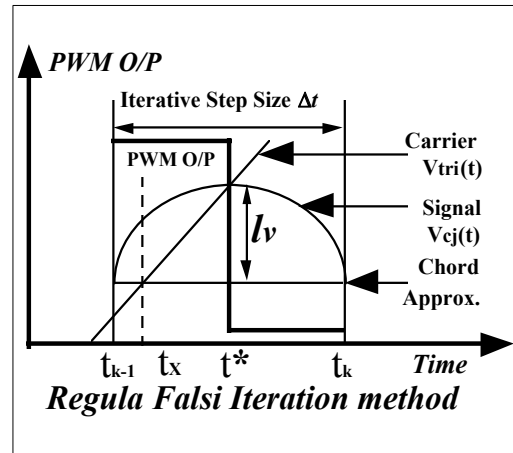


Fig. 16. Regula-falsi iterative search

The duty cycle of the bipolar switch control voltage $v_{sa}(t)$, during one switching period T_s in Figure 12 is determined by the relative magnitude comparison and accurate crossover evaluation, from simulation via the regula-falsi iterative search method shown in Figure 16, of the current control voltage $v_{ca}(t)$ with the dither reference $v_{tri}(t)$. The switch control pulse sequence can be described as

$$v_{sa}(t) = \begin{cases} +V_s & \{v_{ca}(t) \geq v_{tri}(t)\} \\ -V_s & \{v_{ca}(t) < v_{tri}(t)\} \end{cases} \quad (\text{LI})$$

with modulated pulse duration

$$\tau = \begin{cases} T_s & \{v_{ca}(t) \geq A_d\} \\ (1 + m_f) \frac{T_s}{2} & \{|m_f| < 1\} \\ 0 & \{v_{ca}(t) \leq -A_d\} \end{cases} \quad (\text{LII})$$

for carrier amplitude A_d and modulation index (MI) m_f given by

$$m_f = v_{ca}(t)/A_d \quad (\text{LIII})$$

The effect of the switch control voltage on the inverter base drive transistors T_{A+} and T_{A-} under ideal conditions, without delay is illustrated in Figures 13 and 14.

When blanking is introduced inverter switching is postponed until the capacitor voltages of the complementary RC delay circuits, associated with power transistors T_{A+} and T_{A-} , exceeds the threshold level setting V_{th} in the base drivers as shown in Figures 13 and 14 and detailed in Figure 17. The magnitude of the delay δ , typically $20\mu\text{s}$, is given by

$$\delta = RC \ln\left(\frac{2V_s}{V_s - V_{th}}\right) \approx 0.693RC \quad \text{if } V_{th} = 0 \quad (\text{LIV})$$

When phase-a power transistors T_{A+} and T_{A-} , are "OFF" during the blanking period winding current conduction is maintained through free-wheeling protection diodes, as shown in Figures 1 and 15, so that each transistor with its accompanying antiparallel diode functions as a bilateral switch. The relationship between the states of the dc to ac converter phase-a switch transistor pair, denoted by $S_A(k)$ with $k \in \{0,1,2\}$, and the base drive voltages v_{la} & \bar{v}_{la} in Figure 17 can be represented by

$$\begin{aligned} S_A(0) &= \begin{cases} v_{la} < V_{th} \Rightarrow v_{ba}(t) = 0 \Rightarrow T_{A+} \text{ is "OFF"} \\ \bar{v}_{la} \geq V_{th} \Rightarrow \bar{v}_{ba}(t) = V_B \Rightarrow T_{A-} \text{ is "ON"} \end{cases} \\ S_A(1) &= \begin{cases} v_{la} \geq V_{th} \Rightarrow v_{ba}(t) = V_B \Rightarrow T_{A+} \text{ is "ON"} \\ \bar{v}_{la} < V_{th} \Rightarrow \bar{v}_{ba}(t) = 0 \Rightarrow T_{A-} \text{ is "OFF"} \end{cases} \\ S_A(2) &= \begin{cases} v_{la} < V_{th} \Rightarrow v_{ba}(t) = 0 \Rightarrow T_{A+} \text{ is "OFF"} \\ \bar{v}_{la} < V_{th} \Rightarrow \bar{v}_{ba}(t) = 0 \Rightarrow T_{A-} \text{ is "OFF"} \end{cases} \end{aligned} \quad (\text{LV})$$

with similar expressions $S_j(k)$ and $J \in \{A,B,C\}$ for the other two phases. The power transistors in each leg of the inverter are thus alternately switched "ON" and "OFF" according to the tristate expression (LV) with a brief blanking period separating these switched transistor conduction states. The tristate operation of the power converter bridge also determines the phase potential i/p of the stator winding as a result of the PWM gating sequence applied to the basedrive in (LV). The corresponding converter voltages applied between the stator phase winding input connection and ground, denoted by v_{ag} , v_{bg} , and v_{cg} , are then given by

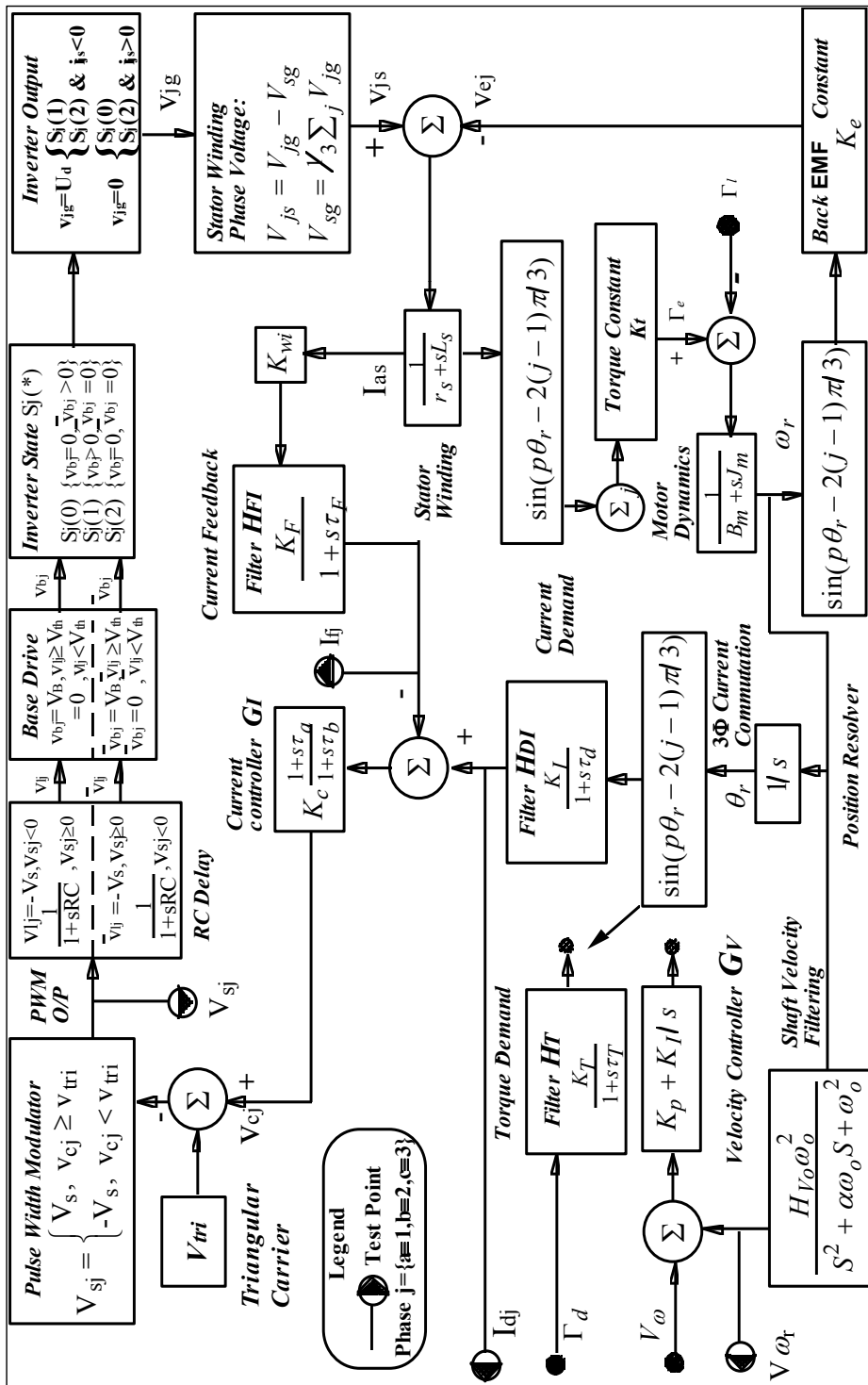


Fig. 17. Transfer Function Block Diagram of a BLMD System (Guinea, 1999)

$$\begin{aligned}
 v_{ag} &= \begin{cases} U_d & \{S_A(1) \text{ or } S_A(2) \& i_{as} < 0\} \\ 0 & \{S_A(0) \text{ or } S_A(2) \& i_{as} > 0\} \end{cases} \\
 v_{bg} &= \begin{cases} U_d & \{S_B(1) \text{ or } S_B(2) \& i_{bs} < 0\} \\ 0 & \{S_B(0) \text{ or } S_B(2) \& i_{bs} > 0\} \end{cases} \\
 v_{cg} &= \begin{cases} U_d & \{S_C(1) \text{ or } S_C(2) \& i_{cs} < 0\} \\ 0 & \{S_C(0) \text{ or } S_C(2) \& i_{cs} > 0\} \end{cases}
 \end{aligned} \tag{LVI}$$

where current flow into a winding is assumed positive by convention. If the phase current flow i_{js} is positive in (LVI) during blanking when power transistors T_{J+} and T_{J-} are “OFF”, as shown in Figure 15, then $v_{jg} = 0$. If, however, i_{js} is negative then $v_{jg} = U_d$ while T_{J+} and T_{J-} are blanked. The tristate operation of the inverter bridge also uniquely determines the phase potential i/p v_{jg} of the stator winding in (LVI) as a result of the PWM gating sequence applied to the basedrive in (LV). The inverter o/p voltage v_{ag} is shown in Figures 18 and 19 for the two cases of current flow direction in phase-a of the stator winding. The potential of the stator winding neutral star point s , from equation (XXIII) with phase current summation

$$\sum_{j=1}^3 i_{js} = i_{as} + i_{bs} + i_{cs} = 0 \tag{LVII}$$

is given by

$$v_{sg} = \frac{1}{3}(v_{ag} + v_{bg} + v_{cg}) \tag{LVIII}$$

with resultant phase voltages

$$\begin{aligned}
 v_{as} &= (v_{ag} - v_{sg}) = \frac{1}{3}(2v_{ag} - v_{bg} - v_{cg}) \\
 v_{bs} &= (v_{bg} - v_{sg}) = \frac{1}{3}(2v_{bg} - v_{ag} - v_{cg}) \\
 v_{cs} &= (v_{cg} - v_{sg}) = \frac{1}{3}(2v_{cg} - v_{ag} - v_{bg})
 \end{aligned} \tag{LIX}$$

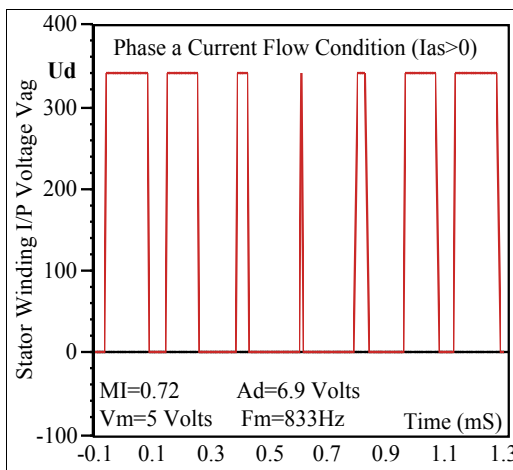


Fig. 18. Inverter o/p Voltage ($i_{as} > 0$)

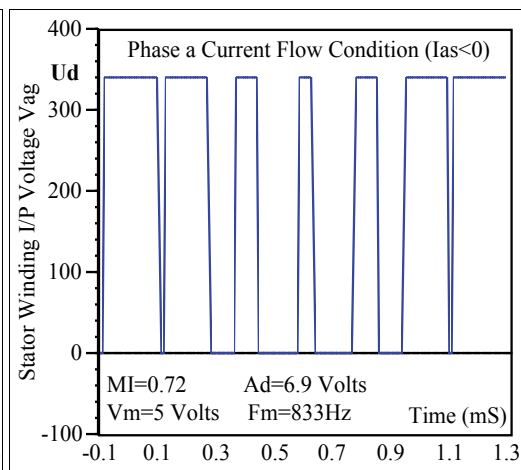


Fig. 19. Inverter o/p Voltage ($i_{as} < 0$)

The complete three phase model of a typical high performance servo-drive system (Moog GmbH, 1989; Guinee, 1999). incorporating equations (XXIII), (XXIV), (XLII), (IL), (L), (LV), (LVI) and (LIX), used in software simulation for parameter identification purposes is displayed in Figure 17.

3. Numerical simulation accuracy and experimental validation of BLMD model

Since the BLMD model is partitioned into linear elements and non linear subsystems, owing to the complexity and discrete temporal nature of the PWM control switching process, numerical integration techniques have to be applied to obtain solutions to the differential electrodynamic equations of motion. Numerical simulation of the continuous-time subsystems, with a transfer function representation based on the Laplace transform, is achieved by means of model difference equations with numerical solutions provided by the use of the backward Euler integration rule (BEIR) (Franklin et al, 1980). In this instance continuous time derivatives are approximated in discrete form using the Z Transform substitution operator $S = \frac{1}{T}(1 - Z^{-1})$. Since the BEIR maps the left half s-plane inside the unit circle in the z-plane these solutions are stable. The choice of this implicit integration algorithm is based on its simplicity of substitution, ease of manipulation with a small number of terms and reduced computation effort in the overall complex BLMD model simulation. An alternative filter discretization process based on Tustin's bilinear method, or the trapezoidal integration rule with the substitution operation $S = \frac{2}{T}(1 - Z^{-1})/(1 + Z^{-1})$, can be implemented with negligible observable differences at the small value of integration step size T actually chosen. The application of the BEIR technique can be visualized for a first order system, as in the case of the current control lag compensator G_I which has a generalized transfer function (Guinee, 2003)

$$G_I(s) = \frac{V(s)}{I(s)} = K_c \frac{1 + \tau_a s}{1 + \tau_b s} \equiv K \frac{\alpha_0 + \alpha_1 s}{\beta_0 + \beta_1 s}, \quad (\text{LX})$$

with continuous-time description given by

$$\beta_0 V(t) + \beta_1 \frac{dV(t)}{dt} = K \left(\alpha_0 I(t) + \alpha_1 \frac{dI(t)}{dt} \right) \quad (\text{LXI})$$

Integrating (LXI) between the discrete time instants t_k and t_{k-1} with a fixed time step size T gives

$$\beta_1 V(t_k) - K\alpha_1 I(t_k) = [\beta_1 V(t_{k-1}) - K\alpha_1 I(t_{k-1})] + K\alpha_0 \int_{t_{k-1}}^{t_k} I(\tau) d\tau - \beta_0 \int_{t_{k-1}}^{t_k} V(\tau) d\tau \quad (\text{LXII})$$

Applying the BEIR, with piecewise constant integrand backward approximations $V(t_k)$ and $I(t_k)$ over the interval $t_k \geq t > t_{k-1}$ yields the input-output difference equation

$$V(t_k)[\beta_1 + \beta_0 T] = \beta_1 V(t_{k-1}) + K[\alpha_1 + \alpha_0 T]I(t_k) - K\alpha_1 I(t_{k-1}) \quad (\text{LXIII})$$

This can be expressed in the Z domain, via the Z Transform, as the transfer function

$$\frac{V(Z)}{I(Z)} = K \frac{\alpha_0 + \alpha_1 \frac{1}{T}(1 - Z^{-1})}{\beta_0 + \beta_1 \frac{1}{T}(1 - Z^{-1})} \equiv k \frac{n_0 + n_1 Z^{-1}}{d_0 + d_1 Z^{-1}} \quad (\text{LXIV})$$

which is equivalent to (LX) through the general BEIR substitution operator $S = \frac{1}{T}(1 - Z^{-1})$. The time evolution of each discretized linear subsystem proceeds according to the BEIR, similar to (LXIII), as an integral part of the overall BLMD numerical simulation with a fixed time step $T = \Delta t$ and input $x(t)$ to output $y(t)$ relationship given by

$$y^k = (n_0 x^k + n_1 x^{k-1}) \frac{k}{d_0} - \frac{d_1}{d_0} y^{k-1} \tag{LXV}$$

The choice of time step size is determined by the resolution accuracy of the PWM switching instants required during simulation for delayed inverter trigger operation as explained in section 3.1 below. The BLMD model program is organized into a sequence of software function calls, representing the operation of the various subsystems.

3.1 PWM simulation with inverter delay

The choice of numerical integration step size Δt , for solution of the set of dynamic system differential equations, is influenced by the PWM switching period T_s ($\approx 200\mu\text{S}$) (Moog, 1989) and the smallest BLMD time constant τ_d ($\sim 28.6\mu\text{S}$) associated with the basedrive ‘lockout’ circuitry. Furthermore the precision with which the pulse edge transitions are resolved in the three phase PWM o/p sequences as in (LI) with inverter blanking included, has a significant effect on the accuracy of the inverter o/p waveforms. This is important in BLMD simulation where model accuracy and fidelity are an issue in dynamical parameter identification for optimal control. The effect of inaccuracy in pulse time simulation can be reduced by choosing a sufficiently small fixed time step $\Delta t \ll T_s$, such as $0.5\% T_s$ or 5% of the inverter dead time δ ($\approx 20\mu\text{S}$) for example, to reflect overall BLMD model accuracy and curtail computational effort in terms of time during lengthy simulation trial runs. Furthermore this choice of step size also provides an uncertainty bound of $+\Delta t$ in the evaluation of PWM switching instants during simulation in the absence of an iterative search of the switch crossover time. This uncertainty can be reduced by an iterative search of the PWM crossover time t^* within a fixed assigned time step size Δt during BLMD simulation for which a width modulated pulse transition has been flagged as shown in Figure 16. A variety of iterative search methods can be employed for this purpose with varying degrees of computation runtime required and complexity. These include, for example, successive application of the bisection method, regula falsi technique and the Newton-Raphson approach (Press et al, 1990) where convergence difficulties can arise with derivative calculations from noisy current control signals. The number of iterations n required for the bisection technique, with a fixed time step Δt , to reach an uncertainty ε in the pulse transition time estimate t_X , is given by the error criterion

$$\Delta t 2^{-(n+1)} \leq \varepsilon \tag{LXVI}$$

The estimate of the PWM switching time t^* obtained via the regula falsi method, from the comparison of the triangular carrier ramp with the piecewise linear approximation of the control signal v_{cj} as shown in Figure 16, is given by the iterative search value t_X as (Guinee, 1998, 2003)

$$t_X = \frac{\{v_{in}(t_{k-1}) - v_{cj}(t_{k-1})\} \Delta t}{\{v_{in}(t_{k-1}) - v_{cj}(t_{k-1})\} - \{v_{in}(t_k) - v_{cj}(t_k)\}} + t_{k-1} \tag{LXVII}$$

The adoption of a single iteration of the regula falsi method along with a small simulation time step Δt simplifies the search problem of the pulse edge transition with sufficient accuracy without the expenditure of considerable computational effort for a modest gain in accuracy by comparison with the other iterative methods available. An indication of the step size required for accurate resolution of PWM inverter operation with delay can be obtained from consideration of the anticipated signal ‘curvature’ due to (a) the signal bandwidth and amplitude at the current controller o/p v_{cj} in the magnitude comparison with the triangular carrier shown in Figure 16 in the comparator modulator and (b) the rate of exponential voltage ramp up to the base drive threshold V_{th} , which controls the inverter dead time, in the RC delay circuits shown in Figure 20.

The maximum harmonic o/p voltage from the high gain current compensator G_I is determined by the carrier amplitude A_d at the onset of overmodulation ($m_f = 1$) in PWM inverter control with a frequency that is limited by the 3dB bandwidth $\omega_F = 1/\tau_F$ ($\sim 3\text{kHz}$ in Table I) of the smoothing filter H_{FI} in the current loop feedback path shown in Figure 17. This may be represented in analytic form as

$$v_{cj}(t) = A_d \sin(\omega_F t) \tag{LXVIII}$$

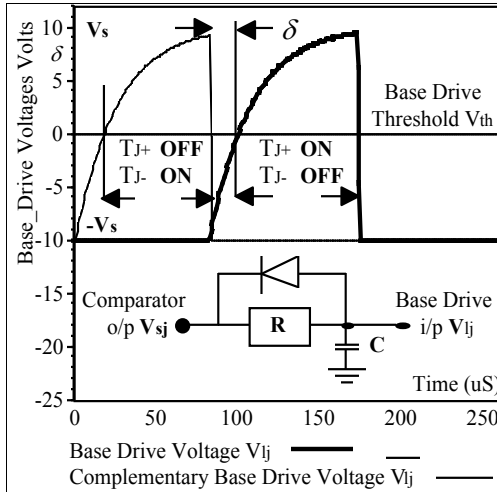


Fig. 20. Delayed basedrive trigger signals

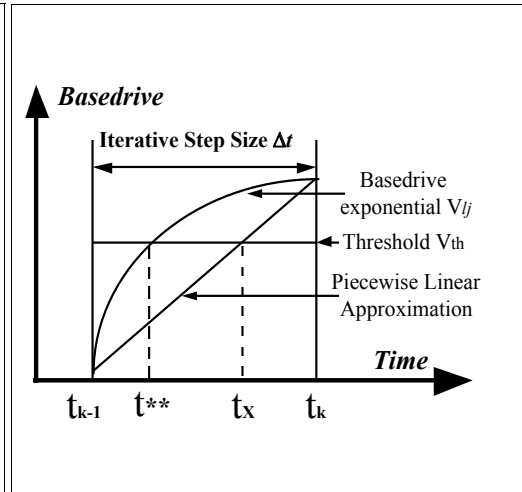


Fig. 21. Basedrive Trigger Time Search

with a quadratic power series approximation about the mid interval point \hat{t} in Δt given by

$$v_{cj}(t) = v_{cj}(\hat{t}) + v'_{cj}(\hat{t})(t - \hat{t}) + \frac{v''_{cj}(\hat{t})}{2!}(t - \hat{t})^2. \tag{LXIX}$$

The accuracy with which the estimated width modulated pulse transition instants t_X are determined can be gauged by comparing the deviation error of the actual intersection time t^* of the triangular carrier with the control signal v_{cj} , due to its curvature, to that t_X obtained with the piecewise linear chord approximation of the signal in the regula-falsi method as illustrated in Figure 16. The ‘curvature’ of the signal in (LXVIII) with time, determined (Kreyszig, 1972) from

$$\kappa = \left| \frac{v''_{cj}}{\sqrt{1 + v'^2_{cj}}} \right|, \tag{LXX}$$

is given by its maximum value

$$\kappa_{\max} = \left| v_{cj}'' \right| = A_d \omega_F^2 \quad (\text{LXXI})$$

at the peak amplitude A_d of $v_{cj}(t)$ corresponding to the instant $t^* = \pi/2\omega_F$ in Figure 16 at which $v_{cj}'(t^*) = A_d \omega_F \cos(\omega_F t^*) = 0$. The peak deviation l_v of the signal due to curvature from the chord approximation through t_{k-1} in Figure 16 occurs at $\hat{t} = t^*$ with zero chord slope. The peak deviation from the chord, through $t_{k-1} = (t^* - \Delta t/2)$, is determined by the Taylor series expansion in (LXIX) about $\hat{t} = t^*$ with

$$v_{cj}(t_{k-1}) = v_{cj}(t^*) + \frac{v_{cj}''(t^*)}{2!} \left(\frac{\Delta t}{2} \right)^2 = A_d \left[1 - \frac{1}{2} \left(\frac{\omega_F \Delta t}{2} \right)^2 \right] \quad (\text{LXXII})$$

giving

$$l_v = \left[v_{cj}(t^*) - v_{cj}(t_{k-1}) \right] = \frac{A_d}{2} \left(\frac{\omega_F \Delta t}{2} \right)^2 \quad (\text{LXXIII})$$

The worst case deviation error of the pulse transition time estimate t_x from t^* is determined by the regula-falsi method at the point of intersection t_x of the carrier ramp, which passes through the signal coordinates $[t^*, v_{cj}(t^*)]$ in Figure 16, with the chord approximation to the signal. The approximation error $(t^* - t_x)$ is determined from the ramp, which has peak-to-peak excursion $2A_d$ over the half period $T_s/2$, with slope $m = 4A_d/T_s$ as

$$\varepsilon = (t^* - t_x) = \left(\frac{l_v}{m} \right) = \left(\frac{T_s}{8} \right) \cdot \left(\frac{\omega_F \Delta t}{2} \right)^2 \quad (\text{LXXIV})$$

Substitution of the set of relevant signal parameters $\{T_s, A_d, f_F\}$, for a step size of $1\mu\text{s}$, with values $\{200 \mu\text{s}, 6.9\text{V}, 3\text{kHz}\}$ result in a negligible approximation error ε relative to the step size Δt of 0.222% which verifies the suitability of the chosen step size for a linear search of the PWM crossover time. The PWM resolution accuracy determines the moment that a modulated pulse edge transition takes place with subsequent onset of inverter blanking, using lockout circuitry, which substantially affects power transfer from the dc supply to the prime mover. The next essential trigger event, that needs to be accurately resolved, is the instant at which retarded firing of the inverter power transistors commences when the RC delay growth voltage exceeds the basedrive threshold $V_{th} = 0$ in Figure 20. The complementary exponential trigger voltages v_{lj} & \bar{v}_{lj} supplied to the basedrive circuitry, for a modulator peak-to-peak o/p swing of $2V_s$, can be expressed as

$$v_{lj} = V_s (1 - 2e^{-t/RC}) \quad (\text{LXXV})$$

The basedrive turnon time t^{**} is given by (LIV) as δ ($\sim 19.82\mu\text{s}$), at the instant at which $v_{lj}(t^{**}) = V_{th}$, for a time constant τ_d ($\sim 28.6\mu\text{s}$). Since delay circuit simulation is employed the trigger instant t_x has to be obtained using piecewise linear approximation of the exponential growth waveform, within the flagged simulation interval as shown in Figure 21, and is given by

$$t_x = t_{k-1} - \frac{v_{lj}(t_{k-1})}{v_{lj}(t_k) - v_{lj}(t_{k-1})} \Delta t \quad (\text{LXXVI})$$

where $t_{k-1} < t_x < t_k$ and $t_{k-1} < t^{**} < t_k$. Assume that t^{**} occurs at the mid interval time $(t_{k-1} + \Delta t/2)$ which thus provides an absolute point of reference for comparison with the search estimate t_x . The effect of basedrive signal 'curvature' on the trigger estimate t_x can be gauged by monitoring the relative contribution of the quadratic terms in the Taylor series expansion about t^{**} as

$$v_{ij}(t_x) = v_{ij}(t^{**}) + v'_{ij}(t^{**})(t_x - t^{**}) + \frac{v''_{ij}(t^{**})}{2!}(t_x - t^{**})^2 \quad (\text{LXXVII})$$

with $v_{ij}(t^{**}) = V_{th} = 0$. The differential error ε in the crossover time estimate in (LXXVI) is given by

$$\varepsilon = (t_x - t^{**}) = \left[\frac{\frac{\Delta t}{e^{2RC} - 1} - \frac{1}{2}}{\frac{\Delta t}{e^{2RC} - e} - \frac{\Delta t}{2RC}} \right] \Delta t \approx 4.37 \times 10^{-3} \Delta t \quad (\text{LXXVIII})$$

and is practically zero for very small time steps which implies a negligible quadratic contribution. Consequently the trigger time estimate obtained by linear approximation of the basedrive voltage about the threshold is very accurate for the time step size chosen.

3.2 Motor dynamic testing and simulation

The steady state controlled torque versus output speed characteristic (Moog, 1988) for the particular motor drive concerned is almost constant over a 4000 rpm speed range for a rated continuous power o/p of 1.5kW. The corresponding dynamic transfer characteristic of o/p motor torque Γ_e versus input torque demand Γ_d voltage is practically linear in the range (0, ± 10) volts. A fixed step signal Γ_d i/p is chosen to provide persistent excitation, as a standard control stimulus for dynamic system response testing, and in particular to gauge the accuracy of the model simulation and parameter extraction process based on the feedback current (FC) response i_{fj} . This response has the transient features of a constant amplitude swept frequency sinusoid, during the acceleration phase of the motor shaft, which are beneficial for test purposes and BLMD model validation in system identification (SI). The phase current feedback simulation can then be checked against experimental test results as the observed target data, for example in phase-a, for both phase and frequency coherence in model validation. Further model validation is provided by the accuracy with which high frequency ripple in the unfiltered current feedback is replicated through BLMD simulation when compared with experimental test data. Examination of the presence of dead time related low frequency harmonics in the simulated current feedback is also used to gauge BLMD model fidelity, through FFT spectral analysis, when compared with measurement data. An input magnitude of 1volt is sufficient to guarantee linear operation and avoid saturation ($m_f > 1$) of the PWM stage by the high gain current controller chosen here as the optimizer module MCO 402B in Table 1. This input step size is also enough to slow down the rate of shaft speed ramp up to allow adequate resolution of the frequency change in the FC target data.

The intrinsic mechanical parameters of motor viscous friction B_m and shaft inertia J_m are initially determined from experimental motor testing and cost surface simulations based on the mean squared error (MSE) between the simulated and measured transient response data for shaft velocity and current feedback. Two examples of known shaft load inertia J_L are

then used in simulated response measurements as a check against BLMD test data for further model accuracy and validation. These simulation results, which correspond to the different inertial loads, are integrated into a parameter identification process, using MSE cost surface simulation, based on a Fast Simulated Diffusion (FSD) optimization technique for the purpose of motor drive shaft parameter extraction. The experimentally determined parameter values listed in Table II for the BLMD model are used in all model simulations.

The back EMF or voltage constant K_e was experimentally determined from an open circuit (o/c) test with the motor configured as a generator driven over a range of speeds by an identical shaft coupled BLMD system. The generator voltage characteristic V_g is linear with drive shaft speed ω_m as shown for the experimental data in Figure 22, according to (XXIV), with slope K_e derived from the fitted linear voltage relationship V_f .

The transducer velocity 'gain' G_{RDC} of the Resolver-to-Digital Converter (RDC) was concurrently estimated along with K_e from the slope of the fitted linear characteristic V_{for} which in addition substantiates the converter linearity, to the speed voltage measurements shown in Figure 23. This value along with the cascaded shaft velocity filter gain is given as the cumulative gain H_{vo} in Table II.

Torque Demand Filter H_T	$K_T=1.0; \tau_T=222\mu\text{S}$	Voltages	$U_d=310$ Volts; $V_{th}=0$; $V_S=10$ Volts
Current Demand Filter H_{DI}	$K_I=1.0; \tau_I=100\mu\text{S}$	Constants	$K_{wi}=6.8 \times 10^{-2}$; $K_e = K_t = 0.3$
Current Feedback Filter H_{FI}	$K_F=5.0; \tau_F=47\mu\text{S}$	Winding	$P=6$; $r_S=0.75$ Ohms; $L_S=1.94\text{mH}$
Basedrive Delay Circuit	RC =28.6 μS	Carrier	$f_S=5\text{kHz}$; $A_d=6.9$ Volts;
Current Controller Type High Gain: MCO 402B Low Gain: MCO 422	$K_C=19.5$; $\tau_a=225\mu\text{s}$; $\tau_b=1.5\text{ms}$ $K_C=5.0$; $\tau_a=223\mu\text{S}$; $\tau_b=0.7\text{mS}$	Motor Dynamics	$J_m=3$ kg.cm ² ; $B_m=2.14 \times 10^{-3}$ Nm.rad ⁻¹ .sec
Shaft Velocity Filter H_V	$H_{vo}=13.5 \times 10^{-3}$; $\alpha=\sqrt{2}$; $\omega_o=2 \times 10^3$ rad.sec ⁻¹	Inertial Loads	$J_{MML}=9.06$ kg.cm ² (Medium Mass -MML) * $J_{LML}=17.8$ kg.cm ² (Large Mass - LML)
*Returned Parameter Estimates: $\hat{J}_{opt} = J_m + \hat{J}_{LML} = 20.838$ kg.cm ² , $\hat{B}_{opt} = 1.959 \times 10^{-3}$ Nm.Sec.Rad ⁻¹			
* Simulated FC Response Surface Estimates: $J_{opt}=20.877$ kg.cm ² , $B_{opt}=1.921 \times 10$ Nm.Sec.Rad ⁻¹			

Table II. BLMD system parameters

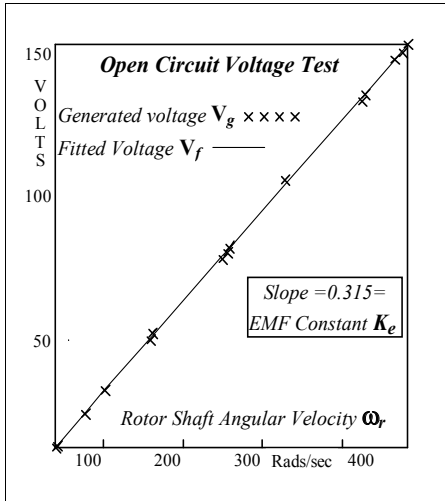


Fig. 22. Estimation of EMF constant K_e

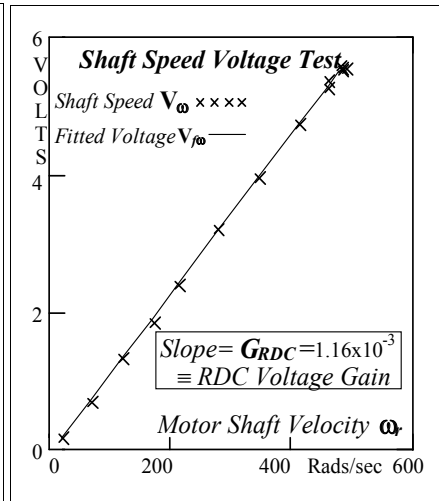


Fig. 23. Estimation of RDC ‘gain’ G_{RDC}

The value of K_e was subsequently used in a motor-generator electrical load test, at different speeds as illustrated in Figure 24, to estimate the stator winding parameters L_s and r_s as a cross check of the nominal catalogued (Moog, 1998) values. The difference ΔV between the measured terminal voltage V_T , across the load resistance R_L , and the generated voltage V_G using the fitted coefficient K_e via (XXIV) is equated to the internal voltage drop of the Thevenin equivalent circuit shown in Figure 24 with

$$\Delta V = V_G - V_T = |Z| I_L \tag{LXXIX}$$

where

$$I_L = V_T / R_L .$$

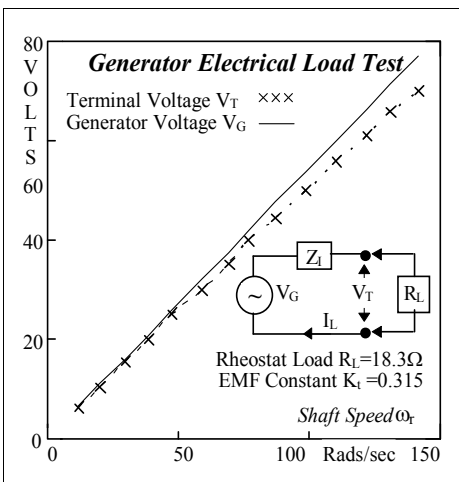


Fig. 24. Motor - generator load test

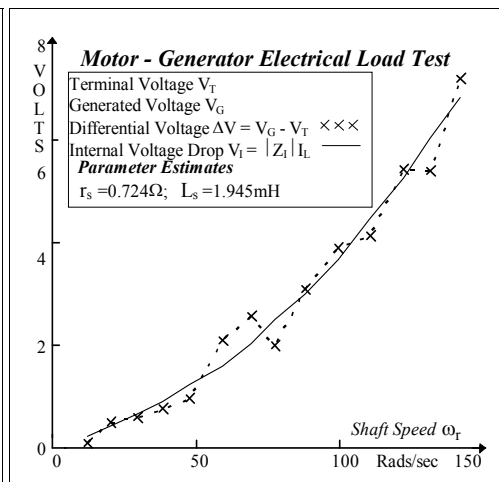


Fig. 25. Winding parameter estimation

The quadratic polynomial expressed in terms of ω_e via the circuit parameters as

$$Z^2 = a_0 + b_0 \omega_e^2, \quad (\text{LXXX})$$

for $\omega_e = p\omega_r$ and constant coefficients $a_0 \equiv r_s^2$ and $b_0 \equiv L_s^2$, is fitted to the derived data $y = (\Delta V/I_L)^2$. The quadratic fit shown in Figure 25 is based on the minimization of the MSE (E), between the sampled y_k and simulated Z_k^2 data, as

$$E = \frac{1}{N} \sum_{k=1}^N [y_k - a_0 - b_0 x_k^2]^2 \quad \text{for } x = \omega_e \quad (\text{LXXXI})$$

with respect to a_0 and b_0 . The cost function minimisation results in the normal equations

$$b_0 = \frac{\sum_k x_k^2 \sum_k y_k - N Y^T X^2}{(\sum_k x_k^2)^2 - (X^2)^T X^2} \quad (\text{LXXXII})$$

$$a_0 = \frac{1}{N} \left[\sum_k y_k - b_0 \sum_k x_k^2 \right] \quad (\text{LXXXIII})$$

with parameter estimates $\hat{L}_s = 1.945\text{mH}$ and $\hat{r}_s = 0.724$ ohms that are very close to the nominal values in Table II.

The motor shaft friction coefficient B_m was obtained from the steady state current feedback I_{fa} in phase-a at various shaft speeds ω_r by means of the torque constant K_t which is numerically equal to the experimentally determined value of K_e when proper units are used. The active component of the steady state current feedback is considered in the calculation of the dissipative friction torque by allowing for the effect of the machine impedance angle φ_z increase, given by

$$\varphi_z = \text{Tan}^{-1} \left(\frac{X_s I_{js}}{r_s I_{js}} \right) = \text{Tan}^{-1} \left(\frac{p\omega_r L_s}{r_s} \right), \quad (\text{LXXXIV})$$

with motor shaft speed and zero load angle β_T in Figure 10. This is necessary in electronic commutated motor drive systems, in which the current controlled applied phase voltage v_{js} at zero load angle is derived from the current demand I_{dj} in Figure 17, without the benefits of adaptive current angle advancement (Meshkat, 1985) to counteract the torque reduction effects of internal power factor angle illustrated in Figure 10. The derived friction torque, from the adjusted measured current feedback $I_{fa} \cos \varphi_z$, is given by

$$\Gamma_f = \left(\frac{3}{2} \right) K_t I_{as} \cos \varphi_z = \left(\frac{3}{2} \right) \left(\frac{K_t}{K_{wi} K_f} \right) I_{fa} \cos \varphi_z \quad (\text{LXXXV})$$

via (XLV) for balanced 3-phase conditions where the current feedback factor K_{wi} and filter gain K_f are considered in the estimation of the stator current flow I_{js} . This is graphed in Figure 26 for the measured FC test data I_{fa} and equated to the steady state mechanical friction torque via (IL) as

$$\Gamma_f = B_m \omega_r. \quad (\text{LXXXVI})$$

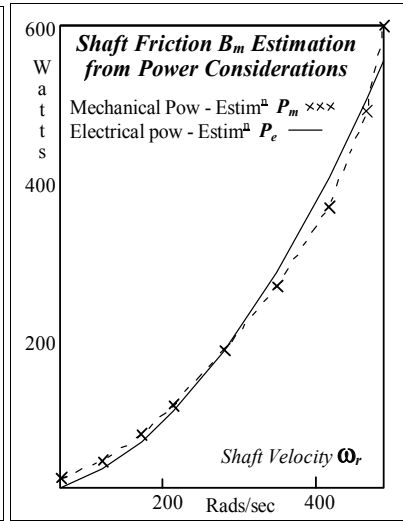
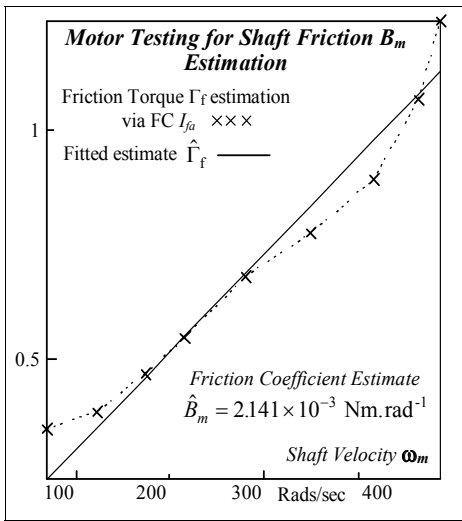


Fig. 26. Friction parameter estimation

Fig. 27. Friction power estimation

The friction coefficient B_m is obtained from a linear first order polynomial fit, displayed in Figure 26, based on expression (LXXXVI) with estimate $\hat{B}_m = 2.141 \times 10^{-3} \text{ Nm}\cdot\text{rad}^{-1}$ as in Table II. Alternative confirmation of the accuracy of the damping factor estimate is obtained from consideration of the electrical power transfer P_e from the coupling field expressed in (XLVII) and comparison with the resultant mechanical power dissipation P_m associated with dynamic friction via (XLVI). The continuous power supplied from the coupling field, necessary to sustain motor rotation with frictional losses at various shaft speeds under steady state conditions, is determined from the rms values of reaction EMF using the measured estimate \hat{K}_e from the o/c test and the experimental FC test data with lagging power factor balanced over three phases as

$$P_e = 3 \left(\frac{I_{fa}}{\sqrt{2}K_{ui}K_f} \cos \phi_z \right) \left(\frac{\hat{K}_e \omega_r}{\sqrt{2}} \right). \tag{LXXXVII}$$

The mechanical power dissipated as frictional heat is evaluated from (LXXXVI) using the measured estimate \hat{B}_m as

$$P_m = \Gamma_f \omega_r = \hat{B}_m \omega_r^2 \tag{LXXXVIII}$$

Both power estimates exhibit a high degree of correlation, with correlation coefficient ρ (Bulmer, 1979) of 99.5%, when plotted in Figure 27 which validates the derived damping factor estimate \hat{B}_m .

3.3 Motor step response testing and simulation results

Synchronized initial conditions for BLMD testing, and resultant comparison with model numerical simulation, are obtained by hand cranking the motor shaft to top dead centre of the phase-a current commutation reference position while monitoring the phase generator o/p waveforms before application of the torque demand step i/p. This is essential for

proper datum time referencing of all waveforms in the eventual comparison process, when formulating a multim minima cost surface for minimization purposes using the least squares error criterion, during parameter identification.

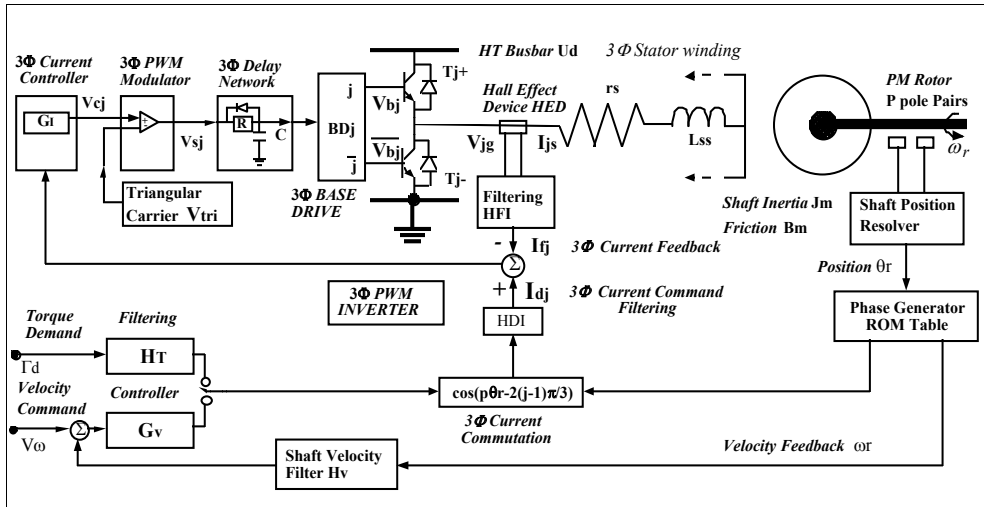


Fig. 28. Network structure of a typical BLMD system

The actual drive system with network structure as shown in Figure 28 was tested at critical internal nodes with multiplexed sampled data waveforms acquired at rates corresponding to the different inertial loaded shaft conditions (J_L) specified in Table III. The length of each data record is fixed at 4095 sample points with a normalized duration of approximately 10 machine FC cycles for reference purposes during comparison with simulated motor response for model validation and accuracy and also during system identification for accurate extraction of drive motor model parameter estimates.

FC Target Data	No Shaft Load (NSL)	Medium Inertial Load (MML)	Large Inertial Load (LML)
No. of machine cycles	~ 9.75	~ 11.5	~ 10.5
Acquisition rate T	20μs	40μs	49.6μs
No. of data points N_d	4095	4095	4095
Simulation time step	1μs	1μs	1μs
Decimation Factor	20	40	50
Waveform Correlation Analysis for BLMD system without inertial shaft loads			
Signal x	$Exp I_{xa}$	$Sim i_{xa}$	Data Correlation Coefficient ρ
Current Feedback	Fig. 29: I_{fa}	i_{fa}	0.985
Current Demand	Fig. 30: I_{da}	i_{da}	0.993
Current Controller o/p	Fig. 31: V_{ca}	v_{ca}	0.98
Motor Shaft Velocity	Fig. 32: $V_{\omega r}$	$v_{\omega r}$	0.98

Table III. Brushless Motor Drive Test and Simulation Results

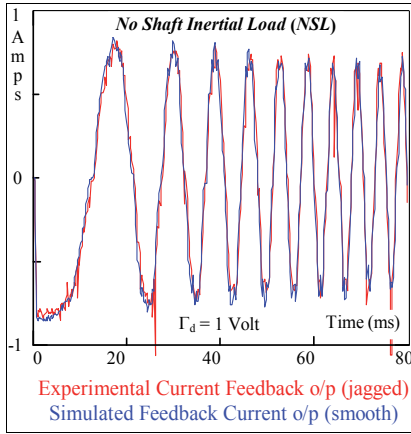


Fig. 29. BLMD current feedback I_{fa}

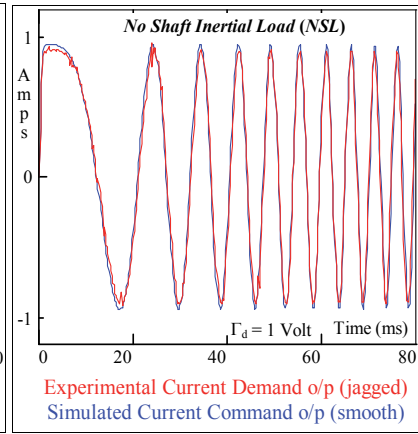


Fig. 30. BLMD current demand I_{da}

Verification of numerical simulation accuracy and BLMD model validation are immediately established by comparing the simulated step response characteristics with the actual test data in Figures 29 to 32 in all cases.

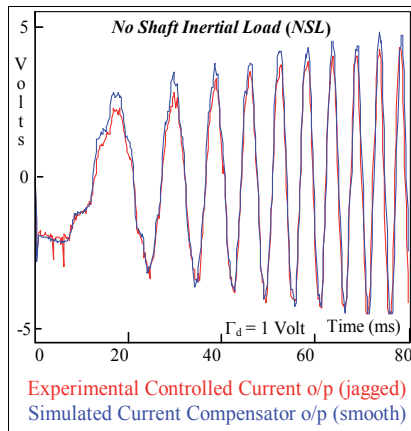


Fig. 31. Current compensator o/p V_{ca}

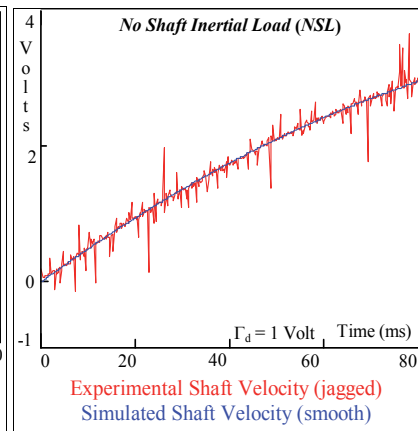


Fig. 32. RDC-rotor shaft velocity V_{ω}

Both the simulated current transients $i_{da}(kT)$ and $i_{fa}(kT)$ exhibit the characteristics of a frequency modulated sinusoid with fixed amplitude and swept frequency due to the exponential buildup of motor shaft speed during the acceleration phase. This can be visualized from the amplitude spectrum shown in Figure 33, for the extended filtered feedback current displayed in Figure 34, which appears constant over the electrical frequency band of 286 Hz corresponding to the swept motor speed range from standstill to 3000 RPM. These simulated waveforms provide an excellent fit in terms of frequency and phase coherence with test data when correlated. The measure of fit in this instance is expressed by the trace response correlation coefficients, listed in Table III, as

$$\rho = \frac{\text{Cov}(I_{xa}, i_{xa})}{\sqrt{V(I_{xa})V(i_{xa})}} \tag{LXXXIX}$$

where $\text{Cov}(I_{xa}, i_{xa})$, $V(I_{xa})$, and $V(i_{xa})$ are the covariance and respective variance measures.

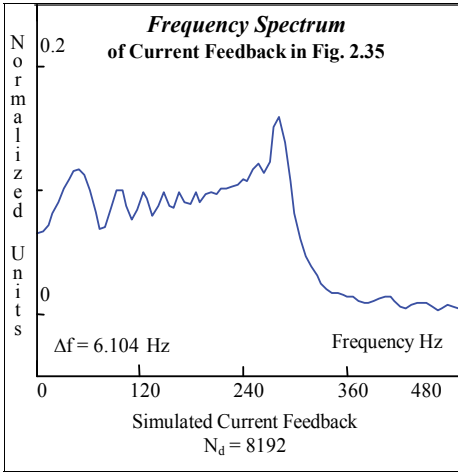


Fig. 33. Spectrum of motor FC $I_{fa}(\omega)$

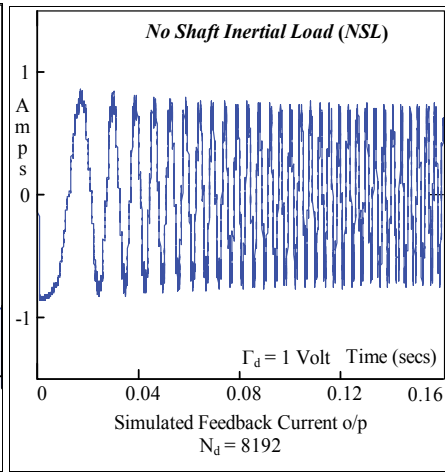


Fig. 34. BLMD model FC I_{fa}

Furthermore the accuracy of fit of the simulated traces consisting of the shaft velocity and current controller output with experimental step response test data, as indicated by the correlation coefficients in Table III, confirms model integrity. The fidelity and coherence of BLMD model trace simulation, when compared with drive experimental test data, is also established for known inertial shaft loads (Guinee, 1998, 1999) which further substantiates model accuracy and confidence. A number of BLMD transient waveform simulations, based on established model accuracy and confidence, at strategic internal nodes provide insight into and confirmation of motor drive operation during the acceleration phase. The filtered feedback current from each phase of the motor winding to the compensators in the three phase current control loop is illustrated in Figure 35. These waveforms show a reduction in the period of oscillation, accompanied by a very slight decrease in amplitude due to the impact of back emf reaction and machine impedance effects, as expected with an increase in shaft speed.

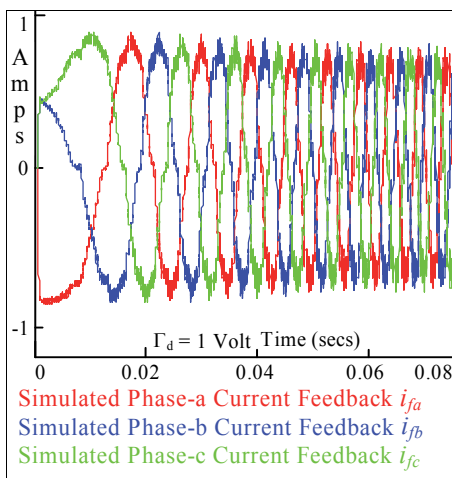


Fig. 35. BLMD 3Φ FC simulation I_{fj}

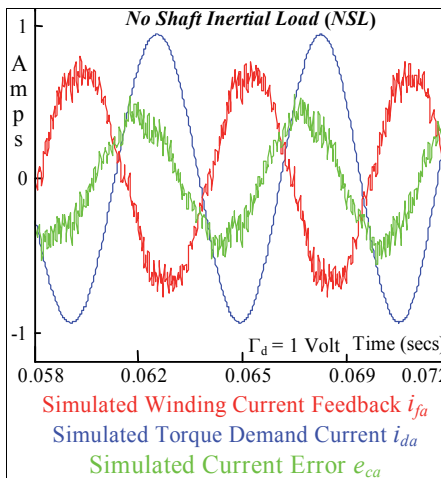


Fig. 36. Current controller inputs

A snapshot in time shows the relative amplitude and phase differences between the simulated phase-a i/p current waveforms i_{fa} and i_{dar} , in the form of the resultant comparison signal error v_{ca} to the current controller, in Figure 36 during motor speed-up. This error is primarily due to the increasing phase difference between the torque command current i_{dar} issued to each phase of the motor winding through the current controlled inverter response voltage v_{asr} , and the actual phase current flow i_{as} as a result of the stator winding impedance angle increase in (LXXXIV) with motor speed.

The simulated complementary turn-on signals issued to the basedrive from the RC delay 'lockout' circuit are shown in Figure 37 over a number of PWM switching periods along with the threshold voltage which determines the basedrive trigger timing. The corresponding PWM inverter controlled 3Φ output pole voltages v_{js} fed to the stator winding i/p, including the neutral potential v_{sg} derived from (LVIII), are shown in Figure 38 over several switching intervals. These simulated binary level width-modulated pulses, which have a voltage excursion from ground potential to the dc busbar high tension level U_{dr} , result in the six step phase voltage waveform v_{as} illustrated in Figure 39.

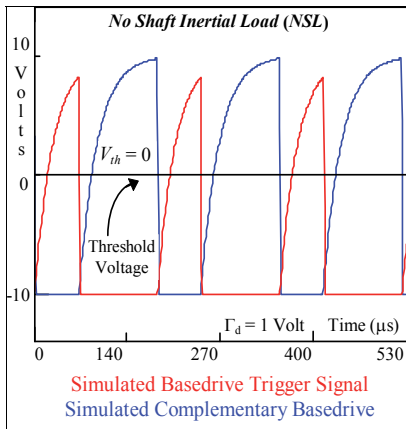


Fig. 37. Basedrive command signals

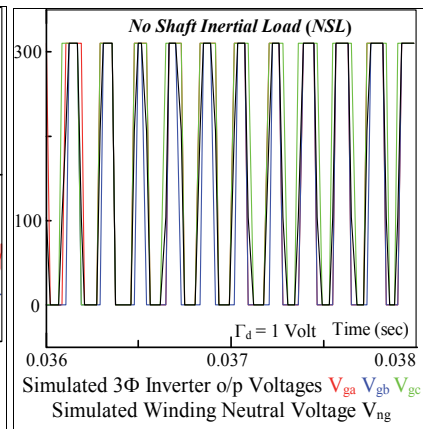


Fig. 38. PWM inverter o/p voltage

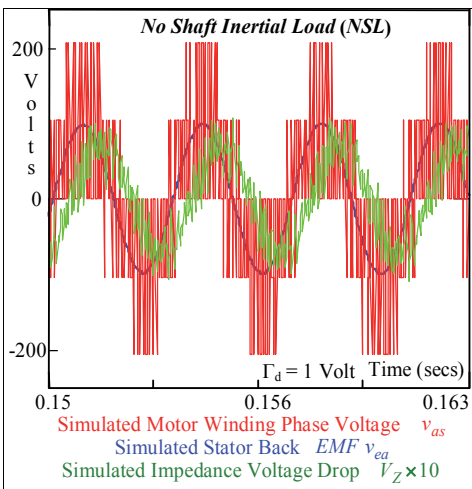


Fig. 39. Stator phase voltages

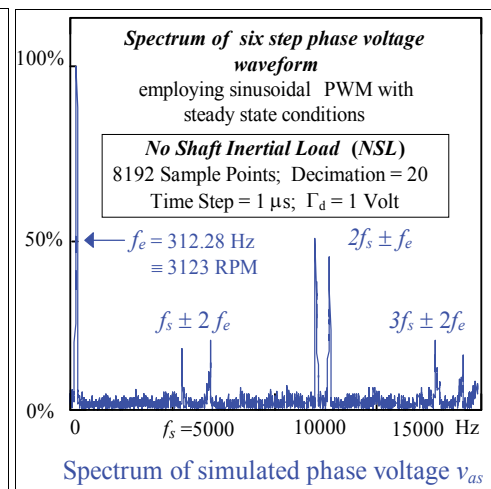


Fig. 40. Spectrum of phase voltage v_{as}

The stator back EMF phase voltage v_{ea} together with the winding impedance voltage drop v_z , which is magnified tenfold for display reasons, are shown in Figure 39 for comparison purposes as the motor rotational speed (~ 3120 rpm) approaches the maximum steady state nominal value of 4000 rpm. The motor impedance voltage $|V_z|$ drop, which is mainly inductive at this speed and determined from

$$V_z = i_{js} \cdot \sqrt{r_s^2 + (p\omega_r L_s)^2} e^{j\phi_z} = |Z| e^{j\phi_z} \cdot i_{js} \tag{XC}$$

with impedance angle ϕ_z as per (LXXXIV), is negligible compared to the reaction EMF as the current required to sustain frictional torque in (LXXXVI) is minimal.

The normalized spectrum of the six step phase voltage, which has a sharp line structure indicative of steady state motor operation close to rated speed, is displayed in Figure 40. This amplitude spectrum, which is the characteristic signature of sub-harmonic PWM inverter operation (Murphy et al, 1998), consists of the fundamental machine electrical frequency f_e (~ 312 Hz) and side frequency component pairs $(kf_s \pm n f_e)$ associated with pulse generation about the triangular carrier switching harmonics kf_s . The side frequency distribution contains even order pairs symmetrically disposed about odd carrier harmonics and odd order pairs about even harmonics with significant amplitudes dependent on the index of modulation m_f in (LIII). These extraneous component contributions are located well outside the machine winding passband, which has a 3dB cutoff frequency f_c determined from the stator electrical time constant $\tau_e = L_s/r_s$ (~ 2.6 ms) in Table I as

$$f_c = (2\pi\tau_e)^{-1} \approx 61.2\text{Hz} , \tag{XCI}$$

by choice of the carrier switching frequency f_s (~ 5 kHz). These distortion components are thus heavily suppressed through attenuation by the stator winding inductance.

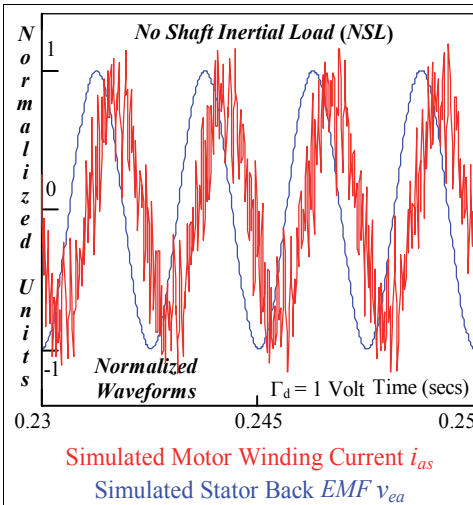


Fig. 41. Phase current & back EMF

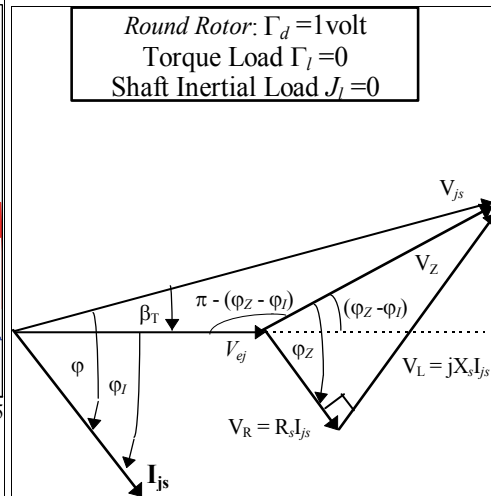


Fig. 42. Stator phasor diagram

The winding currents lag the reaction EMF as shown in Figure 41 by the internal power factor angle $\phi_I \approx 66.6^\circ$, obtained from statistical averaging of the estimated crossover

instants, near rated motor speed. This lag, which can be calculated as 65.7° from the average mechanical power delivered using the rms quantities in Table IV and Figure 42 with

$$P_m = 3V_{ej}I_{js} \cos \varphi_I, \tag{XCII}$$

differs from the machine impedance angle obtained from the BLMD model simulation shown in Figure 43 as $\varphi_Z \approx 78^\circ$ using (LXXXIV) near rated motor speed.

The stator winding voltage and current phasors including relevant phase angles are illustrated in Figure 42 at near rated motor speed for zero torque load conditions with magnitude estimates listed in Table IV. The actual and internal power factor angles, φ and φ_I respectively, are almost identical for zero torque load conditions resulting in negligible load angle β_T . This can be established by geometrically determining from Figure 42 the voltage phasor V_{js} applied to the motor winding as

$$V_{js} = \sqrt{V_{ej}^2 + V_z^2 + 2V_{ej}V_z \cos(\varphi_z - \varphi_I)}. \tag{XCIII}$$

Evaluation Period: $0.2s \leq t \leq 0.24s$	Resistance Voltage $V_R = R_s I_{js} = 1.14v$	Phase Voltage (XCIII): $V_{js} = 81.3v$
Mech-Power (LXXXVIII): $P_m = 141.2 w$	Reactance Voltage $V_L = jX_s I_{js} = j5.9v$	Impedance Angle (LXXXIV): $\varphi_Z = 79.1^\circ$
Shaft Velocity: $\omega_r = 334 \text{ rad.sec}^{-1}$	RMS Impedance Voltage (Fig. 39): $V_Z = 6v$	Int-Pow-Fac Angle (XCII): $\varphi_I = 65.7^\circ$
RMS Current (Fig. 34): $I_{as} = 1.5A$	RMS Reaction EMF (Fig. 39): $V_{ej} = 75.3v$:	Load Angle (XCV): $\beta_T = 1.06^\circ$
Estimated φ_I (Fig. 40) $\varphi_I = 66.55^\circ$	RMS Phase Voltage (Fig. 39) $V_{js} = 78v$	Pow-Factor Angle $\varphi = 66.8^\circ$

Table IV. Evaluation of phasor magnitudes from steady state conditions in figure 42

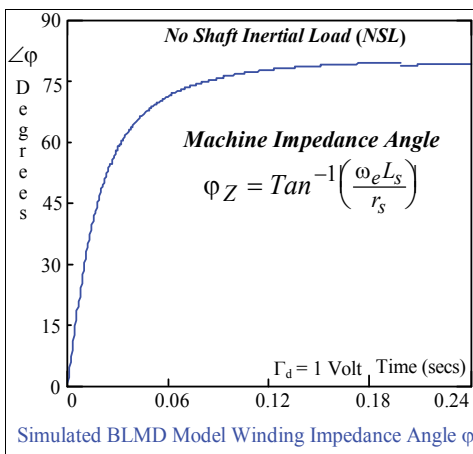


Fig. 43. Motor impedance angle

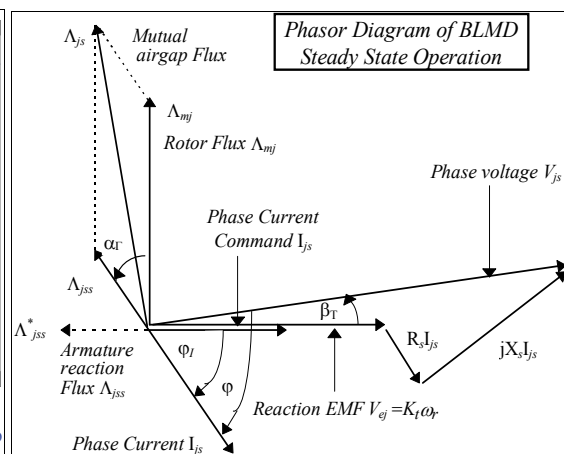


Fig. 44. Phasor diagram of brushless motor

This can then be used in the evaluation of the load angle β_T using

$$\frac{V_z}{\sin \beta_T} = \frac{V_{js}}{\sin\{\pi - (\varphi_z - \varphi_l)\}} \text{ as} \tag{XCIV}$$

$$\beta_T = \sin^{-1} \left\{ \frac{V_z}{V_{js}} \sin(\varphi_z - \varphi_l) \right\} \tag{XCV}$$

with $\beta_T = 1.06^\circ$ upon substitution of the phasor quantities in Table IV. When a finite load torque is applied to the BLMD shaft a noticeable difference develops between the actual and internal power factor angles with an increase in load angle β_T , appropriate to the value of load power necessary to sustain the applied load torque and friction losses, as the motor approaches rated angular velocity ω_{rmax} . In the development of the torque expression in (XLII), which can be re-expressed as

$$\Gamma_e(I_s, \theta_r) = K_e \sum_{j=1}^3 \cos\left(p\theta_r - \frac{2(j-1)\pi}{3}\right) i_{js} = \left(\frac{1}{\omega_r}\right) \sum_{j=1}^3 v_{ej} \cdot i_{js} \tag{XCVI}$$

using (XXIV) it is assumed that the stator winding back EMF v_{ej} is in phase with the forced stator current i_{js} , in response to the equal magnitude current demand i_{dj} from shaft sensor position information, for maximum torque production via the applied and electronically commutated stator terminal voltage v_{sj} . This assumption, however, is not accurate in that a phase lag equal to the power factor angle φ develops with shaft velocity between the injected current I_{js} and voltage V_{js} phasors as shown in Figure 44. During normal motor operation current commutation is used in an attempt to maintain a virtual armature flux phasor Λ_{jss}^* in quadrature with the rotor flux, in accordance with fixed current demand, for maximum motor torque production. As the motor reaches rated speed, for zero shaft load torque conditions, the motor impedance angle φ_z in Figure 42 increases along with the back EMF V_{ej} . The cumulative effect of increased impedance voltage V_z with V_{ej} result in further current lag by the angle φ in order to comply with fixed torque current demand via the applied stator phase voltage V_{js} .

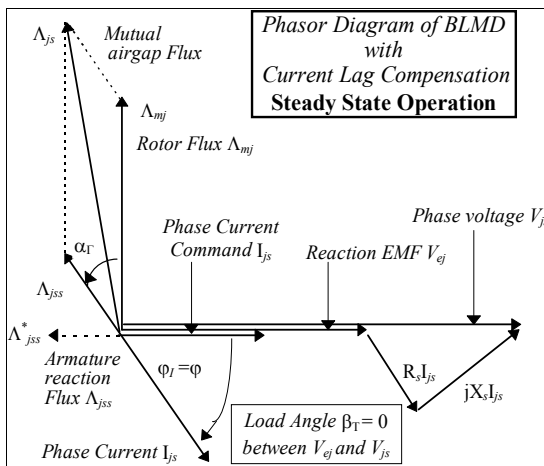


Fig. 45. Current lag compensation

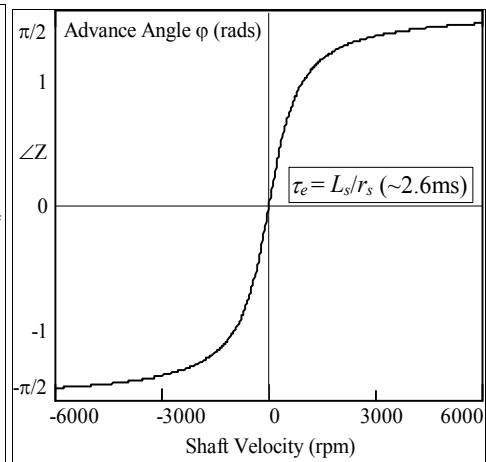


Fig. 46. Commutation phase lead

Consequently the applied torque Γ_e decreases with increased angular displacement ϕ_1 between the inverter controlled stator current flow and EMF phasors in accordance with (XCII) as

$$\Gamma_e = \frac{P_m}{\omega_r} = 3K_t I_{js} \cos \phi_1 . \tag{XCVII}$$

The internal power factor angle adjusts towards 90° to reduce the torque angle α_T in (XLVIII) with reaction EMF increase in compliance with load torque requirements as shown in Figure 44. The increase of current lag ϕ , with impedance angle ϕ_z due to motor speed, can be compensated for with power factor correction by electronically advancing the current command phase angle in accordance with (LXXXIV), in the current commutator circuit of Figures 1 and 28, as

$$p\theta_r - 2(j-1)\frac{\pi}{3} \rightarrow (p\theta_r + \phi_z) - 2(j-1)\frac{\pi}{3} \tag{XCVIII}$$

In this scheme the load angle β_T between the terminal voltage V_{js} and back EMF phasors is forced to zero with inverter controlled winding voltages that are collinear with the current demand I_{ds} phasors as shown in Figure 45. The commutation phase lead angle required to nullify the torque reduction effects at different motor speeds is displayed in Figure 46.

The motor airgap torque Γ_e displayed in Figure 47, which utilizes expression (XLII) during BLMD model simulation, appears to be numerically ‘noisy’. This apparent ‘noisiness’ result from the carrier harmonic contribution as high frequency ripple, due to PWM inverter operation, superimposed on the stator winding current flow. This sawtooth ripple manifestation is transferred via stator winding current injection to the magnetic coupling in the EM torque generation process. This ripple is primarily due to the nonlinear pulse nature of the delayed PWM process manifested as superimposed extraneous phase current harmonics, shown in Figure 48 as phase current ripple, mixing with the fundamental phase reference $\cos[p\theta_r - 2(j-1)\frac{\pi}{3}]$ in the torque product expression (XLIII). The smoothed torque characteristic is also shown in Figure 47 for measurement clarity and reference purposes with ‘noisy’ data filtering identical to the torque demand i/p filter employed.

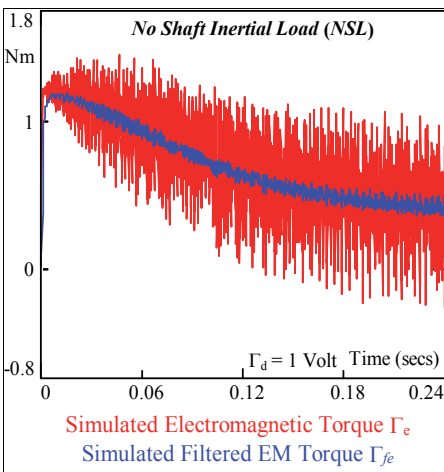


Fig. 47. Simulated airgap torque Γ_e

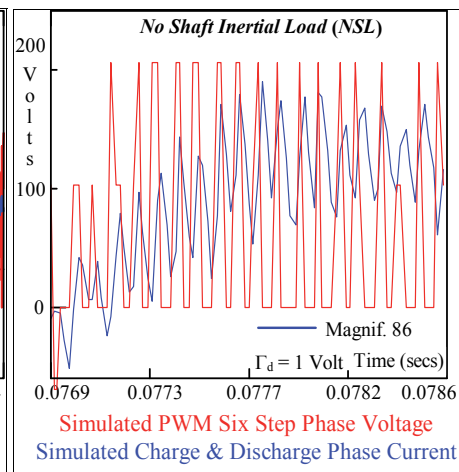


Fig. 48. Phase ripple current

The rotor inertia J_m and damping B_m , inherent in the BLMD system, has a smoothing effect on the generated electromagnetic torque Γ_e by virtue of the integrating action of the equivalent low pass filter characteristics of the motor dynamics given by

$$\frac{\omega_r}{\Gamma_e}(s) = \frac{1}{J_m s + B_m} \tag{XCIX}$$

with a 3dB cutoff radiancy based on parameters from Table II of

$$\omega_m = B_m / J_m \approx 7 \text{ rad. sec}^{-1} \tag{C}$$

This results in the smooth mechanical motion illustrated as the simulated motor shaft velocity in Fig. 49. As the motor reaches rated speed the generated torque decreases to that necessary in (LXXXVI) to sustain motion with frictional torque retardation. The simulated power transfer and the filtered version derived from the developed torque characteristics, depicted in Figure 47 using expression (XLVI), are shown in Figure 50. The net motive power required under steady state conditions, at a motor speed of $\omega_r \sim 310 \text{ rad. sec}^{-1}$, to overhaul mechanical losses is $P_m \sim 182 \text{ watts}$ which correlates reasonably well with the friction power estimate of $P_f \sim 200 \text{ watts}$ obtained from Figure 27.

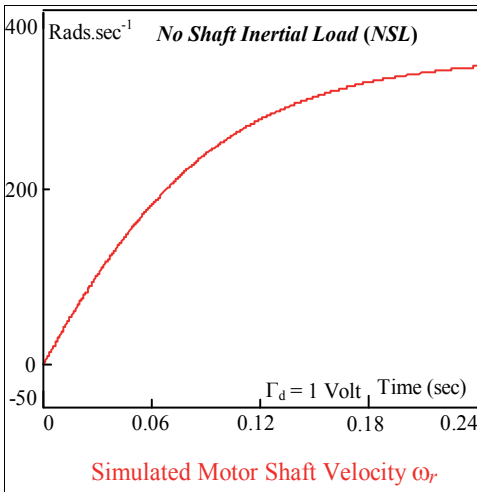


Fig. 49. Simulated shaft velocity

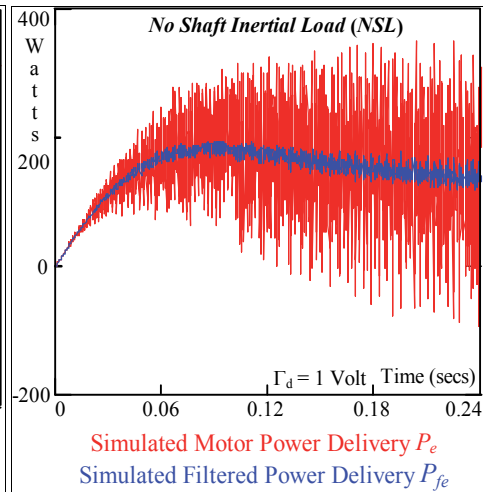


Fig. 50. Mechanical power delivery

3.4 Effects of PWM inverter delay

The influence of inverter delay on both motor torque and speed reduction can be visualized in Figures 51 and 52. Since torque command current magnitude is encoded as a modulated pulse duration τ_m during the PWM process an inverter dead zone is equivalent to a drop in voltage transport to the motor stator windings. The resultant decrease in motor winding current amplitude can be estimated, via (LII) with the aid of Figures 13 and 14, from consideration of the inverter blanking period required for transistor bridge protection with a consequent loss of mechanical torque delivery expressed by (XLV). When current flow i_{js} is positive the modulated pulse ON time of the appropriate power transistor T_{J+} , in the absence of inverter blanking with winding connection to the dc busbar U_d , is given by

$$t_{on} = \tau_m = (1 + m_f) \frac{T_s}{2} \quad (\text{CI})$$

which also corresponds to the OFF time of T_{j-} . When a dead zone is introduced into inverter operation, during which forced winding current injection is impeded but with flywheel conduction maintained through diode D_j in Figure 15 at ground potential, the resulting switch-on time for T_{j+} is given by

$$t_{on}^* = (\tau_m - \delta) = (1 + m_f) \frac{T_s}{2} - \delta \quad (\text{CII})$$

Similar switch-on time expressions hold for T_{j-} operation during negative current flow. The effect of inverter delay can be seen in the BLMD current feedback simulation as crossover distortion in Fig. 53 when contrasted with the FC trace without delay.

The relative percentage current flow with dead time is determined by the ratio of the switch-on times in (CI) and (CII) as

$$t_{on}^*/t_{on} = \left[1 - \frac{2\delta}{(1+m_f)T_s} \right] 100\% \quad (\text{CIII})$$

which for a unit torque demand input with $MI = 0.145$ ($= 1/6.9$), $T_s = 176\mu\text{s}$ and $\delta = 19.6\mu\text{s}$ in Figure 53 is estimated as 80.5%. The percentage ratio of the corresponding rms feedback currents, with and without delay respectively in Figure 53 over the extended time span of 0.24 secs, is 78.5% ($=1.555/1.981$) which is almost identical to that from pulse time considerations. The resultant torque ratio from Figure 51 is also approximately 80%, as it is proportional to the current ratio, in the settled region which corresponds to the torque necessary to overhaul frictional effects. Motor shaft speed exhibits a similar variation in Figure 52, since it is proportional to the time integral of the torque, with delay of about 82.5%.

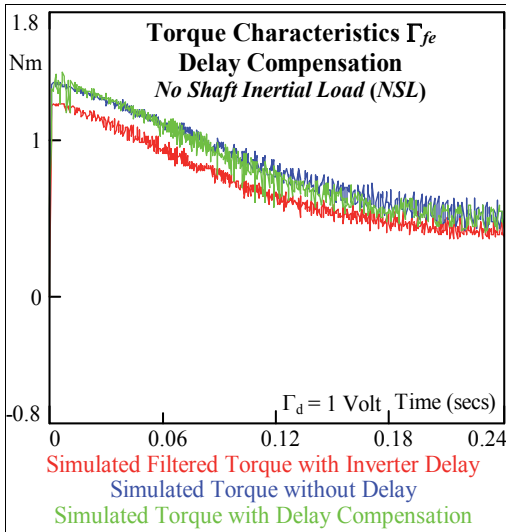


Fig. 51. Torque reduction with lag

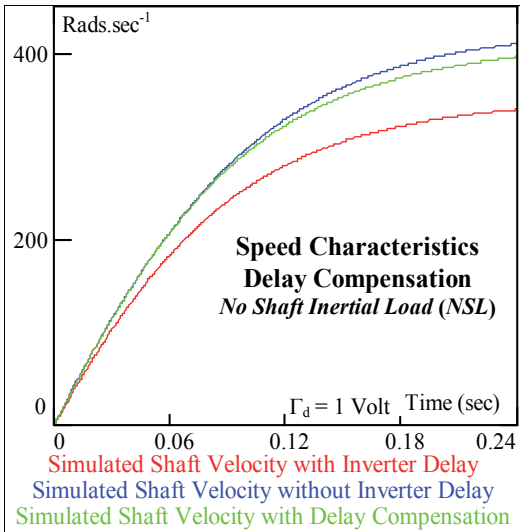


Fig. 52. Motor speed compensation

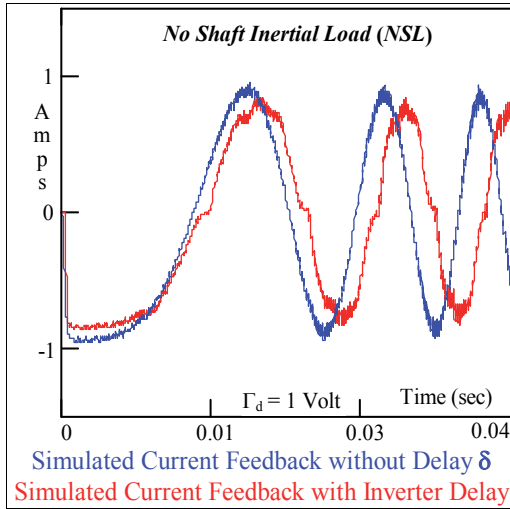


Fig. 53. Effect of inverter lag on FC

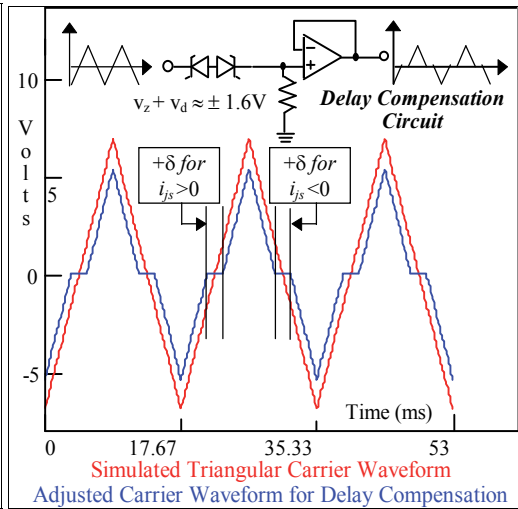


Fig. 54. Inverter delay compensation

3.5 Novel PWM Inverter dead-time compensation

Timing counter circuits with optocoupler isolation (Murai et al, 1985, 1992) have been used for delay correction in each phase during PWM operation of induction motors. A novel and simpler solution is proposed here for simultaneous delay compensation in all three phases through amplitude adjustment of the triangular dither waveform. The technique relies on the simple expedient of additional symmetrical double edge pulse widening during PWM, via the signal magnitude comparison with a reduced carrier amplitude contribution, to counterbalance the effects of inverter lag. The additional modulation index Δm_f required for increased pulse duration using (CI) to nullify the effect of inverter delay in (CII) is

$$\Delta m_f = \frac{\Delta V}{V_{tri}} = \frac{2\delta}{T_s} \approx 0.225 \tag{CIV}$$

which translates into an amplitude reduction of the positive going excursion of the triangular carrier waveform as

$$\Delta V = \Delta m_f V_{tri} = (0.225) \cdot (6.9) = 1.553. \tag{CV}$$

A similar pulse elongation time is associated, during periods of negative winding current flow, with the negative carrier amplitude reduction. The implementation of the requisite bipolar amplitude decrease is facilitated by the back-to-back zener diode combination, with buffer amplifier isolation as shown in Figure 54, which imparts a cumulative voltage clipping V_{CL} of

$$V_{CL} = V_z + V_d = \pm 1.6V \tag{CVI}$$

in the neighborhood of the dither signal $V_{tri}(t)$ polarity changeover where V_z is the zener voltage and V_d is the forward diode voltage drop. The compensatory effect of added pulse time on the torque and speed curves with inverter delay operation is shown in Figures 51 and 52 respectively. These characteristics are almost congruent with model simulations

linked with zero inverter lag over most of the motor speed range. The discrepancy at high speeds, although small, is associated with the lead time distribution about the modulated pulse double edge rather than at the leading edge where it should be concentrated to counteract the effects of inverter blanking. The quality of the lag compensation method can be better gauged from the phase and frequency coherency of the BLMD model FC responses illustrated in Figure 55 which are well correlated with a goodness-of-fit correlation coefficient of 91.7% using (LXXXIX).

4. Conclusions

A detailed and accurate reference model, based on physical principles, of a typical embedded BLMD system used for EV propulsion and high performance motive power industrial applications has been presented for the express purpose of computer aided design and simulation of EV propulsion systems where performance prediction and evaluation are a necessity before fabrication. Model fidelity is confirmed by extensive numerical simulation with particular emphasis at critical internal observation nodes when contrasted with measured data from a high performance PM drive system. Model validation for identification purposes is provided by frequency and phase coherence of simulated data with step response transient current feedback test data possessing FM attributes. A novel and effective delay compensation solution, based on carrier voltage level adjustment for multi-phase operation, is provided to counterbalance the effect of inverter blanking in torque reduction which is substantiated by BLMD model simulation.

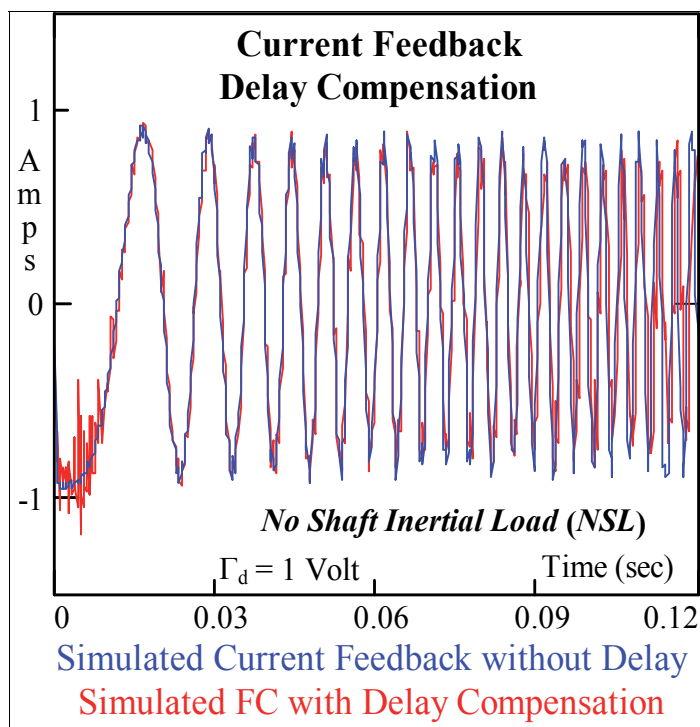


Fig. 55. FC delay compensation

5. Acknowledgment

The author wishes to acknowledge

- i Eolas – The Irish Science and Technology Agency – for research funding.
- ii Moog Ireland Ltd for brushless motor drive equipment for research purposes.

6. References

- Adams, R.D. & Fox, R.S.; (1975). Several Modulation Techniques for a Pulsewidth Modulated Inverter, *IEEE Trans. on Industry Applications*, Vol. IA-8, No. 5.
- Asada, H. & Youcef-Toumi, K.; (1987). *Direct-Drive Robots Theory and Practice*, MIT Press. Camb., Mass.
- Astrom, K.J. & Hagglund, T.; (1988). *Automatic Tuning of PID Controllers*, Instrument Society Of America, ISBN 1-55617-081-5.
- Astrom, K.J. & Wittenmark, B.; (1989). *Adaptive Control*, Addison-Wesley.
- Basak, A.; (1996) *Permanent Magnet DC linear Motors*, Clarendon Press, Oxford
- Boldea, I.; (1996). *Reluctance Synchronous Machines and Drives*, Oxford Science Publications, OUP
- Brickwedde, A.; (1985). Microprocessor-Based Adaptive Speed and Position Control for Electrical Drives, *IEEE Trans. on IAS*, Vol. IA-21, No. 5, pp1154-1161.
- Bulmer, M.G.; (1979). *Principles of Statistics*, Dover Publications Inc., New York.
- Chalam, V.V.; (1987). *Adaptive Control Systems: Techniques and Applications*, Marcel Dekker.
- Crangle, J.; (1991). *Solid State Magnetism*, Edward Arnold Publishers.
- Crowder, R.M.; (1995). *Electric Drives and their Controls*, Clarendon Press, Oxford.
- Dawson, D.M; Hu, J & Burg, T.C.; (1998). *Nonlinear Control of Electric Machinery*, Marcel Dekker.
- Demerdash, N.A; Nehl T.W. & Maslowski E.; (1980). Dynamic modelling of brushless dc motors in electric propulsion and electromechanical actuation by digital techniques, *IEEE/IAS Conf. Rec. CH1575-0/80/0000-0570*.
- Demerdash, N.A. & Nehl, T.W.; (1980). Dynamic Modelling of Brushless dc Motors for Aerospace Applications", *IEEE Trans. On Aerospace and Electronic Systems*, Vol. AES-16, No. 6.
- Dodson, R.C., Evans, P.D., Tabatabaei, H. & Harley, S.C.; (1990). Compensating for dead time degradation of PWM inverter waveforms, *IEE Proc.*, Vol. 137, Pt. B, No. 2.
- Dohmeki, H. & Nasu, M.; (1985). Development of a Brushless DC Motor for Incremental Motion Systems", *Proc. 14th IMCSD annual Symp.*
- Dote, Y.; (1990). *Servo Motor and Motion Control using Digital Signal Processors*, PHI.
- Electrocraft Corp; (1980). *DC Motors, Speed Control, Servo Systems*, 5th Edition.
- El-Sharkawi, M.A. & Huang, C.H.; (1989). Variable Structure Tracking of Motor for High Performance Applications, *IEEE Trans. on Energy Conv.*, Vol. 4, No.4.
- El-Sharkawi, M.A. & Weerasooriya, S.; (1990). Development and Implementation on Self-Tuning Tracking Controllers for DC Motors, *IEEE Trans. on Energy Conv.*, Vol. 5, No. 1.
- EL_Sharkawi, M.A. ; (1991). *Advanced control techniques for High Performance Electric Drives, Control and Dynamic Systems*, Academic Press, pp. 59-130, Vol 44, 1991.

- El-Sharkawi, M.A., El-Samahy, A.A. & El-Sayed, M.L.; (1994). High Performance Drive of DC Brushless Motors Using Neural Network", *IEEE Trans. on Energy Conversion*, Vol.9.
- Emadi, A.; Ehsani, M. & Miller, J. M. (2003). *Vehicular Electric Power Systems: Land, Sea, Air, and Space Vehicles*, CRC Press.
- Evans, P.D. & Close, P.R.; (1987). Harmonic Distortion in PWM inverter output Waveforms", *IEE Proc.*, Vol 134, Pt. B, No. 4.
- Franklin, G.F. & Powell, J.D.; (1980). *Digital Control Of Dynamic Systems*, Addison Wesley.
- Friedrich, G. & Kant, M.; (1998). Choice of drives for electric vehicles: a comparison between two permanent magnet AC machines, *IEE Proc.-Elec. Power Appl.*, Vol. 145, No. 3.
- Grant, D.A. & Seidner, R.; (1981). Ratio Changing in pulse-width-modulated inverters", *IEE Proc.*, Vol. 128, Pt. B, No. 5.
- Grant, D.A., Houldsworth, J.A. & Lower, K.N.; (1983). A New High-Quality PWM AC Drive", *IEEE Trans. on Industry Applications*, Vol IA-19, No. 2.
- Guinee, R.A. & Lyden, C.; (1998). A Novel Single Fourier Series Technique for the Simulation and Analysis of Asynchronous Pulse Width Modulation, *IEEE 13th Annual Applied Power Electronics Conference and Exposition, APEC'98*, Anaheim, California.
- Guinee, R.A. & Lyden, C.; (1998). An Improved Simulation Model of a Brushless DC Motor Drive System for Industrial Applications, *IEEE 9th Mediterranean Electrotechnical Conference, MELECON'98*, Tel-Aviv, ISRAEL.
- Guinee, R.A. & Lyden, C.; (1998). Accurate Modelling and Simulation of a High Performance Brushless DC Motor Drive System for Industrial Applications, *Proc. of the IASTED International Conference Applied Modelling and Simulation*, Honolulu, Hawaii.
- Guinee, R.A. & Lyden, C.; (1999). Accurate Modelling And Simulation Of A DC Brushless Motor Drive System For High Performance Industrial Applications, *IEEE ISCAS'99 - IEEE International Symposium on Circuits and Systems*, May/June 1999, Orlando, Florida
- Guinee, R.A. & Lyden, C.; (1999). Parameter Identification of a Brushless Motor Drive System using a Modified Version of the Fast Simulated Diffusion Algorithm, *Proc. of American Control Conference - IEEE ACC-1999*, San Diego, pp.3467-3471.
- Guinee, R.A. & Lyden, C.; (1999). Accurate Modelling and Simulation of a High Performance Permanent Magnet Adjustable Speed Drive System for Embedded Systems", *8th European Conference on Power Electronics and Applications - EPE'99*, Lausanne, Switzerland.
- Guinee, R.A. & Lyden, C.; (2000) A Novel Application of the Fast Simulated Diffusion Optimization Technique for Brushless Motor Parameter Extraction, *UKACC International Conference on Control*, Cambridge Univ.
- Guinee, R.A. & Lyden, C.; (2001), Motor Parameter Identification using Response Surface Simulation and Analysis, *Proc. of American Control Conference, ACC-2001*, VA, USA.
- Guinee, R.A.; (2003). *Modelling, Simulation, and Parameter Identification of a Permanent Magnet Brushless Motor Drive System*, Ph. D. Thesis, NUI – University College Cork.
- Guinee, R.A.; (2005). Dead Time Compensation in PWM Inverter Transistor operation for Improved Brushless Motor Drive System Performance, *Universities Power Engineering Conference, UPEC 2005*, University College Cork.

- Guinee, R.A.; (2009). *A Novel Dead Time Compensation Circuit for Improved PWM Inverter Operation in Brushless Motor Drive Systems for Electric Vehicle*, 5th IEEE Vehicle Power and Propulsion Conference (VPPC'09), Dearborn, MI 48128, USA
- Hang, C.C. & Sin, K.K.; (1991). "A Comparative Performance Study of PID Auto-Tuners", *IEEE Control Systems*, 0272-1708/91/0800-004.
- Hendershot, J.R. & Miller, T.J.E.; (1994). *Design of Brushless Permanent-Magnet Motors*, Magna Physics Publishing and Clarendon Press, Oxford.
- Jahns, T.M.; (1984). Torque Production in Permanent Magnet Synchronous Motor Drives with Rectangular Current Excitation, *IEEE Trans. on Industry Applications*, Vol IA-20, No. 4.
- Johansson, R.; (1993). *System Modelling and Identification*, Prentice Hall.
- Kuo, B.C. & Tal, J.; (1978). *Incremental Motion Control Systems: DC Motors and Control Systems*, SRL Publ. Co., illinois.
- Kraus, H.L., Bostian C.W. & Raab, F.H.; (1980). *Solid State Radio Engineering*, J. Wiley & Sons.
- Krause, P.C.; (1986). *Analysis of Electric Machinery*, McGraw-Hill
- Krause, P.C. & Wasynczuk, O.; (1989) *Electromechanical Motion Devices*, McGraw-Hill.
- Kreyszig, E.; (1972). *Advanced Engineering Mathematics*, J. Wiley & Sons.
- Leu, M.C., Liu S. & Zhang, H.; (1989). Modelling, Analysis and Simulation of Brushless DC Drive System, *Winter Annual Meeting of ASME*, 89-WA/DSC-1, San Francisco.
- Ljung, L.; (1987). *System identification: Theory For The User*, PHI.
- Ljung, L.; (1991). Issues in System Identification, *IEEE Control Systems*, 0272-1708/91/0100-0025.
- Ljung, L.; (1992). "A Discussion Of Model Accuracy In System Identification", *International Journal Of Adaptive Control and Signal Processing*, Vol.6, pp.161-171, J. Wiley & Sons.
- Matsch, L.W.; (1972). *Electromagnetic and Electromechanical Machines*, Intext Educational Publishers.
- Meshkat, S.; (1985). A new Microprocessor Based Brushless Servo Amplifier for Optimum Current Vector Control, *Proc. 13th IMCSD ann. symp.*, pp 19-24.
- Miller, J.; (2010). *Propulsion Systems for Hybrid Vehicles*, IET, Renewable Energy, 2nd Edition.
- Mohan, N.; (1998). Understanding Basics of Adjustable Speed and Vector-Controlled Induction and Synchronous Motor Drives, Seminar S1, APEC'98 - *Applied Power Electronics Conference and Exposition*, Anaheim, California.
- Moog GmbH; (1988). *Moog Brushless Technology:Brushless Servodrives User Manual*, D310.01.03 En/De/It 01.88, Moog GmbH, D-7030 Böblingen, Germany.
- Moog GmbH; (1989). *Moog Brushless Technology User Manual:D31X-XXX Motors,T158-01X Controllers,T157-001 Power Supply*, , D-7030 Böblingen.
- Murai, Y., Watanabe, T. & Iwasaki, H.; (1985). Waveform Distortion And Correction Circuit For PWM Inverters With Switching Lag Times", *IEEE IAS Annual Meeting*, Toronto, pp436-441, *IEEE CH2207-9/85/0000-0436*.
- Murai, Y., Riyanto, A., Nakamura, H. & Matsui, K.; (1992). PWM Strategy for High Frequency Carrier Inverters Eliminating Current-Clamps during Switching Dead-Time, 0-7803-0634-1/92, Houston, USA.
- Murphy, J.M. & Turnbull, F.G.; (1989). *Power Electronic Control of AC Motors*, Pergammon Press.
- Murugesan, S.; (1981). An Overview of Electric Motors for Space Applications, *IEEE Trans. on Ind. Elec. and Control Inst.*, Vol. IECI-28, No. 4.

- Naitoh, H. & Tadakuma, S.; (1987). Microprocessor-Based Adjustable-Speed DC Motor Drives using Model Reference Adaptive Control", *IEEE Trans. on IAS*, Vol. IA-23, No. 2, pp 313-318.
- Noodleman, S.; (1975). A New Type DC Motor, *IEEE Trans. on Ind. Appl.*, Vol. IA-11, No. 3.
- Persson, E.K. & Buric, M.; (1976). Mathematical Modelling and Simulation of High Performance Brushless DC Motors, *IMCSD 4th annual symp.*
- Pollack, J.J.; (1972). Advanced Pulsewidth Modulated Inverter techniques, *IEEE Trans. on Industry Applications*, Vol. IA-8, No. 2.
- Press, W.H., Flannery, B.F., Teukolsky, S.A. & Vetterling, W.T.; (1990). *Numerical Recipes in C*, CUP.
- Soderstrom, T. & Stoica, P.: (1989), *System Identification*, Prentice Hall Internat.
- Spooner, E. & Williamson, A.C.; (1996). Direct coupled, permanent magnet generators for wind turbine applications, *IEE Proc.-Electr. Power Appl.*, Vol. 143, No. 1.
- Tal, J.; (1976). Design and Analysis of Pulsewidth-Modulated Amplifiers for DC Servo Systems, *IEEE Trans. on Industrial Electronics and Control Instrumentation*, Vol IECI 23, No.1.
- Tomasek, J.; (1979). Brushless Servo Motor - Amplifier Optimization, *Proc. of 8th Ann. Symp. of Incremental Motion Control Systems and Devices*, Univ. of Illinois.
- Tomasek, J.; (1983). Analysis of Torque-Speed Performance Limits in Brushless DC Servo Systems, *Proc. of 12th Ann. Symp. of Incremental Motion Control Systems and Devices*, Illinois Univ
- Tomasek, J.; (1986). "Basic Performance Specifications and Ratings for Sine-Wave Brushless Servo Systems, *Proc. of 15th Ann. Symp. of Incremental Motion Control Systems and Devices*.
- Vas, P; (1998). *Sensorless Vector and Direct Torque Control*, Oxford Univ.
- Weerasooriya, S. & El-Sharkawi, M.A.; (1989). Adaptive Tracking Control for High Performance DC Drives, *IEEE Trans. on Energy Conv.*, Vol. 4, No. 3.

Multiobjective Optimal Design of an Inverter Fed Axial Flux Permanent Magnet In-Wheel Motor for Electric Vehicles

Christophe Versèle, Olivier Deblecker and Jacques Lobry
*Electrical Engineering Department, University of Mons
Belgium*

1. Introduction

Battery electric vehicles (EVs) and hybrid EVs are now at the forefront of transportation researches in order to reduce the emission of pollutant gasses, especially in the inner cities. However, the present performances of EVs are far from being competitive to those of traditional combustion engine vehicles, mainly in terms of autonomy. Therefore, power-saving and mass-saving are of the utmost importance when designing the entire drive system of EVs and their electric motor drives (Tseng & Chen, 1997).

In conventional EVs, the power system consists of battery, electric motors with drives, transmission gears and differentials to the wheels (Yang & Chuang, 2007). The mechanical transmission system contributes greatly to the power loss, through the heat dissipation in the various components, and to the weight of the vehicle. An interesting alternative to this conventional power system is the concept of in-wheel motors or hub-in motors as illustrated in Fig.1. In this concept, the motor is directly integrated into the wheel, thus eliminating transmission gears and differentials with their associated power loss (Yang et al., 2004). Furthermore, the elimination of mechanical components in transmission chains or gears reduces the weight of the vehicle. Each of the in-wheel motors has its own voltage supply inverter (VSI) as well as its own speed or torque controller. All the in-wheel motors are coordinated by a digital vehicular-speed controller with differential gear.

Due to their robustness, low cost, performances and simplicity of design, induction motors (IMs) are often preferred for EVs propulsion. However, in recent years, Neodymium-Iron-Bore (NdFeB) axial flux permanent magnet (AFPM) motors have become an interesting alternative to IMs due to their compactness, low weight and high torque density. Moreover, AFPM motors are pancake-type, fit perfectly the wheel of an automobile vehicle and, thus, can be easily and compactly integrated into the wheel. According to these properties, axial flux motors seem to be a better choice than more conventional radial flux motors for this kind of application. Note that this issue is discussed in (Versèle et al., 2009).

There are many alternatives for the design of AFPM motors (Sahin & Vandenput, 1999): slotted or slotless stator, rotor with interior or surface-mounted permanent magnets (PMs), internal or external rotor, numbers of rotors and stators, etc. In this chapter, a double-sided motor with internal slotted stator and surface-mounted PMs is proposed as basic design choice essentially motivated by the presence of two air gaps doubling the torque.

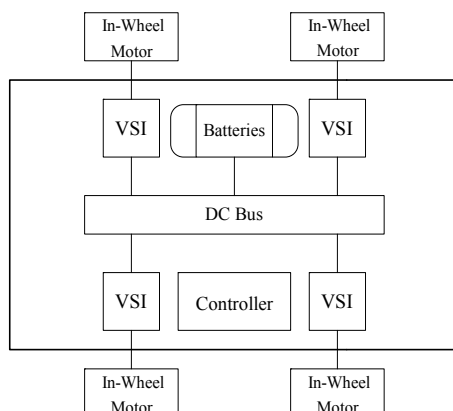


Fig. 1. In-wheel motors drive

Among the various researches, many authors have published papers about the optimal design of in-wheel motors for EVs or wheelchairs (Espanet et al., 1999; Nilssen et al., 2005; Tseng & Chen 1997; Yang et al., 2004) as well as about the optimization of AFPM motors (Azzouzi et al., 2006; Chun et al., 2007; Cvetkovski & Petkovska, 2002).

In this chapter, the objective is to optimize simultaneously one of the four in-wheel motors of an EV and its own VSI in terms of weight and power loss. Note that the simultaneous optimization of the in-wheel motor and its own VSI, rarely discussed in literature, results in a system optimized towards the requirements of the EV.

To do so, a multiobjective optimization (MO) technique based on evolutionary algorithms (EAs) is used. EAs are stochastic search techniques that mimic natural evolutionary principles to perform search and optimization procedure. Among the several approaches to evolutionary optimization, GAs have been chosen and the so-called Elitist Nondominated Sorting Genetic Algorithm (NSGA-II) (Deb, 2002) is used to perform the optimal design of the in-wheel motor and its own VSI. Note that GAs are chosen because they have already proved their efficiency to optimize every kind of electrical machines (Skaar & Nielssen, 2003) and power electronics converters (Helali, 2005; Malyna et al., 2007; Versèle et al., 2010).

The remainder of this chapter is organized as follows. First, the requirements in terms of power and torque of an EV are discussed in Section 2. Then, Section 3 describes the AFPM motor and VSI models used in the design procedure. In Section 4, the MO technique based on GAs as well as the proposed optimization routine are described. Finally, a design example is exposed in Section 5 and the advantages and limitations of the new design procedure are discussed in Section 6.

2. Requirements of an EV

In order to determine the requirements, in terms of power and torque, of one of the four in-wheel motors (considering an EV driven by four in-wheel motors), a computer model of an EV traction system is presented in this section.

The road load on the vehicle consists of three forces (Yang & Chuang, 2007): (1) the rolling resistance F_r , (2) the aerodynamic drag force F_a and (3) the climbing force F_c which are expressed as (Ehsani et al., 2005):

$$F_r = f_r M_v g \tag{1}$$

$$F_a = 0.5 \rho A_f C_D (v + v_w)^2 \tag{2}$$

$$F_c = M_v g \sin(\alpha) \tag{3}$$

where f_r is the rolling resistance coefficient (which is an empirical coefficient depending on the road-tire friction), M_v is the mass of the vehicle, g is the earth gravity acceleration, ρ is the air density, A_f is the frontal area of the vehicle, C_D is the coefficient of aerodynamic resistance (that characterizes the shape of the vehicle), v is the vehicle speed, v_w is the component of the wind speed on the vehicle's moving direction and α is the road angle (deduced from the road slope). According to Newton's second law, the total tractive effort F_t required to reach the desired acceleration a and to overcome the road load is:

$$F_t = M_v a + F_r + F_a + F_c . \tag{4}$$

Once the total tractive effort is computed, the total torque T_t and power P_t required to be produced by the four in-wheel motors can be expressed as:

$$T_t = F_t r_{wheel} \tag{5}$$

$$P_t = T_t \Omega_{wheel} \tag{6}$$

where r_{wheel} is the drive wheels radius and Ω_{wheel} is the rotational wheels speed.

Based on the specifications of an urban EV (Ehsani et al., 2005), summarized in Table 1, and on the above-described EV traction system, the requirements of one in-wheel motor can be easily computed. All the results are presented in Table 2. Note that, in addition to provide its requirements, the in-wheel motor must also respect some constraints. The main constraints are the total weight of each of the four in-wheel motors M_{motor} (imposed by the maximal authorized "unsprung" wheel weight) and the imposed outer radius R_{out} of the motor (imposed by the rim of the wheel). Those are also specified in Table I and Table 2.

Weight M_v	1150 kg
Max. speed v_{max}	13.9 m/s (50 km/h)
Acceleration a	1 m/s ²
Frontal area A_f	2.5 m ²
Coefficient of aerodynamic resistance C_D	0.32
Rolling resistance coefficient f_r	0.015
Max. road angle α	5.7° (10%)
Rim diameter	14''
Number of in-wheel motors	4

Table 1. Specifications of an EV

Torque T_t	$> 107 \text{ Nm}$
Power P_t	$> 8.7 \text{ kW}$
Weight of the motor M_{motor}	$< 43.125 \text{ kg}$

Table 2. Requirements of one in-wheel motor

3. Modeling of the AFPM motor and VSI

In order to evaluate the two objective functions, viz. the weight and the losses of the motor and the VSI, and to verify if the constraints are not violated during the design procedure, two models are necessary: one for the motor and one for the VSI. It should be noticed that analytical models have been chosen in this paper with the aim of reducing the computational time. These models permit to evaluate the weight and the losses of the motor and the VSI as well as to estimate the torque and power developed by the motor.

3.1 AFPM motor model

Analytical design of AFPM motors is usually performed on the average radius R_{ave} of the machine (Parviainen et al., 2003) defined by:

$$R_{ave} = (R_{in} + R_{out})/2 \quad (7)$$

where R_{in} and R_{out} are respectively the inner and outer radius of the machine (see Fig. 2(a)).

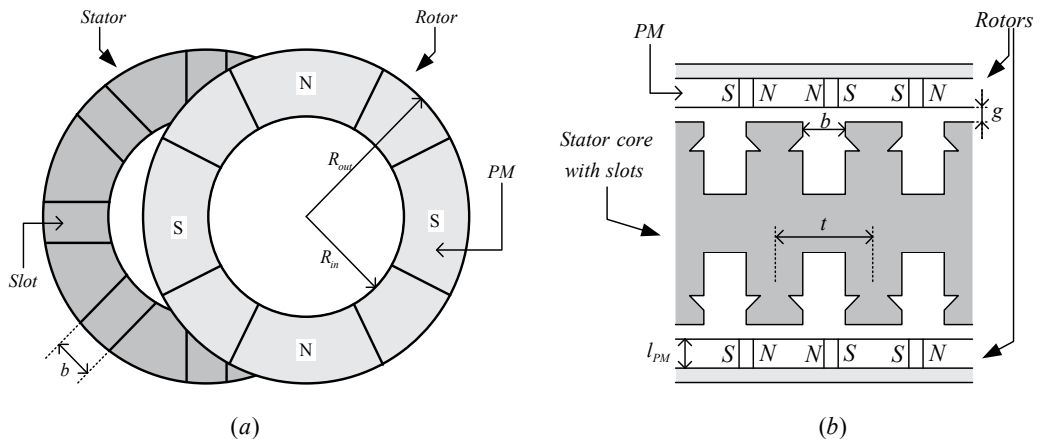


Fig. 2. (a) Stator and rotor of an AFPM machine and (b) doubled-sided AFPM machine with internal slotted stator

The use of the average radius as a design parameter allows evaluating motor parameters and performances based on analytical design methods (Gieras et al., 2004).

The air gap flux density B_g is calculated using the remanence flux density B_r (in the order of 1.2 T for a NdFeB type PM) and the relative permeability μ_{ra} of the PM as well as the geometrical dimensions of the air gap and the PM (thickness and area) according to:

$$B_g = k_{\sigma PM} \frac{B_r}{1 + \mu_{ra} \frac{k_C g S_{PM}}{l_{PM} S_g}} \quad (8)$$

where g and l_{PM} are respectively the air gap thickness and PM thickness (see Fig. 2(b)); S_g and S_{PM} are respectively the air gap area and PM area. Finally, in (8), $k_{\sigma PM}$ (<1) is a factor that takes into account the leakage flux and k_C (>1) is the well-known Carter coefficient.

On the one hand, in order to obtain an accurate estimation of the air gap flux density and torque developed by the motor, the factor $k_{\sigma PM}$ is one of the most essential quantities that must be computed. Indeed, the leakage flux has a substantial effect on the flux density within the air gap and PMs (Qu & Lipo, 2002) and, therefore, on the torque developed by the motor (see (11)). In addition to air gap leakage flux, zigzag leakage flux is another main part of the leakage flux. The zigzag leakage flux is the sum of three portions (Qu & Lipo, 2002): the first part of the zigzag leakage flux is short-circuited by one stator tooth, the second part links only part of the windings of a phase and the third part travelling from tooth to tooth does not link any coil. Note that, in this paper, an analytical model developed by Qu and Lipo (Qu & Lipo, 2002) for the purpose of the design of surface-mounted PM machines is used to compute the factor $k_{\sigma PM}$. This model permits to express this factor in terms of the magnetic material properties and dimensions of the machine. It is thus very useful during the design stage.

On the other hand, the main magnetic flux density in the air gap decreases under each slot opening due to the increase in reluctance. The Carter coefficient permits to take into account this change in magnetic flux density caused by slot openings defining a fictitious air gap greater than the physical one. It can be computed as follows (Gieras et al., 2004):

$$k_C = \frac{t}{t - \gamma g} \quad (9)$$

where t is the average slot pitch (see Fig. 2(b)) and γ is defined by:

$$\gamma = \frac{4}{\pi} \left[\frac{b}{2g} \arctan\left(\frac{b}{2g}\right) - \ln \sqrt{1 + \left(\frac{b}{2g}\right)^2} \right] \quad (10)$$

where b is the width of slot opening (see Fig. 2(b)).

Assuming sinusoidal waveform for the air gap flux density and the phase current, the average electromagnetic torque T of a double-sided AFPM motor can be calculated by:

$$T = 2\pi B_g A_{in} R_{out}^3 (k_d - k_d^3) \quad (11)$$

where A_{in} is the linear current density on the inner radius of the machine and k_d is the ratio between inner and outer radii of the rotor disk. It should be noticed that, for a given outer radius and magnetic and electric loading, the factor k_d is very important to determine the maximum torque developed by the motor. So, this factor will be one of the optimization variables. Figure 3 reports the per-unit (p.u.) electromagnetic torque with respect to this factor k_d . One can remark that the maximum value of the torque is reached for $k_d \approx 0.58$.

The electromagnetic power P can easily be calculated by the product of torque and rotational speed Ω_r of the motor according to:

$$P = T\Omega_r . \quad (12)$$

The double-sided AFPM motor losses are the sum of the stator winding losses, the stator and rotor cores losses, the PMs losses and the mechanical losses, whereas its weight is the sum of the stator and the two rotors weights, the stator winding weight and the PMs weight. Note that the computation of those different parts of the two objective functions can easily be found elsewhere (Gieras et al., 2004) and, so, it is not described in this chapter.

Finally, it should also be pointed out that some electrical parameters of the AFPM motor, such as the stator resistance (R_s) and the direct (L_d) and quadrature (L_q) axes inductances, can be calculated once the motor has been design using the above-described fundamental design equations.

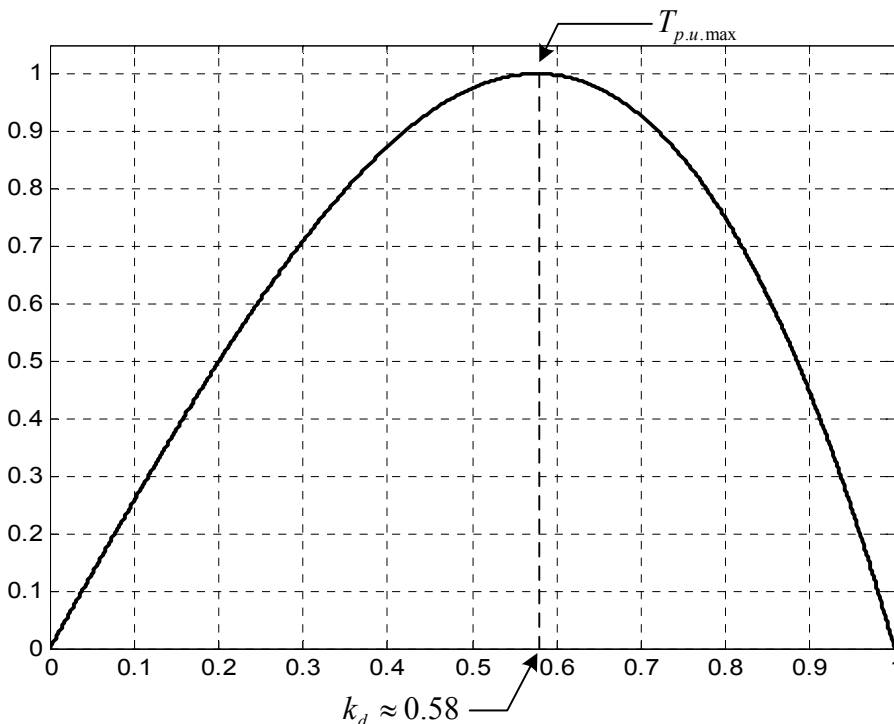


Fig. 3. Per-unit electromagnetic torque $T_{p.u.}$ as a function of the factor k_d

3.2 AFPM motor model validation

In order to validate the analytical AFPM motor model presented in this chapter, analytical and experimental results are compared. To do so, the proposed model is applied to a 5.5 kW, 4000 rpm AFPM motor. The calculated motor parameters are then compared with parameters obtained by classical tests (test at dc level, no-load test, etc.) performed on an existing AFPM pump motor. All the results are reported in Table 3. As can be seen, very small differences are obtained between the analytical and experimental results, whatever the parameters. According to this validation method, one can conclude that the proposed analytical design process gives reasonable results in this particular case and can be used in the optimization procedure of the in-wheel motor of an EV.

Parameters	Analytical results	Experimental results
R_s (dc-resistance)	0.45 Ω	0.423 Ω
L_d	0,129 H	0,117 H
L_q	0,127 H	0,117 H
T	13.97 Nm	15.04 Nm
P	5.85 kW	5.5 kW

Table 3. Analytical and experimental results for the 5.5 kW, 4000 rpm AFPM pump motor

3.3 VSI model

The total loss of the semiconductor devices (IGBTs and diodes) of the VSI (employing sinusoidal pulse-width-modulation) consists of two parts: the on-state losses and the switching losses. The on-state losses of the devices are calculated from their average I_{ave} and rms I_{rms} currents by the well-known expression (Semikron, 2010):

$$P_{on} = V_{th} \cdot I_{ave} + r \cdot I_{rms}^2 \quad (13)$$

where V_{th} represents the threshold voltage and r the on-state resistance, both taken from the manufacturer's data sheets.

The switching losses are, as for them, calculated by the following formula (Semikron, 2010):

$$P_{sw} = f_s \cdot (E_{turn-on} + E_{turn-off})_{T_j, I_C, V_{CE}} \quad (14)$$

where $E_{turn-on}$ and $E_{turn-off}$ are the energies dissipated during the transitions, both taken from the manufacturer's data sheets, at given junction temperature T_j , on-state collector current I_C and blocking voltage V_{CE} . Note that the average and rms values of the current used in (13) can easily be computed.

Based on the total loss of the semiconductor devices, the heatsink can be designed in order to limit the junction temperature to a predefined temperature (typically in the order of 125 °C). This temperature can be estimated from the ambient temperature T_a , the thermal resistances (junction-case: $R_{th,jc}$, case-heatsink: $R_{th,ch}$ and heatsink-ambient: $R_{th,ha}$) and the total loss P_{sc} of all the semiconductor devices by:

$$T_j = T_a + (R_{th,jc} + R_{th,ch} + R_{th,ha}) \cdot P_{sc} \quad (15)$$

From (15), the thermal resistance of the heatsink $R_{th,ha}$ needed to limit the junction temperature to the predefined value can be computed and, then, the heatsink can be selected from the manufacturer's data sheets.

The total weight of the VSI is the sum of the weight of all the semiconductor devices and the weight of the heatsink.

4. Optimization routine based on the NSGA-II

As mentioned previously, in this contribution, a MO technique based on EAs is used. Those are stochastic search techniques that mimic natural evolutionary principles to perform the search and optimization procedures (Deb, 2002).

GAs have been chosen because they overcome the traditional search and optimization methods (such as gradient-based methods) in solving engineering design optimization problems (Deb & Goyal, 1997). Indeed, there are, at least, two difficulties in using traditional optimization algorithms to solve such problems. Firstly, each traditional optimization algorithm is specialized to solve a particular type of problems and, therefore, may not be suited to a different type. As this is not the case with the GAs, no particular difficulties have been met to adapt the considered GA (viz. the NSGA-II, see below) to the multiobjective optimal design of the AFPM motor and its VSI. Only the models of these converters had to be used in combination with the GA in order to evaluate the values of the considered objectives. Secondly, most of the traditional methods are designed to work only on continuous variables. However in engineering designs, some variables are restricted to take discrete values only. In this chapter, this requirement arises, e.g., for the choice of the number of poles pairs.

Mixed-variable optimization problems are difficult to tackle because they pose the problems of the combinatorial and continuous optimization problems (Socha, 2008). For this reason, there are not many dedicated algorithms in literature and most of the approaches used in these algorithms relax the constraints of the problem. The most popular approach consists in relaxing the requirements for the discrete variables which are assumed to be continuous during the optimization process (Deb & Goyal, 1997). This type of approach is, often, referred as continuous relaxation approach.

Apart from the relaxation-based approach, there are methods proposed in literature that are able to natively handle mixed-variable optimization problems. However, only a few such methods have been proposed. Among them, the Genetic Adaptive Search is based on the fact that there are versions of the GAs dedicated to discrete variables and other versions dedicated to continuous variables. So, the GAs can be easily extended to natively handling both continuous and discrete variables. Such an approach has been proposed in (Deb & Goyal, 1997) and will be used in this chapter as it has already proved to be efficient to solve engineering problems (see, e.g. (Deb & Goyal, 1997)). Pattern Search Method (Audet & Dennis, 2001), Mixed Bayesian Optimization Algorithms (Ocenasek & Schwarz, 2002) and Ant Colony optimization (Socha, 2008) are other methods which permit to tackle mixed-variable problems.

Among the several MO techniques using GAs (see, e.g., (Deb, 2007)), the so-called NSGA-II (Deb *et al.*, 2002), described in the next Section, will be used to perform the optimal design.

4.1 NSGA-II

NSGA-II is a recent and efficient multiobjective EA using an elitist approach (Deb, 2002). It relies on two main notions: nondominated ranking and crowding distance. Nondominated ranking is a way to sort individuals in nondominated fronts whereas crowding distance is a parameter that permits to preserve diversity among solutions of the same nondominated front. The procedure of the NSGA-II is shown in Fig. 4 and is as follows (Deb, 2002). First, a combined population R_t (of size $2 \cdot N$) of the parent P_t and offsprings Q_t populations (each of size N) is formed. Then, the population R_t is sorted in nondominated fronts. Now, the solutions belonging to the best nondominated set, i.e. F_1 , are of best solutions in the combined population and must be emphasized more than any other solution. If the size of F_1 is smaller than N , all members of F_1 are inserted in the new population P_{t+1} . Then, the remaining population of P_{t+1} is chosen from subsequent nondominated fronts in order of

their ranking. Thus, the solutions of F_2 are chosen next, followed by solutions from F_3 . However, as shown in Fig. 4, not all the solutions from F_3 can be inserted in population P_{t+1} . Indeed, the number of empty slots of P_{t+1} is smaller than the number of solutions belonging to F_3 . In order to choose which ones will be selected, these solutions are sorted according to their crowding distance (in descending order) and, then, the number of best of them needed to fill the empty slots of P_{t+1} are inserted in this new population. The created population P_{t+1} is then used for selection, crossover and mutation (see below) to create a new population Q_{t+1} , and so on for the next generations.

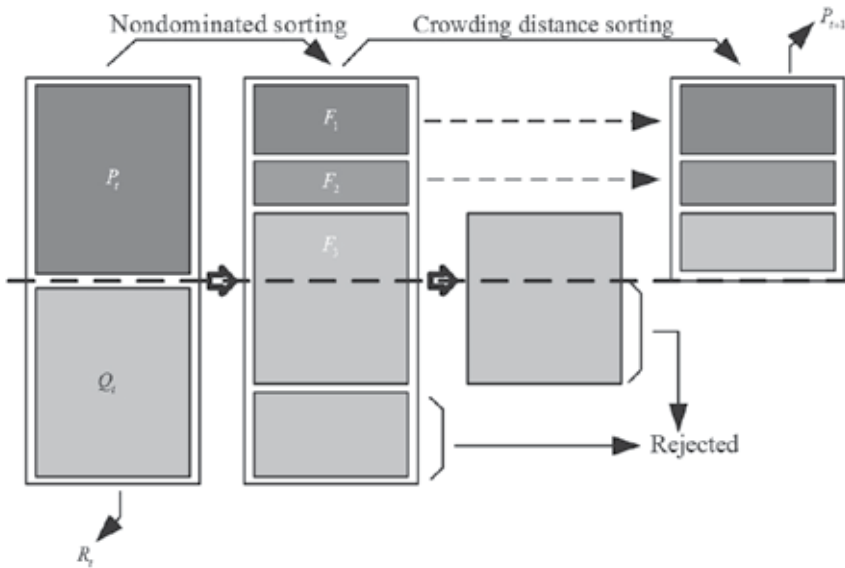


Fig. 4. NSGA-II procedure (Deb, 2002)

NSGA-II has been implemented in Matlab with real and binary coding schemes. So, a discrete variable is coded in a binary string whereas a continuous variable is coded directly. Such coding schemes are used in this paper because the considered optimization variables (see Table 4 in Section 5) belong to the two categories.

These coding schemes allow a natural way to code different optimization variables, which is not possible with traditional optimization methods. Moreover, the real coded scheme for the continuous variables eliminates the difficulties (Hamming cliff problem and difficulty to achieve arbitrary precision) of coding such variables with a binary scheme.

So, e.g., with the coding scheme used in this paper, the structure of the chromosome (composed by the seven considered optimization variables) of the solution #3 (see Table 5 in Section 5) is as follows:

$$\begin{array}{c}
 \underbrace{(k_d)(J)(I_{PM})(g)(f_s)}_{\text{real coded variables}} \quad \underbrace{(p)(q)}_{\text{binary coded variables}} \\
 \downarrow \\
 (0.89)(4.9)(5)(1.9)(1972)\underbrace{(1110)}_{\rightarrow 14}\underbrace{(11011110)}_{\rightarrow 222}
 \end{array}$$

There are three fundamental operations used in GAs: selection, crossover and mutation. The primary objective of the selection operator is to make duplicate of good solutions and eliminate bad solutions in a population, in keeping the population size constant. To do so, a tournament selection (Deb, 2002) based on nondominated rank and crowding distance of each individual is used. Then, the selected individuals generate offsprings from crossover and mutation operators. To cross and to mutate the real coded variables the Simulated Binary Crossover and Polynomial Mutation operators (Deb & Goyal, 1997) are used in this chapter. The single-point crossover (Deb, 2002) is, as for it, used to cross the discrete optimization variables. Note that to mutate this type of variables, a random bit of their string is simply changed from '1' to '0' or *vice versa*.

Finally, the constraints must be taken into account. Several ways exist to handle constraints in EAs. The easiest way to take them into account in NSGA-II is to replace the non-dominated ranking procedure by a constrained non-dominated ranking procedure as suggested by its authors elsewhere (see, e.g., (Deb, 2002)). The effect of using this constrained-domination principle is that any feasible solution has a better nondominated rank than any infeasible solution.

It is important to emphasize that the GA must be properly configured. The size of the population is one of the important parameters of the GA as well as the termination criterion. In this contribution, the size of the population N is taken equal to 100. It is important to note that, on the one hand, N should be large enough to find out small details of the Pareto front whereas, on the other hand, N should not be too large to avoid long time optimization. The termination criterion consists in a pre-defined number of generations which is here also fixed to 400. Finally, the crossover probability and the mutation probability are respectively chosen to be 0.85 and 0.015 as typically suggested in literature (Deb, 2002).

4.2 Design procedure

The overall design procedure, presented in Fig. 5, has been implemented in the Matlab environment. First, a random initial population is generated. Then, the objective functions, i.e. the total weight and the total losses of the VSI-fed AFPM in-wheel motor, are evaluated based on the initial population and on the above-described models (see Section 3). A convergence test is then performed to check for a termination criterion. If this criterion is not satisfied, the reproduction process using genetic operations starts. A new population is generated and the previous steps are repeated until the termination criterion is satisfied. Otherwise, the Pareto front, i.e. the nondominated solutions within the entire search space, is plotted and the optimization procedure ends.

5. Design example

In order to illustrate the design procedure, a VSI-fed AFPM in-wheel motor with the specifications given in Tables 1 and 2 is designed in this Section.

The lower and upper bounds of the seven considered optimization variables, viz. the factor k_d , the current density in the conductors J , the air gap thickness g , the PMs thickness l_{PM} , the number of poles pairs p , the number of slots q and the switching frequency f_s , are specified in Table 4. Note that the variables p and q are discrete ones whereas the others are continuous.

It should also be recalled that the in-wheel motor must provide the requirements of the EV as well as respect some constraints. The main constraints are the total weight M_{motor} of each of the four in-wheel motor and the imposed outer radius of the motor R_{out} . Note that these constraints have already been specified in Tables 1 and 2.

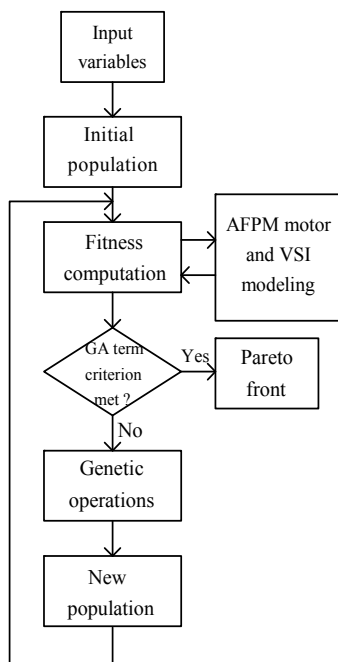


Fig. 5. Flowchart of the design procedure using GAs

Variables	Bounds	Type
k_d	[0.5 ; 0.9]	Continuous
J	[1 ; 6] A/mm ²	Continuous
l_{PM}	[1 ; 20] mm	Continuous
g	[1 ; 5] mm	Continuous
f_s	[1 ; 10] kHz	Continuous
p	[1 ; 15]	Discrete
q	[50 ; 255]	Discrete

Table 4. Optimization variables

The results, i.e. the Pareto front, are presented in Fig. 6. Each point of this Pareto front represents an optimal VSI-fed AFPM in-wheel motor that respects all the constraints. Moreover, the values of the optimization variables corresponding to three particular solutions of the front are detailed in Table 5.

For a practical design, one particular solution of the Pareto front should be chosen. On the one hand, the choice of this particular solution can be let to the designer who can choose *a posteriori* which solution best fits the under consideration application or which objective function to promote. Moreover, in industrial framework, this set of solutions can be confronted with additional criteria or engineer’s know-how not included in models.

On the other hand, the designer can also use some dedicated techniques to choose a particular solution of the Pareto front. These can be categorized into two types (Deb, 2002): post-optimal techniques and optimization-level techniques.

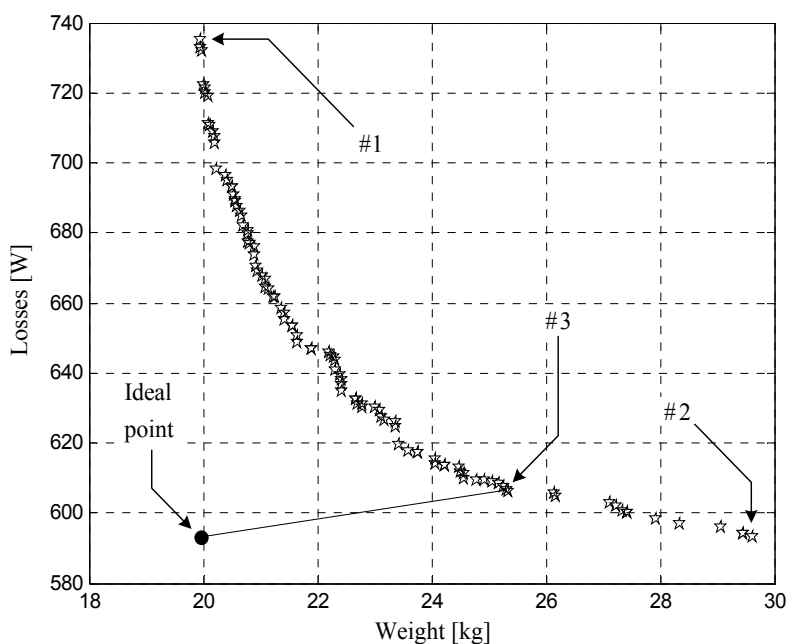


Fig. 6. Pareto front

	#1	#2	#3
k_d	0.89	0.89	0.88
J [A/mm ²]	4.9	5.5	4.9
l_{PM} [mm]	5	5	5
g [mm]	1.9	3.2	1
f_s [Hz]	1972	2110	1410
p	14	15	10
q	222	255	158
T_t [Nm]	207	208	207
P_t [kW]	8.72	8.77	8.72
M_{Motor} [kg]	17.2	15.1	26

Table 5. Details of three particular solutions

In the first approach, the solutions obtained from the optimization technique are analyzed to choose a particular solution whereas, in the second approach, the optimization technique is directed towards a preferred region of the Pareto front. Therefore, only the techniques belonging to the first category are helpful in this chapter. Among these techniques, the Compromise Programming Approach (CPA) (Yu, 1973) is often used in multiobjective problems. The CPA picks a solution which is minimally located from a given reference point (e.g. the ideal point which is a nonexistent solution composed with the minimum value of the two objectives). Note that other techniques, such as the Marginal Rate of Substitution Approach (Miettinen, 1999), the Pseudo-Weight Vector Approach (Deb, 2002) or a method based on a sensitivity analysis (Avila *et al.*, 2006), can also be used.

For instance, using the CPA, the solution #3 of the Pareto front is minimally located from the ideal point. This solution can therefore be considered for a practical design and corresponds, moreover, to a good trade-off between the two objectives.

The evolution of the percentage of individuals belonging to the first nondominated front during the optimization procedure is shown in Fig. 7. From this figure, one can easily conclude that all the individuals are located in the first front at the end of this procedure. Moreover, it can also be observed that new nondominated solutions have been found after approximately 150 generations.

From Fig. 8, it can be concluded that all the individuals respect all the constraints since the fourth generation.

In order to study more in details the evolution of the optimization variables, their values have been plotted along the Pareto front (as a function of the weight) in Fig. 9 to Fig. 15. From these figures, it can be concluded that some of them have converged to an optimal value.

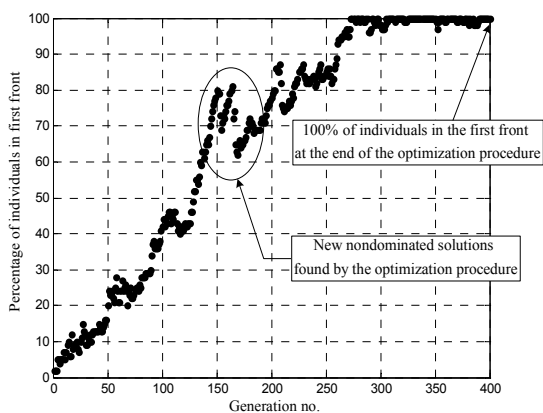


Fig. 7. Evolution of the percentage of individuals belonging to the first nondominated front during the optimization procedure

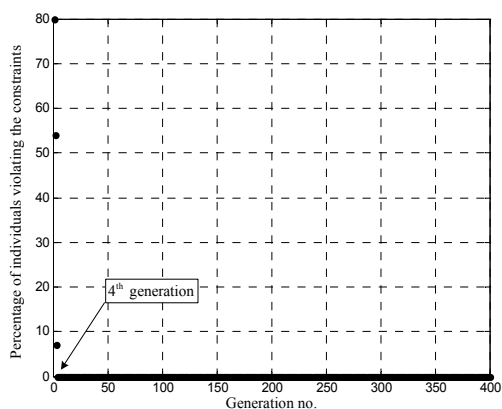
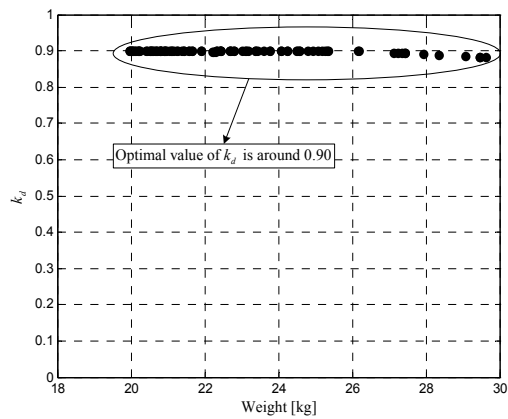
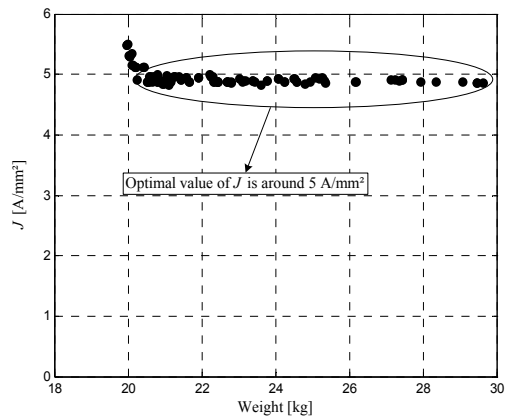
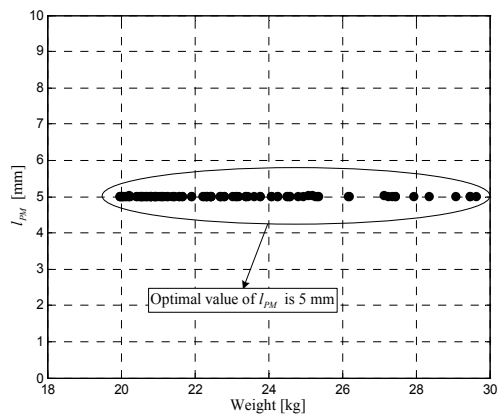


Fig. 8. Evolution of the percentage of individuals violating the constraints during the optimization procedure

Fig. 9. Evolution of k_d along the Pareto frontFig. 10. Evolution of J along the Pareto frontFig. 11. Evolution of l_{PM} along the Pareto front

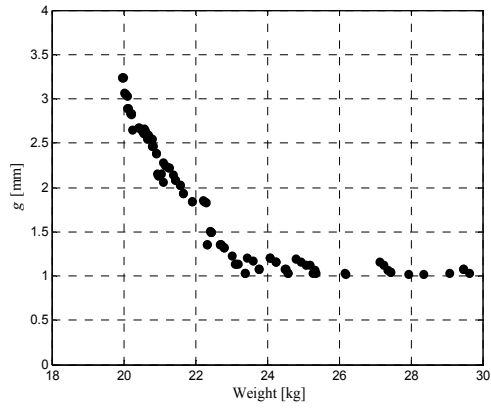


Fig. 12. Evolution of g along the Pareto front

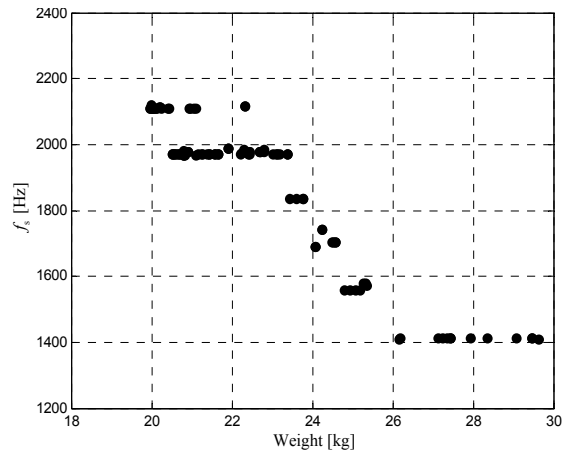


Fig. 13. Evolution of f_s along the Pareto front

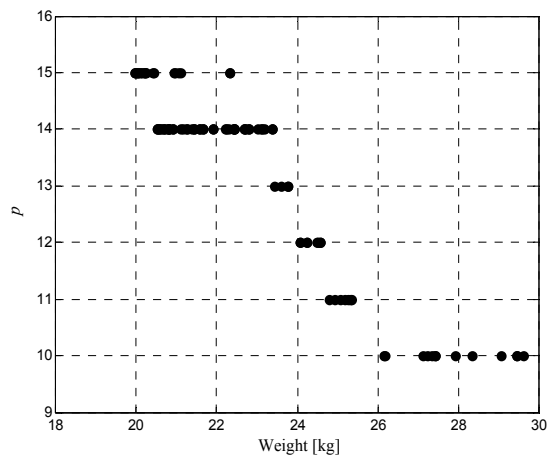


Fig. 14. Evolution of p along the Pareto front

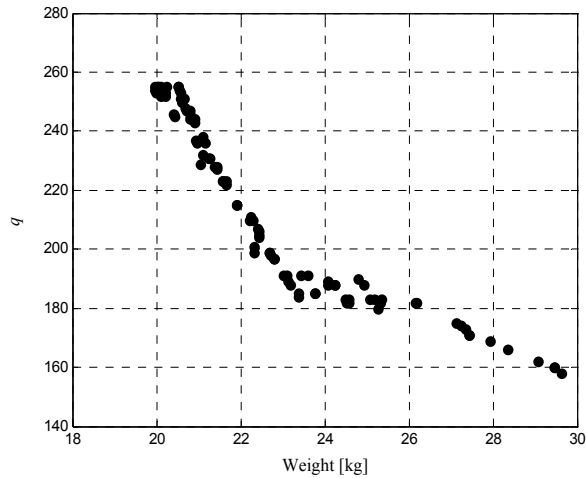


Fig. 15. Evolution of q along the Pareto front

First, the optimal value of the factor k_d is around 0.90 (see Fig. 9). Based on the Fig. 3, one can expect that this value would have converged to 0.58. However, this result is not surprising. Indeed, it has been show elsewhere (Azzouzi et al., 2006) that the maximum value of the torque to weight ratio is obtained for values of k_d around 0.85 and, in this chapter, the weight must be minimized.

Second, the optimal value of J is around 5 A/mm² as shown in Fig. 10 and, third, l_{PM} has converged to the optimal value of 5 mm (see Fig. 11).

In order to further analyze the optimization results, a study of the correlation level between the optimization variables and the objective functions is performed. The results are graphically represented in Fig. 16 and discussed below. Note that a positive value of the correlation factor indicates that the objective function grows when the optimization variable grows whereas a negative value indicates that the objective function reduces when the optimization variable grows.

From Fig. 16, it can be concluded that the optimization variables which have not converged to an optimal value, viz. g , f_s , p and q , have a significant influence on the two objective functions. Indeed, the correlation coefficient between each variable and each objective are, in absolute value, equal or greater than 0.8. The correlations are therefore strong. The fact that the correlation factors between k_d or J and the objective value are smaller is due to the fact that these variables have converged around an optimal value. Moreover, the fact that l_{PM} has converged to an optimal value leads to a correlation coefficient close to zero.

One can easily conclude that the variables p and f_s have the bigger influence on the weight (correlation coefficients equal to -0.94) whereas the variable g has the greater influence on the power loss (correlation coefficient equal to 0.98). Figure 16 also justifies the use of a MO technique. Indeed, the two objective functions are conflicting with respect to the optimization variables (except for l_{PM}) since the correlation levels are of opposite signs.

Finally, the distribution of the weight and the power loss among the AFPM motor and the VSI for the three particular solutions presented in Table 5 are respectively shown in Fig. 17 and Fig. 18 respectively. Figures 19 and 20 present, as for them, the distribution of these two objectives among the several parts of the motor (stator, rotor, PMs and windings).

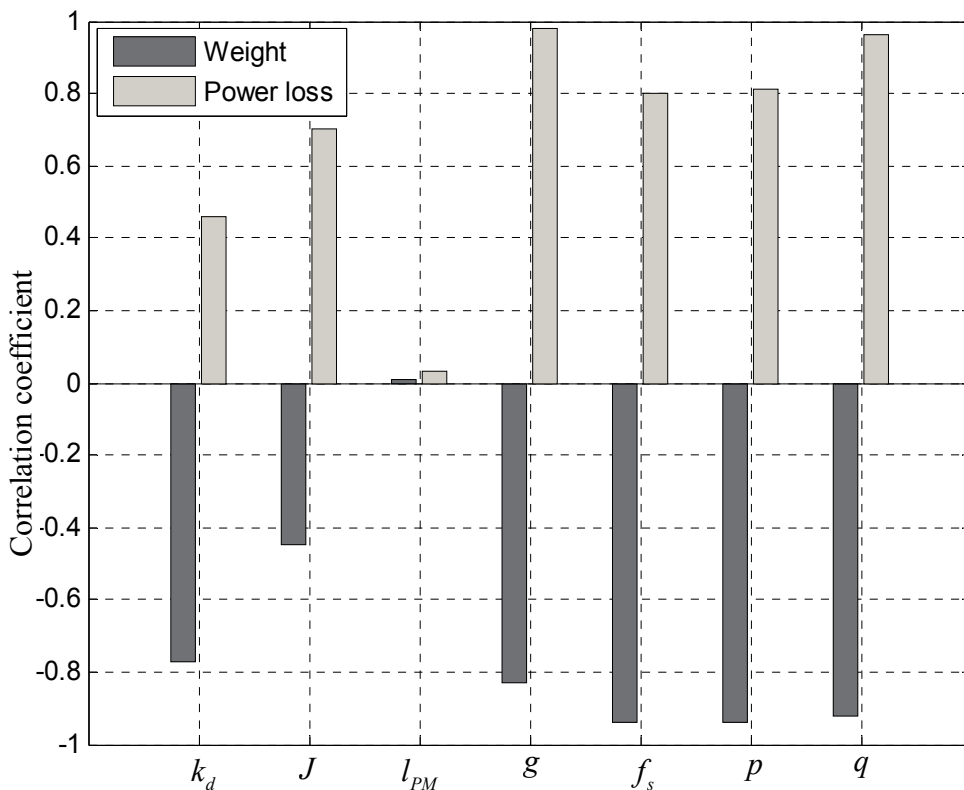


Fig. 16. Correlation between the optimization variables and the objective functions

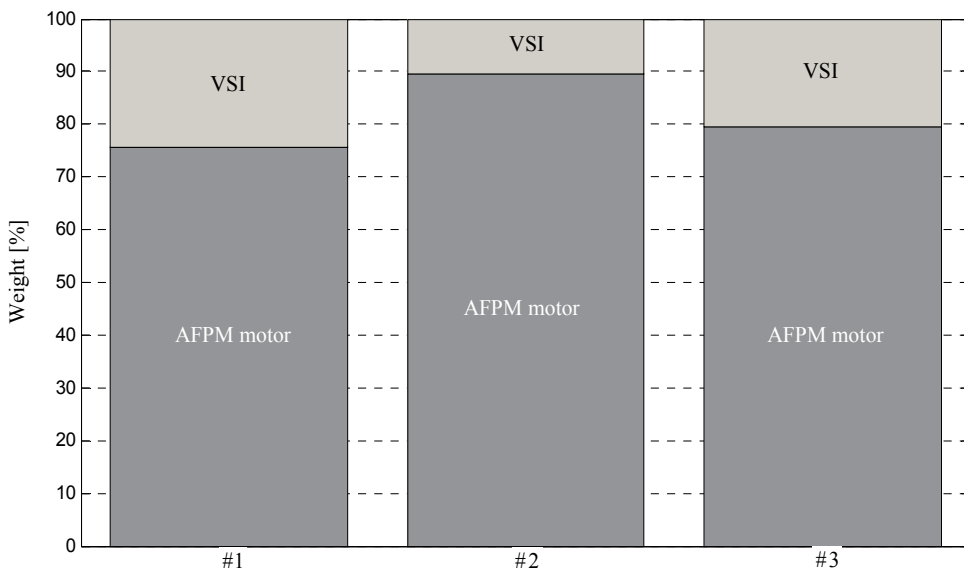


Fig. 17. Distribution of the weight among the AFPM motor and the VSI

Figure 17 shows that the major contributor in weight is the AFPM motor. Indeed, it represents at least 75% of the total weight. Instead, the power loss is, as for it, more equally distributed among the two parts. In fact, approximately 60% of the loss is due to the motor (see Fig. 18).

Figure 19 shows that the PMs are the minor contributor in terms of weight and represent more or less 5% to 10% of the total weight whatever the solution. One can also conclude that the rotor is the heavy part of the AFPM motor.

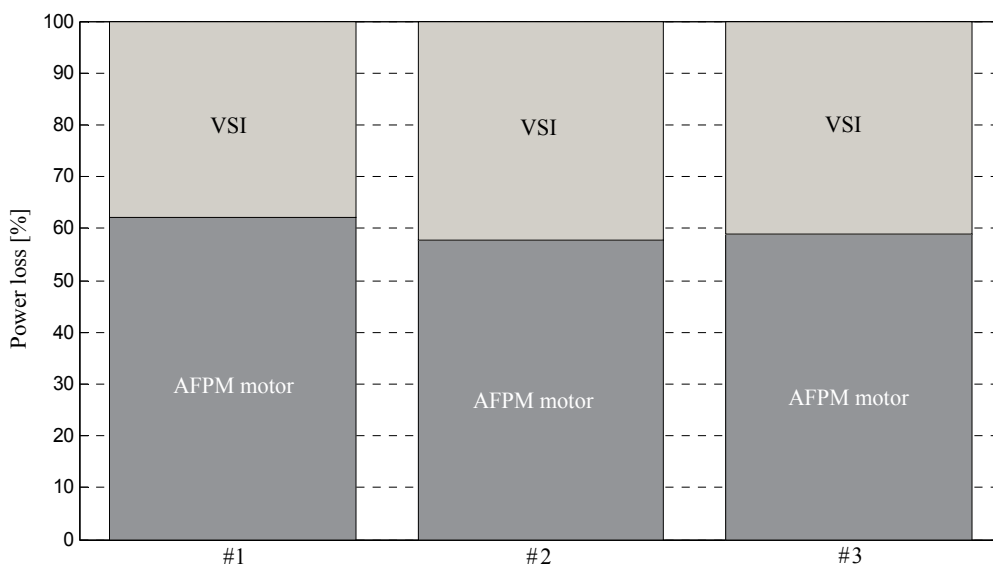


Fig. 18. Distribution of the power loss among the AFPM motor and the VSI

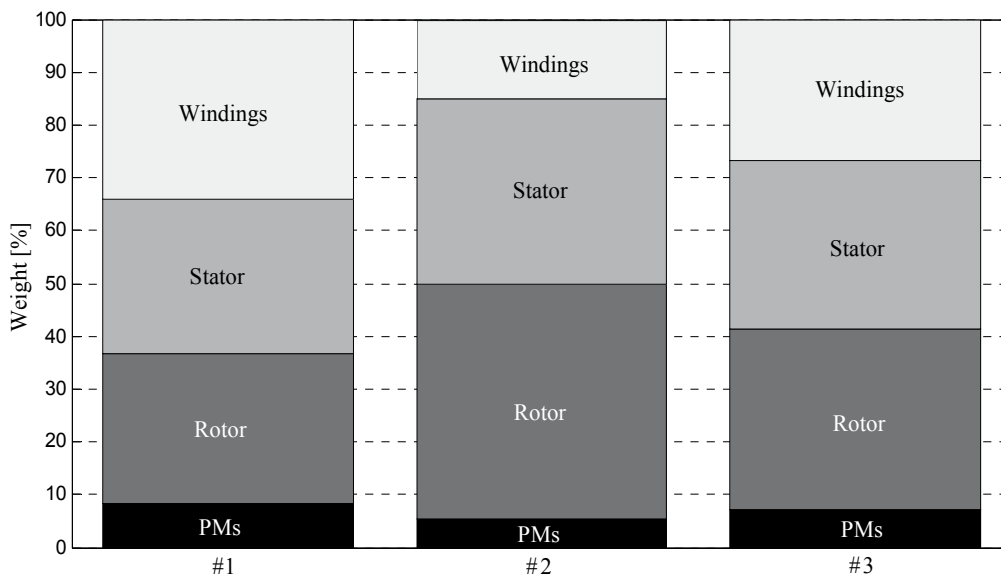


Fig. 19. Distribution of the weight among the several parts of the AFPM motor

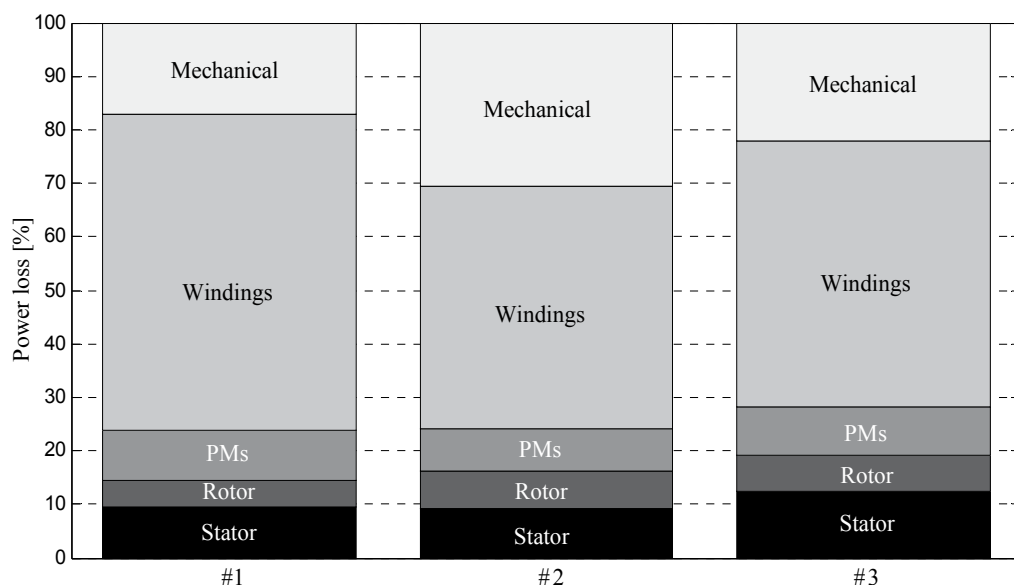


Fig. 20. Distribution of the power loss among the several parts of the AFPM motor

In solution #2, the stator and rotor weights largely dominate the winding and PMs weights compared with the other solutions. This can be explained regarding the value of the flux density in the air gap. Indeed, this value is the greatest among the three solutions (in the order of 0.90 T). So, the stator and rotor must be thick enough to avoid saturation of steel. As these thicknesses are computed using the air gap flux density, the stator and rotor of the solution #2 are thicker and, therefore, heavier. Moreover, the windings of the solution #2 are lighter than the windings of the two other solutions since the frequency is greater. Indeed, according to Faraday's law (Mohan et al., 2003), the windings turns necessary to obtain a same electromotive force is less than in the other solutions which, therefore, yields lighter windings realization.

As can be easily seen from Fig. 20, the mechanical and, more especially, the winding losses are the major contributors in terms of power loss. The fact that the winding losses are so high can be explained by the medium frequency effects (skin and proximity effects).

6. Advantages and limitations of the design procedure

The design procedure proposed in this paper presents several advantages but also some limitations.

A first advantage of this design procedure is that it is multiobjective. So, several conflicting objectives, often present in engineering design problems, can be optimized simultaneously.

A second advantage is the number of solutions considered in a small time. Indeed, the optimization procedure compares a large number of solutions (in the order of several thousands) to retain only the best in a time of approximately 120 s (for 400 generations of 100 individuals with a Pentium (R) D CPU 3.40 GHz, 3 Go RAM).

A third advantage is the simultaneous optimization of the in-wheel motor and its own VSI. Indeed, it results in a system optimized towards the requirements of the EV.

At last, the design procedure has the major advantage that a set of optimal solutions – instead of a single one – is proposed to the designer who can choose *a posteriori* which objective function to promote and, then, select a particular VSI-fed in-wheel motor. So, a degree of freedom is still available at the end of the optimization procedure. Moreover, in industrial framework, this set of solutions can be confronted with additional criteria or engineer's know-how not included in models.

The main limitation of the design procedure is related to the analytical modeling of the AFPM motor. Indeed, an analytical modeling of such motor can lead to a lack of accuracy in some cases, e.g. with a PM shape of higher complexity when the magnet occupation ratio varies along the radius of the rotor (Parviaien et al., 2003). This lack of accuracy arises from the reduction of the 3D design problem to a 2D design problem performed on the average radius of the machine.

It should also be noticed that the most accurate method to predict the performances of an AFPM motor is a 3D finite element analysis (FEA) but it is often too much time consuming to be included in an optimal design procedure in which a large numbers of solutions have to be evaluated. Therefore, the optimal design procedure presented in this contribution is very useful during the first stages of the design, although more sophisticated methods, such as 2D or 3D FEA, are required in more advanced phases of the design.

Note that, in this chapter, the magnet occupation ratio has been considered as constant along the radius of the rotor and, therefore, this limitation is not taken into account in the design of the AFPM motor.

7. Conclusion

This chapter has addressed the problem of MO design of a VSI-fed AFPM synchronous motor using GAs and a new design procedure has been proposed. The weight and the losses of both the motor and the VSI have been chosen as objective functions whereas the factor k_d , the current density in the conductors, the air gap thickness, the PMs thickness, the number of poles pairs, the number of slots and the switching frequency have been chosen as optimization variables. Finally, the design procedure has been illustrated by the design of a VSI-fed AFPM in-wheel motor for an urban EV and some conclusions have been drawn.

Finally, recall that, although many authors have published papers about the optimal design of in-wheel motors for EVs, the simultaneous optimization of the in-wheel motor and its own VSI has, to the authors' knowledge, rarely been discussed in literature.

8. References

- Audet, C. & Dennis Jr., J. (2001). Pattern search algorithms for mixed variable programming. *SIAM Journal on Optimization*, vol. 11, no. 3, (July 2001), pp. 573-594, ISSN 1052-7189.
- Avila, S. L.; Lisboa, A. C.; Krähenbühl L.; Carpes, Jr. W. P.; Vasconcelos, J. A.; Saldanha, R. R.; & Takahashi, R. H. C. (2006). Sensitivity Analysis Applied to Decision Making in Multiobjective Evolutionary Optimization, *IEEE Transactions on Magnetics*, vol. 42, no. 4, (April 2006) , pp. 1103-1106, ISSN 0018-9464.
- Azzouzi, J.; Belfkira, R.; Abdel-Karim, N.; Barakat G. & Dakyo, B. (2006). Design Optimization of an Axial Flux PM Synchronous Machine: Comparison Between DIRECT Method and GAs Method, *Proceedings of 12th International Power Electronics*

- and Motion Control Conference*, ISBN 1-4244-0121-6, Portoroz, Slovenia, September 2006.
- Chun, Y. D.; Koo, D.-H. & Cho, Y.-H. (2007). Multiobjective optimization design of axial flux permanent magnet motor. *International Journal of Applied Electromagnetics and Mechanics*, vol. 25, no. 1, (January 2007), pp. 613-619, ISSN 8273-284.
- Cvetkovski, G. & Petkovska, L. (2008). Efficiency Maximisation in Structural Design Optimisation of Permanent Magnet Synchronous Motor, *Proceedings of 18th International Conference on Electrical Machines*, ISBN 978-1-4244-1736-0, Vilamoura, Portugal, September 2008.
- Deb, K. & Goyal, M. (1997). Optimization Engineering Designs Using a Combined Search, *Proceedings of 7th International Conference on Genetic Algorithms*, ISBN 1-55860-299-2, East Lansing, USA, July 1997.
- Deb, K. (2002). *Multi-Objective Optimization using Evolutionary Algorithms*, John Wiley & Sons, Inc., ISBN 0470743611, New Jersey, USA.
- Deb, K. (2007). Current trends in evolutionary multi-objective optimization, *International Journal for Simulation and Multidisciplinary Design Optimization*, vol. 1, no. 1, (December 2007), pp. 1-8., ISSN 1779-6288.
- Ehsani, M.; Gao, Y.; Gay, S. E. & Emadi, A. (2006). *Modern Electric, Hybrid Electric and Fuel Cell Vehicles: Fundamentals, Theory, and Design*, CRC Press, ISBN 0-8493-3154-4, Florida, USA.
- Espanet, C.; Kauffmann, J. M.; Wurtz, F. & Bignon, J. (1999). Application of a new optimization approach to the design of electrical wheels. *IEEE Transactions on Energy Conversion*, vol. 14, no. 4, (December 1999), pp.952-958, ISSN 0013-4457.
- Gieras, J. F.; Wang, R.-J. & Kamper, M. J. (2004). *Axial Flux Permanent Magnet Brushless Machines*, Kluwer Academic Publishers, ISBN 978-1-4020-6993-2, Netherlands.
- Helali H. et al. (2005). Power converter's optimisation and design. Discrete cost function with genetic based algorithms, *Proceedings of 11th Power Electronics and Applications Conference*, ISBN 91-7636-385-6, Dresden, Germany, September 2005.
- Malyna, D. V.; Duarte, J. L.; Hendrix, M. A. M. & van Horck, F. B. M. (2007). Optimization of Combined Thermal and Electrical Behavior of Power Converters Using Multi-Objective Genetic Algorithms, *Proceedings of 12th Power Electronics and Applications Conference*, ISBN 0-7803-9457-7 Aalborg, Denmark, September 2007.
- Miettinen, K. (1999), *Nonlinear Multiobjective Optimization*, Kluwer Academic Publishers, ISBN 978-0-7923-8278-2, Boston, USA.
- Mohan, N.; Undeland, T. & Robbins, W. (2003), *Power Electronics: Converters, Applications and Design*, John Wiley & Sons, ISBN 978-0-471-22693-2, Hoboken, USA.
- Nilssen, R.; Skaar, S. E.; Lund, R.; Skjellnes, T; Øvrebø, S. & Løvli E. (2005). Design of a permanent magnet synchronous integrated in the wheel rim on wheelchairs, *Proceedings of 11th Power Electronics and Applications Conference*, ISBN 91-7636-385-6, Dresden, Germany, September 2005.
- Ocenasek, J. & Schwarz, J. (2002). Estimation distribution algorithm for mixed continuous-discrete optimization problems, *Proceedings 2nd Euro-International Symposium on Computational Intelligence*, ISBN 1-58603-256-9, Amsterdam, Nederland, September 2002.

- Parviaien, A.; Niemelä, M. & Pyrhönen, J. (2003). Analytical, 2D FEM and 3D FEM Modeling of PM Axial Flux Machine, *Proceedings of 10th Power Electronics and Applications Conference*, ISBN 90-75815-06-9, Toulouse, France, September 2003.
- Qu, R. & Lipo, T. A. (2002). Analysis and Modeling of Airgap & Zigzag Leakage Fluxes in a Surface-Mounted-PM Machine, *Proceedings of 37th Industry Applications Conference*, ISBN 0-7803-7420-7, Pittsburgh, USA, October 2002.
- Sahin, F. & Vandenput, A. J. A. (1999). Design Considerations of the Flywheel-Mounted Axial-Flux Permanent Magnet Machine for a Hybrid Electric Vehicle, *Proceedings of 8th Power Electronics and Applications Conference*, ISBN 90-75815-06-9, Lausanne, Switzerland, September 1999.
- Semikron (2010), "Application Manual", available from http://www.semikron.com/skcompub/en/application_manual-193.htm.
- Skaar, S. E. & Nielssen, R. (2003). Genetic Optimization of Electric Machines, a State of the Art Study, *Proceedings of 10th Power Electronics and Applications Conference*, ISBN 90-75815-06-9, Toulouse, France, September 2003.
- Socha, K. (2008). Ant colony optimization for continuous and mixed-variable domains, *PhD Thesis*, Université Libre de Bruxelles.
- Tseng, K.-J. & Chen, G. H. (1997). Computer-Aided Design and Analysis of Direct-Driven Wheel Motor Drive. *IEEE Transactions on Power Electronics*, vol. 12, no. 3, (May 1997), pp. 517-527, ISSN 0885-8993.
- Versèle, C. et al. (2009). Analytical Design of an Axial Flux Permanent Magnet In-Wheel Synchronous Motor for Electric Vehicle, *Proceedings of 13th Power Electronics and Application Conference*, ISBN 978-1-4244-1742-1, Barcelona, Spain, September 2009.
- Versèle, C.; Deblecker, O. & Lobry, J. (2010). Multiobjective Optimal Design of Medium Frequency Transformers for Full-Bridge DC-DC Converters, *International Review of Electrical Engineering*, vol. 5, no. 4, (July-Augustus 2010), pp. 1354-1363, ISSN 1827-6660.
- Yang, Y.-P.; Luh, Y.-P. & Cheung, C.-H. (2004). Design and Control of Axial-Flux Brushless DC Wheel Motors for Electric Vehicles – Part I: Multiobjective Optimal Design and Analysis. *IEEE Transactions on Magnetics*, vol. 40, no. 4, (July 2004), pp. 1873-1882, ISSN 0018-9464.
- Yang, Y.-P. & Chuang, D.-S. (2007). Optimal Design and Control of a Wheel Motor for Electric Passengers Cars. *IEEE Transactions on Magnetics*, vol. 43, no. 1, (January 2007), pp. 51-61, ISSN 0018-9464.
- Yu, P. L. (1973). A class of solutions for group decision problems, *Management Science*, vol. 19, no. 8, (April 1973), pp. 936-946, ISSN 0025-1909.

DC/DC Converters for Electric Vehicles

Monzer Al Sakka¹, Joeri Van Mierlo¹ and Hamid Gualous²

¹*Vrije Universiteit Brussel,*

²*Université de Caen Basse-Normandie*

¹*Belgium,*

²*France*

1. Introduction

The large number of automobiles in use around the world has caused and continues to cause serious problems of environment and human life. Air pollution, global warming, and the rapid depletion of the earth's petroleum resources are now serious problems. Electric Vehicles (EVs), Hybrid Electric Vehicles (HEVs) and Fuel Cell Electric Vehicles (FCEVs) have been typically proposed to replace conventional vehicles in the near future. Most electric and hybrid electric configurations use two energy storage devices, one with high energy storage capability, called the "main energy system" (MES), and the other with high power capability and reversibility, called the "rechargeable energy storage system" (RESS). MES provides extended driving range, and RESS provides good acceleration and regenerative braking. Energy storage or supply devices vary their output voltage with load or state of charge and the high voltage of the DC-link create major challenges for vehicle designers when integrating energy storage / supply devices with a traction drive. DC-DC converters can be used to interface the elements in the electric power train by boosting or chopping the voltage levels. Due to the automotive constraints, the power converter structure has to be reliable, lightweight, small volume, with high efficiency, low electromagnetic interference and low current/voltage ripple. Thus, in this chapter, a comparative study on three DC/DC converters topologies (Conventional step-up dc-dc converter, interleaved 4-channels step-up dc-dc converter with independent inductors and Full-Bridge step-up dc-dc converter) is carried out. The modeling and the control of each topology are presented. Simulations of 30KW DC/DC converter are carried out for each topology. This study takes into account the weight, volume, current and voltage ripples, Electromagnetic Interference (EMI) and the efficiency of each converter topology.

2. Electric vehicles powertrain

An Electric Vehicle is a vehicle that uses a combination of different energy sources, Fuel Cells (FCs), Batteries and Supercapacitors (SCs) to power an electric drive system as shown in Fig. 1. In EV the main energy source is assisted by one or more energy storage devices. Thereby the system cost, mass, and volume can be decreased, and a significant better performance can be obtained. Two often used energy storage devices are batteries and SCs. They can be connected to the fuel cell stack in many ways. A simple configuration is to

directly connect two devices in parallel, (FC/battery, FC/SC, or battery/SC). However, in this way the power drawn from each device cannot be controlled, but is passively determined by the impedance of the devices. The impedance depends on many parameters, e.g. temperature, state-of-charge, health, and point of operation. Each device might therefore be operated at an inappropriate condition, e.g. health and efficiency. The voltage characteristics also have to match perfectly of the two devices, and only a fraction of the range of operation of the devices can be utilized, e.g. in a fuel cell battery configuration the fuel cell must provide almost the same power all the time due to the fixed voltage of the battery, and in a battery/supercapacitor configuration only a fraction of the energy exchange capability of the supercapacitor can be used. This is again due to the nearly constant voltage of the battery. By introducing DC/DC converters one can chose the voltage variation of the devices and the power of each device can be controlled (Schaltz & Rasmussen, 2008).

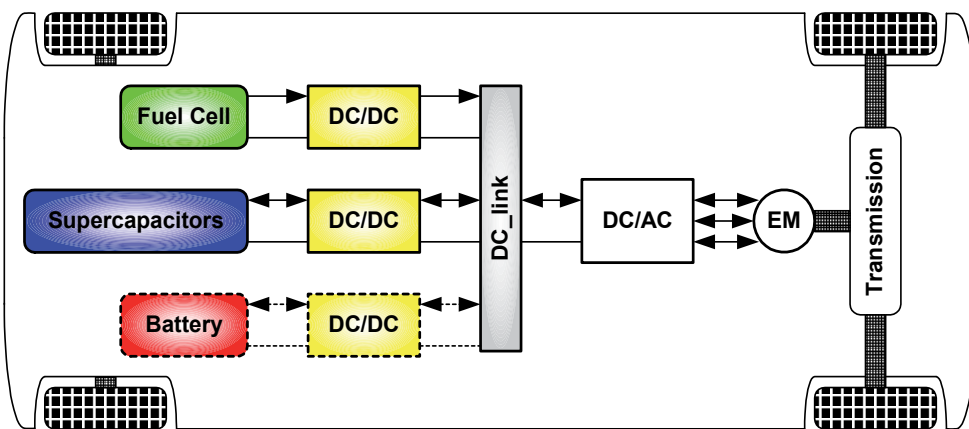


Fig. 1. Electric vehicle drive system.

In reference (Schaltz & Rasmussen, 2008), 10 cases of combining the fuel cell with the battery, SCs, or both are investigated. The system volume, mass, efficiency, and battery lifetime were compared. It is concluded that when SCs are the only energy storage device the system becomes too big and heavy. A fuel cell/battery/supercapacitors hybrid provides the longest life time of the batteries. It can be noticed that the use of high power DC/DC converters is necessary for EV power supply system. The power of the DC/DC converter depends on the characteristics of the vehicle such as top speed, acceleration time from 0 to 100 Km/h, weight, maximum torque, and power profile (peak power, continuous power) (Büchi et al., 2006). Generally, for passenger cars, the power of the converter is more than 20 KW and it can go up to 100 KW.

3. DC/DC converters for electric vehicles

The different configurations of EV power supply show that at least one DC/DC converter is necessary to interface the FC, the Battery or the Supercapacitors module to the DC-link.

In electric engineering, a DC to DC converter is a category of power converters and it is an electric circuit which converts a source of direct current (DC) from one voltage level to another, by storing the input energy temporarily and then releasing that energy to the

output at a different voltage. The storage may be in either magnetic field storage components (inductors, transformers) or electric field storage components (capacitors).

DC/DC converters can be designed to transfer power in only one direction, from the input to the output. However, almost all DC/DC converter topologies can be made bi-directional. A bi-directional converter can move power in either direction, which is useful in applications requiring regenerative braking.

The amount of power flow between the input and the output can be controlled by adjusting the duty cycle (ratio of on/off time of the switch). Usually, this is done to control the output voltage, the input current, the output current, or to maintain a constant power. Transformer-based converters may provide isolation between the input and the output. The main drawbacks of switching converters include complexity, electronic noise and high cost for some topologies. Many different types of DC/DC power converters are proposed in literature (Chiu & Lin, 2006), (Fengyan et al., 2006). The most common DC/DC converters can be grouped as follows:

3.1 Non-isolated converters

The non-isolated converters type is generally used where the voltage needs to be stepped up or down by a relatively small ratio (less than 4:1). And when there is no problem with the output and input having no dielectric isolation. There are five main types of converter in this non-isolated group, usually called the buck, boost, buck-boost, Cuk and charge-pump converters. The buck converter is used for voltage step-down, while the boost converter is used for voltage step-up. The buck-boost and Cuk converters can be used for either step-down or step-up. The charge-pump converter is used for either voltage step-up or voltage inversion, but only in relatively low power applications.

3.2 Isolated converters

Usually, in this type of converters a high frequency transformer is used. In the applications where the output needs to be completely isolated from the input, an isolated converter is necessary. There are many types of converters in this group such as Half-Bridge, Full-Bridge, Fly-back, Forward and Push-Pull DC/DC converters (Garcia et al., 2005), (Cacciato et al., 2004). All of these converters can be used as bi-directional converters and the ratio of stepping down or stepping up the voltage is high.

3.3 Electric vehicle converters requirements

In case of interfacing the Fuel Cell, the DC/DC converter is used to boost the Fuel Cell voltage and to regulate the DC-link voltage. However, a reversible DC/DC converter is needed to interface the SCs module. A wide variety of DC-DC converters topologies, including structures with direct energy conversion, structures with intermediate storage components (with or without transformer coupling), have been published (Lachichi & Schofield, 2006), (Yu & Lai, 2008), (Bouhalli et al., 2008). However some design considerations are essential for automotive applications:

- Light weight,
- High efficiency,
- Small volume,
- Low electromagnetic interference,
- Low current ripple drawn from the Fuel Cell or the battery,
- The step up function of the converter,

- Control of the DC/DC converter power flow subject to the wide voltage variation on the converter input.

Each converter topology has its advantages and its drawbacks. For example, The DC/DC boost converter does not meet the criteria of electrical isolation. Moreover, the large variance in magnitude between the input and output imposes severe stresses on the switch and this topology suffers from high current and voltage ripples and also big volume and weight. A basic interleaved multichannel DC/DC converter topology permits to reduce the input and output current and voltage ripples, to reduce the volume and weight of the inductors and to increase the efficiency. These structures, however, can not work efficiently when a high voltage step-up ratio is required since the duty cycle is limited by circuit impedance leading to a maximum step-up ratio of approximately 4. Hence, two series connected step-up converters would be required to achieve the specific voltage gain of the application specification. A full-bridge DC/DC converter is the most frequently implemented circuit configuration for fuel-cell power conditioning when electrical isolation is required. The full bridge DC/DC converter is suitable for high-power transmission because switch voltage and current are not high. It has small input and output current and voltage ripples. The full-bridge topology is a favorite for zero voltage switching (ZVS) pulse width modulation (PWM) techniques.

4. Electromagnetic compatibility regulation

Fast semiconductor devices make it possible to have high speed and high frequency switching in power electronics converters. High speed switching helps to reduce weight and volume of equipment; however, it causes some undesirable effects such as radio frequency interference (RFI) emission. It is believed that high dv/dt or di/dt due to modern power device switching is mainly responsible for the EMI emissions. Application of electrical equipment especially static power electronic converters in different equipment is increasing more and more. Power electronics converters are considered as an important source of electromagnetic interference and have undesirable effects on the electric networks. Some residential, commercial and especially medical consumers are very sensitive to power system disturbances including voltage and frequency variations. Also, for Electric vehicle, there is limitation of the EMI. The best solution to reduce the interference and improve the power quality is complying national or international EMC regulations. CISPR, IEC, FCC and VDE are among the best known organizations from Europe, USA and Germany who are responsible for determining and publishing the most important EMC regulations. Compliance of regulations is evaluated by comparison of measured or calculated conducted interference level in the mentioned frequency range with the stated requirements in regulations. In European community compliance of regulation is mandatory and products must have certified label to show covering of requirements (Farhadi & Jalilian, 2006). For Electric Vehicle, the maximum interference level should meet the DIN VDE 0879 standard. The limits in this standard are almost the same as the class B of VDE 0871 requirement and limitation on conducted emission.

4.1 Electromagnetic conducted interference measurement

A Line Impedance Stabilization Network (LISN) is typically designed to allow for measurements of the electromagnetic interference existing on the power line, it is a device

used to create known impedance on power lines of electrical equipment during electromagnetic interference testing. The stated situation is shown in Fig. 2.

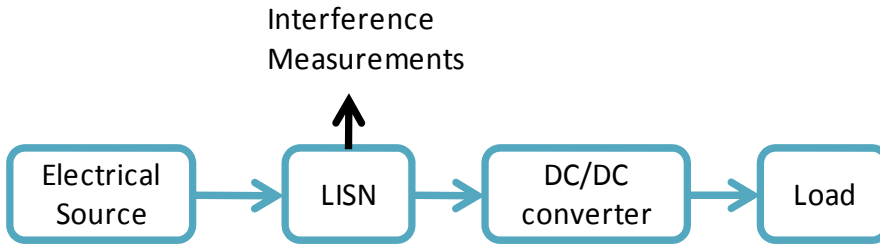


Fig. 2. LISN placement to measure conducted interference.

Variation of level of signal at the output of LISN versus frequency is the spectrum of interference. The electromagnetic compatibility of a device can be evaluated by comparison of its interference spectrum with the standard limitations. The level of signal at the output of LISN in frequency range 10 kHz up to 30 MHz or 150 kHz up to 30 MHz is criteria of compatibility and should be under the standard limitations. Converting the results to dB μ V (Equation 1) makes it possible to compare the spectrum of interference with standard requirements. In practical situations, the LISN output is connected to a spectrum analyzer and interference measurement is carried out. But for modeling and simulation purposes, the LISN output spectrum must be calculated using appropriate software.

$$dB\mu V(x) = 20\log_{10}\left(\frac{x}{10^{-6}}\right) = 20\log_{10}(x) + 120 \quad (1)$$

5. Losses in a power converter

The considered losses in a power converter are the losses produced by the semiconductor switches (IGBTs and DIODES) and the passive components (capacitors and inductors). The aim of this explanation is only to give an idea about the losses estimation. This estimation is used in this study to calculate the efficiency. The efficiency of a power converter is given by:

$$\eta = \frac{P_{Input_power} - \sum Losses}{P_{Input_power}} \quad (2)$$

5.1 IGBT conduction and switching losses

The IGBT conduction losses are given by:

$$P_{IGBT_cond} = V_{CE0} \langle I_{IGBT} \rangle + r_{CE} I_{IGBT_rms}^2 \quad (3)$$

The IGBT characteristics (V_{CE0} and r_{CE}) are given in the datasheet of the IGBT. $\langle I_{IGBT} \rangle$ and I_{IGBT_rms} are the average current and the rms current of the IGBT, respectively.

The IGBT switching losses are given by:

$$P_{IGBT_switch} = (E_{on} + E_{off}) f_s \quad (4)$$

Where, f_s is the switching frequency. E_{on} and E_{off} are the switching losses during the switching on and switching off, respectively.

Energy values are generally given for specific test conditions (Voltage test condition V_{CC}). Thus, to adapt these values to others test conditions, as an estimation the IGBT switching losses are given by (Garcia Arregui, 2007):

$$P_{IGBT_switch} = \frac{V_{IGBT}}{V_{CC}} \left(E_{on}(I_{IGBT_on}) + E_{off}(I_{IGBT_off}) \right) f_s \quad (5)$$

5.2 Diode conduction and switching losses

The Diode conduction losses are given by:

$$P_{D_cond} = V_{F0} \langle I_D \rangle + r_F I_{D_rms}^2 \quad (6)$$

The Diode characteristics (V_{F0} and r_F) are given in the Diode datasheet. $\langle I_D \rangle$ and I_{D_rms} are the average current and the rms current of the Diode, respectively.

The Diode switching losses are given by:

$$P_{D_switch} = E_{rr} f_s \quad (7)$$

Where, f_s is the switching frequency. E_{rr} is the recovery energy.

The recovery energy is given as a function of the voltage, the current, the turn-on and turn off resistances and for a specific test conditions. To adapt the previous expression to another test conditions, as estimation the diode switching losses are given by:

$$P_{D_switch} = \frac{V_D}{V_{CC}} E_{rr}(I_D) f_s \quad (8)$$

5.3 Capacitor losses

The capacitor losses are calculated thanks to the equivalent resistance of the capacitor, which is usually given in the datasheets. The capacitor losses are given by:

$$P_{Capacitor} = r_C I_{C_rms}^2 \quad (9)$$

Where, r_C is the equivalent resistance of the capacitor and I_{C_rms} is the rms current value of the capacitor.

5.4 Inductors losses

In an inductor, there are iron and copper losses. Core losses (or iron losses) are energy losses that occur in electrical transformers and inductors using magnetic cores. The losses are due to a variety of mechanisms related to the fluctuating magnetic field, such as eddy currents and hysteretic phenomena. Most of the energy is released as heat, although some may appear as noise. These losses are estimated based on charts supplied by magnetic core manufacturer. To estimate the total iron losses, the weight of core should be multiplied by the obtained value for a specific flux density and switching frequency. The inductor iron losses are given by:

$$P_{L_Core} = W_{core} P_{core} \tag{10}$$

Where, W_{core} is the weight of the core and P_{core} is the iron losses per Kg. The copper losses or the conduction losses in the inductor are given by:

$$P_{L_copper} = r_L I_{L_rms}^2 \tag{11}$$

Where, r_L is the resistance of the inductor and I_{L_rms} is the rms current value of the inductor.

6. Design, modeling, control and simulation results of 3 DC/DC converters

The modeling of studied converters is done by using the Simpower tools of Matlab/Simulink, and it takes into account the IGBT and Diodes parameters (real components) and the inductors and capacitors losses. To achieve accurate voltage regulation, two control loops are used as shown in Fig. 3. This control mode (current mode control) requires knowledge of the inductor current, which is controlled via the inner loop. The outer loop manages the output voltage error by commanding the necessary current. The control was done using RST controllers.

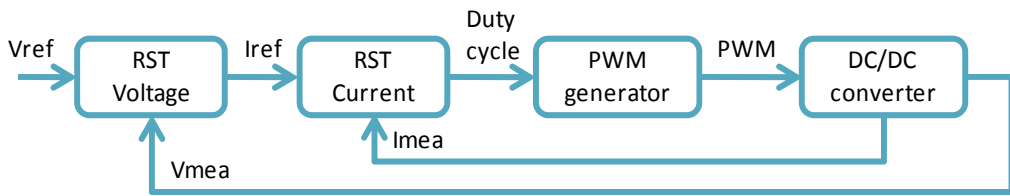


Fig. 3. Block diagram of control mode.

6.1 RST controller

The canonical structure of the RST controller is presented in Fig. 4. This structure has two degrees of freedom, i.e., the digital filters R and S are designed in order to achieve the desired regulation performance, and the digital filter T is designed afterwards in order to achieve the desired tracking and regulation. This structure allows achievement of different levels of performance in tracking and regulation. The case of a controller operating on the regulation error (which does not allow the independent specification of tracking and regulation performance) corresponds to $T=R$. Digital PID controller can also be represented in this form, leading to particular choices of R, S and T (Landau, 1998).

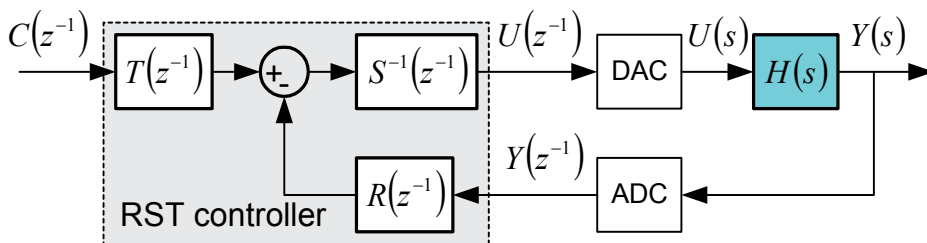


Fig. 4. The RST canonical structure of a digital controller

The equation of the RST canonical controller is give by:

$$S(z^{-1}) \cdot U(z^{-1}) + R(z^{-1}) \cdot Y(z^{-1}) = T(z^{-1}) \cdot C(z^{-1}) \quad (12)$$

Where:

- $U(z^{-1})$: the input of the plant $H(s)$,
- $Y(z^{-1})$: the output of the plant $H(s)$,
- $C(z^{-1})$: the desired tracking trajectory.

The polynomials $R(z^{-1})$, $S(z^{-1})$ and $T(z^{-1})$ have the following form:

$$\begin{cases} R(z^{-1}) = r_0 + r_1 z^{-1} + \dots + r_{n_R} z^{-n_R} \\ S(z^{-1}) = s_0 + s_1 z^{-1} + \dots + s_{n_S} z^{-n_S} \\ T(z^{-1}) = t_0 + t_1 z^{-1} + \dots + t_{n_T} z^{-n_T} \end{cases} \quad (13)$$

The plant and closed-loop models are expressed by expression 14 and expression 15 respectively:

$$H(s) = \frac{Y(s)}{U(s)} = \frac{B(s)}{A(s)} \quad (14)$$

$$H_{CL}(s) = \frac{Y(s)}{C(s)} = \frac{B_{CL}(s)}{A_{CL}(s)} \quad (15)$$

A formal discretization leads to both discrete-time transfer functions as follows, with $m \leq n$ and d is a pure time delay.

$$H(z^{-1}) = z^{-d} \frac{B(z^{-1})}{A(z^{-1})} = z^{-d} \frac{b_1 z^{-1} + b_2 z^{-2} + \dots + b_m z^{-m}}{a_1 z^{-1} + a_2 z^{-2} + \dots + a_n z^{-n}} \quad (16)$$

$$H_{CL}(z^{-1}) = \frac{Y(z^{-1})}{C(z^{-1})} = \frac{B_{CL}(z^{-1})}{A_{CL}(z^{-1})} \quad (17)$$

The closed-loop transfer operator (between $C(z^{-1})$ and $Y(z^{-1})$) is given by:

$$H_{CL}(z^{-1}) = \frac{B(z^{-1})T(z^{-1})}{A(z^{-1})S(z^{-1}) + B(z^{-1})R(z^{-1})} = \frac{B_{CL}(z^{-1})}{A_{CL}(z^{-1})} \quad (18)$$

R , S and T polynomials are determined in order to obtain an imposed closed-loop system. Resolving the Diophantine equation (or Bezout's identity) $AS+BR=A_{CL}$ leads to the identification of S and R polynomials. The polynomial T is determined from the equation $BT=B_{CL}$.

6.1.1 Calculation of RST parameters used in this study

The current and voltage control loops controllers of the three DC/DC topologies compared in this study use the same type of transfer function in open loop which is given by:

$$H(s) = \frac{Y(s)}{U(s)} = \frac{1}{ks} \quad (19)$$

A formal discretization leads to the discrete-time transfer function as follows:

$$\begin{aligned} H(z^{-1}) &= (1 - z^{-1})TFZ\left(\frac{1}{s}H(s)\right) \\ &= (1 - z^{-1})\frac{T_s}{k} \frac{z}{(z-1)^2} = \frac{T_s}{k} \frac{z^{-1}}{1 - z^{-1}} = \frac{B(z^{-1})}{A(z^{-1})} \end{aligned} \quad (20)$$

The sampling period T_s used in the control is equal to the switching frequency of PWM signals.

Choosing the polynomials $R(z^{-1})$ and $S(z^{-1})$:

- The system in closed-loop should be a two order system ($\deg(A_{CL}(z^{-1}))=2$).
- Error Specification: no error in steady state step response and rejection of disturbance.

The polynomials $R(z^{-1})$ and $S(z^{-1})$ are given by:

$$\begin{aligned} \deg(S(z^{-1})) &= \deg(R(z^{-1})) = \deg(A_{CL}(z^{-1})) - 1 \\ \Rightarrow \begin{cases} S(z^{-1}) = 1 - z^{-1} \\ R(z^{-1}) = r_0 + r_1 z^{-1} \end{cases} \end{aligned} \quad (21)$$

In addition, in order to guarantee a unity static gain in closed-loop:

$$\begin{cases} \lim_{z \rightarrow 1} H_{CL}(z^{-1}) = \frac{B(1) \cdot T}{A(1)S(1) + B(1)R(1)} = 1 \Rightarrow T = R(1) = r_0 + r_1 \\ S(1) = 0 \end{cases} \quad (22)$$

Calculation of $S(z^{-1})$ and $R(z^{-1})$ coefficients:

The desired closed loop polynomial is given by:

$$A_{CL}(z^{-1}) = A(z^{-1})S(z^{-1}) + B(z^{-1})R(z^{-1}) = 1 + p_1 z^{-1} + p_2 z^{-2} \quad (23)$$

Replacing $A(z^{-1})$, $S(z^{-1})$, $B(z^{-1})$ and $R(z^{-1})$ by their expressions in Equation 23. The obtained polynomial of the desired closed-loop is represented by:

$$\begin{aligned} A_{CL}(z^{-1}) &= 1 + p_1 z^{-1} + p_2 z^{-2} \\ &= 1 + \left(\frac{T_s}{k} r_0 - 2\right) z^{-1} + \left(\frac{T_s}{k} r_1 - 2\right) z^{-2} \end{aligned} \quad (24)$$

By identification the coefficients r_0 and r_1 are given by:

$$\begin{cases} r_0 = \frac{k}{T_s}(p_1 + 2) \\ r_1 = \frac{k}{T_s}(p_2 - 1) \end{cases} \quad (26)$$

The coefficients p_1 and p_2 are determined according to the desired current and voltage closed-loop dynamics.

Finally, the desired closed loop polynomial can be represented by:

$$A_{CL}(z^{-1}) = (1 - z^{-1}e^{-\omega_n T_s})^2 \quad (26)$$

Where, ω_n is the bandwidth of the control loop.

6.2 Boost DC/DC converter

A boost DC/DC converter (step-up converter shown in Fig. 5.) is a power converter with an output DC voltage greater than its input DC voltage. It is a class of switching-mode power supply containing at least two semiconductor switches (a diode and a switch) and at least one energy storage element (capacitor and/or inductor). Filters made of capacitors are normally added to the output of the converter to reduce output voltage ripple and the inductor connected in series with the input DC source in order to reduce the current ripple.

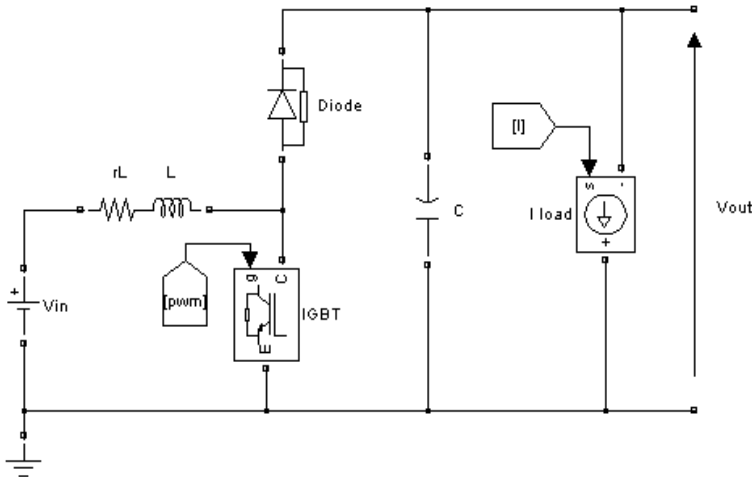


Fig. 5. Standard step-up DC-DC converter.

The smoothing inductor L is used to limit the current ripple. The filter capacitor C can restrict the output voltage ripples. The ripple current in the inductor is calculated by neglecting the output voltage ripple. The inductance value is given by the following equation:

$$L = \frac{V_{out}}{4 \times F \times \Delta I_{L_{max}}} = 400 \mu H \quad (27)$$

The capacitor must be able to keep the current supply at peak power. The output voltage ripple is a result of alternative current in the capacitor.

$$C = \frac{I_{L_{max}}}{4 \times F \times \Delta V_{out_{max}}} = 781 \mu F \quad (28)$$

Where:

- V_{out} : the output voltage,
- $\Delta I_{L_{max}}$: the inductor current ripple,
- F : the switching frequency.
- $I_{L_{max}}$: the maximum input current,
- $\Delta V_{out_{max}}$: the maximum output voltage ripple.

Table 1 shows the specifications of the converter. The inductor current ripple value is desired to be less than 5% of the maximum input current in the case of interfacing a Fuel Cell. A ripple factor less than 4% for the Fuel Cell's output current will have negligible impact on the conditions within the Fuel Cell diffusion layer and thus will not severely impact the Fuel Cell lifetime (Yu et al., 2007).

$\Delta V_{out_{max}}$	Output voltage ripple (1% of $V_{out} = 4$ V)
V_{out}	Output voltage (400 V)
F	Switching frequency (20 KHz)
$I_{L_{max}}$	Inductor current (250 A)
$\Delta I_{L_{max}}$	Inductor current ripple (5% of $I_{L_{max}} = 12.5$ A)

Table 1. Standard boost DC-DC converter parameters

6.2.1 Modeling and control

The output voltage is adjustable via the duty cycle α of the PWM signal switching the IGBT as given in the following expression:

$$\frac{V_{out}}{V_{in}} = \frac{1}{1 - \alpha} \quad (29)$$

The input voltage V_{in} is considered as constant (200V). The inductor and capacitor resistances are not taken into account in the analysis of the converter. The converter can be modeled by the following system of equations:

$$\begin{cases} v_{in} = L \frac{di_L}{dt} + (1 - u)v_{out} \\ i_L(1 - u) = C \frac{dv_{out}}{dt} + i_{out} \end{cases} \quad (30)$$

This model can be used directly to simulate the converter. By replacing the variable u by its average value which is the duty cycle during a sampling period makes it possible to obtain the average model of the converter as illustrated in the following system of differential equations:

$$\begin{cases} v_{in} = L \frac{di_L}{dt} + (1 - \alpha)v_{out} \\ i_L(1 - \alpha) = C \frac{dv_{out}}{dt} + i_{out} \end{cases} \quad (31)$$

Current control loop

The current control loop guarantees limited variations of the current through the inductor during important load variations. The inductor current and voltage models are given by Equation 32 and Equation 33, respectively.

$$IL(s) = \frac{1}{Ls} (V_{in}(s) - (1 - \alpha(s)) \cdot V_{out}(s)) \quad (32)$$

$$VL(s) = V_{in}(s) - (1 - \alpha(s)) \cdot V_{out}(s) \quad (33)$$

To make it simple to define a controller, the behavior of the system should be linearized. The linearization is done by using an inverse model. Thus an expression between the output of corrector and the voltage of the inductor should be found (Lachaize, 2004). Thus, the following expression is proposed:

$$\alpha(s) = 1 + \frac{VL'(s) - V_{in}(s)}{V_{out}(s)} \quad (34)$$

Where, VL' is a new control variable represents the voltage reference of the inductor. Thus, a linear transfer between $VL'(s)$ and $IL(s)$ is obtained by:

$$T_1(s) = \frac{IL(s)}{VL'(s)} = \frac{1}{Ls} \quad (35)$$

The structure of the regulator is a RST form. The polynomials R, S and T are calculated using the methodology explained above. The bandwidth of the current loop ω_i should be ten times lower than the switching frequency.

$$f_i \leq \frac{f}{10}, \omega_i \leq \frac{2\pi f}{10} \quad (36)$$

The inductor current loop is shown in Fig. 6.

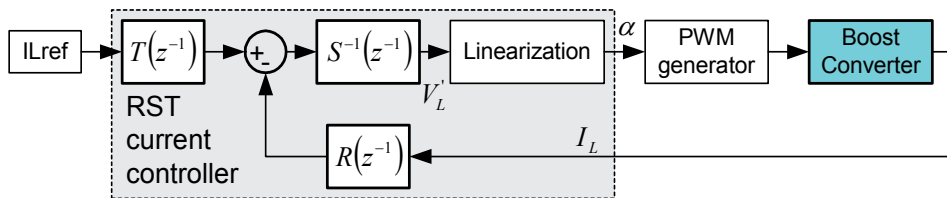


Fig. 6. Boost converter inductor current loop

From the reference value of the current and its measured value, The RST current controller block will calculate the duty cycle as explained above.

Voltage control loop

The output voltage loop was designed following a similar strategy to the current loop. To define the voltage controller, it is assumed that the current control loop is perfect. The capacitor current and voltage models are given by Equation 37 and Equation 38, respectively.

$$IC(s) = (1 - \alpha(s)) \cdot IL(s) - I_{out}(s) \tag{37}$$

$$VC(s) = \frac{1}{Cs} \left((1 - \alpha(s)) \cdot IL(s) - I_{out}(s) \right) \tag{38}$$

The linearization of the system is done by the following expression:

$$IL(s) = \frac{(IC'(s) + I_{out}(s))}{(1 - \alpha(s))} \tag{39}$$

$$\Rightarrow I_{Lref}(s) = \frac{V_{out}(s)}{V_{in}(s)} (IC'(s) + I_{out}(s))$$

Where IC' is a new control variable represents the current reference of the capacitor. Thus, a linear transfer between Vout(s) and IC'(s) is obtained by:

$$T_2(s) = \frac{V_{out}(s)}{IC'(s)} = \frac{1}{Cs} \tag{40}$$

The bandwidth of the voltage loop ω_v should be ten times lower than the current loop bandwidth ω_i which means hundred times lower than the switching frequency.

$$f_v \leq \frac{f}{100}, \omega_v \leq \frac{2\pi f}{100} \tag{41}$$

The output voltage control loop is shown in Fig. 7.

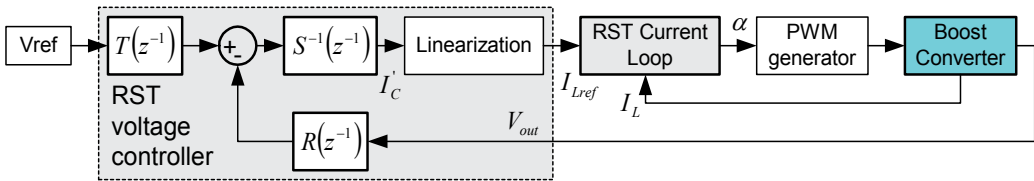


Fig. 7. Boost converter output voltage control loop.

The RST voltage controller operates in the same as the current controller and it has to calculate the current reference which will be the input of the current controller.

Simulation results

The current and voltage ripples are about 10 Amps and 2 Volts, respectively. The results show that the converter follows the demand on power thanks to the good control.

The efficiency of the boost dc/dc converter is about 83% at full load as shown in Fig. 8.

Fig. 9 shows the spectrum of the output signal of the LISN as described in the section “Electromagnetic compatibility regulation”. It is seen that the level of conducted interference due to converter is not tolerable by the regulations. As a consequence EMI filter suppression is necessary to meet the terms the regulations.

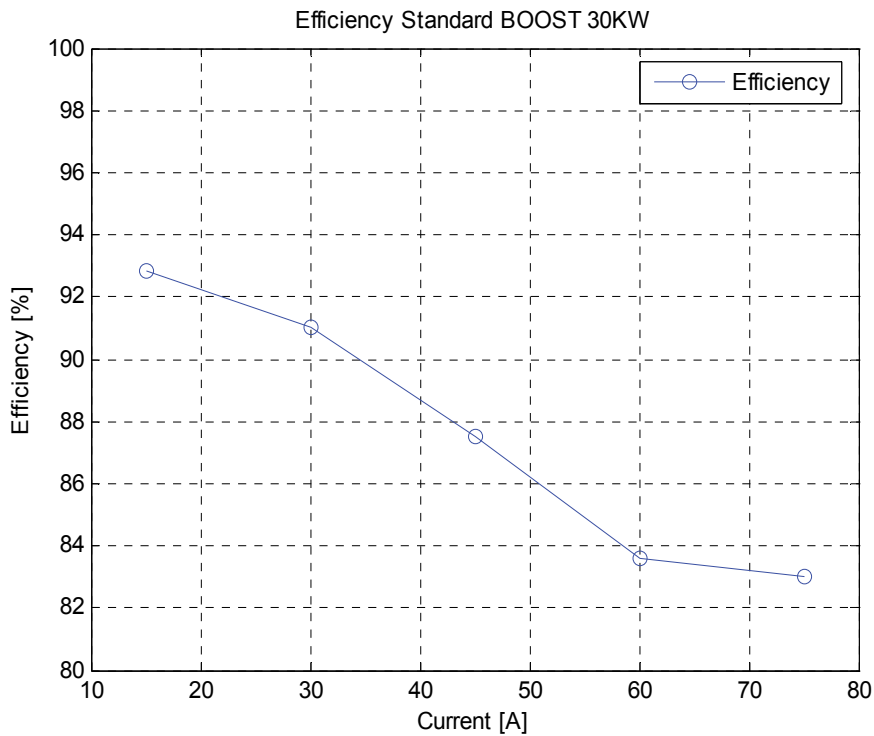


Fig. 8. Boost converter efficiency versus current load

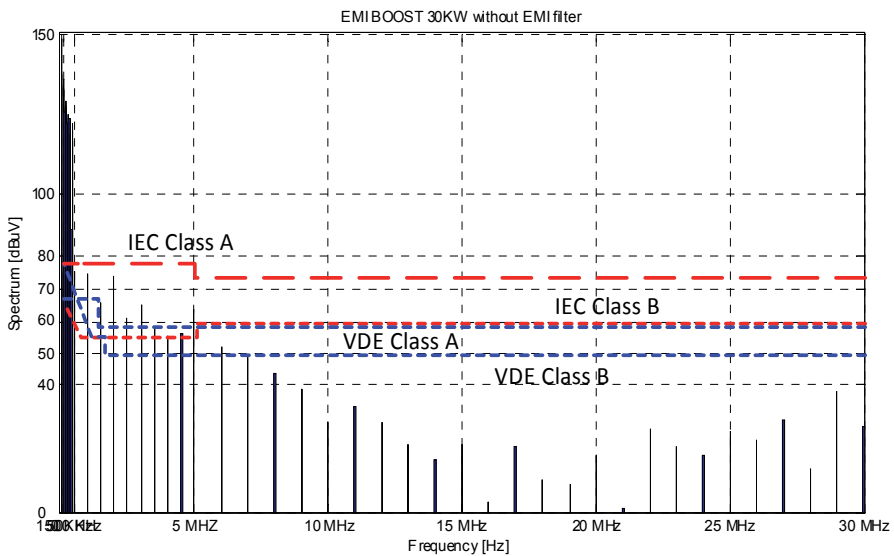


Fig. 9. EMI simulation results of boost DC/DC converter.

6.3 Interleaved 4-channel DC/DC converter

Fig. 10 shows a basic interleaved step-up converter of 4 identical levels where the inductances L_1 to L_4 are built by a separate magnetic core. The gate signals to the power switching devices are successively phase shifted by T/N where T is the switching period and N the number of channels. Thus, the current delivered by the electric source is shared equally between each basic step-up converter level and has a ripple content of period T/N (Destraz et al., 2006).

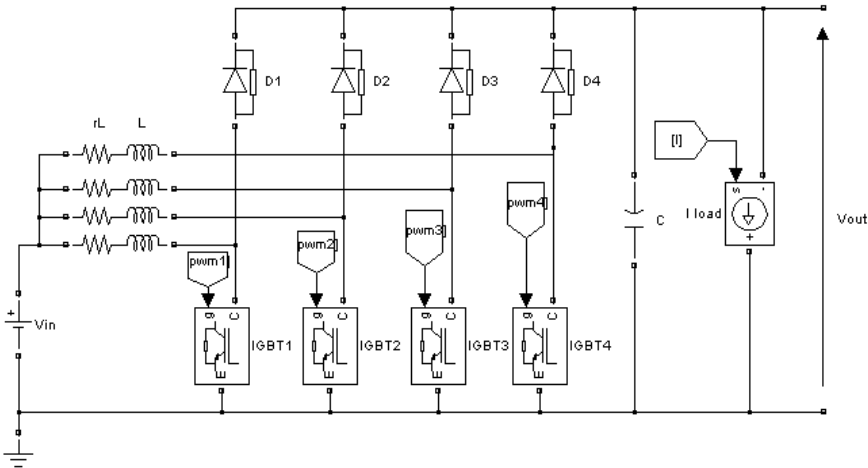


Fig. 10. Interleaved 4-channels step-up DC-DC converter.

The design of the 4-channels converter is the same like the boost one. The output voltage is adjustable via the duty cycle α of the PWM signal switching the IGBTs as given in the following expression:

$$\frac{V_{out}}{V_{in}} = \frac{1}{1 - \alpha} \quad (42)$$

Where:

- α : the duty cycle,
- V_{in} : the input voltage,
- V_{out} : the output voltage.

The inductor value of each channel is given by the following expression:

$$L_k = \frac{V_{out}}{4 \times F \times N \times \Delta I_{In_max}} = 100 \mu H \quad (43)$$

Where:

- N : the number of channels,
- ΔI_{in_max} : the input current ripple,
- F : the switching frequency.
- I_{in_max} : the maximum input current,
- ΔV_{out_max} : the maximum output voltage ripple.

As control signals are interleaved and the phase angle is $360^\circ/N$, the frequency of the total current is N times higher than the switching frequency F . The filter capacitor of the interleaved N -channel dc-dc converter is given by the following expression:

$$C_{f\min} = \frac{I_{In_max}}{4 \times F \times N \times \Delta V_{out_max}} = 195 \mu F \quad (44)$$

Table 2 shows the specifications of the converter.

ΔV_{out_max}	Output voltage ripple (1% of $V_{out} = 4$ V)
V_{out}	Output voltage (400 V)
F	Switching frequency (20 KHz)
I_{In_max}	Inductor current (250 A)
ΔI_{In_max}	Input current ripple (5% of $I_{In_max} = 12.5$ A)

Table 2. Interleaved 4-channels DC-DC converter parameters

6.3.1 Modeling and control

The 4-channel converter is modeled in the same way of the boost converter. The current and voltage loop are designed also using the same methodology used for boost converter. The calculated current reference is divided by 4 (number of channels). The output voltage control loop is shown in Fig. 11.

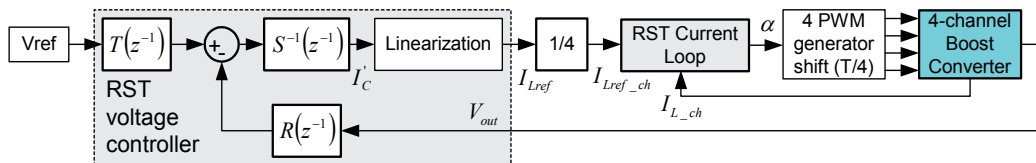


Fig. 11. 4-channels converter output voltage control loop.

In the proposed control, the duty cycle is calculated from one reference channel. The same duty cycle is applied to the other channels. The PWM signals are shifted by $360/4^\circ$.

Simulation results

Thanks to the interleaving technique, the total current ripples are reduced and can be neglected; the voltage ripples are about 0.5V. The results show that the converter follows the demand on power.

The efficiency of the 4-channels dc/dc converter is about 92% at full load as shown in Fig. 12. The drop in efficiency is due to the changing from discontinuous mode (DCM) to continuous mode (CM). In DCM, the technique of zero voltage switching (ZVS) is operating which permits to reduce the switching losses in the switch, thus the efficiency is increased.

Fig. 13 shows the EMI of the interleaved 4-channels DC/DC converter. It is seen that the level of conducted interference due to converter is not tolerable by the regulations. As a consequence this converter without EMI filter suppression does not meet the terms of the regulations. Thus, EMI filter suppression is required.

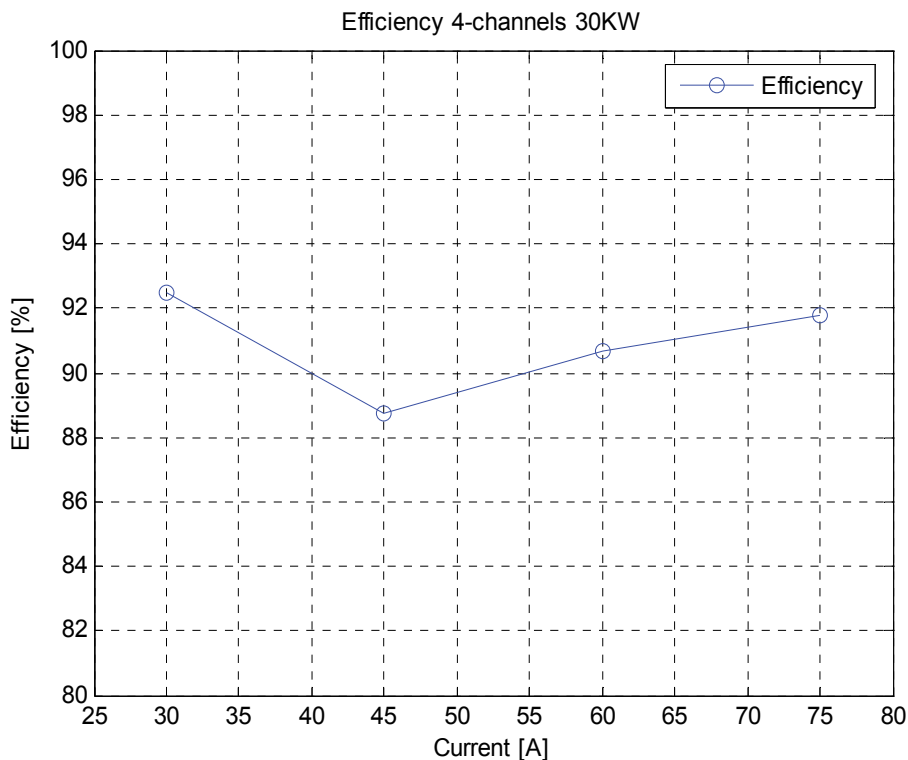


Fig. 12. 4-channels converter efficiency versus current load.

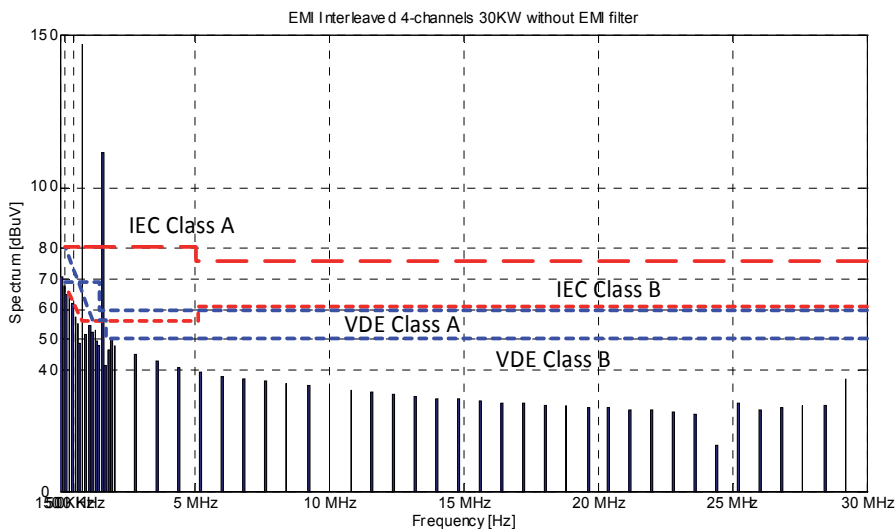


Fig. 13. EMI simulation results of interleaved 4-channels DC/DC converter.

6.4 Full-bridge DC/DC converter

The structure of this topology is given in Fig. 14. The transformer turns ratio n must be calculated in function of the minimum input voltage (Pepa, 2004).

$$n = \frac{N_s}{N_p} = \frac{1}{2\alpha} \times \frac{V_{out}}{V_{in_min}} \quad (45)$$

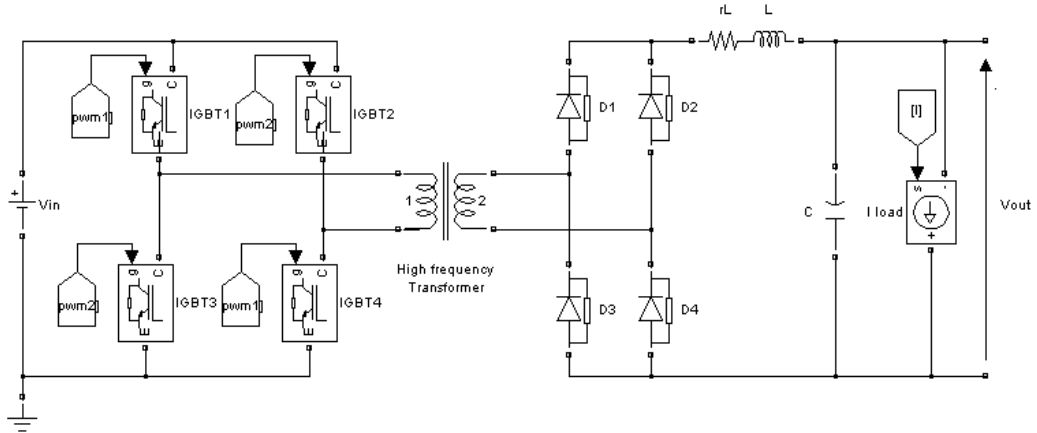


Fig. 14. Full-bridge step-up DC-DC converter

The output filter inductor and capacitor values could be calculated based on maximum ripple current and ripple voltage magnitudes. The calculations are done considering the converter is working in CCM.

$$L = \frac{n \times \alpha \times V_{in}}{2 \times \Delta I_{L_max} \times F} = 1.2\text{mH} \quad (46)$$

The filter capacitor value is given by the following relation based on the inductor current ripple value and the output voltage ripple.

$$C = \frac{\Delta I_{L_max}}{8 \times \Delta V_{out_max} \times F} = 14.64\mu\text{F} \quad (47)$$

Where:

- α : the duty cycle,
- N_s : the number of turns in the secondary winding of the transformer,
- N_p : the number of turns in the primary winding of the transformer,
- V_{in} : the input voltage,
- ΔI_{L_max} : the inductor current ripple,
- F : the switching frequency,
- ΔV_{out_max} is the maximum output voltage ripple.

Table 3 shows the simulations parameters of the converter.

ΔV_{out_max}	Output voltage ripple (1% of $V_{out} = 4$ V)
V_{out}	Output voltage (400 V)
F	Switching frequency (40 KHz)
ΔI_{L_max}	Inductor current ripple (5% of $I_{Lmax} = 3.75$ A)
n	Transformer turns ratio (= 4)

Table 3. Full-Bridge DC-DC converter parameters.

6.4.1 Modeling and control

The Full-Bridge DC/DC converter will have to maintain a constant 400V DC output. By increasing and decreasing the duty cycle $\alpha=t/T$ of the PWM signals, the output voltage can be held constant with a varying input voltage. The output voltage can be calculated as follows:

$$V_{out} = \frac{2}{T} \int_0^t \frac{V_{in}}{n} dt \Rightarrow V_{out} = 2 \times n \times \alpha \times V \quad (48)$$

Where, T is the switching period ($T=1/F$), n is the transformer turns ration ($n=N_s/N_p$), and t is the pulse width time.

The inductor current and voltage models are obtained by expressions 49 and 50, respectively.

$$I_L(s) = \frac{1}{Ls} \left(\frac{4n\sqrt{2}}{\pi} \alpha(s) \times V_{in}(s) - V_{out}(s) \right) \quad (49)$$

$$V_L(s) = \frac{4n\sqrt{2}}{\pi} \alpha(s) \times V_{in}(s) - V_{out}(s) \quad (50)$$

The linearization of the system is done by using an inverse model. Thus an expression between the output of corrector and the voltage of the inductor should be found. Thus, the following expression is proposed:

$$\alpha(s) = \frac{V_L'(s) + V_{out}(s)}{\frac{4n\sqrt{2}}{\pi} \alpha(s) \times V_{in}(s)} \quad (51)$$

Where, V_L' is a new control variable represents the voltage reference of the inductor. Thus, a linear transfer between $V_L'(s)$ and $I_L(s)$ is obtained by:

$$T_1(s) = \frac{I_L(s)}{V_L'(s)} = \frac{1}{Ls} \quad (52)$$

The bandwidth of the current loop ω_i should be ten times lower than the switching frequency.

$$f_i \leq \frac{f}{10}, \omega_i \leq \frac{2\pi f}{10} \quad (53)$$

The inductor current loop is shown in Fig. 15.

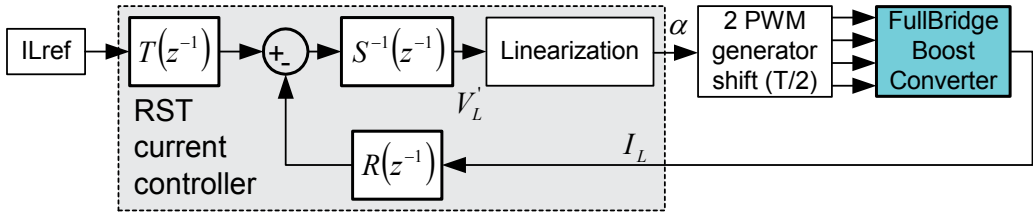


Fig. 15. Full-bridge converter inductor current control loop.

The output voltage loop was designed following a similar strategy to the current loop. To define the voltage controller, it is assumed that the current control loop is perfect. The capacitor current and voltage models are obtained by expressions 54 and 55:

$$I_C(s) = I_L(s) - I_{out}(s) \quad (54)$$

$$V_C(s) = \frac{1}{Cs}(I_L(s) - I_{out}(s)) \quad (55)$$

The linearization of the system is done by the following expression:

$$I_L(s) = I'_c(s) + I_{out}(s) \Rightarrow I_{Lref}(s) = I'_c(s) + I_{out}(s) \quad (56)$$

Where I'_c is a new control variable represents the current reference of the capacitor. Thus, a linear transfer between $V_{out}(s)$ and $I'_c(s)$ is obtained by:

$$T_2(s) = \frac{V_{out}(s)}{I'_c(s)} = \frac{1}{Cs} \quad (57)$$

The bandwidth of the voltage loop ω_v should be ten times lower than the current loop bandwidth ω_i which means hundred times lower than the switching frequency.

$$f_v \leq \frac{f}{100}, \omega_v \leq \frac{2\pi f}{100} \quad (58)$$

The output voltage control loop is shown in Fig. 16.

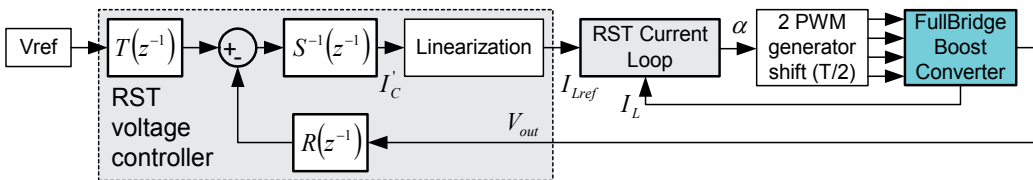


Fig. 16. Full-bridge converter output voltage control loop.

Simulation results

The efficiency of the Full-bridge dc/dc converter is about 91.5% at full load as shown in Fig. 17. The efficiency of this converter can be increased by using phase shifted PWM control and zero voltage switching ZVS technique.

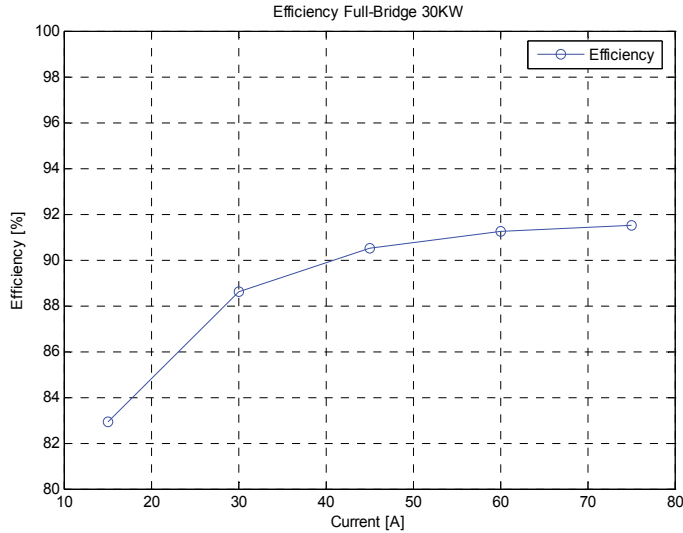


Fig. 17. Full-bridge converter efficiency versus current load.

Fig. 18 shows the spectrum of the EMI of the Full-Bridge converter. The level of conducted interference is not tolerable by the regulations. As a consequence EMI filter suppression is necessary to meet the terms the regulations.

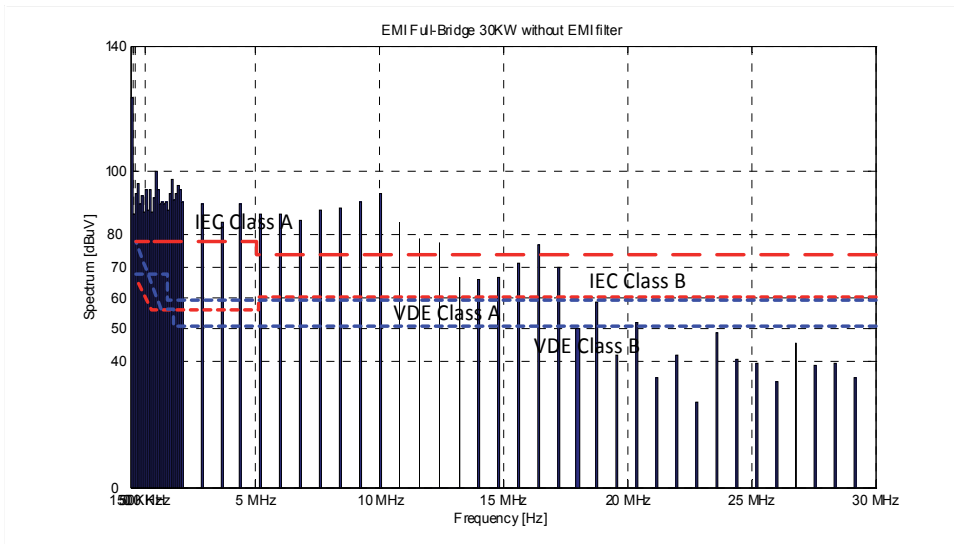


Fig. 18. EMI simulation results of Full-Bridge DC/DC converter.

7. Interpreting and comparing results

Table 4 recapitulates the volume, weight, efficiency and the EMI of each converter. The inductor volume and weight were approximated. It can be noticed that the full-bridge converter has the biggest volume and weight due to the output inductance. This inductance value can be reduced by increasing the switching frequency of the converter. We can notice that the best candidate for the application is the Interleaving multi-channel topology which has the higher efficiency and lower weight and volume. Weight and volume estimation takes into account only the IGBT, DIODE, Inductor and capacitor (transformer for full bridge) and it doesn't take into account the cooling system and the arrangement of components in the casing of the converter.

DC/DC converter	EMI	Volume(cm ³)	Weight(g)	Efficiency at full load
Boost	-+	2167	6325	83%
Interleaved 4-channels	+	1380	3900	92%
Full-Bridge	--	3033	9268	91.5%

Table 4. Recapitulative table.

Fig. 19 gives an idea about the difference in the weight, volume and efficiency of each converter.

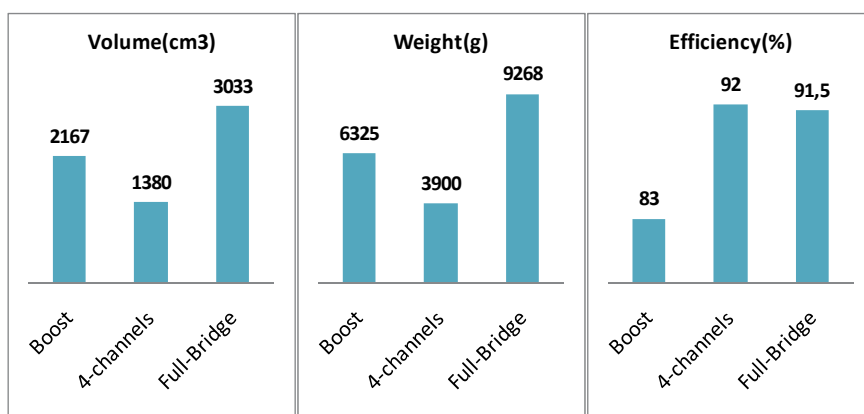


Fig. 19. Efficiency and approximated weight and volume of each converter

8. Conclusion

In this chapter, a comparative study which presents three examples of DC-DC converter topologies (Boost DC/DC converter, interleaved step-up DC/DC converter and Full-bridge step-up DC/DC converter) is carried out. The first structure considers a basic, single step-up converter; the second is based on basic interleaving technique. This structure, even simple, improves the step-up converter quality of the current drawn from the fuel cell and has small weight and volume. However, it presents limits when a high voltage step-up is required. The third topology is the full-bridge converter which has the possibility to high voltage step-up thanks to the High frequency transformer. Simulations are carried out for a three converters of 30 KW. Simulations take into account real components (IGBT and Diode), the

weight and volume of each converter were calculated based on datasheets. The efficiency of each converter was calculated for the worst case condition (maximum losses in the power switches). Simulations results show interleaved 4-channels DC/DC converter as a best candidate to the application. It has low EMI, the higher efficiency, the smaller volume and weight which are required for transport application.

9. References

- Bouhalli, N., Cousineau, M., Sarraute, E., & Meynard, T. (2008). Multiphase coupled converter models dedicated to transient response and output voltage regulation studies, *Proceedings of EPE-PEMC 2008 13th Conference on Power Electronics & Motion Control*, pp. 281 - 287, ISBN 978-1-4244-1741-4, Poznan, Poland, September 1-3, 2008
- Büchi, F., Delfino, A., Dietrich, P., Freunberger, S.A., Kötz, R., Laurent, D., Magne, P.A., Olsommer, D., Paganelli, G., Tsukada, A., Varenne, P. & Walsler, D. (2006). Electrical Drivetrain Concept with Fuel Cell System and Supercapacitor – Results of the «HY-LIGHT» - vehicle, *VDI Tagung Innovative Fahrzeugantriebe 2006*, pp. 415-429, Dresden, Germany, 2006
- Cacciato, M., Caricchi, F., Giuhlii, F. & Santini, E. (2004). A Critical Evaluation and Design of Bi-directional DC/DC Converters for Super-Capacitors Interfacing in Fuel Cell Applications, *Proceedings of IAS 39th IEEE Industry Applications Conference Annual Meeting*, pp. 1127-1133, ISBN 0-7803-8486-5, Rome, Italy, October 3-7, 2004
- Chiu, H.J., & Lin, L.W. (2006). A Bidirectional DC-DC Converter for Fuel Cell Electric Vehicle Driving System, in *Power Electronics IEEE Transactions*, Vol.21 Issue 4, (2006), pp. 950-958, ISSN 0885-8993
- Destraz, B., Louvrier, Y., & Rufer, A. (2006). High Efficient Interleaved Multi-channel dc/dc Converter Dedicated to Mobile Applications, *Proceedings of IAS 41st IEEE Industry Applications Conference Annual Meeting*, pp. 2518-2523, ISBN 1-4244-0364-2, Tampa, Florida, USA, October 8-12, 2006
- Farhadi A., Jalilian A. (2006). Modeling and Simulation of Electromagnetic Conducted Emission Due to Power Electronics Converters, *Proceedings of PEDES'06 International Conference on Power Electronics, Drives & Energy Systems*, pp. 1-6, ISBN 0-7803-9772-X, New Delhi, India, December 12-15, 2006
- Fengyan, W., Jianping, X., & Bin, W. (2006). Comparison Study of Switching DC-DC Converter Control Techniques, *Proceedings of International Conference on Communications, Circuits & Systems*, pp. 2713-2717, ISBN 0-7803-9584-0, Guilin, Alberta, Canada, June 25-28, 2006
- Garcia Arregui, m. (2007). Theoretical study of a power generation unit based on the hybridization of a fuel cell stack and ultracapacitors, *Laboratoire Plasma et Conversion d'Énergie*, Toulouse, France, 2007
- Garcia, O., Flores, L.A., Oliver, J.A., Cobos, J.A., & De la Pena, J. (2005). Bi-Directional DC/DC Converter For Hybrid Vehicles, *Proceedings of PESC'05 IEEE 36th Power Electronics Specialists Conference*, pp. 1881-1886, ISBN 0-7803-9033-4, Recife, Brazil, June, 2005
- Lachaize, J. (2004). Etude des stratégies et des structures de commande pour le pilotage des systèmes énergétiques à Pile à Combustible (PAC) destinés à la traction, *Laboratoire d'Electrotechnique et d'Electronique Industrielle de l'ENSEEIH*T, Toulouse, France, 2004

- Lachichi, A., Schofield, N. (2006). Comparison of DC-DC Converter Interfaces for Fuel Cells in Electric Vehicle Applications, *Proceedings of VPPC'06 IEEE Conference on Vehicle Power & Propulsion*, pp. 1-6, ISBN 1-4244-0158-5, Windsor, UK, September 6-8, 2006
- Landau, I. D. (1998). The R-S-T digital controller design and applications, *Journal of Control Engineering Practice*, Vol.6, Issue 2, (February 1998), pp. 155-165
- Pepa, E. (2004). Adaptive Control of a Step-Up Full-Bridge DC-DC Converter for Variable Low Input Voltage Applications, *Faculty of the Virginia Polytechnic Institute and State University*, Blacksburg, Virginia, 2004
- Schaltz, E., & Rasmussen, P.O. (2008). Design and Comparison of Power Systems for a Fuel Cell Hybrid Electric Vehicle, *Proceedings of IAS'08 IEEE Industry Applications Society Annual Meeting*, pp. 1-8, ISBN 978-1-4244-2278-4, Edmonton, Alberta, Canada, October 5-9, 2008
- Yu, W., & Lai, J.S. (2008). Ultra High Efficiency Bidirectional DC-DC Converter With Multi-Frequency Pulse Width Modulation, *Proceedings of APEC 2008 23rd Annual IEEE Conference and Exposition on Applied Power Electronics*, pp. 1079-1084, ISBN 978-1-4244-1873-2 Austin, Texas, USA, February 24-28, 2008
- Yu, X., Starke, M.R., Tolbert, L.M., & Ozpineci, B. (2007). Fuel cell power conditioning for electric power applications: a summary, *Journal of IET electric power applications*, Vol.1, No.5, (2007), pp. 643-656, ISSN 1751-8660

A Comparative Thermal Study of Two Permanent Magnets Motors Structures with Interior and Exterior Rotor

Naourez Ben Hadj, Jalila Kaouthar Kammoun,
Mohamed Amine Fakhfakh, Mohamed Chaieb and Rafik Neji
*Electrical Engineering Department/ University of Sfax
Tunisia*

1. Introduction

Considering the large variety of electric motors, such as asynchronous motors, synchronous motors with variable reluctances, permanent magnets motors with radial or axial flux, the committed firms try to find the best choice of the motor conceived for electric vehicle field.

The electric traction motor is specified by several qualities, such as the flexibility, reliability, cleanliness, facility of maintenance, silence etc. Moreover, it must satisfy several requirements, for example the possession of a high torque and an important efficiency (Zire et al., 2003; Gasc, 2004; Chan., 2004).

In this context, the surface mounted permanent magnets motor (SMPMM) is characterized by a high efficiency, very important torque, and power-to-weight, so it becomes very interesting for electric traction.

In the intension, to ensure the most suitable and judicious choice, we start by an analytical comparative study between two structures of SMPMM which are the permanent magnets synchronous motor with interior rotor (PMSMIR) and the permanent magnets synchronous motor with exterior rotor (PMSMER), then, we implement a methodology of design based on analytical modelling and the electromagnetism laws. Also, in order to understand the thermal behaviour of the motor, we implant a comparative thermal performance of the two structures illustrated with careful attention to the manufacturing techniques used to produce the machine, and the associated thermal resistances and capacitances, to obtain good steady state and transient thermal performance prediction.

2. Modelling of two SMPMM structures

2.1 Structural data

The structures of motors allowing the determination of the studied geometry are based on three relationships.

The ratio β is the relationship between the magnet angular width L_m and the pole-pitch L_p . This relationship is used to adjust the magnet angular width according to the motor pole-pitch.

$$\beta = \frac{L_m}{L_p} \quad (1)$$

$$L_p = \frac{\pi}{p} \quad (2)$$

The ratio R_{ldla} is the relationship between the angular width of a principal tooth and the magnet angular width. This ratio is responsible for the regulation of the principal tooth size which has a strong influence on the electromotive force form.

$$R_{ldla} = \frac{A_{tooth}}{L_m} \quad (3)$$

The R_{did} ratio is the relationship between the angular width of the principal tooth and the angular width of the inserted tooth A_{toothi} . This relationship fixes the inserted tooth size.

$$R_{did} = \frac{A_{tooth}}{L_m} \quad (4)$$

2.2 Geometrical structures of PMSMIR and PMSMER

This part is devoted to an analytical sizing allowing calculation of geometrical sizes of the two SMPMM configurations which are the PMSMER and the PMSMIR.

Figure 1 represents the PMSMER and the PMSMIR with the number of pole pairs is $p=4$ and a number of principal teeth is 6, between two principal teeth, an inserted tooth is added to improve the wave form and to reduce the leakage flux (Ben Hadj, N. et al., 2007). The slots are right and open in order to facilitate the insertion of coils and to reduce the production cost (Magnussen, F. et al., 2005; Bianchi, N. et al., 2003; Libert, F. et al., 2004).

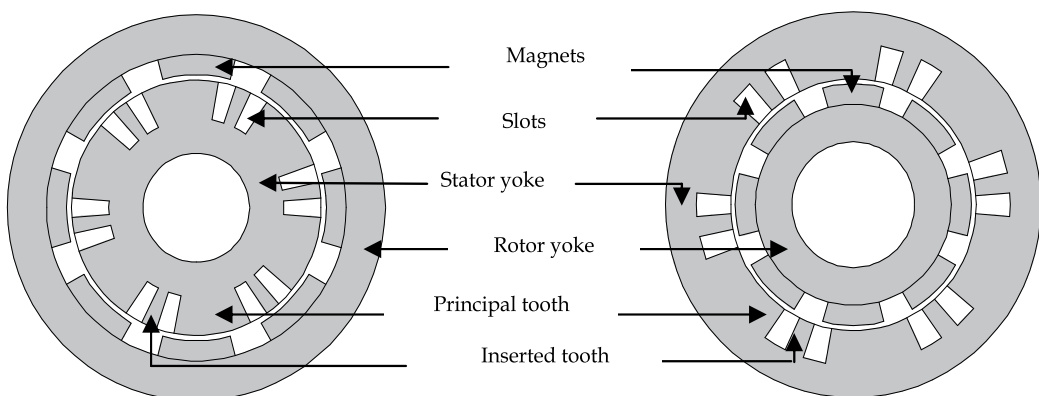


Fig. 1. Permanent magnets motors with exterior rotor and interior rotor

2.3 Analytical sizing of the two SMPMM structures

The analytical study of motor sizing is based on the schedules data conditions parameters (Table 1), the constant characterizing materials (Table 2), the expert data and configurations of the two motors.

Definition	Symbol	Value
Electric vehicle mass	M	1000 kg
Angle of starting	α_d	3°
Time of starting	t_d	4 s
Outside temperature	T_{out}	40°C
Maximum motor power	P_{mmax}	21,635 kW
Winding temperature	T_w	95°C
Base speed of the vehicle	V_b	30 km/h
Maximum Speed of the vehicle	V_{max}	100 km/h
Slots load factor	k_r	0,44
Current density in the slots	δ	7 A/mm ²

Table 1. The schedules data conditions

Definition	Symbol	Value
Remanent magnetic induction of the magnets	B_m	1,175 T
Demagnetization Induction	B_c	0,383 T
Magnetic induction in teeth	B_{tooth}	0,9 T
Magnets permeability	μ_a	1,05
Mechanical losses coefficient	k_m	1%
Copper resistivity at 95°C	R_{cu}	17,2 10 ⁻⁹ Ωm
The copper resistivity variation coefficient	α	0,004
Density of the electrical sheets	M_{vt}	7850 kg
Density of magnets	M_{va}	7400 kg
Density of copper	M_{vc}	8950 kg
Sheets quality coefficient	Q	1,1

Table 2. Specific constants of materials

Expert data

The expert data are practically represented by three sizes which are, the magnetic induction in the air gap B_e , the magnetic induction in the stator yoke B_{sy} and the magnetic induction in the rotor yoke B_{ry} . It should be noted that the zone of variation of these three parameters varies between 0,2 to 1,6T (Ben Hadj et al., 2007).

Structural data

For the two configurations, we adopted the same number of pole pairs $P=4$, with an air gap thickness equivalent to 2mm, with a relationship β equal to 0,667 and $R_{l dia}$ equal to 1,2.

Data identified by the finite elements method

K_{fu} is the leakage flux coefficient of the PMSMIR which is fixed to 0,95 whereas for the PMSMER, k_{fu} is equal to 0,98. In this context, we define a ratio R_{did} equal to 0,2.

2.4 Geometrical sizes

Geometrical parameters of the two structures motors are defined in figure 2. Where:

1. The magnet height, h_m
2. The slots height h_s and the tooth height h_{tooth}
3. The rotor yoke height, h_{ry}
4. The stator yoke height, h_{sy}
5. The air gap thickness, e

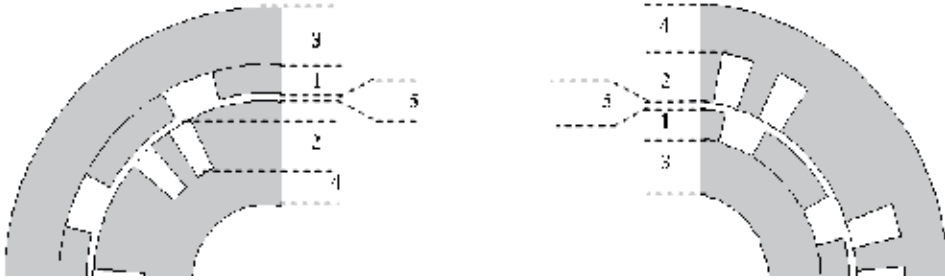


Fig. 2. PMSMER and PMSMIR parameters

In the stator of the PMSMIR, geometrical sizes are defined by:

The slot average width: W_s

$$W_s = \frac{D_m + e + h_{tooth}}{2} A_s \quad (5)$$

The principal tooth section: S_{tooth}

$$S_{tooth} = \frac{D_m + e}{2} A_{tooth} l_m \quad (6)$$

Where l_m , D_m are the average motor length and the average motor diameter.

The inserted tooth section: S_{toothi}

$$S_{toothi} = \frac{D_m + e}{2} A_{toothi} l_m \quad (7)$$

The slot section: S_s

$$S_s = \frac{1}{2} \left[\frac{2\pi}{N_{tooth}} - A_{tooth} - A_{toothi} \right] \frac{D_m + e}{2} l_m \quad (8)$$

In the stator of the PMSMER, geometrical sizes are defined by:

The slot average width: W_s

$$W_s = \frac{D_m - e - h_{tooth}}{2} A_s \quad (9)$$

The principal tooth section: S_{tooth}

$$S_{tooth} = \frac{D_m + e}{2} A_{tooth} I_m \quad (10)$$

The inserted tooth section: S_{toothi}

$$S_{toothi} = \frac{D_m + e}{2} A_{toothi} I_m \quad (11)$$

The slot section: S_s

$$S_s = \frac{1}{2} \left[\frac{2\pi}{N_{tooth}} - A_{tooth} - A_{toothi} \right] \frac{D_m - e}{2} I_m \quad (12)$$

The teeth height h_{tooth} of the PMSMIR and the PMSMER are expressed by equation 13 and 14 where N_{sph} is the number of turns per phase, I_n is the rated current and N_{teeth} in the number of teeth.

$$h_{tooth} = \sqrt{\frac{N_{sph} \cdot I_n}{N_{teeth} \delta K_r A_s} + \left(\frac{D_m + e}{2} \right)^2} - \frac{D_m + e}{2} \quad (13)$$

$$h_{tooth} = \sqrt{\frac{N_{sph} \cdot I_n}{N_{teeth} \delta K_r A_s} + \left(\frac{D_m - e}{2} \right)^2} - \frac{D_m - e}{2} \quad (14)$$

The stator yoke thickness h_{sy} is obtained by the application of the flux conservation theorem, where B_{tooth} is the magnetic induction in the tooth.

$$h_{sy} = \frac{B_{tooth} S_{tooth}}{2 l_m B_{sy}} \quad (15)$$

In the rotor of the two structures, geometrical sizes are defined by:

The expression of the magnet height h_m is the same one in the two structures. It is obtained by the application of the Ampere theorem.

Where μ_a is the air permeability and k_{fu} is the flux leakage coefficient.

$$h_m = \frac{\mu_a B_e e}{M(Ta) - \frac{B_e}{k_{fu}}} \quad (16)$$

Where the magnet induction $M(Ta)$ at $Ta^\circ\text{C}$ is defined by:

$$M(Ta) = M[1 + \alpha_m(Ta - 20)] \quad (17)$$

The rotor yoke thickness h_{ry} is defined:

$$h_{ry} = \frac{B_e S_{tooth}}{2k_{fu} l_m B_{ry}} \quad (18)$$

2.5 Electrical sizing

The electromotive force in the two SMPMM structures is expressed by:

$$EMF_i(t) = \frac{8}{\pi} N_{sph} l_m D_m B_e \sin\left(\frac{\pi\beta}{2}\right) \sin\left(\frac{\pi}{2}\beta R_{llda}\right) \Omega_m \sin(p\Omega_m t) \quad (19)$$

The motor electric constant : K_e

$$K_e = \frac{12}{\pi} N_{sph} l_m D_m B_e \sin\left(\frac{\pi\beta}{2}\right) \sin\left(\frac{\pi}{2}\beta R_{llda}\right) \quad (20)$$

The electromagnetic torque : T_{em}

$$T_{em}(t) = \frac{1}{\Omega} \sum_{i=1}^3 EMF_i(t) i_i(t) \quad (21)$$

where EMF_i , i_i and Ω_m represent respectively the electromotive force, the current of the i phase and the angular speed of the motor.

The motor rated current I_n is the ratio between the electromagnetic torque and the motor electric constant.

$$I_n = \frac{T_{em}}{K_e} \quad (22)$$

The phase resistance of the motor : R_{ph}

$$R_{ph} = R_{co}(T_w) \frac{N_{sph} \delta L_{sp}}{I_n / \sqrt{2}} \quad (23)$$

where $R_{co}(T_w)$ is the copper receptivity at the temperature of winding T_w and L_{sp} is the spire average length (Ben Hadj et al., 2007).

3. Comparative thermal study between the two SMPMM

In this study, the comparison between the two SMPMM structures consists on the thermal analysis which is based upon lumped-circuit analysis. It represents the thermal problems by using the thermal networks, analogous to electrical circuits. The thermal circuit in the steady state consists of thermal resistances and heat sources connected between motor component nodes. For transient analysis, the heat/thermal capacitances are used additionally to take into account the change in internal energy of the body with time. The thermal resistances for conduction and convection can be obtained by:

$$R_{convection} = \frac{l}{Ak} [K / W] \quad (24)$$

$$R_{conduction} = \frac{l}{A_c h} [K / W] \quad (25)$$

Where l is the distance between the point masses and A is the interface area, k is the heat conductivity, A_c is the cooling cross section between the two regions and h is the convection coefficient calculated from proven empirical dimensionless analysis algorithms.

The heat capacitance is defined as follow:

$$C = V \rho c [Ws / K] \quad (26)$$

Where V is the volume, ρ is the density and c is the heat capacity of the material. The simplified stator for the thermal study of the two SMPMM structure are given by figures 3 and 4, also the thermal model for the two structures are implemented in MATLAB simulator where the different radius for the PMSMER dimensions are defined as follow:

$$R_{carter} = R_1 = R_f + \frac{e}{2} + h_m + h_{ry} + e_{carter} \quad (27)$$

$$R_{rotoryoke} = R_2 = R_f + \frac{e}{2} + h_m + h_{ry} \quad (28)$$

$$R_{magnet} = R_3 = R_f + \frac{e}{2} + h_m \quad (29)$$

$$R_4 = R_f + \frac{e}{2} \quad (30)$$

$$R_{slot} = R_5 = R_f - \frac{e}{2} \quad (31)$$

$$R_{insolator} = R_6 = R_5 - h_s \quad (32)$$

$$R_7 = R_5 - h_s - t_{insolator} \quad (33)$$

$$R_8 = R_7 - h_{sy} \quad (34)$$

The thermal resistances are calculated along the radial direction. The R_i radius are calculated from dimensions of motor, where R_f is the Bore raduis and $t_{insolator}$ is the thickness insulator.

The different radius for the PMSMIR dimensions are defined as follow:

$$R_1 = R_f + \frac{e}{2} \quad (35)$$

$$R_2 = R_f + \frac{e}{2} + h_{tooth} \quad (36)$$

$$R_3 = R_f + \frac{e}{2} + h_{tooth} + t_{insolator} \quad (37)$$

$$R_4 = R_f + \frac{e}{2} + h_{tooth} + t_{insolator} + h_{sy} \quad (38)$$

$$R_5 = R_f + \frac{e}{2} + h_{tooth} + t_{insolator} + h_{sy} + t_{carter} \quad (39)$$

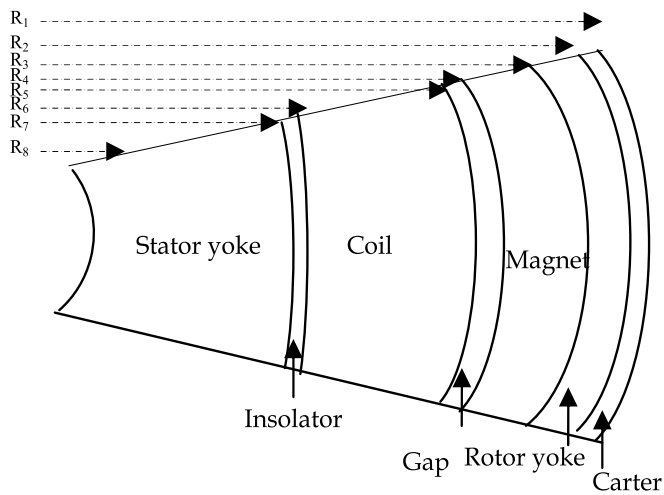


Fig. 3. Simplified stator for the thermal study in the PMSMER

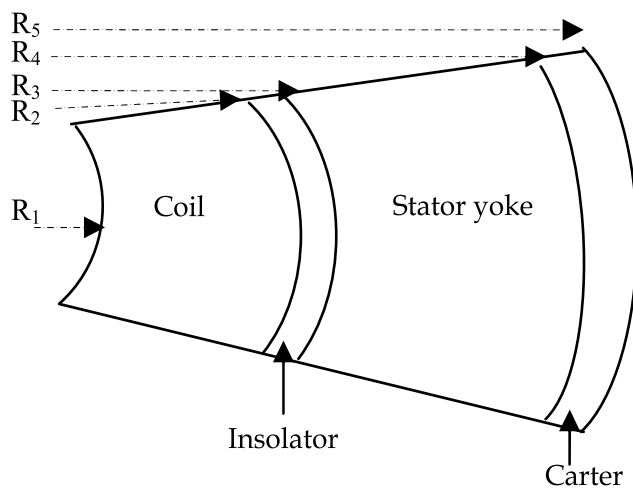


Fig. 4. Simplified stator for the thermal study in the PMSMIR

As described earlier, the thermal resistance values are automatically calculated from motor dimensions and material data.

Figure 5 shows the thermal model in transient behaviour of the PMSMIR.

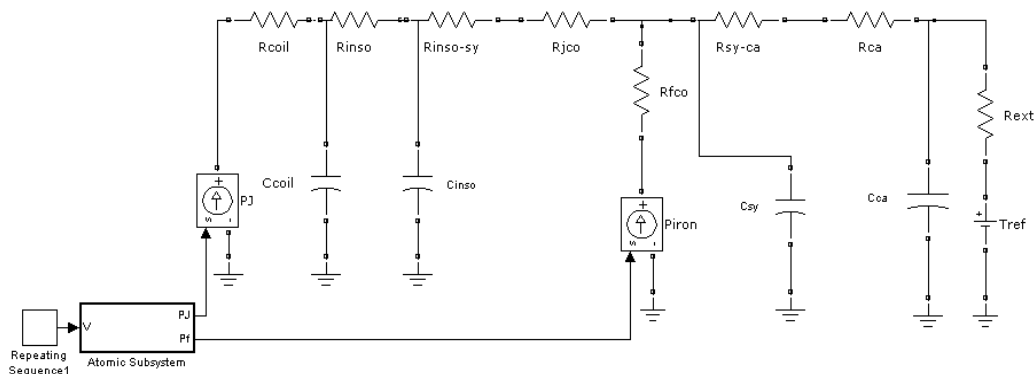


Fig. 5. Thermal model of the PMSMIR in transient behaviour

In this model, the heat sources are respectively the copper losses and iron losses in the stator. The T_i variables are the temperatures in various points of the motor. The expressions of thermal resistances of the PMSMIR result from the resolution of the heat equation at the fields borders.

R_{coil} represents the coil thermal resistance ($K.W^{-1}$).

$$R_{coil} = \frac{1}{4\pi l_m \lambda_{coil}} \left[1 - 2 \frac{R_1^2}{R_2^2 - R_1^2} \ln \frac{R_2}{R_1} \right] \quad (40)$$

R_{inso} represents the isolator thermal resistance ($K.W^{-1}$).

$$R_{inso} = \frac{\ln \frac{R_3}{R_2}}{2\pi \lambda_{inso} l_m} \quad (41)$$

$R_{inso-sy}$ represents the contact thermal resistance between insulator and the stator yoke ($K.W^{-1}$).

$$R_{inso-sy} = \frac{1}{\frac{300}{2\pi R_3 l_m}} \quad (42)$$

R_{jco} represents the thermal resistance of stator yoke ($K.W^{-1}$).

$$R_{jco} = \frac{\ln \frac{R_4}{R_3}}{2\pi \lambda_{iron} l_m} \quad (43)$$

R_{fco} represents the thermal resistance of conduction in the stator yoke ($K.W^{-1}$).

$$R_{fco} = \frac{1}{4\pi l_m \lambda_{iron}} \left[1 - 2 \frac{R_3^2}{R_4^2 - R_3^2} \ln \frac{R_4}{R_3} \right] \quad (44)$$

R_{sy-ca} represents the thermal resistance between stator yoke and the carter ($K.W^{-1}$).

$$R_{sy-ca} = \frac{1}{2\pi R_4 l_m} \quad (45)$$

R_{ca} represent the thermal resistance of carter ($K.W^{-1}$).

$$R_{ca} = \frac{\ln \frac{R_5}{R_4}}{2\pi \lambda_{ca} l_m} \quad (46)$$

R_{ext} represents the convection thermal resistance between the carter and ambient air ($K.W^{-1}$).

$$R_{ext} = \frac{l}{h S_{ext}} \quad (47)$$

In the previous expression, S_{ext} represents the outer surface of the motor and h is the heat transfer coefficient between the carter and the ambient air. It can be between 20 and 40 $K.W^{-1} m^{-2}$ for a motor with natural ventilation, and may exceed 80 $K.W^{-1} m^{-2}$ for the motor forced air.

To calculate the outer surface of SMPMM, we considered only the outer surface of the cylinder with radius R_5 and height l_m (Gasc, 2004; Chan., 2004).

$$S_{ext} = 2\pi R_5 l_m \quad (48)$$

The expressions of heat capacities of the PMSMIR are given by the following equations:

C_{coil} represents the heat capacity of coil (JK^{-1}).

$$C_{coil} = \rho_{co} V_{co} C_{th-co} \quad (49)$$

C_{inso} represents the heat capacity of insulator (JK^{-1}).

$$C_{inso} = \rho_{inso} V_{inso} C_{th-inso} \quad (50)$$

C_{sy} represents the heat capacity of stator yoke (JK^{-1}).

$$C_{sy} = \rho_{iron} V_{sy} C_{th-iron} \quad (51)$$

C_{ca} represents the capacity of carter (JK^{-1}).

$$C_{ca} = \rho_{alu} V_{ca} C_{th-alu} \quad (52)$$

Figure 6 shows the thermal model in transient behaviour of the PMSMER.

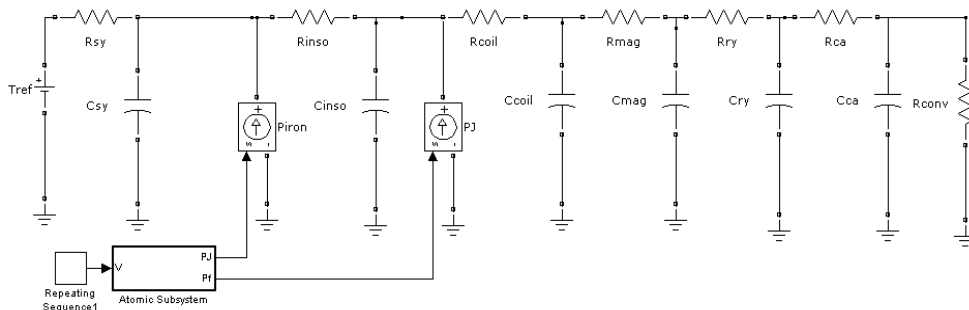


Fig. 6. Thermal model of the PMSMER in transient behaviour

The expressions of the PMSMER thermal resistances obtained from the resolution of the heat equation at the fields borders.

R_{sy} represents the stator yoke thermal resistance ($K.W^{-1}$).

$$R_{sy} = \frac{1}{4\pi l_m \lambda_{iron}} \left[1 - 2 \frac{R_8^2}{R_7^2 - R_8^2} \ln \frac{R_7}{R_8} \right] \quad (53)$$

R_{inso} represents the insulator thermal resistance ($K.W^{-1}$).

$$R_{inso} = \frac{1}{4\pi l_m \lambda_{inso}} \left[2 \frac{R_7^2}{R_6^2 - R_7^2} \ln \frac{R_6}{R_7} \right] \quad (54)$$

R_{coil} represents the coil thermal resistance ($K.W^{-1}$).

$$R_{coil} = \frac{1}{4\pi l \lambda_{co}} \left[1 - 2 \frac{R_6^2}{R_5^2 - R_6^2} \ln \frac{R_5}{R_6} \right] \quad (55)$$

R_{mag} represents the magnet thermal resistance ($K.W^{-1}$).

$$R_{mag} = \frac{\ln \frac{R_1}{R_2}}{2\pi \lambda_{mag} l_m} \quad (56)$$

R_{ry} represents the rotor yoke thermal resistance ($K.W^{-1}$).

$$R_{ry} = \frac{\ln \frac{R_2}{R_3}}{2\pi \lambda_{iron} l_m} \quad (57)$$

R_{ca} represents the thermal resistance of carter. ($K.W^{-1}$)

$$R_{ca} = \frac{\ln \frac{R_1}{R_2}}{2\pi \lambda_{ca} l_m} \quad (58)$$

To calculate the outer surface of SMPMM, we considered only the cylinder outer surface with radius R_1 and the height l_m .

$$S_{ext} = 2\pi R_1 l_m \quad (59)$$

The expressions of heat capacities of the PMSMER are given by the following equations: C_{mag} represents the heat capacity of magnet (JK^{-1}).

$$C_{mag} = \rho_{mag} V_{mag} C_{th-mag} \quad (60)$$

C_{ry} represents the heat capacity of rotor yoke (JK^{-1}).

$$C_{ry} = \rho_{iron} V_{ry} C_{th-iron} \quad (61)$$

C_{coil} represents the heat capacity of coil (JK^{-1}).

$$C_{coil} = \rho_{co} V_{co} C_{th-co} \quad (62)$$

C_{inso} represents the heat capacity of insulator (JK^{-1}).

$$C_{inso} = \rho_{inso} V_{inso} C_{th-inso} \quad (63)$$

C_{sy} represents the heat capacity of stator yoke (JK^{-1}).

$$C_{sy} = \rho_{iron} V_{sy} C_{th-iron} \quad (64)$$

The below table presents the different thermal conductivities of materials (Jérémi, R., 2003)

Material	Conductivities (Wm-1K-1)	Mass heat capacity (Jkg-1K-1)	Density (Kgm-3)
Copper (Coil)	$\lambda_{co}=5$	$C_{th-co}= 398$	$\rho_{co} = 8953$
Insulator	$\lambda_{inso} = 0.25$	$C_{th-inso} = 1250$	$\rho_{inso} = 1200$
(Iron)Stator Yoke	$\lambda_{iron} = 25$	$C_{th-iron} = 460$	$\rho_{iron} = 7650$
Magnet	$\lambda_{mag} = 6.5$	$C_{th-mag} = 420$	$\rho_{mag} = 7400$
aluminium (Carter)	$\lambda_{ca} = 180$	$C_{th-alu} = 883$	$\rho_{alu} = 2787$

Table 3. The thermal conductivities of materials

6. Results and simulations

Simulation results with Matlab software allowed us to obtain the curves of temperatures specific to different materials of the PMSMER and PMSMIR structures. The thermal results at steady and transient state is reached by figures 7, 8.

According to the results, we find that the steady state in the PMSMIR is reached after 4000s. However, the steady state in the PMSMER is achieved after 2000s.

By comparing the results in steady and transient state between the two configurations, we note that temperatures of different parts in PMSMIR are higher than temperatures in PMSMER (especially the coil temperature). That's why, we choose the PMSMER configuration as the best solution in electric traction field.

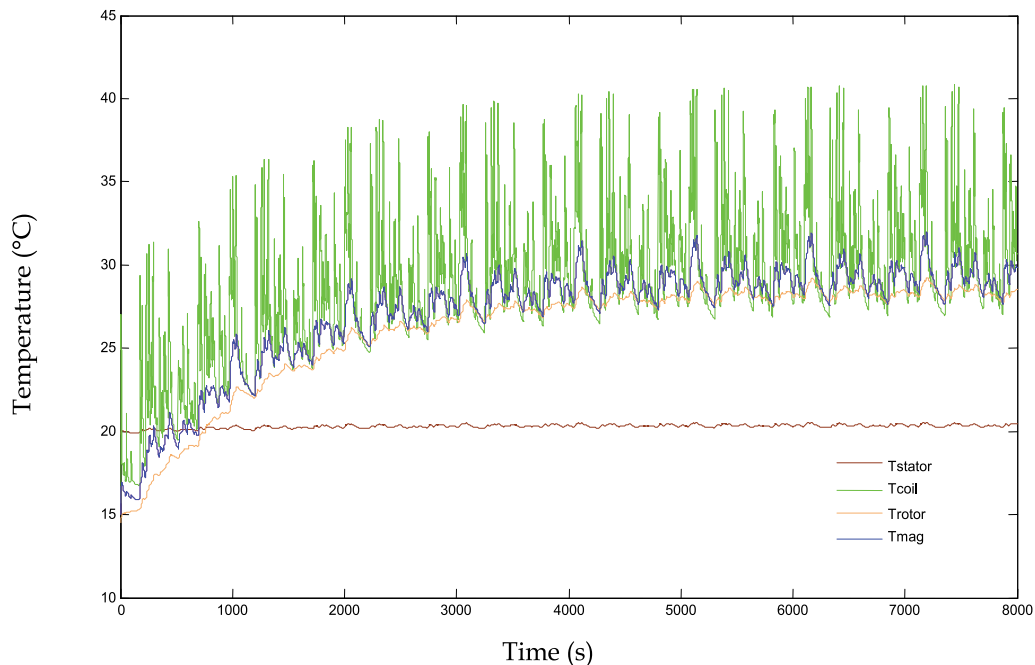


Fig. 7. Various temperatures in different parts of the PMSMER in transient state.

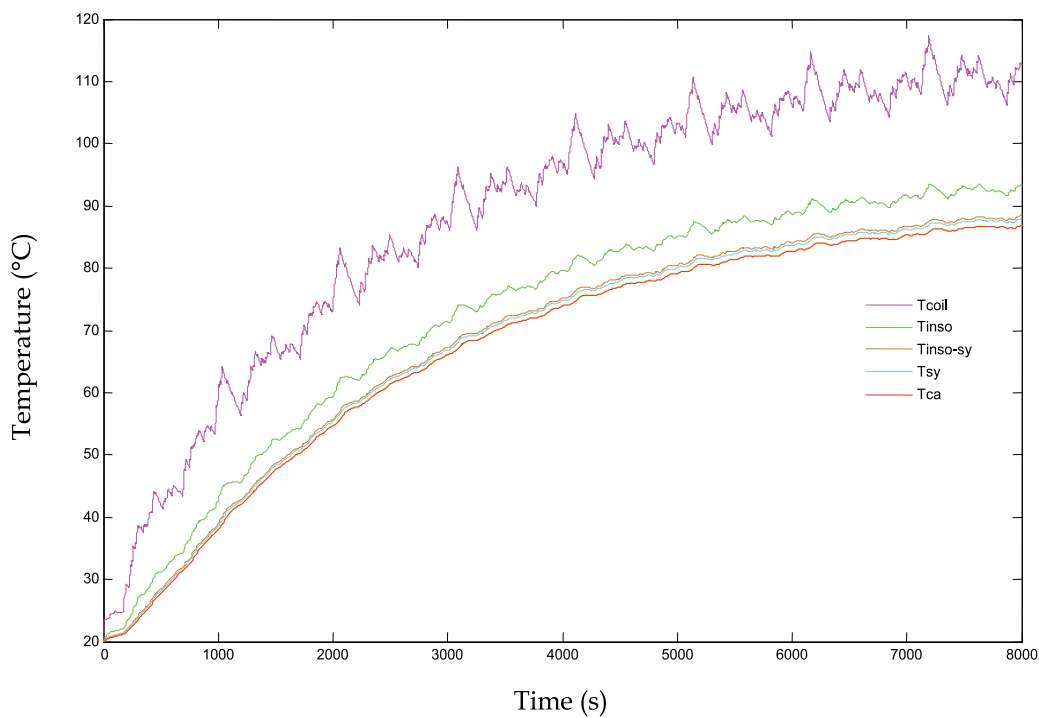


Fig. 8. Various temperatures in different parts of the PMSMIR in transient state.

Moreover, we always look to get a permissible values of coil temperature, based on the proper choice of motors geometric parameters in order to ensure a good compromise between geometric dimensioning and thermal modeling motor.

7. Conclusion

In this paper, a thermal model of two SMPMM with interior rotor and exterior rotor was realised, the intension to compare the evolution of the temperatures of different parts of the two motor configurations and especially the modeling of temperature at the coil is made.

8. References

- Chan, C. C. (2004). The Sate of the Art of Electric Vehicles, *Journal of Asian Electric Vehicles*, Vol. 2, No. 2, pp.579-600.
- Junak, J. ; Ombach, G. ; Staton, D. (2008). Permanent Magnet DC Motor Brush Transient Thermal Analysis, 978-1-4244-1736-0/08/\$25.00 ©2008 IEEE.
- Dorrell David, G. ; Staton Malcolm, A. ; McGilp, I. (2006). Thermal Approach to High Performance Specification, IEEE.
- Magnussen, F. ; Lendenmann, H. (2005). Parasitic Effects in PM Machines with Concentrated Windings, IAS 40th Annual Meeting Hong Kong , Volume 2, pp 1045- 1049.
- Ben Hadj, N. ; Tounsi, S. ; Neji, R. and Sellami, F. (2007). Real coded Genetic algorithm for permanent magnet motor mass minimization for electric vehicle application, 3rd International Symposium on Computational Intelligence and Intelligent Informatics, Agadir-Morocco, March 28-30, 2007, pp.153-158.
- Chin, Y.K.; Nordlund, E.; Staton, E.A. (2003). Thermal analysis - Lumped circuit model and finite element analysis. Sixth International Power Engineering Conference (IPEC), pp. 952- 957.
- Staton, D.A. (2001). Thermal analysis of electric motors and generators, Tutorial course at IEEE IAS Annual Meeting , Chicago, USA .
- Holman, J.P. (1992). Heat Transfer, Seventh Edition, McGraw-Hill Publication.
- Tounsi, S. (2006). Modélisation et optimisation de la motorisation et de l'autonomie d'un véhicule électrique. Thèse de Doctorat, ENI Sfax
- Jérémi, R. (2003). Conception de systèmes hétérogènes en Génie Électrique par optimisation évolutionnaire multicritère, thèse de doctorat, Institut National Polytechnique de Toulouse.
- Gasc, L. (2004). Conception d'un actionneur à aimants permanents à faibles ondulations de couple pour assistance de direction automobile Approches par la structure et par la commande, Thèse de doctorat, Institut national Polytechnique de Toulouse.

Minimization of the Copper Losses in Electrical Vehicle Using Doubly Fed Induction Motor Vector Controlled

Saïd Drid

*University of Batna, Electrical Engineering Department Research Laboratory LSPiE
Algeria*

1. Introduction

The electric vehicle (EV) was conceived in the middle of the previous century. EV's offer the most promising solutions to reduce vehicular emissions. EV's constitute the only commonly known group of automobiles that qualify as zero-emission vehicles. These vehicles use an electric motor for propulsion, batteries as electrical-energy storage devices and associated with power electronics, microelectronics, and microprocessor control of motor drives.

The doubly fed induction motor (DFIM) is a wound rotor asynchronous machine supplied by the stator and the rotor from two external source voltages. This machine is very attractive for the variable speed applications such as the electric vehicle and the electrical energy production. Consequently, it covers all power ranges. Obviously, the requested variable speed domain and the desired performances depend of the application kinds (Vicatos & Tegopoulos, 2003, Akagi & Sato, 1999, Debiprasad et al., 2001, Leonhard, 1997, Wang & Ding, 1993, Morel et al., 1998 and Hopfensperger et al., 1999).

The use of DFIM offers the opportunity to modulate power flow into and out of the rotor winding in order to have, at the same time, a variable speed in the characterized super-synchronous or sub-synchronous modes in motor or in generator regimes. Two modes can be associated to slip power recovery: sub-synchronous motoring and super-synchronous generating operations. In general, while the rotor is fed through a cycloconverter, the power range can attain the MW order which presents the size power often reserved to the synchronous machine (Vicatos & Tegopoulos, 2003, Akagi & Sato, 1999, Debiprasad et al., 2001, Leonhard, 1997, Wang & Ding, 1993, Morel et al., 1998, Hopfensperger et al., 1999a, 1999b, Metwally et al., 2002, Hirofumi & Hikaru, 2002 and Djurovic et al., 1995). The DFIM has some distinct advantages compared to the conventional squirrel-cage machine. The DFIM can be controlled from the stator or rotor by various possible combinations. The disadvantage of two used converters for stator and rotor supplying can be compensated by the best control performances of the powered systems (Debiprasad et al., 2001). Indeed, the input-commands are done by means of four precise degrees of control freedom relatively to the squirrel cage induction machine where its control appears quite simple. The flux orientation strategy can transform the non linear and coupled DFIM-mathematical model into a linear model leading to one attractive solution for generating or motoring operations (Sergeial, 2003).

It is known that the motor driven systems account for approximately 65% of the electricity consumed in the world. Implementing high efficiency motor driven systems, or improving existing ones, could save over 200 billion kWh of electricity per year. This issue has become very important especially following the economic crisis due to the oil prices raising, the new energy saving technologies are appearing and developing rapidly in this century (Leonhard, 1997, Longya & Wei, 1995, Wang & Cheng, 2004, Zang & Hasan, 1999, David, 1988 and Rodriguez et al., 2002). In this framework, the DFIM continues to find great interest since the birth of the idea of the double flux orientation (Drid et al., 2005a, 2005b). The philosophy of this idea is to get a simpler machine model expression (ideal machine) (Drid et al., 2005a). Consequently, in the same time, we can solve a non linear problem presented by the DFIM control and step up from many digital simulations toward the experimental test by the use of the system dSPACE-1103. This method gives entire satisfaction and consolidates our theory, especially using the Torque Optimization Factor TOF strategy (Drid et al., 2005b). Always the search for a solution has more optimal, us nap leans towards the minimization of the copper losses in the DFIM.

In this chapter we developed an optimization factor Torque Copper Losses Optimization TCLO. The chapter will be organized as follows. The DFIM mathematical model is presented in section 3. In section 4, the robust nonlinear feedback control is exposed. Section 5 concerns the two energy torque optimization strategies TOF and TCLO. In the section 6, simulation results are exposed and comparative illustration shows the performances in energy saving between TOF and TCLO.

2. The DFIM model

Its dynamic model expressed in the synchronous reference frame is given by Voltage equations:

$$\begin{cases} \bar{u}_s = R_s \bar{i}_s + \frac{d\bar{\phi}_s}{dt} + j\omega_s \bar{\phi}_s \\ \bar{u}_r = R_r \bar{i}_r + \frac{d\bar{\phi}_r}{dt} + j\omega_r \bar{\phi}_r \end{cases} \quad (1)$$

Flux equations:

$$\begin{cases} \bar{\phi}_s = L_s \bar{i}_s + M \bar{i}_r \\ \bar{\phi}_r = L_r \bar{i}_r + M \bar{i}_s \end{cases} \quad (2)$$

From (1) and (2), the state-all-flux model is written like:

$$\begin{cases} \bar{u}_s = \frac{1}{\sigma T_s} \bar{\phi}_s - \frac{M}{\sigma T_s L_r} \bar{\phi}_r + \frac{d\bar{\phi}_s}{dt} + j\omega_s \bar{\phi}_s \\ \bar{u}_r = -\frac{M}{\sigma T_r L_s} \bar{\phi}_s + \frac{1}{\sigma T_r} \bar{\phi}_r + \frac{d\bar{\phi}_r}{dt} + j\omega_r \bar{\phi}_r \end{cases} \quad (3)$$

The electromagnetic torque is done as

$$C_e = \frac{PM}{\sigma L_s L_r} \Im m \left[\bar{\phi}_s \phi_r^* \right] \quad (4)$$

The copper losses are giving as:

$$P_{cl} = R_s i_s^2 + R_r i_r^2 \quad (5)$$

The motion equation is:

$$C_e - d = J \frac{d\omega}{dt} \quad (6)$$

In DFIM operations, the stator and rotor mmf's (magneto motive forces) rotations are directly imposed by the two external voltage source frequencies. Hence, the rotor speed becomes depending toward the linear combination of these frequencies, and it will be constant if they are too constants for any load torque, given of course in the machine stability domain. In DFIM modes, the synchronization between both mmf's is mainly required in order to guarantee machine stability. This is the similar situation of the synchronous machine stability problem where without the recourse to the strict control of the DFIM mmf's relative position, the machine instability risk or brake down mode become imminent.

3. Nonlinear vector control strategy

3.1 Double flux orientation

It consists in orienting, at the same time, stator flux and rotor flux. Thus, it results the constraints given below by (7). Rotor flux is oriented on the d-axis, and the stator flux is oriented on the q-axis. Conventionally, the d-axis remains reserved to magnetizing axis and q-axis to torque axis, so we can write (Drid et al., 2005a, 2005b)

$$\begin{cases} \phi_{sq} = \phi_s \\ \phi_{rd} = \phi_r \\ \phi_{sd} = \phi_{rq} = 0 \end{cases} \quad (7)$$

Using (7), the developed torque given by (4) can be rewritten as follows:

$$C_e = k_c \phi_s \phi_r. \quad (8)$$

where, $k_c = \frac{PM}{\sigma L_s L_r}$

ϕ_s Appears as the input command of the active power or simply of the developed torque, while ϕ_r appears as the input command of the reactive power or simply the main magnetizing machine system acting.

3.2 Vector control by Lyapunov feedback linearization

Separating the real and the imaginary part of (3), we can write:

$$\begin{cases} \frac{d\phi_{sd}}{dt} = f_1 + u_{sd} \\ \frac{d\phi_{sq}}{dt} = f_2 + u_{sq} \\ \frac{d\phi_{rd}}{dt} = f_3 + u_{rd} \\ \frac{d\phi_{rq}}{dt} = f_4 + u_{rq} \end{cases} \quad (9)$$

Where f_1, f_2, f_3 and f_4 are done as follows :

$$\begin{cases} -f_1 = \gamma_1 \phi_{sd} - \gamma_2 \phi_{rd} - \omega_s \phi_{sq} \\ -f_2 = \gamma_1 \phi_{sq} - \gamma_2 \phi_{rq} + \omega_s \phi_{sd} \\ -f_3 = -\gamma_3 \phi_{sd} + \gamma_4 \phi_{rd} - \omega_r \phi_{rq} \\ -f_4 = -\gamma_3 \phi_{sq} + \gamma_4 \phi_{rq} + \omega_r \phi_{rd} \end{cases} \quad (10)$$

With:

$$\gamma_1 = \frac{1}{\sigma T_s} ; \gamma_2 = \frac{M}{\sigma T_s L_r} ; \gamma_3 = \frac{M}{\sigma T_r L_s} ; \gamma_4 = \frac{1}{\sigma T_r}$$

Tacking into account of the constraints given by (7), one can formulate the Lyapunov function as follows

$$V = \frac{1}{2} \phi_{sd}^2 + \frac{1}{2} \phi_{rq}^2 + \frac{1}{2} (\phi_{sq} - \phi_s)^2 + \frac{1}{2} (\phi_{rd} - \phi_r)^2 > 0 \quad (11)$$

From (11), the first and second quadrate terms concern the fluxes orientation process defined in (7) with the third and fourth terms characterizing the fluxes feedback control. Where its derivative function becomes

$$\begin{aligned} \dot{V} = \phi_{sd} \dot{\phi}_{sd} + \phi_{rq} \dot{\phi}_{rq} + (\phi_{sq} - \phi_s) (\dot{\phi}_{sq} - \dot{\phi}_s) + \\ (\phi_{rd} - \phi_r) (\dot{\phi}_{rd} - \dot{\phi}_r) \end{aligned} \quad (12)$$

Substituting (9) in (12), it results

$$\begin{aligned} \dot{V} = \phi_{sd} (f_1 + u_{sd}) + \phi_{rq} (f_4 + u_{rq}) + \\ (\phi_{sq} - \phi_s) (f_2 + u_{sq} - \dot{\phi}_s) + \\ (\phi_{rd} - \phi_r) (f_3 + u_{rd} - \dot{\phi}_r) \end{aligned} \quad (13)$$

Let us define the following law control as (Khalil, 1996):

$$\begin{cases} u_{sd} = -f_1 - K_1 \phi_{sd} \\ u_{rq} = -f_4 - K_2 \phi_{rq} \\ u_{sq} = -f_2 + \dot{\phi}_s - K_3 (\phi_{sq} - \phi_s) \\ u_{rd} = -f_3 + \dot{\phi}_r - K_4 (\phi_{rd} - \phi_r) \end{cases} \quad (14)$$

Hence (14) replaced in (13) gives:

$$\begin{aligned} \dot{V} = & -K_1 \phi_{sd}^2 - K_2 \phi_{rq}^2 - K_3 (\phi_{sq} - \phi_s)^2 \\ & - K_4 (\phi_{rd} - \phi_r)^2 < 0 \end{aligned} \quad (15)$$

The function (15) is negative one. Furthermore, (14) introduced into (9) leads to a stable convergence process if the gains K_i ($i=1, 2, 3, 4$) are evidently all positive, otherwise:

$$\begin{cases} \lim_{t \rightarrow +\infty} \phi_{sd} = 0 \\ \lim_{t \rightarrow +\infty} \phi_{rq} = 0 \\ \lim_{t \rightarrow +\infty} (\phi_{rd} - \phi_r^*) = 0 \\ \lim_{t \rightarrow +\infty} (\phi_{sq} - \phi_s^*) = 0 \end{cases} \quad (16)$$

In (16), the first and second equations concern the double flux orientation constraints applied for DFIM-model which are define above by (7), while the third and fourth equations define the errors after the feedback fluxes control. This latter offers the possibility to control the main machine magnetizing on the d-axis by ϕ_{rd} and the developed torque on the q-axis by ϕ_{sq} .

3.3 Robust feedback Lyapunov linearization control

In practice, the nonlinear functions f_i involved in the state space model (9) are strongly affected by the conventional effect of induction motor (IM) such as temperature, saturation and skin effect in addition of the different nonlinearities related to harmonic pollution due to the supplying converters and to the noise measurements. Since the control law developed in the precedent section is based on the exact knowledge of these functions f_i , one can expect that in real situation the control law (14) can fail to ensure flux orientation. In this section, our objective is to determine a new vector control law making it possible to maintain double flux orientation in presence of physical parameter variations and measurement noises. Globally we can write:

$$f_i = \hat{f}_i + \Delta f_i \quad (17)$$

On, \hat{f}_i : True nonlinear feedback function (NLFF)

f_i : Effective NLFF

Δf_i : NLFF variation around f_i .

Where: $i = 1, 2, 3$ and 4 .

The Δf_i can be generated from the whole parameters and variables variations as indicated above. We assume that all the Δf_i are bounded as follows: $|\Delta f_i| < \beta_i$; where are known bounds. The knowledge of β_i is not difficult since, one can use sufficiently large number to satisfy the constraint $|\Delta f_i| < \beta_i$.

The Δf_i can be generated from the whole parameters and variables variations as indicated above.

Replacing (17) in (9), we obtain

$$\begin{cases} \frac{d\phi_{sd}}{dt} = \hat{f}_1 + \Delta f_1 + u_{sd} \\ \frac{d\phi_{sq}}{dt} = \hat{f}_2 + \Delta f_2 + u_{sq} \\ \frac{d\phi_{rd}}{dt} = \hat{f}_3 + \Delta f_3 + u_{rd} \\ \frac{d\phi_{rq}}{dt} = \hat{f}_4 + \Delta f_4 + u_{rq} \end{cases} \quad (18)$$

The following result can be stated.

Proposition: Consider the realistic all fluxes state model (18). Then, the double fluxes orientation constraints (7) are fulfilled provided that the following control laws are used

$$\begin{cases} u_{sd} = -\hat{f}_1 - K_1 \phi_{sd} - K_{11} \operatorname{sgn}(\phi_{sd}) \\ u_{rq} = -\hat{f}_4 - K_2 \phi_{rq} - K_{22} \operatorname{sgn}(\phi_{rq}) \\ u_{sq} = -\hat{f}_2 + \dot{\phi}_s - K_3 (\phi_{sq} - \phi_s) - K_{33} \operatorname{sgn}(\phi_{sq} - \phi_s) \\ u_{rd} = -\hat{f}_3 + \dot{\phi}_r - K_4 (\phi_{rd} - \phi_r) - K_{44} \operatorname{sgn}(\phi_{rd} - \phi_r) \end{cases} \quad (19)$$

where $K_{ii} \geq \beta_i$ and $K_{ii} > 0$ for $i=1; 4$.

Proof. Let the Lyapunov function related to the fluxes dynamics (18) defined by

$$V_1 = \frac{1}{2} \phi_{sd}^2 + \frac{1}{2} \phi_{rq}^2 + \frac{1}{2} (\phi_{sq} - \phi_s)^2 + \frac{1}{2} (\phi_{rd} - \phi_r)^2 > 0 \quad (20)$$

One has

$$\begin{aligned} \dot{V}_1 = & \phi_{sd} (\Delta f_1 - K_{11} \operatorname{sgn}(\phi_{sd})) + \phi_{rq} (\Delta f_2 - K_{22} \operatorname{sgn}(\phi_{rq})) \\ & + (\phi_{sq} - \phi_s) (\Delta f_3 - K_{33} \operatorname{sgn}(\phi_{sq})) + (\phi_{rd} - \phi_r) (\Delta f_4 - K_{44} \operatorname{sgn}(\phi_{rd})) + \dot{V} < 0 \end{aligned} \quad (21)$$

where \dot{V} is given by (15). Hence the Δf_i variations can be absorbed if we take:

$$\begin{aligned}
 K_{11} > |\Delta f_1| \quad K_{11} > |\Delta f_1| \\
 K_{22} > |\Delta f_2| \quad K_{22} > |\Delta f_2| \\
 K_{33} > |\Delta f_3| \quad K_{33} > |\Delta f_3| \\
 K_{44} > |\Delta f_4| \quad K_{44} > |\Delta f_4|
 \end{aligned}
 \tag{22}$$

The latter inequalities are satisfied since $K_i > 0$ and $|\Delta f_i| < \beta_i < K_{ii}$
Finally, we can write:

$$\dot{V}_1 < \dot{V} < 0
 \tag{23}$$

Hence, using the Lyapunov theorem (Khalil, 1996), one concludes that

$$\left\{ \begin{array}{l}
 \lim_{t \rightarrow +\infty} \phi_{sd} = 0 \\
 \lim_{t \rightarrow +\infty} \phi_{rq} = 0 \\
 \lim_{t \rightarrow +\infty} (\phi_{rd} - \phi_r^*) = 0 \\
 \lim_{t \rightarrow +\infty} (\phi_{sq} - \phi_s^*) = 0
 \end{array} \right.
 \tag{24}$$

The design of these robust controllers, resulting from (19), is given in the following figure 2
The indices w can be : sd, sq, rd and rq , ($i = 1, 2, 3$ and 4)

4. Energy optimization strategy

In this section we will explain why and what is the optimization strategy used in this work.
Fig. 1 illustrates the problem which occurs in the proposed DFIM vector control system when the machine magnetizing excitation is maintained at a constant level.

4.1 Why the energy optimization strategy?

Considering an iso-torque-curve (hyperbole form), drawn from (8) for a constant torque in the (ϕ_s, ϕ_r) plan and lower load machine (Fig.1), on which we define two points **A** and **B**, respectively, corresponding to the two machine magnetizing extreme levels. These points concern respectively an excited machine ($\phi_r = 1 \text{ Wb} = \text{Const}$) and an under excited machine ($\phi_r = 0.1 \text{ Wb} = \text{Const}$). Both points define the steady state operation machine or equilibrium points. The machine rotates to satisfy the required reference speed acted by a given slope speed acceleration $\alpha = \frac{d\Omega}{dt} = \text{Const}$. So, the machine in both magnetizing cases must develop a transient torque such as:

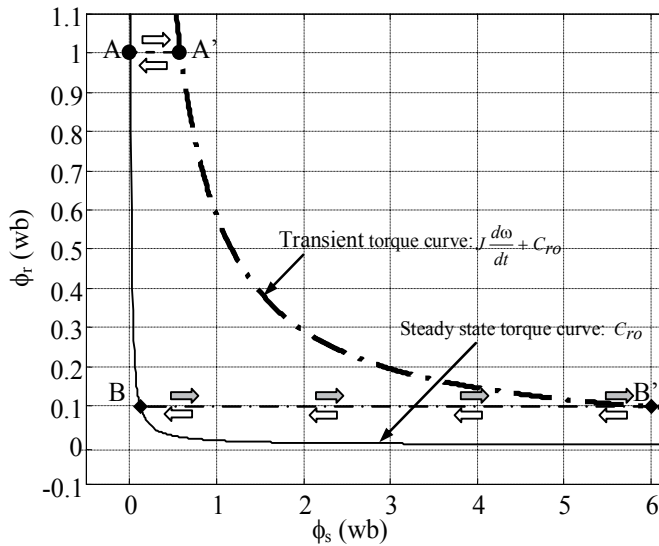


Fig. 1. Illustration of the posed problem in the DFIM control system with constant excitation.

$$C_{eT} = C_{r0} + J \frac{d\Omega}{dt} = C_{r0} + J\alpha \tag{25}$$

On the same graph, we define a second iso-torque-curve $C_{eT} = \text{Const}$ in the (ϕ_s, ϕ_r) plan. This curve is a transient one on which we place two transient points A' and B' . Here we distinguish the first transitions $A-A'$ and $B-B'$ due to the acceleration set, respectively for each magnetizing case. Both transitions are rapidly occurring in respect to the adopted control.

Once the machine speed reaches its reference, the inertial torque is cancelled ($\alpha = 0$), then the developed torque must return immediately to the initial load torque C_{r0} , characterized by the second transitions $A'-A$ and $B'-B$ towards the preceding equilibrium points A and B . One can notice that during the transition $B-B'$, corresponding to the under excited machine, the stator flux can attain very high values greater than the tolerable limit $(\phi_{s \max})$, and can tend to infinite values if the load torque C_{r0} tends to zero. So the armature currents expressed by the following formula deduced from (2) and (7) are strongly increased and can certainly destruct the machine and their supplied converters.

$$\begin{aligned} \bar{i}_s &= \lambda \cdot \phi_r + j\gamma \cdot \phi_s \\ \bar{i}_r &= \chi \cdot \phi_r + j\lambda \cdot \phi_s \end{aligned} \tag{26}$$

Where, $\lambda = -\frac{M}{\sigma \cdot L_S \cdot L_R}$; $\gamma = \frac{1}{\sigma \cdot L_S}$; $\chi = \frac{1}{\sigma \cdot L_R}$

In the other hand, for the case A (excited machine), if the $A-A'$ transition remains tolerable, the armature currents can present prohibitory magnitude in the steady state operation due to the orthogonal contribution of stator and rotor fluxes at the moment that the machine is sufficiently excited. The steady state armature currents can be calculated by (26), where we can note the amplification effect of the coefficients λ , γ and χ .

4.2 Torque optimization factor (TOF) design

In the previous sub-section, the problem is in the transient torque, especially when the machine is low loaded. So it becomes very important to minimize the torque transition such as (Drid, 2005b):

$$\frac{dC_e}{dt} \rightarrow 0 \quad (27)$$

where,

$$dC_e = \frac{\partial C_e}{\partial \phi_s} d\phi_s + \frac{\partial C_e}{\partial \phi_r} d\phi_r \quad (28)$$

This condition should be realized respecting the stator flux constraint given by

$$\phi_s \leq \phi_{s \max} \quad (29)$$

In this way the rotor and stator fluxes, though orthogonal, their modulus will be related by the so-called TOF strategy which will be designed from the resolution of the differential equations (27-28) with constraint (29) as follows:

$$\begin{cases} \dot{\phi}_s \phi_r + \dot{\phi}_r \phi_s = 0 \\ \phi_s \leq \phi_{s \max} \end{cases} \quad (30)$$

from (29) we can write

$$-\dot{\phi}_s \phi_r = \dot{\phi}_r \phi_s \leq \dot{\phi}_r \phi_{s \max} \quad (31)$$

thus,

$$-\frac{\dot{\phi}_s}{\phi_{s \max}} \leq \frac{\dot{\phi}_r}{\phi_r} \quad (32)$$

the resolution of (32) leads to

$$-\frac{\phi_s}{\phi_{s \max}} + C \leq \ln \phi_r \quad (33)$$

where C is an arbitrary integration constant, therefore

$$\phi_r \geq e^{\left(\frac{\phi_s}{\phi_{s \max}} - C\right)} \quad (34)$$

Since, the main torque input-command in motoring DFIM operation is related to the stator flux, it becomes dependent on the speed rotor sign and thus we can write

$$\phi_{sq} = \phi_s \operatorname{sgn}(\Omega) = \begin{cases} +\phi_s & \text{if } \Omega > 0 \\ -\phi_s & \text{if } \Omega < 0 \end{cases} \quad (35)$$

with (35), (34), the rotor flux may be rewritten as follows

$$\phi_r = e^{-\left(\frac{|\phi_{sq}|}{\phi_{s\max}} - C\right)} \tag{36}$$

The resolution of (32) gives place to the arbitrary integration constant C from which the TOF-relationship (36) can be easily tuned. This one can be adjusted by a judicious choice of the integration constant, while figure 2 presents TOF effect on armature DFIM currents with C-tuning. Note that this method offers the possibility to reduce substantially the magnitude of the armature currents into the machine and we can notice an increase in energy saving. Hence using TOF strategy, we can avoid the saturation effect and reduce the magnitude of machine currents from which the DFIM efficiency could be clearly enhanced.

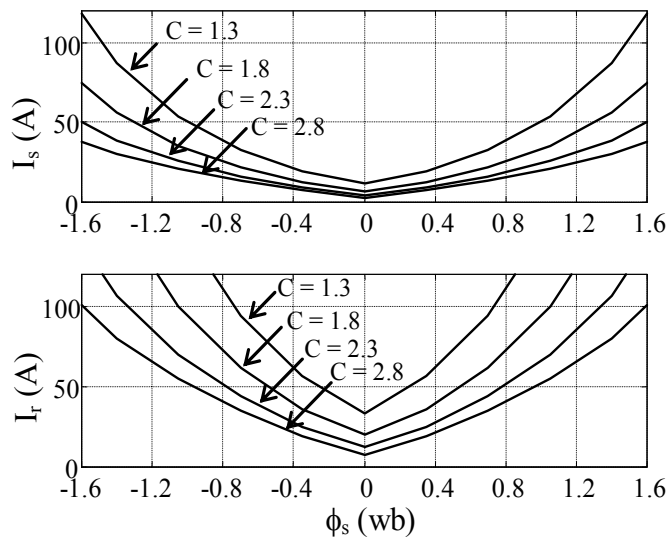


Fig. 2. TOF effect on armature DFIM currents

4.3 Torque-copper losses optimization (TCLO) design

In many applications, it is required to optimize a given parameter and the derivative plays a key role in the solution of such problems. Suppose the quantity to be minimized is given by the function $f(x)$, and x is our control parameter. We want to know how to choose x to make $f(x)$ as small as possible. Let’s pick some x_0 as the starting point in our search for the best x . The goal is to find the relation between fluxes which can optimize the compromise between torque and copper losses in steady state as well as in transient state, (i.e. for all $\{C_e\}$ find (ϕ_s, ϕ_r) let $\min\{P_{cl}\}$) (Drid, 2008). From (5), (8) and (26), the torque and copper losses can be to written as:

$$\begin{cases} C_e = k_c \cdot \phi_r \cdot \phi_s \\ P_{cl} = a_1 \phi_r^2 + a_2 \phi_s^2 \end{cases} \tag{37}$$

$$a_1 = \left(\frac{R_r}{(\sigma \cdot L_r)^2} + \frac{R_s M^2}{(\sigma \cdot L_r \cdot L_s)^2} \right)$$

with :

$$a_2 = \left(\frac{R_r M^2}{(\sigma \cdot L_r \cdot L_s)^2} + \frac{R_s}{(\sigma \cdot L_s)^2} \right)$$

The figure 3 represents the layout of (37) for a constant level of torque and copper losses in the (ϕ_s, ϕ_r) plan. These curves present respectively a hyperbole for the iso-torque and ellipse for iso-copper-losses. From (37) we can write:

$$a_1 k_c^2 \phi_r^4 - k_c^2 \phi_r^2 \Delta P_{cl} + a_2 C_{el}^2 = 0 \quad (38)$$

To obtain a real and thus optimal solution, we must have:

$$\Delta = k_c^4 \Delta P_{cl}^4 - 4a_1 k_c^2 a_2 C_{el}^2 = 0 \quad (39)$$

The equation (39) represents the energy balance in the DFIM for one working DFIM point as shown in fig.3. Then, one can write:

$$\Delta P_{cl} = \sqrt{\frac{4a_1 a_2 C_{el}^2}{k_c^2}} \quad (40)$$

This equation shows the optimal relation between the torque and the copper losses.

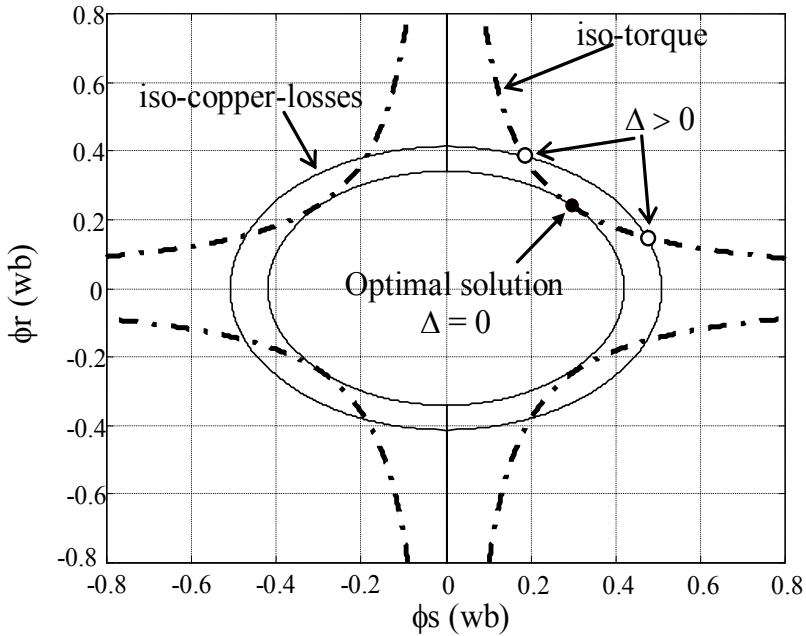


Fig. 3. The iso-torque curves and the iso-losses curves in the plan (ϕ_s, ϕ_r)

4.4 Finding minimum Copper-losses values

The Rolle's Theorem is the key result behind applications of the derivative to optimization problems. The second derivative test is used to finding minimum point.

We can rewrite (37) as:

$$\begin{cases} \phi_s = \frac{C_e}{k_c \cdot \phi_r} \\ P_{cl} = a_1 \phi_r^2 + a_2 \frac{C_e^2}{k_c^2 \cdot \phi_r^2} = \frac{a_1 k_c^2 \phi_r^4 + a_2 C_e^2}{k_c^2 \cdot \phi_r^2} \end{cases} \quad (41)$$

The computations of the first and second derivatives show that the critical point is given by:

$$\phi_{rc} = \pm \left(\frac{C_e^2 a_2}{a_1 k_c^2} \right)^{\frac{1}{4}} \quad (42)$$

For which:

$$\frac{d^2 P_{cl}(\phi_{rc})}{d\phi_r^2} = \frac{2a_1 k_c^2 \phi_{rc}^4 + 6a_2 C_e^2}{k_c^2 \cdot \phi_{rc}^4} = 8a_1 > 0 \quad (43)$$

We can see that the second derivative is positive and conclude that the critical point is a relative minimum.

5. Simulation

Figure 4 illustrates a general block diagram of the suggested DFIM control scheme. Here, we can note the placement of optimization block, the first estimator-block which evaluates torque and the second estimator-block which evaluates firstly the modulus and position fluxes, respectively ϕ_s , ϕ_r , ρ_s and ρ_r , from the measured currents using (2) and secondly the feedback functions f_1 , f_2 , f_3 , f_4 given by (10). Optimization process allows adapting the main flux magnetizing defined by rotor flux to the applied load torque characterized by the stator flux. With the analogical switch we can select the type of the reference rotor flux. The switch position 1, 2 gives respectively TCLO and TOF for optimized operation and the position 3 for a magnetizing constant level.

The Figure 5 shows the speed response versus time according to its desired profile drawn on the same figure. Figure 6 illustrate the fluxes trajectory of the closed-loop system. It moves along manifold toward the equilibrium point. We can notice the stability of the system. Figures 7 and 8 show respectively the stator and the rotor input control voltages versus time during the test. Figure 9 present the copper losses according to the stator flux variations in steady state operation and we can see the contribution of the TCLO compared to the TOF. Finally figure 10 present the dissipated energy versus time from which we can observe clearly the influence of the three switch positions on the copper losses in transient state. We can conclude that the TCLO is the best optimization.

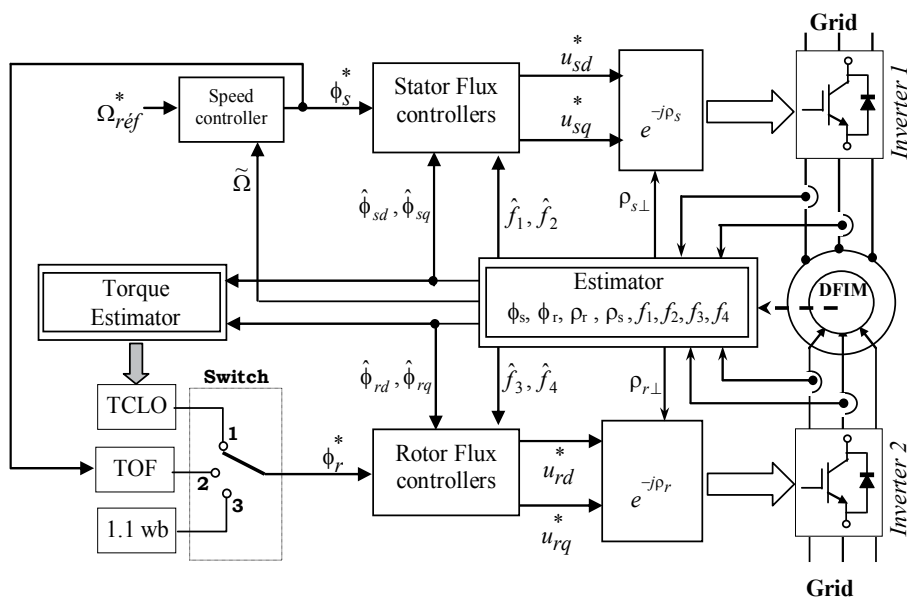


Fig. 4. General block diagram of control scheme

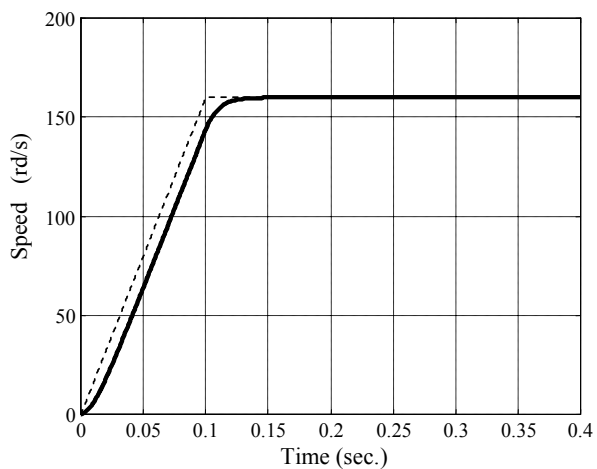


Fig. 5. Speed response

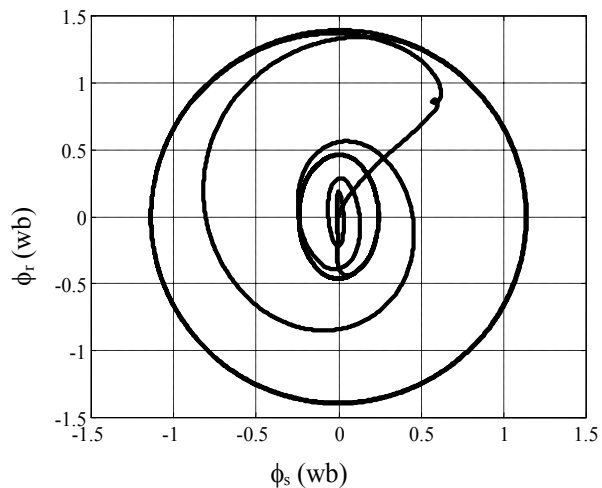


Fig. 6. Fluxes trajectories of the closed-loop system

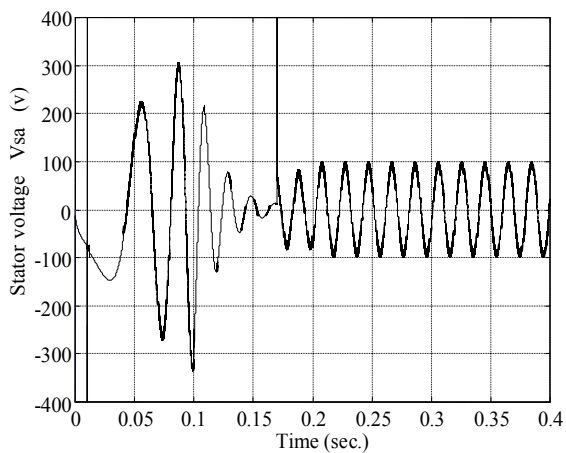


Fig. 7. The input control stator voltage response in the stator reference frames with TCLO

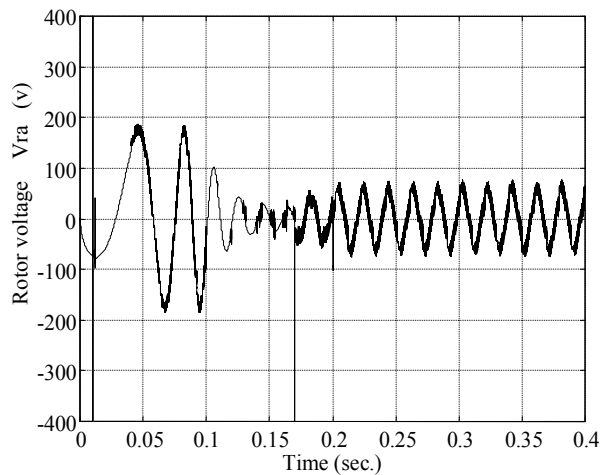


Fig. 8. The input control rotor voltage response in the stator reference frames with TCLO

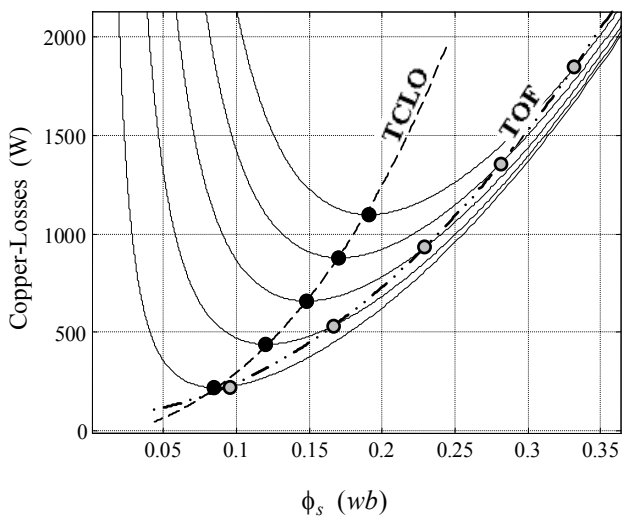


Fig. 9. Minimized copper losses in steady state operation with TOF and TCLO

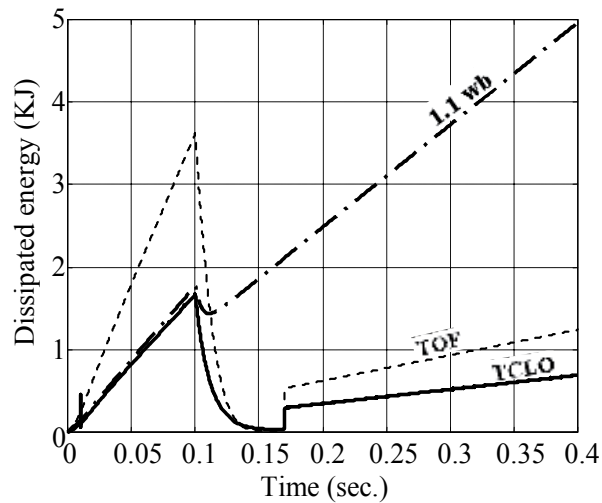


Fig. 10. Total copper losses versus time during test for the three switch positions (Energy saving illustration)

6. Conclusion

In this chapter was presented a vector control intended for doubly fed induction motor (DFIM) mode. The use of the state-all-flux induction machine model with a flux orientation constraint gives place to a simpler control model. The stability of the nonlinear feedback control is proven using the Lyapunov function.

The simulation results of the suggested DFIM system control based on double flux orientation which is achieved by the proposed DFIM control demonstrates clearly the suitable obtained performances required by the references profiles defined above. The speed tracks its desired reference without any effect of the load torque. Therefore the high control performances can be well affirmed. To optimize the machine operation we chose to minimize the copper losses. The proposed TCLO factor performs better than the already designed TOF. Indeed, the energy saving process can be well achieved if the magnetizing flux decreases in the same way as the load torque. It results in an interesting balance between the core losses and the copper losses into the machine, so the machine efficiency may be largely improved. The simulation results confirm largely the effectiveness of the proposed DFIM control system.

7. Appendix

The machine parameters are:

$R_s = 1.2 \Omega$; $L_s = 0.158 \text{ H}$; $L_r = 0.156 \text{ H}$; $R_r = 1.8 \Omega$; $M = 0.15 \text{ H}$; $P = 2$; $J = 0.07 \text{ Kg.m}^2$; $P_n = 4 \text{ Kw}$; $220/380\text{V}$; 50Hz ; 1440tr/min ; $15/8.6 \text{ A}$; $\cos\phi = 0.85$.

8. Nomenclature

s, r	Rotor and stator indices.
d, q	Direct and quadrature indices for orthogonal components
\bar{x}	Variable complex such as: $\bar{x} = \Re[\bar{x}] + j.\Im[\bar{x}]$.

\bar{x}	It can be a voltage as \bar{u} , a current as \bar{i} or a flux as $\bar{\phi}$
\bar{x}^*	Complex conjugate
R_S, R_R	Stator and rotor resistances
L_S, L_R	Stator and rotor inductances
T_S, T_R	Stator and rotor time-constants ($T_{s,r} = L_{s,r} / R_{s,r}$)
σ	Leakage flux total coefficient ($\sigma = 1 - M^2 / L_r L_s$)
M	Mutual inductance
θ	Absolute rotor position
p	Number of pairs poles
δ	Torque angle
ρ_s, ρ_r	Stator and rotor flux absolute positions
ω	Mechanical rotor frequency (rd/s)
Ω	Rotor speed (rd/s)
ω_s	Stator current frequency (rd/s)
ω_r	Induced rotor current frequency (rd/s)
J	Inertia
d	Unknown load torque
C_e	Electromagnetic torque
\sim	Symbol indicating measured value
\wedge	Symbol indicating the estimated value
$*$	Symbol indicating the command value
DFIM	Doubly Fed Induction Machine
TOF	Torque Optimization Factor
TCLO	Torque Copper Losses Optimization

9. References

- Vicatos, M.S. & Tegopoulos, J. A. (2003). A Doubly-Fed Induction Machine Differential Drive Model for Automobiles, *IEEE Transactions on Energy Conversion*, Vol.18, No.2, (June 2003), pp. 225-230, ISSN 0885-8969
- Akagi, H. & Sato, H. (1999). Control and Performance of a Flywheel Energy Storage System Based on a Doubly-Fed Induction Generator-Motor, *Proceedings of the 30th IEEE Power Electronics Specialists Conference*, pp. 32-39, vol1, ISBN 0275-9306, Charleston, USA, 27 June-1 July, 1999
- Debiprasad, P. et al (2001). A Novel Control Strategy for the Rotor Side Control of a Doubly-Fed Induction Machine. *IEEE Industry Applications Conference and Thirty-Sixth IAS Annual Meeting*, pp. 1695-1702, ISBN: 0-7803-7114-3, Chicago, USA, 30 September-04 October 2001
- Leonhard, W. (1997). Control Electrical Drives, Springer verlag, ISBN 3540418202, Berlin Heidelberg, Germany
- Wang, S. & Ding, Y. (1993). Stability Analysis of Field Oriented doubly Fed induction Machine drive Based on Computed Simulation, *Electrical Machines and Power Systems*, Vol. 21, No. 1, (1993), pp. 11-24, ISSN 1532-5008
- Morel, L. et al. (1998). Double-fed induction machine: converter optimisation and field oriented control without position sensor, *IEE proceedings Electric power applications*, Vol. 145. No. 4, (July 1998), pp. 360-368, ISSN 1350-2352

- Hopfensperger, B. et al., (1999) Stator flux oriented control of a cascaded doubly fed induction machine, *IEE proceedings Electric power applications*, Vol. 146. No. 6, (November 1999), pp. 597-605, ISSN 1350-2352
- Hopfensperger, B. et al., (1999) "Stator flux oriented control of a cascaded doubly fed induction machine with and without position encoder, *IEE proceedings Electric power applications*, Vol. 147. No. 4, (July 1999), pp. 241-250, ISSN 1350-2352
- Metwally, H.M.B. et al. (2002). Optimum performance characteristics of doubly fed induction motors using field oriented control, *Energy conversion and Management*, Vol. 43, No. 1, (2002), pp. 3-13, ISSN 0196-8904
- Hirofumi, A. & Hikaru, S. (2002). Control and Performance of a Doubly fed induction Machine Intended for a Flywheel Energy Storage System, *IEEE Transactions on Power Electronics*, Vol. 17, No. 1, (January 2002), pp. 109-116, ISSN 0885-8993
- Djurovic, M. et al. (1995). Double Fed Induction Generator with Two Pair of Poles, *IEE Conferences of Electrical Machines and Drives*, pp. 449-452, ISBN 0-85296-648-2, Durham, UK, 11-13 September 1995
- Leonhard, W. (1988). Adjustable-Speed AC Drives, Invited Paper, *Proceedings of the IEEE*, vol. 76, No. 4, (April 1988), pp.455-471. ISSN 0018-9219
- Longya, X. & Wei C. (1995). Torque and Reactive Power control of a Doubly Fed Induction Machine by Position Position Sensorless Scheme. *IEEE Transactions on Industry Applications*, Vol. 31, No. 3, (May/June 1995), pp 636-642 ISSN 0093-9994
- Sergei, P., Andrea, T. & Tonielli, A. (2003). Indirect Stator Flux-Oriented Output Feedback Control of a Doubly Fed Induction Machine, *IEEE Trans. On control Systems Technology*, Vol. 11, No. 6, (Nov. 2003), pp. 875-888, ISSN 1063-6536
- Wang, D.H. & Cheng, K.W.E. (2004). General discussion on energy saving Power Electronics Systems and Applications. *Proceedings of the First International Conference on Power Electronics Systems and Applications*, pp298-303, ISBN 962-367-434-1, USA, 9-11 Nov. 2004
- Zang, L. & Hasan K.H, (1999). Neural Network Aided Energy Efficiency control for a Field Orientation Induction Machine Drive. *Proceeding of Ninth International conference on Electrical Machine and Drives*, pp. 356-360, ISSN 0537-9989, Canterbury, UK, 1-3 September 1999
- David, E. (1988). A Suggested Energy-Savings Evaluation Method for AC Adjustable-Speed Drive Applications," *IEEE Trans. on Industry Applications*, Vol. 24, No. 6, (Nov/Dec. 1988), pp1107-1117, ISSN 0093-9994
- Rodriguez, J. et al. (2002). Optimal Vector Control of Pumping and Ventilation Induction Motor Drives. *IEEE Trans. on Electronics Industry*, vol. 49, No. 4, (August 2002), pp.889-895, ISSN 0278-0046
- Drid, S., Nait_Said, M.S. & Tadjine, M. (2005). Double flux oriented control for the doubly fed induction motor. *Electric Power Components & Systems Journal*, Vol. 33, No.10, (October 2005), pp. 1081-1095, ISSN 1532-5008
- Drid, S., Tadjine, M. & Nait_Said, M.S. (2005). Nonlinear Feedback Control and Torque Optimization of a Doubly Fed Induction Motor. *JEEEC Journal of Electrical Engineering Elektrotechnický časopis*, vol. 56, No. 3-4, (2005), pp. 57-63, ISSN 1335-3632
- Drid, S., Nait_Said, M.S., Tadjine M. & Makouf A.(2008), Nonlinear Control of the Doubly Fed Induction Motor with Copper Losses Minimization for Electrical Vehicle, *CISA08, 1st Mediterranean Conference on Intelligent Systems and Automation, AIP Conf. Proc.*, Vol. 1019, pp.339-345, Annaba, Algeria, June 30-July 02, 2008
- Khalil, H., (1996), *Nonlinear systems*. Prentice Hall, ISBN 0-13-067389-7, USA

Predictive Intelligent Battery Management System to Enhance the Performance of Electric Vehicle

Mohamad Abdul-Hak, Nizar Al-Holou and Utayba Mohammad
Electrical & Computer Engineering Department, University Of Detroit Mercy, Detroit, USA

1. Introduction

The Electric Vehicle (EV) is emerging as state-of-the-art technology vehicle addressing the continually pressing energy and environment concerns. The benefits of EV emerge from these vehicles' capability of sustaining their energy demands through electric grid rather than fossil fuel consumption. Well- to-Wheel studies have shown that electric drive (E-drive) offers the highest fuel efficiency and consequently the lowest emission of green house gases. Grid electricity in the United States of America has been shown to be four times cheaper than fuel given gasoline prices at \$3/gallon. Consequently, it is crucial to further optimize the electric-drive mode for EV. Battery capacity should be designed to allow EV drivers reach their destination while avoiding unnecessary stops to recharge their vehicles. However, this additional battery capacity would impact the vehicle's space, weight and cost. In view of these limitations, we propose integrating EVs with the vision of Intelligent Transportation Systems (ITS). This chapter starts out by putting the design of EVs into a broader perspective by proposing a Predictive Intelligent Battery Management System (PIBMS), which will enhance the overall performance of EVs including energy consumption and emissions using the ITS infrastructure.

At the end of this chapter, the reader should have an understanding of the capabilities and limitations of the PIBMS. It lays out the design foundation for the future implementation of an interconnected EV equipped with PIBMS, which further contributes to the optimization of energy efficiency and reduced emissions.

2. EV design challenges

Recent advancement in battery and charging technologies has allowed the Electric Vehicle (EV) to be considered as the new generation of automotive transportation. However, the physical dimensions, packaging environment and charging of EV batteries continues to be the main challenge and the focus of attention in the development of EVs. Battery technology selection continues to be the primary challenge in order to achieve the proper balance in the EV design as illustrated in Figure 1 and described below.

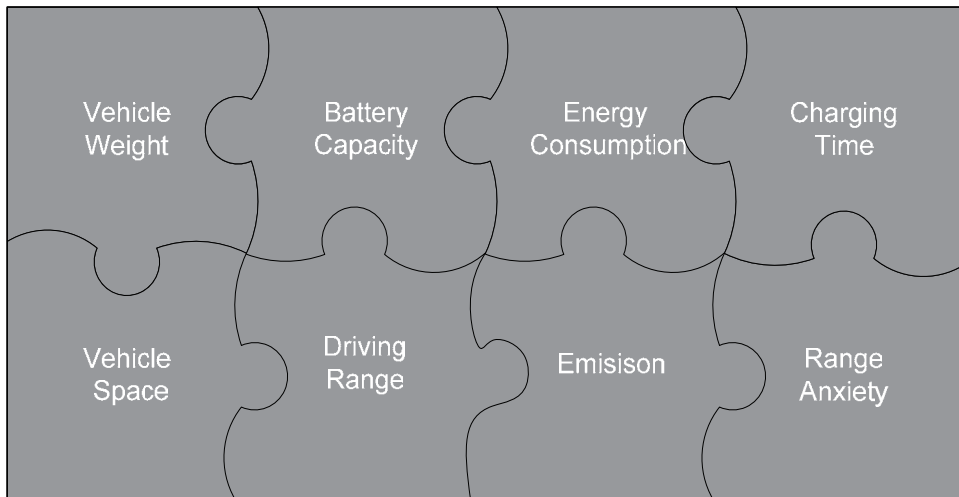


Fig. 1. EV Design Parameters

- **Battery Capacity:** EV battery capacity is predetermined by the battery design and cell chemistry. Lithium polymer batteries are the target implementation for EV due mainly to their high power-to-weight ratio.
- **Vehicle Weight:** EVs weight increases proportionally to battery capacity increase.
- **Vehicle Space:** Vehicle operators favor personal use of vehicle space. EV requires more packaging space to house the battery in a safe environment. Generally, the battery is packaged in the center of the vehicle where vehicle operators conventionally utilize this space.
- **Driving Range:** EV can only run for 100-200 miles before recharging compared to gasoline vehicle, which can drive more than 300 miles before refueling.
- **Charging time:** EV has no internal source for recharging the battery. EV charging time ranges between 3-8 hours compared to 2-4 minutes of refueling for gasoline vehicle.
- **Range Anxiety:** EV operators are usually concerned with their vehicles' limited driving range, inadequate charging infrastructure, and long charging time.
- **Energy Consumption:** EV propulsion systems offer around 85% efficiency compared to about 25 % efficiency for Internal Combustion Engines (ICE).
- **Emission:** EV emits no pollutants; however, power plant generating the EV electricity may emit them.

While battery manufacturers are still pursuing further improvement in energy capacity, the navigation technology and rapid advances in wireless communication technology can be used to achieve the vehicle performance balance described as "Target" and presented in Table 1.

Table 1 clearly shows the limitations for utilizing battery capacity as the only design variable for achieving a balanced EV design that is acceptable for EV operators. To realize the success of EVs, achieving the "Target" design option shall be exerted. This call for considering two crucial aspects in addition to battery technology: Traffic information and wireless communication.

The need to identify traffic conditions and the ability to transfer these conditions constitutes the success of optimizing energy consumption and emission reduction in EVs.

Realizing emission reduction in EVs is a crucial step toward emission free vehicles. However, it requires a better understanding of emission free EVs and the ensuing energy sources. These topics are addressed in the following section: EV Emission.

Parameter	Design Options		
	A	B	"Target"
Battery Capacity			
Vehicle Weight			
Vehicle Space			
Driving Range			
Charging Time			
Range Anxiety			
Energy Consumption			
Emission			

Positive Impact
 Negative Impact

Table 1. EV System Design Option Evaluation

2. EV emission

2.1 Electrical energy source

An accurate assessment of EV emission requires the inclusion of the electrical energy source associated emission with the generation and transmission. Electrical energy is generated from two main sources as illustrated in Figure 2:

- Non-renewable source: Coal, natural gas, nuclear, petroleum
- Renewable source: wind, solar and geothermal

Non-renewable energy produces elevated Greenhouse Gas (GHG) emissions. Coal is leading all other energy sources in terms of GHG emissions.

Renewable energy investment has to some extent been very limited due to the associated high development cost. However government subsidiaries continue to make the renewable energy investment more affordable.

The claim of EV proponents is that this type of vehicle is a Zero Emission Vehicle (ZEV). This claim depends on many factors, but a key factor shall be highlighted. The EV operating energy emission is a function of the energy source. The upstream Greenhouse gases (GHG) emission is based on power plant types and efficiency. The claim of EV technology proponents that this type of propulsion technology will offer a potential to reduce a long-

term GHG emission can be verified with the implementation of the Well-To-Wheel (WTW) emission model to analyze the GHG emission of the electrical energy source.

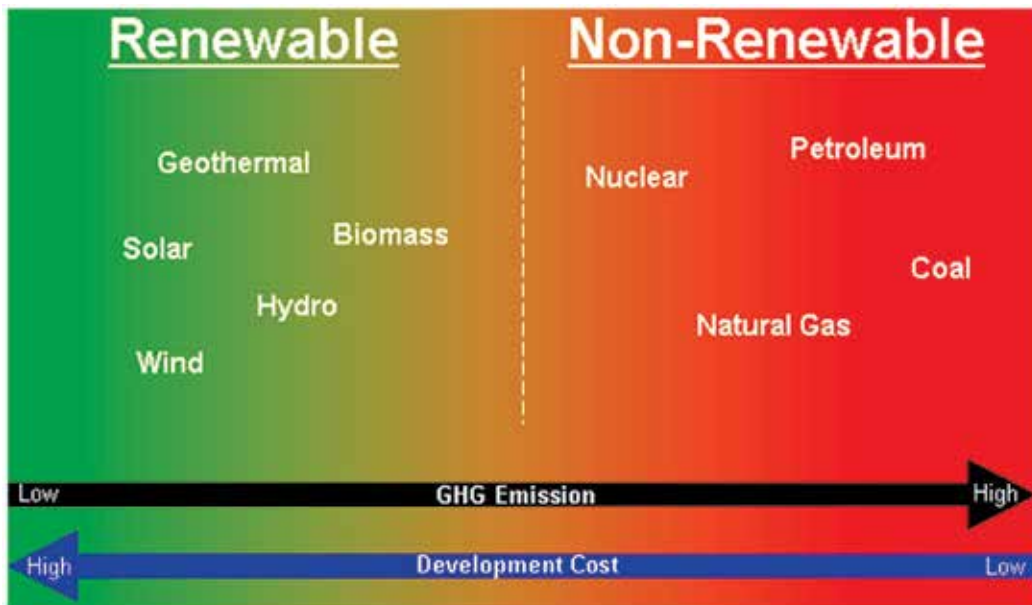


Fig. 2. Electrical Energy Source

2.2 EV configuration

The EV is mainly a conventional vehicle with the following main differences illustrated in Figure 3 and listed below:

1. High voltage electric battery rather than a fuel tank to store and supply the required operational energy
2. Electric motor rather than an internal combustion engine to propel the vehicle
3. Gear box rather than a transmission to couple the power from the electric motor to the drive shaft
4. On Board or Off Board Charger to allow for recharging of the high voltage electric battery
5. Direct current / Alternating current (DC/AC) inverter to convert the DC high voltage battery into AC to drive the E-motor
6. DC/DC converter to convert the DC high voltage battery into DC low voltage battery (Conventionally identified as 12 Volt battery)

2.3 EV efficiency

The EV overall efficiency can be classified in three main categories. The following section describes the categories and their respective components:

2.3.1 Charging efficiency

Automotive charging standards are currently being developed worldwide to allow for DC (Direct Current) charging. In contrast AC/DC (Alternating Current / Direct Current)

charging standards have already been established and are currently being implemented in a number of alternative vehicle technology production models such as the Chevy Volt, EV SMART, Mitsubishi MIEV, Nissan Leaf and Tesla. DC charging enables the vehicle's high voltage DC battery to be directly charged from the charge station bypassing the vehicles' on board charger thus further improving charging efficiency and time. DC charging is the target implementation for public charging enabling fast charge. Due to the associated high cost of DC charging infrastructure, AC/DC charging will be the alternative and only solution for residential charging.

The EV charging efficiency is the ratio of energy transferred to the high voltage battery to the energy consumed from the AC source. Charging efficiency is highly dependent on charging power and operating temperature. Figure 4 depicts a typical EV charging efficiency operated at room temperature and utilizing an AC/DC onboard charger with a maximum output power of 3500 W.

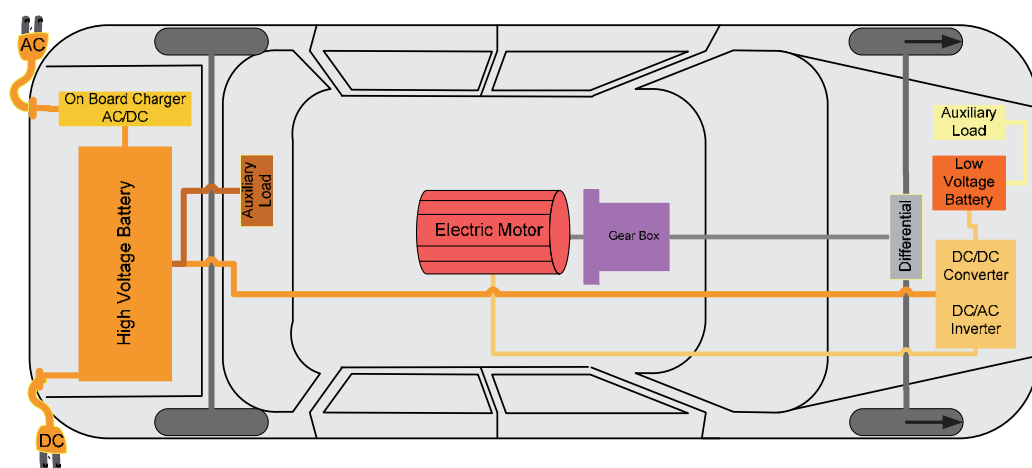


Fig. 3. Electric Vehicle Model

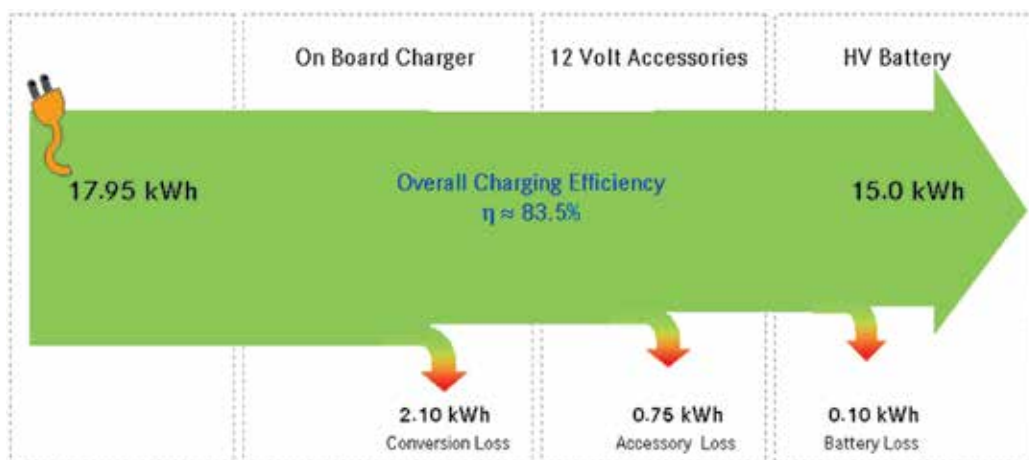


Fig. 4. EV Charging Energy Flow and Efficiency Diagram

2.3.2 Operational efficiency

Generally the efficiency of the EV Electrical Motor (EM) is exceptionally high $\sim 85\%$ compared with an Internal Combustion Engine (ICE) $\sim 25\%$. Power losses in an EV are negligible, in this section we will focus on power losses from key components occurring in an electrical propulsion system during driving mode due to power conversion, operation and propulsion. As illustrated in Figure 5 approximately 81.3% of the energy stored in the HV battery is utilized to propel the EV. Combining the EV overall charging efficiency with the EV overall operational efficiency, the EV efficiency becomes $\sim 67.9\%$ around four times more efficient than an ICE propelled vehicle with an overall efficiency of $\sim 14\%$.

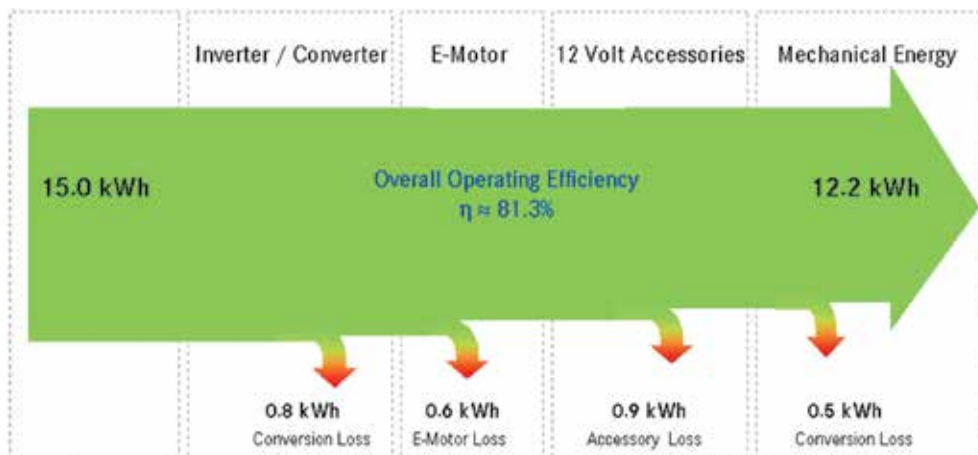


Fig. 5. EV Operating Energy Flow and Efficiency Diagram

2.3.3 Power source generation and transmission efficiency

For a full representation of energy and emission calculation, it is important to consider the efficiency involved in energy recovery, processing and transportation. Complete vehicle energy-cycle analysis tools, commonly known as Well-To-Wheel (WTW) analysis tools are needed to provide an accurate assessment of EV overall efficiency and emission.

The U.S Environmental Protection Agency's (EPA) offers an emission database "National Emissions Inventory" (NEI); the database includes annual emissions associated with electric energy generation.

To fully evaluate emission impact of EV, a Well-to-Wheel emission model shall be considered such as the Greenhouse Gases, Regulated Emissions, and Energy Use in Transportation (GREET). GREET was developed by the U.S. Department of Energy (U.S. DOE) to allow researchers to evaluate emissions from a full fuel cycle for EVs and other various propulsion technologies as depicted in Figure 6.

3. PIBMS architecture

Current EV architecture incorporates a Battery Management System (BMS) which is a vehicle integrated electrical module responsible for monitoring State Of Charge (SOC) and maintaining a suitable state of health (SOH) of the EV high voltage battery through controlled charging and discharging processes of the battery cells.

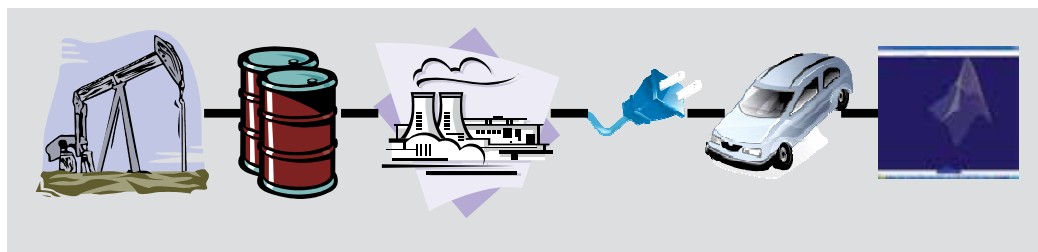


Fig. 6. WTW Emission Modeling

Adding a predictive and an intelligent component to the BMS design can make the architecture of the EV more energy and emission efficient, as it would facilitate acquiring traffic condition; offer a dynamic response to all future stochastic traffic flow situations through travel route and drive profile advisement. The integration of the predictive and intelligent components with the BMS led to the concept of the Predictive Intelligent Battery Management System (PIBMS).

With the rapid advances in wireless communication, global positioning system and the introduction of smartphones, the world is transitioning from being an online connected world to become a mobile connected world. The PIBMS concept will be based on further developing and integrating the existing technologies of the Global Positioning System (GPS), the wireless communication technology “Dedicated Short Range communication” (DSRC), and the advanced computing mobile phones identified as smartphone. The PIBMS receives traffic information from traffic light controllers and roadside units, location data from GPS and charge point data in the vicinity as depicted in Figure 7.

3.1 Intelligent Transportation System (ITS)

The technological progress in wireless communication, Global Positioning System (GPS) and vehicle electronics is enabling the introduction of advanced technologies into the transportation system commonly referred to as the Intelligent Transportation system (ITS).

3.1.1 Dedicated Short Range Communication (DSRC)

Dedicated Short Range Communication (DSRC) defined by the framework of the international standards organization ASTM and standardized by the IEEE 802.11, IEEE P1609.x and SAE J2735 standards, is a two-way short- to medium range (~1000 meters) wireless communication designed for automotive application and currently being systematically deployed throughout the U.S transportation system across the nation and sponsored by the U.S Department of Transportation Research and Innovative Technology Administration (RITA). DSRC enables the attainment of the following vehicle safety critical components for vehicle communication:

- **Fast Network Acquisition:** To allow immediate establishment of communication between vehicles and road side units
- **Low Latency:** To allow least execution time
- **High Reliability:** To allow high level of user reliability

DSRC offers the base and single wireless communication technology for future vehicular safety communications; furthermore DSRC is gaining momentum among researchers for future vehicular applications focused on energy optimization and emission reductions.

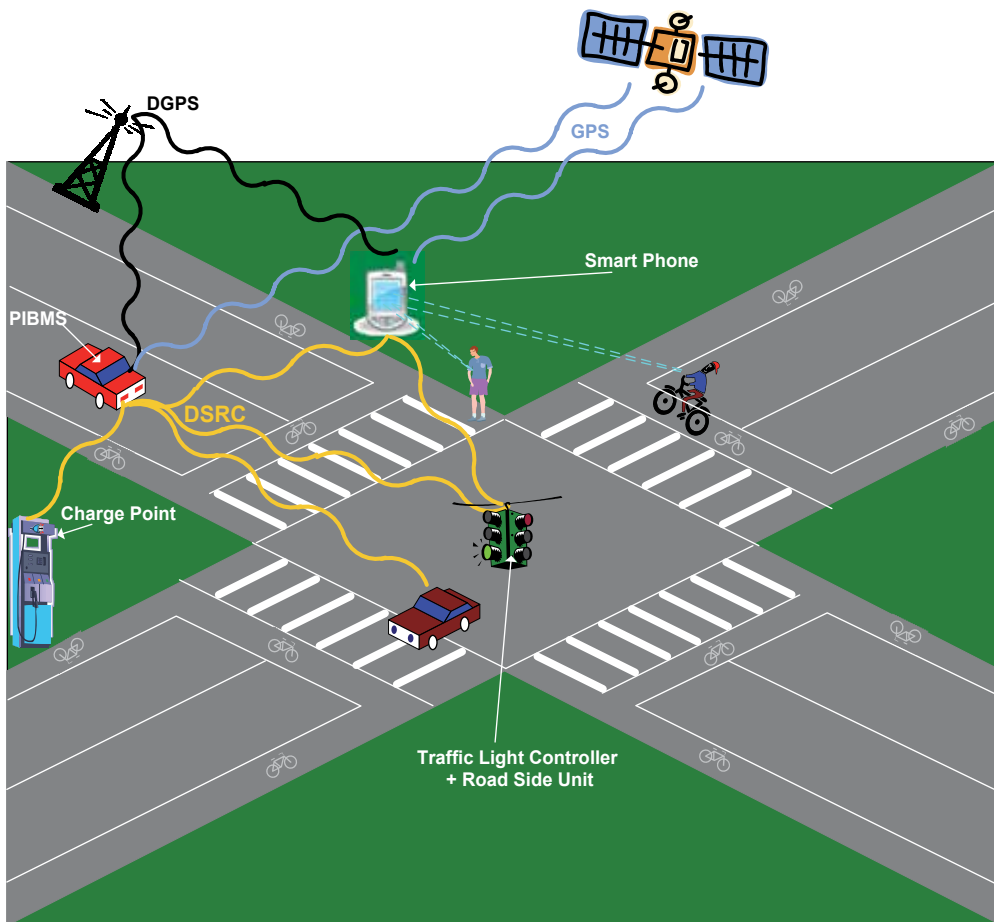


Fig. 7. PIBMS Communication Block Diagram

3.1.2 Positioning system

Real time vehicle position is required with a very high level of accuracy; this would allow the system to optimize the output with both high confidence and reliability.

Several satellite receivers' manufacturers offer systems with an extremely superior accuracy such as the Topcon GR-3 receiver. The Topcon GR-3 is compatible with the US satellite system GPS, the Russian satellite system GLONASS and the European satellite system GALILEO. This receiver system claims a static accuracy of 3mm, a Real-Time Kinetic (RTK) accuracy of 10 mm.

It is important to note than in cases where satellite navigation coverage is not available due to for example driving through tunnels, Differential GPS data shall be used which would offer in this case a slightly reduced accuracy.

3.2 PIBMS design

The PIBMS distinctive features are the predictive and the intelligent:

- The predictive feature of the PIBMS is viable through the capability of the EV to integrate the capability of vehicular wireless communication technology (DSRC) to communicate traffic, charging infrastructure and vehicle data.
 - The intelligent feature is offered through the application of a 2-scale dynamic programming optimization approach onboard the PIBMS operated EV. The proposed PIBMS architecture consists of six modules illustrated in Figure 8 and described below:
1. Traffic Data Extractor (TDE): To extract the future traffic data from the ITS network including traffic flow, intersection light status. This data is consequently used to determine if alternative routes should be considered.
 2. Vehicle Operation Mode (VOM): To provide the vehicle’s current operation modes including vehicle speed, gear and SOC.
 3. Trip Model Identifier (TMI): To learn the route road condition including slope and distance, this is accomplished through the use of GPS data.
 4. Trip Model Deflector (TMD): To re-route trip as found necessary following the processing of future traffic data.
 5. State Of Charge Optimizer (SOCO): To optimize battery energy the intelligent algorithm found in this module is expected to have two key criteria: agile and dynamic.
 6. Driver Feedback Control (DFC): To provide the driver feedback relative to drive style including speed, acceleration, and deceleration.

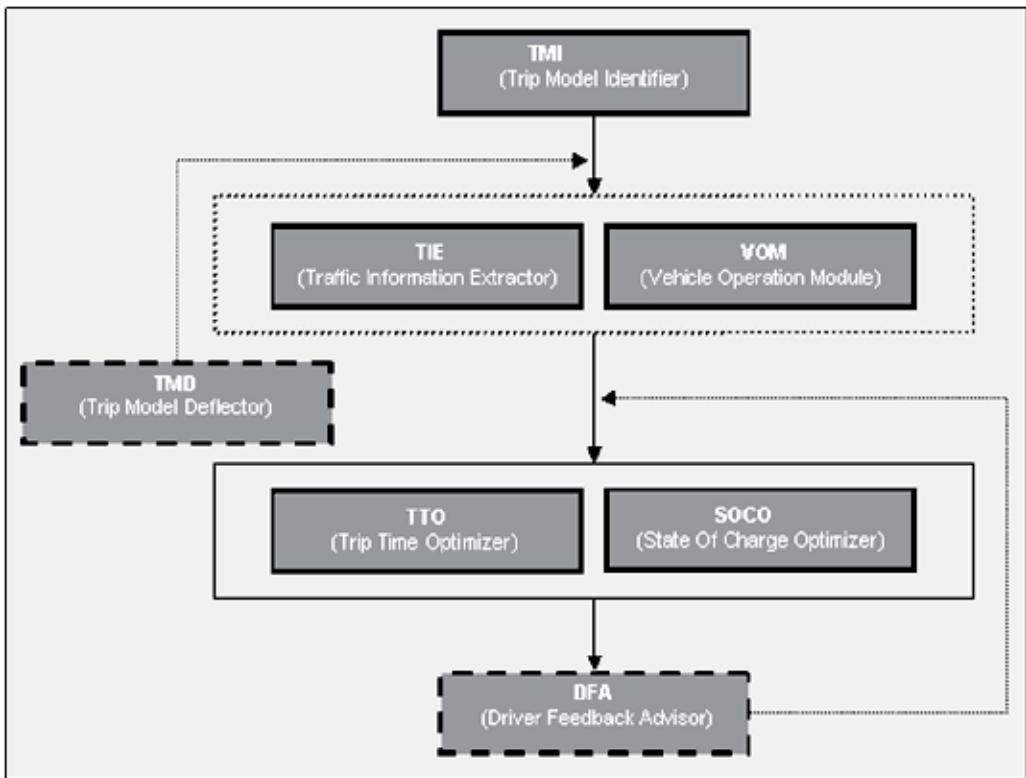


Fig. 8. PIBMS Architecture

3.2.1 Design realization

The system design is to offer the user the ability to follow advised upon route model, trip model and electrical accessory model to optimize the following queries:

1. Energy consumption
2. Emission
3. Travel Time

The system design consists of three phases:

- Phase I uses initial vehicle and route parameters at origin to advise the driver for an initial drive and route profiles based on the historical traffic data.
- Phase II uses the driver input to arrange the cost function to be optimized based on driver selective or combined selection of optimization criteria: energy consumption, vehicle emission and travel time.
- Phase III uses energy, emission and travel time cost function to plan optimized route, drive and accessories profiles.

The PIBMS in combination with the Intelligent Transportation Systems (ITS) data offers the capability of operating the EV amid additional energy optimization and emission reduction. Figure 9 illustrates a block diagram of the Predictive Intelligent Battery Management Sub-Systems and the interfaces to vehicle sub-systems and road infrastructure.

The historical traffic data is utilized for initialization of the system, where vehicle has not yet established a real-time connection with the infrastructure and other vehicle's communication system.

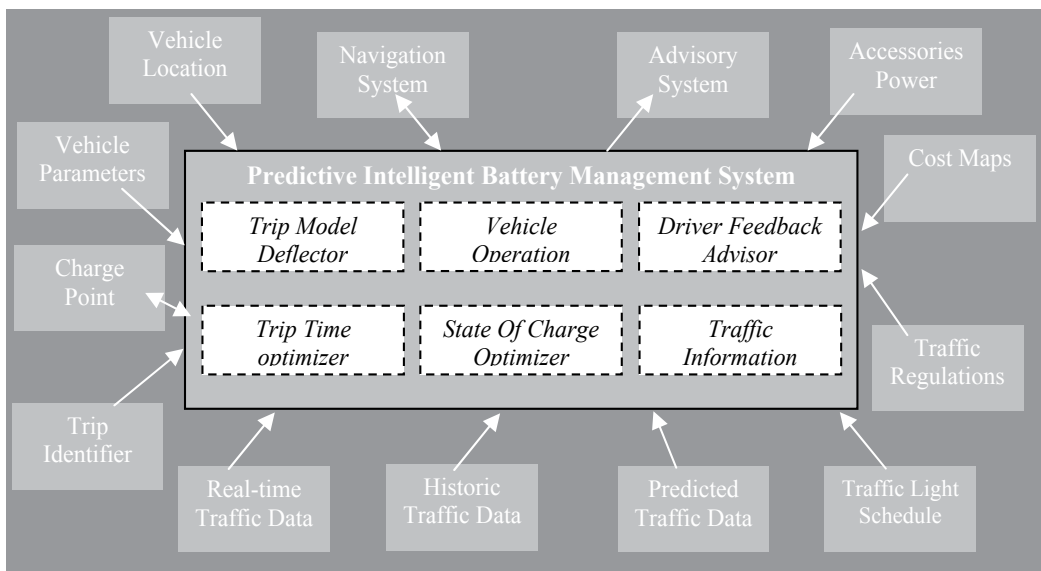


Fig. 9. PIBMS Interface Block Diagram

Referring now to Figure 10, the PIBMS is first initialized with an array of input data including: vehicle position, destination, and the maximum allowed arrival time as set by the driver. The PIBMS in coordination with the navigation system will generate an energy and emission efficient route and drive profile based on historical traffic data. The route will be established in multiple segments. The PIBMS will determine the number of route segments

and assign a maximum constraint in terms of consumed time, energy, and emission to travel those N segments. The PIBMS selects the Kth sequence associated with the expected segment to be traveled next. Through current and predicted traffic data, the PIBMS again in coordination with the navigation system will iteratively seek, compute and compare energy, emission and travel time of the selected segment. If the segment meets or is inferior to original estimated time, emission and energy consumption target costs, driver is advised to maintain driving through the formerly selected segment with its associated driving profile. Lest the originally selected segment does not meet the energy, emission and time constraints, an alternative segment is inquired and projected by the navigation system as an advisory path and drive profile. The navigation system will continuously seek alternative segments; if none are obtained the PIBMS will select the segment with the least calculated cost function. The driver is then advised to follow the recommended segment and driving profile to reduce energy consumption and emissions. In all cases, when driving and route profiles are established, they will be communicated to the Road Side Unit (RSU) to be then utilized as predictive traffic data for other PIBMS equipped vehicles seeking their respective optimized drive and route profiles, in addition to pre-scheduling arrival time to charge point as necessary. It is very critical for EV operators not to be abandoned mid-route where vehicle have no other self propelling means, an alternative route offering re-charge station is recommended to the driver. Provided that final segment has been computed and selected, thus indicating that driver is to commence driving the last segment of the route thus arriving to destination.

3.2.1.1 Phase I: Initialization

At initialization the system calculates a drive and route profiles based on historical traffic data provided by the roadside unit server. The historical traffic data includes current traffic flow conditions for the route profile from origin to destination in addition to charge point locations and energy source emission.

3.2.1.2 Phase II: Optimization

In this phase the route is divided into segments, for each possible path in the segment the travel time, energy consumption and emission are calculated in advance.

3.2.1.2.1 Cost Function

The parameters to be selectively or in combination optimized are travel time $T(i)$ energy $\delta(i)$, and emission $E(i)$, thus the cost function to be minimized can be stated as follow:

$$C = \sum_{i=0}^{j-1} [\alpha.t(i) + \beta.\delta(i) + \omega.E(i)] = \sum_{i=0}^{j-1} TC[x(i), u(i)] \quad (1)$$

where j is the period of the route, α , β and ω are the respective weights for travel time, energy consumption and energy source emission. The PIBMS is to allow the driver to select at initialization the priority of travel time, energy consumption and energy source emission through associating the weights α ; β ; ω , TC is total cost of route as well as energy, emission and time, $x(i)$ is the dynamic state vector of the vehicle such as vehicle speed, energy capacity, motor torque, vehicle route and $u(i)$ is the control vector of the vehicle such as the recommended vehicle speed, the recommended acceleration, the recommended deceleration, the recommended route and the recommended charge point. The optimization problem becomes the search for the control vector $u(i)$.

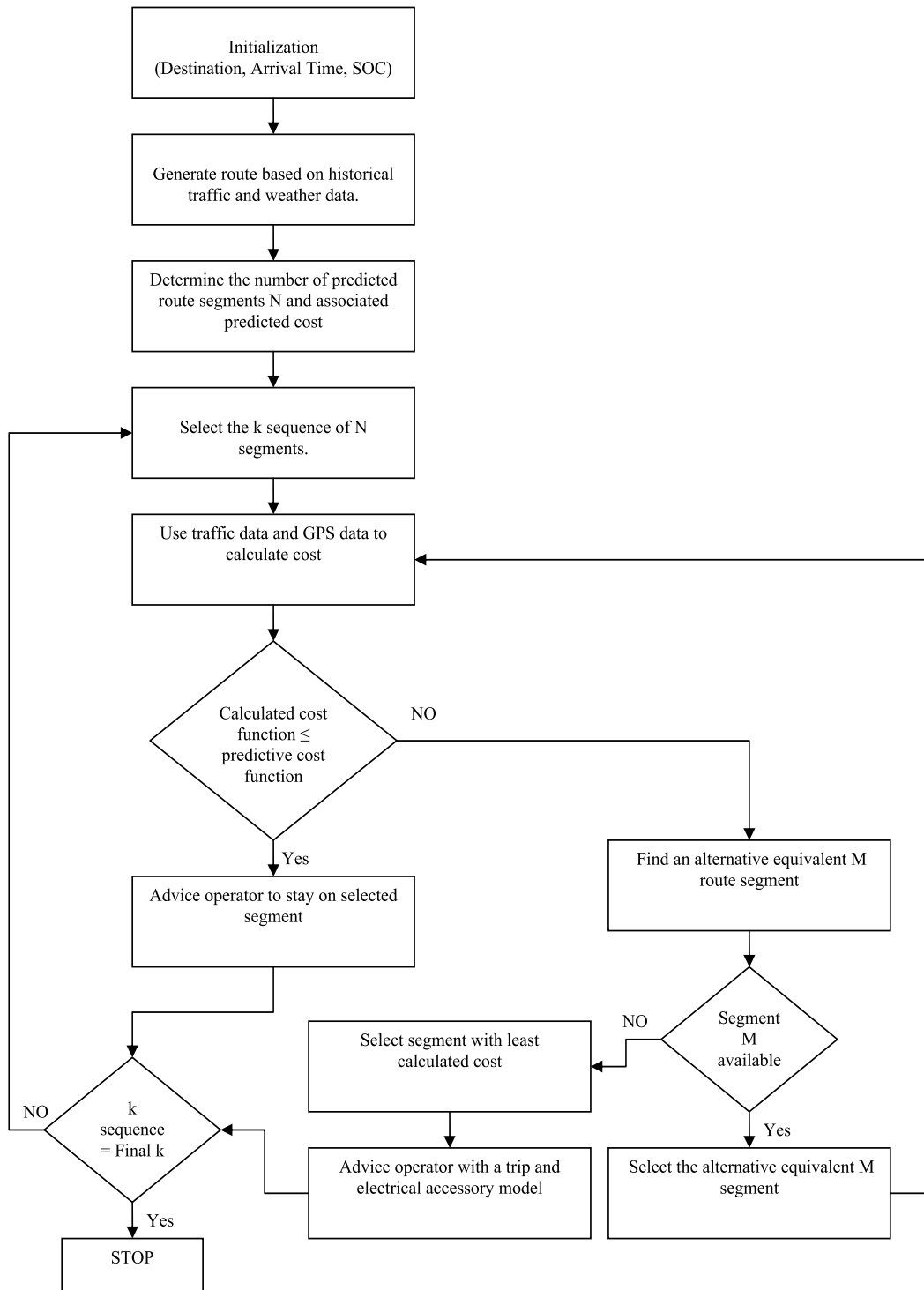


Fig. 10. PIBMS Operational Flow chart Diagram

The cost function will be subject to the targeted EV model thus resulting in the following constraints:

$$\delta_{\min} \leq \delta(i) \leq \delta_{\max} \quad (2a)$$

$$E_{\min} \leq E(i) \leq E_{\max} \quad (2b)$$

$$T_{\min} \leq T(i) \leq T_{\max} \quad (2c)$$

$$V_v(i) = V_{v\text{-req}} \quad (2d)$$

$$\tau_{em}(i) = \tau_{em\text{-req}}(i) \quad (2e)$$

$$V_v(i) \leq V_{v\text{-max}} \quad (2f)$$

$$V_{\min\text{limit}} \leq V(i) \leq V_{\max\text{limit}} \quad (2g)$$

$$\text{Acc}_{v\text{-min}} \leq \text{Acc}_v(i) \leq \text{Acc}_{v\text{-max}} \quad (2h)$$

$$\tau_{em}(i) \leq \tau_{em\text{-max}}(i) \quad (2i)$$

where V_v is vehicle velocity, $V_{v\text{-req}}$ is requested vehicle velocity, $V_{v\text{-max}}$ is vehicle maximum velocity, $V_{\min\text{limit}}$ is minimum speed limit, $V_{\max\text{limit}}$ is maximum speed limit, $\text{Acc}_{v\text{-min}}$ is vehicle minimum acceleration, $\text{Acc}_{v\text{-max}}$ is vehicle maximum acceleration, τ_{em} is electric motor torque and $\tau_{em\text{-req}}$ is electric motor torque requested, $\tau_{em\text{-max}}$ is electric motor torque maximum.

3.2.1.3 Phase III: 2-Scale Predictive Dynamic programming

In this phase a modified 2-scale predictive dynamic programming approach is implemented for obtaining the optimal drive and route solutions. Route is divided into segments, for each possible path in the segment the energy consumption and emission are calculated. The 2-scale predictive dynamic programming approach is implemented based on Bellman's Principle of Optimality; the optimal solution is obtained by identifying the initial and terminal conditions of the state. The optimized solution is then for segment k ($0 < k < i-1$) realized by minimizing the cost function defined as:

$$C_i^*[x(i)] = \min_{u(i)} \left\{ TC[x(i), u(i)] + \left[C_{x+1}^*[x(i+1)] \right] \right\} \quad (3)$$

The algorithm shows how to plan optimized drive and route profile based on energy, emission and travel time. The PIBMS will generate advisory audible/visual recommendations to the driver, including optimized routes, optimized drive profiles, and optimized electrical load profiles. The optimization algorithms will take into consideration improving traffic safety, congestion, energy consumption, emission and travel time.

The current and predicted traffic conditions are maintained by the RSU. In order to reduce bandwidth utilization for communication between RSU and PIBMS, repeating traffic data will be communicated to PIBMS only in case of traffic condition change thus eliminating message overhead.

4. Simulation environment

To evaluate the performance of the PIBMS a simulation tool integrating traffic, vehicle and network models shall be employed. The simulation platform PIBMST (Predictive Intelligent Battery Management Simulation Tool) consists of three main building blocks described below and illustrated in Figure 11. The traffic, vehicle and network models are to allow for bidirectional coupling among each other, thus resulting in enhanced simulation accuracy however at the cost of increased computation time.

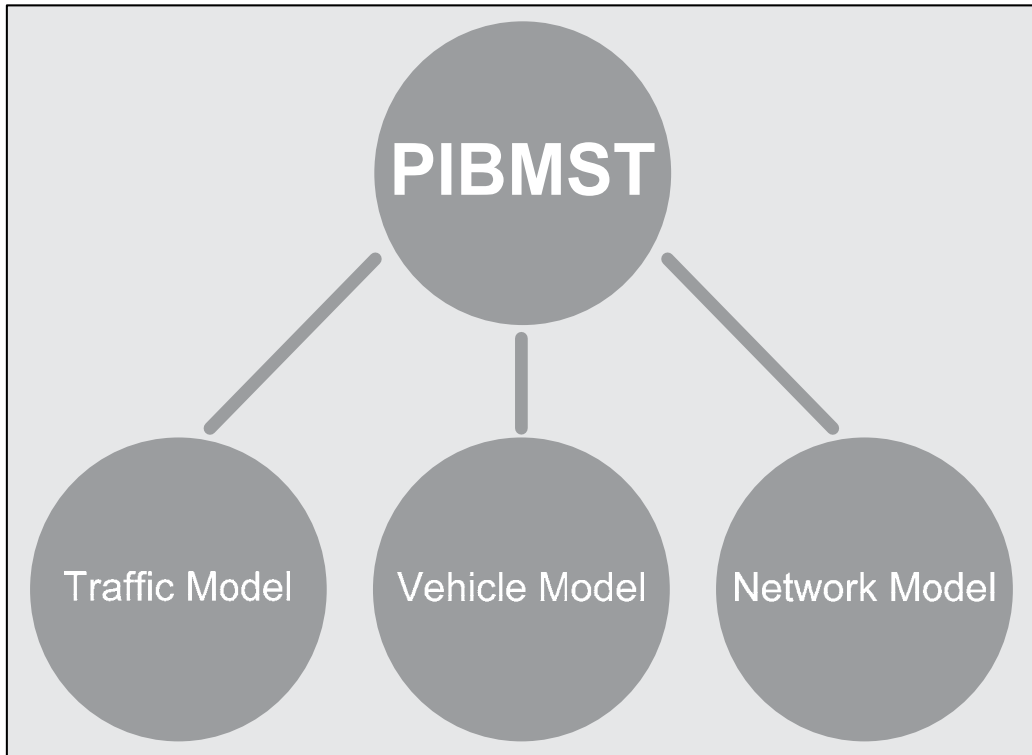


Fig. 11. PIBMST Platform

4.1 Traffic model

A recent study has proven that the traffic mobility model can be represented by trace-based models based on generated vehicular traces. The traces are real world based on mapping the positions of the vehicles. The traffic models are in general classified in two categories:

- Macroscopic: Mathematical model to simulate major traffic characteristics such as average speed, density, and flow.
- Microscopic: In contrast to the macroscopic mathematical model, the microscopic model is to simulate single vehicle traffic characteristics.

Traffic flow is a dynamic problem, influenced by several variables thus for any beneficial performance of the trip model the microscopic traffic model is implemented in PIBMST.

4.2 Vehicle model

The EV model represents a series of mathematical equations representing the characteristics of the identified EV components in Figure 3 and the forces applied to the vehicle as depicted in Figure 12

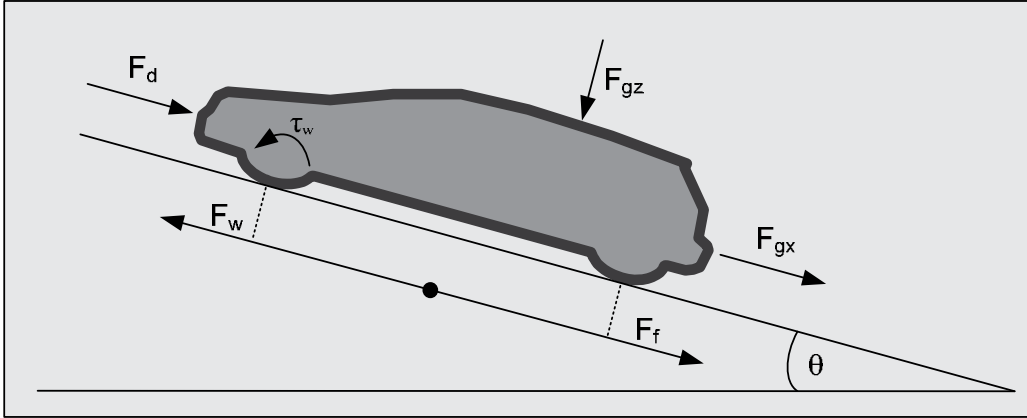


Fig. 12. Applied Forces to the EV

The earth's gravitational force imposes a force F_g on the vehicle. F_g is derived from Newton's second law where a body of mass m endure an acceleration a resulting in an applied net force F .

$$F = mg \quad (4)$$

The gravitational normal force applied to the vehicle shall take into consideration the slope angle θ , when vehicle is moving uphill or downhill.

$$F_{gz} = mg \cos \theta \quad (4.1)$$

$$F_{gx} = mg \sin \theta \quad (4.2)$$

In order to move the vehicle a wheel force F_w is applied on the wheel. F_w is the resulting force from the generated torque in the electric motor applied to the vehicle's wheels through a gear box with a fixed differential ratio. F_w is then represented as the ratio of the torque applied to the wheel τ_w to the wheel radius, r_w .

$$F_w = \frac{\tau_w}{r_w} \quad (4.3)$$

When vehicle is moving the aerodynamic drag force F_d is created. F_d depends on the air density ρ , the vehicle frontal area A_v , the drag coefficient C_d , and the vehicle velocity V_v .

$$F_d = \frac{1}{2} C_d \rho V_v^2 A_v \quad (4.4)$$

The contact surfaces between the vehicle's wheels and the road results into a friction force F_f . The product of the friction coefficient μ_f and the vehicle's gravitational force F_g results in the corresponding frictional force F_f .

$$F_f = \mu_f F_{gz} \quad (4.5)$$

The total force acting on the vehicle F_t is the sum of all applied forces on the vehicle in the driving direction.

$$F_t = F_w - F_{gx} - F_d - F_f \quad (4.6)$$

The acceleration of the vehicle is determined by the torque applied to the wheels. The wheel torque τ_w is the product of the E-motor torque τ_{em} the gear box ratio G_b

$$\tau_w = \tau_{em} G_b \quad (4.7)$$

The acceleration of the vehicle a_v through the application of Newton's second law is the ratio of the total force acting on the vehicle to the mass of the vehicle

$$\begin{aligned} F_t &= \frac{F_w - F_{gx} - F_d - F_f}{m} \\ &= \frac{\tau_w}{r_w m} - g \sin \theta - \frac{1}{2m} C_d \rho V_v^2 A_v - \mu_f g \cos \phi \\ &= \frac{\tau_{em} G_b G_i}{r_w m} - g \sin \theta - \frac{1}{2m} C_d \rho V_v^2 A_v - \mu_f g \cos \phi \end{aligned} \quad (4.8)$$

The angular velocity of the E-motor ω_{em} is the angular velocity in rotation per minute (RPM) multiplied by the E-motor turnover rate 2π and divided by 60 (to transform RPM into revolution per second)

$$\omega_w = \frac{2\pi \omega_{em}}{60 G_b} \quad (4.9)$$

The vehicle speed is the product of the wheel radius and the angular velocity of the wheel. rotation per minute (RPM) multiplied by the E-motor turnover rate 2π and divided by 60

$$V_v = r_w \omega_w = \frac{r_w 2\pi \omega_{em}}{60 G_b} \quad (4.10)$$

4.2.1 Emission model

The emission model considers the emission associated with the generation and transportation of electricity in addition to the operation of the EV as illustrated in Figure 13. The EV emission model is to be based on governmental accredited agencies such as the U.S. Environmental Protection Agency's (EPA's) electric power plant emission database. The EV emission is the product of consumed electrical energy in Kilo Watt hour (KWh) and the associated emission of the electrical energy source and transmission to the EV in grams (g) per KWh according to EPA. The results are presented in g/KWh of VOC, CO, CO₂, NO_x, PM₁₀ and SO_x.

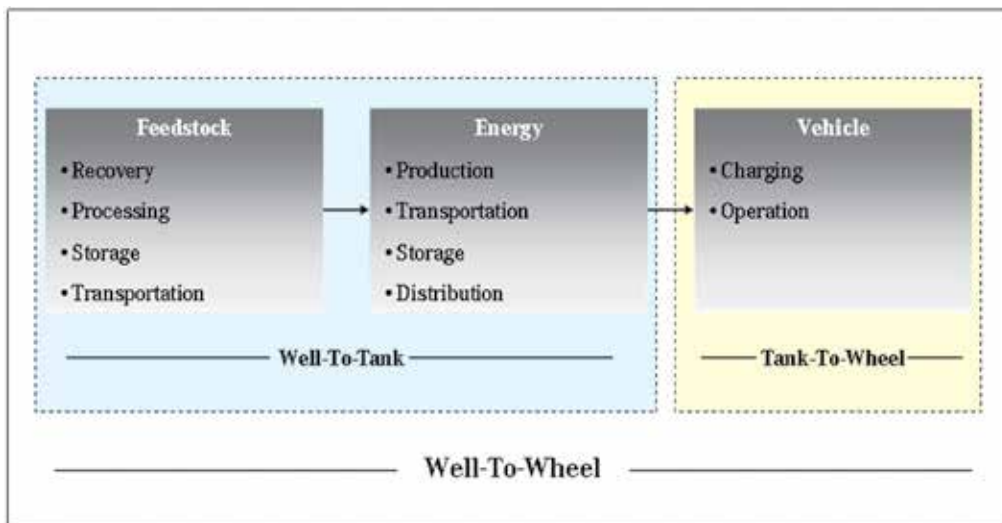


Fig. 13. Well-To-Wheel Emission Analysis Model

4.3 Network model

The roadway includes dynamic nodes such as vehicles, cyclists and pedestrians, and the static nodes such as Road Side Unit, Traffic Light Controller and Charge Point. The simulation of the nodes will require the implementation of a Vehicular ad-hoc network (VANET) capable of simulating the behaviour of the DSRC network. The network data model simulation is a discrete event simulator, implementing the protocol stack Wireless Access in Vehicular Environments (WAVE)/ Dedicated Short Range Communication (DSRC) as illustrated in Figure 14.

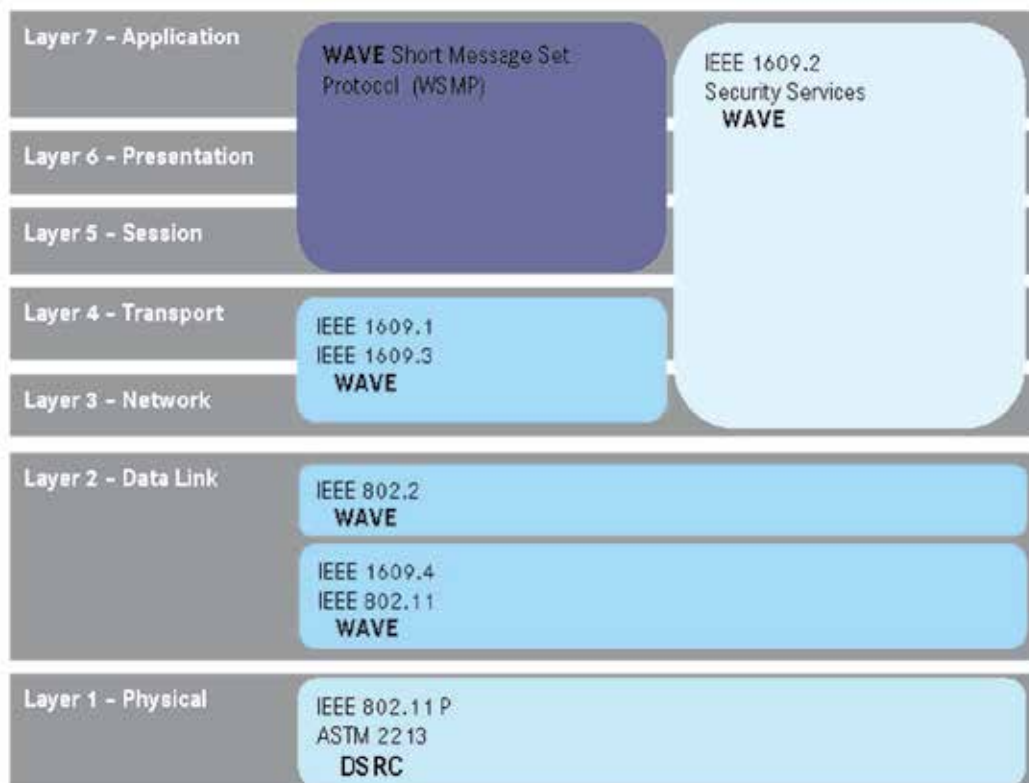


Fig. 14. Protocol Stack

5. Conclusion

Due to the single propulsion system design in the EV, the latter offers the consumers a greater reliability, simplicity of maintenance and vehicle cost compared to Plug-In Hybrid Electric Vehicle (PHEV). Further more compared with the Fuel Cell Vehicle (FCV) the EV is more advantageous relative to vehicle cost, recharging infrastructure and safety.

The automotive industry is being reshaped with the development of the EV. The new generation of automobiles are demanded to meet the market's conventional demands from vehicle space, driving range and convenience; furthermore new requirements have been shaped by the market to include energy consumption and environmental impact.

The EV will lead the way among the alternative vehicle technologies to target energy consumption and emission reduction.

This chapter offered the conceptual framework for the PIBMS application using DSRC and GPS technologies to offer EV operators an enhanced energy efficiency and decreased emission. Furthermore the proposed framework is designed to target near future implementation for relatively negligible cost using existing equipments and technologies.

6. References

- [1] Martin Eberhard and Marc Tarpenning, "The 21st Century Electric Car," Tesla Motors Inc, July 19, 2006
- [2] Romm, J. J. and Frank, A. A. "Hybrid Vehicles Gain Traction," Scientific American, v 294,n4, April 2006,p 763-770
- [3] M.Abdul-Hak, N.Al-Holou "ITS based Predictive Intelligent Battery Management System for plug-in Hybrid and Electric vehicles" Vehicle Power and Propulsion Conference, 2009. VPPC apos;09. IEEE Volume , Issue , 7-10 Sept. 2009 Page(s):138 - 144
- [4] Brinkman, N; Wang, M; Weber, T & Darlington,T (May 2005), Well-to-Wheels Analysis of Advanced Fuel/Vehicle Systems – A North American Study of Energy Use, Greenhouse Gas Emissions, and Criteria Pollutant Emissions, Available from <http://greet.es.anl.gov/>
- [5] ASTM E2213-02e1 Standard Specification for Telecommunications and Information Exchange Between Roadside and Vehicle Systems - 5 GHz Band Dedicated Short Range Communications (DSRC) Medium Access Control (MAC) and Physical Layer (PHY) Specifications
- [6] 802.11p-2010 - IEEE Standard for Local and Metropolitan Area Networks - Specific requirements Part 11: Wireless LAN Medium Access Control (MAC) and Physical Layer (PHY) Specifications Amendment 6: Wireless Access in Vehicular Environments
- [7] IEEE 1609.x - IEEE Family of Standards for Wireless Access in Vehicular Environments (WAVE)
- [8] SAE J2735 – SAE Standard for Dedicated Short Range Communications (DSRC) Message Set Dictionary

-
- [9] Fehr, W; (March 2011) The Vehicle-to-Vehicle (V2V) and Vehicle-to-Infrastructure (V2I) Technology Test Bed - Test Bed 2.0: Available for Device and Application Development, Available from http://www.its.dot.gov/factsheets/v2v_v2i_tstbd_factsheet.htm
- [10] Topcon, (March 2011) Tripple Constellation Receiver, Available from <http://www.topconpositioning.com/products/gps/geodetic-receivers/integrated/gr-3.html>
- [11] M. Boban, T. T. V. Vinhoza, Modeling and Simulation of Vehicular Networks: towards Realistic and Efficient Models, Source: Mobile Ad-Hoc Networks: Applications, Book edited by: Xin Wang, ISBN: 978-953-307-416-0, Publisher: InTech, Publishing date: January 2011
- [12] Lighthill, M.H., Whitham, G.B.,(1955), On kinematic waves II: A theory of traffic flow on long, crowded roads. Proceedings of The Royal Society of London Ser. A 229, 317-345
- [13] L. Bloomberg and J. Dale, Comparison of VISSIM and CORSIM Traffic Simulation Models on a Congested Network. Transportation Research Record 1727:52-60, 2000

Design and Analysis of Multi-Node CAN Bus for Diesel Hybrid Electric Vehicle

XiaoJian Mao, Jun hua Song, Junxi Wang, Hang bo Tang and Zhuo bin
*School of Mechanical Engineering, Shanghai Jiaotong University,
China*

1. Introduction

Automobile industry will face great evolution in the 21st century. Developing Energy saving and low emission products become the two directions of automobile industry. People have begun to focus on HEV since 1970s. HEV integrates power devices such as engine, motor, battery, which allow its both strong points of pure electric and traditional automobile. CAN is a serial communication protocol initially developed by BOSCH [1]. CAN supports distributed real-time control applications with dependability requirements. CAN is used widely in automotive electronics, with bit rates up to 1 Mbit/s [2-4]. CAN is a multi-master, broadcast protocol with collision detect and a resolution mechanism based on message priorities. Each message on the CAN bus has a unique priority and is only transmitted from a single node on the bus. J1939 is a protocol developed by SAE[5]. The J1939 protocol is a vehicle application layer built on the CAN protocol. The central entity is the Protocol Data Unit (PDU), which carries all the important information needed for determination of a message's priority and size.

In this paper, a multi-node CAN bus of diesel hybrid electric vehicle is designed, based on CAN2.0 protocol and J1939. The design methods of hardware and software for CAN bus are presented.

2. System overview

In general, according to powertrain configuration, HEV can be classified into three types, namely serial hybrid, parallel hybrid and serial parallel hybrid electric vehicle. In this study, parallel hybrid electric vehicle is adopted, as shown in Fig.1. The motor here is Integrated Starter Generator (ISG). This design has many advantages such as better inherited of former buses in structure, facility in application and wider applied range. And this method is applied widely in China.

3. Multi-node CAN bus for HEV

3.1 Analysis of CAN topology

According to requirement of HEV, CAN communication regular among ECU is worked out. CAN bus topology structure is designed. Hierarchical control method is used in the HEV controlled system, and the kernel controller of this powertrain is Hybrid Control Unit

(HCU). The controllers of lower level include Engine Management System (EMS), which is a diesel controller in this system, Battery Packets Control Module (BPCM), Automation Disconnect Module (ADM), Drive Motor Control Module (DMCM). And the main communication between controllers is CAN communication. Main CAN nodes of HEV powertrain are shown Fig. 2. HCU receives information form other lower ECU in order to know the whole vehicle state, at the same time HCU sends control message to them.

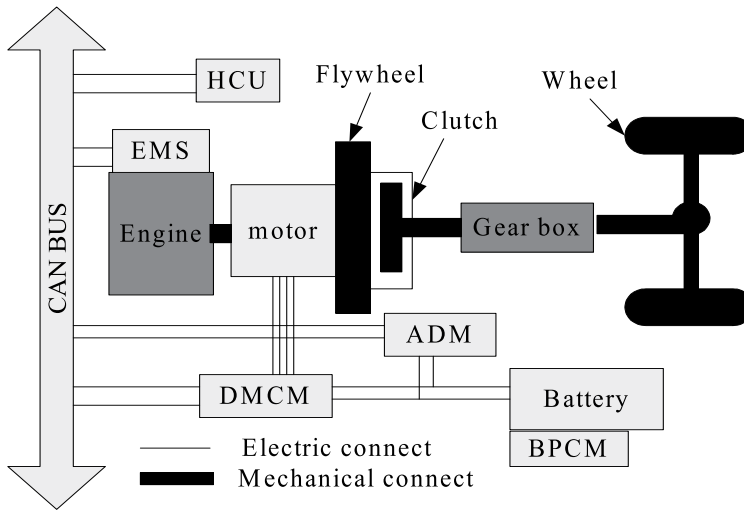


Fig. 1. Structure of Diesel Hybrid Electric Vehicle

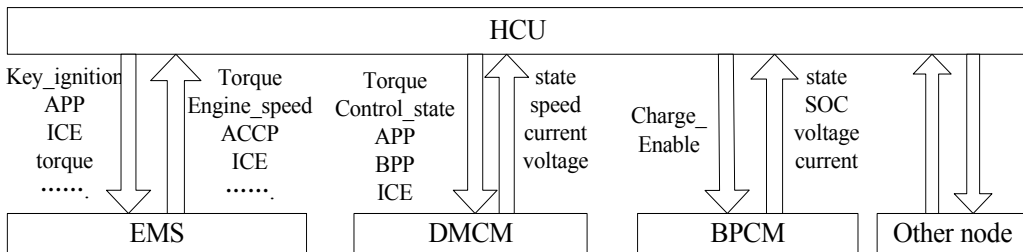


Fig. 2. Hierarchical control diagram of hybrid vehicle powertrain system

3.2 Design of CAN bus for hybrid electric vehicle

HCU is designed based on the microprocessor MC68376[6], and multi-node CAN is developed based on 29bits extended frame . This MCU integrates one TouCAN module which meets CAN2.0B protocol, and this module has 16 buffers. Specific address is assigned for each CAN node, so it is not necessary for declare and modification of each ECU. The address is defined when HCU under power on reset. The information of CAN frame is shown in the table 1. There are two trigger methods for CAN frame, one is period trigger mode, the other is interrupt trigger mode. The period of every node is designed based on the requirement of sampling velocity for vehicle control. Each node has different transmitting and receiving (TR) period. This method can full the control requirement and reduce the road rate of CAN bus, so improve the response time of the system.

CANbuffer	Use	Communiaca-tion period
buffer0	HCU→DMCM	20ms
buffer1	HCU→BPCM	1000ms
buffer3	HCU→ADM	20ms
buffer4	DMCM1→HCU	20ms
buffer6	DMCM2→HCU	50ms
buffer7	HCU→Calibration	interrupt trigger
buffer8	BPCM1→HCU	1000ms
buffer9	BPCM2→HCU	1000ms
buffer10	ADM→HCU	20ms
buffer11	Calibration→HCU	Interrupt trigger
buffer12	HCU→DCN1/ LFE→HCU	20ms /100ms
buffer13	HCU→DCN2/ ET→HCU	20ms /100ms
buffer14	HCU→DCN3	20ms
buffer15	EEC3→HCU	50ms

Table 1. Information of CAN frames

Byte position	Data definition
1	DM_State_Flg bit1-4 DM_Dig_Flg bit5-8
2	High byte of DM_Trq_Actual
3	low byte of DM_Trq_Actual
4	high byte of DM_Spd_Actual
5	low byte of DM_Spd_Actual
6	high byte of DM_I_Actual
7	low byte of DM_I_Actual
8	Set FF

Table 2. Detail data format of DMCM to HCU

Data combination and data split are applied, when data's addresses were defined. For example, the detail data definition is shown in Table2. Some variables which have two or three bits are combined in one same byte, while some variables which occupy two bytes were split high byte and low byte which in two bytes. These methods can improve the ability of CAN transmitting, which can save the space of transmitting. In addition, the load rate of CAN bus could be reduced.

4. Hardware and software design of CAN communication

4.1 Design of hardware circuit of CAN communication

TouCAN module integrated MC68376 and CAN transceiver 82C250 are adopted in the hardware design of CAN circuit. In order to improve the reliability of communication, power isolation and optoelectronic isolation are applied in the hardware design of CAN communication circuit. DC/DC isolation circuit module is used for power isolation. 6N137 is applied for optoelectronic isolation. The block diagram of CAN circuit is shown in Fig.3. Anti-jamming design should be considered in hardware design. Shield wire, impedance match of bus and electromagnetic filtering are applied in hardware design to improve the communication quality.

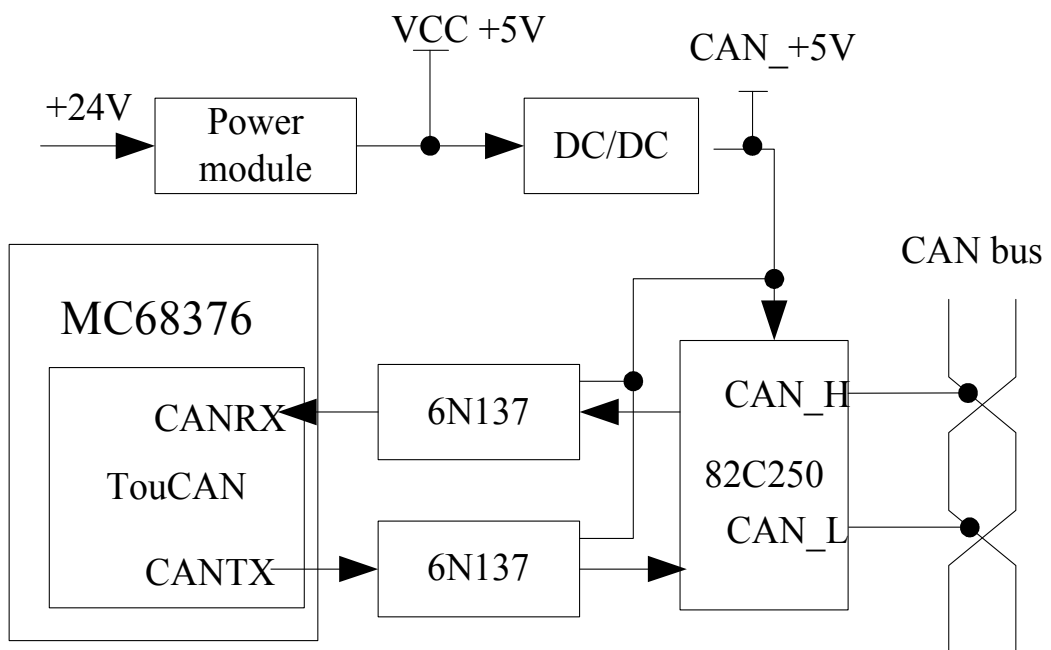


Fig. 3. Block chart of CAN circuit

4.2 Design of CAN communication software algorithmic

4.2.1 Buffer time-sharing

TouCAN module that meets CAN2.0B protocol, has sixteen buffers. There are eighteen data frames in our control system. In this study, a method of buffer sharing is designed, which two frames use the same buffer, named buffer time sharing. For example, the frames of HCU→DCN1 and LFE→HCU use the same buffer twelve. The flowchart of this the soft structure is shown in the figure5. Buffer time-sharing applies the mechanism of arbitration of CAN bus to avoid data conflict. What's more, buffer time-sharing can approve the hardware usage of HCU.

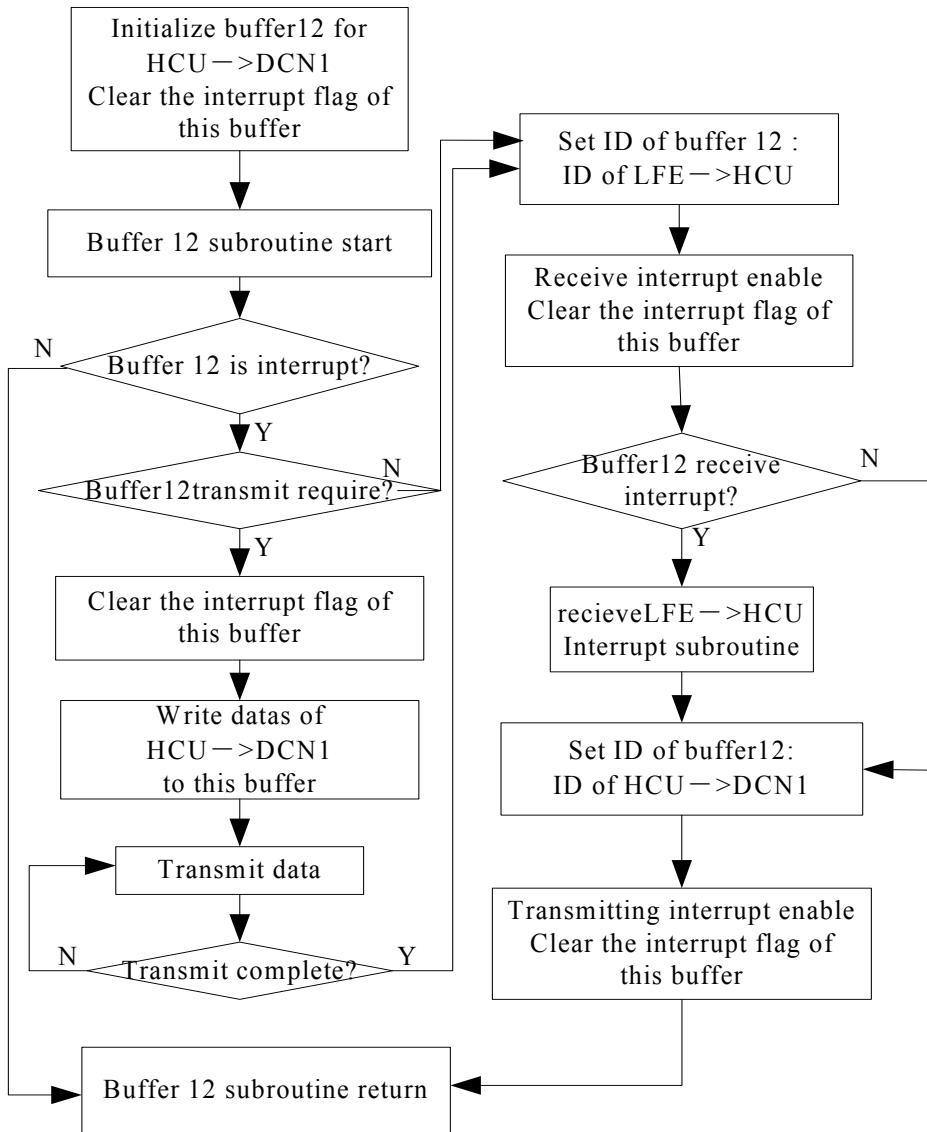


Fig. 4. Flowchart of buffer time-sharing program

4.2.2 Time-sharing receiving and transmitting

The infra program of CAN is designed according to HCU. The method of time-sharing receiving and transmitting (TSRT) is applied to ensure quality of communication. The communication period is determined according to requirement of control system. TSRT is an effective way to improve the efficiency of communication. On one hand, TSTR could shorten the running time of CAN subroutines because of all timer subroutine don't achieve at same time. On the other hand, amount of data transmitted on CAN bus is changed, according to time. So the road rate of CAN bus is changed at different time. When there is one timer subroutine operated, the road rate is lower. This is the most ordinary condition.

4.2.3 Optimization design of CAN drivers

CAN communication module is one of the most important subroutine of infra program. As an interrupt subroutine, CAN driver subroutine may lead to longer time of interrupt relay and affect the ability of interrupt performance of system. A Real Time Operating System (RTOS) is needed in optimization of the control system software. Multi-task is applied in the CAN subroutine design.

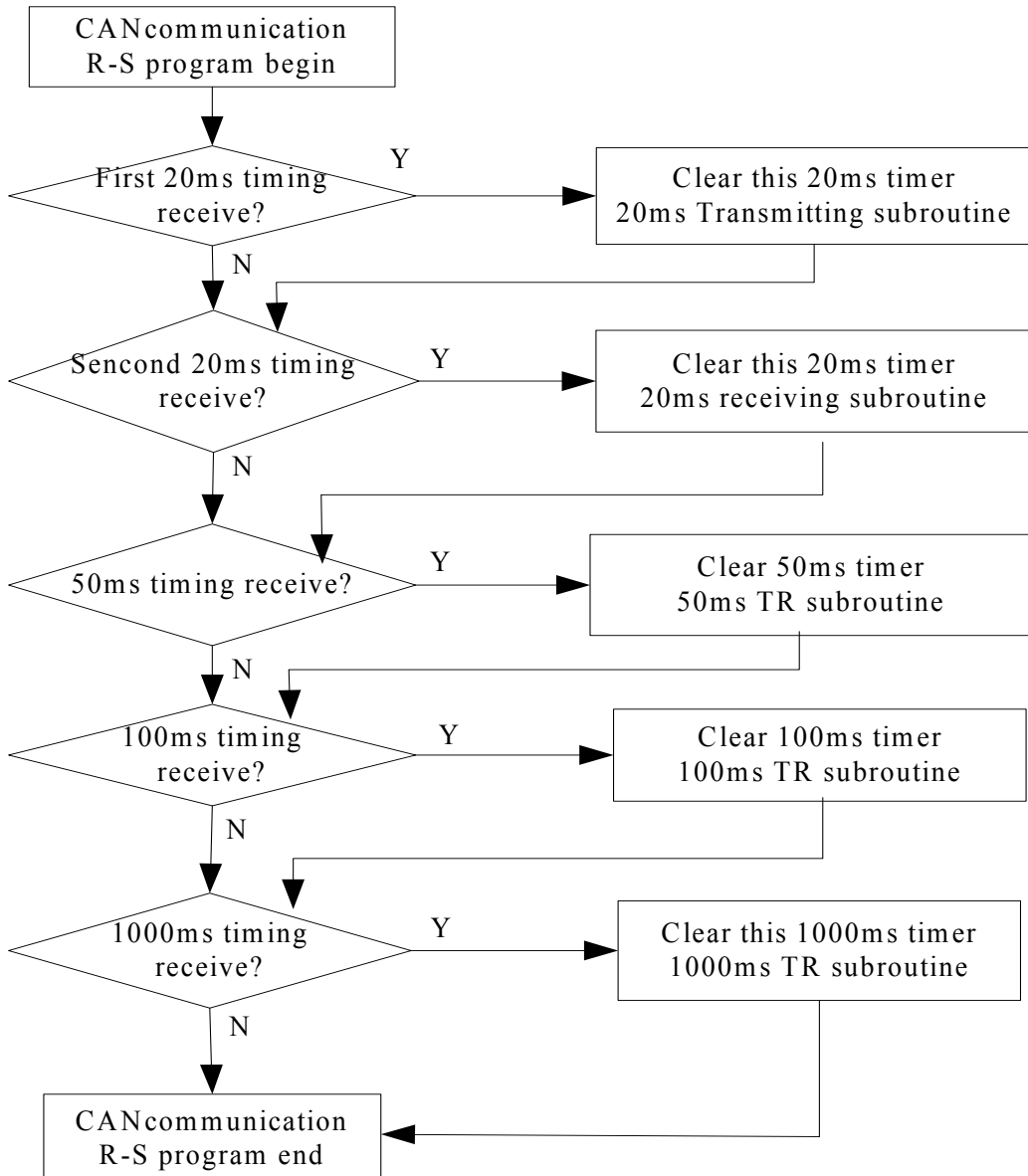


Fig. 5. Flowchart of time-sharing program

The setting of response time of parameters should consider these two conditions.

1. Interrupt trigger is used in the events that need handle immediately. For example, control instruction between HCU and EMS, and calibration instructions between HCU and calibration tools.
2. Considering the response time of control parameters are different, as shown in Table.3. CAN messages are divided into four degrees, 20ms, 50ms, 100ms, 1000ms. At the same time, the priorities of these tasks raise when communication period become short.

Parameter	response time
Pedal signal	10ms
Brake signal	10ms
Speed of engine	20ms
Speed of vehicle	1000ms
State of charge(SOC)	1s
Torque of driver motor	20ms
Torque of engine	20ms

Table 3. Response time of control parameters

The new structure of CAN communication is shown in Fig.6. Priority assignment is applied in this new structure. Each task is triggered by event interrupt. If there are two or more tasked triggered at the same time, the task of higher priority is responded firstly. Multi-task method can optimizes the resource of HCU, and supplies an effective means to extend CAN communication program.

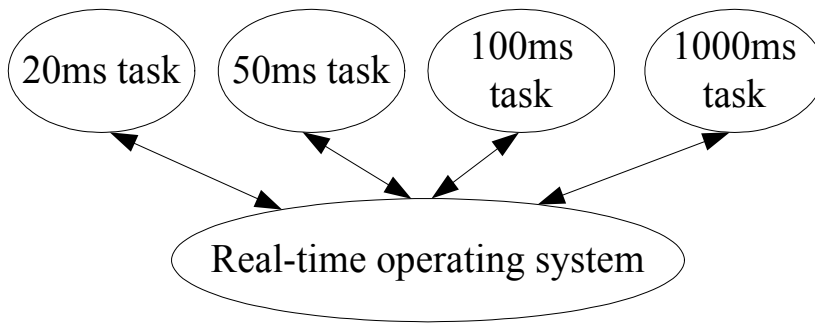


Fig. 6. Structure of CAN communication in the RTOS

4.3 CAN bus road rate analysis

The average road rate of CAN bus is defined as the sum total of each communication flame transmitting occupy in bus. It is conducted one equation as following:

$$U_t = \sum_{j=1}^m (S_j \times \tau) / T_j \tag{1}$$

In which, U_t is road rate of whole bus, T is TR period of each communication flame, τ is bit time of CAN data transmitting, S_m is maximum number of TR data bit, m is the number

of all communication frames. According to CAN2.0B and J1939, the data can be calculated by Table 4.

If there are i bytes data in one CAN frame, from the definition and specification of CAN 2.0B, the maximum number of stuff bits of one frame can be calculated by equation as follow:

$$\frac{54 + 8i}{5} \quad (1)$$

The maximum bits of each frame TR can be calculated by following equation [7]:

$$s = \frac{54 + 8i}{5} + 67 + 8i \quad (2)$$

In which, i is the bytes data of each frame TR. The bit time τ is 4us, when baud rate is 250Kb/s. From equation (1) and equation (2), the maximum road rate can be calculated is about 28.05%, which is enough for bus communication.

	Extend CAN (number of bits)	Bit stuffing?
Start of Frame	1	yes
Arbitration Field	11+1+1+18+1=32	yes
Control field	6	yes
Data field	8*i	yes
CRC	15	yes
CRC delimiter	1	no
ACK field	2	no
EOF	7	no

Table 4. Data frame of CAN message

4.4 CAN Calibration Protocol (CCP)

One of important parts for multi-node CAN bus design is CCP driver. CCP is a CAN based application protocol for calibration and measurement data acquisition of ECUs. It is accepted by many corporations such as VECTOR, DSPACE, ETAS, and become standardization.

CCP driver is needed for ECU which parameters can be calibrated. A CCP driver software is integrated in the infra program of HCU. A basic implementation of CCP driver needs only a few control unit resources such as RAM, ROM, and CPU time. The CCP driver occupies two CAN buffers, which should be assigned low bus priority to avoid influencing other bus communication [8]. The trigger mode of CCP driver is interrupt mode. CCP driver is the foundation of calibration platform. The calibration platform structure is shown as Fig.7. CCP driver achieves data upload, download and calibration of controlled parameters. This calibration system provided reliable, accurate and quickly CAN communication between calibration platform and ECU. It has been used successfully in HEV controlled system.

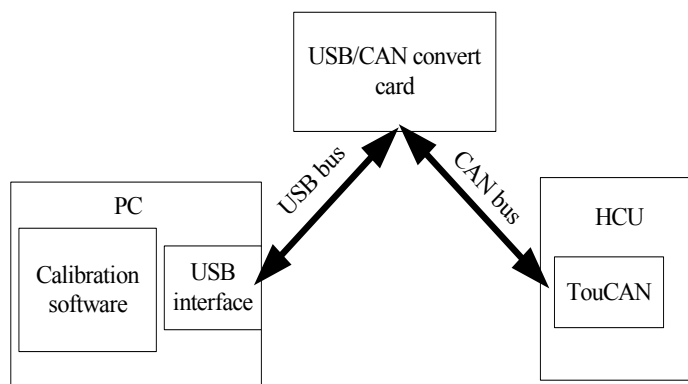


Fig. 7. Structure of CCP Calibration platform

5. Verify

The verify tests of CAN bus include three parts: Single module verify, hardware in loop (HIL) simulation test, and bench test.

5.1 Single module verify

The structure of single module verification is shown as Fig.8. CAN transmitting and receiving (TR) program of single module is carried out in personal computer (PC). The communication between USB/CAN card and single ECU, can verify the CAN hardware function and transmitting and receiving subroutine of the ECU. Single module verification can find the error of hardware or infra TR program as early as possible, which makes well preparation for subsequent tests.

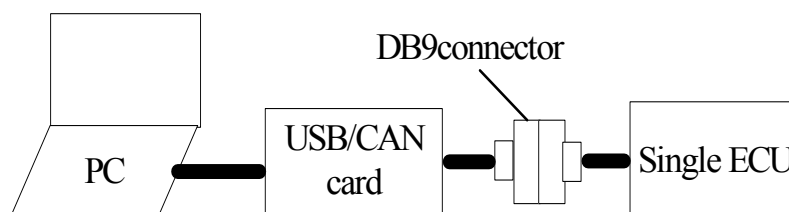


Fig. 8. Structure of single control module

5.2 Hardware in the loop test

Hardware in the loop test is one of important steps in controller design [9]. The structure of HIL simulation is shown in Fig.9. In HIL system are divided into two important parts: Simulation ECU and upper program of PC. The models of HEV (include engine model, motor model, battery model, ADM model and vehicle model) and monitoring interface are handled in the PC. Communication between HCU and simulation ECU is CAN communication, which uses USB/CAN converter card. The interface of monitoring is developed by Labview. This method of HIL has many advantages. It avoids double RAM communication. The ability of PC could be achieved as vehicle models that are computed in the PC. Multi-thread technology is used in the program design to reduce the response time of communication.

Hardware function can be tested by HIL test. CAN data can display clearly in the monitoring interface. So data communicated can be checked easily. And debug schedule can be quickly. HIL test shows that HCU operates normally, and sampling of sensor's signals are real time, output signals are accurate, and the CAN communication is reliable.

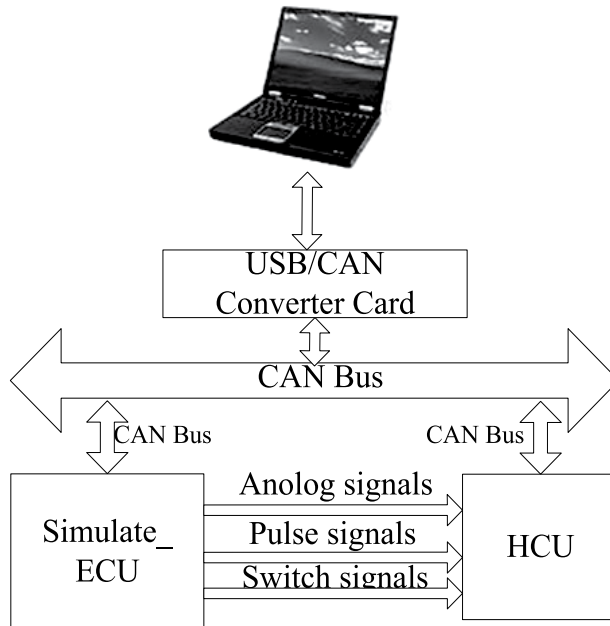


Fig. 9. Block diagram of hardware in the loop

5.3 Bench test

The multi-node test of CAN bus is applied in the bench test of HEV. HCU, EMS, ADM, DMCM and BPCM are concluded. Each ECU simulates the HEV running state, the CAN communication is tested in HEV bench. Figure 10 shows one curve of bench test, which include stages of motor starts engine and motor helps engine.

A reliable CAN bus could be verified from the engine running and monitoring data. The results of bench test shows that CAN hardware circuit has reliability and ability of anti-jamming. At the condition of 2600 rpm engine speed, four CAN nodes work normally. The real time communication between HCU and EMS or BPCM or other node can be achieved. What's more, the calibration instruction and monitoring instruction can be realized regularly. The CAN communication is reliable and real time.

6. Conclusion

A multi-node CAN bus is designed based on CAN 2.0B and J1939. The structure of HEV control system is introduced. According to the requirement of control system, a CAN topology is developed. The methods of hardware and software design of CAN bus are discussed. Based on the 32-bit MC68376, power isolation and optoelectronic isolation are applied in the hardware design of CAN communication circuit. The design methods of software algorithmic are emphasized. Buffer sharing and time sharing are applied in the

program design of CAN bus. The idea of multi-task is introduced. Task assignment and scheduler could optimize the real time of CAN communication, by event interrupt. Road rate of multi-node CAN bus is analyzed. In order to calibrate the ECU, the CCP driver is designed, which can achieve the data upload and download for calibration.

There are many tests to verify the multi-node CAN bus, single module test, HIL test and bench test. The multi-node CAN bus design can be accomplished quickly through these tests. All tests showed that the hardware and software design of multi-node CAN bus could meet the requirements of HEV system. The quality of CAN communication is reliable and real time.

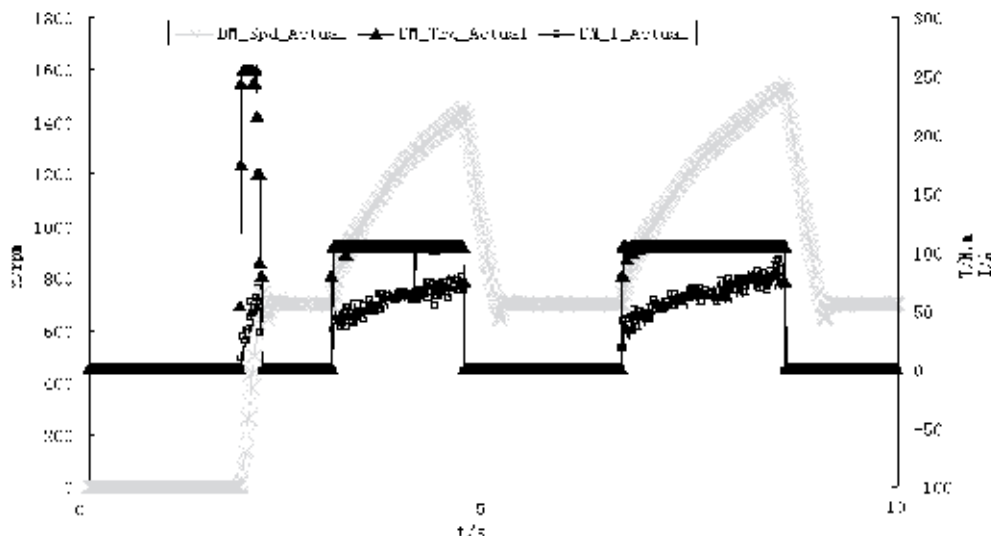


Fig. 10. Curve of bench test

7. Acknowledgement

The authors could like to acknowledge Xu Jian for his assistance in the project.

8. References

- [1] Robert B G. CAN Specification Version 2.0. 1991.
- [2] Massimo C., Paolo C., et al. CAN_LabView based development platform for fine-tuning hybrid vehicle management systems. IEEE, 2005; p433-438
- [3] Dai X. H., Zhu J. X., Peng Y. G., et al. Development of EV control system communication based on CAN bus[J]. Application of Electronic technology, 2004, 8; p37-39
- [4] Yao Z., Liu F. M., Li Y. X.. Design of Node in CAN Bus for Hybrid Electric Vehicle. Computer and Communications, 2005, 5; p121- 123
- [5] Society of Automotive Engineering INC. Data Link Layer (1994-07). <http://www.sae.org>
- [6] Motorola INC. MC68336/376 User's Manual. <http://www.freescale.com>
- [7] Roger Johansson, Jan Torin. On calculating guaranteed message response times on the SAE J1939 bus. Chalmers Lindholmen University College. Report no.10, Feb. 2002

- [8] J-X Wang, J Feng, X-J Mao, L Yang, B Zhuo. Development of a new calibration and monitoring system for invehicle electric control units based on controller area network calibration protocol. Proc. IMechE vol.219 PartD: J. Automobile engineering:p1381-1389
- [9] Tang H. B., Gong Y. M., Tan W. C., Zhuo B. The hardware design of Hardware-in-Loop Simulation System of Diesel Engine High Pressure Common-Rail ECU Based on CAN Bus. Vehicle Engine.No.1:p24-28

Sugeno Inference Perturbation Analysis for Electric Aerial Vehicles

John T. Economou and Kevin Knowles
Intelligent Propulsion and Emissions Laboratory
Aeromechanical Systems Group
Cranfield University, Defence Academy of the United Kingdom
UK

1. Introduction

The Chapter is focusing in the area of the Electrically-powered Unmanned Aerial Vehicles (UAVs) in association to bounded sensor noise. The increased requirements for airworthiness and safety of such vehicles have resulted in the requirement of improving the analytical methods for subsystem level mathematical modelling, such as for example the electrical propulsion system. The Takagi-Sugeno fuzzy inference has been formulated in the context of bounded multi-sensor errors for a range of error classes. The modelled system is an electrical propulsion system together with the associated sensor boundaries in relation to a typical UAV operation.

Unmanned aerial vehicles have been used in various operational conditions where other vehicles fail to operate. UAVs have been used to inspect hazardous areas such as flooded areas, earthquake areas, and generally areas that may have a high risk of radioactive contaminants. The immediate result of the effective use of UAVs is reducing the risk of endangering human lives while still capable of operating safely and efficiently. This chapter addresses the issue of sensor operational boundaries and the UAV's electrical thruster parametric variation due to altitude variations. UAVs normally operate over a range of altitudes Kladis et al. (2010) depending on their operational role. Hence, these can be exposed to a range of temperature conditions which can affect their normal operation. This chapter addresses this specific consideration which can have airworthiness implications, and focuses on the description of the electrical permanent magnet direct current thrusters in the context of UAVs and operations .

The UAV's propulsion options can vary depending on the user and operational requirements, however the focal point for the work described in this chapter is for an electrical thruster system. Such systems being supplied from a fuel cell are described in more detail in Karunaratne et al. (2007). In particular, the work in Karunaratne et al. (2007), describes for a given example UAV operation the effectiveness of the electric propulsion option together with the importance of a sophisticated power management system utilising intelligent based methods. In Miller (2004), the propulsion system options are described within the context of power and energy and thus assist towards the importance of electro-mechanical systems for propulsion. In Ehsani et al. (2005), the authors

contribute towards a structured approach towards the theory of propulsion systems and the general design considerations surrounding these systems. Both resources together with this chapter will enhance the readers' awareness towards the power and energy design considerations in relation to sensing and the boundaries that these systems have when related to UAV operations.

In particular in this chapter, the electrical thruster is modelled as an ordinary differential equation which can operate in either motoring or generator mode depending on the operational shaft angular velocity and the motor torque. The theoretical parts present the Sugeno fuzzy inference in association to the fuzzy-hybrid concept developed by Economou & Colyer (2005). The latter is demonstrated from the simulated behaviour of the PMDC thruster. Part of the electrical thruster, based on Economou & Colyer (2005) can be presented in an ordinary differential equation representation while when the UAV altitude is included then the model exerts partially a Sugeno type fuzzy behaviour. The collection of these behaviours is shown in this chapter.

In effect part of the thruster is modelled utilising physical system modelling methods while the remaining part of the system is modelled using an intelligent based method (fuzzy logic). Overall the thruster is a fuzzy-hybrid system as per Economou & Colyer (2005). In particular, the fuzzy inference system utilised in this chapter is a Sugeno system Sugeno (1999).

Furthermore when a system is realised in practice it is also highly likely to contain some deviations from its nominal measurements Economou et al. (2007). The sensors are expected due to operational temperature variations for example to incorporate an error deviating from the nominal value. For the UAV electrical thruster the consequence is that the thruster angular velocity will tend to deviate from the expected nominal value and this could lead to loss of aerodynamic propeller thrust and can therefore lead to airworthiness and safety implications. This chapter clearly shows that the thruster's angular velocity can vary from its nominal (expected value), when the additional effects of sensor error boundaries and temperature variation (due to altitude), are both included in the mathematical modelling. The resulting analysis is demonstrated for a given operational UAV scenario, indicating that the percentage errors exceeded the value of 20% over the nominal value for the armature thruster's resistance.

2. Analysis

2.1 Sugeno output perturbation

Fuzzy logic is a methodology which results in representing a system or controlling a system using If-Then rules. For the purpose of this Chapter a Sugeno type inference is utilised as a modelling tool. The system n -th rule can be represented as follows:

$$\begin{array}{c}
 n: \text{ IF } \underbrace{z_1 \text{ is } Z_n^1 \text{ AND } z_2 \text{ is } Z_n^2 \text{ AND } \dots z_j \text{ is } Z_n^j \dots}_{\text{Antecedent}} \\
 \dots \text{ THEN } \underbrace{h_n = f_n(z_1, z_2, \dots, z_j)}_{\text{Consequent}}
 \end{array}$$

The membership functions represent the belonging of the sampled variable at a specific time instant $t = \tau$ to the specific membership function Z_n^j for rule (n) and sensor (j). The corresponding (j -th) membership functions which are not the left and right edge membership functions are Gaussian type functions (1):

$$Z_n^j(z_j) = e^{-\frac{(z_j - c_j)^2}{d_j}} \tag{1}$$

(1) is valid for $n = 2, 3, \dots, n_{\max} - 1$ i.e. the membership functions representing the centred membership functions. The left edge ($n=1$) and right edge ($n=n_{\max}$) are sigmoid type of membership functions. These are given from the following expressions (2a) and (2b):

$$Z_1^j = \begin{cases} Z_1^j = \frac{1}{1 + e^{z_j}} \end{cases} \tag{2a}$$

$$Z_{n_{\max}}^j = \begin{cases} Z_{n_{\max}}^j = \frac{1}{1 + \eta e^{-z_j}} \end{cases} \tag{2b}$$

The graphical illustration of the membership functions is shown next in Figure 1 for the j -th sensor.

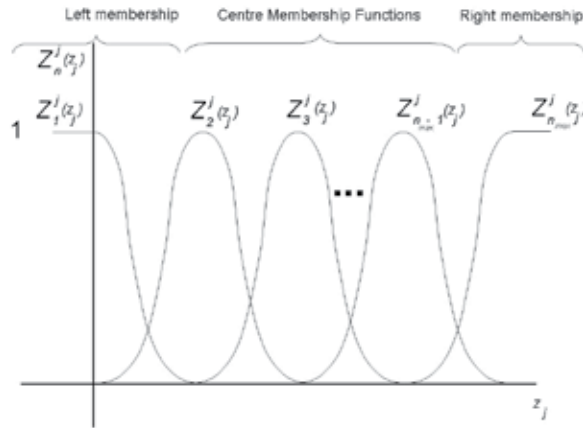


Fig. 1. Generalised Membership Functions for the j -th sensor

The polynomial for each Sugeno rule is given from the following expression (3):

$$\forall n : h_n := b_n + \sum_{j=1}^{j_{\max}} \varsigma_{jn} z_j \tag{3}$$

Based on the general Sugeno rule description the resulting defuzzyfied output is given from the following expanded equation (4) for time $t = \tau$ which represents the nominal system response:

$$H^*(\tau) = \frac{\gamma_1 h_1 + \gamma_2 h_2 + \dots + \gamma_{n_{\max}} h_{n_{\max}}}{\gamma_1 + \gamma_2 + \dots + \gamma_{n_{\max}}} = \frac{\sum_{n=1}^{n_{\max}} \gamma_n h_n}{\sum_{n=1}^{n_{\max}} \gamma_n} \quad (4)$$

The antecedent “AND” operator results into the following expressions (5):

$$\begin{aligned} \gamma_1 &= Z_1^1(z_1).Z_1^2(z_2).Z_1^3(z_3) \dots Z_1^{j_{\max}}(z_{j_{\max}}) \\ \gamma_2 &= Z_1^1(z_1).Z_2^2(z_2).Z_2^3(z_3) \dots Z_2^{j_{\max}}(z_{j_{\max}}) \\ \gamma_3 &= Z_1^1(z_1).Z_1^2(z_2).Z_3^3(z_3) \dots Z_3^{j_{\max}}(z_{j_{\max}}) \\ \gamma_4 &= Z_1^1(z_1).Z_2^2(z_2).Z_1^3(z_3) \dots Z_1^{j_{\max}}(z_{j_{\max}}) \\ \gamma_5 &= Z_1^1(z_1).Z_2^2(z_2).Z_1^3(z_3) \dots Z_2^{j_{\max}}(z_{j_{\max}}) \\ \gamma_6 &= Z_1^1(z_1).Z_2^2(z_2).Z_1^3(z_3) \dots Z_3^{j_{\max}}(z_{j_{\max}}) \\ &\vdots \\ &\vdots \\ &\vdots \\ \gamma_{n_{\max}} &= Z_{n_{\max}}^1(z_1).Z_{n_{\max}}^2(z_2).Z_{n_{\max}}^3(z_3) \dots Z_{n_{\max}}^{j_{\max}}(z_{j_{\max}}) \end{aligned} \quad (5)$$

From (5) it can be deduced that if the “left” edge triggers only uniformly for all rules (n_{\max}), then the following equality (6) holds:

$$\gamma_1 = Z_1^1(z_1).Z_1^2(z_2).Z_1^3(z_3) \dots Z_1^{j_{\max}}(z_{j_{\max}}) \quad (6)$$

It can also be deduced that if a “right” edge trigger only triggers then the following equality holds (7):

$$\gamma_{n_{\max}} = Z_{n_{\max}}^1(z_1).Z_{n_{\max}}^2(z_2).Z_{n_{\max}}^3(z_3) \dots Z_{n_{\max}}^{j_{\max}}(z_{j_{\max}}) \quad (7)$$

For all other remaining conditions the following “centred” rules can trigger as shown from the set of equations in (8):

$$\begin{aligned} \gamma_2 &= Z_1^1(z_1).Z_1^2(z_2).Z_1^3(z_3) \dots Z_2^{j_{\max}}(z_{j_{\max}}) \\ \gamma_3 &= Z_1^1(z_1).Z_1^2(z_2).Z_1^3(z_3) \dots Z_3^{j_{\max}}(z_{j_{\max}}) \\ \gamma_4 &= Z_1^1(z_1).Z_2^2(z_2).Z_1^3(z_3) \dots Z_1^{j_{\max}}(z_{j_{\max}}) \\ \gamma_5 &= Z_1^1(z_1).Z_2^2(z_2).Z_1^3(z_3) \dots Z_2^{j_{\max}}(z_{j_{\max}}) \\ \gamma_6 &= Z_1^1(z_1).Z_2^2(z_2).Z_1^3(z_3) \dots Z_3^{j_{\max}}(z_{j_{\max}}) \\ &\vdots \\ \gamma_{n_{\max}-1} &= Z_{n_{\max}-1}^1(z_1).Z_{n_{\max}-1}^2(z_2).Z_{n_{\max}-1}^3(z_3) \dots Z_{n_{\max}-1}^{j_{\max}}(z_{j_{\max}}) \end{aligned} \quad (8)$$

2.2 Sugeno output perturbation models

Based on the research work in Economou & Colyer (2005) it can be deduced that the preferred architecture of a fuzzy-hybrid is the following equation (9):

$$y = f_1(\underline{p})u_1 + f_2(\underline{p})g(u_2)H^* + f_3(\underline{p}) \tag{9}$$

Where $f_1(\underline{p}), f_2(\underline{p}), f_3(\underline{p})$ are the parametric functions with respect to a vector p . u_1, u_2 are the fuzzy-hybrid system inputs. And $g(u_2)$ is a function of the input u_2 . The mathematical expression (9) will be associated to the electric propulsion equation. The (H^*) term represents the fuzzy Sugeno non-singleton type system which will associate to sensor perturbations $\delta\beta_n = \varepsilon_n$ and thus observe how key variables can potentially drift from their expected nominal value for given conditions. Hence, by incorporating the work in Economou et al. (2007), the Singleton type inference is provided from the following equation:

$$H_+^* = \frac{\sum_{n=1}^{n_{\max}} \gamma_n h_n + \sum_{n=1}^{n_{\max}} (\gamma_n \delta\beta_n)}{\sum_{n=1}^{n_{\max}} \gamma_n} \tag{10a}$$

$$H_-^* = \frac{\sum_{n=1}^{n_{\max}} \gamma_n h_n - \sum_{n=1}^{n_{\max}} (\gamma_n \delta\beta_n)}{\sum_{n=1}^{n_{\max}} \gamma_n} \tag{10b}$$

Which assumes that (11) is true for (10a) and (10b).

$$\sum_{j=1}^{j_{\max}} \varsigma_{jn} z_j \neq 0 \tag{11}$$

Where the term $\delta\beta_n$ is the perturbation for the n-th rule for the given antecedent conditions.

2.3 Static error bound models

2.3.1 Class of Static Isotropic Error Bounds (SIEB)

For this class of errors we have a set with lower and upper bounds for each sensor (j), $S_1 : \varepsilon_j \in [\underline{\varepsilon}_j, \bar{\varepsilon}_j]$. These errors are valid for the entire observation interval $t \in [0, t_f]$. For this class of errors it is possible that the errors for each sensor (j) are equal. Hence we could have the special case that for the sets,

$$S_1 : \varepsilon_1 \in [\underline{\varepsilon}_1, \bar{\varepsilon}_1] = [-\bar{\varepsilon}_1, \bar{\varepsilon}_1], \varepsilon_2 \in [\underline{\varepsilon}_2, \bar{\varepsilon}_2] = [-\bar{\varepsilon}_2, \bar{\varepsilon}_2], \dots, \varepsilon_j \in [\underline{\varepsilon}_j, \bar{\varepsilon}_j] = [-\bar{\varepsilon}_j, \bar{\varepsilon}_j],$$

$$\underline{\varepsilon}_1 = \underline{\varepsilon}_2 = \dots = \underline{\varepsilon}_j, \bar{\varepsilon}_1 = \bar{\varepsilon}_2 = \dots = \bar{\varepsilon}_j,$$

Although it is more often the case that the following condition will be true:

$$\underline{\varepsilon}_1 \neq \underline{\varepsilon}_2 \neq \dots \neq \underline{\varepsilon}_j, \bar{\varepsilon}_1 \neq \bar{\varepsilon}_2 \neq \dots \neq \bar{\varepsilon}_j.$$

2.3.2 Class of Static Anisotropic Error Bounds (SAEB)

In the case the upper and lower bound errors are considered to be anisotropic which therefore result in the following condition:

$$S_2 : \varepsilon_1 \in [\underline{\varepsilon}_1, \bar{\varepsilon}_1], \varepsilon_2 \in [\underline{\varepsilon}_2, \bar{\varepsilon}_2] \dots \varepsilon_j \in [\underline{\varepsilon}_j, \bar{\varepsilon}_j], \varepsilon_1 \neq -\bar{\varepsilon}_1, \varepsilon_2 \neq -\bar{\varepsilon}_2, \dots, \varepsilon_j \neq -\bar{\varepsilon}_j$$

2.3.3 Class of Static Clustered Isotropic Error Bounds (SCIEB)

For this particular class of systems identical classes of sensors can be used in order to acquire experimental data. For these cases the numbering order of the sensors will result in a unique system representation. Hence the following figure can be used in order to refer to a selection of choices,

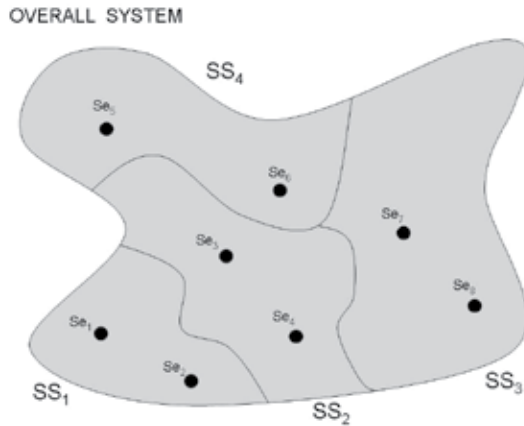


Fig. 2. SCIEB representation for a Generalised System with 8 sensors (Se) and 4 clusters (SS).

For this system the following expression exists:

$$\begin{aligned} SS_1 : \varepsilon_1 \in [\underline{\varepsilon}_1, \bar{\varepsilon}_1], \varepsilon_2 \in [\underline{\varepsilon}_2, \bar{\varepsilon}_2], \varepsilon_1 = -\bar{\varepsilon}_1 = \underline{\varepsilon}_2 = -\bar{\varepsilon}_2 \\ SS_2 : \varepsilon_3 \in [\underline{\varepsilon}_3, \bar{\varepsilon}_3], \varepsilon_4 \in [\underline{\varepsilon}_4, \bar{\varepsilon}_4], \varepsilon_3 = -\bar{\varepsilon}_3 = \underline{\varepsilon}_4 = -\bar{\varepsilon}_4 \\ SS_3 : \varepsilon_7 \in [\underline{\varepsilon}_7, \bar{\varepsilon}_7], \varepsilon_8 \in [\underline{\varepsilon}_8, \bar{\varepsilon}_8], \varepsilon_7 = -\bar{\varepsilon}_7 = \underline{\varepsilon}_8 = -\bar{\varepsilon}_8 \\ SS_5 : \varepsilon_5 \in [\underline{\varepsilon}_5, \bar{\varepsilon}_5], \varepsilon_6 \in [\underline{\varepsilon}_6, \bar{\varepsilon}_6], \varepsilon_5 = -\bar{\varepsilon}_5 = \underline{\varepsilon}_6 = -\bar{\varepsilon}_6 \end{aligned}$$

Figure 2 for the same system, sensors and clusters is not unique because it is based on the ordering of the subsystems and the ordering of the individual sensors.

2.4 Dynamic error bound models

The dynamic error bounds are time based and therefore represent the variation in a polynomial form and can be similarly divided into three main categories similar to the static case but with the error bounds being represented in a polynomial form. These are divided into the Class of dynamic isotropic error bounds (DIEB), Class of dynamic anisotropic error bounds (DAEB), Class of dynamic clustered isotropic error bounds (DCIEB). The results shown for the UAV application are based on the SIEB type of errors for illustration purposes.

2.5 Relation of sugeno perturbation and error type classification

For the SIEB type of perturbation equations (10a) and (10b) hold, while for the case of SAEB the perturbations are unequal for each sensor and therefore the following expression holds:

$$Z_+^* = \frac{\sum_{n=1}^{n_{max}} \gamma_n I_n + \sum_{n=1}^{n_{max}} (\gamma_n \delta\beta_n^+)}{\sum_{n=1}^{n_{max}} \gamma_n} \tag{12a}$$

$$Z_-^* = \frac{\sum_{n=1}^{n_{max}} \gamma_n I_n - \sum_{n=1}^{n_{max}} (\gamma_n \delta\beta_n^-)}{\sum_{n=1}^{n_{max}} \gamma_n} \tag{12b}$$

$$\delta\beta_n^+ \neq \delta\beta_n^- \tag{12c}$$

Where $\delta\beta_n^+ \neq \delta\beta_n^-$ corresponds to the asymmetry of the perturbations in the consequent fuzzy component. Subject to the constraint (12d):

$$\sum_{j=1}^{j_{max}} \varsigma_{jn} z_j \neq 0 \tag{12b}$$

2.6 Application: Electric aerial vehicle propulsion system

2.6.1 System description

The system is an unmanned aerial vehicle electrical propulsion permanent magnet system linked via a gearbox to the propeller. It is assumed that suitable power electronics/controls and energy sources are in place for supplying the electrical thrusters. The aerial vehicle is capable of flying over a range of altitudes and therefore the thrusters and propeller are capable of meeting a range of angular velocity and load torque demands.

2.6.2 Mathematical problem modelling

The electric machine (permanent magnet d.c.) is modelled as a dual mode ordinary differential equation representing using fuzzy switching the two operational modes.

Case 1: Motoring mode (Torque , speed quadrants 1,3):

$$V_a(t) = K_a \omega(t) + R_a i_a(t) + L \frac{di_a(t)}{dt} \tag{13a}$$

Case 2: Generator mode (Torque, speed quadrants 2,4):

$$E_a(t) = V_a(t) + R_a i_a(t) + L \frac{di_a(t)}{dt} \tag{13b}$$

For case 1, an applied external voltage is required in order to provide rotor motion while also the motor provided torque is sufficient to drive at any given time the applied load and

mathematically presented in (13a). For case 2, the expression is shown in (13b) while the rotor is rotating due to an external mechanical force (generation) as long as the back *emf* voltage is higher than V_a then generation occurs (it is assumed that the power electronics will satisfactory re-root the power back into a rechargeable battery source and therefore store energy). For both modes the following equations are valid. The motor back *emf* is provided from (13c):

$$E_a = K_a \omega(t) \quad (13c)$$

The rotor angular velocity is given from (13d):

$$\frac{d\theta(t)}{dt} = \omega(t) \quad (13d)$$

The motor shaft torque is given from (14):

$$T_m(t) = i_a(t)K_T \quad (14)$$

The motor supplied torque is linked to the mechanical system load as shown next (15):

$$T_m(t) = (J_a + J_L \left(\frac{N_1}{N_2}\right)^2) \frac{d^2\theta}{dt^2} + (B_a + B_L \left(\frac{N_1}{N_2}\right)^2) \frac{d\theta}{dt} \quad (15)$$

Revisiting the equations from case 1 and case 2 can both be generalised and result in equation (16):

$$V_a(t) = K_a \omega(t) + \text{sign}(P_m) \cdot R_a i_a(t) + \text{sign}(P_m) \cdot L \frac{di_a(t)}{dt} \quad (16)$$

The “*sign*” function is provided as shown next in (17):

$$\text{sign}(P_m) = \begin{cases} +1 & P_m > 0 \\ 0 & P_m = 0 \\ -1 & P_m < 0 \end{cases} \quad (17)$$

Alternatively the *sign* function can also be approximated to equation (18):

$$\text{sign}(P_m(t)) \approx \frac{P_m(t)}{\sqrt{(P_m(t))^2 + \rho^2}} = \psi(P_m(t), \rho), \rho \in \mathfrak{R}^+ \quad (18)$$

The variable P_m is the mechanical motor power. Modes 1 and 2 from (16) and equation (18) will result in the following expression (19).

$$V_a(t) = K_a \omega(t) + \frac{P_m(t)}{\sqrt{(P_m(t))^2 + \rho^2}} R_a i_a(t) + \frac{P_m(t)}{\sqrt{(P_m(t))^2 + \rho^2}} L \frac{di_a(t)}{dt} \quad (19)$$

Allowing an armature resistance variation with reference to the aerial vehicle altitude (h) and environmental conditions such as air moisture parameter (ξ) given from equation (20):

$$R_a = R_{ref}[1 + \alpha_c(T - T_{ref})] = f(\zeta, \xi) \tag{20}$$

Hence by combining the results from (19) and (20) the following expression is obtained (21):

$$V_a(t) = K_a\omega(t) + \frac{P_m(t)}{\sqrt{P(t)_m^2 + \rho^2}} i_a(t)f(\zeta, \xi) + \frac{P_m(t)}{\sqrt{P(t)^2 + \rho^2}} L \frac{di_a(t)}{dt} \tag{21}$$

This can be simplified to equation (22):

$$V_a(t) = \underbrace{K_a\omega(t)}_{\text{Term 1}} + \underbrace{\psi(P_m(t), \rho)i_a(t)f(\zeta, \xi)}_{\text{Term 2}} + \underbrace{\psi(P_m(t), \rho)L \frac{di_a(t)}{dt}}_{\text{Term 3}} \tag{22}$$

With reference to equation (22), term 1 represents the mechanical equivalent voltage which causes the aircraft propeller to rotate. Term 2, corresponds to the motor windings copper voltage loss which is temperature-sensitive, due to a change of aircraft altitude and air moisture for example. The third term relates to the propeller motor thrust equivalent voltage. When a change of thrust is required for the same shaft angular velocity, then the current will vary with time and therefore the inductive element will become active. The ordinary differential equation with respect to the thruster armature current is given from (23):

$$\frac{di_a(t)}{dt} = -\frac{1}{\psi(P_m(t), \rho)L} (K_a\omega(t) - \psi(P_m(t), \rho)i_a(t)f(\zeta, \xi)) + \frac{1}{\psi(P_m(t), \rho)L} V_a(t) \tag{23}$$

Equation (23) as time $t \rightarrow 0$ can be simplified to the following expression (24a):

$$V_a(t) = K_a\omega(t) + \psi(P_m(t), \rho)f(\zeta, \xi)i_a(t) \tag{24a}$$

Equation (24) can be rearranged to obtain the EPS angular velocity (24b).

$$\omega(t) = -\psi(P_m(t), \rho)f(\zeta, \xi) \frac{1}{K_a} i_a(t) + \frac{1}{K_a} V_a(t) \tag{24b}$$

When (24b) is compared to the fuzzy-hybrid topology shown in (9) the following equalities are valid:

$$\begin{aligned} y &= \omega(t) \\ f_1(\underline{p}) &= \frac{1}{K_a} \\ u_1 &= V_a(t) \\ f_2(\underline{p}) &= -\frac{\psi(P_m(t), \rho)}{K_a} \\ f_3(\underline{p}) &= 0 \\ g(u_2) &= i_a(t) \\ H^* &= f(\zeta, \xi) \end{aligned} \tag{24}$$

2.6.3 Electrical propulsion power consumers

The electrical propulsion system has several power consumers. In order to illustrate these, the power flow equation needs to be considered first which relates the input thruster power to the power consumers.

The power inserted to the electrical actuator $P_a(t)$ is provided from the following expression (25):

$$P_a(t) = \underbrace{K_a \omega(t) i_a(t)}_{\text{Term1}} + \underbrace{\psi(P_m(t), \rho) i_a^2(t) f(\zeta, \xi)}_{\text{Term2}} + \underbrace{\psi(P_m(t), \rho) L \frac{di_a(t)}{dt} i_a(t)}_{\text{Term3}} \quad (25)$$

In equation (25) term 3 is normally non-zero when there is a change in thrust and therefore armature current and can be neglected for quasi-static conditions. Term 2 represents the conductive armature resistance losses while the useful power is the mechanical power shown as term 1. Normally, the following inequality (26) is desired:

$$K_a \omega(t) i_a(t) \gg \psi(P_m(t), \rho) i_a^2(t) f(\zeta, \xi) + \psi(P_m(t), \rho) L \frac{di_a(t)}{dt} i_a(t) \quad (26)$$

However in practice efficiencies can vary depending on the angular velocity and loading over a wide operational envelope. For a UAV application the expected efficiencies are typically very high due to the near to optimum angular velocity operation.

2.7 Sensor class and simulation demonstration of implications to the electric application

For the Unmanned Aerial Vehicle (UAV) application our objective is to investigate the effects that the user implicitly incurs to the UAV. In particular when the UAV operator, due to mission requirements, selects to change altitude in the range of 0-6km, for example, then the ambient temperature conditions can cause the temperature to drop several degrees (K) per 1000m increase in altitude (7K/km) for given moisture conditions.

Consequently, the electrical propulsion system will experience a temperature drop which results in variation of the coil armature resistance. Therefore, the angular velocity of the propulsion will be affected thus resulting in further changes to the UAV propeller thrust.

The purpose of this analysis is to demonstrate the effects of these variations and error tolerance in the temperature sensing and show how these can affect UAV performance via the loss of thrust. Figure 3 illustrates this:

The exogenous altitude variations represent the source of altitude and air moisture which both affect the ambient temperature and therefore both can affect the UAV operation and deviate this from its nominal (or expected) behaviour due to variations in the Electrical Propulsion System (EPS).

Although Figure 3, shows four interconnections in essence these are repetitive. After the first sequence from stage 1 to 4 has lapsed then the operator does receive visual feedback and therefore reacts in order to compensate according to the mission plan. Therefore, the effects of the EPS parametric variation and the effects of the perturbation for the temperature sensing boundaries will be investigated, as shown in Figure 4.

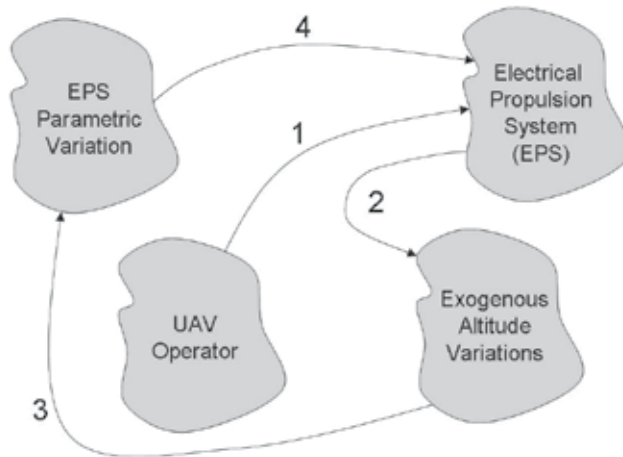


Fig. 3. UAV operator and EPS performance for varying altitudes

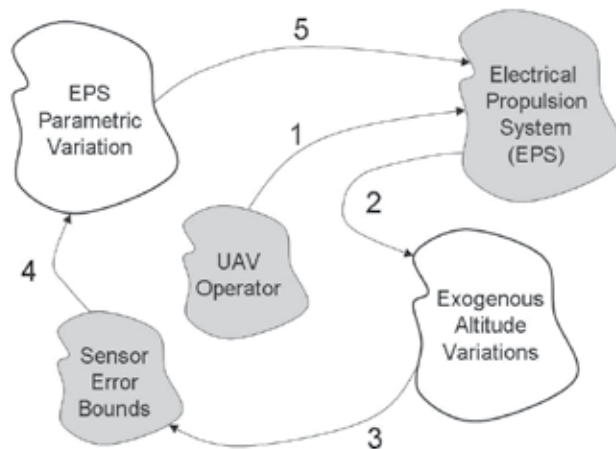


Fig. 4. EPS Parametric Variation and Exogenous Altitude Variations

The proposed simulation block diagram for the UAV which incorporates a perturbation and the fuzzy-hybrid model for the UAV thrusters is presented as shown next in Figure 5:

Figure 6 shows the system’s operational requirements for a near to sea level UAV altitude thus having overall a constant armature resistance. Figure 6. shows a similar block diagram which includes the UAV Altitude Profile, UAV “dry/moist” profile which provide an estimate for the perturbed temperature via a Sugeno-type Fuzzy Inference System (FIS). The armature resistance variation with temperature and the electrical thrusters are based on physical system modelling. The fuzzy Sugeno system produces a nominal armature resistance variation which is related to the UAV altitude and air moisture conditions. Lastly figure 8 shows the Sugeno FIS which produces the perturbed armature resistance values for the electrical thruster. Two inputs, the UAV armature voltage and UAV current profile are

driving the electrical thruster for the given airframe and associated aerodynamics. Meanwhile the thruster's armature resistance will vary significantly depending on the UAV altitude. Furthermore, the thruster's angular velocity variation can be observed for given system demands and compared to the nominal and the expected (perturbation) values obtained in the later figures clearly showing the key variations.

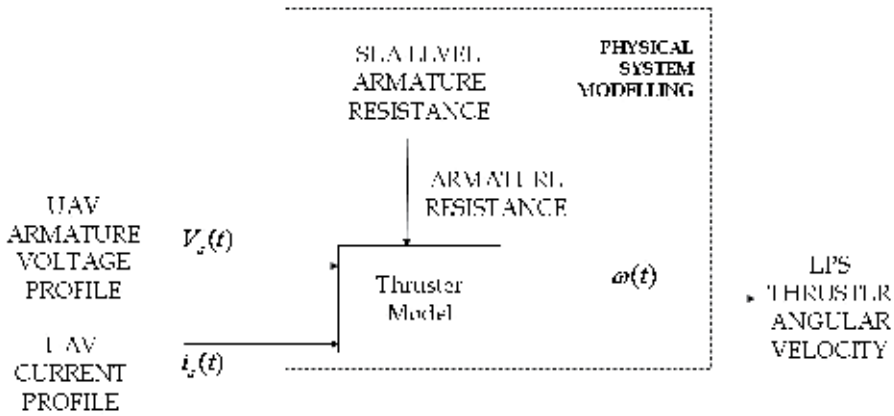


Fig. 6. UAV EPS Model near sea level altitude

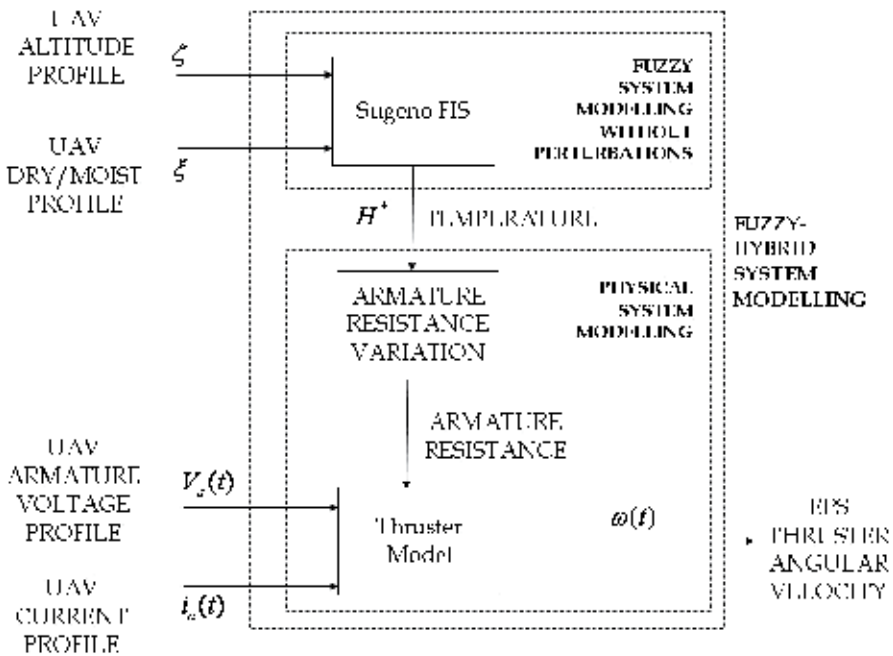


Fig. 7. UAV EPS Model at variable exogenous conditions with Sugeno (fuzzy-hybrid system)

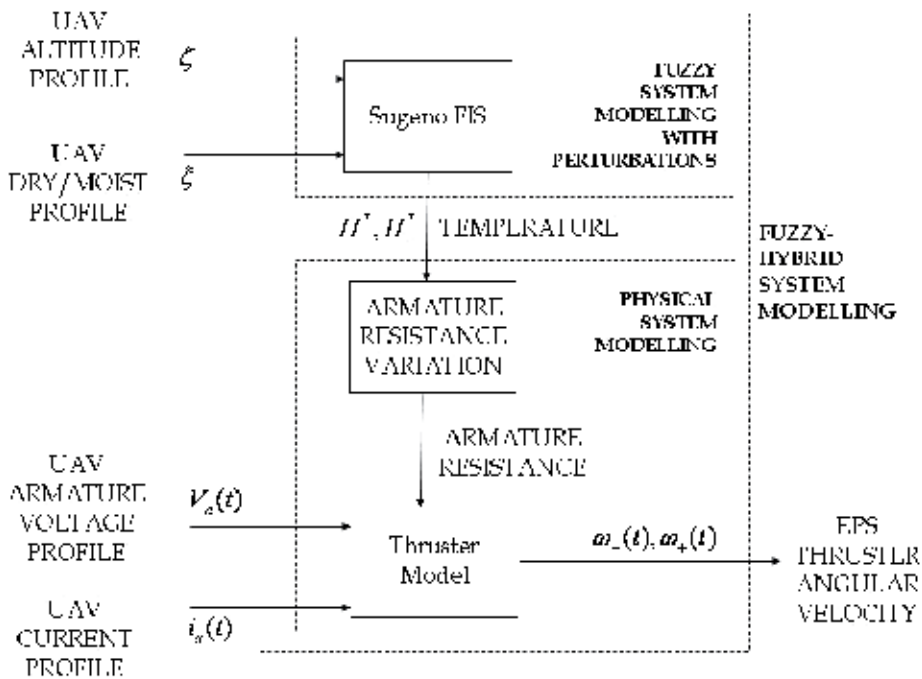


Fig. 8. UAV EPS Model at variable exogenous conditions with Sugeno (fuzzy-hybrid system) and Sugeno parameter perturbations.

The inputs of Figure 5 are shown next in Figure 9 (top, centre graphs) while the resulting thruster's input electrical power is also shown (lower graph). The quasi-static approach shows that the armature input electrical power does vary in order to balance the UAV flight requirements for altitude and overcome the atmospheric air moisture conditions.

Clearly, Figure 10, shows a realisable UAV test scenario. Initially the UAV starts at ground (sea level) and gradually gains altitude with a realisable climb rate. During its mission the UAV remains at a fixed altitude and then gains altitude again reaching before its 6 km requirement, where it remains for a given time (25 min) until it starts to descend back to sea level.

Meanwhile, the air moisture varies between two fuzzy logic extremes of "1" and "0.5" each representing a different condition, "dry air" and "saturated moist air" respectively. The moist air affects the temperature variation as the UAV altitude varies and hence was modelled utilising the Sugeno FIS topology.

Based on the chapter hypothesis, the armature resistance will affect the propeller shaft angular velocity for given conditions. Therefore, the next step is to observe the armature resistance during the UAV mission and compare this to the nominal (sea level) conditions. Figure 11, successfully demonstrates the nominal "blue line" armature resistance at sea level and the variable resistance due to the altitude and air moisture conditions.

In Figure 11, the dotted upper and lower lines demonstrate the injected $\pm 10\%$ perturbation in the Sugeno consequent. Both the effects of altitude, air moisture and the sensor SIEB type of perturbations affect the thruster's armature resistance and therefore it is expected to observe this variation to cascade also to the thruster's variables such as the propeller shaft angular velocity.

Figure 12, shows more clearly the injected $\pm 10\%$ perturbations in the Sugeno consequent and the effect of these. Typically, the boundaries (upper and lower) indicate the line for instantaneous measurements where the sensor measurement is used rather than the exact value of the sensor.

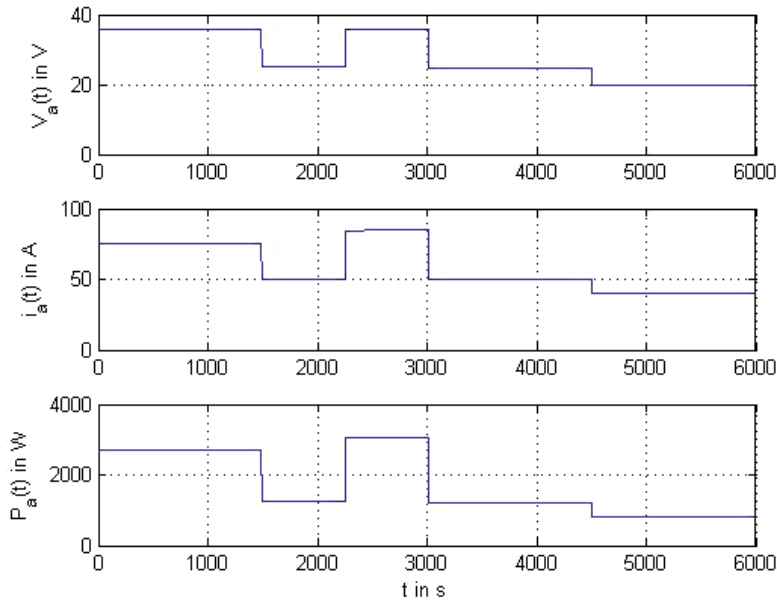


Fig. 9. UAV thruster armature voltage, current and input electrical power.

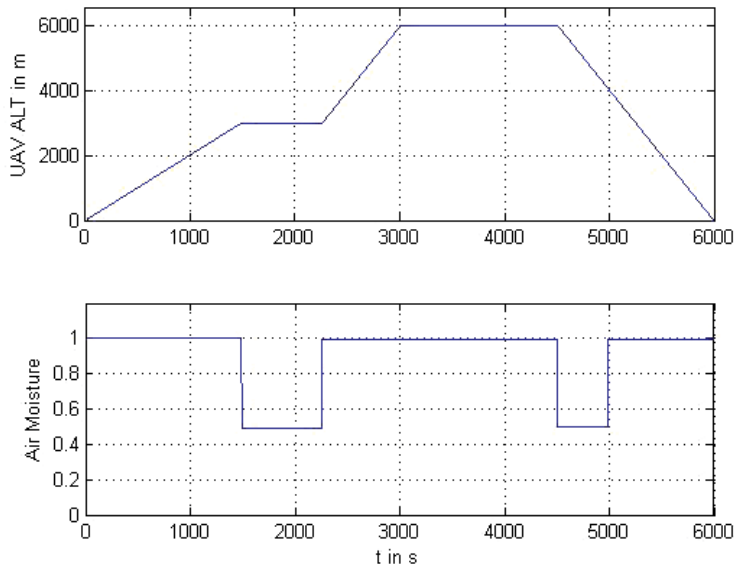


Fig. 10. UAV operational scenario, indicating altitude and air moisture conditions.

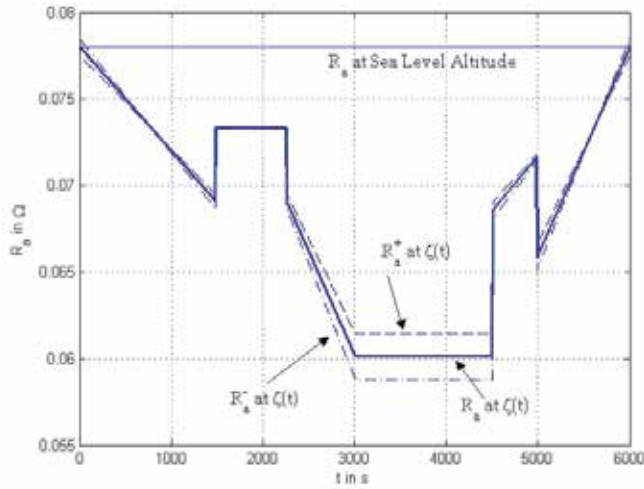


Fig. 11. Thruster armature resistance for nominal conditions (blue) and altitude based conditions (red).

Normally, UAV propulsion pack designs have a limited maximum rated electrical power which is available for use, including the propeller power requirements and thruster’s power losses. Figure 12, shows the armature resistance related copper losses for the given UAV test scenario. Clearly, the power copper losses relating to the nominal (sea level) when compared to the variable altitude and air moisture conditions result in different losses. In particular the variable altitude scenario power losses are less than the sea level equivalent, hence resulting in a gain in net power available for thrust for the same power pack.

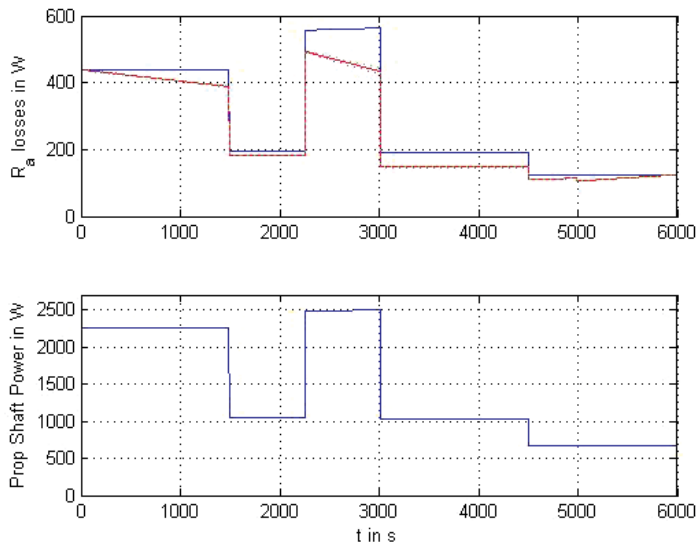


Fig. 12. Nominal (blue) and altitude based copper losses and propeller shaft powers.

Figure 12, (lower graph), shows the propeller shaft available power for the test scenario shown earlier. During time intervals (0,1500)s and (2200,3000)s the UAV requires its maximum rated power in order to climb to the desired altitudes of 3000 m and 6000 m.

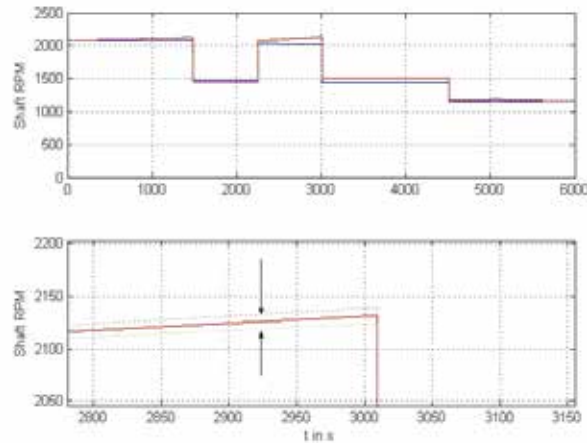


Fig. 13. Geared shaft RPM for nominal (blue) and altitude based (red), second graph showing the percent variation in the shaft RPM.

Figure 13, shows (top graph) the propeller geared shaft RPM for the nominal (in blue) and the altitude varied angular velocity (in red). As expected because the power pack has a maximum rated power capability and the armature resistance losses reduce, the propeller shaft mechanical power increases for the same rated input power. Hence, while the propeller loading remains as shown in the previous profiles the angular velocity at the propeller shaft is expected to increase as shown from the analysis.

Figure 13, also shows a zoomed version (lower graph) clearly showing the implications of the added phenomenon of speed changing due to an example injected $\pm 10\%$ perturbations in the Sugeno sensor. It appears that this specific injected perturbation does not cause a substantial change compared to the altitude based angular velocities.

Figure 14. shows the armature resistance percentage error when compared to the sea level conditions. Clearly the expected error (top graph) exceeds 20% from nominal, therefore demonstrating the importance of the Sugeno fuzzy inference modelling within the context of the fuzzy-hybrid modelling process. The armature resistance percentage error for both the upper and lower boundaries (centre graph), are approximately 2.5 % for the upper/lower boundary or 5% for both boundaries. This indicates that the Sugeno perturbation based on SIEB-type errors can indeed affect the model behaviour. The (last graph), shows the SIEB errors with reference to the sea level equivalent. These are expected to be high and exceeding 20% due to the inclusion of the fuzzy-hybrid model which includes the altitude/moisture and perturbation effects.

Figure 15 shows the thruster's angular velocity error comparing the sea level and altitude based models. Clearly the error (top graph) is nearly 5% and variant throughout the UAV flight scenario. The centre graph shows the thruster's upper and lower injected $\pm 10\%$ perturbations in the Sugeno FIS and compared to the non-perturbation model. The error resulting from this test run is less than 1%, thus shown some influence of the armature

resistance variations cascading and affecting the propeller shaft angular velocity. However, (last graph), when the perturbation model is compared to the sea level model the error increased by approximately 10 times reaching a percentage error of up to 6%.

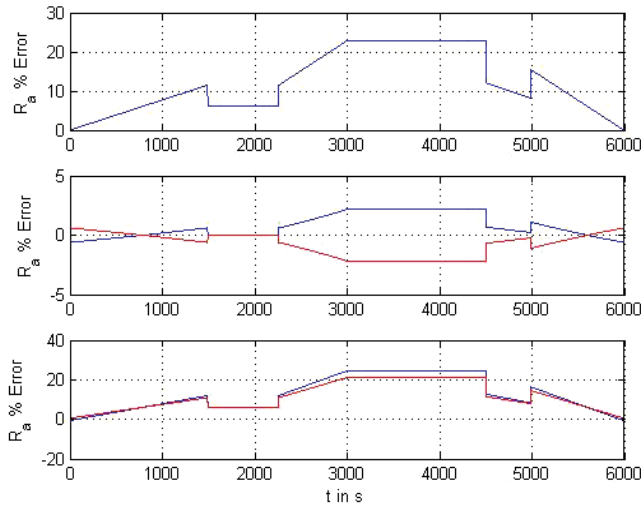


Fig. 14. Altitude-based armature resistance error with respect to the nominal (top graph); altitude-based armature resistance error wrt $\pm 10\%$ FIS Consequent perturbation (Centre graph); the lower graph is showing the error due to $\pm 10\%$ FIS Consequent perturbation wrt the nominal armature resistance.

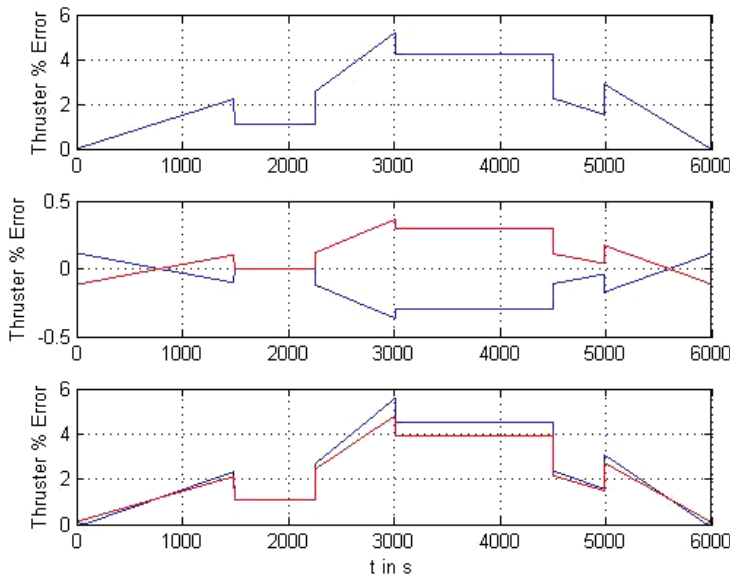


Fig. 15. Altitude-based shaft angular velocity error with respect to the nominal (top graph); altitude-based angular velocity error wrt $\pm 10\%$ FIS Consequent perturbation (Centre graph); the lower graph is showing the error due to $\pm 10\%$ FIS Consequent perturbation wrt the nominal angular velocity.

3. Conclusion

In this chapter we have learned how to incorporate sensor perturbations via the Sugeno fuzzy logic inference for electrical thruster systems which are propelling a class of electrically-powered unmanned aerial vehicles. Therefore, design considerations have included the UAV altitude variation and atmospheric moisture via the fuzzy logic Sugeno design framework.

Furthermore the necessity of the fuzzy-hybrid modelling topology became apparent for the electrical thruster system. While the thruster was modelled utilising an ordinary differential equation form, the additional UAV operational conditions such as altitude and atmospheric moisture required the inclusion of the Sugeno-based fuzzy inference system thus *amalgamating* the two topologies into a single fuzzy-hybrid topology.

4. Nomenclature

Nomenclature (Units are in SI)

n	Rule number
n_{max}	Maximum number of rules
j	Number of Sensors
j_{max}	Maximum number of sensors
z_j	j-th sensor variable
Z_n^j	Membership function for the
h_n	n-th rule function
$f_n(z_1, z_2, z_3)$	Linear polynomial in terms of z_1, z_2, \dots, z_j
c_j	Centre for Gaussian type membership function for the j-th sensor
d_j	Dispersion for Gaussian type membership function for the j-sensor
η	Horizontal shift operator
b_n	Rule consequent offset
ς_{jn}	n-th rule j-th sensor polynomial coefficients
h^*	Sugeno FIS output at time τ .
γ_n	n-th rule rule firing
ε_j	j-th sensor error
$\bar{\varepsilon}_j$	j-th sensor error upper boundary
$\underline{\varepsilon}_j$	j-th sensor error lower boundary
$V_a(t)$	PMDC Armature thruster voltage
$\omega(t)$	Thruster angular velocity
$i_a(t)$	Thruster Armature Current
K_a	Thruster back emf constant
R_a	Thruster armature resistance
R_a^+	Sugeno upper bound for armature resistance for different altitudes

R_a^-	Sugeno lower bound for armature resistance for different altitudes
L	Thruster inductance
E_a	Thruster equivalent back emf voltage
$\theta(t)$	Shaft angle
K_T	Thruster torque constant
T_m	Thruster produced torque
J_a	Thruster armature inertia
J_L	Load inertia
B_a	Thruster armature viscous angular damping
B_L	Load viscous angular damping
N_1	Thruster side gear teeth
N_2	Load side gear teeth
P_m	Thruster mechanical power
ρ	Constant in W
R_{ref}	Reference resistance for thrusters armature at temperature T_{ref}
a_c	Coefficient of thermal expansion for copper
ζ	UAV Altitude in m
ξ	Air moisture condition
T	Temperature at altitude ζ
T_{ref}	Reference temperature

5. References

- Kladis, G.P.; Economou, J.T.; Knowles, K.; Lauber, J. & Guerra T.M. (2010). *Energy conservation based fuzzy tracking for unmanned aerial vehicle missions under a priori known wind information*, Journal of Engineering Applications of Artificial Intelligence, Vol. 24, Issue 2, pp. 278-294.
- Karunarathne, L.; Economou J.T. & Knowles, K. (2007). Adaptive neuro fuzzy inference system-based intelligent power management strategies for fuel cell/battery driven unmanned aerial vehicles, Journal of Aerospace Engineering, Vol/ 224, No. G1, pp 77 – 88.
- Sugeno, M. (1999). On stability of fuzzy systems expressed by fuzzy rules with singleton consequents, IEEE Transactions on Fuzzy Systems, Vol. 7, Issue 2, pp 201-224.
- Economou, J.T. & Colyer, R.E. (2005). *Fuzzy-hybrid modelling of an Ackerman steered electric vehicle*, International Journal of Approximate Reasoning, Vol.41, No.3, pp. 343-368.
- Ehsani, M.; Gao, Y.; Gay, S.E. & Emadi, A., (2005). Modern Electric, Hybrid Electric, and Fuel Cell Vehicles, CRC Press, ISBN 0 8493 3154 4, USA.
- Economou, J.T.; Tsourdos, A. & White B.A. (2007). *Fuzzy logic consequent perturbation analysis for electric vehicles*, Journal of Automobile Engineering, Proceedings of the IMech E PART D., Vol. 221, No D7, pp 757-765.

Miller, J.M., (2004). *Propulsion Systems for Hybrid Vehicles*, IEE Power & Energy Series 45, ISBN 0 86341 336 6, UK.

Extended Simulation of an Embedded Brushless Motor Drive (BLMD) System for Adjustable Speed Control Inclusive of a Novel Impedance Angle Compensation Technique for Improved Torque Control in Electric Vehicle Propulsion Systems

Richard A. Guinee
*Cork Institute of Technology
Ireland*

1. Introduction

As already stated for the reasons given in a previous chapter a good continuous time model, of low complexity, of a BLMD system is essential to adequately describe mathematically the PWM inverter switching process with dead time and subsequent binary waveform generation in terms of the switching instant occurrences for accurate computer aided design (CAD) of embedded BLMD model simulation in proposed electric vehicle (EV) propulsion systems. In this chapter a complete software model of the BLMD system as a set of difference equations representing subsystem functionality, the organization of these subsystem activities into flowchart form and the processing details of these modular activities as software function calls in C-language for simulation purposes (Guinee, 2003) is presented.

Furthermore in this the second chapter, concerning BLMD model fidelity for EV applications, BLMD model simulation accuracy for embedded EV CAD is next checked for a range of restraining shaft load torques via numerical simulation and then extensively compared and benchmarked for accuracy against theoretical estimates using known manufacturer's catalogued specifications and motor drive constants (Guinee, 2003).

Model simulation accuracy is further substantiated and validated through evaluation of the shaft velocity step response rise time when cross checked against (i) experimental test data and (ii) that evaluated from the catalogued performance index relating to the brushless motor dynamic factor (Guinee, 2003). Numerical simulation with outer velocity loop closure is used to demonstrate the accuracy of the completed BLMD reference model, based on established model confidence in torque control mode, in ASD configuration when compared with experimental test data.

In addition to the BLMD model structure presented in the previous chapter for actual drive emulation two innovative measures which relate to increased drive performance are also provided. These novel techniques (Guinee, 2003), which include

i. inverter dead time cancellation and
 ii. motor stator winding impedance angle compensation,
 are encapsulated within the BLMD model framework and simulated for validation purposes and prediction of enhanced drive performance in EV systems. An approximate analysis is given to support the approach taken and verify the performance outcome in each case.

In the first of these BLMD performance enhancements a novel compensation method has already been presented in the first chapter to offset the torque reduction effects of inverter delay during BLMD operation. This simple expedient relies on the zener diode clamping of the triangular carrier voltage during the carrier waveform comparison with the modulating current control signal in the comparator modulator to nullify power transistor turnon delay. This approach obviates the need for separate compensation timing circuitry in each phase as required in other schemes. The accuracy of this methodology is supported by current feedback, EM torque generation and shaft velocity trace simulation when compared with similar traces from the BLMD benchmark reference model with the effects of the inverter basedrive trigger delay neglected.

The second proposed innovative improvement, presented in this chapter, relates to the progressive introduction of commutation phase lead with increased shaft speed as BLMD impedance angle compensation which forces the impedance angle to the same value as the internal power factor angle. This effect maintains zero load angle between the stator winding terminal voltage and the back emf. It also results in rated load torque delivery at lower shaft speeds with minimal rise time, overshoot and settling time in the generated torque for a range of torque demand input values. This novel technique greatly enhances the dynamic performance of the embedded BLMD prime mover in EV applications without overstressing mechanical assembly components during periods of rapid acceleration and deceleration. The incorporation of this novel impedance angle compensation technique thus minimizes component wear-out such as gear boxes, transmission shafts and wheel velocity joints and consequently enhances overall EV reliability improvement. BLMD simulation is provided in torque control mode at rated torque load conditions, for the actual drive system represented, with and without impedance angle compensation to gauge model performance accuracy over a range of torque demand step input values.

2. BLMD model structure and program sequence of activities

The BLMD model structure is composed of interconnected subsystems with feedback as shown in Figure 1, of varying complexity according to physical principles. Consequently it can be described by a discrete time configuration of first order digital filter realizations for linear elements cascaded with difference equations representing nonlinear PWM inverter behaviour into a complete software model for simulation purposes as illustrated in Figure 2. The BLMD model program is organized into a sequence of software activities, coded in C-language as function calls, representing the functionality of various subsystem modules shown as the flowchart in Figure 3. All subsystem output (o/p) variable quantities in the cascaded activity chain are assumed to remain constant, once computed irrespective of feedback linkage, throughout the remainder of the time step interval Δt_k based on the simulation sampling rates ($1/\Delta t_k$) chosen from considerations given in section 3.1 of the previous chapter. The essential features of the BLMD model program in Figure 3 can be explained by means of the linked modular software configuration encoded as the functional block sequence in Figure 2 along with the appropriate C-language code segments illustrated in Figure 4.

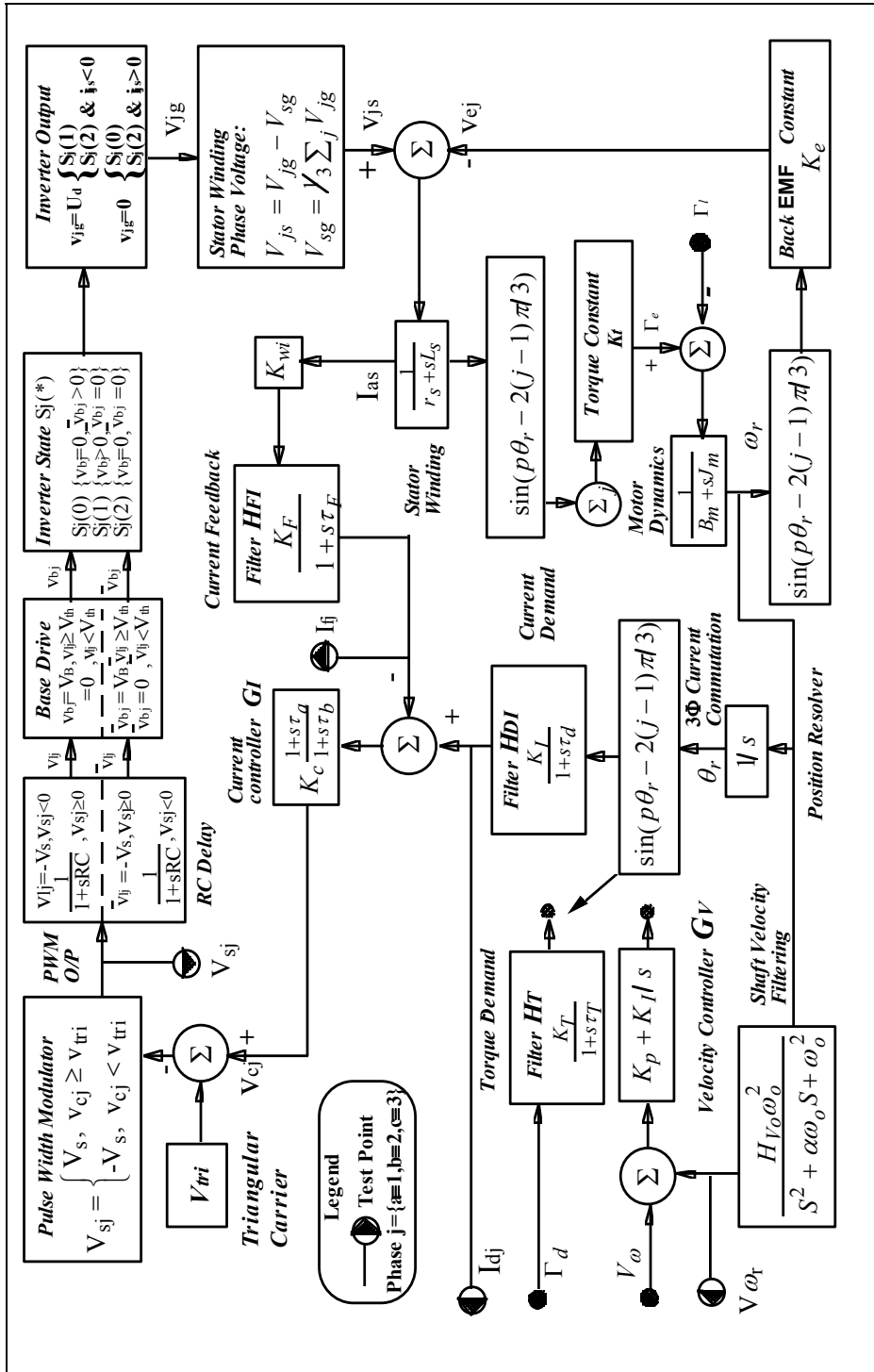


Fig. 1. Transfer Function Block Diagram of a BLMD System (Guinee, 1999)

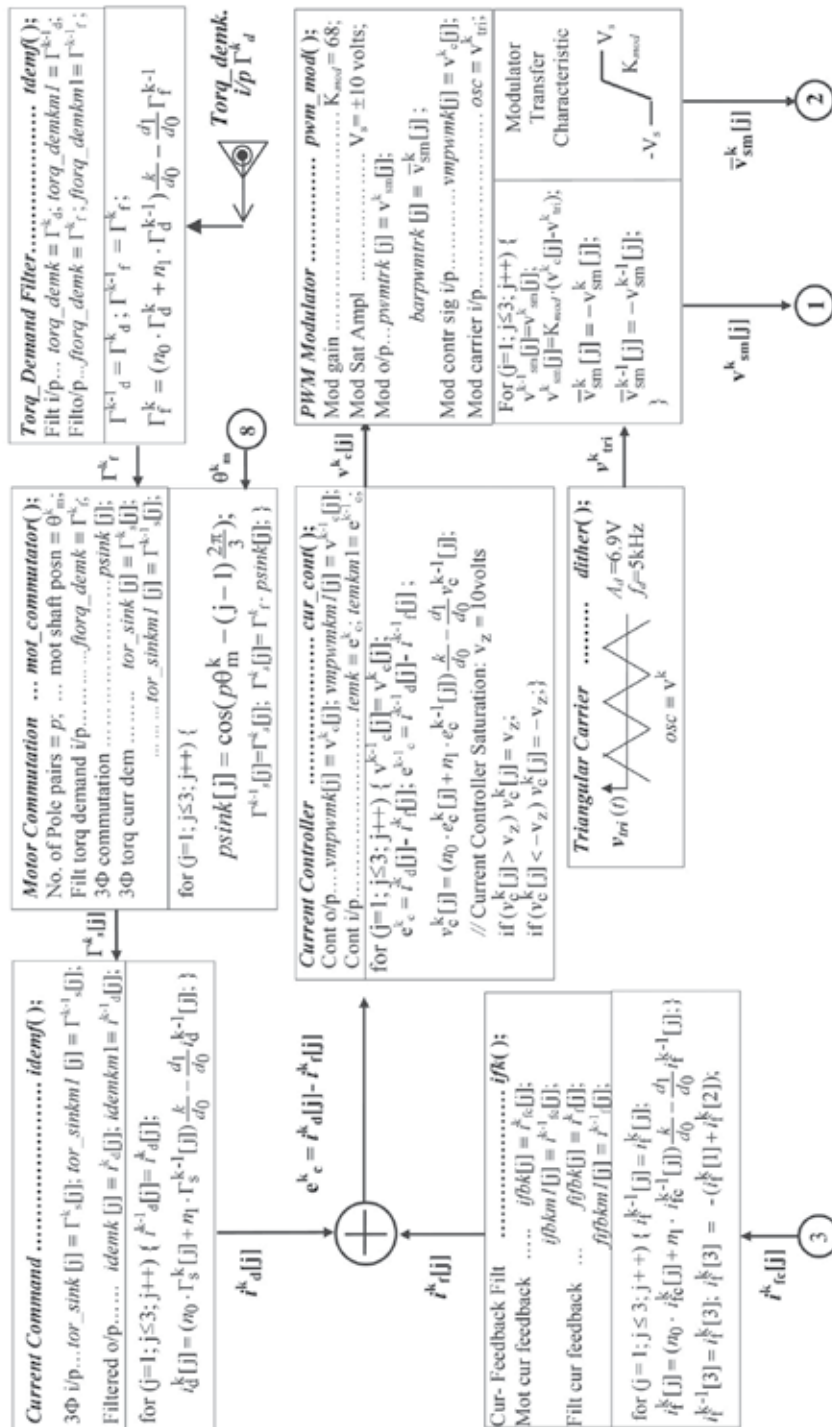


Fig. 2-A. Software Functional Block Diagram (Guinee, 2003) of a BLMD System

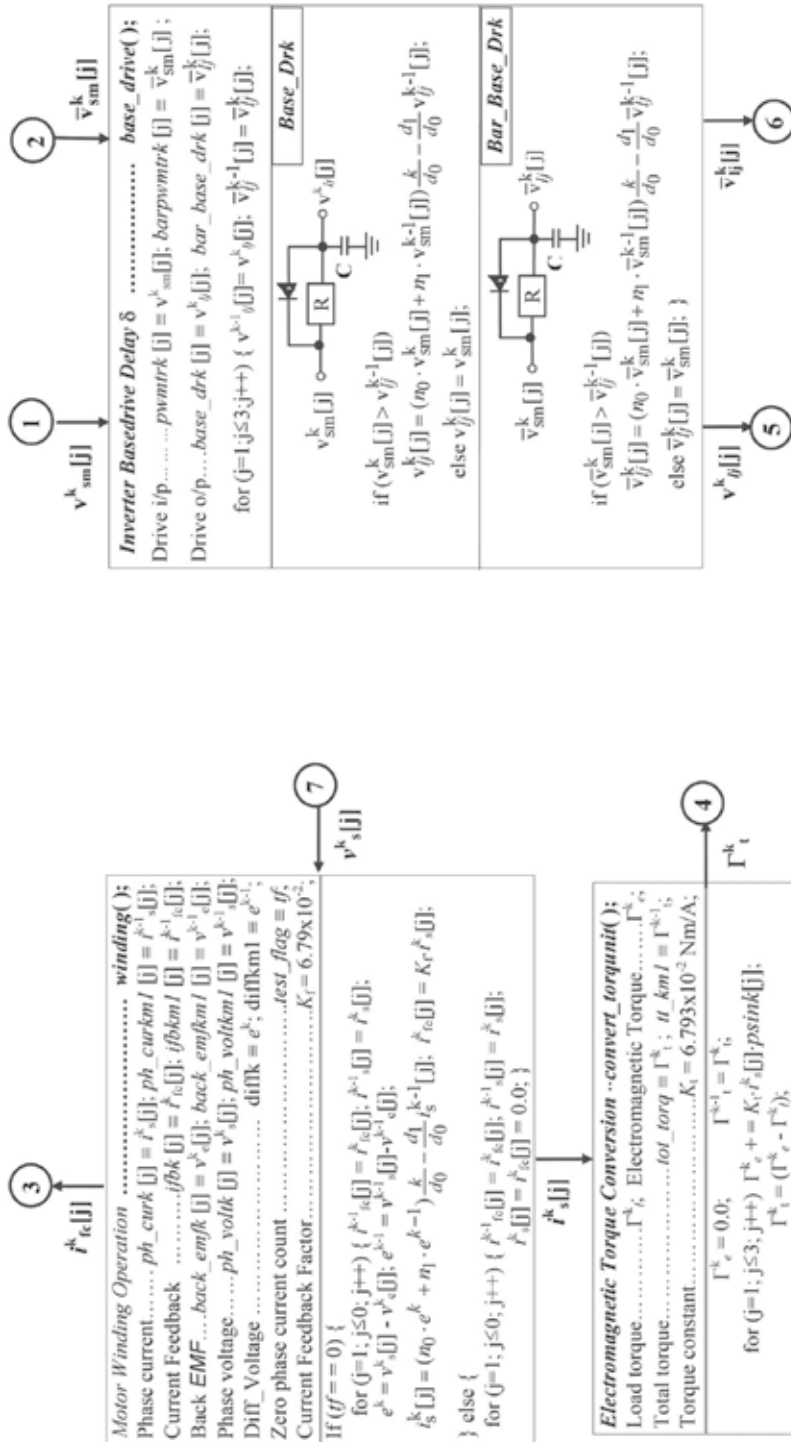


Fig. 2-B. Software Functional Block Diagram of a BLMD System

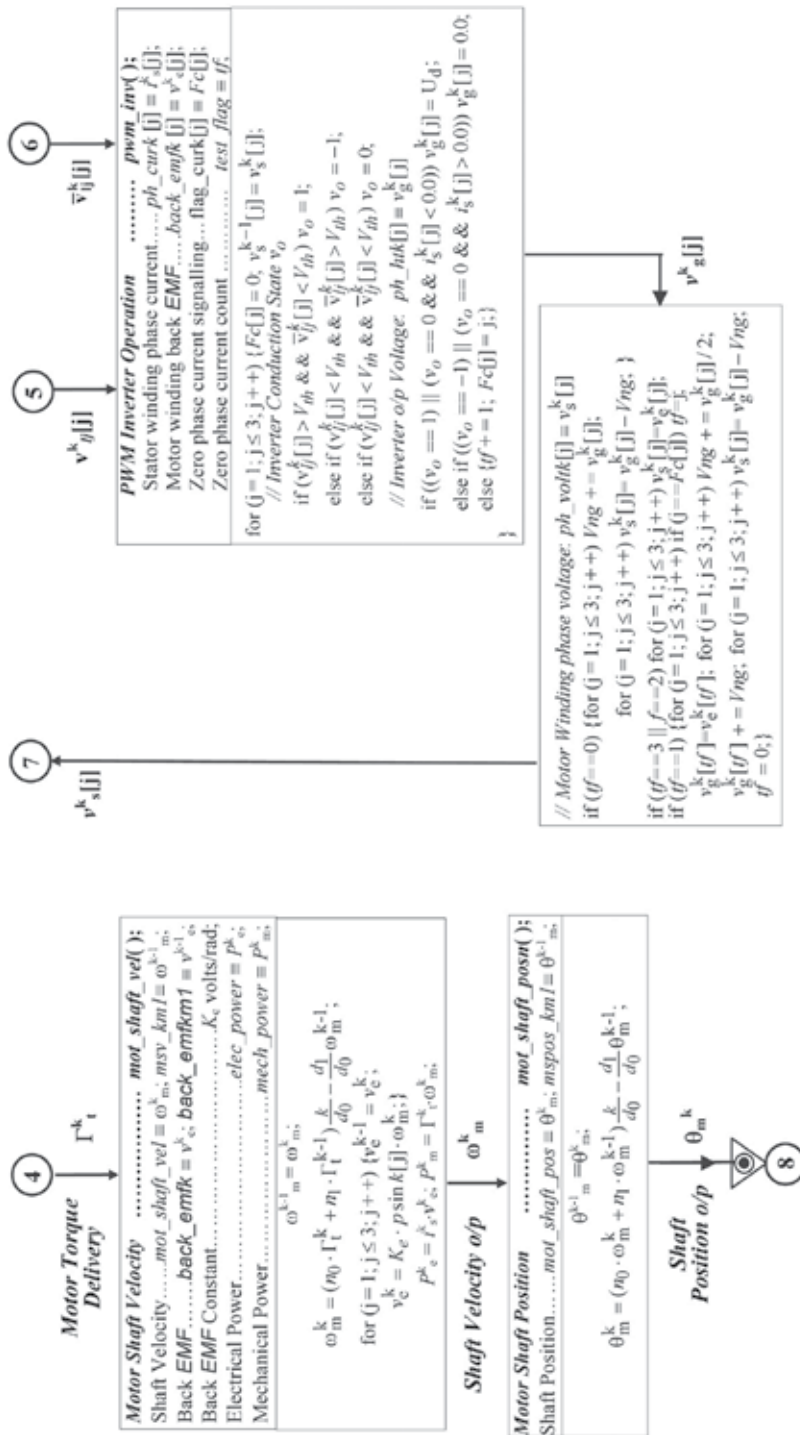


Fig. 2-C. Software Functional Block Diagram of a BLMD System

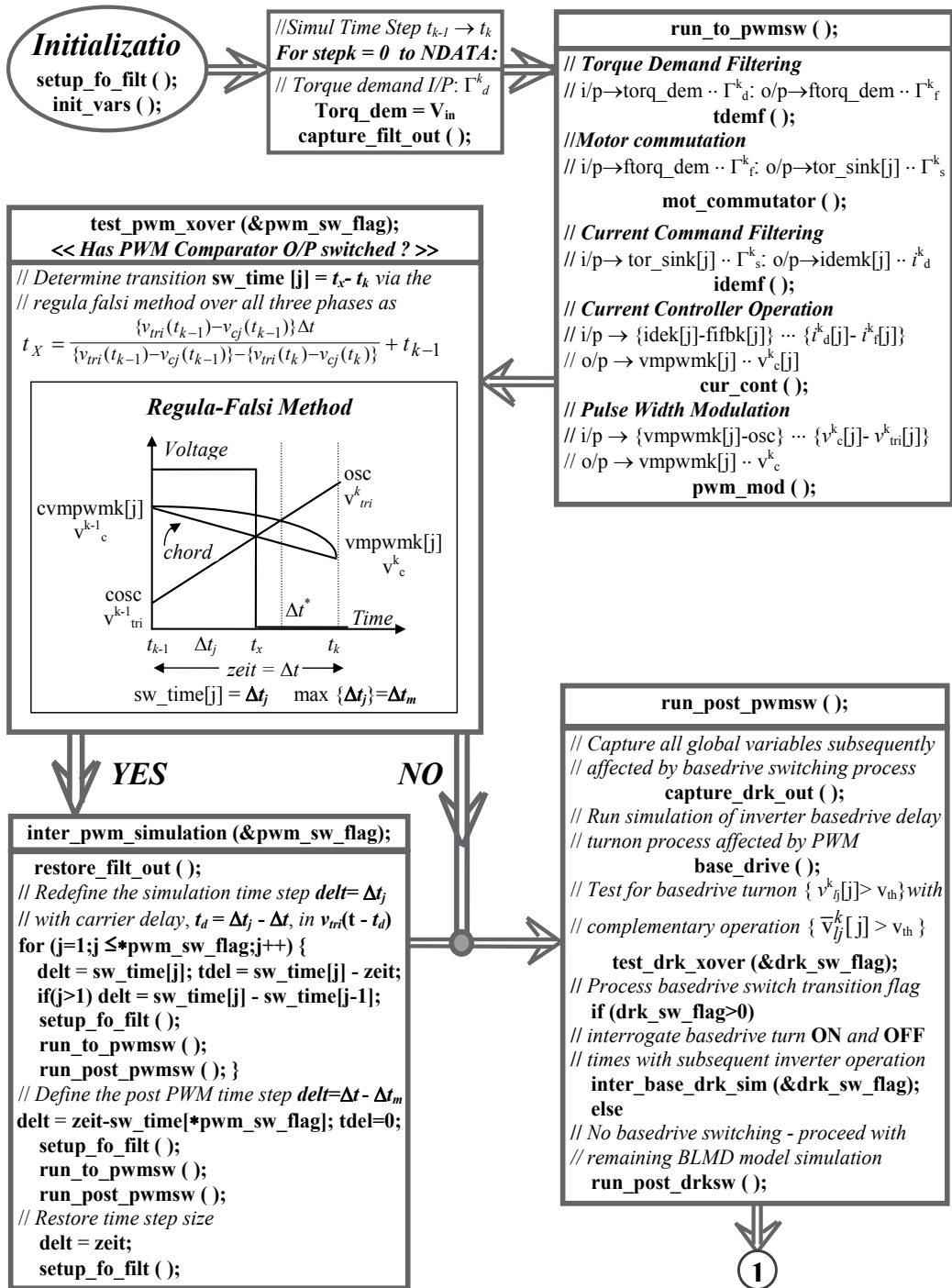


Fig. 3-A. Program Flow Diagram (Guinee, 2003) for BLMD Model Simulation

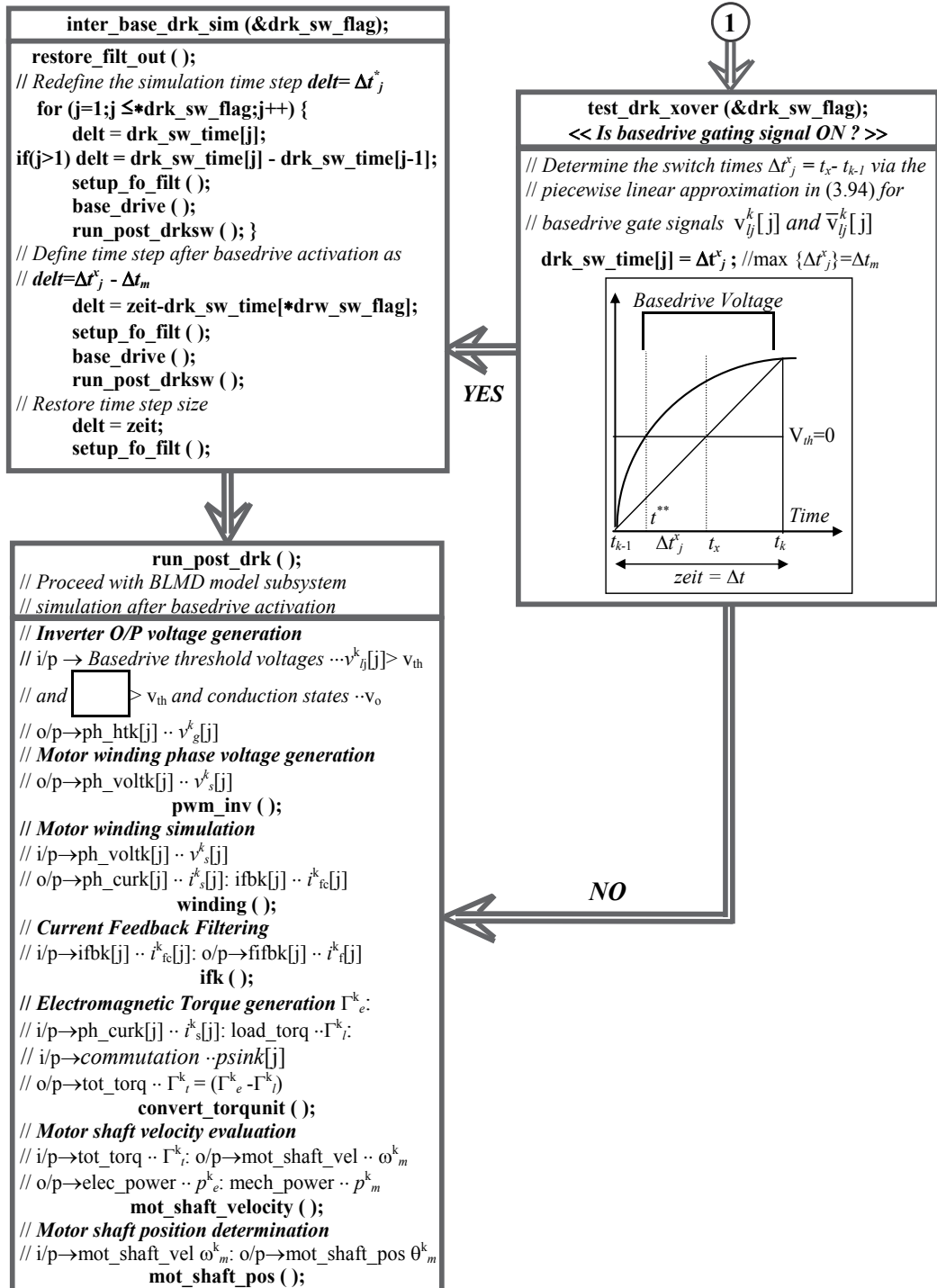


Fig. 3-B. Program Flow Diagram for BLMD Model Simulation

2.1 BLMD model simulation

Numerical simulation commences with the declaration of known BLMD system parameters followed by a declaration with initialization of variables and three phase (3Φ) arrays for global usage, over the program linked function call sequence, as outlined in the code blocks shown in Figure 4-1.

```

    ≈ Define BLMD System Parameters in Fig.5 ≈
    // Define all filter constants:
    KT=1.0; τT=222μS; // Torque Demand Filter HT
    KI=1.0; τI=100μS; // Current Demand Filter HDI
    KF=5.0; τF=47μS; //Current Feedback Filter HFI
    Kwf ≡ Kf; // Current Feedback Factor
    KC=19.5; τa=225μS; τb=1.5mS; //Current Controller GI
    Hvo=13.5x10-3; α=√2; ωo=2x103 rad.s-1; //Velocity Filter HV
    Kd=1.0; τd=28.6μS; // RC Delay
    rS=0.75Ω; LS=1.94mH; p = 6 pole pairs; // Motor Winding
    Ke = Kt = 0.3 // Motor torque & Back EMF Constants
    Jm=3 kg.cm2; Bm=2.14x10-3 Nm.rad-1; // Motor Dynamics
    Ud=310 Volts; Vth=0; VS=10 Volts; // Voltage Constants
    fS=5.7kHz; Ad=6.9 Volts; // Carrier Waveform Constants

    ≈ Define Global Variables ≈
    stepk // kth iteration time step
    delta_t // Fixed simulation Time Step Size Δt = (tk - tk-1)
    delT // Variable simulation Time Step Size Δti
    tdel // Carrier vtri(t-td) time delay td
    osc // Carrier amplitude vktri
    torq_dem // motor i/p torque demand Γkd
    ftorq_dem // Filtered torque demand Γkf
    mot_shaft_pos // Motor shaft position Θkm
    mot_shaft_vel // Motor shaft velocity ωkm
    tot_torq // Net drive torque Γkf

    ≈ Define Global Array variables for j=1 to3 ≈
    ppsinkm1[j] // 3-phase commutation psink[j]
    tor_sink[j] // 3-phase torque demand Γks[j]
    idemk[j] // 3-phase current demand ikd[j]
    fjfbk[j] // Filtered current feedback ikf[j]
    ifbk[j] // Current feedback ikfc[j]
    vmpwmk[j] // Current controller o/p vkc[j]
    pwmtrk[j] // Modulator o/p vksm[j]
    base_drk[j] // Basedrive o/p vkg[j]
    bar_base_drk[j] // Complementary basedrive o/p vkg[j]
    ph_voltk[j] // Stator winding Phase voltage vks[j]
    back_emfk[j] // Motor back EMF vke[j]
    ph_curk[j] // Stator winding Phase current iks[j]

    ≈ init_vars ( ) ≈
    // Function initializes all global variables and arrays to 0.0
    
```

Fig. 4-1. Declaration and Initialization (Guinee, 2003)

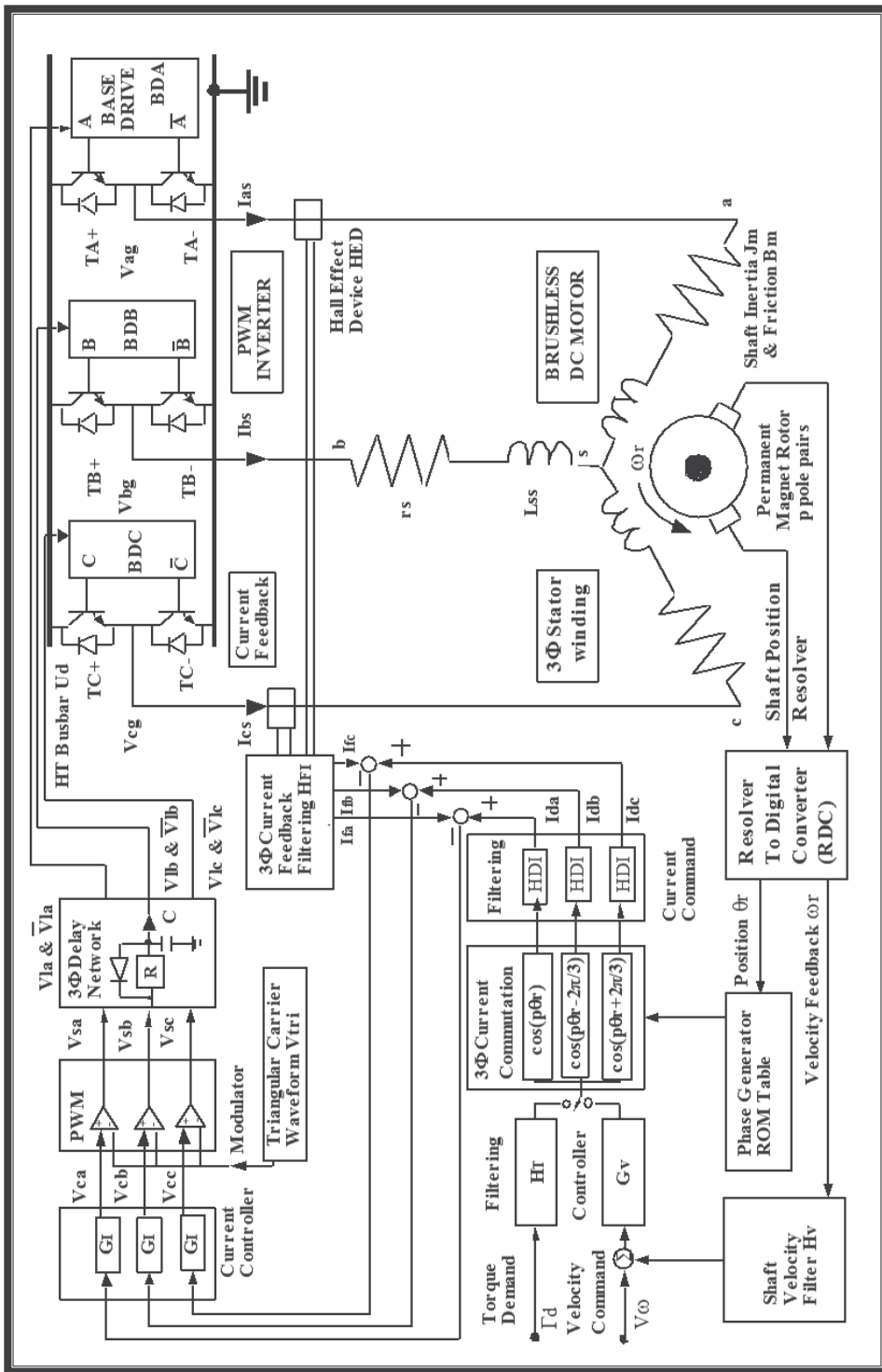


Fig. 5. Network Structure (Guinee, 1999) of a Typical Brushless Motor Drive System

All first order linear system discretization is accomplished by complex variable substitution of the Euler backward rectangular rule using the Z transform. The alternative filter discretization process using Tustin's bilinear method (Franklin et al, 1980) or the trapezoidal integration rule (Balabanian, 1969) can also be used but with negligible observable differences at the step size Δt chosen. Resultant digital filter implementation for simulation purposes is facilitated by transfer of the appropriate filter time constant and gain coefficients using the C-language 'structure' mechanism in the function call *setup_fo_filt ()* illustrated in Figure 4-2.

```

        ≈ setup_fo_filt ( ) ≈
// Function sets up and discretizes all first order BLMD
// linear subsystems H(s) in Figures 1 & 5 according
// to expressions (LX) and (LXIV) in the previous chapter as

$$H(s) = K_c \frac{1+\tau_a s}{1+\tau_b s} \frac{s \sim \frac{1}{T}(1-z^{-1})}{d_0+d_1 z^{-1}} \rightarrow k \frac{n_0+n_1 z^{-1}}{d_0+d_1 z^{-1}}$$

// using function call discrete1( );
// with discrete filter coefficients {k, n0, n1, d0, n1}, such as
tdemf( ); idemf( ); ifk( ); cur_cont( ); winding( );
mot_shaft_vel( ); mot_shaft_posn( );
dtrdfilt( ); // drive transistor RC delay network

≈ First Order System Discretization Process discrete1 ( ) ≈
typedef struct
{
    double k;
    double n0;
    double n1;
    double d0;
    double d1;
} tf1;

// Tustin's Bilinear Method
//  $s \sim \frac{2}{T} \frac{1-z^{-1}}{1+z^{-1}}$ 
tf1 discrete1(tf1 temp)
{
    tf1 discrete;
    double at,bt,ts;
    double k,n0,n1,d0,d1;
    ts=delt;
    bt=temp.d0*ts/2.0;
    at=temp.n0*ts/2.0;
    discrete.n0=at+temp.n1;
    discrete.n1=at-temp.n1;
    discrete.d0=bt+temp.d1;
    discrete.d1=bt-temp.d1;
    discrete.k=temp.k;
    return discrete;}

// Euler's Backward Integration Rule
//  $s \sim \frac{1}{T}(1-z^{-1})$ 
double delt;
tf1 discrete1(tf1 temp)
{
    tf1 discrete;
    double at,bt,ts;
    double k,n0,n1,d0,d1;
    ts=delt; k=temp.k;
    n0=temp.n0; n1=temp.n1;
    d0=temp.d0; d1=temp.d1;
    at=ts*n0; bt=ts*d0;
    n0=at+n1; d0=bt+d1;
    if(n1!=0.0) {
        discrete.k=k*n1/d1;
        discrete.n0=n0/n1;discrete.n1 = -1.0;
        discrete.d0=d0/d1; discrete.d1 = -1.0;
    } else {
        discrete.k=k*n0/d1;
        discrete.n0=1.0;
        discrete.n1 = 0.0;
        discrete.d0=d0/d1;
        discrete.d1 = -1.0;
    }
    return discrete; }
    
```

Fig. 4-2. Linear Subsystem Discretization

Before proceeding with model program execution in the k^{th} time step ($t_{k-1} \rightarrow t_k$) all global variables and arrays are captured in the function call *capture_filt_out* () for later reinstatement, during accurate resolution of the width modulated pulse edge transition time via the regula-falsi method, with *restore_filt_out* () in Figure 4-3.

```

≈ capture_filt_out ( ) ≈
// Capture all global variables and arrays for PWM evaluation
void capture_filt_out(void)
{
  int j;
  cftorq_dem=ftorq_dem; cosc=osc;
  ctot_torq=tot_torq; cmot_shaft_vel=mot_shaft_vel;
  cmot_shaft_pos=mot_shaft_pos;
  for(j=1;j<=3;j++) {
    cidemk[j]=idemk[j]; ctor_sink[j]=tor_sink[j];
    cvmpwmk[j]=vmpwmk[j]; cpwmtrk[j]=pwmtrk[j];
  }
  return;}

≈ restore_filt_out ( ) ≈
//Function reinstates arrays and global variables
ftorq_dem = cftorq_dem; //etc. for all other variables
for (j=1;j<=3; j++) {
  idemk[j] = cidemk[j]; tor_sink[j]=ctor_sink[j];
  vmpwmk[j]=cvmpwmk[j]; pwmtrk[j]=cpwmtrk[j];
}

```

Fig. 4-3. Variable capture and restoration

The instruction code group *run_to_pwm*sw () processes the sequence of BLMD software activities up to the comparator modulator o/p using the following list of function calls in Figures 4-1 and 4-4.

<i>tdemf</i> ()	filters the i/p torque demand signal <i>torq_dem</i> with o/p <i>ftorq_dem</i> .
<i>mot_commutator</i> ()	establishes the 3-phase reference <i>psink[j]</i> , from the computed shaft rotor displacement θ_{m}^k , for 3 phase stator winding voltage commutation with modulated amplitude.
<i>tor_sink[j]</i>	based on the filtered torque demand <i>ftorq_dem</i> .
<i>idemf</i> ()	filters the i/p torque related current command signal <i>tor_sink[j]</i> with o/p <i>idemk[j]</i> .
<i>cur_cont</i> ()	The lag compensator 'optimizes' the current error as the difference between the current command <i>idemk[j]</i> and the filtered stator winding current feedback <i>fifbk[j]</i> in each phase of the 3Φ current control loop. The o/p <i>vmpwmk[j]</i> from each of the high gain controllers is amplitude limited to the saturation voltage levels $\pm V_z$ (~10v) by zener diodes.
<i>pwm_mod</i> ()	produces a width modulated o/p pulse sequence <i>pwmtrk[j]</i> for each phase in accordance with the amplitude comparison of the modulating control signal <i>vmpwmk[j]</i> o/p and the triangular dither signal <i>osc</i> . The modulator has a gain K_{mod} with complementary outputs, for basedrive operation, that are hard limited to $\pm V_z$ (~10v) by zener diodes.

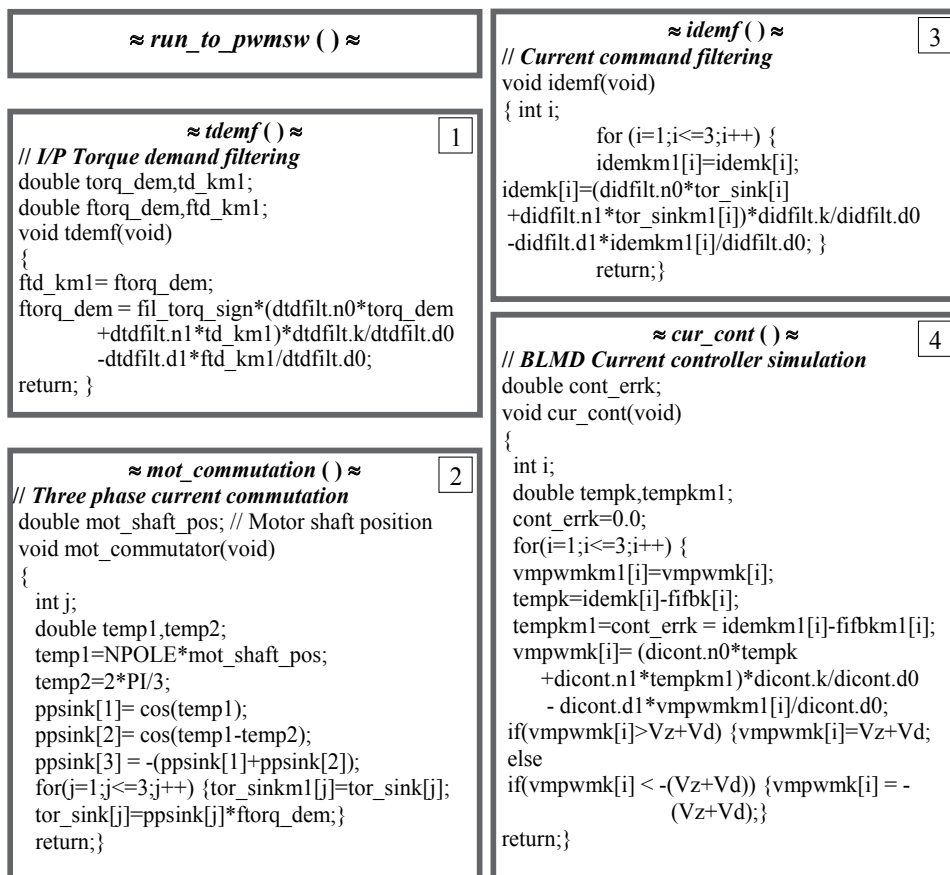


Fig. 4-4. Call Sequence to PWM O/P

A test is used to interrogate the o/p status of the simulated comparator modulator by monitoring any observational sign change in the o/p polarity ($\pm V_z$), which is indicative of a modulated pulse edge transition, after execution of the software code module *pwm_mod ()* as shown in Figure 4-5.

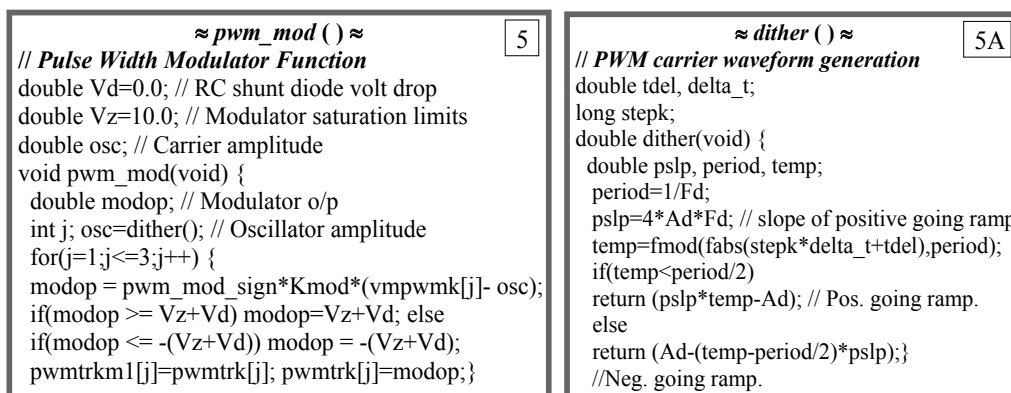


Fig. 4-5. Simulation of PWM

The o/p status of the comparator modulator is examined by comparing the trapped value $cpwmtrk[j]$ at the beginning of the time step t_{k-1} with the new o/p $pwmtrk[j]$ at t_k for each phase j and signalling any change via the pwm_test_flag in the function call $test_pwm_xover()$ detailed in Figure 4-6. If a crossover event occurs during simulation then the transition interval $\Delta t_x = (t_x - t_{k-1})$, denoted by min_time , is determined by the regula falsi method in (LXVII) in the previous chapter.

```

    ≈ test_pwm_xover (&pwm_test_flag) ≈
// PWM Pulse Edge Transition Time Detection
void test_pwm_xover(int *flag)
{
    int i, j, ref_sign, act_sign, sigfl;
    double min_time, tol;
    *flag=0; // Reset pwm_sw_flag
    tol=0.001; // Tolerance limit on the time resolution
    for(j=1;j<=3;j++) { // Examine all 3 Φ for PWM X-over
        sigfl=0;
        if(cpwmtrk[j]<0.0) ref_sign = -1; else ref_sign=1;
        if(pwmtrk[j]<0.0) act_sign = -1; else act_sign=1;
        if(ref_sign!=act_sign) { // PWM Crossover Check
            min_time=delt*(cosc-cvmpwmk[j])/(vmpwmk[j]
                -cvmpwmk[j]-osc+cosc); // Expression (3.85)
            if(min_time<0.0)
                nerror("PWM Switch_time calculation error");
            if(min_time<=(1-tol)*delt) { // switch-time ≤ Δt = T
                if(*flag>=1) {
                    for(i=1;i<=(*flag);i++)
                        if(min_time>=sw_time[i]-tol*delt &&
                            min_time<=sw_time[i]+tol*delt) sigfl=1;
                    // Switch times are identical - stall flag increase!
                    if(sigfl==0) { ++(*flag); phase_flag[*flag]=j;
                        sw_time[*flag]=min_time; } // Store switch time
                    } else { ++(*flag); phase_flag[*flag]=j;
                        sw_time[*flag]=min_time; }
                } // switch-time ≅ Δt = T
            } else ; // No Crossover!
        } // End 3-phase X-over search!
        if(*flag>0) { // Adjust phase switching times
            // in order of increasing magnitude
            for(i=1;i<=(*flag);i++) { min_time=1.0;
                for(j=i;j<=(*flag);j++) {
                    if(sw_time[j]<min_time) {
                        min_time=sw_time[j]; ref_sign=j;
                    }
                }
            }
            if(i!=ref_sign) { // Define swap (a,b,c): c←a, a←b, b←c
                SWAP(sw_time[i],sw_time[ref_sign],min_time);
                SWAP(phase_flag[i],phase_flag[ref_sign],act_sign);
            }
        }
    }
    return;
}

```

Fig. 4-6. Search for PWM X-over

A check is made to see if this value occurs within the imposed tolerance limit ($tol * \Delta t_k$) at the end of the time step interval Δt_k , denoted by Δt , in which it is discarded in the affirmative without test flag registration. If multiple crossover events occur within the simulation interval, corresponding to different phases, then all transition times with the appropriate phase tag number are logged in the respective $sw_time[j]$ and $test_flag[j]$ arrays along with the signaled transition count via the PWM test flag. A check is also performed for identical multiple switch transition times without an increase in test flag count. The test routine is completed by arranging the multiple switch times, with corresponding phase listing, in increasing order of magnitude for subsequent detailed PWM simulation in the function call $inter_pwm_simulation()$. Accurate internal simulation of a modulated pulse transition, indigenous to the time step, commences with restoration of the captured global variables preceding the time step and temporary storage of the original step size ($zeit$) and time delay (t_del) settings, relevant to the $dither()$ signal source, for later retrieval. The new time step (Δt) is initially set to the smallest switching interval Δt_X ($sw_time[1]$) for discretization of all first order linear subsystems using the call function $setup_fo_filt()$ as per the C-code module in Figure 4-7.

```

≈ inter_pwm_simulation (&pwm_sw_flag) ≈
// Simulate 3Φ- PWM with accurate transition times  $t_X$ 
void inter_pwm_simulation(int *flag)
{
    int i,ref_sign,act_sign;
    double zeit, t_del, tol=0.001;
    zeit=zeit; t_del=t_del; // Retain original time step info.
    restore_filt_out();
    for(i=1;i<=(*flag);i++) {
delt=sw_time[i]; // Adjust  $\Delta t = (t_X - t_k)$  to X-over time  $t_X$ 
        if(i>1) del = sw_time[i-1];
        tdel=t_del-zeit+sw_time[i];
        setup_fo_filt();
        run_to_pwmsw();
        if(pwmtrk[phase_flag[i]<0.0) act_sign = -1;
        else act_sign=1;
        if(cpwmtrk[phase_flag[i]<0.0) ref_sign = -1;
        else ref_sign=1;
        if(ref_sign==act_sign) pwmtrk[phase_flag[i]] *= -1.0;
        // Force PWM X-over
        run_post_pwmsw();
    } // adjust  $\Delta t$  to complete interval ( $t_k - t_X$ )
    del=zeit-sw_time[*flag];
    tdel=t_del; // Restore original timing to  $V_{ri}(t)$ 
    setup_fo_filt();
    run_to_pwmsw(); run_post_pwmsw();
    del=zeit; // Restore original time step
    setup_fo_filt();
    return;
}

```

Fig. 4-7. PWM X-Over Simulation

The necessary delay offset t_d ($tdel$) is determined by back tracking ($\Delta t_k - \Delta t_X$) from t_k for proper time registration in the execution of the carrier function $dither()$ and rerun of the call sequence $run_to_pwmsw()$ followed by the block function call $run_post_pwmsw()$. The post PWM

simulation call list contains the additional BLMD model basedrive switching features as an embedded layer in the nested *base_drive* () and associated switch event signalling *test_drk_xover* () program routines. The complete BLMD model program is subsequently exercised for other multiple switch time intervals $\Delta t^{i>1}_x$ with updated linear system discretization and adjusted delay offset. Termination of the remainder of the original time step simulation is accomplished by setting the integration interval *delt* equal to the time step residue ($\Delta t_k - \Delta t^{max}_x$) followed by the call sequences *run_to_pwm*sw () and *run_post_pwm*sw () and exiting to the main program with a reinstatement of original time settings

Numerical BLMD model simulation proceeds to the next program step in the flowchart cycle shown in Figure 3, by processing the call sequence *run_post_pwm*sw (), with the execution of the switch event routine *base_drive* () associated with the basedrive turn-on/off as a consequence of the PWM process. The relevant global variables and arrays associated with this call sequence run are trapped by the command *capture_drk_out* () as a precursor to basedrive simulation. The 'lockout' circuit routine, illustrated in Figure 4-8, consists of the integrating capacitor action when the PWM comparator o/p $v^{k_{sm}}[j]$ exceeds $v^{k-1}_{lj}[j]$ and charge dumping when $v^{k_{sm}}[j] < v^{k-1}_{lj}[j]$ as shown in Figure 3 for the basedrive **BDJ** with a similar microprogram description for complementary basedrive **BDJ** operation. The exponential trigger voltage growth on the timing capacitor, due to the inherent RC circuit delay in (LIV) in the previous chapter, along with the basedrive voltage threshold V_{th} (≈ 0.0) setting determines the inverter turn-on time. The charge dump action by the shunt diode across the delay timing resistor is virtually instantaneous when the switched comparator PWM output $v^{k_{sm}}[j] = K_{mod} \cdot (v^{k_c}[j] - v^{k_{tri}})$ is hard limited to $-v_z$.

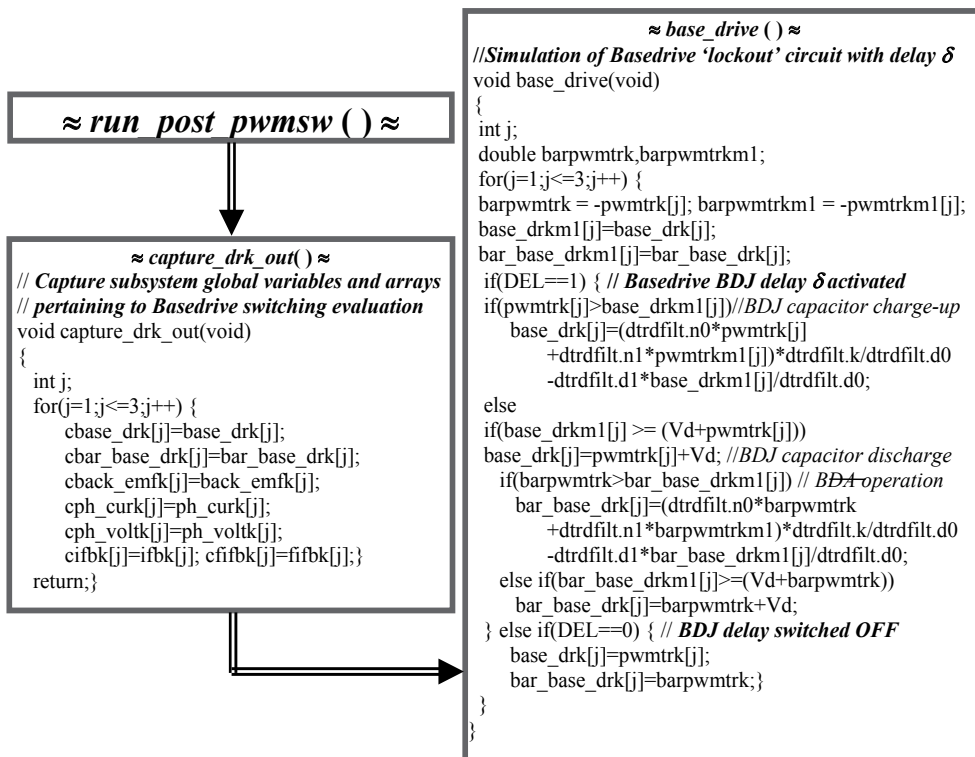


Fig. 4-8. Basedrive simulation

This effect results in swift basedrive turn-off with zero delay when referenced to the trailing edge of the PWM o/p. However the capacitor discharge can be gradual, when the PWM o/p is soft switched ($v_z > v_{sm}^k[j] > -v_z$), due to the limited magnitude of the product combination of modulator gain K_{osc} (~ 68) and error response $v_c^k[j]$ of the current loop controller which is implicitly dependent on the filtered current feedback response $i_f^k[j]$ for fixed current demand $i_d^k[j]$. The gradual reduction in capacitor voltage protracts the basedrive switch-off time, when referenced to the initial point of the logic “1-to-0” transition, associated with the PWM trailing edge. This delay has to be accounted for in an accurate inverter software model description with a search of the basedrive turn-off in addition to the turn-on times associated with exponential voltage growth.

The BLMD program test function *test_drk_xover* (&*drk_test_flag*), which is shown in Figure 4-10 and is very similar to *test_pwm_xover* () in code content, checks for basedrive on/off firing signal occurrence within a simulation time step interval. This search is complemented with the evaluation of associated multiple phase activation times Δt_x for both normal **BDJ** and complementary **BDJ** inverter drive modes of operation. These inverter trigger instants t_x are determined by piecewise linear approximation using (LXXVI) in the previous chapter, ranked in increasing order of magnitude and phase tagged via the global storage arrays *drk_sw_time[j]* and *drk_phase_flag[j]* for subsequent use in detailed basedrive simulation. Accurate simulation of the basedrive trigger timing signals for subsequent inverter operation is achieved using the software routine call *inter_base_drk_loop_sim* (&*drk_test_flag*) which is shown in Figure 4-11 and has similar execution features to *inter_pwm_simulation* ().

The function call begins with the reinstatement of the global arrays at the beginning (t_{k-1}) of the time step using *restore_drk_out* (), illustrated in Figure 4-9, and temporary storage (*zeit*) of the original step size Δt . The routine proceeds with linear system discretization appropriate to and with execution of the *base_drive* () function and the subsequent call sequence *run_post_drksw* (), listed in Figure 4-12, for progressive substitution of multiple differential switch times as the temporary variable *delt*.

This simulation call is completed with restoration of the original time step size followed by first order system discretization with a return to the main BLMD program to begin the new time step $t_k \rightarrow t_{k+1}$. The function call group *run_post_drksw* (), summoned during main program execution in the flowchart of Figure 3, processes the following sequence of modular software activities illustrated in Figures 4-12 and 4-13 pertaining to BLMD system electrodynamic operation with inverter interaction.

pwm_inv () generates the 3 Φ inverter output HT binary voltage *ph_htk[j]* $\equiv v_g^k[j]$ in response to the PWM basedrive gating signals v_{bj} & \bar{v}_{bj} shown in Figure 1. The magnitude of the simulated complementary trigger signals v_{lj}^k & \bar{v}_{lj}^k in relation to the basedrive **BDJ** threshold voltage V_{th} establish the conduction states $S_J(k)$ for $k \in \{0,1,2\}$ as per (LV) in the previous chapter, by means of the tristate switching indicator V_o , of the complementary power transistor pair T_{j+} and T_{j-} in each leg **J** of the 3 Φ inverter shown in Figure 15 in the previous chapter. The tristate flag condition in conjunction with the sustained stator winding current flow *ph_curk[j]* $\equiv i_s^k[j]$ through the free wheeling shunt diodes establish the inverter o/p binary voltage as 0 or V_{dc} . The neutral star point voltage *Vng* (v_{sg}) of the stator winding is determined from (LVIII) in the previous chapter for subsequent evaluation of the phase voltages *ph_voltk[j]* $\equiv v_s^k[j]$ via (LIX) in the previous chapter.

<pre> ≈ test_drk_xover (&drk_sw_flag) ≈ // Basedrive switch transition time t_X void test_drk_xover(int *flag) { int i,j_ref_sign,act_sign,sigfl; double min_time,tol; *flag=0; tol=0.001; // Switching time resolution for(j=1;j<=3;j++) { if(cbase_drk[j]<0.0) ref_sign = -1; else ref_sign=1; if(base_drk[j]<0.0) act_sign = -1; else act_sign=1; // Check basedrive switching times if(ref_sign!=act_sign){ min_time=cbase_drk[j]*delt/(cbase_drk[j]-base_drk[j]); if((min_time < 0.0) (min_time > delt)) nerror("Base Drive Switch_time error"); if(min_time<=(1-tol)*delta_t) { // switch time < Δt if(*flag>=1) { for(i=1;i<=(*flag);i++) // identical switch times if(min_time>=drk_sw_time[i]-tol*delta_t && min_time<=drk_sw_time[i]+tol*delta_t) sigfl=1; if(sigfl==0) { ++(*flag); drk_phase_flag[*flag]=j; drk_sw_time[*flag]=min_time;} } else { ++(*flag); drk_phase_flag[*flag]=j; drk_sw_time[*flag]=min_time;} } } else { if(cbar_base_drk[j]<0.0) ref_sign = -1; else ref_sign=1; if(bar_base_drk[j]<0.0) act_sign = -1; else act_sign=1; if(ref_sign==act_sign); else // Check complementary switch times if(ref_sign!=act_sign){ } min_time=cbar_base_drk[j] *delt/(cbar_base_drk[j]-bar_base_drk[j]); if((min_time < 0.0) (min_time > delt)) nerror("Base Drive Switch_time error"); if(min_time<=(1-tol)*delta_t) { // switch time < Δt if(*flag>=1) { for(i=1;i<=(*flag);i++) // identical switch times if(min_time>=drk_sw_time[i]-tol*delta_t && min_time<=drk_sw_time[i]+tol*delta_t) sigfl=1; if(sigfl==0) { ++(*flag); drk_phase_flag[*flag]=j; drk_sw_time[*flag]=min_time;} } else { ++(*flag); drk_phase_flag[*flag]=j; drk_sw_time[*flag]=min_time;} } } } } } } </pre>	<pre> ≈ test_drk_xover (&drk_sw_flag) ≈ Contd if(*flag>0) { // Adjust switching times in increasing order for(i=1;i<=(*flag);i++) { min_time=1.0; for(j=i;j<=(*flag);j++) { if(drk_sw_time[j]<min_time) { min_time=drk_sw_time[j]; ref_sign=j;} } if(i!=ref_sign) { SWAP(drk_sw_time[i],drk_sw_time[ref_sign],min_time); SWAP(drk_phase_flag[i],drk_phase_flag[ref_sign],act_sign);} } } return;} </pre>
	Figure 4-10

Fig. 4-10. Search for Basedrive X-Over

```

≈ restore_drk_out ( ) ≈
// Global array restoration for evaluation
// of basedrive switch transition time
void restore_drk_out(void)
{
    int j;
    for(j=1;j<=3;j++)
        base_drk[j]=cbase_drk[j];
        bar_base_drk[j]=cbar_base_drk[j];
        back_emfk[j]=cback_emfk[j];
        ph_voltk[j]=cph_voltk[j];
        ph_curk[j]=cph_curk[j];
        ifbk[j]=cifbk[j]; ffbk[j]=cffbk[j];
}
return;}
    
```

Fig. 4-9. Restore basedrive variables

```

≈ inter_base_drk_loop_sim (&drk_sw_flag) ≈
//Simulate basedrive with accurate switching times
void inter_base_drk_loop_sim(int *flag)
{
    int i;
    double zeit;
    zeit=delt; // Retain original time step info.
    restore_drk_out(); // Recover global variables
    for(i=1;i<=(*flag);i++) {
        delt=drk_sw_time[i]; // simulate to switching instant tx
        if(i>1) delt -= drk_sw_time[i-1];
        setup_fo_filt(); base_drive(); run_post_drksw(); }
    delt=zeit-drk_sw_time[*flag];
    setup_fo_filt(); //Complete time step interval Simn.
    base_drive(); run_post_drksw();
    delt=zeit; // Restore original time step interval Δt
    setup_fo_filt();
    return;}
    
```

Fig. 4-11. BDJ X-over Simulation

```

≈ run_post_drksw ( ) ≈
≈ pwm_inv ( ) ≈
// Inverter O/P and Motor Phase Voltage Generation
double vng;
int test_flag;
void pwm_inv(void)
{
    int j,vo; // Vo ≡ inverter Tristate switching indicator
    test_flag=0; // Phase winding count with zero current flow
    vng=0.0; // Stator winding neutral voltage w.r.t. ground
    // PWM Inverter Conduction State
    for(j=1;j<=3;j++) { flag_cur[j]=0;
        ph_htkm1[j]=ph_htk[j]; ph_voltkm1[j]=ph_voltk[j];
        if(base_drk[j]>Vth && bar_base_drk[j]<Vth) vo=1;
        else
            if(base_drk[j]<Vth && bar_base_drk[j]>Vth) vo = -1;
        else
            if(base_drk[j]<Vth && bar_base_drk[j]<Vth) vo=0;
        else nerror("NO PWM Inverter Control");
    }
    if((vo==1) || (vo==0 && ph_curk[j]<0.0)) ph_htk[j]=Vdc;
    else
        if((vo == -1) || (vo==0 && ph_curk[j]>0.0)) ph_htk[j]=0.0;
    else { test_flag += 1; flag_cur[j]=j;}
    // Motor Winding Phase Voltage Generation
    if((test_flag == 3) || (test_flag == 2))
        for(j=1;j<=3;j++) ph_voltk[j]=back_emfk[j];
    if(test_flag == 0) {
        for(j=1;j<=3;j++) vng += ph_htk[j]/3;
        for(j=1;j<=3;j++) ph_voltk[j]=ph_htk[j]-vng;}
    if(test_flag==1) {
        for(j=1;j<=3;j++) if(j==flag_cur[j]) test_flag=j;
        ph_htk[test_flag]=back_emfk[test_flag];
        for(j=1;j<=3;j++) vng += ph_htk[j]/2.0;
        ph_htk[test_flag] += vng;
        for(j=1;j<=3;j++) ph_voltk[j]=ph_htk[j]-vng;
        test_flag=0;}
    return;}
    
```

Fig. 4-12. Post Basedrive Operation

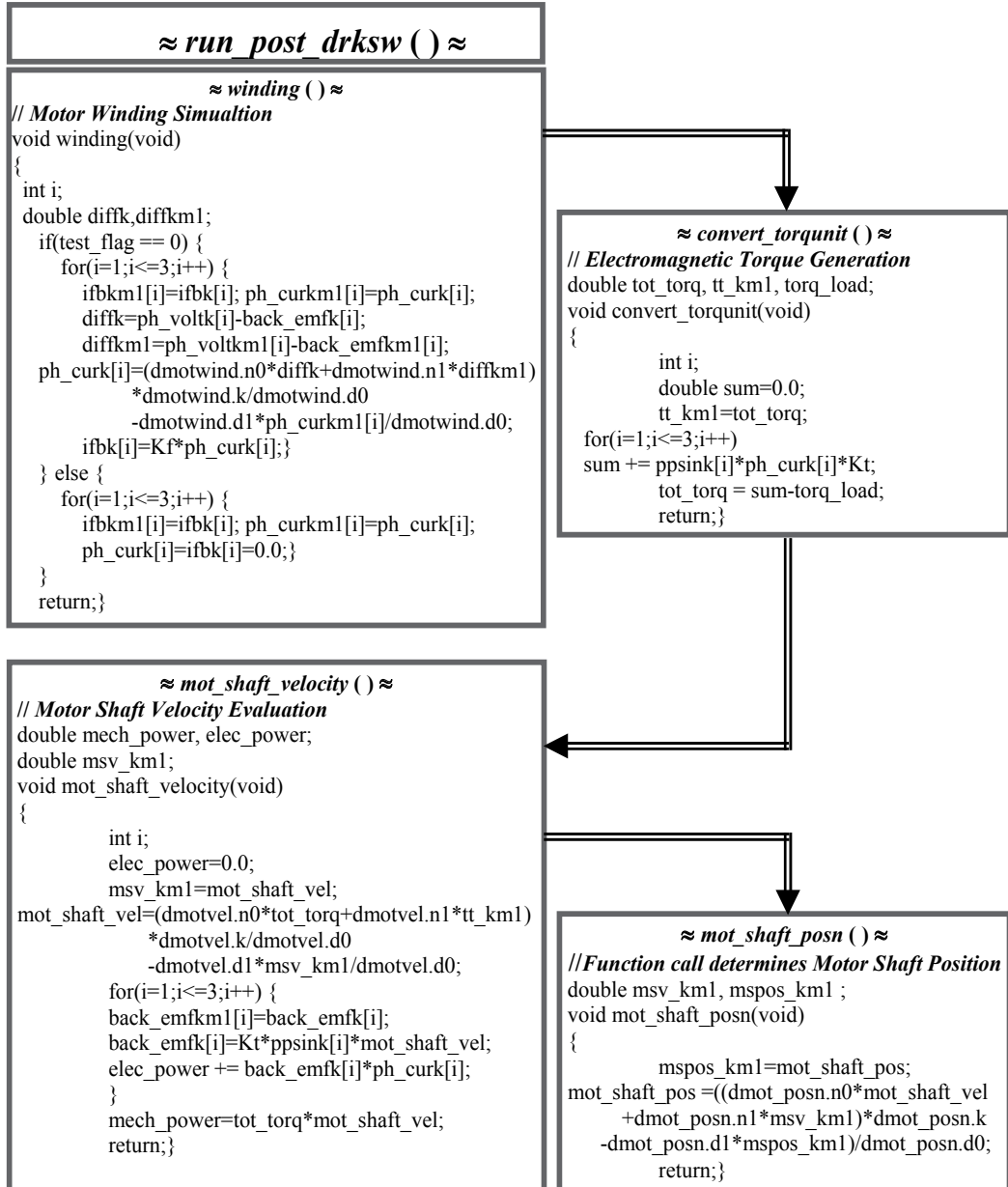


Fig. 4-13. Post Basedrive Call Sequence For Inverter Fed Motor Operation

If one or more phase currents are zero during the condition $V_O = 0$ a *test_flag* \equiv *tf* is incremented by unity for each null occurrence and the relevant phases are tagged using the *test_cur[j]* array for later identification in the computation of the relevant motor winding phase voltages. A test flag count of 2 or 3 indicates that the phase voltages are identical to the back EMF voltages *back_emfk[j]* \equiv $v_e^k[j]$ from the previous simulation step using expressions (XXIII) and (LVII) in the previous chapter. If the test flag (*u*) value is unity the associated phase current *ph_curk[test_flag]* is zero and the following relations result

$$\begin{aligned} v_{jg} &= v_{js} + v_{sg} = r_s i_{js} + L_s \frac{di_{js}}{dt} + v_{ej} + v_{sg}; \forall j \neq tf \equiv u \\ v_{us} &= v_{eu}; \quad \therefore i_{us} = 0 \\ v_{sg} &= \frac{1}{2} \left[\sum_{j \neq u} v_{jg} + v_{us} \right]; \quad \therefore \sum_{j \neq u} i_{js} = 0 \ \& \ \sum_j v_{ej} = 0 \end{aligned} \quad (I)$$

which enable the phase voltages to be calculated from the 3 Φ inverter o/p.

winding ()

determines the stator winding current *ph_curk [j]* from a knowledge of the phase voltages and motor parameters $\{r_s, L_s\}$ encoded in the discrete filter representation of the winding electrical behaviour.

convert_torqunit ()

computes the developed electromagnetic torque, manifested in the winding current flow, via the 3 Φ commutation vector *psink[j]* and motor torque constant K_t for dynamic operation.

mot_shaft_vel ()

evaluates the rotor shaft velocity *mot_shaft_vel* \equiv ω_m^k from the net torque *tot_torq* \equiv Γ^k available, with the effects of load torque retardation *torq_load* \equiv Γ^{k_l} considered, using a discrete filter representation of the rotor dynamics as per (II) in the previous chapter with parameters $\{J_m, J_l, B_m\}$. The back emf can be determined via the motor voltage constant K_e , along with the mechanical (*mech_power*) and electrical (*elec_power*) power delivery, once the shaft velocity is known.

mot_shaft_pos ()

evaluates the motor shaft position *mot_shaft_pos* from the rotor velocity.

3. BLMD model simulation with restraining shaft load torque

The effect of a fixed applied shaft load Γ_l on BLMD model behaviour can be monitored via its simulation characteristics, in torque control mode with and without impedance angle compensation considered, for a range of torque demand step input stimuli capable of matching the posed restraining torque. A suitable choice for the target load magnitude is based on the manufacturers continuous rated stall torque of 5Nm for the particular motor type specified in Table I of the previous chapter. The set of motor shaft velocity step response characteristics $\{\omega_r | 4v \leq \Gamma_d \leq 9v, \Delta\Gamma_d = 1v\}$ for the indicated torque demand Γ_d range is displayed in Figures 6 and 7 without impedance angle compensation.

The response time T_{res} required for the motor drive to reach the maximum shaft velocity of $\omega_{rmax} = 419 \text{ rads.sec}^{-1}$ in each case, corresponding to the rated output of 4000 rpm in Table I of the previous chapter, improves with increased motor shaft acceleration via the "dynamic factor" $[(\Gamma_e - \Gamma_l)/J_m]$ as a consequence of its dependency on torque demand input. The corresponding generated torque step response family of characteristics

$\{\Gamma_e | 4v \leq \Gamma_d \leq 9v \ \& \ \Delta\Gamma_d = 1v\}$ for the specified variation in torque demand inputs are shown in Figures 8 and 9.

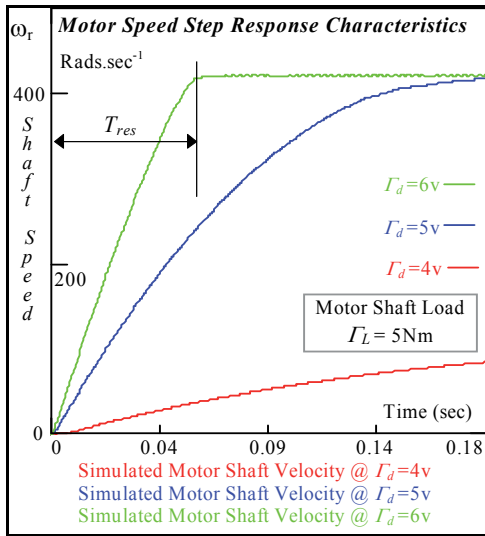


Fig. 6. Shaft Velocity Step Response

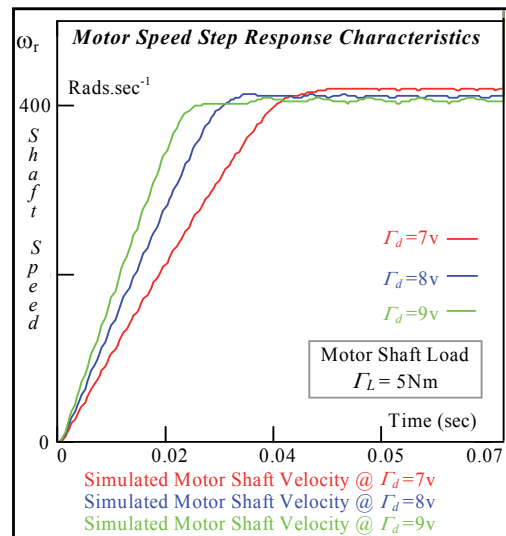


Fig. 7. Shaft Velocity Step Response

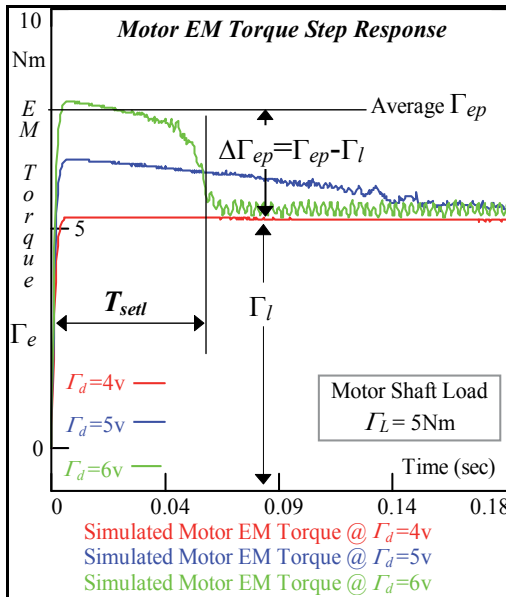


Fig. 8. Generated Torque Response

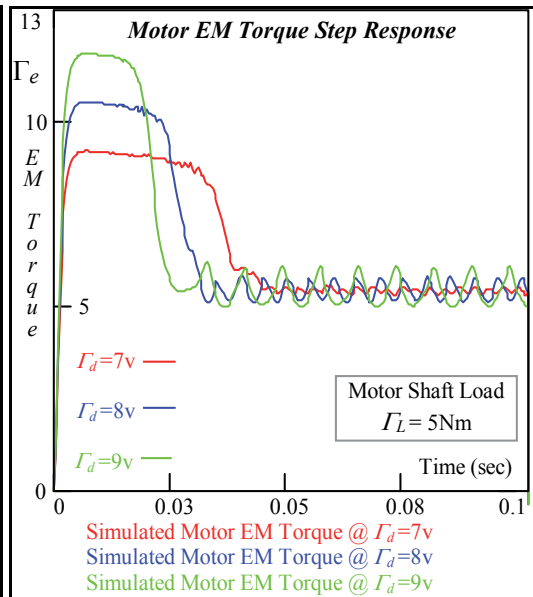


Fig. 9. Generated Torque Response

All the torque response characteristics, with the exception of that at $\Gamma_d = 4v$, exhibit overshoot before settling to the required value of $\sim 5.3\text{Nm}$ to overhaul the fixed restraining load torque (5Nm) and frictional effects. The degree of overshoot increases in proportion to the torque demand i/p, as exhibited in Figure 10 for the average peak EM torque Γ_{ep}

responsible for overshoot $\Delta\Gamma_{ep}$, accompanied by a corresponding reduction in settling time as shown in Figure 11.

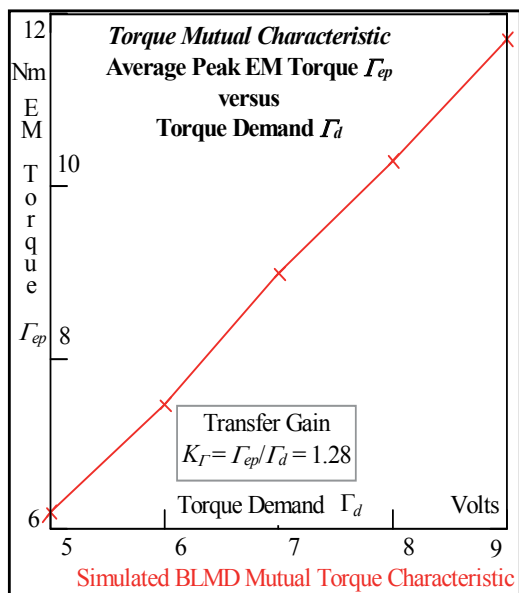


Fig. 10. Mutual Torque Characteristic

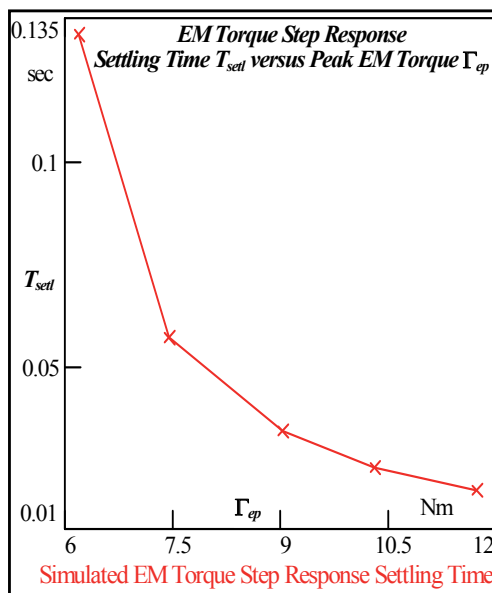


Fig. 11. Torque Settling Time

3.1 Theoretical consideration of motor accelerative dynamical performance

The reduction in settling time is paralleled by the shaft velocity response time improvement in reaching rated motor speed. It is evident from inspection of the velocity and torque simulation traces that a direct correlation exists between the EM torque settling time and motor shaft velocity response time as indicated in Table I.

Torque Load $\Gamma_l = 5\text{Nm}$		"Inertial" Time Constant $\tau_m = J_m / B_m = 0.318$			Tran. Gain (Fig.10) $K_\Gamma = 1.28$	
Torq-Dem Γ_d (Volts)	Av. Peak EM Torq Γ_{ep} (Nm)	Torque Overshoot $\Gamma_{ep} - \Gamma_l$ (Nm)	Torq. Settling Time T_{setl} (sec) Figs. 8/9	Shaft Velocity Rise Time T_{res} (sec) Figs. 6/7	Theoretical Rise Time T_r (sec) Eqn. (IV)	Rise Time T_α (sec) via Dyn-Fac. Eqn (VI)
5	6.2	1.2	~0.13	~0.13	0.131	0.107
6	7.45	2.45	~0.06	~0.06	0.057	0.0524
7	8.98	3.98	~0.04	~0.037	0.034	0.0323
8	10.29	5.29	~0.03	~0.027	0.025	0.0243
9	11.634	6.634	~0.024	~0.022	0.02	0.02

Table I. Correlation of EM Torque Settling Time with Shaft Velocity Response Time

The shaft velocity step response rise time, as defined in Figure 6, can be obtained directly from the solution of the transfer function (XCIX) from the previous chapter in the time

domain with a step input approximation for the average peak torque overshoot $\Delta\Gamma_{ep} = (\Gamma_{ep} - \Gamma_l)$ in Figure 8 as

$$\omega_r(t) = \frac{\Delta\Gamma_{ep}}{B_m} \left[1 - e^{-t/\tau_m} \right] \quad (II)$$

with time constant

$$\tau_m = J_m / B_m \quad (III)$$

The step response time, for the shaft velocity under load conditions to reach maximum speed $\omega_{r,max}$, can be determined from (II) for different torque demand i/p and corresponding peak torque values as per the above Table I with

$$T_r = \tau_m \ln \left[\frac{\Delta\Gamma_{ep}}{\Delta\Gamma_{ep} - B_m \omega_{r,max}} \right] \quad (IV)$$

The estimated rise times are in excellent agreement with the approximate settling and response times obtained from the BLMD model simulation traces. An alternative crude estimate of the response time can be obtained from the motor “dynamic factor”

$$\alpha = \frac{d\omega_r}{dt} = \frac{(\Gamma_{ep} - \Gamma_l)}{J_m} \quad (V)$$

for average peak torque endurance as the acceleration time

$$T_\alpha = \frac{\omega_{r,max}}{\alpha} \quad (VI)$$

from standstill to maximum speed assuming a shaft velocity linear transient response which is valid for torque demand values in excess of 5 volts.

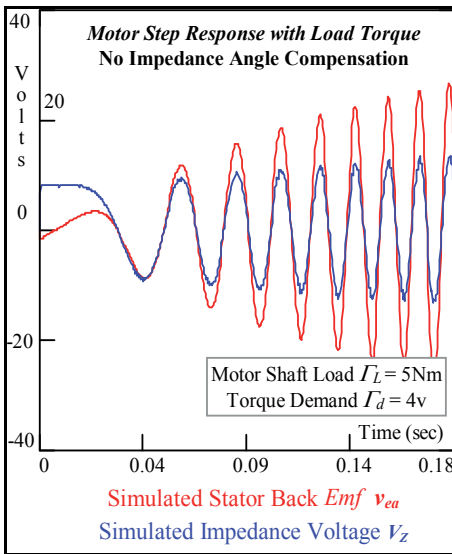


Fig. 12. Motor Winding Voltages

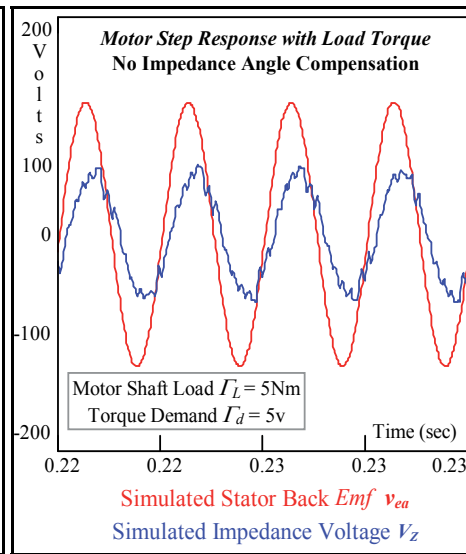


Fig. 13. Motor Winding Voltages

These response estimates, given in above Table I, are in good agreement with those already obtained except for that at $\Gamma_d = 5v$ where the rise time is longer with exponential speed ramp-up.

3.2 Torque demand BLMD model response - internal node simulation

The simulated back-EMF along with the stator impedance voltage drop are illustrated in Figures 12 and 13 for two relatively close values of torque demand i/p. In the former case the torque demand i/p of 4volts results in sufficient motor torque to meet the imposed shaft load constraint (5Nm) without reaching rated speed and saturation ($\pm 10v$) of the current compensator o/p trace shown in Figure 14. The corresponding reaction EMF exceeds the winding impedance voltage V_Z and is almost in phase with the stator current, which is proportional to V_Z , at the particular low motor speed reached. The torque demand i/p of 5v in the latter case results in the onset of a clipped current controller o/p in Figure 15 due to saturation (± 10) at rated motor speed ω_{rmax} .

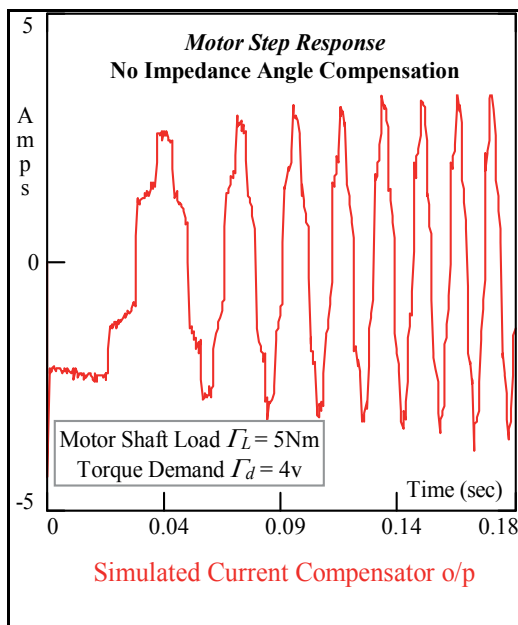


Fig. 14. Current Compensator o/p

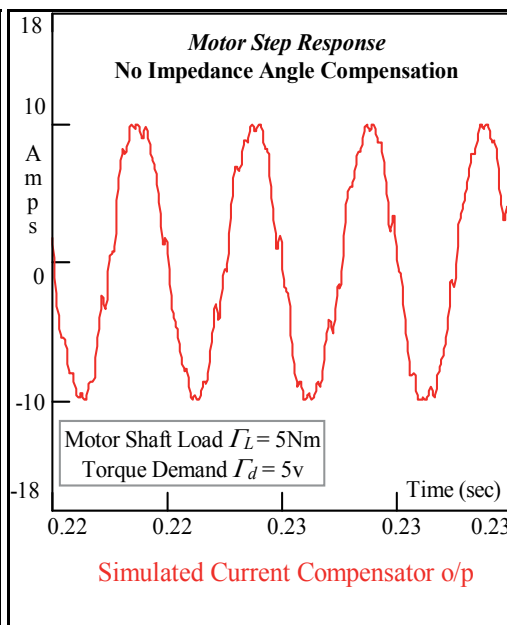


Fig. 15. Current Compensator o/p

The back-EMF generated at this speed greatly exceeds the winding impedance voltage, as in the former case, and leads the stator current necessary to surmount the torque load by the internal power factor (PF) angle ($\sim 27^\circ$) with a correspondingly low power factor (~ 0.7).

The stator winding currents corresponding to the inputs $\Gamma_d \in \{5v, 9v\}$ are displayed in Figures 16 and 17 respectively which indicate the marked presence of peak clipping in the latter case with loss of spectral purity due to heavy saturation of the current controller o/p for $\Gamma_d > 5v$.

The simulated motive power characteristic with the steady state threshold value of $\sim 2.3kW$ necessary to sustain shaft motion, for $\Gamma_d = 5v$ with restraining load torque and friction losses is shown in Figure 18 at base speed $\omega_{rmax} \cong 420 \text{ rad.sec}^{-1}$.

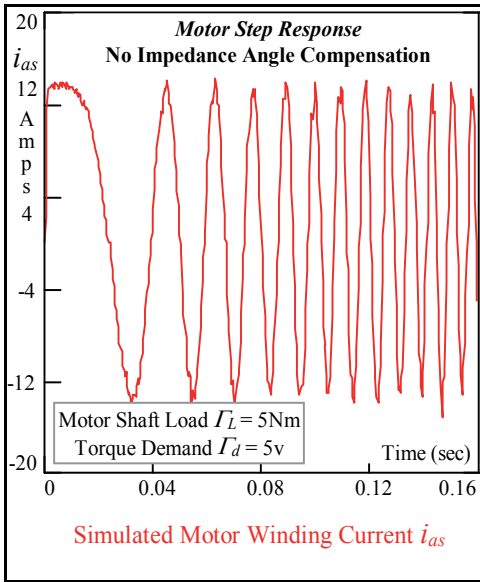


Fig. 16. Stator Winding Current

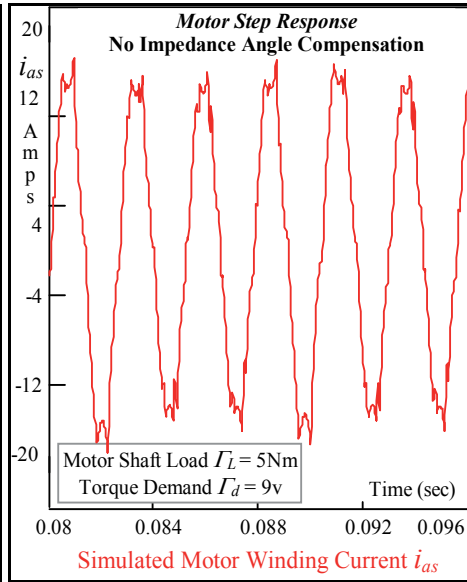


Fig. 17. Stator Winding Current

This can be rationalized from the power budget required to sustain the load torque at rated speed via (LXXXVIII) in the previous chapter as

$$P_l = \Gamma_l \omega_{r_{max}} = (5)(420) = 2.1\text{kW} \tag{VII}$$

The excess coupling field power required to surmount mechanical shaft friction losses is shown simulated in Figure 19 with a steady state estimate of ~200 watts.

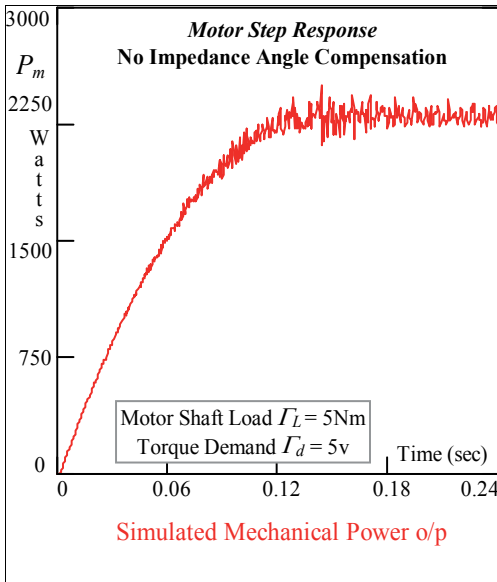


Fig. 18. Mechanical Power Delivery

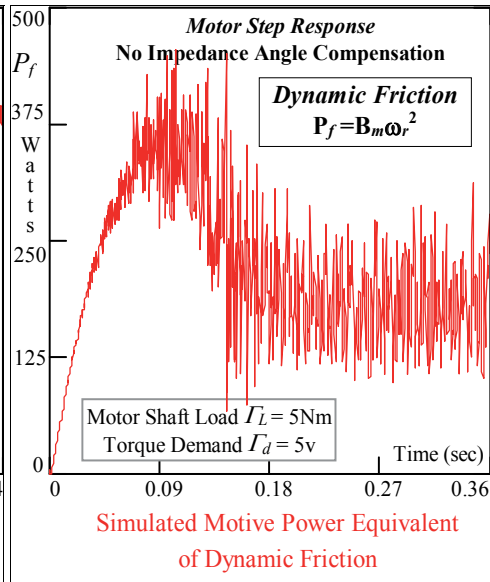


Fig. 19. Dynamic Friction Loss

Stator Winding Phasor RMS Magnitude Estimation as per Figure 44 in previous chapter via BLMD Model Simulation						
Torq_Dem Γ_d Step i/p	Shaft_Vel ω_{rmax} rad.sec ⁻¹	Elec_Power P_e volts (XLVII) - Prev. Chap	Back_EMF $ V_{ej} $ volts	Imped_Vol $ V_z $ volts (XC) - Previous Chap	Ph_Cur $ I_{js} $ amps	
5v	419.2	2301	94.82	44.87	9.09	
6v	420.3	2305	95.24	48	9.7	
7v	418.9	2298	94.78	50.89	10.32	
8v	410.3	2251	92.05	52.42	10.84	
9v	405.5	2224	91.5	53.66	11.23	
Derived Phase Quantities as per Figure 42 in previous chapter						
Torq_Dem Γ_d volts	Int. PF Ang ϕ_I (XCII) - Prev. Chap.	ϕ_I Estimate via Figure 13	Ph_Vol V_{js} (XCIII) - Prev. Chap	Imp_Ang ϕ_z (LXXXIV) - Prev. Chap.	Load Ang β_T (XCIV) - Prev. Chap	PF Ang ϕ $\phi_I + \beta_T$
5	27.13°	27.13°	126.44v	81.26°	15.52°	42.65°
6	33.7°	32.16°	131.75v	81.28°	15.6°	49.3°
7	38.43°	38.74°	136.56v	81.26°	14.68°	53.11°
8	41.24°	42.58°	136.5v	81.08°	13.83°	55.07°
9	43.8°	45.12°	138.1v	80.97°	13.58°	57.38°

Table II. Phase Angle Evaluation for BLMD Steady State Operation with $\Gamma_l = 5Nm$

The effect of shaft load on the BLMD model simulation characteristics for $\Gamma_d > 5v$ is summarized in above Table II for steady state conditions with the aid of the general phasor diagram in Figure 42 of the previous chapter.

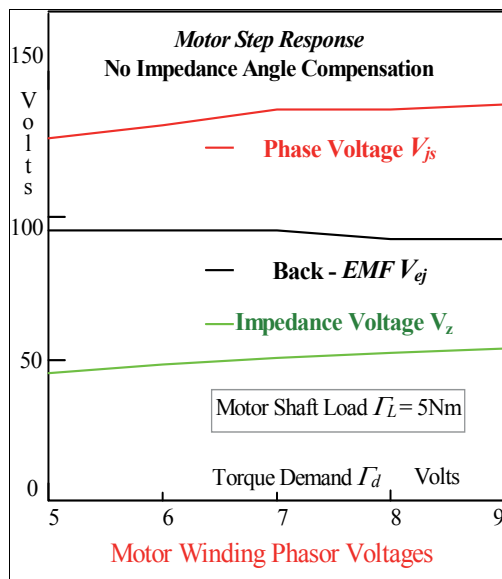


Fig. 20. Motor RMS Phasor Voltages

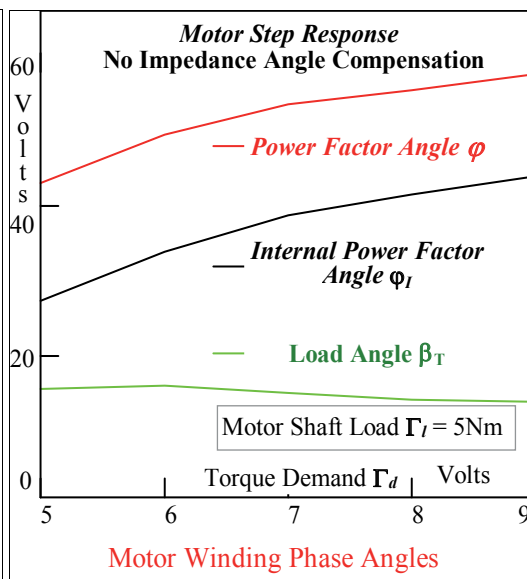


Fig. 21. Stator Winding Phase Angles

It is evident from the table that the back EMF has reached its peak rms value with the onset of maximum shaft velocity, for all values of $\Gamma_d > 5V$, with

$$V_{ej_{\max}} = \frac{K_e}{\sqrt{2}} \omega_{r_{\max}} = \left(\frac{0.315}{\sqrt{2}} \right) (420) = 93.6V \quad (\text{VIII})$$

Furthermore the impedance voltage drop V_z in (XC) of the previous chapter is limited to a very small increase with torque demand current I_{dj} listed in Table II and is shown almost stabilized to a constant value in Figure 20. This voltage clamping effect, due to current compensator o/p saturation in response to tracking current feedback, is controlled to achieve the desired rms level of clipped current flow in the stator winding as shown in Figure 17 to satisfy torque load requirements. The rms winding current flow necessary at unity internal power factor to meet steady state torque load and friction demands at $\sim 5.4N\text{m}$ in Figures 8 and 9 can be determined from (XLV) in the previous chapter as

$$\hat{I}_{js} = \left(\frac{\sqrt{2}}{3} \right) \left(\frac{\Gamma_e}{K_e} \right) = \left(\frac{\sqrt{2}}{3} \right) \left(\frac{5.42}{0.315} \right) = 8.11 \text{ Amps} \quad (\text{IX})$$

This is almost identical to the rms values obtained from BLMD model simulations in Table II, which are consistent with increased torque current demand, when internal power factor self adjustments are accounted for as in

$$\hat{I}_{js} = I_{js} \cos \varphi_1 \approx 8.1 \text{ Amps} \quad (\text{X})$$

The internal power factor angles, listed in Table II and displayed in Figure 21, are deduced for $\Gamma_d > 5v$ from the mechanical power transfer by substituting the rms quantities obtained from back EMF and winding current simulations in expression (XCII) of the previous chapter. These angles, which increase with torque demand i/p, can be alternatively calculated from the simulated winding current response using (X) with knowledge of \hat{I}_{js} .

The tabulated angle estimates obtained statistically as the phase lag between the current and back EMF waveforms in Figure 13, for example, are in close agreement with those from (XCII) of the previous chapter. The motor winding impedance angle φ_z , which is fixed at rated machine speed $\omega_{r_{\max}}$ is determined from (LXXXIV) as $\sim 81.2^\circ$ in Table II.

The rms winding voltage V_{js} is obtained in its pure spectral form, instead of the PWM version furnished by the current controlled inverter, upon application of (XCIII) to the known rms phasor quantities given in Table II for different values of $\Gamma_d > 5V$.

Knowledge of the relevant phasor magnitudes with corresponding phase angles enable the load angle β_T to be determined from (XCV) of the previous chapter for given shaft load conditions. This is approximately fixed, at $\sim 15^\circ$ as indicated in Table II with about 2° variation, over the torque demand i/p range as shown in Figure 21. The resulting power factor angle φ listed in Table II increases with φ_l , for fixed load angle over the torque demand i/p range as shown, in a way that is commensurate in (X) with motor current requirements towards sustaining shaft load torque with a decreasing power factor as illustrated in Figure 22.

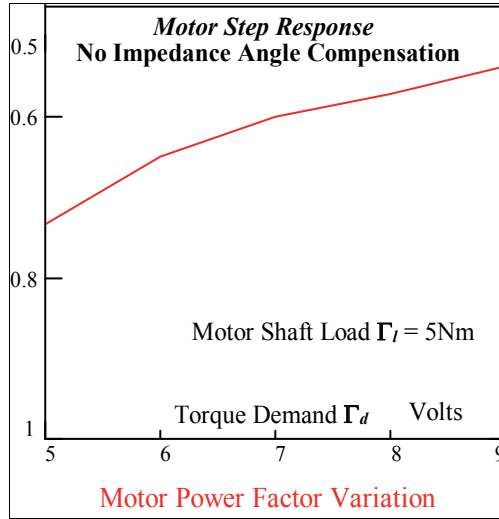


Fig. 22. Power Factor Variation

3.3 BLMD model simulation with novel impedance angle compensation

The effect of motor impedance angle compensation (MIAC), manifested as commutation phase lead angle incorporated into the BLMD model in (XCVIII) of the last chapter as $p\theta_r - 2(j-1)\frac{\pi}{3} \rightarrow (p\theta_r + \varphi_z) - 2(j-1)\frac{\pi}{3}$ on the motor step response velocity and torque characteristics is illustrated in Figures 23 and 24 for the torque command i/p range $4\text{v} \leq \Gamma_d \leq 9\text{V}$ at step size intervals of $\Delta\Gamma_d = 1$ volt .

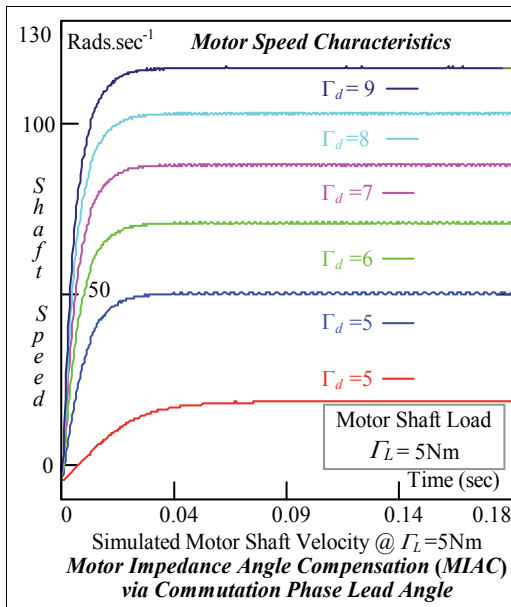


Fig. 23. Shaft Velocity with MIAC

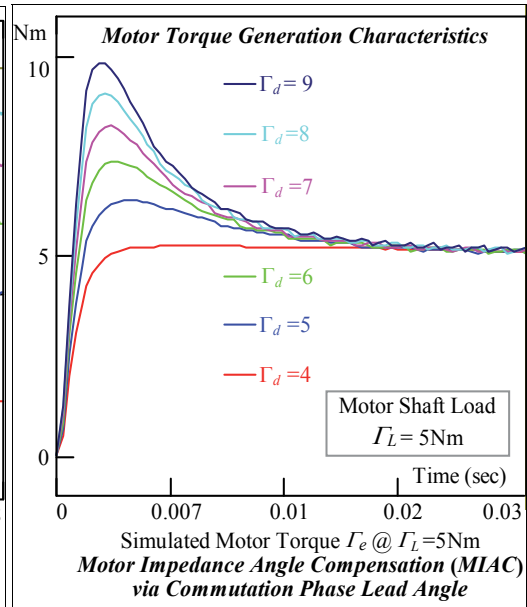


Fig. 24. Torque Response with MIAC

The variation of peak torque overshoot with i/p demand, displayed as the mutual characteristic in Figure 25, is linear with a transfer gain that is lower than that without MIAC in Figure 10. Consequently the maximum peak torque delivery, for a given i/p demand to sustain shaft load requirements, is lower in amplitude and of shorter overshoot pulse duration as seen in Figure 24 when compared with that without MIAC in Figures 8 and 9. Furthermore the persistence of torque overshoot is lower with a much reduced settling time (<0.015 sec), in reaching steady state sustained load conditions in all cases albeit at lower acceleration and much smaller drive speeds, thereby exerting less mechanical stress on the drive shaft components and minimizing shaft flexure in EV propulsion applications.

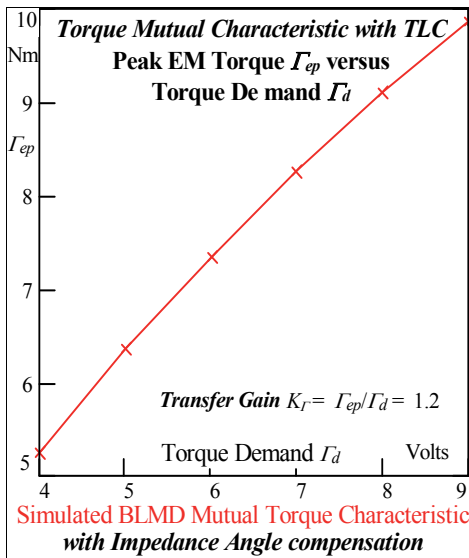


Fig. 25. Mutual Torque with MIAC

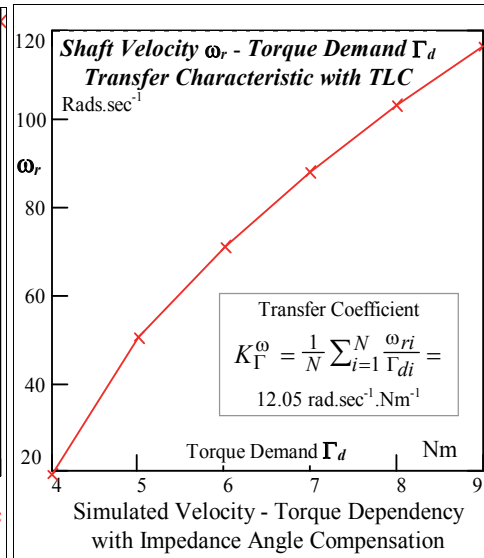


Fig. 26. Torque - Velocity Transfer Curve

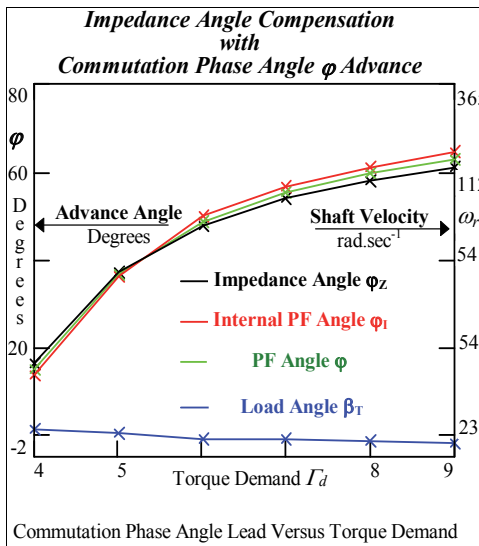


Fig. 27. Impedance Angle Compensation

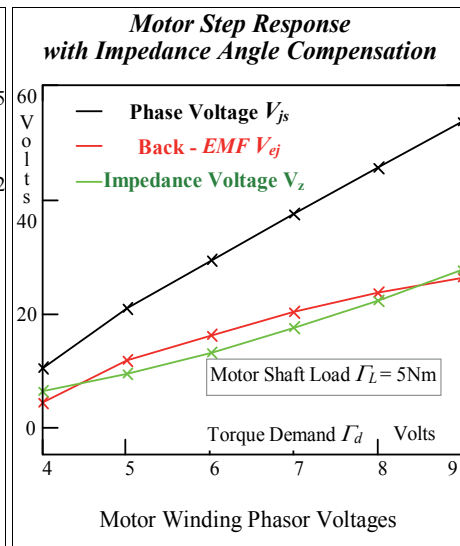


Fig. 28. Phasor Voltages with MIAC

The shaft velocity characteristics also indicate a much lower steady state motor run speed, with MIAC deployed, which never reaches velocity saturation $\omega_{r\max} = 419 \text{ rad.s}^{-1}$ over the permissible torque demand i/p range of $-10\text{V} \leq \Gamma_d \leq 10\text{V}$. The relevant command torque to shaft velocity transfer characteristic is approximately linear as shown in Figure 26 which indicates a maximum motor operating speed of $\omega_{r\max}^* \approx 120 \text{ rad.s}^{-1}$ with $\omega_{r\max}^* < 30\% \omega_{r\max}$ under rated load conditions (5Nm) for a maximum demand i/p of $\Gamma_{d\max} = 10\text{V}$. This speed reduction is singly due to the maintenance of an almost zero load angle β_T shown in Figure 27, between the motor terminal V_{js} and back EMF V_{ej} rms voltage phasors in Figure 45 of the previous chapter, by commutation phase angle advance for optimal torque production as indicated from the BLMD simulation results in Table III.

This phase compensation technique results in back EMF and winding impedance voltage V_z phasors that appear approximately equal in magnitude over the allowable torque demand input range as shown in Figure 28. Furthermore the internal power factor angle ϕ_I is forced to adopt approximately the same value as the machine impedance angle ϕ_z as indicated in Table III, by the phase advance measure ϕ_z in the current commutation circuit, with a consequent collinear alignment of phasors V_{ej} and V_z in Figure 45. This collinear arrangement can only be sustained at a particular machine speed that is dependent on the torque demand i/p which determines the subsequent winding current flow and thus the necessary impedance angle for alignment. This reasoning can be deduced as follows by noting that for a given torque load Γ_l the rms winding current flow is linear with torque demand i/p as per Table III and Figure 29.

Stator Winding Phasor RMS Magnitude Estimation as per Figure 45 of the Previous Chapter via BLMD Model Simulation					
Torq_Dem Γ_d Step i/p	Shaft_Vel $\omega_{r\max}$ rad.sec ⁻¹	Elec_Power P_e (XLVII) in Prev. Chap.	Back_EMF V_{ej} volts	Imped_Vol V_z volts - (XC) in Prev. Chap.	Ph_Cur I_{js} amps
4v	18.6	94.44	4.17	6.06	7.76
5v	48.95	257.2	11.5	9.23	9.7
6v	70.87	363.67	16.01	13.05	11.71
7v	87.9	452.6	19.95	17.33	13.66
8v	102.9	531.2	23.28	22.18	15.7
9v	116.3	602.2	26.3	27.45	17.74
Derived Phase Quantities as per Figure 42 of the Previous Chapter					
Torq_Dem Γ_d volts	Int. PF Ang ϕ_I (XCII) in Prev. Chap.	Ph_Vol V_{js} (XCIII) in Prev. Chap.	Imp_Ang ϕ_z (LXXXIV) in Prev. Chap.	Load Ang β_T (XCV) in Prev. Chap.	PF Ang ϕ $\phi_I + \beta_T$
4	13.75°	10.23	16.1°	1.39°	15.14°
5	36.13°	20.73	37.22°	0.51°	36.64°
6	49.71°	29.06	47.72°	-1.0°	48.71°
7	56.38°	37.27	53.76°	-1.22°	55.16°
8	61.02°	45.44	57.95°	-1.5°	59.52°
9	64.52°	53.73	61.01°	-1.79°	62.73°

Table III. Phase Angle Evaluation at $\Gamma_l = 5\text{Nm}$ with Motor Impedance Angle Compensation

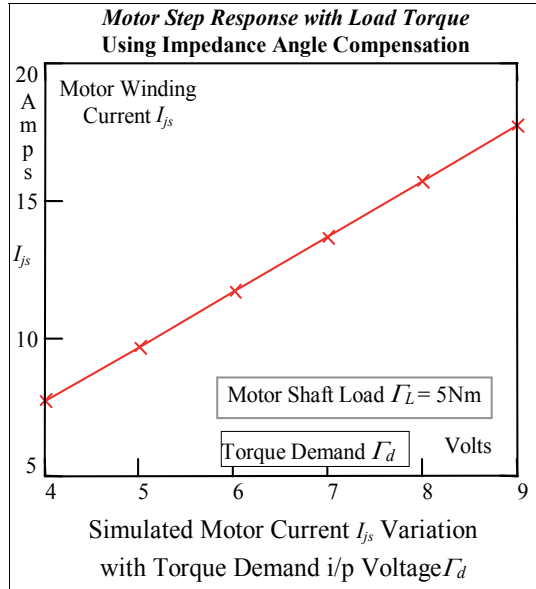


Fig. 29. Motor Current Variation

3.3.1 MIAC substantiation via theoretical analysis and validation

The internal power factor angle φ_I can be determined theoretically for fixed winding current flow corresponding to a given torque demand i/p using (IX) and (X), assuming negligible dynamic friction at the shaft speeds concerned with $\Gamma_I \gg \Gamma_f$, as

$$\varphi_I = \cos^{-1} \left\{ \left(\frac{\sqrt{2}}{3} \right) \frac{\Gamma_I}{K_t I_{js}} \right\} \quad (\text{XI})$$

The motor terminal voltage i/p V_{js} in (XCIII) from previous chapter can be optimized with respect to the motor impedance angle φ_z , which is unknown, in terms of the rms phasor quantities V_{ej} , V_z and the fixed internal power angle φ_I from (XI) by letting

$$\frac{dV_{js}}{d\varphi_z} = 0 \Rightarrow \sin(\varphi_z - \varphi_I) = 0 \quad (\text{XII})$$

This procedure results in the impedance angle φ_z in terms of the known angle φ_I as

$$\varphi_z = \varphi_I \quad (\text{XIII})$$

with

$$\max V_{js} = \sqrt{V_{ej}^2 + V_z^2 + 2V_{ej}V_z} = (V_{ej} + V_z) \quad (\text{XIV})$$

which is unknown as both V_{ej} and V_z depend on the motor shaft velocity ω_r . The shaft velocity can now be determined from (LXXXIV) from previous chapter using expression (XIII) as

$$\omega_r = \left(\frac{r_s}{pL_s} \right) \tan \varphi_I \quad (\text{XV})$$

Theoretical Estimation of RMS Phasor Magnitudes						
Torq_Dem Γ_d Step i/p	Ph_Cur I_{js} Table III	Int_PF ϕ_I Eqn. (XI)	Shaft_Vel ω_r Eqn (XV)	Back_EMF V_{ej} Eqn (VIII)	Imp_Vol V_z Eqn. (XC) in Prev. Chap.	Ph_Vol V_{js} Eqn. (XIV)
4v	7.76 A	15.37°	17.71 rad/s	3.94v	6.04v	9.98v
5v	9.70 A	39.52°	53.17 rad/s	11.84v	9.43v	21.27v
6v	11.71 A	50.28°	77.55 rad/s	17.27v	13.74v	31.01v
7v	13.66 A	56.79°	98.43 rad/s	21.92v	18.71v	40.63v
8v	15.70 A	61.54°	118.87 rad/s	26.48v	24.71v	51.19v
9v	17.74 A	65.05°	138.49 rad/s	30.85v	31.54v	62.39v

Table IV. Motor Impedance Angle Compensation

This value of ω_r can be used to theoretically generate the rms voltage phasors V_{ej} , V_z and V_{js} using expressions (VIII), (XC) and (XCIII) in the previous chapter respectively from a knowledge of the motor winding phasor current I_{js} as per Table IV over the i/p torque demand range range $\Gamma_d \geq 4V$. The quantities obtained from BLMD simulations in Table III compare reasonably well with those derived in Table IV from theoretical considerations which reinforces model validation and confidence. The optimized internal power factor angle, which is almost identical to that in Table III, results in a zero load angle β_T from (XCV) in the previous chapter due to the phasor collinearity and thus improved torque control via the PWM voltage supplied by the current controlled inverter. The power factor angle ϕ , internal power factor angle ϕ_I and machine impedance angle ϕ_z variations with torque demand i/p, which are displayed in Figure 27 using estimates extracted from BLMD model simulation in Table III for $\Gamma_d \geq 4V$, are almost congruent with a mismatched difference manifested as the negligible load angle ($\beta_T \approx 0$).

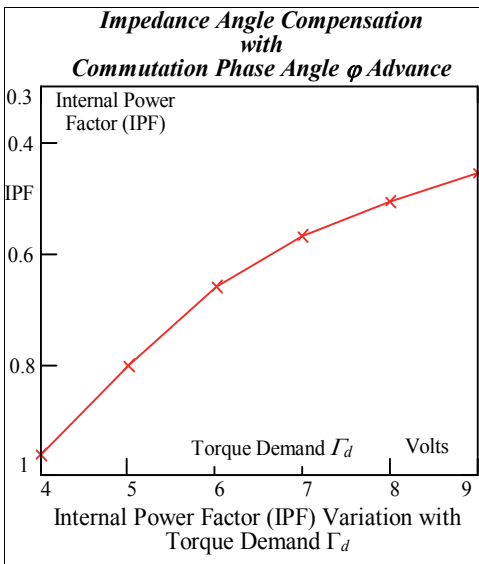


Fig. 30. Motor Power Factor

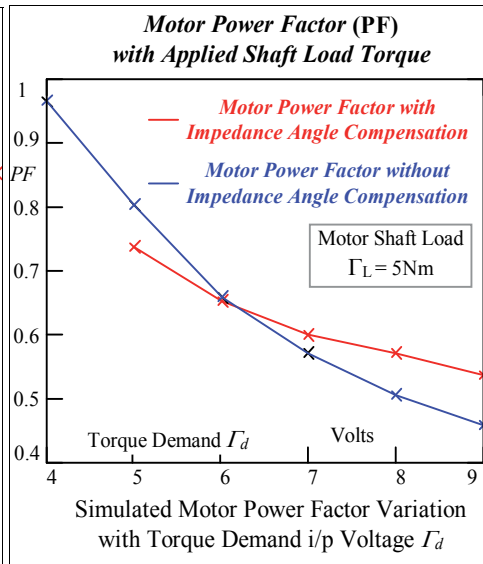


Fig. 31. Power Factor Comparison

The internal power factor $\cos\varphi_l$ shows a gradual deterioration with increasing torque demand i/p in Figure 30 as expected with the accompanying internal power factor angle φ_l adjustment, from the mirrored motor current increase in Figure 29, constrained by a fixed shaft load in (X). Impedance angle compensation results in a improved motor power factor as shown in Figure 31 than that without MIAC over the torque demand i/p range $4V \leq \Gamma_d \leq 6V$ necessary to meet load requirements Γ_l .

Motor speed reduction is also mirrored with a decrease of the shaft velocity step response rise time as shown Figure 32 with maximum values falling below the velocity time response floor of the uncompensated BLMD model. This results in constant motor speed operation, though small by comparison to that without phase angle advance, well below the rated value in torque control mode with smooth torque delivery to satisfy load requirements.

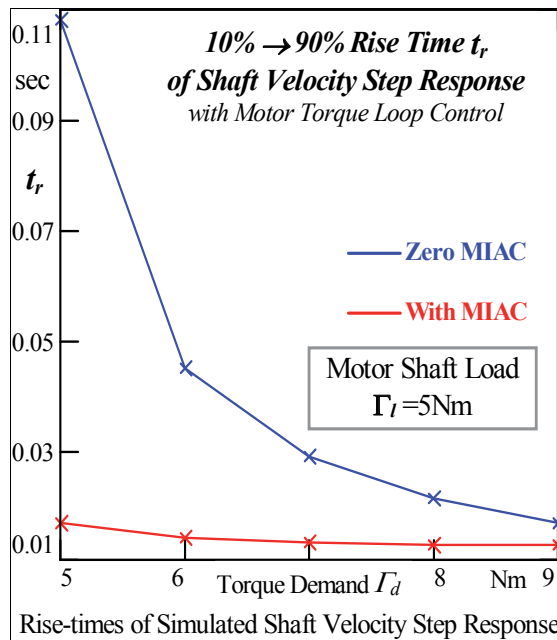


Fig. 32. Shaft Velocity Rise Times

The simulated motor winding impedance and back EMF voltages for mid (5V) and full range (9V) torque demand input values, which result in developed torque capable of surmounting the fixed restraining shaft load (5Nm), are displayed in Figures 33 and 34. Both sets of characteristics exhibit comparable amplitudes appropriate to the level of torque demand i/p, with speed related motor current phase lags φ_l as per Table III, that are much lower than those without MIAC in Figure 13. The impedance and back EMF voltages are interrelated which can be shown as follows by starting with expression (XC) for V_z and using (IX) and (X) giving

$$V_z = |Z| |I_{js}| = |Z| \left(\frac{\sqrt{2}}{3} \right) \left(\frac{\Gamma_l}{K_t} \right) \cos\varphi_l \quad (\text{XVI})$$

This can be rewritten by using (LXXXIV) in the previous chapter with optimized value of φ_l in (XIII) as

$$V_z = \left(\frac{\sqrt{2}}{3}\right) \left(\frac{\Gamma_L}{K_t}\right) \left(\frac{r_s^2 + (p\omega_r L_s)^2}{r_s}\right) \tag{XVII}$$

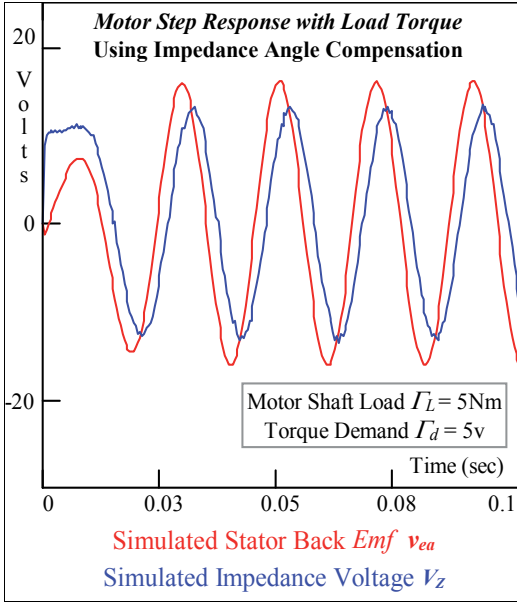


Fig. 33. Motor Winding Voltages

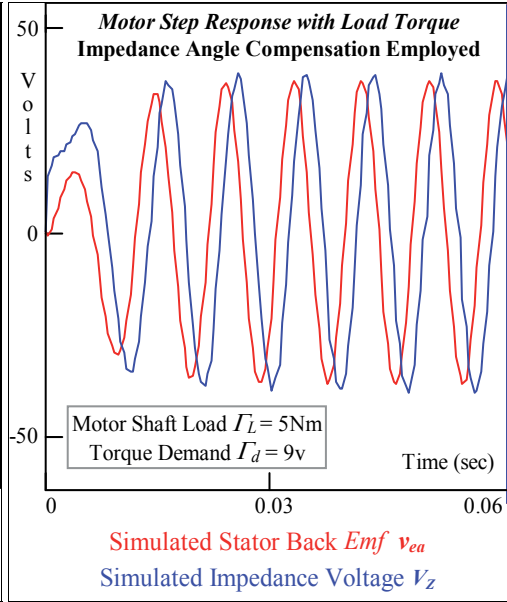


Fig. 34. Motor Winding Voltages

The shaft velocity ω_r , linking the back EMF, can be replaced in (XVII) by using (VIII) yielding

$$V_z = K_1 [1 + K_2 V_{ej}^2] \tag{XVIII}$$

where

$$K_1 = r_s \left(\frac{\sqrt{2}}{3}\right) \left(\frac{\Gamma_L}{K_t}\right) = 5.612 \tag{XVIII}$$

and

$$K_2 = \left(\frac{\sqrt{2} p L_s}{K_t r_s}\right)^2 = 4.855 \times 10^{-3} \tag{XIX}$$

from substitution of parameters in Table I of the previous chapter and $\Gamma_L = 5\text{Nm}$. The impedance voltage in (XVII) is expressed as a quadratic equation in terms of the back EMF with points of equality corresponding to

$$V_{ej} \in \{6.915\text{v}, 29.79\text{v} | V_z = V_{ej}\} \tag{XX}$$

which are visible in Figure 28 as points of intersection of the two voltage traces.

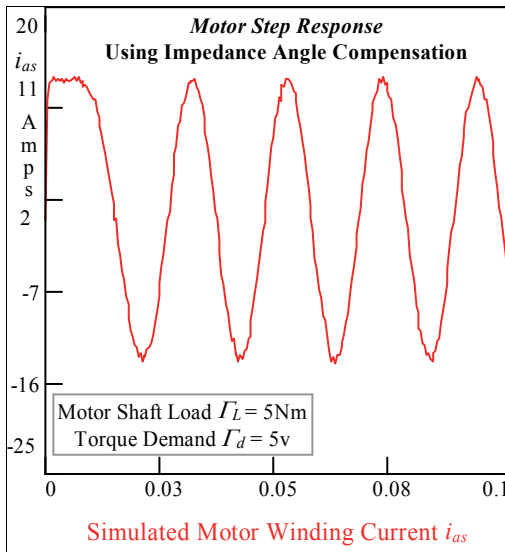


Fig. 35. Stator Winding Current Flow

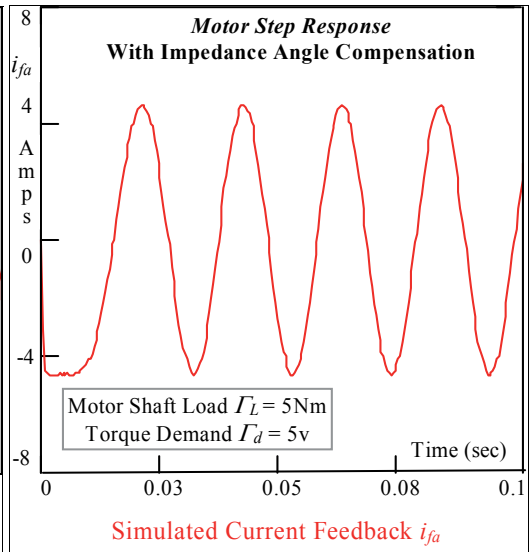


Fig. 36. Motor Current Feedback

These crossover points divide the rms V_z amplitude variation along with V_{ej} in Figure 28 into three distinct regions, over the usable torque demand i/p range as per Table IV, with

$$\begin{aligned}
 &V_z > V_{ej} \text{ for } V_{ej} < 6.9\text{v} \\
 &V_z < V_{ej} \text{ for } 6.9\text{v} < V_{ej} < 29.8\text{v} \\
 &V_z > V_{ej} \text{ for } V_{ej} > 29.8\text{v}
 \end{aligned}
 \tag{XXI}$$

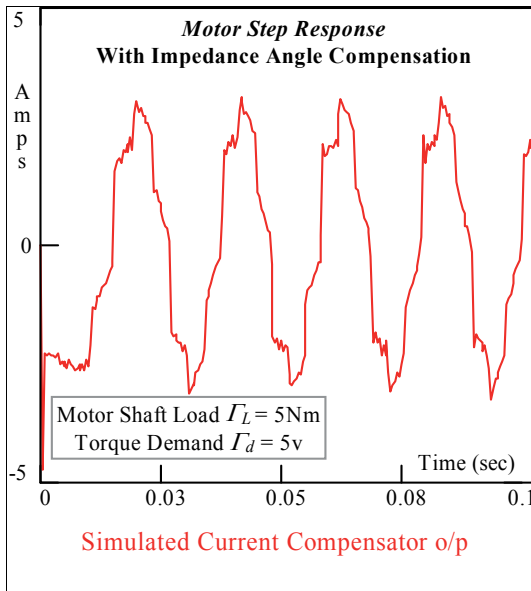


Fig. 37. Current Controller o/p

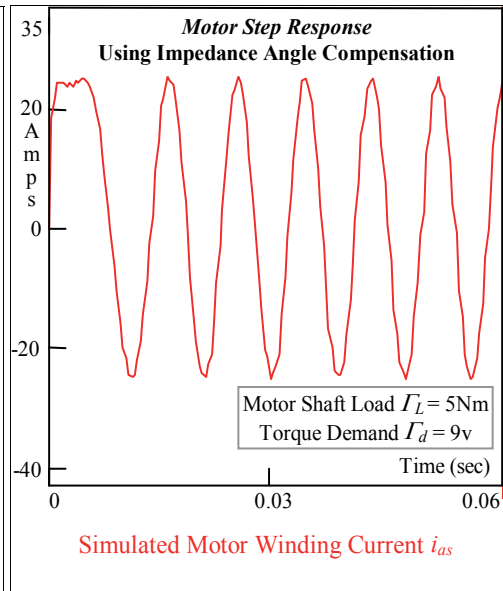


Fig. 38. Stator Winding Current Flow

These regions can also be inferred from the voltage amplitude traces in Figure 33 and 34 where V_{ej} exceeds V_z in the former case with $\Gamma_d = 5v$ and vice versa for $\Gamma_d = 9v$ in the latter diagram.

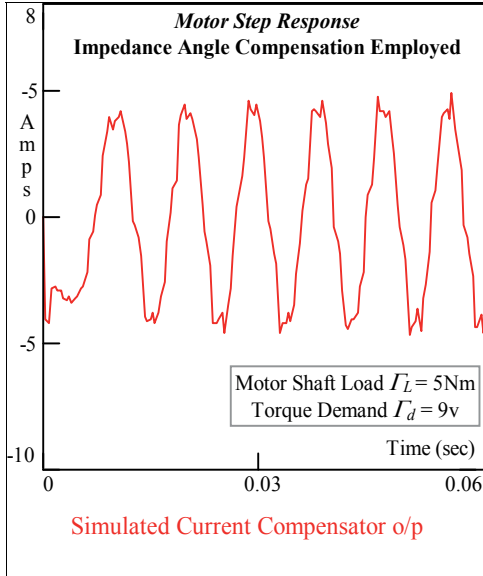


Fig. 39. Motor Current Feedback

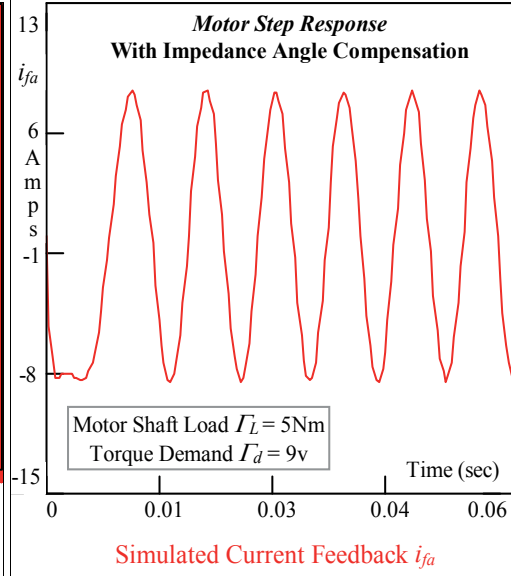


Fig. 40. Current Controller o/p

The simulated stator winding current along with current feedback response and current controller o/p are displayed in Figures 35, 36 and 37 respectively for $\Gamma_d = 5v$ without saturation related distortion in the current compensator o/p. The BLMD model simulation current characteristics corresponding $\Gamma_d = 9v$ are also shown in Figures 38, 39 and 40 without saturation effects.

4. BLMD reference model simulation in velocity control mode

In this section the BLMD reference model performance as an ASD emulator is examined and compared with experimental step response data for shaft inertial load conditions with $J_l \sim 3J_m$. Adjustable speed drive operation, with embedded inner PWM current control, is effected by closing the outer velocity loop via a two term PI term controller G_v as shown in Figures 1 and 5. The analog velocity controller shown in Figure 41, which has an inbuilt velocity offset adjustment and speed gain control adjustment K_s for the chosen BLMD system modelled here (Moog GmbH, 1989) has a transfer function

$$G_v(s) = K_e \left(K_p + \frac{K_I}{s} \right) \tag{XXII}$$

with proportional and integral compensation gain settings K_p and K_I respectively. The inclusion of this outer loop velocity compensator, in addition to the inner torque control current loop, results in a complete holistic BLMD reference model that can now be used for ASD simulation and performance evaluation in embedded applications. Proportional and

integral control is easily incorporated in C-language routine during BLMD simulation of velocity closed loop operation as a digital filter code module via (LXV) of the previous chapter using the backward Euler method in (LXIV) of the previous chapter. The resulting ASD model was exercised at low and high shaft velocities corresponding to 36.4% and 73.6% of rated motor speed n_o in Table 1 of the previous chapter and compared with experimental test data at critical internal nodes in Figure 1 for model validation and simulation accuracy.

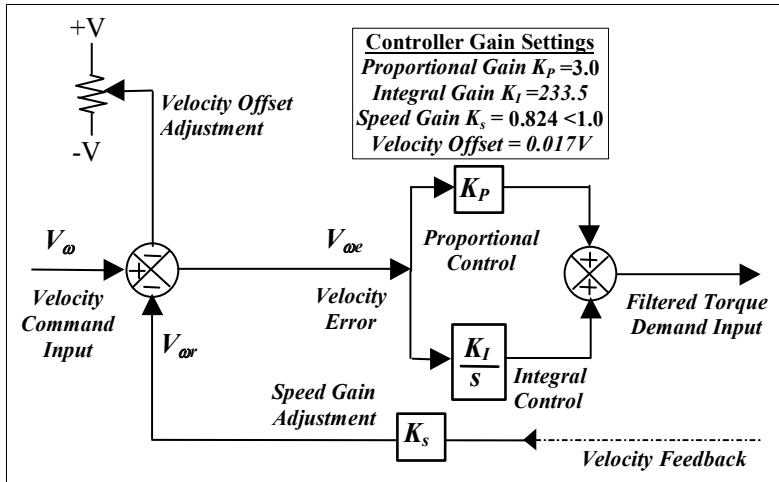


Fig. 41. BLMD Velocity Controller

The current controller G_I step response simulation traces for a velocity step command input V_{ω} of 2volts, corresponding to 36% of rated motor speed ($\sim 4000\text{rpm}$), are exhibited in Figures 42 to 44 for linear pulsewidth modulator operation.

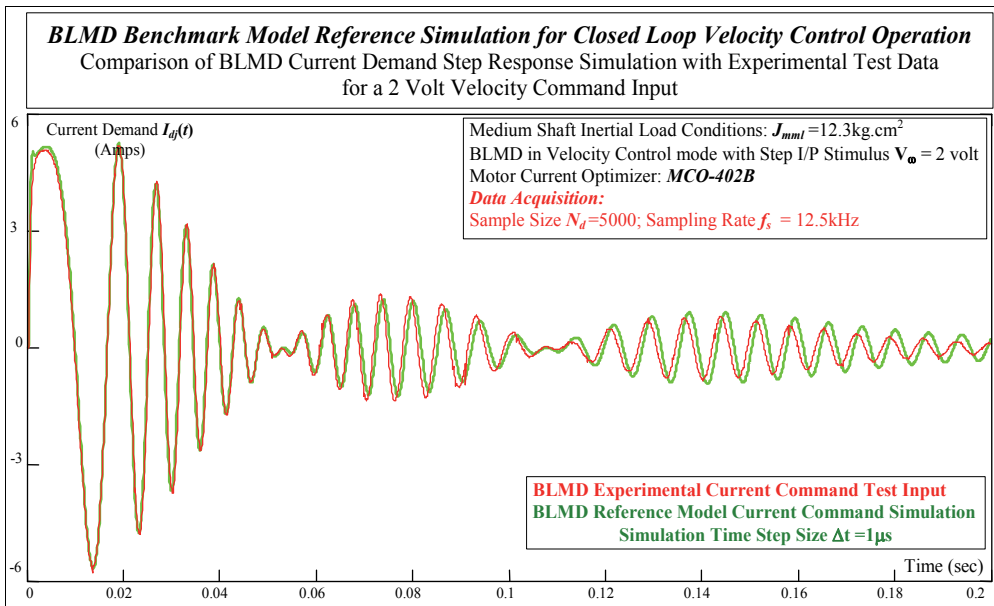


Fig. 42. ASD Reference Model Current Demand Comparison with Experimental Test Data

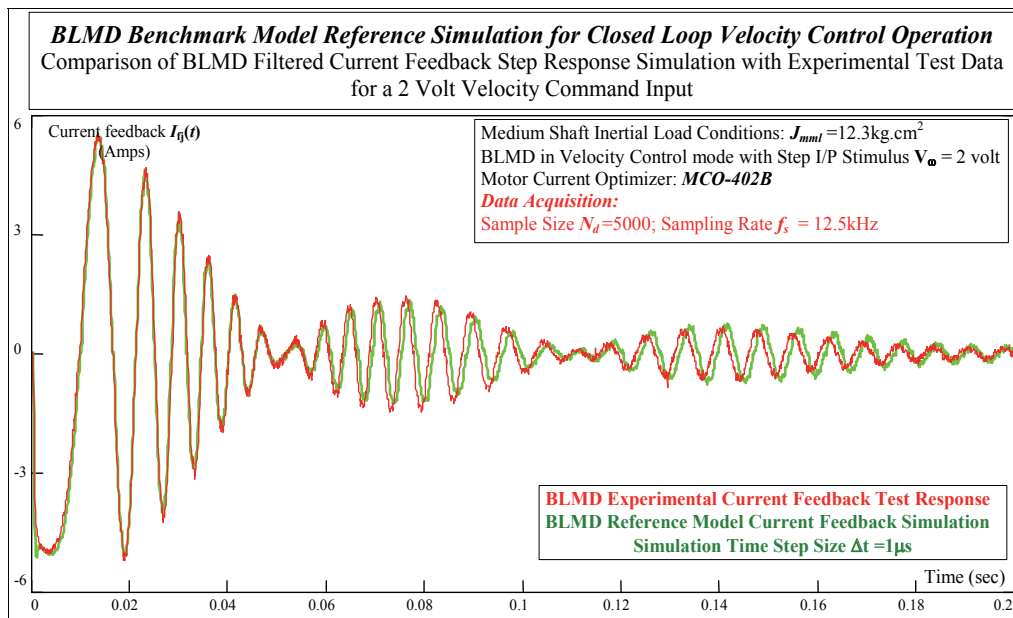


Fig. 43. ASD Model Reference Current Feedback Comparison with Experimental Test Data

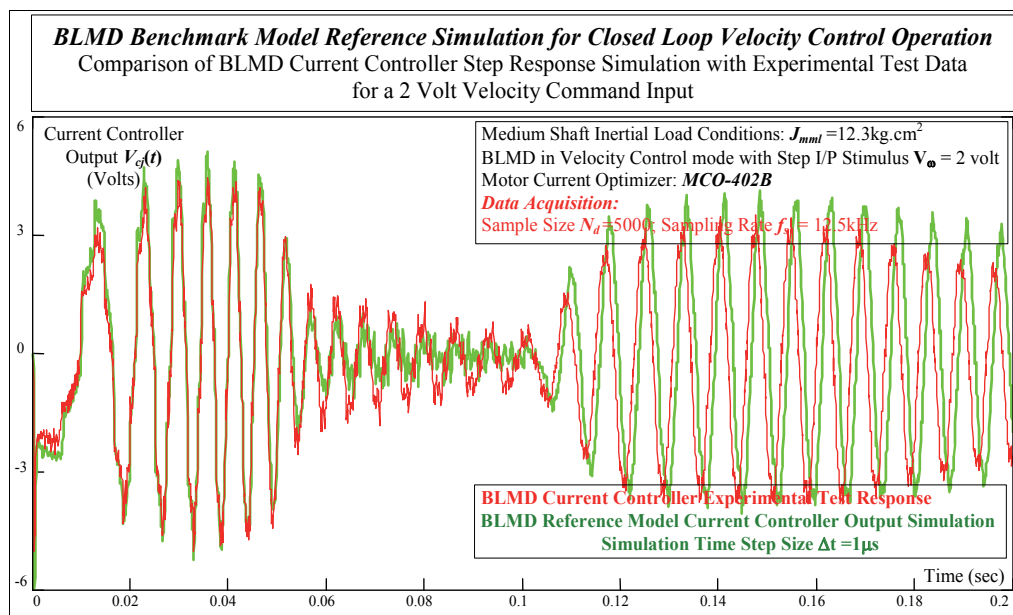


Fig. 44. ASD Model Current Controller o/p Comparison with Experimental Test Data

The accuracy of these simulation traces, which capture the essence of the velocity transient step response V_{ω} or overshoot in Figure 45, is characterized by a large waveform correlation coefficient of fit in Table V which provides a good indication of the model fidelity when matched with experimental data.

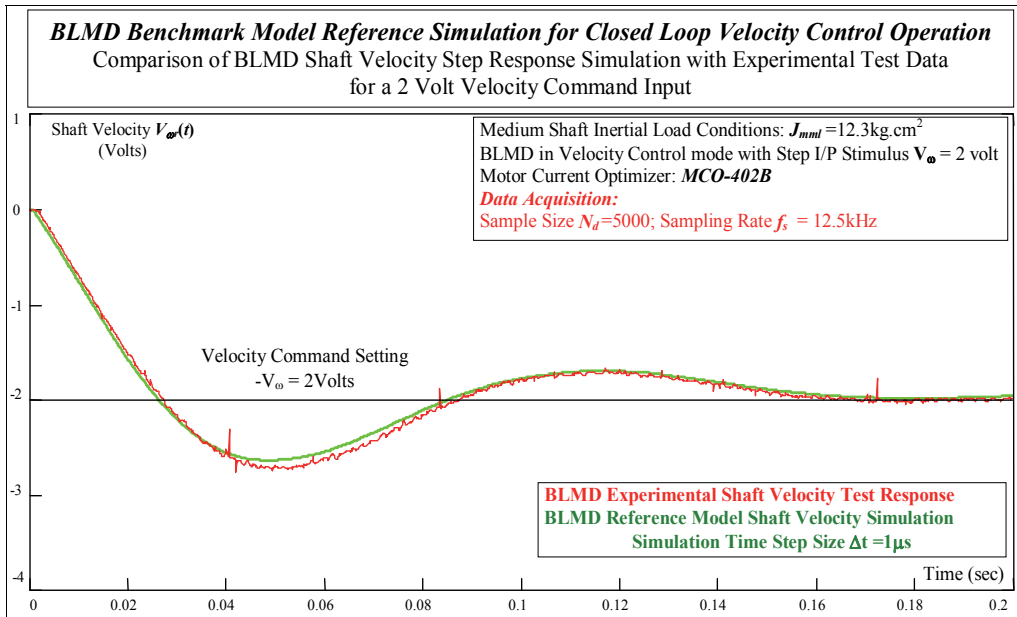


Fig. 45. ASD Model Reference Shaft Velocity Comparison with Experimental Test Data

Target Data Length $N_D = 3000$	Data Sampling Rate: 12.5kHz	BLMD Simulation Time Step: $1\mu\text{s}$
Waveform Correlation Analysis for Total Inertial Shaft Load $J_{Tot} = J_I + J_m = 12.3\text{kg}\cdot\text{cm}^2$		
ASD Waveform	Velocity Command i/p $V_{\omega} = 2\text{V}$	Velocity Command i/p $V_{\omega} = 4\text{V}$
Current Demand I_{dj}	96.8%	92.85%
Current Feedback (FC) I_{ff}	97.26%	93.27%
Current Compensator output V_{cj}	59.81%	45.46%
Motor Shaft Velocity output $V_{\omega r}$	99.8%	99.68%

Table V. ASD Model Trace Simulation Comparison with Experimental Test Data

The simulated current demand and feedback waveforms, which have high matching coefficients with test data, exhibit an amplitude modulated step response with velocity transient overshoot and ringing, before eventually setting to negligible constant amplitude traces with fixed frequency commensurate with reached shaft speed ω_r demanded ($V_{\omega r} \sim 2\text{V}$) in Figure 45.

The compensated velocity error output for 2Volts operation $V_{\omega r}$ in the BLMD network structure in Figure 5 is equivalent to the filtered torque demand Γ_{df} , as the velocity control effort $V_{\omega e}$ shown in Figure 46, applied to the inner closed loop for motor current control and BLMD output torque regulation. This optimized velocity error $V_{\omega e}$ in Figure 46 is a short duration pulse for reasons of fast BLMD shaft velocity risetime T_{res} and short setting time T_{setl} as required in high performance ASD industrial applications.

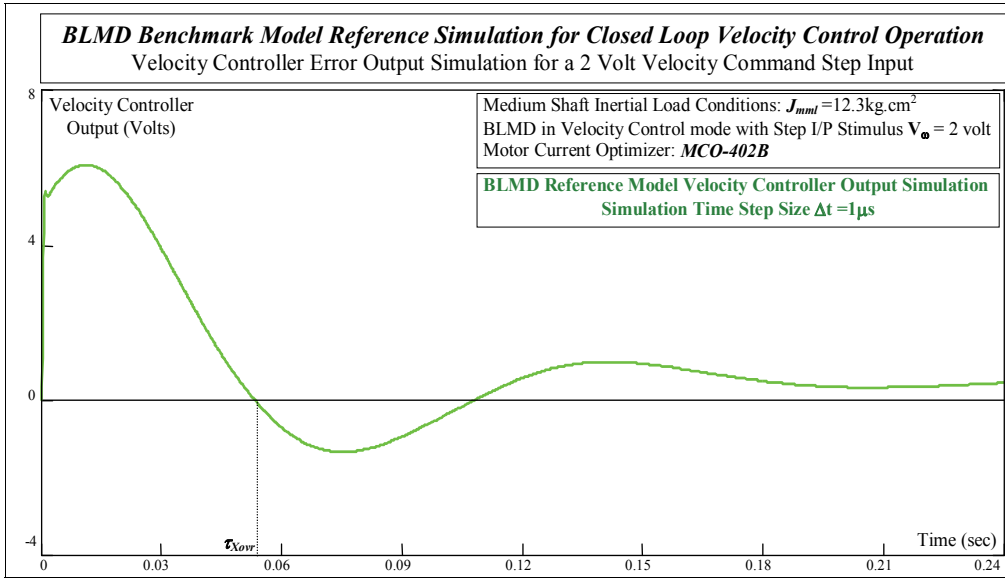


Fig. 46. ASD Reference Model Compensated Velocity Error Output

The presence of overshoot in the BLMD velocity step response in Figure 45 is due to the non-optimal tuning of the velocity controller PI parameters required to ensure stiff dynamical operation for the total drive shaft inertial load $J_{Tot} = J_m + J_l$ in question.

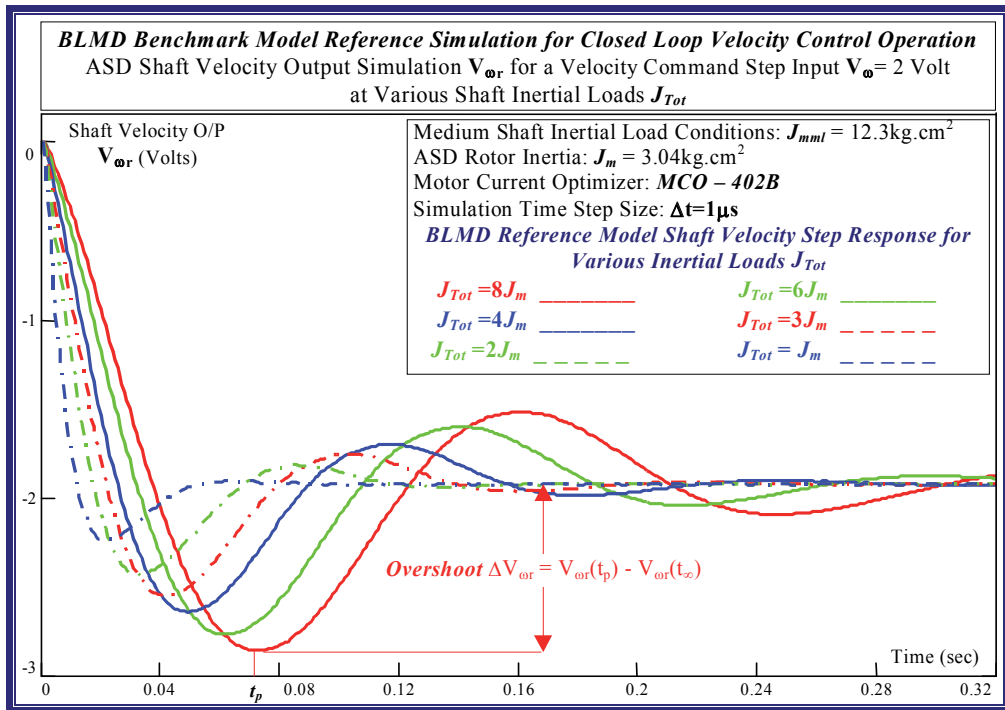


Fig. 47. ASD Shaft Velocity Step Response Variation with Rotor Inertial Load J_{Tot}

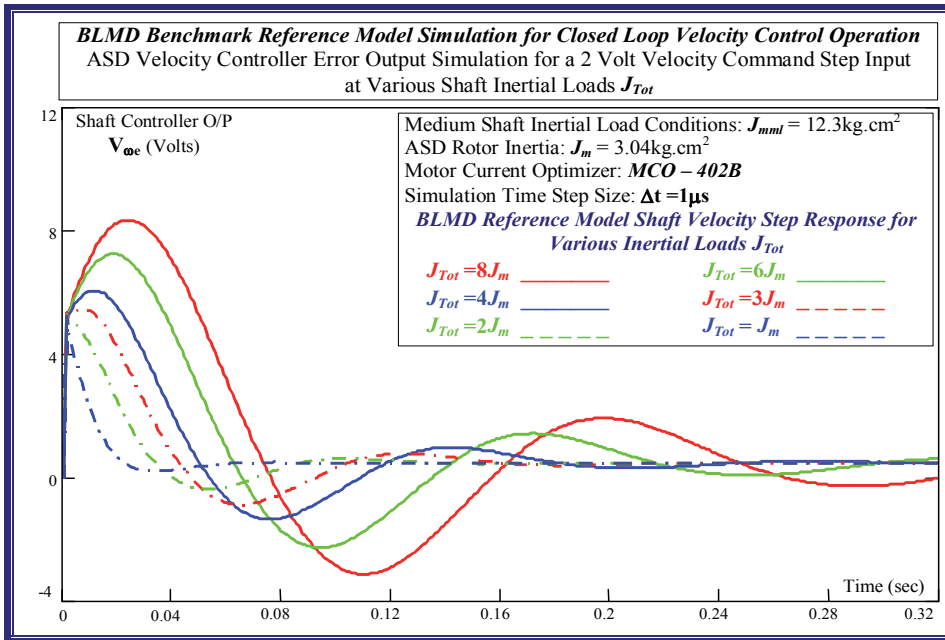


Fig. 48. Variation of ASD Velocity Control Effort with Rotor Inertial Load J_{Tot}

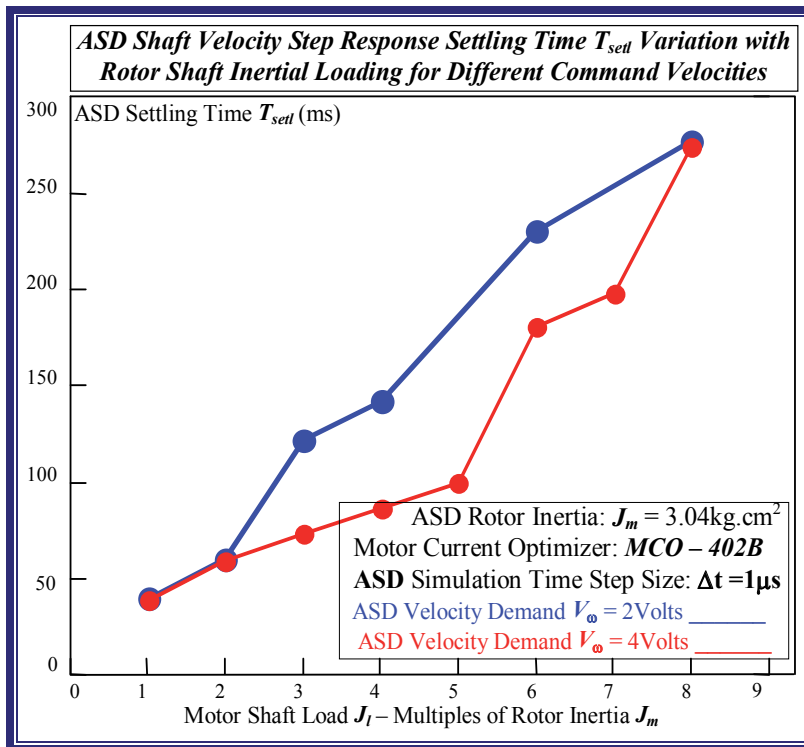


Fig. 49. Variation of ASD Settling Time with Inertial Loading

Examination of the ASD velocity step response trace simulations over a range of shaft inertial load multiples of the rotor value J_m in Figure 47 reveal that the PI parameters have been optimized only at zero load with $J_{Tot} = J_m$ for good drive dynamic transient performance with little overshoot. The effect of increased shaft inertia on the velocity control effort $V_{\omega e}$ in Figure 48, for a velocity command input of 2 volts, is a greater sustained oscillation accompanied by longer settling times T_{setl} manifested in the simulated ASD velocity step response as shown in Figure 49. This behaviour is mirrored by an increased overshoot, as defined in Figure 47, in the BLMD shaft velocity step response with shaft load inertia as shown in Figure 50.

The effect of increased load inertia on ASD dynamic performance also translates into slower rise times T_{res} as shown in Figure 51 for a non optimally tuned velocity controller.

Further ASD step response simulation and comparison with experimental measurements in Figures 52 to 55, for a 4 volts velocity command input which corresponds to 74% of rated motor speed n_0 with resulting saturated pulsewidth modulator operation in Figure 54 for the load inertia considered ($\sim 12.3\text{kg}\cdot\text{cm}^2$), reveal good BLMD model accuracy.

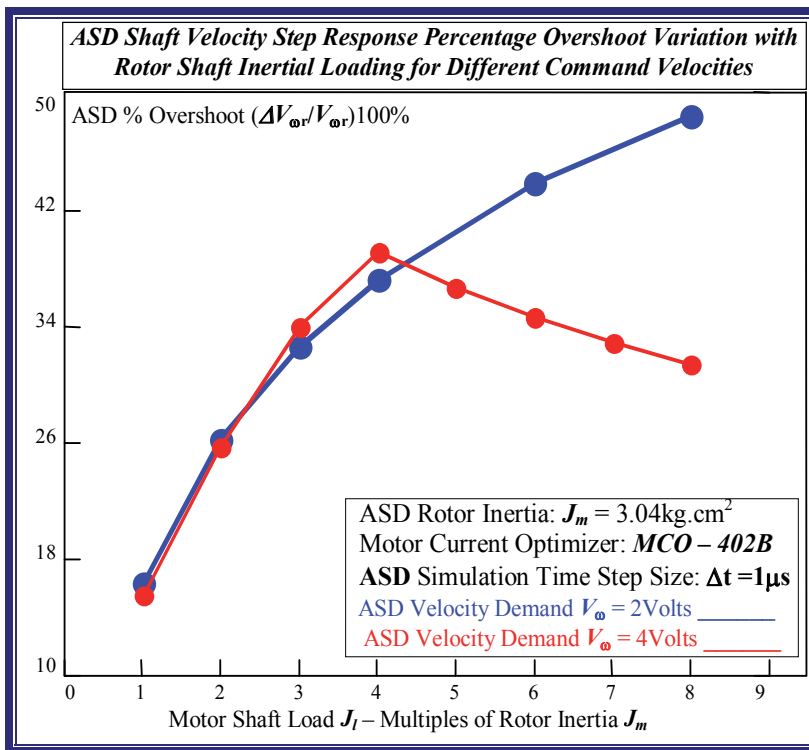


Fig. 50. Variation of ASD Shaft Velocity Overshoot with Inertial Loading

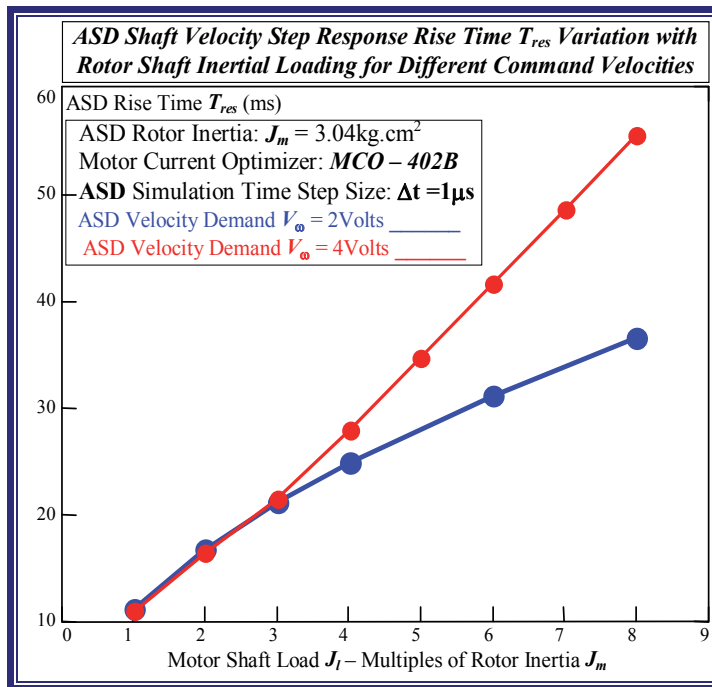


Fig. 51. Variation of ASD Velocity Response Rise Time with Load Inertia

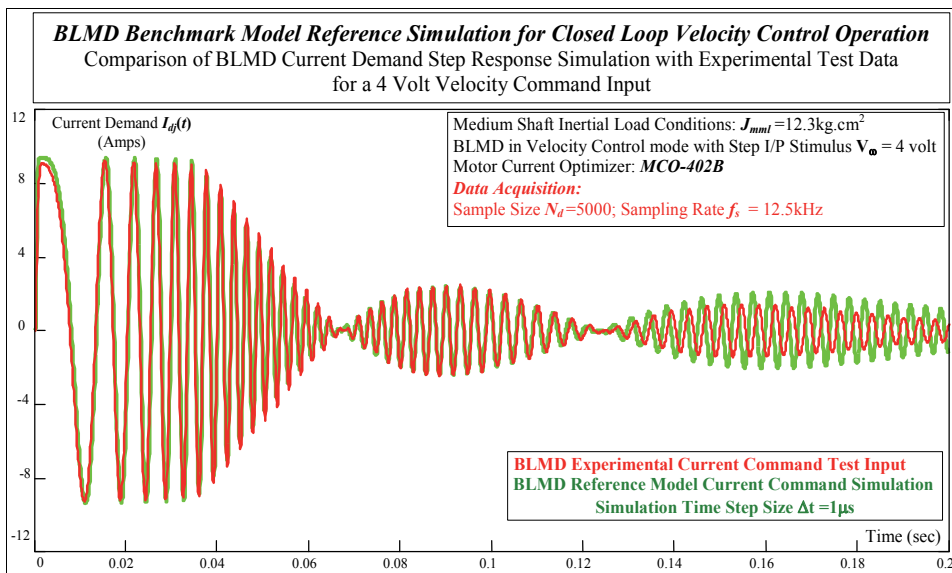


Fig. 52. BLMD Reference Model Current Demand Comparison with Experimental Test Data

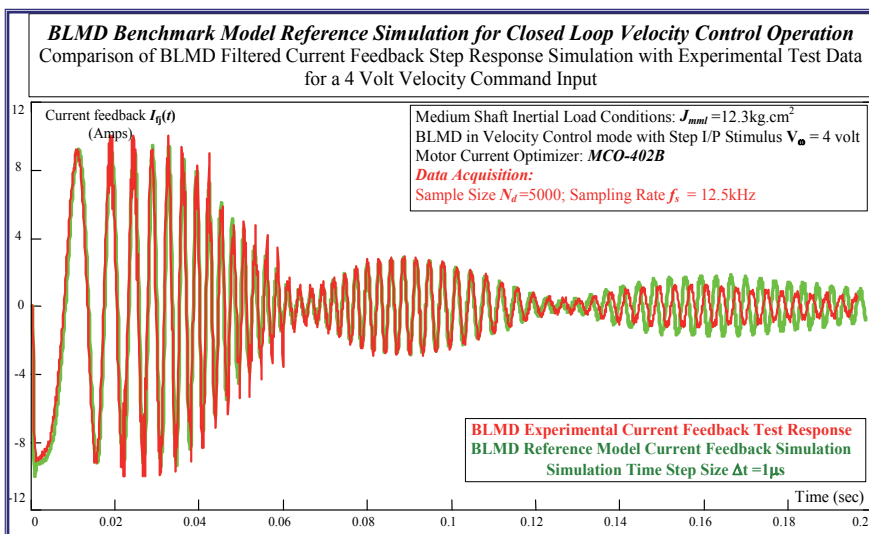


Fig. 53. BLMD Model Current Feedback Comparison with Experimental Test Data

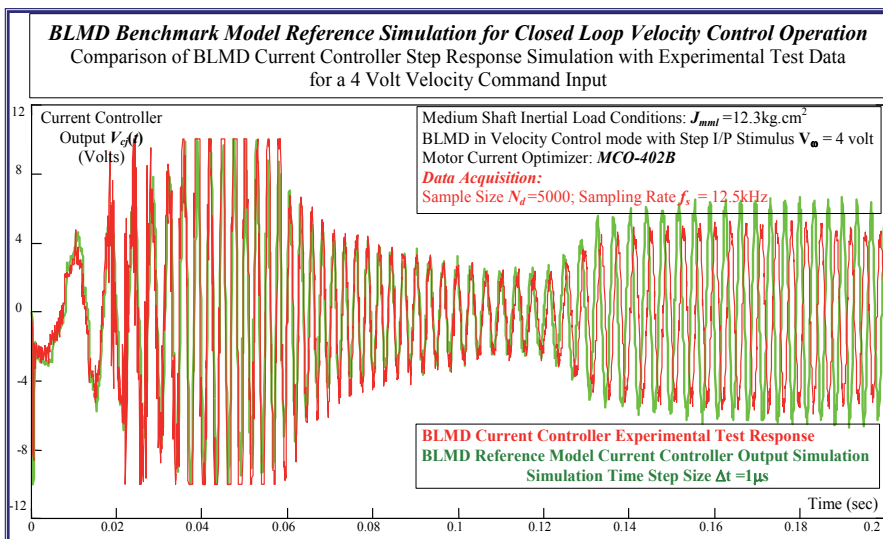


Fig. 54. BLMD Model Current Controller Output Comparison with Experimental Test Data

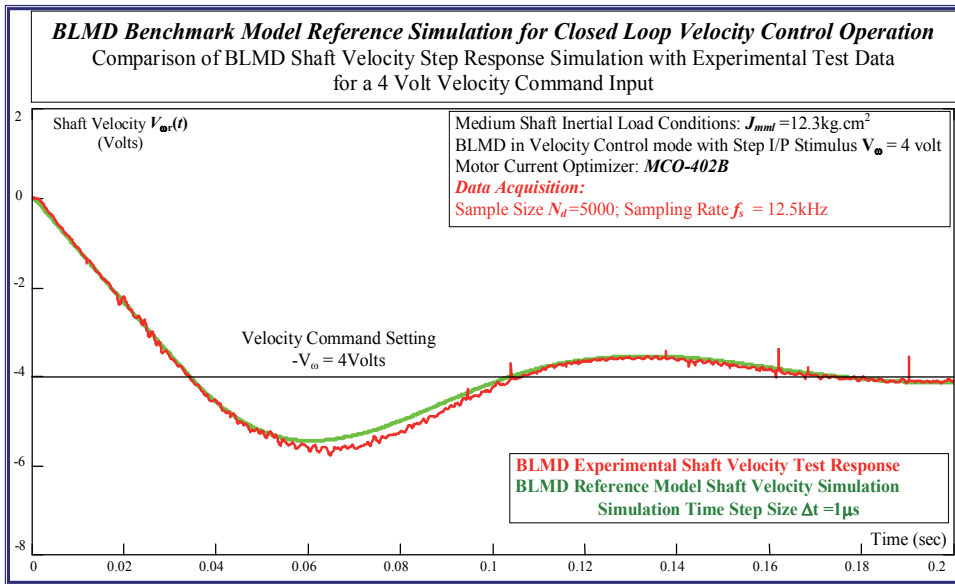


Fig. 55. BLMD Model Shaft Velocity Comparison with Experimental Test Data

The quality of ASD simulation trace match with test data is indicated by the high value of the waveform correlation coefficients given in Table V.

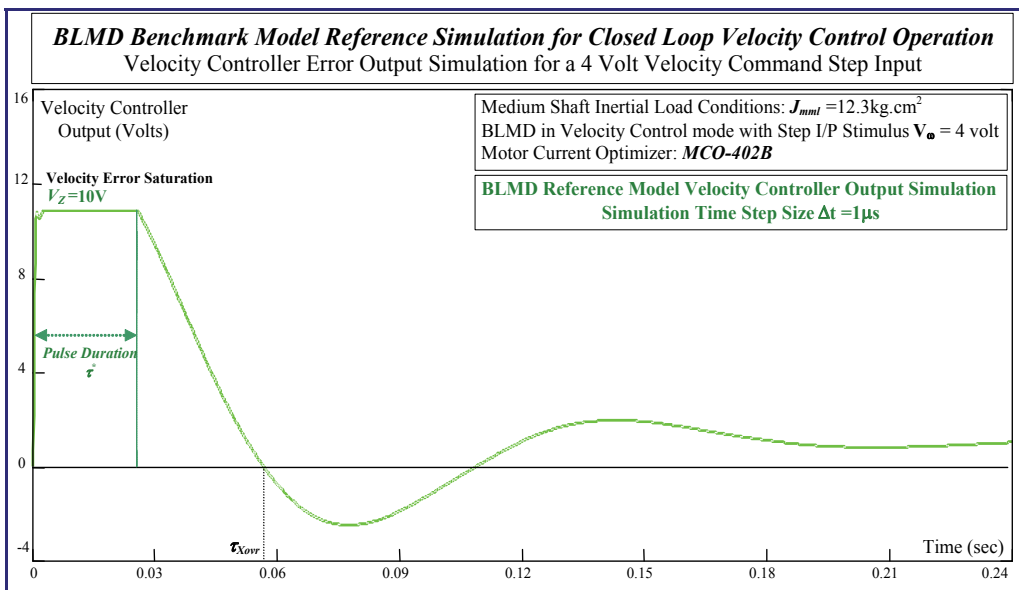


Fig. 56. BLMD Reference Model Compensated Velocity Error Output

The velocity loop derived torque command input stimulus $V_{\omega e}$ in Figure 56 has a pulse duration that is much shorter than the time constant ($\tau_{ml} \sim J_{tot}/B_m$) of the load dynamics, eventhough the pulse amplitude is of sufficient strength to force the shaft velocity to the value demanded ($V_{\omega} \sim 4$ volts). The endurance τ^* of the velocity control effort in Figure 56, associated with pronounced PWM saturation in Figure 54, is a measure of the maximum sustained EM torque necessary to accelerate the total BLMD inertial load masses to the appropriate shaft velocity demanded by the ASD command setting V_{ω} . This velocity error pulse has amplitude that is clipped to a maximum saturation limit of 10 volts at the three phase current generator input, which limits the size of the torque loop input stimulus, in the derivation of the BLMD current command signals.

Examination of the family of characteristics pertaining to velocity control effort over a range of motor shaft inertial loads in Figure 57 indicate peak saturation over long pulse intervals τ^* proportional to the inertial masses as in Figure 58 to be accelerated to the required speed $V_{\omega r}$. This velocity error saturation is absent in the characteristics displayed in Figure 48 for 2volt ASD operation and results in linear PWM operation with a BLMD acceleration torque delivery commensurate with the velocity effort.

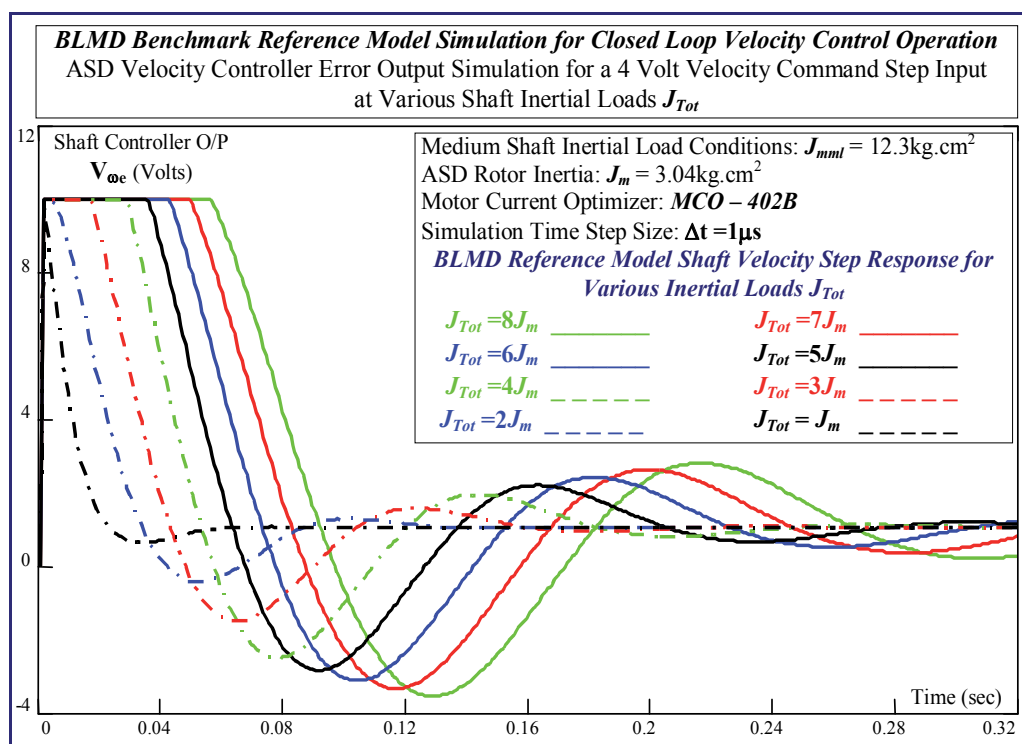


Fig. 57. Variation of Velocity Control Effort with Motor Shaft Inertial Load J_{Tot}

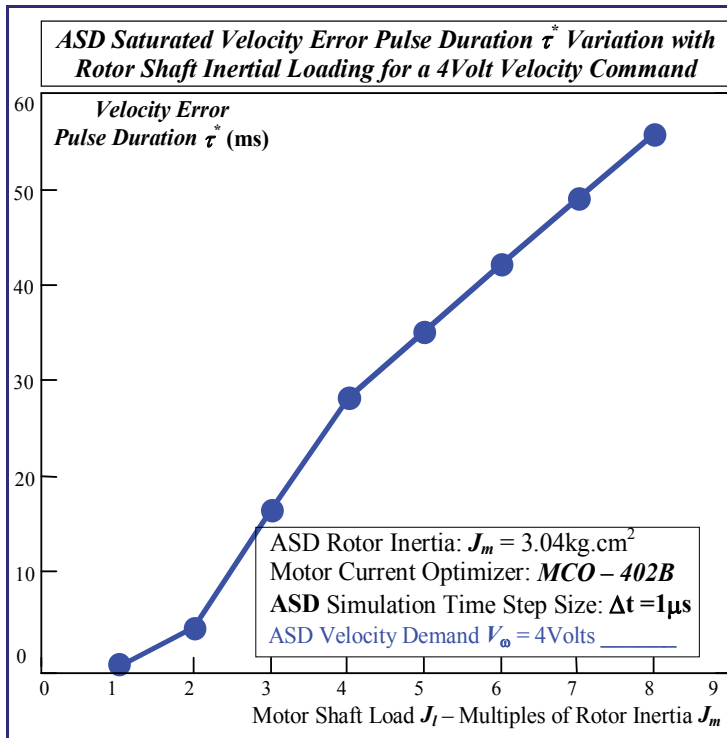


Fig. 58. Variation of Saturated Velocity Error Pulse Duration with Load Inertia

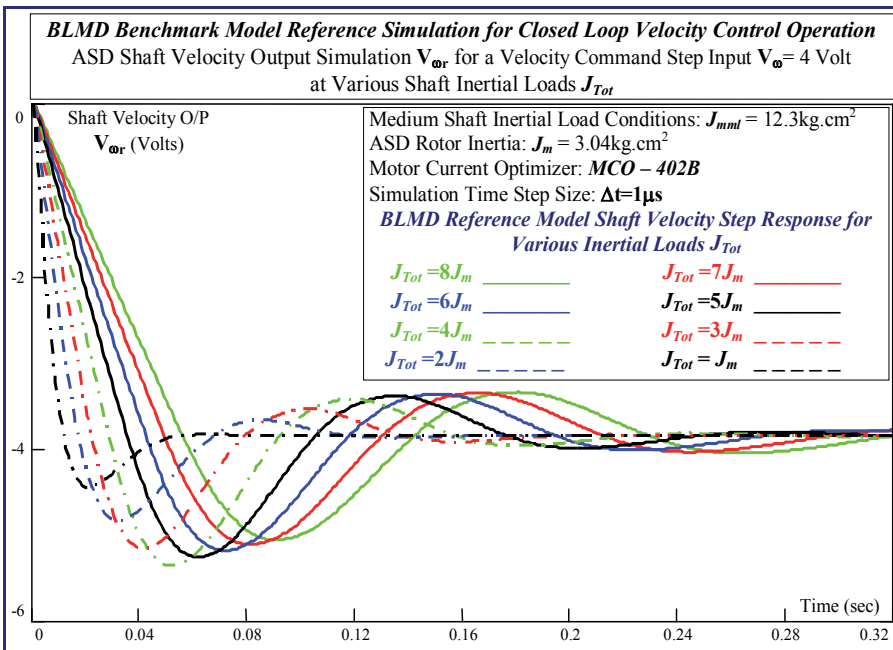


Fig. 59. ASD Velocity Step Response Variation with Inertial Shaft Load

The variation of the simulated ASD velocity step response overshoot and settling time with shaft inertial load for a 4volt velocity command corresponding to 75% of rated shaft speed in Figures 50 and 49 respectively appear to be lower than those for 2 volt ASD operation at 36% rated speed. This is due to the saturation effect of the velocity error in ASD torque generation, which limits the peak amplitude swing of the oscillatory step response on velocity overshoot in Figure 59. However the rise time is longer in this instance as indicated through ASD simulation in Figure 51 for higher velocity command input (~4V) and increases almost linearly with shaft inertial load. The bigger the load inertia being handled during normal ASD operation the greater the corrective action required in the control effort to limit shaft velocity overshoot with inertial deceleration and settling time with reached velocity experienced with a non optimal speed controller during large step changes in velocity command input.

Unless the inertial load is known apriori in this scenario the variable PI parameters cannot be optimally selected for fast risetime and minimum overshoot except through offline manual tuning approximation procedures during the installation and commissioning phase (Moog GmbH, 1988) of the embedded drive in industrial applications. Inertial load parameter extraction in new ASD industrial applications, using the BLMD reference model with step response testing in an offline identification strategy for autotuning purposes, is difficult without knowledge of the initial PI settings of the velocity controller for zero load conditions before drive hookup to the embedded application. In this instance the procedure of accurate inertia parameter extraction using the ASD model in any identification strategy is complicated by the control action of outer velocity loop closure on the wideband inner torque loop when the variable PI settings are unknown. The ASD parameter identification problem in this case has to incorporate evaluation of the existing PI term settings in addition to the inertial load parameter in the new application in order to optimally design the embedded drive velocity controller. However if the drive is configured in torque control mode, thereby eliminating the velocity controller during step response testing in the commissioning phase, inertial load parameters are more amenable to extraction using low torque command input stimuli (<1V) for linear BLMD behaviour with small perturbation of the drive dynamics. The identification problem in this case has to focus only on the extraction of inertial load parameter J_{Tot} and also on the friction coefficient B_m if required.

5. Conclusions

Further BLMD simulation for various load torque settings, based on model confidence, yield results that compare favourably with those obtained from theoretical considerations using catalogued data for the actual drive concerned. The introduction of stator impedance angle compensation at high shaft speed results in improved motor power factor and better BLMD steady state performance. This is verified theoretically and illustrated through model simulation. Detailed BLMD simulation, configuration as an ASD with velocity feedback, is provided at internal observation nodes and checked against measured data at low and high command speed settings for confirmation of model accuracy and validation purposes.

6. Acknowledgment

The author wishes to acknowledge

- i. Eolas - The Irish Science and Technology Agency - for research funding.
- ii. Moog Ireland Ltd for brushless motor drive equipment for research purposes.

7. References

- Balabanian, N. & Bickart, T.A.; *Electrical Network Theory*, 1969, J.Wiley & Sons
- Franklin, G.F. & Powell, J.D.; *Digital Control Of Dynamic Systems*, Addison Wesley, 1980
- Guinee, R.A.; (2003). *Modelling, Simulation, and Parameter Identification of a Permanent Magnet Brushless Motor Drive System*, Ph. D. Thesis, NUI – University College Cork.
- Guinee, R.A. & Lyden, C.; (1999). Accurate Modelling And Simulation Of A DC Brushless Motor Drive System For High Performance Industrial Applications, IEEE ISCAS'99 - IEEE International Symposium on Circuits and Systems, May/June 1999, Orlando, Florida
- Moog GmbH; (1988). *Moog Brushless Technology:Brushless Servodrives User Manual*, D310.01.03 En/De/It 01.88, Moog GmbH, D-7030 Böblingen, Germany.
- Moog GmbH; (1989). *Moog Brushless Technology User Manual:D31X-XXX Motors,T158-01X Controllers,T157-001 Power Supply, , D-7030 Böblingen.*



Edited by Seref Soylu

In this book, modeling and simulation of electric vehicles and their components have been emphasized chapter by chapter with valuable contribution of many researchers who work on both technical and regulatory sides of the field. Mathematical models for electrical vehicles and their components were introduced and merged together to make this book a guide for industry, academia and policy makers.

Photo by Smoczyslaw / iStock

IntechOpen

